The Evolution of Matter

From the Big Bang to the Present Day

I. N. Tolstikhin and J. D. Kramers

CAMBRIDGE

CAMBRIDGE www.cambridge.org/9780521866477

This page intentionally left blank

THE EVOLUTION OF MATTER

This book explains how matter in the Universe developed from the primordial production of light elements within minutes of the Big Bang, and from subsequent stellar processes that continue to create heavier elements at the expense of lighter ones. It also describes the evolution of interstellar matter and its differentiation during the accretion of the planets and the history of the Earth.

Much emphasis is placed on isotopic data. Variations in the stable isotope compositions of many elements help us to understand the underlying chemical and physical processes of differentiation. Radioactive isotopes, and their radiogenic daughter isotopes, allow the time and duration of numerous natural processes to be constrained. Unlike many books on geochemistry, this volume follows the chemical history of matter from the very beginning to the present, demonstrating connections in space and time. It provides solid links from cosmochemistry to the geochemistry of the Earth, in the context of astrophysical and planetary processes.

The book presents comprehensive descriptions of the various isotope systematics and fractionation processes occurring naturally in the Universe, using simple equations and helpful tables of data. With a glossary of terms and over 900 references, the text is accessible to readers from a variety of disciplines, whilst providing a guide to more detailed and advanced resources. This volume is should prove to be a valuable reference for researchers and advanced students studying the chemical evolution of the Earth, the solar system and the wider Universe.

IGOR TOLSTIKHIN was awarded a Ph.D. in geochemistry from the St Petersburg Mining Institute in 1966 and a D.Sc. from the Vernadsky Institute, Moscow, in 1975. He is currently a Senior Research Scientist in the Space Research Institute and the Geological Institute at Kola Scientific Center, both of which are part of the Russian Academy of Sciences, where his research has encompassed noble gases, radiogenic isotope geochemistry, isotope hydrology and geochemical modelling. His more recent contributions include a chemical Earth model with a wholly convective mantle.

JAN KRAMERS was awarded a Ph.D. from the University of Berne in Switzerland in 1973 and went on to work in South Africa, the UK and Zimbabwe before returning to the University of Berne, where he is currently Professor of Geochemistry in the Institute of Geological Sciences. Professor Kramers' research interests include mantle geochemistry (kimberlites, diamonds), the origin of Archaean continental crust, global radiogenic isotope systematics, the early evolution of the Earth's atmosphere and, more recently, palaeoclimate research using the speleothem archive.

THE EVOLUTION OF MATTER

From the Big Bang to the Present Day Earth

IGOR TOLSTIKHIN
Kola Scientific Centre, Russian Academy of Sciences

JAN KRAMERS
Institute of Geological Sciences, University of Bern

CAMBRIDGE
UNIVERSITY PRESS

CAMBRIDGE UNIVERSITY PRESS
Cambridge, New York, Melbourne, Madrid, Cape Town, Singapore, São Paulo

Cambridge University Press
The Edinburgh Building, Cambridge CB2 8RU, UK
Published in the United States of America by Cambridge University Press, New York

www.cambridge.org
Information on this title: www.cambridge.org/9780521866477

First published in print format 2008

ISBN-13 978-0-511-40891-5 eBook (EBL)

ISBN-13 978-0-521-86647-7 hardback

Contents

Introduction *page* 1

Part I The elements 5

1 Isotopes: weights and abundances 7
- 1.1 Introduction: nuclei and their behaviour 7
- 1.2 Atomic nuclei and binding energy, with some predictions on isotope abundances 10
- 1.3 Summary 17

2 Introduction to the Universe: the baryonic matter 19

3 Element and isotope abundances: reference collection 24
- 3.1 Hydrogen and helium and their special significance 24
- 3.2 Metal-poor stars: the most ancient matter of the Galaxy 25
- 3.3 Presolar grains 26
- 3.4 The solar system element and isotope abundances 31
- 3.5 Summary 42

4 Cosmological nucleosynthesis: production of H and He 44
- 4.1 The expanding Universe and the Big Bang hypothesis 44
- 4.2 Big Bang nucleosynthesis (BBN) 44
- 4.3 The age of the Universe 46
- 4.4 Summary 49

5 Stellar nucleosynthesis: lower-mass stars and the s-process 52
- 5.1 Introduction 52
- 5.2 Formation of stars 52
- 5.3 Hydrogen and He burning and the evolution of a low-mass star 56
- 5.4 Slow nucleosynthesis (s-process) 59
- 5.5 Summary 67

6 Stellar nucleosynthesis: r- and associated processes 68
6.1 Introduction to rapid nucleosynthesis (r-process): what does "rapid" mean? 68
6.2 Evolution of massive stars 69
6.3 Core-collapse supernovae (SNe II) and rapid nucleosynthesis 70
6.4 SNe Ia: nucleosynthesis and luminosity 76
6.5 Summary 77
7 Timing of stellar nucleosynthesis 79
7.1 Cosmochronology from long-lived radioactive elements 79
7.2 The uranium isotopes: age and evolution of stellar nucleosynthesis 80
7.3 The age of stellar clusters: luminosity–temperature relationships 81
7.4 Summary 82
8 Chemical evolution of the Galaxy 83
8.1 Introduction: processes governing galactic chemical evolution 83
8.2 Milky Way evolution 84
8.3 The sources of short-lived radionuclides 91
8.4 Milky Way evolution: models and results 94
8.5 Summary 97
Part II Early solar system: nebula formation, evolution and lifetime 99
9 Introduction to the solar nebula 101
10 The primary solar system objects and related processes 106
10.1 Solar nebula: initial composition and early development 106
10.2 Calcium–aluminium inclusions 108
10.3 An "absolute" age for the earliest solar system objects 117
10.4 Short-lived nuclides: further evidence for early CAI formation 120
10.5 Oxygen isotopes in nebula objects: the CAI array 128
10.6 CAI formation: concluding remarks 131
11 Chondritic meteorites 134
11.1 Introduction to chondritic meteorites: compositions and taxonomy 134
11.2 Chondrules and matrix 137
11.3 Metamorphism and equilibration in chondrites 142

11.4 Highly volatile elements: hydrogen, carbon and nitrogen 144
11.5 Highly volatile elements: noble gases 146
11.6 Chondritic meteorites: time scales 152
11.7 Chondritic meteorites: formation processes 158
11.8 Summary: chondritic meteorites and early evolution of the solar nebula 161
12 Highly processed meteorites 163
12.1 Introduction: non-chondritic meteorites and their relationships 163
12.2 Magmatic fractionation and trace-element partitioning 164
12.3 Major and trace elements in non-chondritic meteorites 168
12.4 The chronology of planetesimal processing 175
12.5 Formation of non-chondritic stony and iron meteorites: processes and time scales 186
12.6 Summary: late nebular processes as recorded by non-chondritic meteorites 189
13 A summary of early solar system chronology 191
Part III Accretion of the Earth 197
14 Introduction to the planetary system, Earth and Moon 199
14.1 The solar system: the planets and satellites 199
14.2 A first look at the post-accretion Earth and Moon 201
15 Introduction to planetary accretion 208
15.1 Orderly growth 208
15.2 Runaway growth 209
15.3 Planet formation 210
16 Earth accretion: the giant impact(s) 211
16.1 Giant impacts: impactor mass and energy deposited 211
16.2 The post-impact Earth model 212
17 The post-accretion silicate Earth: comparison with meteorites 214
17.1 Introduction: principal reservoirs of the post-accretion Earth 214
17.2 The silicate Earth: ways of reconstruction 215
17.3 Major elements 216
17.4 Trace elements 218
17.5 Concept of a terrestrial magma ocean: the role of convection 225
17.6 Summary 230

18 Core segregation 231
18.1 Introduction: siderophile elements in the silicate mantle and light elements in the core 231
18.2 Successful core-formation models 236
18.3 Time constraints on terrestrial core segregation 240
19 Heavy "crust" on the top of the core 243
19.1 Introduction: geochemical indicators for the occurrence of an early-formed apparently isolated reservoir 243
19.2 Present-day status: the core–mantle transition zone 245
19.3 Early formation of the core–mantle transition 246
19.4 Summary: geochemical importance of the core–mantle transition zone 248
20 The early atmo-hydrosphere 250
20.1 Introduction 250
20.2 Noble-gas inventories and constraints on atmosphere evolution 251
20.3 Mechanisms for the loss of volatile elements from the planetary atmospheres 258
20.4 Major volatile species: inventories and sources 261
20.5 Summary 266
21 Light from the Moon . . . 267
21.1 Introduction 267
21.2 Bulk composition and formation of the Moon 268
21.3 Early lunar crust and mantle 271
21.4 Early evolution of the lunar mantle and crust 281
21.5 Summary 286
Part IV Global evolution of the Earth 289
22 First look at the Earth 291
23 The plate-tectonic concept: some phenomenology 293
23.1 Major geotectonic units: the plates 293
23.2 Plate motions: processes on the plate boundaries 294
23.3 Intraplate magmatism: plumes 297
23.4 The moving forces of plate tectonics 298
23.5 Summary: the major terrestrial factories reworking matter 300
24 Ocean-ridge and island magmatism 301
24.1 Introduction to anhydrous mantle melting 301
24.2 Tholeiitic basalts: major products of ocean-ridge magmatism 303
24.3 Mid-ocean ridge magmatism: evidence from stable trace elements 305

24.4 Mid-ocean ridge magmatism: evidence from radioactive trace elements 310
24.5 Main features of a MORB melting model: evidence from trace elements and radioactive nuclides 314
24.6 Features specific to ocean-island basaltic magmatism 317
24.7 Summary 319
25 Subduction and island-arc magmatism 321
25.1 Introduction: subduction, associated processes and the crucial role of water 321
25.2 Major-element chemistry of arc magmatic rocks 323
25.3 Trace-element chemistry of primitive arc volcanics 324
25.4 Development of slab rocks during subduction: introduction to metamorphism 331
25.5 Metamorphism in the slab: fluid production and release 335
25.6 Melting of subducting slab: supercritical liquids 338
25.7 Melting in the mantle wedge 339
25.8 Summary 341
26 Composition of the continental crust: magmatic, metamorphic and sedimentary processes 344
26.1 Introduction: the continental crust 344
26.2 The upper continental crust: magmatic rocks 346
26.3 Sedimentary rocks and processes related to them 359
26.4 The lower continental crust: complement to the upper? 365
26.5 The crustal age distribution function 368
26.6 The mean composition of crustal reservoirs 371
26.7 Processes governing crustal mass and composition 372
26.8 Summary 380
27 Isotopic records of the evolution of Earth's accessible reservoirs 382
27.1 Introduction 382
27.2 The Lu–Hf, Sm–Nd, Rb–Sr and Th–U–Pb isotopic systematics of the mantle 385
27.3 Sources of OIB magmatism 391
27.4 Light rare gases in the mantle 394
27.5 Mantle xenology 399
27.6 Isotopes of Sr, Nd and Pb in the continental crust 403
27.7 Relationships between the Sm–Nd and Lu-Hf isotope families 409
27.8 Isotopic traces from earliest Earth history and evolutionary trends 413
27.9 Evolutionary trends recorded by sedimentary rocks 418
27.10 Summary 425

28 Geochemical Earth model 427
28.1 Introduction to geochemical modelling 427
28.2 Multireservoir Earth model 428
28.3 Results: isotope geochemical constraints on Earth's evolution 432
28.4 Summary 440
References 442
Glossary 489
Abbreviations 507
Meteorites, rocks and minerals 510
Index 517

Introduction

This book is a cross between a textbook and a monograph, and it was started as an attempt to link depth with breadth in cosmo- and geochemistry. The need for this becomes obvious when one sees the two opposing trends in this science. On the one hand, much excellent research goes into great depth in a relatively narrow field, unnoticed except by specialists and, on the other hand, wide-ranging textbooks capture the imagination of a broader audience but cannot do justice to the actual data-gathering and interpretation. Thus, if one is interested in cosmochemistry, or the solar system or planetary formation and evolution, one can readily find a number of specific, well-written, textbooks. However, those who want to examine critically how these issues are related, and who would like to see the "big picture" and realize how it came to be, have to dive into the often rather complicated original literature.

As is the case with most branches of science, cosmochemistry and geochemistry have made huge leaps forward in the last 20 years but have become more fragmented. A bewildering amount of isotopic evidence has amassed that links Earth's history to that of the early solar system and, in turn, early solar system history to the evolution of the Galaxy and of the Universe itself. The many papers in which these data have appeared necessarily address specialized issues and although the connection to a grand unifying theme is normally made clear, there is mostly no direct contact with other specialized work that relates to the theme from another niche. This means that possible contradictions, but also cases where different angles of research have strengthened the results, may go unnoticed.

This fragmentation is not necessary, and we have felt that a "history book" describing how matter could have evolved from primordial nucleosynthesis through stellar processes, the formation of a solar nebula and planetary evolution could actually present and discuss large amounts of original data without becoming fragmented and losing sight of the big picture itself.

In pursuing this aim, we have placed much emphasis on isotope data. One reason for this is that relative isotope abundances are fingerprints of the processes in

which isotopes were produced or their ratios modified. Isotope compositions of some elements serve as "stellar-thermometers" or "stellar-dosimeters" highlighting intimate features of the birth of the elements. In many cases the relationships between parent and daughter isotopes allow the time of events to be constrained, which is of prime importance if the subject is evolution. On the other hand, in most cases isotope abundance ratios have been much less disturbed than element abundances. They are therefore robust tracers of the early events that set their values. In cases where isotope abundance ratios are fractionated, their behaviour follows simple laws of nature and the resulting variations of isotope compositions help us to understand the underlying chemical and physical processes.

Another reason is that there is simply a very large amount of high-quality isotope data in the literature that combines to tell fascinating and convincing stories but is not sufficiently taken note of in textbooks. The reason for this may be that isotope-ratio interpretation is considered to be difficult and to require involved arguments. This is, however, mostly not the case. Precisely because of their lack of chemical fractionation, isotope data are the easiest geochemical results to interpret. This is why we have chosen a mainly (but not exclusively) isotopic perspective for this book.

This book is aimed at a varied readership: lecturers preparing courses for advanced undergraduate classes; graduate students; young scientists (in any branch of cosmo- or geochemistry) requiring a background in global geochemistry, particularly in its isotopic aspects; and a broader audience interested in examining the basis for our knowledge of the matter from which the Earth was built and how it formed and evolved. The book does not require a specialized knowledge of astrophysics, geology, geochemistry or isotopes: a general science background is probably enough. We have attempted to provide a coherent picture of the history of matter through time, as seen from the perspective of first astrophysics, then solar system origin and early history, including the formation of the Earth and Moon, and finally through geological time on Earth. In this effort at a continuum, we have tried to show at all stages in Earth's evolution how the particular chemical budget, or setup, that we live in, came about. Subjects that are not dealt with, as they are very well covered in many current textbooks, are the question of the origin of life or when this happened, the evolution of life, biogeochemistry and present-day environmental developments.

The book consists of four parts. Broadly, Part I deals with the principles of nucleosynthesis, the evolution of stars and episodes in which they are particularly nucleosynthetically active and the manner in which matter is conserved in interstellar space so that it can be inherited by nascent stars and solar systems. Isotopes play a large part here, first as actors and products in nucleosynthetic processes (so that their abundance ratios act as stellar thermometers and flux indicators), then (in

the case of short-lived radioactive isotopes) as the illuminators of clouds of supernova ejecta, providing information on their nucleosynthetic processes and finally (in the case of long-lived radioactive isotopes) as clocks for the time scale of nucleosynthesis. Stellar processes also provide an interesting and unusual perspective for isotope geochemists and cosmochemists in that most decay "constants" are not constant in stellar environments. Light-stable-isotope variations in presolar grains are also covered in this chapter, as these data provide an important foundation for improved models of the nucleosynthetic processes that produced them.

In Part II the early evolution of the solar system from a disk of gas and dust to planetesimals such as chondrite and achondrite parent bodies, via coagulation, evaporation, recondensation and melting processes, is described using the available data and by modelling. In this part of the book the systematics of stable-isotope fractionation and their relevance to sources of matter and early solar system processes are described. Further, chronological techniques using both the long-lived decay systems (such as U–Pb) yielding absolute ages and the short-lived decay systems (such as Al–Mg), yielding precise relative time spans are dealt with in as much detail as is necessary. The incredibly well-constrained time scale of processes in the first 10 million years of the solar system and some minor contradictions in it are discussed.

Part III of the book concerns planetary accretion. This is first described in general terms and then specifically applied to the Earth–Moon system. The processes associated with planetary accretion, such as core formation, and the apparent paradoxes of the siderophile-element concentrations are considered together with the time scale derived from Hf–W isotope systematics. Also included are the results of new modelling of the core-formation process and the concept of a deep-seated reservoir in the Earth from which primitive noble gases still emanate today. The formation of the Moon by a giant impact is discussed along with the contrast between the ensuing terrestrial mantle-wide magma ocean, which apparently did not fractionate silicates, and the lunar magma ocean, which did. Lunar geochemical and isotope data are tied in with the terrestrial data to provide a consistent picture of the earliest history of our planet. A discussion of the constraints on the earliest atmosphere and its extensive loss is also included. This draws mainly on noble-gas abundance data, including radiogenic and fissiogenic Xe, but also considers the major atmospheric components.

In Part IV, the present-day Earth dynamics and geochemistry are reviewed, as well as the available isotopic and geochemical data base that constitutes "hard data" on the Earth's history. These include, for instance, Hf-isotope data on the oldest terrestrial (detrital) zircons and their interpretation. Present-day data yield important mass-balance considerations relating to mantle dynamics, and the total data set provides constraints for models of the geochemical evolution of the Earth's

crust and mantle, which are described in some detail. One important question here is whether the mantle convects as a whole entity or in two layers, and another concerns the growth of the amount of continental crust and its partial recycling into the mantle through geological time. In setting up and discussing such models it is a great advantage to have the conclusions of the previous chapters immediately to hand, as these determine the initial geochemical and isotope compositions for the Earth. Further, it is a requirement for successful scenarios to satisfy the principal geochemical and isotope constraints (the Rb–Sr, Sm–Nd, Lu–Hf, U–Th–Pb and K–Ar systematics and the noble-gase abundances); one cannot be eclectic. The interaction of the different reservoirs of planet Earth with one another appears to be essential in all successful models.

Finally a world picture emerges that, in terms of chemistry and isotope compositions, traces its roots back to the very origins of the Universe. In this picture the major processes are mapped out with reasonable confidence but major problems are also highlighted.

We have made frequent use of equations in the text to illustrate points quantitatively. Equations have the advantage of not being vague. However, they usually need explaining and we have padded them in text to cover sharp edges. Systematics such as trace-element partitioning, radiogenic-isotope chronology and geochemistry and stable-isotope fractionation are explained in dedicated sections that are slotted in where they are first needed in the narrative; they are thus distributed over the book but are referred to where necessary and can be readily located using the table of contents.

Further, a comprehensive glossary is included. We have tried to avoid creating new abbreviations; it may be that "SOS" for the solar system is our only invention (which perhaps reflects our concern about what is going on with Nature). Overall we have used those abbreviations that are very frequent in the literature, such as the "H–R diagram" with "RGB and AGB stars" in it and "MORBs and OIBs" for astrophysicists and geologists respectively. Such abbreviations are explained in an appendix. There is also a list of rock and mineral names used in the text as well as a list of meteorite names and a glossary.

We are grateful for help and financial support from the International Space Science Institute in Bern, the Max Planck Institute for Chemistry in Mainz and Clare Hall College at the University of Cambridge. We thank A. W. Hofmann, R. K. O'Nions, B. Polyak, A. Sobolev, Yu. Kostitsyn, Yu. Pushkarev, V. Vetrin, V. Balagansky and U. Ott for lively discussions, V. and R. Vetrin for technical support, Yu. Kostitsyn for two figures and A. Zimmer for library support.

Finally we thank Elena and Elaine for their great patience and for keeping our feet on the ground.

Part I

The elements

In this part of the book the processes of nucleosynthesis and the environments in which they are occurring, and have occurred are sketched out.

To understand the principles of nucleosynthesis, it is important to appreciate the factors that determine the relative stability of different nuclides, and this subject is treated in Chapter 1. The grand scene is introduced in Chapter 2, without too much detail. Chapter 3 deals with data and observations concerning the chemical and isotopic composition of stars, galaxies and the solar system. This follows a broad chronological order, starting with the D/H and He/H ratios that lend support to the hypothesis of Big Bang nucleosynthesis, following through with the most primitive stellar matter and heterogeneities in presolar grains and then focussing on the composition of the solar system. Models and explanations of these data are contained in Chapters 4 to 8, which relate the data to results derived from astrophysical modelling. This helps us to understand first how the chemical elements were and are produced and second how they were scattered in space, to be incorporated in stars and solar systems that formed later.

1

Isotopes: weights and abundances

1.1 Introduction: nuclei and their behaviour

Atoms are the smallest units of matter that characterize a chemical element. An atom consists of a positively charged core or nucleus and negatively charged electrons orbiting around the core. In nuclear physics, a host of different particles is known to make up atomic cores, but for the purpose of cosmochemistry and geochemistry the simplified model suffices, in which we consider just two kinds of nuclear particles (nucleons): positively charged protons, p, and neutral neutrons, n. For a neutral atom the number of protons in the core, Z (the atomic number), is equal to the number of electrons around it. As Z determines the electron configuration and therefore the chemical behaviour, a family of atoms of equal Z constitutes a chemical element. Such a family generally includes nuclei with a varying number of neutrons, N. The atomic mass number $A = Z + N$, the total number of nucleons, then varies accordingly. Atoms of an element that have different values of N (and therefore A) are called isotopes, a term with Greek roots indicating that these different nuclides occupy the same position in the periodic table. The lightest element, hydrogen, includes three isotopes, ^{1}H, ^{2}H (D) and ^{3}H, having 0, 1 and 2 neutrons in the core, respectively. Most elements consist of a larger number of isotopes; therefore the approximately 100 currently known elements include approximately 1000 isotopes.

Many isotopes exist indefinitely, at least in normal conditions, and these are known as stable isotopes, S. The nuclei of the great majority of isotopes are, however, not stable and can spontaneously decay, i.e. turn into other nuclei, by emitting or absorbing a particle as summarized in Fig. 1.1. These decaying isotopes are termed radioactive or parent isotopes, $^{\mathrm{r}}R$, and the decay products are radiogenic or daughter isotopes, $^{\mathrm{r}}D$. Generally after decay an excited daughter nucleus "cools down", emitting γ-rays (high-frequency electromagnetic radiation). Each radioactive isotope species has its own specific rate of decay, λ, known as the

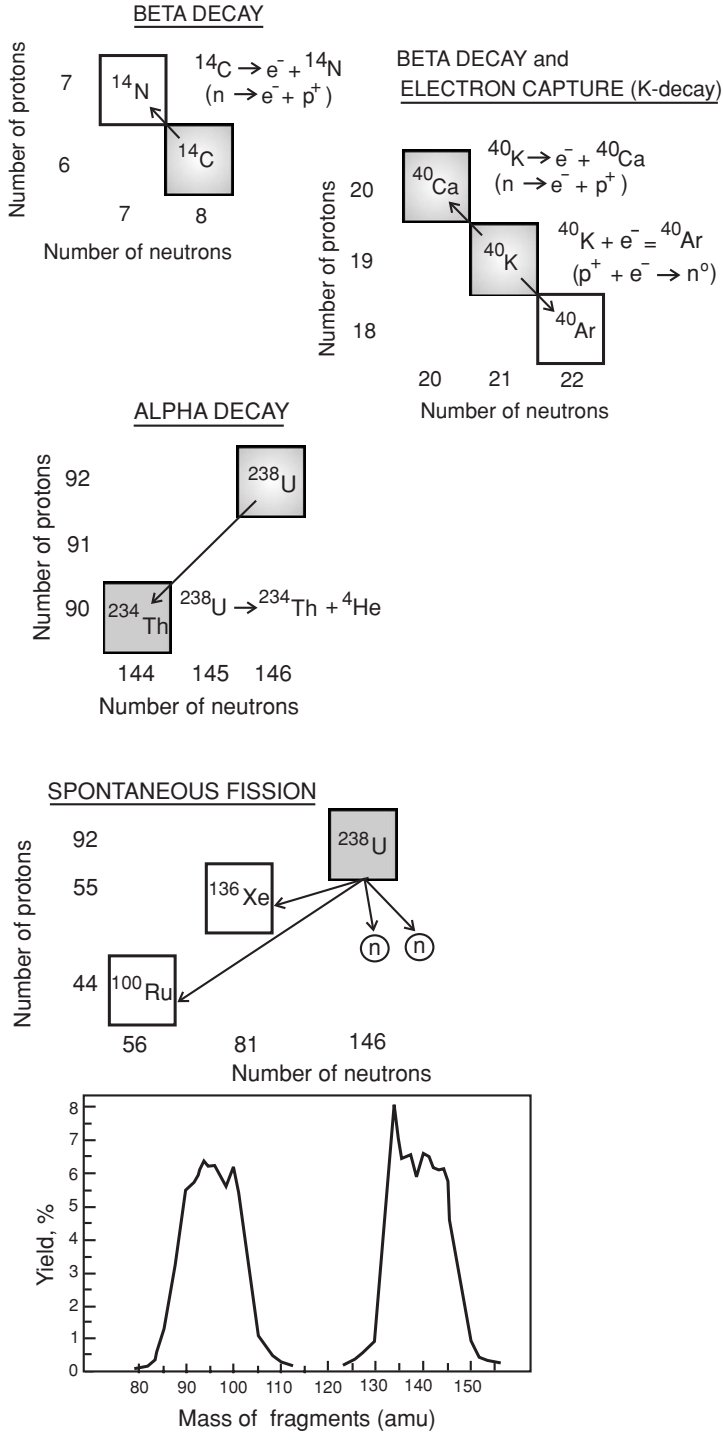
BETA DECAY
Number of protons
7
6
^{14}N
^{14}C
7
8
Number of neutrons
$^{14}C \rightarrow e^- + {}^{14}N$
$(n \rightarrow e^- + p^+)$
BETA DECAY and
ELECTRON CAPTURE (K-decay)
Number of protons
20
19
18
^{40}Ca
^{40}K
^{40}Ar
20
21
22
Number of neutrons
$^{40}K \rightarrow e^- + {}^{40}Ca$
$(n \rightarrow e^- + p^+)$
$^{40}K + e^- = {}^{40}Ar$
$(p^+ + e^- \rightarrow n^o)$
ALPHA DECAY
Number of protons
92
91
90
^{238}U
^{234}Th
144
145
146
Number of neutrons
$^{238}U \rightarrow {}^{234}Th + {}^{4}He$
SPONTANEOUS FISSION
Number of protons
92
55
44
^{238}U
^{136}Xe
^{100}Ru
n
n
56
81
146
Number of neutrons
Yield, %
0
1
2
3
4
5
6
7
8
80
90
100
110
120
130
140
150
Mass of fragments (amu)

decay constant; if R is the number of radioactive atoms then the decay is described by

$$\mathrm{d}R/\mathrm{d}t = -\lambda R. \tag{1.1}$$

The solution of Eqn (1.1) gives

$$R = R_0 \mathrm{e}^{-\lambda t} \equiv R_0 \exp(-\lambda t), \tag{1.2}$$

where t is the time elapsed since some time t_0 in the past and $R_0 \equiv R(t_0)$. Commonly, the decay is also characterized by the time interval τ during which the number of atoms R decreases by a factor 2; this is the half-life of the isotope. As $R(\tau) = R_0/2$, the relation between the decay constant and the half-life τ of a radioactive nuclide is $\tau \equiv \ln 2/\lambda$. The mean life of a radioactive isotope is $1/\lambda = \tau \ln 2$. Some radioactive isotopes decay by more than one mechanism, producing different daughter nuclides; for example ^{40}K can decay into ^{40}Ca (with corresponding λ_{Ca}) or into ^{40}Ar (λ_{Ar}), so that the total decay rate is $\lambda_{40} \equiv \lambda_{\mathrm{Ca}} + \lambda_{\mathrm{Ar}}$ and the number of $^{40}\mathrm{Ar}^*$ atoms generated by ^{40}K decay during time t equals $(\lambda_{\mathrm{Ar}}/\lambda_{40})\ ^{40}\mathrm{K} \exp(-\lambda_{40} t)$. In some cases decay competes with nuclear reactions (Section 5.4). The general term for such situations is branching.

It should be noted that the term "decay constant" does not apply to stellar environments, where β-decay rates can vary by orders of magnitude owing to the extreme temperatures and pressures. These variations, when known, shed light on nucleosynthetic processes (see for example Section 5.4). For planetary conditions λ values are constant, with some rare exceptions; for instance, the λ_3 value for ^{3}H β-decay is measurably dependent on the chemical state of hydrogen (Akulov and Mamyrin, 2004) and the value for ^{7}Be increases with pressure, by about 1% at 40 GPa (Liu and Huh, 2000).

←

Fig. 1.1 Radioactive decay and fission.
Top left, β-decay: a neutron n in the nuclei of carbon-14 decays to a proton p^+ and electron e^-, which is then emitted leaving behind nitrogen-14.
Top right, e-capture: a proton in the nucleus of ^{40}K captures an electron from the innermost orbit to produce a neutron and the nucleus of ^{40}Ar. Potassium-40 nuclei also decay via β-emission. Middle, α-decay: a nucleus of the heavy radioactive element ^{238}U emits an α-particle consisting of two protons and two neutrons; the resulting isotope is ^{234}Th. Bottom, nuclear fission: the nucleus of ^{238}U disintegrates into two fragments (generally the mass ratio is $\sim 1/2$) and emits two to three neutrons. As the fragments initially have too many neutrons relative to protons (for the given mass range), β-decay occurs until the "stability valley" (Fig. 1.3) is reached. When short-lived heavy isotopes ($A \sim 260$) exhibit fission, the fragment mass ratio approaches 1.

Nuclei can be modified not only by spontaneous decay but also by nucleus–particle (or nucleus–γ) interactions known as nuclear reactions. These can be destructive (breaking nuclei up) or constructive (building heavier nuclei). The interaction of nuclei with other nuclei or with protons is impossible at low temperatures, as both are positively charged. However, at $T \sim 10^7$ K or higher temperatures, this "Coulomb barrier" can be overcome: nuclei can collide and fuse, which is the basis for the existence of all nuclides other than the proton, ^{1}H.

Neutrons can easily penetrate nuclei even at low temperatures. For instance,[1] neutron capture by ^{56}Fe(n, γ)^{57}Fe and ^{57}Fe(n, γ)^{58}Fe gives rise to heavier iron isotopes. Further n-capture, ^{58}Fe(n, γ)^{59}Fe, followed by β-decay yields the next element, cobalt: $^{59}\text{Fe} \rightarrow \beta^- \rightarrow {}^{59}\text{Co}$. Such n-capture and associated β-decay has produced all the elements beyond Fe. These are therefore called n-capture elements. An example of a destructive nuclear reaction is the nuclear fission of ^{235}U: after neutron capture, ^{235}U disintegrates into two heavy fragments with different masses and a few neutrons (Fig. 1.1). Its heaviest brother, ^{238}U, exhibits spontaneous fission in addition to α-decay, but with a much lower probability. Another important example is ^{6}Li(n, α)^{3}H: this reaction produces radioactive ^{3}H (tritium), which β-decays into daughter ^{3}He.

Investigations of the heaviest nuclei have shown that the heavier a nucleus is, the higher the probability that it will disintegrate via fission. Extrapolation of the relationships between Z, A and the fission rate suggests a limit of $Z \sim 120$, $A \sim 310$ for possible nuclei. Thus, the full range of the elements extends from hydrogen (1 amu) to an, as yet unknown, superheavy element ($\sim$ 300 amu).

1.2 Atomic nuclei and binding energy, with some predictions on isotope abundances

Mass, energy and binding energy

The atomic nuclei are quite small: the radius r_A of a nucleus with atomic mass number A is about $1.4 \times 10^{-13} A^{1/3}$ cm. Thus, for the heaviest possible nuclides, $r_A \sim 10^{-12}$ cm. The shape of atomic nuclei varies between spheroidal and ellipsoidal. The whole atom, i.e. the nucleus plus the electronic cloud, is a factor $\sim 10^5$ larger. For example, the radius of the first electronic orbit of the hydrogen atom is 0.53×10^{-8} cm. However, the nucleus makes up almost all the mass of an atom. Generally this mass is measured in so-called atomic mass units, defined as 1/12 of the mass of the neutral isotope ^{12}C; i.e. 1 amu $\equiv 1.660\,53 \times 10^{-24}$ g. Thus the mass of an atom in amu is numerically $\approx A$, the atomic mass number. The precise masses of the proton, $M_\text{p} = 1.007\,282\,6$ amu, and neutron, $M_\text{n} = 1.008\,671\,3$ amu, are larger

[1] The following notation abbreviates $^{56}\text{Fe} + \text{n} \rightarrow {}^{57}\text{Fe} + \gamma$ etc.

by a factor of about 2×10^3 than the mass of the electron, $m_e = 0.000\,548\,58$ amu. The nuclear masses and radii (e.g. $238 \times 1.66 \times 10^{-24}$ g corresponds to $\sim 10^{-12}$ cm) allow the density of nuclear matter to be estimated at $\sim 10^{14}$ g cm^{-3}.

High-resolution mass spectrometry allows the isotope masses $M(A, Z)$ to be obtained precisely. These masses are without exception smaller than the sum of the masses of the constituent particles, protons + neutrons + electrons:

$$[Zm_p + (A - Z)M_n + ZM_e] - M(A, Z) = \Delta M > 0. \tag{1.3}$$

Note that the measured $M(A, Z)$ also includes Zm_e, so that ΔM is the difference in nuclear mass. From this, the binding energy of nuclei can be calculated. According to the Einstein relationship,

$$E = Mc^2 \tag{1.4}$$

where E is the energy in ergs; $c = 3 \times 10^{10}$ cm s^{-1} is the light velocity in vacuum and M is the relativistic mass in g: $M = M_0/\sqrt{(1 - (v/c)^2)}$, where M_0 is the rest mass and v is the velocity of the body. One atomic mass unit is thus equivalent by (1.4) to the energy 1.49×10^{-3} erg or 0.932×10^9 eV = 932 MeV (1 MeV $\equiv 1.60 \times 10^{-6}$ erg). Substituting ΔM from Eqn (1.3) into Eqn (1.4) gives the total binding energy ΔW of a nucleus,

$$\Delta W = \Delta Mc^2, \tag{1.5}$$

and the binding energy per nucleon for that nucleus,

$$\varepsilon = \Delta W/A. \tag{1.6}$$

A comparison of the mass of deuterium, 2.014 74 amu, with the total mass of its constituent proton and neutron, 2.017 12 amu, gives $\Delta M = 0.0024$ amu, $\Delta W =$ 2.2 MeV and $\varepsilon = 1.1$ MeV nucleon^{-1}. This is the energy yield from deuterium nucleosynthesis. Conversely, a neutron is heavier than a proton by about 1 MeV and readily decays, when in isolation, producing a proton, electron and neutrino. A similar estimate for the ^{4}He nucleus gives $\Delta W = 28$ MeV and $\varepsilon = 7$ MeV nucleon^{-1}.

It is instructive to compare nuclear energy values with those for chemical interactions, say, that required to separate an electron from a hydrogen atom. The total energy of an electron having a charge $e = -1.6 \times 10^{-19}$ C and orbiting the nucleus at a distance $r = 0.53 \times 10^{-8}$ cm is the sum of its kinetic and potential energies:

$$E = \frac{mv^2}{2} - \frac{e^2}{4\pi\epsilon r} = \frac{-e^2}{8\pi\epsilon r},$$

where ϵ, the permittivity of free space, equals 8.85×10^{21} $C^2 g^{-1} cm^{-3} s^2$. Substituting values we obtain

$$E = \frac{-(1.6 \times 10^{-19})^2}{2 \times 4\pi \times 8.85 \times 10^{21} \times 0.53 \times 10^{-8}} = -2.17 \times 10^{-11}\ \text{erg} = -13.6\,\text{eV} \quad (1.7)$$

which is a factor 10^5 to 10^6 less than the binding energy of an atomic nucleus. This comparison illustrates how powerful nuclear energy is.

Nuclear forces originate from the interactions of a number of elementary particles, the characterization of which is beyond the scope of this book. Instead, the discussions below are based simply on the observed atomic masses, and we will show that even this simple approach leads to several far-reaching inferences about nuclide-producing processes and the abundances of isotopes and elements.

Relationships between binding energy and atomic mass

Figure 1.2 shows a sharp increase in ε with nuclear mass at lower masses, approaching $\varepsilon \approx 8.8$ MeV nucleon^{-1} for the iron-peak elements at $A \sim 50$ to 60. This is followed by a smooth decrease to 7.4 MeV nucleon^{-1} for heavier nuclei, $60 < A < 209$; $A = 209$ is the atomic mass number of the heaviest stable isotope, ^{209}Bi. The cause of this important feature is that the forces holding nuclei together work on a very short distance and a nucleon does not interact with all others in the nucleus, especially when A becomes large, around 60. The Coulomb forces, however, work over longer distances and they increase with the total charge of the nucleus. For nuclei to be stable, it is required that the Coulomb repulsion between protons be less than the nucleon attraction. For example, for two protons at a distance similar to the size of the ^{4}He nucleus ($A = 4$), $r \approx 1.4 \times 10^{-13}\, A^{1/3} \approx 2 \times 10^{-13}$ cm, the potential energy due to Coulomb repulsion is

$$E_p = \frac{e^2}{4\pi\epsilon r} \approx \frac{(1.6 \times 10^{-19})^2}{4\pi \times 8.85 \times 10^{21} \times 2 \times 10^{-13}} \approx 1\,\text{MeV}. \quad (1.8)$$

This is much less than the binding energy per nucleon for ^{4}He. In contrast, the Coulomb interaction within a heavy nucleus, for example $E_p \approx 5$ MeV for $A \approx 200$, is comparable with ε. In heavier elements, the stability of the nucleus is achieved by neutron–proton ratios > 1 (Fig. 1.3). Thereby the distance between protons is increased and the destructive tendency caused by the Coulomb forces is diminished.

An important consequence of the hump-like shape of the binding energy per nucleon curve is that the generation of elements with $A \leq 60$ from lighter ones produces energy, whereas production of those with $A > 60$ requires an energy input.

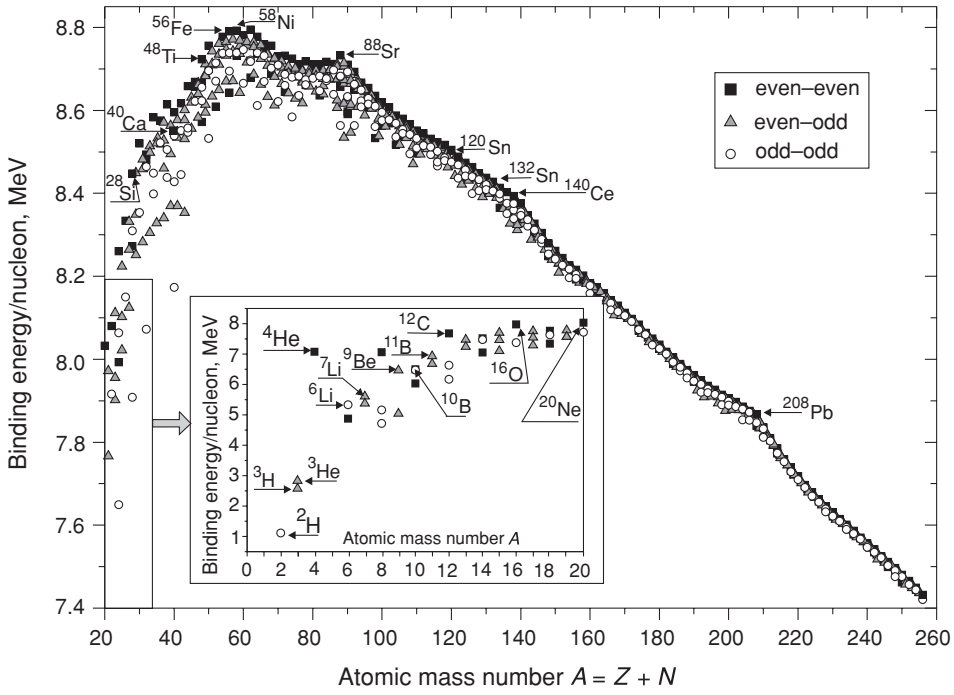

Fig. 1.2 Relationships between the atomic binding energy per nucleon and the atomic mass number, the prime importance characteristics of nuclei controlling their synthesis, abundance, and stability. Even–even nuclei show higher binding energy than the others; this predicts the higher abundances of the even–even isotopes in nature (see Fig. 3.9). Several highs along the array correspond to the magic numbers of nucleons in nuclei. The iron peak is of special importance: all elements heavier than this have lower binding energy, which means that an energy input is required to generate them. Lithium, Be, B show lower binding energies than ^{4}He (see inset); these are fragile and therefore should be of low abundance. The α-particle, the nucleus of ^{4}He, has a very high binding energy, and so nuclei consisting of α-particles (e.g. ^{16}O) also show high binding energies; these nuclei are strong, stable and abundant. The rather low binding energies of nuclei heavier than ^{209}Bi impel their spontaneous disintegration.

Therefore, in principle, the heavier nuclei can only be produced in an environment where the nucleosynthesis of lighter elements provides the necessary energy. As early as 1950, stellar interiors were shown to be a suitable astrophysical environment for such a combined production.

The strong nuclear binding of Fe-group elements around $A \sim 60$ predicts that they should be anomalously abundant in galaxies. This is indeed the case (see Figs. 3.8, 3.9). Some elevations along the $\varepsilon(A)$ curve reflect an especially high binding energy for nuclei with so-called magic numbers of nucleons: N or $Z = 2$, 8, 20, 50, 82 and $N = 126$ (e.g. the Sn isotopes, with $Z = 50$, Fig. 1.2). Nuclei having magic

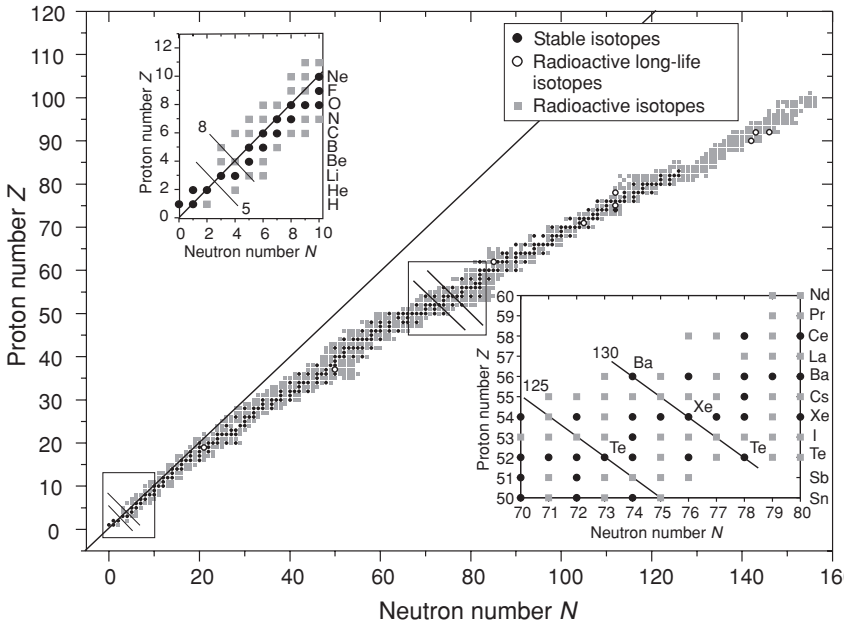

Fig. 1.3 Relationships between neutron number and proton number (atomic number) in nuclei. The neutron/proton ratio in atomic nuclei increases together with their mass. Only certain combinations of N and Z allow stable nuclei, constituting a narrow stability valley. The long-lived radioactive isotopes that have survived the 4.570 Gyr since solar system formation are also shown. Note that no stable nuclides exist on the fifth and eighth isobars, i.e. lines of equal $A = Z + N$ (top-left inset); this prevented a substantial yield of elements heavier than ^{4}He in the Big Bang nucleosynthesis. Generally only one stable isotope exists for an odd-isobar family (e.g. ^{125}Te), whereas there are generally two or three stable nuclides on even isobars (e.g. ^{130}Ba, ^{130}Xe and ^{130}Te, bottom-right inset; see the main text and Fig. 1.4). Also, elements having even Z typically have several isotopes (e.g. Xe has nine) in contrast with elements with odd Z. No stable isotopes exist beyond the "almost stable" ^{209}Bi (half-life 2×10^{17} yr) because the binding energies per nucleon are too low (Fig. 1.2).

numbers of both protons and neutrons are called double-magic nuclei: their shapes are closest to spherical, and therefore these nuclei are especially tightly bound (e.g. ^{132}Sn, ^{208}Pb; Fig. 6.1).

Odd, even and even–odd families

Nuclei with even numbers of both protons and neutrons are called "even–even." They are more strongly bound than even–odd and odd–odd nuclei because there is a very tight link (i.e. high ε value) for proton–neutron pairs and particularly for the combination two protons + two neutrons. For example, ε is much higher for

^{4}He than for its neighbour Li (see the inset in Fig. 1.2). Elements that formed by trapping α-particles (^{4}He nuclei), e.g. ^{12}C, ^{16}O, ^{28}Si, etc., are called α-elements: these elements are especially strongly bound. This translates into a higher number of even–even nuclides: the fractions of even–even, even–odd and odd–odd stable nuclei are approximately 0.65, 0.25 and 0.014 respectively. Figure 1.4 illustrates this for isobaric nuclides, which share a single value of $A = Z + N$.

Along an odd isobar, all nuclides have Z odd and N even, or vice versa, and clearly belong to one family: their binding energies are approximated by one parabola. Each nuclide sitting on the arms of the parabola is unstable and decays to a daughter radioactive nuclide with a greater binding energy. The decay continues until the single nuclide with the highest binding energy for a given isobar family is reached; this surviving nuclide is situated at the very bottom of the parabola. Therefore generally only one stable nuclide exists in each odd-isobar family.

In contrast, the nuclei constituting an even isobar are separated into odd–odd and even–even families, whereby the odd–odd nuclides plot on a parabola with higher ΔM (lower ε) than the even–even ones (Fig. 1.4). Near the bottom of the lower parabola, even–even nuclei, because of their strong nuclear bonds, cannot decay into odd–odd ones. The only way to strengthen their bonds is to decay to a neighbouring even–even nuclide, but this would involve double β-decay, for which the probability appears to be extremely low. Therefore generally two or three stable nuclides coexist in one even–even isobar family whereas odd–odd nuclei are particularly prone to disintegration: among the 1000 or so nuclides seen in Fig. 1.2 only four odd–odd nuclides are stable, ^{2}H, ^{6}Li, ^{10}B and ^{14}N.

The comparison of odd and even isobar families predicts another feature of the natural abundance of nuclides. The abundance of a single stable isotope from an odd family (^{125}Te in Fig. 1.4) comprises all precursor nuclides on the isobar that have been produced, whereas some even–even isotopes (^{130}Ba) have no precursors. Therefore the abundance curve for odd isobars should be smoother than that for even ones. Figure 3.9 illustrates the validity of this prediction.

The distribution of the binding energy per nucleon and the consideration of isobar families also predict a sawtooth pattern in elemental abundances, elements with even Z being more abundant than those with odd Z by (on average) an order of magnitude. The main reason is the greater binding energy of even–even nuclei. Further, in elements with odd Z (with four odd–odd exceptions) only odd–even isotopes are possible, and the single isobar for even–odd nuclides means that mostly these elements have only one stable isotope. In contrast, both even–even and even–odd isotopes are possible for elements with even Z, so that a number of stable isotopes occur, even–even ones dominating. This results in a lower overall elemental abundance for odd-Z elements, which is the second reason for the sawtooth pattern (Fig. 3.8).

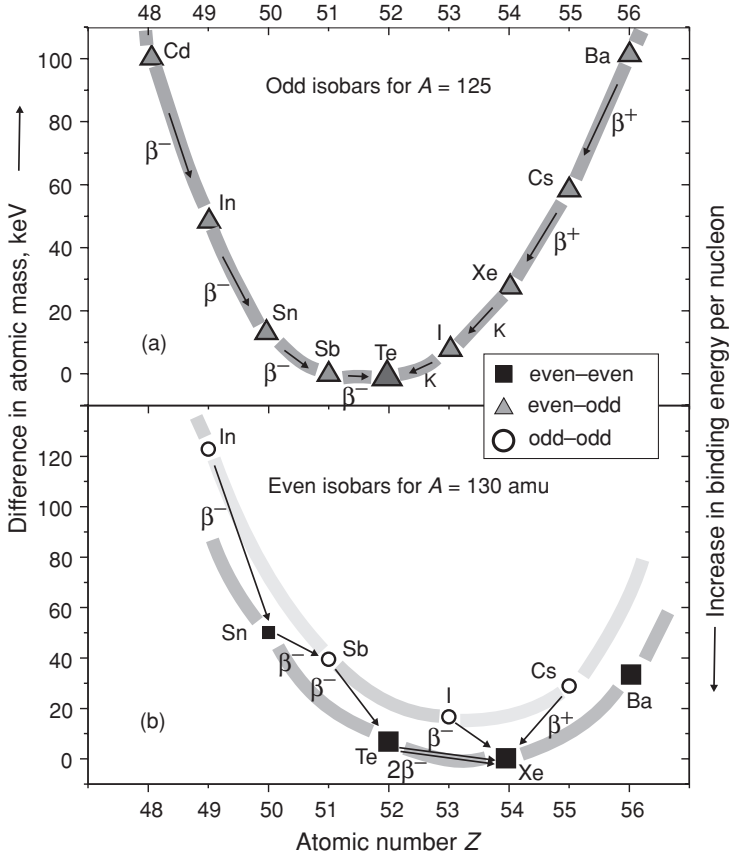

Fig. 1.4 Plots of mass differences vs. Z for examples of isobars with even and odd A. The difference in atomic mass is equal to the atomic mass of each individual nucleus minus the atomic mass of the nucleus with the lowest mass in the isobar; these are ^{125}Te and ^{130}Xe in the top and bottom plots respectively: the higher the mass difference the lower the binding energy per nucleon. (a) Atomic masses on an odd-A isobar can be approximated by a single parabola; all the nuclei belong to the same family, and β-decay or e-capture result in one stable isotope for the family, i.e. ^{125}Te (large triangle) for the $A = 125$ isobar. (b) Even isobars are separated into odd–odd and even–even families. Odd–odd nuclei readily decay to even–even ones by β^- or β^+ decay. Even–even nuclei that do not have the highest binding energy can decay into other even–even nuclei only through double β-decay, e.g. $^{130}\text{Te} \rightarrow 2\beta \rightarrow {}^{130}\text{Xe}$. Such decay is an extremely rare event: here the half-life is $\sim 10^{24}$ yrs (!) (Kirsten, 1983). Because of this there are three stable even–even nuclei in the 130 amu family (the large solid squares) whereas no odd–odd species have survived.

Heavy elements and radioactive isotopes

A continuous decrease in ε for $A > 60$ signals the progressively diminishing stability of the heavier isotopes. Thus, the magic Pb comprises four stable isotopes and the following odd-Z Bi only one; all isotopes heavier than ^{209}Bi are unstable because their total binding energy εA is lower than the sum of the corresponding constituents. For example, the product $\varepsilon(^{238}\mathrm{U}) \times 238$ is 4.25 MeV less than the sum of the corresponding products for ^{234}Th and ^{4}He: U is unstable to α-decay, which indeed liberates this energy. Further, ^{238}U has a lower binding energy than the sum of two constituents of similar mass and therefore undergoes spontaneous nuclear fission (Fig. 1.1). Thus the roots of radioactivity are found in the binding energy inventories.

1.3 Summary

The binding energy per nucleon ε can be derived from the difference ΔM between the mass of a nuclide and the sum of its components and is an important model-independent parameter characterizing each isotope. When plotted as a function of atomic mass number A, ε shows a hump-like shape, increasing from hydrogen to iron (and neighbouring elements at $A \sim 60$) and then smoothly decreasing towards the heaviest elements. This pattern yields important inferences on the origin, abundance and stability of the elements.

The synthesis of nuclei below the iron peak occurs with release of nuclear energy, whereas the production of heavier elements requires an energy input. For example, the synthesis of one helium nucleus from two protons and two neutrons releases 28 MeV (or 4.5×10^{-5} erg) of atomic energy, which exceeds the typical energy of chemical interactions by a factor $\sim 10^6$ (!). If synthesis occurs in some hypothetical thermo-isolated environment, extremely high temperatures can result, leading to further interaction of charged particles in nucleosynthetic processes.

The total binding energy depends on the numbers of protons and neutrons in the nuclei. Competition of the short-distance nuclear forces (tending to keep the nucleons together) and the Coulomb repulsion forces (tending to disunite them) leads to neutron–proton ratios > 1 in heavy nuclei. In a plot of the number of protons versus the number of neutrons, the "stability valley" departs from the isoline after the doubly magic ^{40}Ca, approaching a neutron-to-proton ratio of 1.5 for the heaviest isotopes.

Strongly bound elements with a high ε value should be more abundant than fragile ones, and the most strongly bound, iron, is expected to be especially abundant. For isotopes with $A > 60$, ε decreases steadily with increasing nuclear mass, so that their abundance is expected to decrease also. A limit for the mass of stable isotopes

is expected because of the increasing Coulomb forces in the nucleus; the heaviest stable nuclide is ^{209}Bi. The binding energy of some heavy nuclei is less than the binding energies of their constituents (e.g. the binding energy of ^{238}U is less than the binding energies of ^{4}He and ^{234}Th), and this relationship predicts their nuclear decay and fission.

As elements with an even number of protons can have many stable isotopes and those with an odd number of protons generally only one, a sawtooth shape of the elemental abundance curve is predicted. Also, because only a single stable isotope exists in an odd-isobar family, this isotope comprises all precursor nuclides, whereas even–even isotopes have generally no precursors. Therefore the abundance curve for odd isobars is smoother than that for even isobars.

2

Introduction to the Universe: the baryonic matter

The major goal of Part I of the book is to present the observed abundances of the elements and isotopes and their variations in space and time, describe the relevant nucleosynthetic processes and outline the evolution of the elements in the Galaxy. In order to provide a context for the observations and models, this chapter is a brief excursion through the Universe, as a unique assembly of matter, and the galaxies within it. Only the small visible baryonic part of the assembly is considered here; it is ≈ 0.04 of the total. Small but important, as we are made of it! To appreciate dark matter, dark energy etc., we refer the reader to the recent book by Peacock (1999), and also to the fascinating breakthrough in understanding the Universe following from recent measurements of the microwave background radiation and high-redshift supernovae (e.g. Spergel *et al.*, 2003).

In Fig. 2.1 the major constituents of the evolving Universe are shown schematically together with the relevant interactions and time scales. The lightest elements, H and He, originated simultaneously with the Universe, in a single explosion-like event, the Big Bang, for which the age is now reliably known, 13.7 ± 0.2 Gyr (Section 4.3). From denser fragments of the early expanding Universe galaxies were formed, giant stellar systems comprising most of the baryonic mass of the Universe. The time scale of galaxy formation is ~ 1 Gyr or less, and some models envisage a relatively long infall of intergalactic matter up to several Gyr (Chiappini *et al.*, 2001).

The baryonic matter in a galaxy is divided among the interstellar medium, stars (some with planetary systems) and stellar remnants. Gas (mainly H and He) is the major constituent of the interstellar medium. In some regions of the galaxy the gas is dense and cold compared with others and forms molecular clouds that also generally contain dust. Under certain circumstances a cloud can contract to form a star. At present the average gas–star mass ratio of our Galaxy is between ~ 0.1 and ~ 0.2, and in the early Galaxy the proportion of gas is thought to have been higher. From a mass-balance point of view the compositions of both interstellar clouds

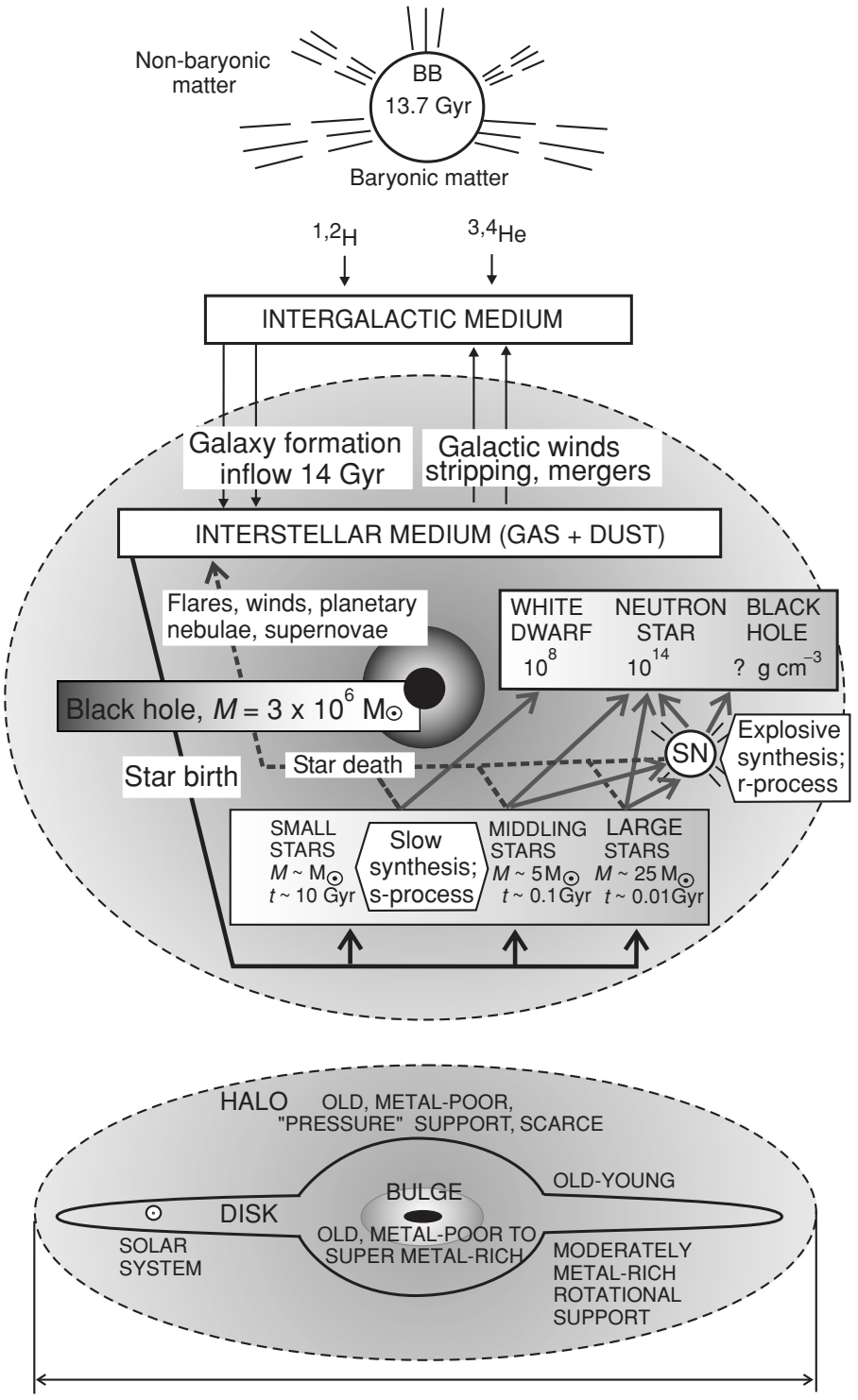
Non-baryonic matter
BB
13.7 Gyr
Baryonic matter
1,2H
3,4He
INTERGALACTIC MEDIUM
Galaxy formation inflow 14 Gyr
Galactic winds stripping, mergers
INTERSTELLAR MEDIUM (GAS + DUST)
Flares, winds, planetary nebulae, supernovae
WHITE DWARF
NEUTRON STAR
BLACK HOLE
10^8
10^14
? g cm^-3
Black hole, M = 3 x 10^6 M⊙
Star birth
Star death
SN
Explosive synthesis; r-process
SMALL STARS
M ~ M⊙
t ~ 10 Gyr
Slow synthesis; s-process
MIDDLING STARS
M ~ 5M⊙
t ~ 0.1Gyr
LARGE STARS
M ~ 25 M⊙
t ~ 0.01Gyr
HALO
OLD, METAL-POOR, "PRESSURE" SUPPORT, SCARCE
BULGE
OLD-YOUNG
DISK
SOLAR SYSTEM
OLD, METAL-POOR TO SUPER METAL-RICH
MODERATELY METAL-RICH ROTATIONAL SUPPORT

and stars are thus representative and important. Stellar remnants ("dead stars"), i.e. white dwarfs, neutron stars and black holes, at present account for ~ 0.1 of the mass of the Galaxy (Pagel, 1994; Chiappini *et al.*, 2001).

Spectroscopic investigations of the interstellar clouds allow the average compositions of large regions of the Galaxy to be evaluated. In addition to H (mass fraction $\sim 70\%$) and He ($\sim 28\%$), the heavier elements O, C, N, Ne, S, Ar, Fe and others (contributing all together $\sim 2\%$) are also present in the clouds. In hot regions of clouds (known as HII), e.g. around hot stars, all elements including H may be ionized, while in cold regions molecules and even grains are formed. Even though the grains, generally ~ 1 μm in size, comprise only $\sim 1\%$ of the mass of a cloud, they are an important store of the refractory, heavier, elements. Some interstellar grains condensed before the formation of the solar system are preserved in meteorites, and thus present a unique opportunity to study interstellar matter directly in the laboratory. This has shed light on the initial prestellar abundances of nuclides, nuclear reactions in stars, mixing caused by convection or stellar shells or winds, condensation in cooling stellar ejecta and on the respective time scales. Some grains indicate substantial reworking and remixing within a cloud and thus bear evidence of intracloud processes.

Stars are hot luminous objects that originated from interstellar clouds by gravitational collapse. With the exception of a few that are close to our solar system, they are observed only as point sources of light and other electromagnetic radiation. The outermost, relatively cool, shells of a star are collectively known as its atmosphere:

←

Fig. 2.1 Introduction to the Milky Way Galaxy. After light elements had been produced in the Big Bang nucleosynthesis (top figure), the expanding matter formed denser clumps called galaxies. The middle and bottom figures give a plan view and elevation of our Galaxy. The local collapse of the interstellar medium – gas, and later gas and dust grains, – gave rise to stars, small, middling or large. Nuclear burning in stellar interiors produces energy supporting a star against collapse, generates radiation and yields heavier elements (up to iron) at the expense of lighter ones; n-capture processes (e.g. the slow s-process operating in small stars and the rapid r-process operating in large stars) yield elements heavier than iron. The elements newly generated in a star, together with the pre-existing matter, are (repeatedly) expelled from the stellar outer envelope(s) back to the interstellar medium (and partially even to the intergalactic medium) as stellar winds, planetary nebulae, etc. (broken-line arrows). When the nuclear fuel is exhausted, the star dies: the outer shells are finally ejected as planetary nebulae or supernova outburst, whereas the stellar core collapses into a dense compact object, a white dwarf, neutron star or black hole. There is probably a very massive black hole at the centre of our Galaxy. The parameters of our Galaxy are as follows: size $\sim 10^5$ light years (10^{23} cm); mass $\sim 10^{44}$ g; lifetime ~ 13 Gyr; number of stars $\sim 10^{10}$–10^{11}; stars/gas mass ratio ~ 5, dust/gas mass ratio $\sim 1/1000$ in solar neighbourhood. After Pagel (1994) and Chiappini *et al.* (2001).

these shells are of low density and are transparent, and thus allow energy to dissipate from the inner layers of the star. Spectroscopic measurements give element abundances in the stellar atmospheres and planetary nebulae. Observations on different stars at different stages of their evolution allow modelling of nucleosynthetic processes in stars.

The temperature T, pressure P and density ρ of the gas increase towards the stellar centre. Depending on the stellar mass and evolution, a core and several shells can exist within a star. The cores and/or internal shells around it have temperatures high enough to ignite nuclear fusion, and here heavier nuclides are produced at the expense of lighter ones. Elements up to those of the Fe group, which have extreme values of the binding energy per nucleon (Fig. 1.2), are thus produced by fusion. Because of the increasing Coulomb barrier, this process cannot produce elements with $A > 60$ and these are yielded mainly via n-capture reactions. These can proceed during the quiescent evolution of small stars of mass between 1 and 5 $M_\odot$, yielding s-process nuclides such as Sr, Zr, La, Ce (Chapter 5). An important feature of the s-process is that the time scales for n-capture reactions are long relative to the half-lives of the interim radioisotopes within and adjacent to the stability valley (Fig. 1.3). The evolution and explosive death of big stars, e.g. ~ 25 $M_\odot$, results in the production of r-process n-capture nuclides, Eu, Ho, Ir, U, Th and others (Chapter 6). In this case n-captures follow each other much faster than β-decay, and n-rich radioactive nuclides outside the stability valley are yielded first and then decay into stable r-process nuclei. Convection operating at different stages of stellar evolution transfers the newly yielded elements to the outer shells of the star, where they are mixed with those available in proto-stellar material. Stars eject part (or even all) of their material back into the interstellar medium, supplying it with freshly synthesized nuclides and thus increasing the proportion of heavy elements. Another portion of the stellar material can be preserved in a stellar remnant.

Among stellar remnants, only white dwarfs, left over after the death of small stars (Fig. 2.1), preserve their matter in the form of chemical elements, and their photospheric abundance can be derived e.g. from the analysis of radio spectra (Isern *et al.*, 2001; Reddy *et al.*, 2003). Matter in the heavier and much denser neutron stars and black holes cannot be described in terms of a chemical composition. Here the composition of the preceding material may in some cases be (partially) reconstructed e.g. via investigations of an accompanying star, which orbits the "black dead object" and could have trapped products of its final explosion (Israelian *et al.*, 1999). The amount of material conserved in neutron stars and black holes is difficult to estimate. Probably it varies between different segments of a galaxy. Thus, towards the centre of our Galaxy, an increasing portion of the mass is concentrated in stellar remnants. There is also convincing evidence from the parameters of stellar

orbits, that a large black hole, of mass $3.7 \pm 1.5\ 10^6\ M_\odot$, occurs in the centre of the Galaxy (Schodel *et al.*, 2002).

To compare the compositions of various objects or regions of the Galaxy and the Universe, the relative abundances of elements heavier than He in these objects are used, quantified as their metallicities (see the Glossary). The density and metallicity both increase from the periphery to the centre of the Galaxy, by factors ~ 100 and ~ 1.5 respectively. Also, stellar metallicities increase smoothly with time and at present many stars show a higher metallicity than our 4570-Myr- old Sun. A galaxy should thus be treated as a complicated, fundamentally heterogeneous, system, parts of which evolve at different rates. However, even with these complications, it is possible to study the origin and evolution of the elements. The observational data used for this include:

- average element abundances of interstellar clouds, first of all D/H and He/H ratios, but also those of the heavier elements (Section 3.1);
- element abundances in stars of different ages including the most ancient stars, which portray early nucleosynthesis, enabling one to outline the evolutionary trend (Section 3.2);
- elemental and isotopic data on presolar dust grains, bearing evidence on stellar nucleosynthesis and subsequent processes in the solar neighbourhood (Section 3.3);
- the average solar system element abundances as the reference composition at least for the solar neighbourhood (Section 3.4);
- the evidence for short-life nuclides from studies of early solar system materials (Section 3.4).

3

Element and isotope abundances: reference collection

3.1 Hydrogen and helium and their special significance

The lightest isotope, hydrogen, with $A = 1$, is the prime building block for the elements, and spectroscopic measurements show that H is the most abundant element in stars and interstellar clouds in our Galaxy and in the Universe as a whole: nine out of ten atoms are hydrogen. The second stable hydrogen isotope, deuterium (D), with $A = 2$, is much less abundant: it has a low binding energy per nucleon (Fig. 1.2), and upon collision with baryons and heavier particles it is readily fused to form ^{3}He or He. As nuclear processes in stars thus tend to destroy D, this nuclide must have been generated in another process, i.e. in the earliest prestellar nucleosynthesis.

This hypothesis can be tested by measuring the prestellar D/H ratio of galaxies. This can be achieved by the spectroscopy of interstellar clouds lying along the line of sight to a remote very bright object. Some of these clouds represent nearly virgin samples of prestellar cosmic material with $\sim$ 1000 times lower metallicity than that in the solar system (the metallicity of a system is a measure of the abundance of elements heavier than helium). High-resolution spectroscopic measurements of the H and D abundances in these clouds gave D/H = $(30 \pm 2) \times 10^{-6}$ (Schramm and Turner, 1998). Recent detections gave a slightly lower value $(26 \pm 2) \times 10^{-6}$ (Pettini and Bowen, 2001), which is indistinguishable from the primordial D/H value, $(26.2 \pm 0.2) \times 10^{-6}$, derived from the cosmological model based on the cosmic microwave background radiation (Spergel *et al.*, 2003). This remarkable agreement is important evidence in favour of the Big Bang nucleosynthesis model (Chapter 4).

In contrast with D, the ^{4}He nucleus is very tightly bound; therefore the ^{4}He abundance has increased over time owing to H fusion in stars (Chapter 5), and evolved astrophysical objects generally show enhanced helium/hydrogen ratios. The primordial abundance of ^{4}He can be derived from the dependence between

the ^{4}He/H and O/H ratios observed in low-metallicity clouds. Extrapolation of this dependence to O/H = 0 gives a mass ratio ^{4}He/H = 0.236 ± 0.02, in full accord with predictions from the Big Bang nucleosynthesis model (Schramm and Turner, 1998).

The even–odd fragile ^{3}He is much less abundant than ^{4}He: spectroscopic measurements give a value ∼ 6600 for the primordial ^{4}He/^{3}He ratio (Rood *et al*., 1998). This value is close to the best estimate of the presolar ^{4}He/^{3}He ratio, 6020 ± 200, measured in Jupiter's atmosphere (Mahaffy *et al*., 1998) and to the present-day value measured in the interstellar medium in the solar neighbourhood, 7100 ± 2300 (Salerno *et al*., 2001). Observed prestellar ^{4}He/^{3}He ratios thus vary by a factor ∼ 1.2 only, and there appears to be no systematic trend (Reeves, 1998).

Importantly, ^{3}He is a nuclide complementary to D, as it was converted to ^{3}He during early stellar evolution. This allows an independent estimate of the primordial D to be made. The solar abundance of ^{3}He is known from measurements of the composition of the solar wind (SW), and $^3\mathrm{He}_{\mathrm{SW}}$ is the sum of the primordial D and ^{3}He: $\mathrm{D}_{\mathrm{PRIM}} + {}^3\mathrm{He}_{\mathrm{PRIM}} = {}^3\mathrm{He}_{\mathrm{SW}}$. The latter is more invariant against stellar processing than D alone. This approach gives a presolar D/H = 21 ± 5 ppm, much the same as the values discussed above (Geiss and Gloeckler, 1998).

Thus, the data on the relative abundances of the lightest nuclides that originated in the Big Bang nucleosynthesis are remarkably consistent.

3.2 Metal-poor stars: the most ancient matter of the Galaxy

The study of near-primeval matter can be extended to heavier elements. The increase of metallicity with time appears to be a general trend of the evolution of matter in a galaxy (Chapter 8). Therefore low-metallicity astrophysical objects should be targeted for such a study. The stars with the lowest metallicity index, [Fe/H] ≈ −5.0, show an extreme overabundance of the light CNO elements, so that their C/Fe ratios exceed solar values by a factor 10 000. The abundance ratios [Na/Fe], [Mg/Fe], [Al/Fe] and [Sr/Fe] are also much higher than those in the solar system, whereas the heavy elements, $A > 100$, are virtually absent in the spectra of these newly discovered stars (Frebel *et al*., 2005).

In contrast, the next generation of metal-poor halo stars, with [Fe/H] below −3.0, shows high abundances of n-capture heavy nuclides. A comparison with solar system abundances reveals both similar and different features (Fig. 3.1). The relative abundances of the heavy n-capture elements ($A > 130$, e.g. Sm, Eu, Gd, Tb, Dy, Ho, Er, Pb) in metal-poor stars are very similar to solar values, thus highlighting the universality of nucleosynthetic process(es) operating in different objects, including very ancient ones.

However, the agreement of the abundance pattern of light n-capture elements (Sr to Cd, especially Ag and Y) with that of the solar system is not as good as that for

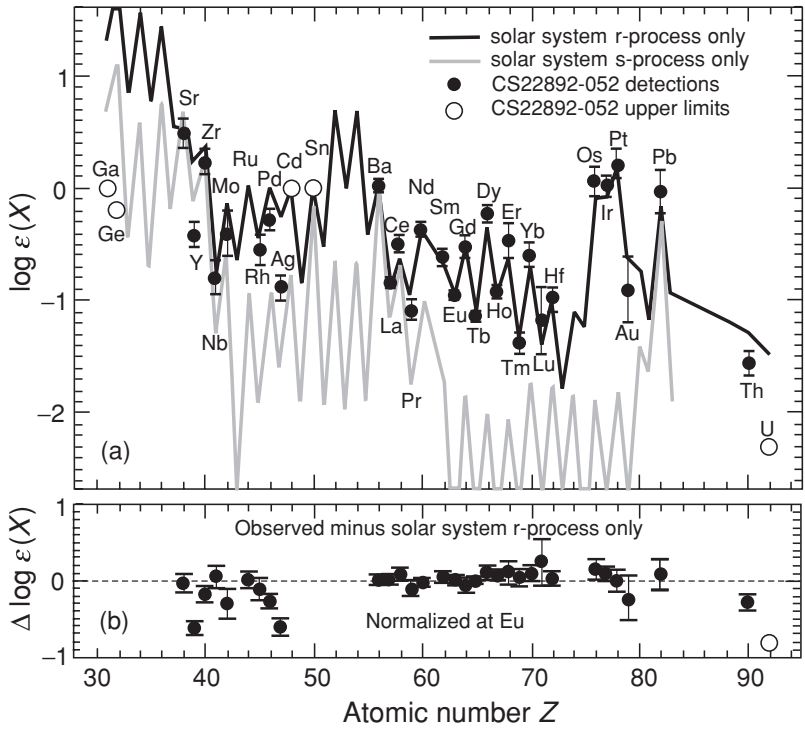

Fig. 3.1 Solar-normalized abundances of heavy elements in an ancient metal-poor star. (a) The metallicity of the star is [Fe/H] = −3.0. The abundances of the n-capture elements are expressed as log ε (X) = log (X/H) +12 (see the Glossary). The black line is the solar system r-process abundance curve normalized to the observed abundance of Eu considered as an only-r-process element. The grey line corresponds to the solar s-process element abundance pattern, normalized to the Sr–Zr group of mainly s-process elements. (b) The small difference between the solar abundances of heavy r-process elements and those observed in metal-poor stars points to the universality of the main r-process, whereas the lighter elements (e.g. the mainly r-process Ag) do not fit so well. From Cowan and Sneden (2006). Reproduced by permission from Macmillan Publishers Ltd., © 2006.

the heavy ones. Moreover, studies of a large sample of very metal-deficient stars show that the abundance ratios of light and heavy n-capture elements, e.g. Sr/Ba, scatter over more than an order of magnitude even though both are mainly generated in s-process nucleosynthesis. This implies the production of the lighter elements in different nucleosynthetic processes. Beers and Christlieb (2005) presented a detailed review of this new and exciting topic of astrophysics.

3.3 Presolar grains

Dust is an important host for the heavy refractory elements in interstellar clouds. Primitive meteorites that escaped intensive processing during solar system

formation preserve presolar dust, grains of which can be separated and directly studied in laboratories on Earth. Their typical size is $\sim$ 1 μm or smaller, down to $\sim$ 1 nm. They are set apart from other meteoritic constituents by refractory (and sometimes unusual) chemical compositions and mineralogy, including carbon-rich phases (graphite, diamond, SiC), oxides (such as corundum or Al-rich hibonite) and rare minerals such as silicon nitride. The chemical and isotopic compositions of interstellar grains can preserve a record of their formation and evolution; reading this record is a new branch of science, known as grain astrophysics (Zinner, 1998).

These grains were originally formed from stellar material ejected into the interstellar media; this material included species inherited from the prestellar cloud and those generated within the star. When ejected, this became mixed with interstellar gas; it then cooled down and the refractory component condensed (Sedlmayr and Kruger, 1997).

Shocks, sputtering, thermal annealing, irradiation by cosmic rays, coagulation and other mechanisms further affected the grains. Depending on the shock energy and grain chemistry, grains could be partially or completely vaporized and then recondense. The mean residence time of an atom in a grain is estimated at $\sim$ 0.3 Gyr and the mean residence time of a metal atom in the interstellar medium is $\sim$ 1 Gyr; that means that most particles were modified or completely reworked while in the cloud (Draine, 2003). Finally the grains studied on Earth also endured solar system formation, irradiation by the furious early Sun and the agglomeration and accretion of meteorite parent bodies as well as subsequent metamorphic processes, irradiation and ablation on the way to Earth and weathering on the Earth's surface.

These numerous processes have indeed affected the compositions of presolar grains and the degree of their preservation. Therefore their presently observed abundances in meteorites depend on meteorite class (i.e. the conditions of formation and metamorphism) and on grain compositions (Huss *et al*., 2004). Diamonds are the most resistant minerals and their inferred abundances in carbonaceous chondrites are larger and less variable, from $\sim$ 300 to 1500 μg g^{-1}, than those of SiC (0.01 to 14 μg g^{-1}) and graphite (0.1 to 10 μg g^{-1}). Notwithstanding these low abundances and complicated evolution, presolar grains have yielded a large amount of robust data which cannot be derived from other sources. The fact of their preservation itself validates solar nebula models that envisage only partial vaporization and recondensation of presolar dust in the asteroid belt, where meteorite parent bodies were formed (Fig. 14.1). The isotopic compositions of major and trace elements constituting the grains are particularly important, as they are used to test models of stellar nucleosynthesis (Chapters 5, 6 and 8). Their huge isotopic heterogeneities highlight the fact that a multitude of stars ($\sim 10^3$) contributed to the matter in the solar system, which thus reflects many types of nucleosynthetic stellar processes.

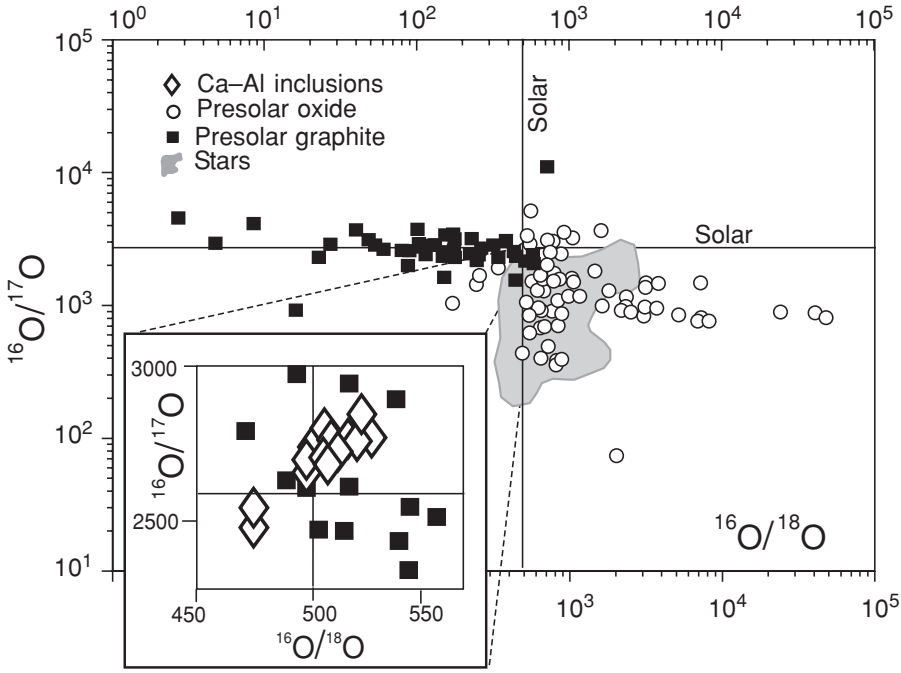

Fig. 3.2 Oxygen-isotope compositions in presolar grains. Stellar (main figure) and solar system (inset) compositions are shown for comparison. Note the much greater variations in O-isotope compositions in presolar grains than those in solar system materials. The oxygen compositions in presolar graphite differ from observable stellar compositions. After Zinner (1998) and Nittler (1997).

Figures 3.2–3.4 present the isotopic abundances of O, N, C and Si in such grains. Oxygen-isotope ratios (Fig. 3.2) show trends towards ^{18}O enrichment in graphite and ^{18}O depletion in oxide grains. Both these trends deviate greatly from the population seen in stellar atmospheres, towards end-member ratios hardly observed in any stars. Also the extremely heavy oxygen discovered in Si-rich grains from the Murchison meteorite does not fit the stellar yield of oxygen isotopes (Aleon *et al*., 2005). These unusual grains show solar (i.e. terrestrial) Si-isotope composition, in contrast with those of mainstream and anomalous presolar grains (Fig. 3.4).

In most SiC grains (Figs. 3.3, 3.4), the C, N and Si compositions all show a main population lying in the field of carbon-rich stars; the anomalously low $^{12}C/^{13}C$ ratios correspond to those observed in the atmospheres of a minor population of carbon stars (Section 8.2). In individual mainstream SiC grains an excess of ^{99}Ru is a product of the decay of s-process-yielded ^{99}Tc. This points to the operation of s-process nucleosynthesis in the course of the evolution of low-mass stars (Section 5.4).

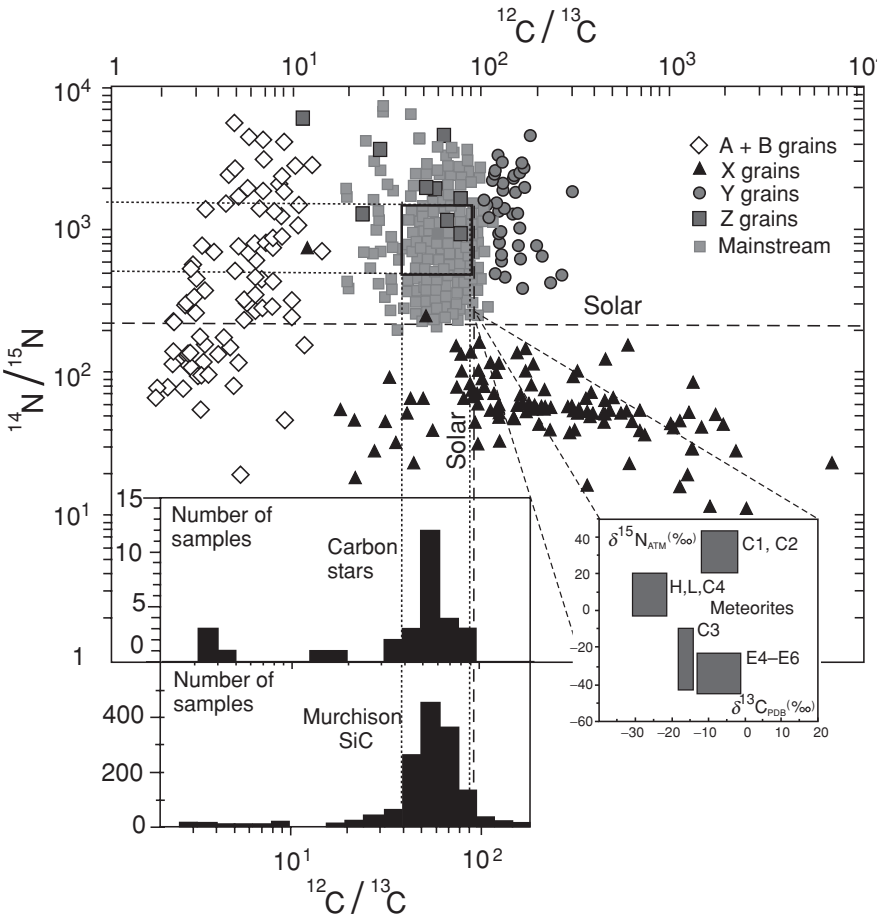

Fig. 3.3 Main figure, C- and N-isotope compositions in presolar grains. Stellar and meteoritic compositions (left- and right-hand insets) are shown for comparison. Note the similarity in the C-isotope compositions of grains from Murchison C1 (mainstream carbon) and carbon stars; the bottom right inset shows N- and C-isotope compositions typical of these stars. Many grains display anomalous compositions (see the classification at top right). The N- and C-isotope compositions in bulk meteorites vary within a much narrower range than those for presolar grains: the mixing of matter in the solar nebula was quite efficient! See the Glossary entry for "abundance" for a definition of the δ notation. After Kung and Clayton (1978), Hoppe and Ott (1997), Zinner (1998) and Ott (2003).

High $^{12}C/^{13}C$ and low $^{14}N/^{15}N$ ratios and high abundances of ^{28}Si have no present stellar-atmosphere equivalent (Figs. 3.3 and 3.4). An excess of ^{28}Si also appears to be correlated with an inferred excess of ^{44}Ti (Fig. 3.5): abundances of the stable daughter nuclide of the latter, ^{44}Ca, are extremely high (a factor $\sim$ 100 above the SOS value) thus implying a nucleosynthetic source but also identifying this source

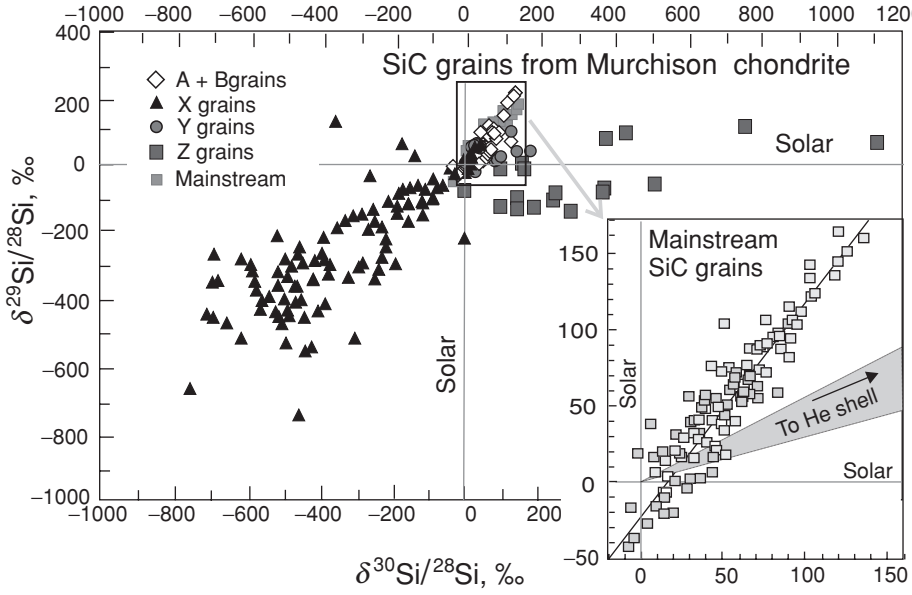

Fig. 3.4 Silicon-isotope compositions in presolar grains. The various types of anomaly are discussed in the text. Note that the solar Si-isotope composition appears to be anomalous relative to the mainstream SiC range, in contrast with the O, C and N compositions. After Zinner (1998). Reproduced by permission from *Annual Reviews*, © 1998.

as supernovae (Chapter 6). This would explain why the isotope signature of this group does not correspond to any presently observed stellar atmosphere.

These isotopic fingerprints allow us to identify the grain sources and further to understand the nature of other "cosmopolitan" nuclides in a grain, such as ^{27}Al and ^{41}Ca: these important isotopes are abundant in some grains and in principle could be generated in both small and massive stars (Zinner *et al.*, 2006). The respective models are discussed in Chapters 5, 6 and 8. Here we merely note that isotope signatures seen in presolar grains may be in the main related to two types of stellar source: stars of up to five solar masses at late stages of their evolution (RGB and AGB) on the one hand and supernovae on the other hand (Zinner, 1998; Amari *et al.*, 2001a).

Isotopic anomalies also shed light on the efficiency of mixing in the presolar cloud and nebula. Of the ^{14}N/^{15}N and ^{12}C/^{13}C anomalies discussed above, there is no trace in any solar system materials other than the presolar grains themselves. Oxygen-isotope ratios show a small heterogeneity among meteorite parent bodies and planets, particularly in early-formed highly refractory Ca–Al inclusions in chondritic meteorites. This heterogeneity is generally considered to reflect multiple sources for the solar nebula. Its largest extent is shown in Fig. 3.2, where its

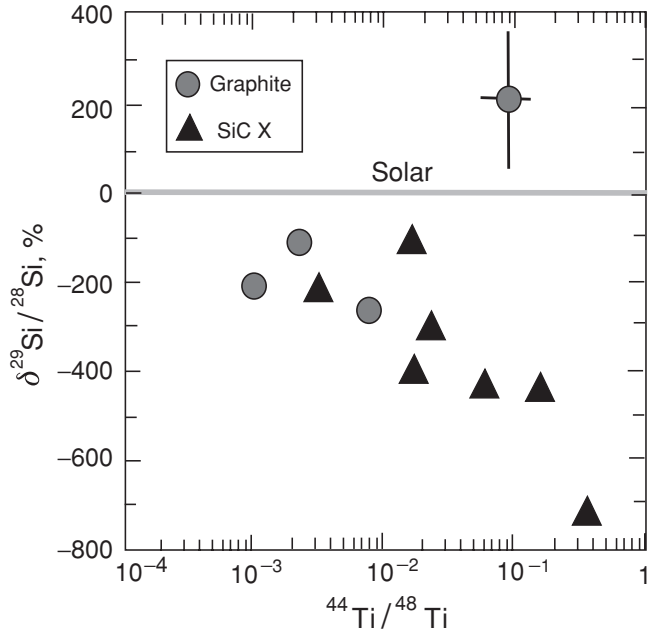

Fig. 3.5 Titanium- and silicon-isotope correlation in presolar grains. Note that ^{44}Ti is a radioactive isotope ($\tau_{44} = 85$ yr) and its abundance is measured via a ^{44}Ca anomaly. Titanium-44-bearing grains must have condensed within ~ 100 yr after the explosion, otherwise no ^{44}Ca anomaly could have built up in them. The correlation (except for one grain) indicates that the ^{28}Si and ^{44}Ti were probably produced by the same process (Section 6.3). After Zinner (1998). Reproduced by permission from *Annual Reviews*, © 1998.

insignificance compared to the large heterogeneity in presolar grains is apparent. Obviously highly efficient mixing characterized solar nebula formation.

3.4 The solar system element and isotope abundances

Environments, processes and behaviour of the elements: some phenomenology

The Sun, our closest star, together with the planetary system allows an average elemental and isotope composition of matter typical of the solar neighbourhood (a 4.5-Gyr-old segment of the Milky Way Galaxy near the Sun) to be established. This so-called standard or reference composition is widely used in the astronomical literature for comparison with other objects or regions. The Sun is a typical low-mass star situated within the main sequence in the Hertzsprung–Russell (H–R) diagram (Fig. 5.1). The chemical composition of the Sun appears to be typical for a number of stars having similar size and evolution, so the solar composition may be considered as a convenient reference.

Table 3.1 *Chemical classification of the elements*[a] *using volatility and affinity to metallic or silicate phases as criteria*[b]

Elements	Lithophile (silicate)	Siderophile and/or chalcophile
refractory $T_C = 1400$ to 1850 K[c]	Al, Ca, Ti, Be, Ba, Sc, Sr, Y, Zr, Nb, REE, Hf, Ta, Th, U, Pu	V, Mo, Ru, Rh, W, Re, Os, Ir, Pt
transitional $T_C = 1250$ to 1350 K	Mg, Si, Cr, Li	Fe, Ni, Co, Pd
moderately volatile $T_C = 700$ to 1230 K	Mn, P, B, Na, Rb, K, F, Zn	Au, Cu, Ag, Ga, Sb, Ge, Sn, Se, S, Te, As
highly volatile $T_C < 700$ K	Cl, Br, I, Cs, H, C, O, He, Ne, Ar, Kr, Xe	Cd, In, Tl, Bi, Pb, Hg

[a] Elements are not listed in order of increase of the given characteristics.
[b] After Wasson (1985), McDonough and Sun (1995), Palme (2000) and Palme and Jones (2003).
[c] T_C is the condensation temperature at a pressure of 10^{-4} bar.

Several independent approaches can be applied to determine the chemical and isotopic composition of the solar system: spectroscopy of the Sun's photosphere; measurements of solar-wind implantations in manmade and natural materials; the study of objects orbiting the Sun, e.g. planets, satellites, meteorite parent bodies and comets.

Deriving an inventory from all these data sources is not straightforward, for many reasons. Regarding the raw material, interstellar grains are greatly heterogeneous (Section 3.3) and differ in isotope composition from interstellar gas. Even after substantial mixing, traces of initial heterogeneity are observed in present-day solar system materials and the compositions depend on the origin and evolution of each given object. During the accretion of solid bodies in the solar nebula, chemical fractionation generally took place, at least in the inner segment where the terrestrial planets were formed. If the behaviour of a given element is known, it is possible to predict the effect that such fractionation processes could have on it. There are several classifications of the elements based on their behaviour in different natural fractionation processes (Table 3.1). For example, during condensation and crystallization from a hot gas in circumstellar or nebula environments, minerals formed by refractory elements such as Zr (which forms zircon) or Al (which forms corundum) grow first while other elements are still in the gas phase (Chapter 10). If some process subsequently separates the gas and solid phases, elements having different volatilities will be fractionated. Another example

is the separation of metallic iron from silicate material in meteorite parent bodies or planetary interiors. In this process siderophile elements were presumably partitioned into the metal, leaving the silicate mantles depleted in these elements (Chapter 18).

Some bodies in the asteroid belt (Fig. 14.1) have undergone only minor processing and therefore may be used to reconstruct the bulk solar system composition. Collisions have allowed samples of these bodies to be delivered to our planet as meteorites. The class of meteorites known as chondrites contains small spheroids called chondrules (hence their name) and have a complicated, non-equilibrium, texture, indicating relatively primitive material. Traditionally, C1, carbonaceous, chondrites are considered to be the most primitive, and their composition is used as a reference even though unfortunately they have not avoided hydrous alteration (Chapter 11). Even though C1 meteorites contain volatile-rich low-temperature material, as solid bodies they have preserved only a tiny portion of gases. Therefore the solar abundances of the highly volatile elements H, C, N and of the noble gases have to be derived from spectroscopic measurements on the solar atmosphere, solar-wind studies and investigations of the giant planets.

C1-meteorite, solar and terrestrial element and isotope abundances: a comparison

Except for the highly volatile elements (the last row in Table 3.1) the agreement between the two reservoirs, C1 meteorites and the solar photosphere, appears to be remarkably good for the majority of elements. The similarity for the refractory siderophile and lithophile elements, measured with relatively good precision, is the most impressive (Fig. 3.6). Anders and Grevesse (1989) discussed reasons for the discrepancies observed for several elements.

In contrast with C1 meteorites, the terrestrial planets are highly differentiated bodies that have experienced a complicated evolution, as discussed below in Parts III and IV of the book, and no terrestrial sample could ever be imagined to represent the bulk Earth composition. To some degree, the refractory lithophile elements present an exception. Although the abundances of Al, Zr, Nb, the rare Earth elements (REEs), U, Th and some others are found to be fractionated, in the Earth's accessible reservoirs (EARs), they nevertheless enable us to postulate a tight affinity of terrestrial and chondritic matter.

Isotopic arguments reinforce the affinity of solar, meteoritic and terrestrial matter. The similar chemical behaviour of the isotopes of one element tends to restrict their relative fractionation in chemical processes. This is the case for most elements, especially those that are refractory. Figure 3.7 illustrates the similarity of solar and chondritic isotopic compositions for several abundant elements; the solar data

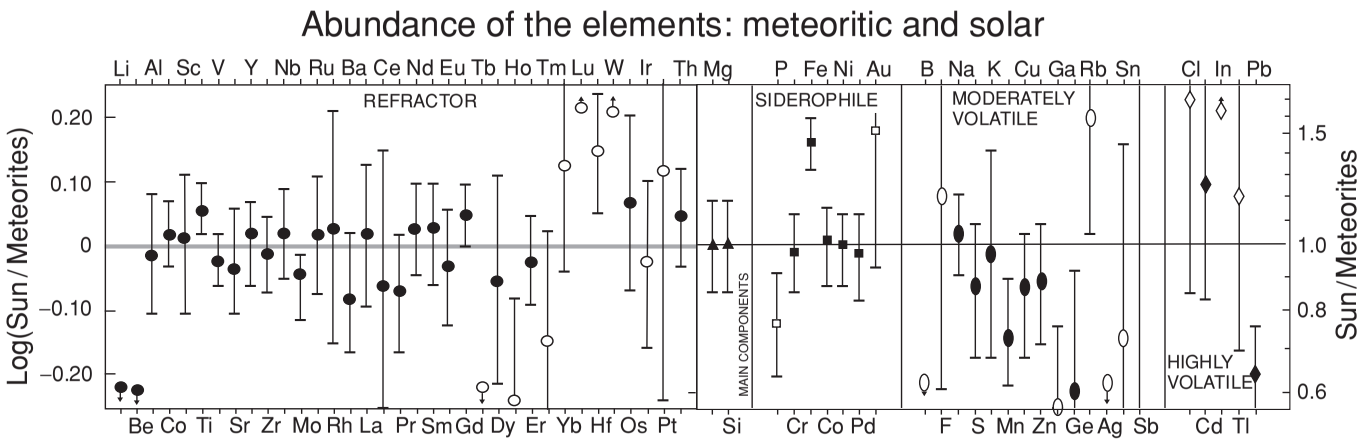

Fig. 3.6 Comparison of solar and meteoritic abundances of the elements. Agreement between the solar and C1 abundances of the elements appears to be remarkably good, especially taking into account that both reservoirs, the solar photosphere and the C1 parent bodies, represent a negligibly small portion of solar system material. From Anders and Grevesse (1989), © Pergamon Press 1989, reproduced by permission of Elsevier Science.

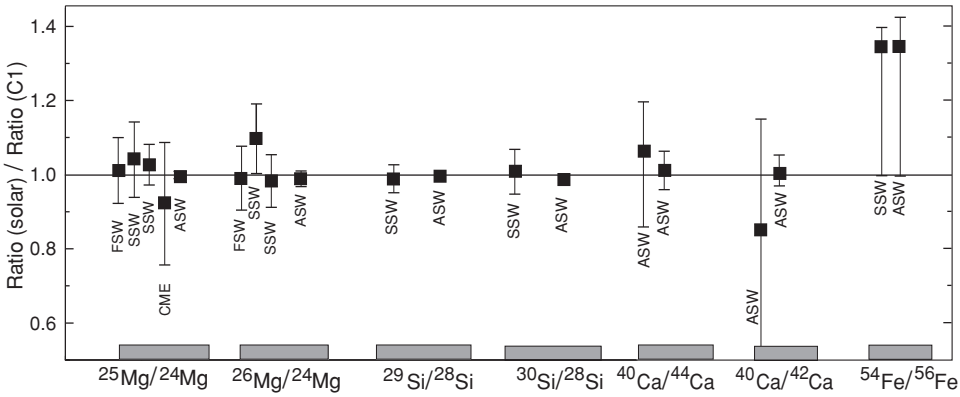

Fig. 3.7 The isotope compositions of several abundant elements in solar emissions and in C1 chondrites are indistinguishable (within the precision of the measurements). SSW, slow solar wind; FSW, fast solar wind; ASW, average solar wind; CME, coronal mass ejection. After Anders and Grevesse (1989), Wimmer-Schweingruber *et al.* (1998, 1999a, b) and Kallenbach (2001).

were obtained from solar-wind analyses. Even though solar-wind propagation itself probably causes some fractionation, the observed agreement is quite good. These abundant elements are among the major building blocks of the Earth, together constituting more than half the Earth's mass. Their terrestrial, lunar and meteoritic isotopic compositions are indistinguishable except in presolar grains, as discussed above. Moreover, the initial ratios of daughter radiogenic and stable reference isotopes, e.g. $^{87}Sr/^{86}Sr$ or $^{143}Nd/^{144}Nd$, comprise a self-consistent set of systematics for meteorites and the Earth.

The comparison of elemental abundances together with the isotopic arguments leaves little doubt that the solar system as a whole was made from the same relatively well (but not completely) mixed material (Figs. 3.6, 3.7).

Solar system elemental and isotope abundances

Following the above discussion, a reference solar system composition may be synthesized from two principal sets of objects:

- the solar atmosphere and neighbouring interstellar clouds, which are especially important for constraining the abundances of H, the noble gases and some other volatile elements;
- meteoritic and planetary materials, as well as the matter in other objects within the solar nebula.

The first-order trend seen in the integrated solar system abundances of the elements is a decrease in abundance as the atomic number increases: the more massive the element, the lower the abundance (Fig. 3.8 and Table 3.2). Against the

Table 3.2 *Solar system abundance of the elements, from Anders and Grevesse (1989), © Pergamon Press 1989, reproduced by permission of Elsevier Science*

Z	Element	Atoms per 10^6 atoms of Si
1	H	2.79×10^{10}
2	He	2.72×10^{9}
3	Li	57.1
4	Be	0.73
5	B	21.2
6	C	1.01×10^{7}
7	N	3.13×10^{6}
8	O	2.38×10^{7}
9	F	843
10	Ne	3.44×10^{6}
11	Na	5.74×10^{4}
12	Mg	1.07×10^{6}
13	Al	8.49×10^{4}
14	Si	1.00×10^{6}
15	P	1.04×10^{4}
16	S	5.15×10^{5}
17	Cl	5.24×10^{3}
18	Ar	1.01×10^{5}
19	K	3.77×10^{3}
20	Ca	6.11×10^{4}
21	Sc	34.2
22	Ti	2.4×10^{3}
23	V	293
24	Cr	1.35×10^{4}
25	Mn	9.55×10^{3}
26	Fe	9.0×10^{5}
27	Co	2.25×10^{3}
28	Ni	4.93×10^{4}
29	Cu	522
30	Zn	1.26×10^{3}
31	Ga	37.8
32	Ge	119
33	As	6.56
34	Se	62.1
35	Br	11.8
36	Kr	45
37	Rb	7.09
38	Sr	23.5
39	Y	4.64
40	Zr	11.4
41	Nb	0.698
42	Mo	2.55
44	Ru	1.86
45	Rh	0.344
46	Pd	1.39

Table 3.2 *(cont.)*

Z	Element	Atoms per 10^6 atoms of Si
47	Ag	0.486
48	Cd	1.61
49	In	0.184
50	Sn	3.82
51	Sb	0.309
52	Te	4.81
53	I	0.9
54	Xe	4.7
55	Cs	0.372
56	Ba	4.49
57	La	0.446
58	Ce	1.136
59	Pr	0.167
60	Nd	0.828
62	Sm	0.258
63	Eu	0.097
64	Gd	0.33
65	Tb	0.06
66	Dy	0.394
67	Ho	0.089
68	Er	0.251
69	Tm	0.038
70	Yb	0.248
71	Lu	0.037
72	Hf	0.154
73	Ta	0.021
74	W	0.133
75	Re	0.052
76	Os	0.675
77	Ir	0.661
78	Pt	1.34
79	Au	0.187
80	Hg	0.34
81	Tl	0.184
82	Pb	3.15
83	Bi	0.144
90	Th	0.0335
92	U	0.009

background of this trend several important features are readily recognized, some of which result from the particular binding energy characteristics of nuclei (Section 1.2). The light elements Li, Be and B, having low binding energies, are of low abundance. Iron and its neighbouring elements, which have the highest binding energies (Fig. 1.2), are overabundant, constituting the iron peak. Some other tightly

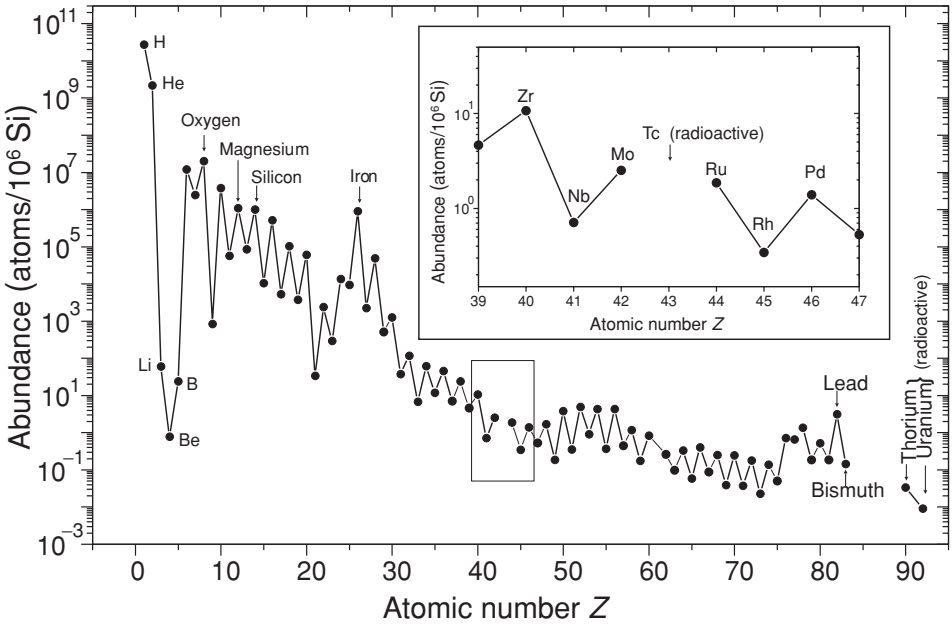

Fig. 3.8 Abundance of the elements in the solar system. Note the overall smooth decrease in abundance except for a severe underabundance of the light fragile elements and several peaks related to species with magic proton and neutron numbers. The Fe peak is especially distinct because its isotopes have the highest binding energy per nucleon (see Fig. 1.2). The inset shows the only gap in the abundance curve: all Tc isotopes are radioactive ($\tau \sim 10^5$ yr or less) and Tc is observed only in stellar photospheres, thus indicating that it is produced in stars. After Anders and Grevesse (1989).

bound elements (e.g. Pb, with doubly magic ^{208}Pb) are more abundant than their neighbours. The heaviest elements, having low binding energy, are unstable and show negligibly low natural abundances except for relatively long-lived U and Th. The short-lived element Tc is also absent (see the inset in Fig. 3.8).

The sawtooth shape of the abundance curve is also predicted. For the heavy elements it results primarily from the fact that elements with even Z can have many isotopes, whereas in the light elements the greater binding energy of even–even nuclei is the most important factor (Section 1.2).

These and other features are also seen in Fig. 3.9, which summarizes the solar system isotopic abundances (Anders and Grevesse, 1989). The odd–odd nuclei are characterized by quite low binding energy, and only four of these nuclei are stable. The abundances of the even–odd species can be approximated by a smoother curve than that for the even–even species. This results from the differing decay chains for odd and even isobars (Fig. 1.4). Most even–even nuclei are at the top of the isotope

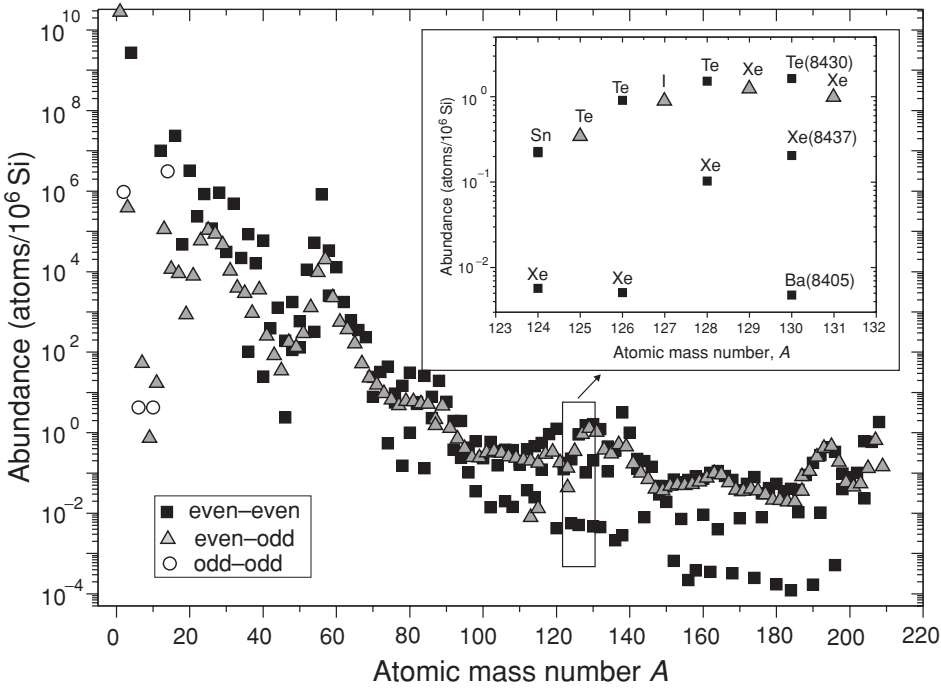

Fig. 3.9 Abundances of the isotopes in the solar system. In accordance with predictions from the binding energy data (see Fig. 1.2), even–even isotopes, having higher binding energies, are generally more abundant than even–odd ones. Also, the abundance curve for even–odd species is smoother than the distribution of even–even isotopes as a result of the averaging via radioactive decay of the precursors (see Fig. 1.4). The inset shows that, for a given isobar, generally only one even–odd stable isotope is in existence whereas two to three even–even species occur; the reason for this phenomenon is illustrated in Fig. 1.4. The different abundances of isobars, e.g. ^{130}Te, ^{130}Xe and ^{130}Ba (for which the numbers in parentheses show the binding energy in keV per nucleon) are discussed in the main text. After Anders and Grevesse (1989).

abundance trend, in overall accord with their high binding energy (see the inset in Fig. 3.9).

However, the abundances of heavy even–even nuclides ($A > 100$) belonging to one isobar family generally differ by up to a factor 1000, although the neighbouring nuclides have similar binding energies (Fig. 1.2). A convincing example is presented by ^{130}Te, ^{130}Xe and ^{130}Ba (see the inset in Fig. 3.9): the last is much less abundant even though the binding energies of the trio are almost equal. What is different for these n-capture nuclides is their site in the N–Z plot (see the lower inset in Fig. 1.3): abundant Te isotopes occupy the lowest line of the stability valley and therefore could have been yielded via n-capture + β-decay processes, whereas ^{130}Ba stays on the opposite side of the valley and is screened from these processes by the chain

of stable Xe isotopes. The occurrence of several isotopes (belonging to different elements) within one even-isobar family is governed by the binding energies of odd–odd and even–even isotopes (Fig. 1.4). Here the binding energy distributes the priorities of formation of n-capture elements and the nucleosynthetic processes follow these priorities (Chapters 5 and 6).

A comparison of the reference solar abundances with those obtained from modelling the chemical evolution of our Galaxy indeed shows good conformity. Realistic models of galactic chemical evolution should take into account not only the various nucleosynthetic sources but also the complicated mixing processes illustrated by the data on presolar grains. Clearly the solar system abundances represent some grand average (Timmes *et al*., 1995). It is further noteworthy that recent investigations of the local interstellar clouds show little difference between their composition and that of the solar neighbourhood 4.6 Gyr ago, as represented by the solar system itself. It would appear that the chemical evolution of the Galaxy, at least in the solar vicinity, has been relatively minor during the last $\sim$ 5 Gyr (Gloeckler and Geiss, 2001; Salerno *et al*., 2001).

Solar system sample of short-lived nuclides

Above we discussed the abundances of the stable or long-lived radioactive isotopes observable at present. Although the short-lived radioactive isotopes incorporated during solar system formation have all decayed, their daughter isotopes can be detected by the isotope analysis of meteoritic materials (Section 10.4). The isotopic systematics of these nuclides and their daughter isotopes are cosmochronometers that present a unique opportunity to measure short time intervals relevant to the formation of the solar system (Table 3.3). Thus, the evidence for radioactive nuclides with $\tau < 1$ Myr (^{41}Ca, ^{26}Al) in refractory inclusions in meteorites limits the time interval between the generation of these nuclides in stellar nucleosynthesis and the formation of first solid grains in the solar nebula to < 1 Myr, unless these nuclides were generated within the nebula (Section 8.3).

Also, these systematics shed light on the processes that could have triggered the collapse of an interstellar cloud and subsequent star formation. For example, it is likely that ^{182}Hf (half-life 9 Myr) is only produced in explosive stellar nucleosynthesis. It was incorporated into meteorites and even planets, which indicates a short time interval between nucleosynthesis and the formation of large solid objects within the solar system. This lends support to the idea that the interaction of a shock wave from a stellar explosion and a cold presolar cloud could have triggered the collapse of the latter, leading to the formation of the Sun and the solar nebula (Boss and Vanhala, 2000).

Table 3.3 *Short-lived radioactive isotopes ^{r}R in the solar system, their production processes[a] and fractionation processes[b]. Listed for each ^{r}R are a stable "brother" ^{s}R, the daughter nuclide ^{r}D, a stable "brother" ^{s}D of the daughter isotope and the $^{r}R/^{s}R$ ratios for stellar production. All ratios are atomic*

Source[c]	Radio-nuclide ^{r}R	Half- life, Myr	Ref. nuclide ^{s}R	Nucleosynth. prod. ratio	SOS initial $^{r}R/^{s}R$	Daughter nuclide ^{r}D	Ref. nuclide ^{s}D	SOS initial $^{r}D/^{s}D$
(1)	^{41}Ca	0.10	^{40}Ca	3×10^{-3}	1.5×10^{-8}	^{41}K	^{39}K	0.072
(2)	^{26}Al	0.73	^{27}Al	4×10^{-3}	5×10^{-5}	^{26}Mg	^{24}Mg	0.1393
(3)	^{60}Fe	1.49	^{56}Fe	1×10^{-5}	3.5×10^{-7}	^{60}Ni	^{58}Ni	0.382 18
(4)	^{10}Be	1.52	^{9}Be	7×10^{-2}	8.8×10^{-4}	^{10}B	^{11}B	0.2538
(5)	^{53}Mn	3.7	^{55}Mn	0.13	8.5×10^{-6}	^{53}Cr	^{52}Cr	0.113 45
(6)	^{107}Pd	6.5	^{108}Pd	0.65	2×10^{-5}	^{107}Ag	^{109}Ag	1.11
(7)	^{182}Hf	9	^{180}Hf	0.21	1.01×10^{-4}	^{182}W	^{184}W	0.864 48
(8)	^{129}I	15.7	^{127}I	1.4	1×10^{-4}	^{129}Xe	^{130}Xe	6.27
(9)	^{244}Pu	81	^{238}U	0.7	1×10^{-2}	^{136}Xe	^{130}Xe	1.79
(10)	^{146}Sm	103	^{144}Sm	0.1	7.5×10^{-3}	^{142}Nd	^{144}Nd	1.1416

[a] Nucleosynthesis processes (Chapters 5, 6, 8) and isotopes produced by them: O burning (^{41}Ca); H-shell burning, explosive Ne burning (^{26}Al); s-process (^{41}Ca, ^{107}Pd, ^{182}Hf); explosive Si burning (^{53}Mn); nuclear statistical equilibrium (^{60}Fe, ^{53}Mn); supernovae Ia (^{60}Fe, ^{53}Mn, ^{146}Sm); r-process (^{107}Pd, ^{129}I, ^{182}Hf, ^{244}Pu); p-process (^{146}Sm); energetic particle irradiation in circumstellar disk (^{10}Be, ^{26}Al, ^{41}Ca, ^{53}Mn).

[b] Major fractionation processes (for systematics shown in parentheses): degassing (^{244}Pu $\rightarrow$ $^{136-131}$Xe); degassing, hydrous alteration (^{129}I $\rightarrow$ ^{129}Xe); volatility difference (^{41}Ca $\rightarrow$ ^{41}K, ^{107}Pd $\rightarrow$ ^{107}Ag); partitioning in coexisting metal and silicate phases (^{182}Hf $\rightarrow$ ^{182}W, ^{60}Fe $\rightarrow$ ^{60}Ni); partitioning between coexisting silicate solid and melted phases (^{146}Sm $\rightarrow$ ^{142}Nd); partitioning between coexisting silicate and oxide phases (^{26}Al $\rightarrow$ ^{26}Mg); partitioning between coexisting silicate minerals and spinel (^{53}Mn $\rightarrow$ ^{53}Cr).

[c] Modified after Meyer and Clayton (2000) using the following contributions: (1) Srinivasan *et al.* (1996); (2) Hsu *et al.* (2000); (3) Tachibana and Huss (2003) and Mostefaoui *et al.* (2004); (4) Chaussidon *et al.* (2006) and Gounelle *et al.* (2006); (5) the initial ^{53}Cr/^{52}Cr ratio varied within the inner nebula; here the ratio for the asteroid belt is presented as determined from the CC isochron. From Lugmair and Shukolyukov (1998) and Shukolyukov and Lugmair (2006); (6) Chen and Wasserburg (1996); (7) SOS parameters after Jacobsen (2005); (8), (9) from Table 28.1; (10) Amelin and Rotenberg (2004).

The short-lived isotopic systematics are important tracers of fractionation and mixing in the solar nebula. It is particularly important that they allow short time intervals between the formation of different objects or materials to be reliably determined (Lugmair and Shukolyukov, 1998).

The decay of short-lived nuclides generates heat, and this source could be important for the development of planetesimals in the early planetary nebula (LaTourrette and Wasserburg, 1998). This may apply to ^{26}Al because of the sufficiently high abundance and refractory behaviour of this nuclide as well as the high energy released by its decay.

For these reasons, a discussion of the generation of the short-lived nuclides and their evolution is included in the sections mentioned below. The ^{26}Al–^{26}Mg systematics are especially important and have been widely investigated in meteorites and presolar grains (Section 8.3). The half-life of ^{26}Al (0.72 Myr) is much longer than the time of formation of solid grains in an expanding stellar envelope (Section 6.3); the highest ratios observed should come close to the production values. In some SiC grains (those of type X) the initial ^{26}Al/^{27}Al ratio approaches 0.2 (Huss *et al.*, 1997). Such observations are a stimulus for further, more refined, nucleosynthesis modelling.

3.5 Summary

In this chapter we have summarized the observed abundances of the elements, mainly within our Galaxy, which will help us to address the question of which processes were chiefly responsible for the production and evolution of the elements.

In juvenile low-metallicity interstellar clouds, H and He are major constituents. The binding energy considerations and the uniform abundances at which they are observed in such clouds imply that H and He isotopes might have been generated first and have served as raw material for the heavier elements.

Small ancient ultra-metal-poor stars present a set of elements synthesized very early, in the first stellar generations: light α-capture and heavy n-capture elements were abundant in the early Galaxy, in contrast with elements having intermediate atomic masses, around and above the iron peak. The pattern of relative abundances of the heavy elements in these stars is indistinguishable from that in the solar system, indicating a unique universality of the nucleosynthetic process that formed them.

The production of the heavy elements in stars and their ejection into the interstellar medium leads to the condensation of dust grains that contain the refractory heavy-element budget of interstellar clouds. Presolar grains found in primitive meteorites show a spread of isotopic compositions over several orders of magnitude for a number of elements and bring important constraints to bear on the sources and nucleosynthetic processes involved.

The average solar system element and isotopic abundances are constrained much better than those in any other astrophysical objects. The abundances of almost all elements in the least processed meteorites have been found to be almost indistinguishable from the solar values, indicating that the Sun and the planetary system were formed from the same material. The isotopic compositions of the abundant elements Mg, Si, Ca, Fe are very similar in meteorites and solar emissions. This similarity of solar and planetary material is in full accord with dynamical models of the formation of stars and circumstellar disks. The isotopic homogeneity of the solar system in comparison with the presolar grain population indicates that the nebular stage of solar system evolution involved a great amount of mixing.

The observed solar system abundances of the elements and isotopes are in good agreement with the predictions from the binding energy of their nuclei, which include an excess of iron-group elements relative to their neighbours, a sawtooth abundance pattern and an overabundance of the magic isotopes. This agreement implies that the binding strength of a nucleus played an important role in the nucleosynthetic processes discussed in the following chapters.

4

Cosmological nucleosynthesis: production of H and He

4.1 The expanding Universe and the Big Bang hypothesis

Friedmann (1922) was the first to postulate the model of an expanding Universe that originated in one explosion-like event. Soon afterwards Hubble (1929) discovered the relationship between the redshifts, due to the Doppler effect, in the spectra of distant stars, galaxies or galactic clusters and the distances to these objects: the further the object the larger the redshift, i.e. the greater the outward velocity (see Section 4.3). These relationships were considered as the first important confirmation of Friedmann's model, which is now generally accepted.

Later, further supporting evidence was found. The uniform He/H ratio in astrophysical objects with low metallicity, discussed in Section 3.1, was shown to be identical to that predicted by the Big Bang nucleosynthesis (BBN) model. Further, important support for the Big Bang hypothesis was the observation of the cosmic microwave background radiation (Penzias and Wilson, 1965), which had been predicted by Gamow's Big Bang model. From recent high-precision satellite-based measurements of this radiation, several important cosmological parameters including the Hubble parameter and the primeval D/H ratio have been inferred, and these are in excellent agreement with the values actually observed (Spergel *et al*., 2003). Also, all independent estimates of the age of BBN and of the most ancient objects formed in the Galaxy are remarkably consistent (Sections 4.3 and 7.2).

Thus the model of an expanding Universe that originated in one short single explosion-like event appears to be by far the most convincing; Big Bang nucleosynthesis yielded the primeval baryonic matter of the Universe, and this is discussed briefly below.

4.2 Big Bang nucleosynthesis (BBN)

The BBN model envisages the synthesis of the lightest elements to have occurred during the first 30 minutes of the history of the Universe in an "expanding box",

while the temperature and density decreased from 10^{11} to 10^9 K and from 10 to 10^{-5} g cm^{-3} respectively (Schramm and Turner, 1998). At very high temperatures around a few MeV (which is somewhat below 10^{11} K), weak interactions maintain the proton–neutron equilibrium:

$$\begin{aligned} \mathrm{n} + \mathrm{e}^+ &\leftrightarrow \mathrm{p} + \nu_\mathrm{e}^*, \\ \mathrm{p} + \mathrm{e}^- &\leftrightarrow \mathrm{n} + \nu_\mathrm{e}. \end{aligned} \tag{4.1}$$

Here ν_e and ν_e^* are the electron neutrino and antineutrino, and p and n are the principal building blocks of nuclei. The n/p ratio depends on the binding energy and temperature as follows:

$$\mathrm{n/p} = \exp(-\varepsilon_\mathrm{n}/kT) \tag{4.2}$$

where $\varepsilon_\mathrm{n} = (m_\mathrm{n} - m_\mathrm{p})c^2$ is the neutron–proton rest-mass difference, 1.293 MeV (Schramm and Turner, 1998). The production of nuclei is controlled by two competing factors: the binding energy, which favours the stability of nuclei, and the entropy, which disfavours the stability of nuclei via interactions with energetic photons. When the temperature had decreased to $\approx 5 \times 10^9$ K, the corresponding n/p ratio was $\sim 1/6$ (Eqn 4.2). At that temperature the weak interactions (Eqn 4.1) were sharply terminated as the photon energies were insufficient to disrupt nuclei. The system departed from nuclear equilibrium, the number of neutrons was frozen and the accumulation of heavier species started following the pathways shown in Fig. 4.1. The time scale of BBN was shorter than the neutron half-life outside the nucleus (see Fig. 4.3); therefore ^{4}He, having an extreme binding energy, succeeded in trapping almost all neutrons. The mass fraction of ^{4}He produced was thus

$$Y(^4\mathrm{He}) \approx \frac{2(\mathrm{n/p})}{1 + (\mathrm{n/p})} \approx 0.28, \tag{4.3}$$

which is close to the measured value, 0.24 ± 0.02 (Section 3.1).

Fragile D and ^{3}He (see Fig. 1.2) were substantially underabundant relative to ^{4}He (Fig. 4.2), and Li and heavier nuclei were even more underabundant because there are no stable isobars with $A = 5$ or 8 (Fig. 4.1): only reactions 7 and 10 between charged nuclei were able to overcome the gaps, and these reactions have very high Coulomb barriers. Also, fragile ^{7}Li and ^{7}Be easily disintegrate back to ^{4}He via reactions 11 and 12. These peculiarities and the rapid cooling of the expanding envelope prevented the cosmological synthesis of heavier elements (Schramm and Turner, 1998; Burles *et al*., 2001).

During and after BBN fragile D-nuclei were being destroyed by collisions with baryons (nucleons and nucleon-like particles); the total destruction over time depends on the baryonic density ρ_B of the Universe. Figure 4.2 shows the model

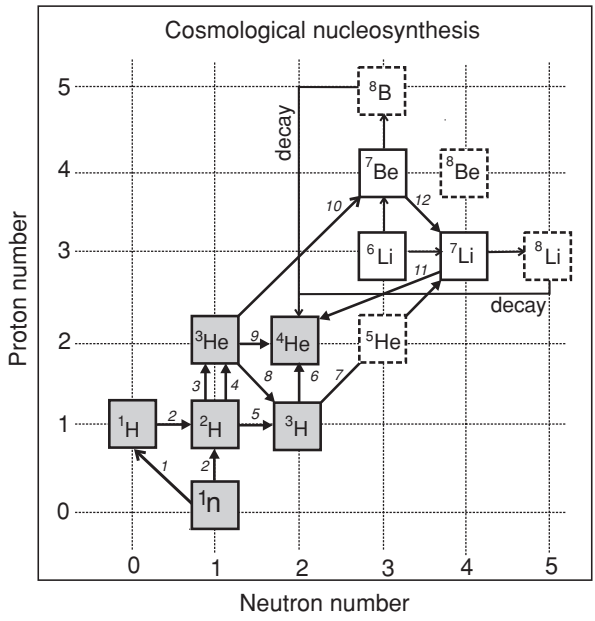

1. $n \rightarrow p + e^{-} + \nu_e$
2. $^{1}H + n \rightarrow ^{2}H + \gamma$
3. $^{2}H + p \rightarrow ^{3}He + \gamma$
4. $^{2}H + d \rightarrow ^{3}He + n$
5. $^{2}H + d \rightarrow ^{3}H + p$
6. $^{3}H + d \rightarrow ^{4}He + n$
7. $^{3}H + \alpha \rightarrow ^{7}Li + \gamma$
8. $^{3}He + n \rightarrow ^{3}H + p$
9. $^{3}He + d \rightarrow ^{4}He + p$
10. $^{3}He + \alpha \rightarrow ^{7}Be + \gamma$
11. $^{7}Li + p \rightarrow ^{4}He + \alpha$
12. $^{7}Be + n \rightarrow ^{7}Li + p$

Fig. 4.1 Plot of proton number Z vs. neutron number N for light isotopes undergoing cosmological nucleosynthesis. The numbers labelling the arrows identify the nuclear processes involved and the relevant pathways. Isotopes below $A = 5$ can be yielded by interactions of nuclei with a proton or neutron (shaded squares). Note that stable isobars with $A = N + Z = 5$ and 8 are non-existent, which prevents the efficient nucleosynthesis of heavier elements. The latter can be obtained only via (nucleus, α-particle) reactions (7, 10), for which the cross sections are small owing to the high Coulomb barrier. After Schramm and Turner (1998).

relationship, from which the value $\rho_B \sim 2.5 \times 10^{-31}$ g cm^{-3} may be derived. During the first half-hour or so the baryonic matter of the Universe was produced (Fig. 4.3).

4.3 The age of the Universe

Distance–redshift relationship: Doppler effect and redshift

The model of an expanding Universe that originated in a single short event implicitly suggests that it should be possible to estimate the age of this event. To obtain the

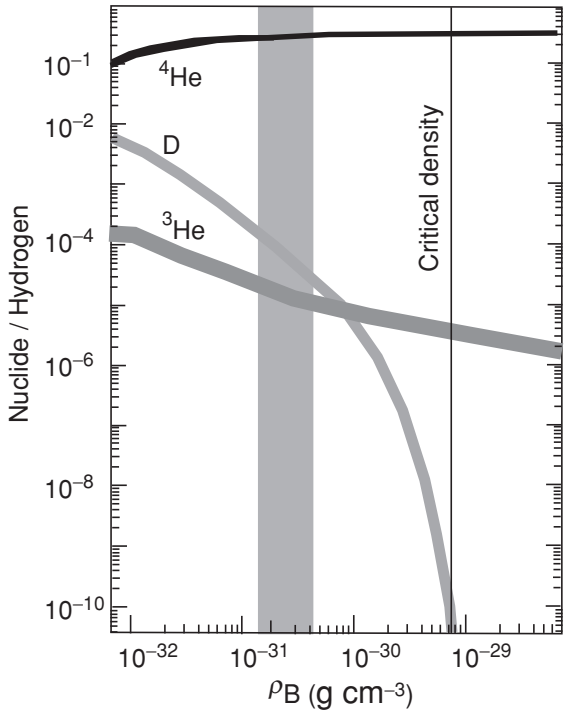

Fig. 4.2 Abundance of the He isotopes and D relative to H as predicted from models of the Big Bang nucleosynthesis; ^{4}He/H is a mass ratio; the others are atomic ratios. The ^{4}He abundance is insensitive to the baryonic density of the Universe ρ_B (i.e. the density of the heavy particles having $m \geq 1$ amu); therefore the comparison of the model and observed ^{4}He abundances is crucial to establishing the Big Bang nucleosynthesis of this nuclide. The ^{4}He abundance contrasts with the sharp dependence of the D abundance on ρ_B. The shaded vertical band shows the baryonic density derived from the observed D abundance corrected for stellar processing of the nuclide. Astrophysicists prefer a density about 20 times higher, which corresponds to a more plausible model of the Universe. Simplified from Schramm and Turner (1998). Reproduced by permission, © 1998 American Physical Society.

rate of expansion, distances between remote objects as well as the differences in their velocities must be measured.

If a light source and receiver move away from each other, photons arriving at the receiver show a lower frequency than those emitted, i.e. in the optical range their frequency is shifted to the red side of the spectrum (hence, redshift). The velocity difference between source and receiver Δv and the frequency difference $\Delta f = f(\text{emitted}) - f(\text{observed})$ are related as (Aller, 1971)

$$\Delta f/f = \Delta v/c \tag{4.4}$$

where c is the speed of light.

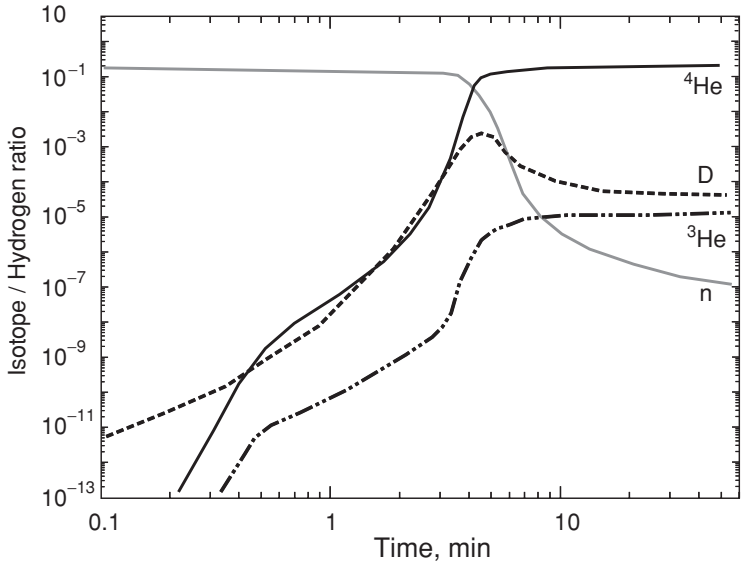

Fig. 4.3 Evolution of the abundances of the light elements during Big Bang nucleosynthesis. All ratios are atomic except for the ^{4}He/H ratio, which is the weight fraction. After Schramm and Turner (1998). Reproduced by permission, © 1998 American Physical Society.

Hubble discovered that in the Universe the velocity difference Δv increases proportionally to the distance d between the emitter and observer, so that $\Delta v/d$ is a constant equal to H_0, the Hubble parameter. Defining the redshift ζ via $1 + \zeta \equiv \lambda_{\rm OBS}/\lambda_{\rm EMIT}$ and substituting wavelengths for frequencies in Eqn (4.4) gives

$$\zeta = \Delta v/c \approx H_0 d/c. \tag{4.5}$$

Thus the slope of the regression between relative velocity (or redshift) and distance gives H_0 in s^{-1} (or conventionally in km s^{-1} Mpc^{-1}).

The measured redshift is affected by several other effects, e.g. local (inhomogeneous) movement of matter within the observed object (such as an expanding stellar envelope) and the reddening of the light as it passes through the interstellar and intergalactic media, etc. However, modelling of the relevant features of the object and the environment allows one to isolate the ζ-component related to the expansion of the Universe. This is particularly robust for the class of supernovae termed Ia (SNe Ia, Section 6.4).

Distance–redshift relationship: distances

Several approaches are used to estimate distances at the scale of the Universe. Trigonometric parallax with the Earth's orbit as a base allows measurements of

the relatively short distances to the closest stars ($\sim 10^{20}$ cm). When the distance travelled by the Sun and the solar system over many years, and many stars (with similar parallaxes) are taken into account, measurable distances can be extended up to 10^{21} cm.

Much longer distances can be estimated from the luminosity of the brightest stars or galaxies. The ratio of the apparent brightnesses of two similarly bright objects depends mainly on the ratio of the inverse squares of their distances from the Sun: $I_2/I_1 = R_1^2/R_2^2$. After the *I–R* relationship for relatively close objects (with known R_1) has been quantified to $C = R_1^2/I_1$, this approach can be extended to larger distances up to $\sim 10^{10}$ light years ($\sim 10^{46}$ cm): $R_2 = \sqrt{C/I_2}$. The major uncertainties here stem from the postulate that the objects involved have similar intrinsic brightness and the fact that light, especially from a remote object, can be affected during propagation through "dusty" interstellar clouds.

An important observation is that the brightest red-giant stars in a galaxy have nearly uniform luminosity and can be used as "standard candles" (Harris *et al.*, 1998). This is also valid, after some corrections, for the brightest galaxy in a cluster (Peacock, 1999). Supernovae Ia (SNe Ia) appear to be the most suitable objects: they not only have uniform light spectra, as noted above, but also exhibit a striking uniformity in maximum luminosity and light-curve shape (Fig. 6.2); therefore SNe Ia observations have been successfully used to measure the Hubble parameter at large distances.

The Hubble parameter and the age of the Universe

Figure 4.4 shows the Hubble diagram of recession velocities versus distances obtained by observations on supernovae SNe Ia. The slope of the regression line gives $H_0 = 72 \pm 2$ km s^{-1} Mpc^{-1}. The inset presents less distant objects, with an inferred $H_0 = 75 \pm 8$ km s^{-1} Mpc^{-1}. Thus the velocity–distance dependence seen in Fig. 4.4 appears to be valid for both remote and neighbouring objects, from which the light signals travel ~ 1 Gyr and ~ 1 Myr respectively. Recently a fully independent determination of the Hubble parameter, based on measurements of the cosmic microwave background radiation, has yielded 71 ± 4 km s^{-1} Mpc^{-1}, in excellent agreement with the redshift-derived value. This agreement confirms the model of the expanding Universe, and from these observations the time when expansion started, i.e. the age of the Universe, can be derived. The best-fit value is 13.7 ± 0.2 Gyr (Spergel *et al.*, 2003; Freedman and Turner, 2003).

4.4 Summary

Friedmann (1922) invented the now generally accepted model of the expanding Universe that originated in one explosion-like event, named the Big Bang. Hubble

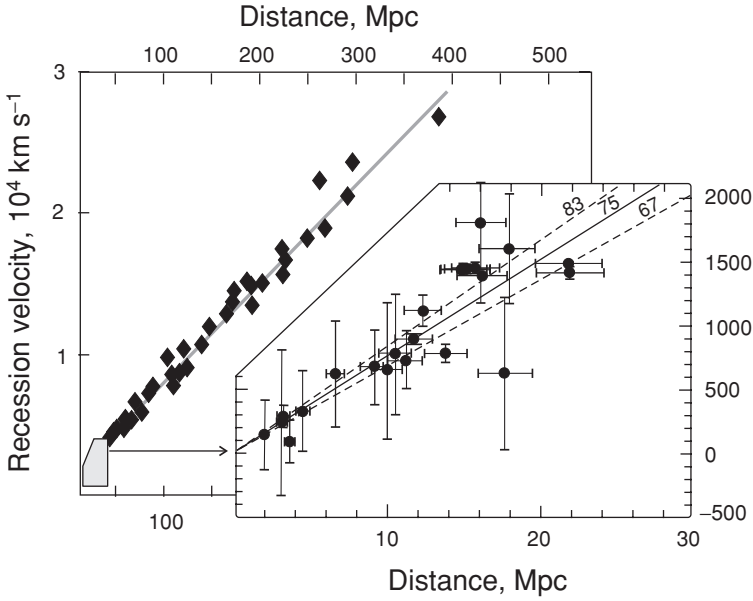

Fig. 4.4 Distance–velocity relationships for different objects of the Universe. Circles, data for distances < 25 Mpc; diamonds, distances > 25 Mpc. (1 Mpc = 3×10^{19} km.) The good correlation between the two parameters (grey line) obtained for SNe Ia gives the Hubble parameter $H_0 = 72 \pm 2$ km s^{-1} Mpc^{-1}. Less distant objects give $H_0 = 75 \pm 8$ km s^{-1} Mpc^{-1}, identical to the former value within error limits. From these and other observations and models the best-fit value, 71 ± 4 km s^{-1} Mpc^{-1}, and the age of the Universe, 13.7 ± 0.2 Gyr, are inferred. After Freedman *et al.* (2001) and Freedman and Turner (2003).

(1929) discovered a linear relationship between the distance from distant objects and redshift in their light spectra, which supported this model. Subsequent precise measurements of redshift and distance, together with evaluations of the cosmic microwave background, have allowed the age of the Universe to be determined with great precision and confidence at 13.7 ± 0.2 Gyr.

The Big Bang provides a setting for the formation of baryonic matter. Models predict that the first baryonic particles, protons and neutrons, were formed at a late stage of the explosion, when the temperature dropped below 10^{11} K. During a time interval of ~ 30 min the temperature decreased from 10^{11} to 10^9 K and the density from 10 to 10^{-5} g cm^{-3}, and H, D, ^{3}He and ^{4}He were formed. The BBN models predict relative abundances for these nuclides close to those directly observed in primitive prestellar matter. Hydrogen and ^{4}He were dominant, and the ^{4}He mass fraction (~ 0.28) is determined by the neutron/proton ratio, which became fixed at $\sim$ one-sixth when weak interactions were terminated, at $\sim 5 \times 10^9$ K.

The fragile nuclides D and ^{3}He are less abundant at present. Modelling of the decline of D during late stages of the nucleosynthesis process allows the baryonic density of the Universe to be estimated in the range (1–5) $\times$ 10^{-31} g cm^{-3}. This is 20 times less than is required for the Universe to be "closed" and is much lower than the total matter density of the Universe derived from the "emerging standard cosmological model" (Spergel *et al*., 2003).

5

Stellar nucleosynthesis: lower-mass stars and the s-process

5.1 Introduction

From the discussion of the Big Bang nucleosynthesis in the previous chapter it follows that H and He, but not the heavier elements, could have been produced in this very early event. Since the classical publication by Burbidge *et al.* (1957) there has been no doubt that these heavier elements are produced in stellar nucleosynthesis, and the real problem is to discover how similar model stars and the nuclear processes in them are to reality.

After the collapse of a cold molecular cloud and the formation of a star, nuclear burning becomes the major source of energy in a star and also the process producing heavier elements from lighter ones. The production of heavy elements with $A > 60$ is controlled by neutron fluxes, which can be slow (Section 5.4) or rapid (Section 6.1), and also by several associated nuclear processes. The elements used by a star at its formation as well as newly produced elements are (partially) returned to the interstellar medium by stellar winds or explosions and mix with the matter already there. Another part of the stellar matter could be held in stellar remnants for a long time.

In this chapter we describe nucleosynthesis processes in stars up to ~ 4 solar masses. These include H and He burning, which produces C, N and O in abundance and small amounts of the elements up to Si (Section 5.3), as well as the generation of elements heavier than Fe by the slow neutron capture s-process. It should be noted that the iron-peak elements, the seed for s-process nucleosynthesis, are not yielded in small stars: Fe-peak nuclides must thus be inherited from the source molecular cloud.

5.2 Formation of stars

Following astrophysical observations and theory, the gravitational collapse of interstellar clouds appears to be the principal star-forming process (e.g. Larson, 1981; Shu *et al.*, 1987; Evans, 1999). As an example we discuss the simplest scenario

for this, based on an approximately spherical cloud at rest (neither contracting nor expanding), with only thermal support. The limit of gravitational stability for such a cloud can be estimated using the virial theorem,

$$2E_{\mathrm{K}} + U_{\mathrm{G}} = 0, \tag{5.1}$$

where U_{G} is the potential gravitational energy of the system, which is considered as still being in hydrostatic equilibrium (in the steady-state approximation), and E_{K} is the kinetic energy due to thermal movements of particles, their rotation relative to the centre of mass of the system etc. The internal nuclear energy of the particles is not considered in the virial theorem approach. In Eqn (5.1) the terms are

$$U_{\mathrm{G}} \approx -GM^2/R \tag{5.2}$$

and

$$E_{\mathrm{K}} = 3MkT/2m, \tag{5.3}$$

where G is the gravitational constant, M and R are the mass and radius of the system, k is the Boltzmann constant, T is the temperature of the gas and m is the mass of a particle. Taking into account that the mass and radius of the system are related through the density, $\rho = M/[(4/3)\pi R^3]$, and assuming that the cloud consists of H alone, then Eqns (5.1–5.3) give the Jeans critical mass,

$$M_{\mathrm{C}} \sim (kT/Gm_{\mathrm{H}})^{3/2}\rho^{-1/2}. \tag{5.4}$$

A cloud having a mass exceeding M_{C} undergoes contraction unless magnetic fields, rotation or turbulence support the cloud in addition to the thermal support (see the discussion of these factors by Shu *et al.*, 1987; Evans, 1999; Hartmann *et al.*, 2001).

The critical mass M_{C} can thus be estimated from the two parameters temperature (T) and density (ρ). In sterile regions with a low rate of star formation, typical values are $\rho \sim 10^3$ amu cm^{-3} and $T \sim 10$ K. Several mechanisms can stimulate the contraction of a cloud. For example, when it crosses the spiral arms of a galaxy it could be compressed by interaction with the denser gas constituting the arms. Processes associated with already formed stars, e.g. shock waves or stellar winds, could also trigger contraction. The post-trigger density exceeds $\sim 10^4$ cm^{-3}, which leads to shielding, preventing the temperature in the cloud core (estimated at ≤ 15 K) from rising sufficiently to stabilize it. A similar temperature is expected for the dust particles, and under such conditions efficient coupling of hydrogen atoms could occur: H atoms could remain adsorbed on a grain surface long enough to locate another H atom and react. This leads to the formation of a dense cold molecular cloud. Hartmann and colleagues have shown that when the density approaches the value needed for molecular shielding, the self-gravitating forces become important and collapse is inevitable. This is the basic reason why star formation is presently

occurring in almost all molecular cloud complexes of significant size in the solar neighbourhood. Observations show that collapse and subsequent star formation follow the development of cold molecular clouds without delay; the time scale is $\sim$ 1 Myr (Hartmann *et al.*, 2001).

The final size of the star-forming cloud and the resulting configuration (single star, stellar system or planetary system) depend crucially on several factors, mainly the mass, composition, triggering mechanism and angular momentum. Regarding the mass, the upper limit for a single star is around several hundred $M_\odot$. On the one hand, more massive stars could hardly be formed: their luminosity during formation would be so extreme that the radiative pressure would blow gas and dust away from the accreting envelope. On the other hand, in stars lighter than $\sim 0.1\ M_\odot$ the internal temperature could not become high enough to ignite nuclear burning. Generally the mass of a star-forming cloud varies within the range $0.1\ M_\odot < M < 100\ M_\odot$ (Shu *et al.*, 1987; Beech and Mitalas, 1994).

The standard model envisages an initially gradual and then rapid collapse of the cloud. If the gravitational acceleration is not retarded by internal pressure, the free-fall time $T_{\rm ff}$ of the collapse is (Cameron *et al.*, 1997):

$$T_{\rm ff} = [3\pi/(32G\rho)]^{1/2}. \tag{5.5}$$

Substitution of the above density gives $T_{\rm ff} \approx 2 \times 10^5$ yr, and a mean infall rate for a solar-like star $\mathrm{d}M/\mathrm{d}t \approx 10^{-5}\ M_\odot\ \mathrm{yr}^{-1}$. When a proto-stellar core with radius $R_{\rm C} \sim 10\ R_\odot$ and mass $M_{\rm C} \sim 1\ M_\odot$ has been formed, such an infall produces the luminosity

$$L = GM_{\rm C}(\mathrm{d}M/\mathrm{d}t)/R_{\rm C} \approx 30\ L_\odot \tag{5.6}$$

assuming that essentially all the kinetic energy of the infalling material is converted into radiation (Shu *et al.*, 1987). The virial theorem allows the central temperature $T_{\rm C}$ to be estimated: solving Eqns (5.1–5.3) for T gives

$$T_{\rm C} \approx GM_{\rm C}m/(3kR_{\rm C}) \approx 10^6\ \mathrm{K}. \tag{5.7}$$

The star enters the D-burning stage (see below); the released energy powers intense stellar surface activity. The enhanced luminosity and accompanying stellar winds provide a negative feedback to stellar accretion: these factors counteract and then terminate the infall. The star can now be followed in the framework of the Hertzsprung–Russell (H–R) diagram (Fig. 5.1). This is a plot of two observable parameters, the effective surface temperature and the luminosity, and allows evolutionary star models to be tested against observation. Below we follow the evolution of a low-mass star ($\sim$1–4 solar masses). The star moves up towards the main sequence during the relatively long, $\sim$ 10 Myr, T-Tauri stage, discussed in Part II. The stellar radius decreases slowly, approaching $R_\odot$. The corresponding central (subscript c)

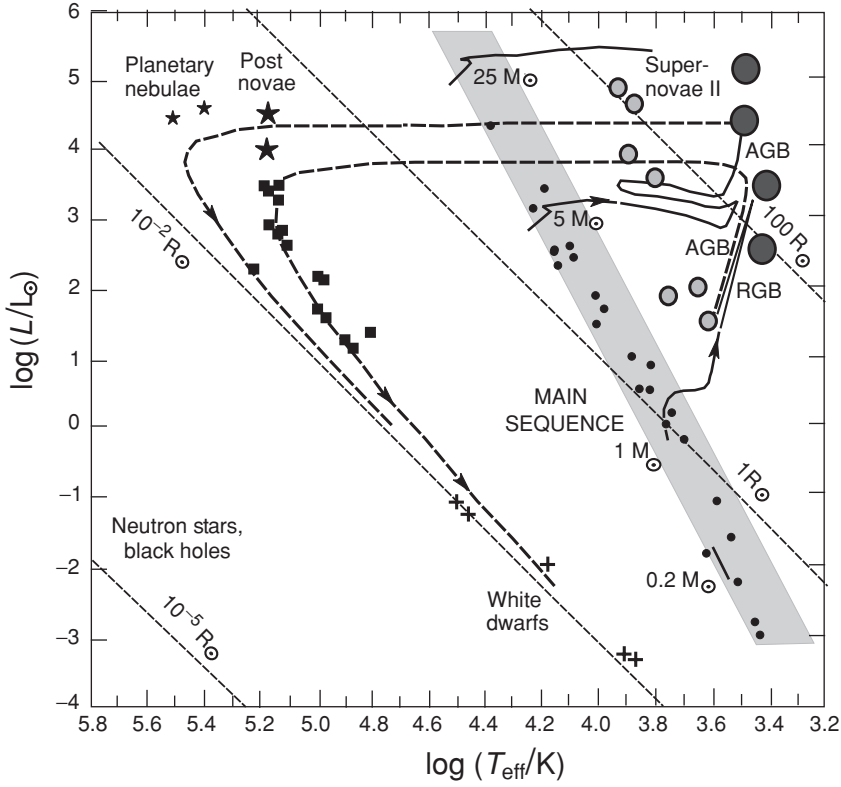

Fig. 5.1 Hertzsprung–Russell (H–R) diagram: model trends and observations. Coordinates: the effective temperature $T_{\rm eff}$ is in K; the luminosity L is measured relative to the solar luminosity. The broken lines of negative slope show stellar radii relative to the solar radius. The circles are single stars: core-hydrogen-burning main-sequence stars are shown as small circles within the main sequence (the grey band); core-helium-burning stars are shown as medium circles; red giants or red supergiants burning hydrogen or helium in a shell are shown as large circles. The large star symbols indicate post novae and the small star symbols indicate the central stars of planetary nebulae. The solid curves are evolutionary tracks for single stars having masses 0.2, 1.0, 5 and 25 $M_\odot$. The broken-line curves are the tracks of the dying 1 and 5 $M_\odot$ stars, which lose most of their hydrogen-rich envelope and evolve into white dwarfs (crosses). The locations of stars passing through the red-giant-branch and asymptotic-giant-branch stages of evolution are indicated by RGB and AGB respectively. Simplified from Wallerstein *et al.* (1997). Reproduced by permission, © 1997 American Physical Society.

temperature $T_{\rm c} \approx 10^7$ K, the mean solar density $\rho_\odot = 1.41$ g cm^{-3} and the tabulated coefficient $(\rho_{\rm c}/\rho_\odot) \approx 60$ (for solar-like stars) give $\rho_{\rm c} \approx 100$ g cm^{-3}. At this temperature and density, H burning is ignited in the core (see below) and becomes a major source of stellar energy, increasing the pressure of the gas in the core and thus counteracting the gravitational attraction and effectively stabilizing the star.

5.3 Hydrogen and He burning and the evolution of a low-mass star

Hydrogen burning

When a young star approaches the main sequence, fragile D is consumed via reaction (2) in Eqn (5.8) below, increasing the ^{3}He abundance. Then H burning is initiated in the stellar core at $T \approx 10^7$ K. In the beginning, proton–proton reaction chains are responsible for heating the core; one of these, the ppI chain, includes the following nuclear reactions:

$$\begin{aligned} &(1) \quad \mathrm{p(p,\, e^+ + \nu)D + 1.44\ MeV},\\ &(2) \quad \mathrm{D(p,\, \gamma)^3He + 5.49\ MeV},\\ &(3) \quad \mathrm{^3He(^3He,\, p + p)^4He + 12.8\ MeV}. \end{aligned} \tag{5.8}$$

The first reaction, which is the principal one for H burning, has never been observed experimentally because of its extremely low probability. In order to yield a deuteron, the proton + proton interaction must overcome the Coulomb barrier, for which the energy is ~ 1 MeV or almost 10^{10} K. At $T \approx 10^7$ K the probability that a proton reaches the required energy is only $\sim 10^{-8}$. Further, the time of the interaction is extremely short, $\sim 10^{-21}$ s, and during this time one of the two excited protons must emit a positron and turn into a neutron. However, thanks to the very high density of protons in a stellar interior this "improbable" reaction can proceed, albeit slowly. The positron is immediately annihilated by interaction with an electron, $\mathrm{e^+ + e^-} \rightarrow 2\gamma$, and the neutrino leaves the star (Shklovsky, 1977). Reactions (5.8) and similar ones all terminate at ^{4}He because of its rather high binding energy, and this nuclide accumulates in the core. Meanwhile, the low probability of reaction (1) above and the abundance of fuel for it ensure a very long duration of the H burning stage, ~ 10 Gyr for a star of solar mass (Section 7.3).

If the temperature slightly exceeds 10^7 K and the heavier elements C, N and O are present in the stellar interior then reactions of the C–N (CNO) cycle can take place parallel to those of the pp chains, also yielding ^{4}He (Table 5.1; Meyer, 1997).

During all this time H is still the major constituent of the star, which moves along the main sequence as the effective temperature T_{eff} and luminosity L increase; the major stellar parameters, the pressure P, density n and temperature T, are related by the ideal gas equation:

$$p = nkT. \tag{5.9}$$

Similar equations of state are valid for the pressure of the ions, P_{i}, and of the electrons, P_{e}, and for high densities it is convenient to present the total pressure as $P = P_{\mathrm{i}} + P_{\mathrm{e}}$ (Cameron, 1976).

Table 5.1 *The CNO bi-cycle*

Reaction	The CN cycle	Reaction	The ON cycle
1	$^{12}C(p, \gamma)^{13}N$	7	$^{15}N(p, \gamma)^{16}O$
2	$^{13}N \rightarrow {}^{13}C + e^{+} + \nu$	8	$^{16}O(n, \gamma)^{17}F$
3	$^{13}C(p, \gamma)^{14}N$	9	$^{17}F \rightarrow {}^{17}O + e^{+} + \nu$
4	$^{14}N(p, \gamma)^{15}O$	10	$^{17}O(p, {}^{4}He)^{14}N$
5	$^{15}O \rightarrow {}^{15}N + e^{+} + \nu$		
6	$^{15}N(p, {}^{4}He)^{12}C$		

The electron density decreases in the course of stellar evolution. All relevant reactions consume electrons, e.g. Eqn (5.8) transfers four protons having four electrons into one ^{4}He atom having two electrons. Lowering the electron density in the core diminishes the scattering of photons on electrons and therefore increases the radiative conductivity of the star. This increases the stellar luminosity, and the star moves upwards in the H–R diagram (Fig. 5.1). The main-sequence lifetime depends on the *PT* conditions, which are mainly determined by the stellar mass (Section 7.3).

As hydrogen burning continues, ^{4}He "ash" accumulates in the core. When all the H in the core has been burnt, the latter cools and contracts, releasing gravitational energy and thus heating the H-shell around it. This ignites H burning in the shell. Now H burning in the shell becomes the principal source of energy in the star and the core continues to accumulate He ash. The mass and density of the core increase slowly. The energy released by core growth and contraction is being lost, and the pressure in the core increases without substantial heating. The core gas becomes "degenerate", that is, atoms lose their individual electron shells to a common "electron gas", which now supports the outer layers of the star by the Pauli pressure.

The thermal conductivity of the degenerate core is high, and the gravitational energy, released as it slowly contracts, is readily transferred to the outer envelope. Heating of the envelope increases the stellar radius and the star expands. The growth of the stellar surface, which has area $\sim R^2$, causes a decrease in the effective temperature, whereas the total luminosity remains almost constant, and the model star moves to the right off the main sequence (Fig. 5.1). These processes also lead to a steepening of the temperature profile within the envelope and thus initiate convection.

This convection extends deeply and transfers heat (along with partially processed material) to the outer envelope. This transfer allows more energy to be dissipated,

so that the luminosity increases. The star now enters the red-giant-branch (RGB) phase (Fig. 5.1), also known as the first dredge-up. The contribution of freshly generated nuclides, i.e. the enhanced abundance of newly produced ^{4}He together with heavier nuclides from CNO cycling, changes the surface composition of the outer shells: the ^{4}He mass fraction increases by a factor ~ 3, the ^{12}C/^{13}C ratio drops from ~ 90 to ~ 20 (reactions 1 and 2, Table 5.1) and ^{14}N increases at the expense of ^{12}C (reactions 1–3 in Table 5.1) by $\sim 30\%$. The C-isotope composition in interstellar dust grains (see Fig. 3.3) is especially diagnostic for these processes: reactions 1 and 2 produce ^{13}C, whereas He burning, see Eqn (5.10) below, does not. Convection also stimulates stellar winds. With mass-loss rates of up to 10^{-6} $M_\odot$ yr^{-1}, a substantial portion of the stellar mass could be blown away.

Meanwhile the ^{4}He-rich core continues to grow and as its mass approaches ~ 0.5 $M_\odot$, contraction and resultant heating to $\sim 2 \times 10^8$ K lead to He ignition (Wallerstein *et al.*, 1997).

Helium burning

Helium burns according to the following reactions:

$$\begin{aligned} &(1) \qquad 3^4\mathrm{He} \rightarrow {}^{12}\mathrm{C} + \gamma, \\ &(2) \quad {}^{12}\mathrm{C} + {}^4\mathrm{He} \rightarrow {}^{16}\mathrm{O} + \gamma, \end{aligned} \tag{5.10}$$

and ^{16}O accumulation terminates this stage. The energy produced via He burning heats the core, which expands. This expansion leads to the cooling of the base of the H-shell and thus terminates H burning. Convection in the shell ceases, energy transfer to the surface is less efficient, the stellar luminosity decreases and the star moves down in the H–R diagram (Fig. 5.1). The time scale for the He-burning stage is much less than the main-sequence stellar residence time, by a factor ~ 0.25 for Sun-like stars or a factor ~ 0.1 for massive stars.

When He is exhausted in the core, the latter contracts again; He burning can start in the previously H-burning shell, and H burning can start higher up. Once again the star ascends the giant branch; this second ascent is known as the asymptotic-giant-branch (AGB) stage. The He or H shells are blazing, whereas the core grows slowly via the addition of ^{12}C and ^{16}O ash and then becomes degenerate. The He-shell is unstable during this phase, and the star enters the thermally pulsing part of the AGB phase, which is important because such stars produce a substantial portion of the nuclides heavier than Fe (Section 5.4). When the H-burning shell comes close to the surface, the He layer cools below the temperature required for He burning. After this only H burning continues. A high-energy flux through the relatively thin outer shells maintains a high outward pressure, which initially merely supports these shells but finally overcomes the gravity forces. Then the outer shells are blown

away, the remaining star contracts by four orders of magnitude while increasing $T_{\rm eff}$ (it moves to the left in the H–R diagram) and evolves into a C–O white dwarf. A core with mass ≤ 1.4 $M_\odot$ (the so-called Chandrasekhar limit) can be supported by the electronic gas in the degenerate matter, so that the star is prevented from collapsing into a neutron star or black hole. Therefore numerous stars with masses up to ~ 3 $M_\odot$ turn, after this stage, into white dwarfs with $M \sim 0.6$ to 0.7 $M_\odot$ (Hansen and Liebert, 2003).

5.4 Slow nucleosynthesis (s-process)

What is meant by "slow"?

The nucleosynthetic processes described above involve the interactions of nuclei with other positively charged particles (α-particles and protons). Processes of this kind can also produce heavier elements, up to Fe. However, to enter a nucleus a charged particle must overcome the Coulomb repulsion barrier and, for elements heavier than Fe, the required temperature is $\sim 10^{10}$ K, well above the highest temperature reached in the normal, quiescent, evolution of a star: reactions of nuclei + neutrons are therefore the only route to the synthesis of heavy elements.

The abundant Fe-peak nuclides inherited by low-mass stars during their formation act as "seeds" for this process. A chain of nucleus + n reactions can be traced, starting, for example, from ^{60}Ni (Fig. 5.2). First, two (n, γ) reactions produce the stable isotopes ^{61}Ni and ^{62}Ni, but further neutron capture yields the radioactive nuclide ^{63}Ni ($\tau_{63} = 4 \times 10^9$ s). Now there are two possibilities: either ^{63}Ni decays to generate stable ^{63}Cu ($^{63}\text{Ni} \rightarrow {}^{63}\text{Cu} + \text{e}^- + \nu^*$, an antineutrino) or its nucleus absorbs another neutron to yield stable ^{64}Ni. In the latter case ^{63}Cu and ^{64}Zn would be found to be underabundant. However, ^{64}Zn is the most abundant Zn isotope in the solar system and it can thus be concluded that normally ^{63}Ni has had enough time to decay. This means that the mean time interval between two subsequent neutron captures, $\tau_{\rm n}$, is longer than the mean life of ^{63}Ni: $\tau_{\rm n} \geq 1/\lambda_{63}$.

The mean interval $\tau_{\rm n}$ is directly related to the neutron density $n_{\rm n}$ in cm^{-3} by (Kappeler *et al.*, 1989)

$$\tau_{\rm n} = \frac{1}{n_{\rm n}\langle\sigma\rangle v_T} \tag{5.11}$$

where $\langle\sigma\rangle$ is the probability of a (neutron, nucleus) reaction, expressed as the size of the target in cm^2 and known from laboratory experiments, and v_T is the relative velocity in cm s^{-1} and is governed by the stellar temperature. Considering a temperature $\sim 10^8$ K (corresponding to $v_T \sim 10^8$ cm s^{-1}) and a typical cross section ~ 0.1 barn $\sim 10^{-25}$ cm^2, the product $\langle\sigma\rangle v_T \sim 10^{-17}$ cm^3 s^{-1}. For the

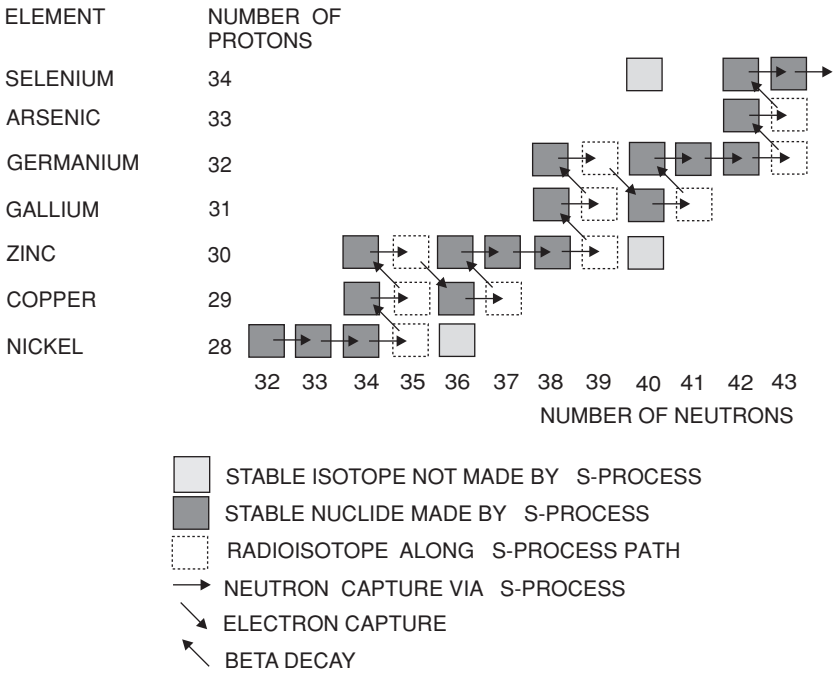

Fig. 5.2 Slow-process pathway, starting at the iron peak. After Broecker (1985).

above example we have $\tau_{\rm n} \geq \tau_\beta = 4 \times 10^9$ s, so the corresponding neutron density $n_{\rm n}$ is

$$n_{\rm n} \leq \frac{1}{\tau_{\rm n} \sigma v_T} \approx \frac{1}{4 \times 10^9 \times 10^{-17}} \approx 2.5 \times 10^7 \,{\rm cm}^{-3}. \tag{5.12}$$

It is of interest to compare this value with the seed-species density. A solar Fe/H ratio $\sim 10^{-5}$ (Table 3.2) and a total core density $\rho \sim 100$ g cm^{-3} (Section 5.2) give Fe $\sim 10^{21}$ cm^{-3} and a low neutron/seed ratio, $\sim 10^{-14}$.

Even though these estimates are valid at best to within an order of magnitude (see the more detailed discussion below), they allow us to quantity "slow" in the context of an s-process: "slow" means that the neutron density is very small compared with the abundance of the target atoms and that radionuclides formed in the course of the s-process by n-capture generally decay before they trap another neutron. The neutron/seed ratio is an important factor determining the nature of the s-process, and therefore the abundance of the elements generated also depends on the metallicity (e.g. Busso *et al.*, 1999, 2001; Aoki *et al.*, 2001).

An important feature of the s-process is that only one stable isotope, that with the lowest Z, is produced for each isobar family, to be a seed for further n-capture nucleosynthesis. This allows reliable identification of the s-produced species.

Neutron sources

Even though not many neutrons are required for the s-process, they must still be generated. One possible environment is provided by the late AGB stages in the evolution of a low-mass star, (1.5–4) $M_\odot$, when He or H burn in narrow shells above a core rich in ^{12}C and ^{16}O (Section 5.3). Hydrogen burning produces He, which accumulates in a thin layer around the core. Protons penetrating into the core boundary layer interact with ^{12}C, yielding ^{13}C via ^{12}C(p, γ)^{13}N(β, ν)^{13}C. This leads to formation of a ^{13}C-rich and α-particle-rich pocket in which the reaction

$$^{13}\mathrm{C}(\alpha, \mathrm{n})^{16}\mathrm{O} \tag{5.13}$$

yields neutrons. Typical parameters for this stage are a duration of $\sim 10^5$ yr, a neutron density $\sim 10^7$ cm^{-3} and temperatures $\sim 10^8$ K (Busso *et al.*, 2001).

As soon as a critical mass of He has accumulated, He burning is initiated. Now the reaction

$$^{22}\mathrm{Ne}(\alpha, \mathrm{n})^{25}\mathrm{Mg} \tag{5.14}$$

guarantees a neutron supply during the convective thermal pulses driven by unstable He burning (i.e. He flashing). This source can provide neutron densities up to 10^{10} cm^{-3}. The convection causes the "dredge-up" of freshly synthesized matter including ^{12}C. The helium is exhausted on a time scale of $\sim$ 100 yr, but H burning restarts in the overlying shell and ^{12}C is converted to ^{13}C, supplying fresh fuel for reaction (5.13), which drives the so-called weak s-process. Meanwhile He accumulates anew from H burning, and later on starts to flash again, so that this episode can be repeated.

S-process and non-s-process species

An examination of the *N–Z* isotope plot (Fig. 1.3) reveals that one or more nucleosynthesis mechanisms other than the s-process must exist. For example, the inset in Fig. 1.3 shows that stable ^{130}Te could not have been yielded by the slow process, with τ_n as long as one month, because the β-decay of the precursor isotope ^{129}Te is too fast ($\tau_{129} = 72$ min) and it decays before it traps a neutron. Further, the most neutron-rich long-lived radioactive isotopes, ^{232}Th, ^{235}U and ^{238}U, constitute an island separated from the contiguous range of stable nuclides by a sea of radioactive nuclides, some of which have short half-lives, in the range of seconds. These three isotopes could thus never have been produced by the s-process.

To identify the nuclides not generated by the s-process, observations on low-metallicity stars are important: the iron-peak elements are highly underabundant in these stars and therefore could not serve as seeds for the much more abundant heavy n-capture elements. By using as a reference species that cannot be produced by

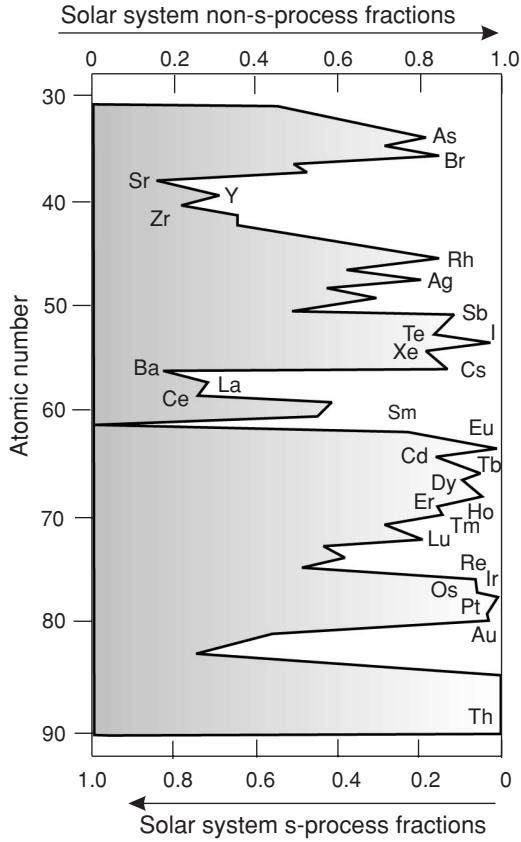

Fig. 5.3 Solar system abundances of s-process and non-s-process elements. The elements heavier than Fe were mainly synthesized in supernovae, by the r-, p- and ν-processes discussed in Chapter 6. Supernovae appear to be the most important phenomena developing the composition of matter in the Galaxy. After Wallerstein *et al*. (1997). Reproduced by permission, © 1997 American Physical Society.

the s-process (e.g. ^{232}Th), the pattern in Fig. 3.1 can be subtracted from a bulk observed pattern, e.g. from the solar abundances (Table 3.2, Fig. 3.8) to yield the relative abundances of s-process species (see Burris *et al.*, 2000 for a detailed discussion). The resulting s- and non-s-process contributions to nuclide abundances in the solar system are shown in Fig. 5.3.

Comparison of model-derived and observed s-process nuclide abundances

In modelling the s-process abundances of isotopes there are two free parameters, the abundances of ^{56}Fe and of other seed nuclides in the s-process environment and the mean neutron exposure time τ_{n}. Therefore modelling is limited to the relative

abundances (i.e. the shape of the abundance curves). In general terms, nuclides with large neutron-capture cross sections are expected to be less abundant than those with small cross sections.

Figure 5.4 presents for comparison the product $\langle\sigma\rangle N$, where N is the solar system abundance of s-process nuclides, and the model-derived values. Good agreement between the observed and calculated trends for nuclides with $A > 90$, termed the main s-component, strongly supports the models and thus allows the stellar s-process environments to be constrained. Yin *et al.* (2006) have shown recently that measured REE isotope abundances in presolar SiC grains are consistent with the theoretical predictions except for the relatively volatile Yb and Eu (Fig. 10.1(a), (b)).

Four important features are clearly apparent in Fig. 5.4: (1) the overall smoothness of the $\langle\sigma\rangle N$ product curve; (2) the model underproduction of nuclides with masses with $A \approx 60$–90, termed the weak s-process component; (3) several flat plateaux separated by steep steps; and (4) several deep valleys. These features are briefly discussed below.

(1) The smoothness of the $\langle\sigma\rangle N$ curve allows an inverse problem to be solved, namely, estimating the product σN for nuclides with poorly constrained abundances N. For example, the abundances of the Xe isotopes, produced by the s-process, were determined in this way (Anders and Grevesse, 1989).
(2) The discrepancy between the observed abundances for the relatively light mass range $60 \leq A \leq 90$ and those calculated for the main s-process can be resolved if a component from an s-process environment with a low neutron density is postulated. A suitable site for such a "weak" s-process appears to be the hydrogen-burning core in a massive star, where the neutron flux is supported by reaction (5.13), which operates on the relatively short time scale of $\sim 10^5$ yr (Wallerstein *et al.*, 1997).
(3) The steps are caused by the anomalously small cross sections of neutron reactions with magic nuclei (Section 1.2), which act as bottlenecks for the neutron capture flow thus decreasing the abundances of the heavier elements.
(4) The valleys seen in Fig. 5.4 result from branching, as discussed below.

Stellar β-decay enhancement: are the decay constants really constant and are the stable isotopes really stable?

As already mentioned in Section 1.1, the β-decay rates of certain nuclides under stellar pressures and temperatures can greatly exceed values measured under "normal" low temperatures (Fig. 5.5). Moreover, some isotopes, which are stable under Earth conditions, e.g. ^{163}Dy and ^{179}Hf, become radioactive in the s-process environment. The physics of this phenomenon is not fully understood. The thermal excitation of nuclei and the high degree of ionization appear to control the stellar

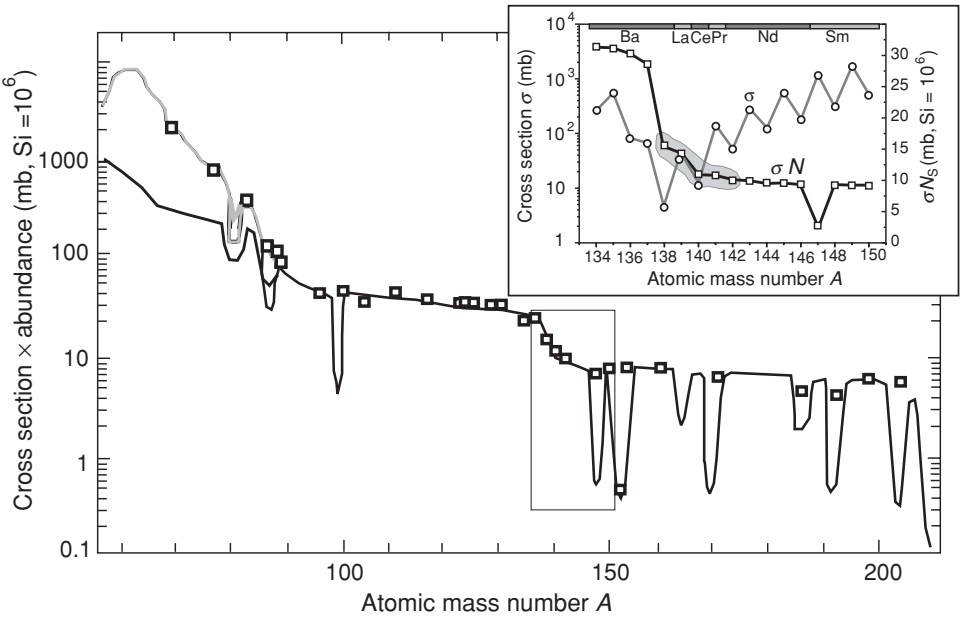

Fig. 5.4 Observed and model-predicted abundances of s-process elements. The squares are products of the cross sections σ (1 mb $\equiv 10^{-27}$ cm^2) and the observed abundances N_s of s-process nuclides (Si $\equiv 10^6$); the curves show σN_s products derived from the main s-process model (black) and the weak s-process model (grey). Note the good agreement of the observed and predicted abundances, especially for the main s-process nuclides with $A \geq 90$. Some modification of the s-process (i.e. the addition of the weak s-process) is required to obtain a similar fit for the lighter nuclides (A between 60 and 90). The sharp valleys result from branching. The distinct steps in the σN curve are due to the small neutron-capture cross sections for nuclei with magic numbers, e.g. 82 neutrons for ^{138}Ba, ^{139}La and ^{140}Ce as shown in the inset. Except for the branching and the "magic" nuclides, the σN_s products of neighbouring nuclides are similar; for example the observed ratio σ_{148} ^{148}Sm/σ_{150} ^{150}Sm is 0.87. After Wallerstein *et al.* (1997). Reproduced by permission, © 1997 American Physical Society.

β-decay enhancement, but it is quite difficult to study these relationships since excited nuclear states decay much faster via γ-emission than by β-decay. The only experimentally investigated example of β-decay from an excited state is that of ^{79}Se. The most extreme known case of temperature dependence of the β-decay rate is ^{176}Lu, for which the "normal" half-life $\tau_{176} = 37$ Gyr is reduced to a few years at s-process temperatures (Takahashi and Yokoi, 1987; Wallerstein *et al.*, 1997).

The decay rates of radioactive isotopes are important parameters, which allow the physical conditions of s-process nucleosynthesis to be quantified using branching: this occurs where the rate of neutron capture can compete with that of β-decay. In cases where the β-decay rate is strongly temperature dependent (e.g. ^{176}Lu) this can

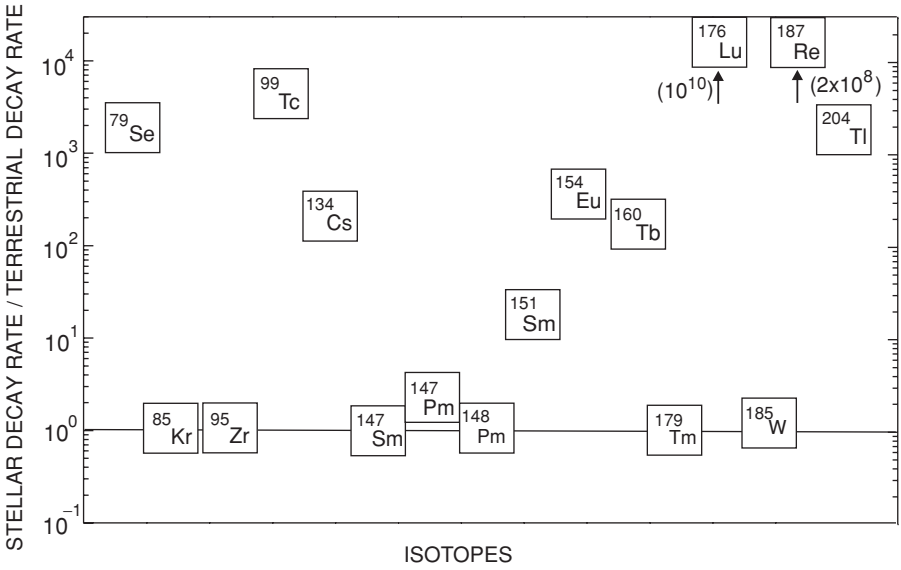

Fig. 5.5 Stellar enhancement of β-decay at $T \sim 10^8$ K. Note the very large variation in the temperature effect, in the extreme case a factor $\sim 10^{10}$ for ^{176}Lu. From Wallerstein *et al*. (1997). Reproduced by permission, © 1997 American Physical Society.

be used to estimate stellar temperatures. In the case of temperature independence (e.g. ^{148}Pm), the neutron density can be constrained. The latter case is discussed below as an example.

Branching: isotope abundance as a measure of neutron density in the s-process environment

In the REE mass region, the stable isotopes ^{148}Sm and ^{150}Sm are considered to be products of the s-process (Fig. 5.6). The radioactive isotopes ^{147}Nd, ^{147}Pm and ^{148}Pm could affect their abundances. Among this trio,^{148}Pm has the highest (n, γ) cross section and the shortest half-life ($\lambda_{148} = 1.54 \times 10^{-6}$ s^{-1}), therefore it is the principal isotope for branching. As the ^{148}Pm decay rate is temperature independent (Fig. 5.5), the branching shown in Fig. 5.6 can be used to estimate the neutron density (Reifarth *et al.*, 2003).

If $\lambda_{148} \ll \lambda_n = \ln 2/\tau_n$ then ^{148}Pm traps neutrons before it decays, and the daughter isotope ^{148}Sm would have been underproduced relative to ^{150}Sm and so would have defined a valley in the $\langle\sigma_i\rangle\, ^iN$ curve. This is not observed (see the inset in Fig. 5.4), indicating that the opposite is true: the s-process path runs mainly through ^{148}Sm, and $\langle\sigma_{148}\rangle^{148}\text{Sm} \approx \langle\sigma_{150}\rangle^{150}\text{Sm}$. However, ^{147}Sm is indeed underabundant: the parent ^{147}Pm has a relatively long life, so it traps a neutron before β-decay, thus giving the constraint $\lambda_{147} < \lambda_n < \lambda_{148}$.

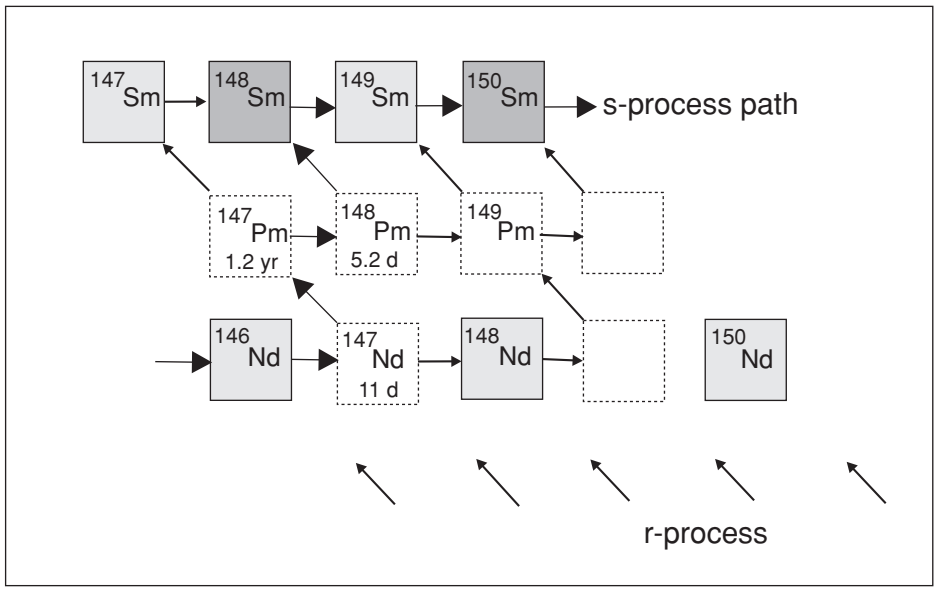

Fig. 5.6 Branching: the competition between rates of neutron capture and of β-decay. The open and light-grey squares are radioactive and stable isotopes respectively, in a branching s-process path. The darker-grey ^{148}Sm and ^{150}Sm are stable isotopes for which the abundance ratio depends strongly on the branching. The half-lives shown for the radioactive nuclides are stellar ones. Note that ^{148}Sm and ^{150}Sm are shielded from the r-process by the isobars ^{148}Nd and ^{150}Nd respectively; these isotopes must be mainly products of the s-process. From Wallerstein *et al.* (1997). Reproduced by permission, © 1997 American Physical Society.

Generally, the strength of branching f_β is defined as

$$f_\beta \equiv \lambda_\beta/(\lambda_\beta + \lambda_\mathrm{n}) \approx \langle\sigma_i\rangle\, {}^{i}N/\langle\sigma_j\rangle\, {}^{j}N. \tag{5.15}$$

For the above example $f_\beta \approx \langle\sigma_{148}\rangle^{148}\mathrm{Sm}/\langle\sigma_{150}\rangle^{150}\mathrm{Sm} = 0.87$ (Wisshak *et al.*, 1993), and this gives $\lambda_\mathrm{n} = 2.3 \times 10^{-7}$ s^{-1}. Substituting this value in $\lambda_\mathrm{n} = n_\mathrm{n}\langle\sigma\rangle v_T$ (see Eqn 5.11) gives a neutron density $n_\mathrm{n} \approx 4.6 \times 10^8$ cm^{-3} for the main s-process component, $T \approx 3 \times 10^8$ K (Kappeler *et al.*, 1989; Reifarth *et al.*, 2003).

Arlandini *et al.* (1999) investigated branchings in the neutron-capture path at ^{141}Ce and ^{142}Pr that affect the s-process abundance of ^{142}Nd, for which the SOS abundance is important for the understanding of early Earth processes (Fig. 27.16(a), (b)). In their refined model for AGB stars these authors considered variations in the neutron density of almost two orders of magnitude.

If the neutron density in the s-process environment and the temperature–decay-rate relationships are known, then branching via nuclides that have temperature-dependent stellar decay rates, e.g. ^{176}Lu, allows s-process temperatures to be estimated at $T \sim 3 \times 10^8$ K (Wallerstein *et al.*, 1997).

5.5 Summary

Small and medium-size stars are the main producers of the light elements C and N, as well as of heavy n-capture s-process elements, at different stages of their evolution.

Slow H burning in a small (solar-like) star can sustain its luminosity and stabilize it against gravitational collapse during ~ 10 Gyr. Helium-4 is the principal product of this burning. As H burning proceeds, He accumulates in the core and, after the H is burnt out, core contraction and heating ignite He burning. This leads to the production and accumulation of C, N and O (especially ^{17,18}O), which are the final products of nuclear burning in a low-mass star. When the He in the core is exhausted, H burning in the shell starts again. At that late relatively short stage of stellar evolution, H and He burning in thin shells around the core replace each other several times. These episodes are accompanied by convection, the mixing of matter from different shells and mass loss from the outer stellar envelope. Small amounts of nuclides up to Si are produced by fusion, and some reactions yield neutrons. Then heavy elements are generated via interactions of nuclei with neutrons in the s-process. The use of radioactive–stable-isotope systematics allows the testing of neutron density and temperatures in the s-process sites.

Although additional observations and modelling are needed, it appears that there is a good understanding of nuclear burning and s-process nucleosynthesis in small and medium-mass stars. Generalizing, the solar system s-process element abundances can be understood as a result of mixing of the outputs of medium-size stars (a few solar masses) of different stellar generations, born with different metallicities and producing somewhat different patterns of s-process nuclei (Wallerstein *et al.*, 1997; Busso *et al.*, 1999, 2001; Abia *et al.*, 2001; Travaglio *et al.*, 2001c). Massive stars, however, follow a very different evolutionary path, discussed in the next chapter.

6

Stellar nucleosynthesis: r- and associated processes

6.1 Introduction to rapid nucleosynthesis (r-process): what does "rapid" mean?

The n-capture pathways to non-s-process elements answer the question, what is a rapid process? The pathway to the ^{232}Th–^{235}U–^{238}U island is separated from the stability valley by radioactive isotopes A decaying on rather short time scales, $\tau_A \sim 1$ s and less. To generate the above trio by n-capture of the closest stable nuclides (Pb, Bi) these short-lived nuclides must be bridged, and some of their half-lives require a neutron density a factor $\sim 10^{10}$ greater than that of the slow s-process (Eqn 5.12). Even higher neutron densities, 10^{23} to 10^{24} cm^{-3}, are required for the r-process models (Kratz *et al.*, 1993; Kratz, 2001).

Thus, the rapid or r-process requires an enormous neutron flux that cannot be reached during quiescent stellar evolution. Weak interactions, encountered earlier in Big Bang nucleosynthesis (Chapter 4), appear to be the only plausible neutron sources, e.g.

$$\mathrm{p} + \mathrm{e}^- \rightarrow \mathrm{n} + \nu_\mathrm{e}. \tag{6.1}$$

These are initiated at $\geq 5 \times 10^9$ K, which exceeds the highest temperature reached in Si burning and can be generated in several mechanisms, such as core collapse in a massive star, fast accretion on a C–O white dwarf or the merging of two stars.

All these mechanisms lead to a short explosive stage (known as a supernova), during which the star releases an enormous amount of energy, up to $\sim 10^{53}$ erg, more than the radiation from all $\sim 10^{10}$ stars in a galaxy combined, and then dies. Supernovae (SNe) are the most energetic events in the Universe, second only to the Big Bang (Wooden, 1997; Burrows, 2000). Two different types of SNe are distinguished. Supernovae of type II are explosions of massive stars (generally about 20 to 40 $M_\odot$), with intense H-lines in the spectrum (indicating a high abundance of hydrogen) and variable bolometric light curves (Section 6.3). Supernovae of type

I are explosions of low-mass stars (generally $< 1.4\ M_\odot$) and do not show strong H-lines. Type I supernovae are classified into three subclasses, one of which, SNe Ia, allows a precise measurement of the Hubble parameter (Section 4.3); this model is discussed in Section 6.4.

The short explosive stages of stellar evolution are extremely complicated phenomena that have not yet been adequately modelled or fully understood in detail. The outline given in the following sections is merely intended to illustrate the principles of r-process nucleosynthesis in the SNe environment.

6.2 Evolution of massive stars

The evolution of massive stars with $M > 10\ M_\odot$ is faster and more complicated than that of small ones. Because a higher core temperature is reached than in low-mass stars, the duration of H burning in the core is short, ~ 10 Myr for $M \sim 30\ M_\odot$, and all other stages are also much shorter. After He has accumulated in the core, the star evolves into the red-giant region, similarly to the evolution of low-mass stars (Fig. 5.1). However, because of the higher temperatures, the densities in massive star interiors are lower than in low-mass stars and therefore He burning starts before the core becomes degenerate. In the course of He burning the core expands, thus terminating H burning in the shell. The outer shells then become compressed and the star moves back towards the main sequence. After the He in the core is exhausted, the core, which now consists mainly of C and O ash, is compressed and becomes degenerate, whereas He or H burning resumes in the expanding shells and the star moves once again towards the red-giant region. The massive star passes along several such loops (Fig. 5.1). Each pass is accompanied by a convective dredge-up (up to four episodes) and mass loss into the interstellar medium. As the star matures, more heavy elements are being produced in the stellar interior. Carbon and oxygen burning produce heavier elements according to the reactions

$$\begin{aligned} {}^{12}\mathrm{C} + {}^{12}\mathrm{C} &\rightarrow {}^{20}\mathrm{Ne} + {}^{4}\mathrm{He} + 4.617\ \mathrm{MeV} \\ &\rightarrow {}^{23}\mathrm{Na} + \mathrm{p} + 2.241\ \mathrm{MeV} \\ &\rightarrow {}^{23}\mathrm{Mg} + \mathrm{n} + 2.599\ \mathrm{MeV} \end{aligned} \tag{6.2}$$

and

$$\begin{aligned} {}^{16}\mathrm{O} + {}^{16}\mathrm{O} &\rightarrow {}^{28}\mathrm{Si} + {}^{4}\mathrm{He} + 9.95\ \mathrm{MeV} \\ &\rightarrow {}^{31}\mathrm{P} + \mathrm{p} + 7.67\ \mathrm{MeV} \\ &\rightarrow {}^{31}\mathrm{S} + \mathrm{n} + 1.50\ \mathrm{MeV} \\ &\rightarrow {}^{30}\mathrm{Si} + 2\mathrm{p} + 0.381\ \mathrm{MeV} \\ &\rightarrow {}^{30}\mathrm{P} + \mathrm{D} + 2.41\ \mathrm{MeV}. \end{aligned} \tag{6.3}$$

The released α-particles, protons and neutrons interact with the available nuclei to produce a number of isotopes below the iron peak.

The last stage of element burning results in the production and accumulation of the most tightly bound nuclei of the iron peak, at very high temperatures, $\sim 3 \times 10^9$ K. At such temperatures, however, the photon disintegration of heavy nuclei also occurs:

$$^{28}\mathrm{Si} + \gamma \rightarrow 7\,^{4}\mathrm{He}. \tag{6.4}$$

The resulting large density of ^{4}He together with heavier nuclides enables such reactions as

$$^{28}\mathrm{Si} + 7\,^{4}\mathrm{He} \rightarrow {}^{56}\mathrm{Ni}. \tag{6.5}$$

A number of reactions within this mass range yield nuclei lighter than ^{56}Ni. This stage is short, a few weeks, as the temperature approaches 3×10^9 K. When the most tightly bound Fe and Ni isotopes (Section 1.2 and Fig. 1.2) have accumulated in the core, the nuclear fuel is exhausted and a star enters its most dramatic, final, episode.

The model of a pre-explosive massive star, the SNe II progenitor, has several shells, with the heavier constituent elements towards the centre. The shells are thought to contain He and N, He and C, C and O, O and C, O and Ne, O and Si, Si and S, and there is a massive Fe–Ni core.

6.3 Core-collapse supernovae (SNe II) and rapid nucleosynthesis

Supernovae type II (SNe II)

As the mass of the iron core increases and its matter becomes degenerate, there comes a point when the electron gas cannot counteract the gravitational pressure, and core collapse starts. The heat produced by the release of gravitational energy then causes the central core temperature to rise above that of Si burning. The partial photodissociation of Fe nuclei back to α-particles occurs. Because an Fe nucleus has a much higher binding energy per nucleon than He (Fig. 1.2), this dissociation consumes energy, thus preventing heating and allowing the collapse to proceed. Only after the Fe has been largely dissociated can energy released by the collapse be translated into heat, and the temperature then approaches $\sim 10^{10}$ K. Then alpha particles dissociate to protons and neutrons, thus preventing, for the same reason as above, any more heating of the core, which then collapses further.

While the central core density increases, the supersonic infall of material on it builds up the pressure and temperature, thus stimulating weak neutrino-producing interactions (6.1). The neutrinos escape from the core and a neutron-rich core starts

to form, the embryo of a neutron star or a black hole. The outward flux of neutrinos also carries away energy released in the core. However, as the density of the inner core approaches that of nuclear matter, $\sim 10^{14}$ g cm^{-3} (Section 1.2), it cannot collapse further. Then the whole enormous energy of the outer-core collapse must be transformed into heat, which is mainly deposited within the so-called "gain" region of the core. The sharp temperature upturn in this region generates a shock wave, which for a few milliseconds reverses the collapse.

Severe energy losses by photodisintegration of iron nuclei and neutrino emission terminate the reversal, and the dense, hot, neutron-rich core (a proto-neutron star, PNS) is accreting further mass at a rate $\sim M_\odot$ s^{-1}. At this point two quite different outcomes are possible. If such intense accretion continues for about 1 second, the proto-neutron star develops into a black hole, thus preventing explosion (Woosley *et al.*, 2002). In the case of somewhat less intense and longer accretion, the inner-core neutrinos yielded via weak interactions approach the outer PNS layer, giving rise to an enormous neutrino flux from the star's surface: a "neutrino star" is born deep inside the dying star. The PNS contracts, giving up its binding energy (up to 10% of its rest mass, or about 3×10^{53} erg). As it settles down into a neutron star, a gravity-powered neutrino explosion (partially) blows away the material outside its ~ 10 km radius. During this few-seconds-long pulse the SNe neutrino luminosity can exceed the total optical output of the observable Universe (Burrows, 2000; Woosley and Janka, 2005).

The expanding envelope is convectively unstable because of the extremely high temperature of the matter closest to the PNS, and so convection carries the energy deposited in its small innermost region to the outer parts, thus heating the envelope, stimulating the explosion and developing non-radial deformations. Indeed, observations suggest an asymmetric explosion: neutron stars have high velocities (generally ~ 500 km s^{-1}) and eccentric orbits, indicating a violent kick at birth. Highly asymmetric explosion mechanisms may be a necessary ingredient of core-collapse supernovae models (Burrows, 2000; Cameron, 2001a, c; Wang *et al.*, 2001).

Supernova explosions eject stellar material into the interstellar medium: in the SNe II model ($M_{\rm SN} \sim 30\ M_\odot$), the total mass of ejected material could approach $0.9 M_{\rm SNe}$. Initially plasma is ejected that transforms into a gas, and solid grains are formed soon afterwards. Radiogenic species in such grains allow the relevant time scales to be evaluated. Tellurium and xenon isotopic anomalies in presolar nano-diamonds formed after a supernova explosion imply a time interval from a few hours to one day between the termination of the nucleosynthetic process and the formation of these first grains (Ott, 1996; Richter *et al.*, 1998; Qian *et al.*, 1999).

In the case of a binary system, material lost by a supernova could be trapped by an accompanying star. This star then shows enrichment of the α-elements,

typical products of the explosive burning of SNe II stars, in accord with explosive nucleosynthesis in the outer parts of SNe II models (Israelian *et al.*, 1999).

Explosive nucleosynthesis: r-process and explosive burning

Within the framework of the core-collapse model, a plausible environment for the main r-process appears to be the region between the surface of the newly formed neutron star embryo ($T \sim 10^{10}$ K, $\rho \geq 10^{10}$ g cm^{-3}), and the expanding envelope below the Si-rich shell. The neutrino wind carries neutrons and protons away from the surface of the neutrino star: as the wind blows outward the star cools, and the n/p ratio increases via the weak interaction (Eqn 6.1); α-particles are produced, also causing the consumption of free protons, so that matter consisting mainly of α-particles and neutrons is formed (the inverse of Big Bang nucleosynthesis, Chapter 4). As the temperature drops from 10^{10} to 3×10^9 K, some α-particles assemble into heavy nuclei ($A \sim 100$), seeds for the r-process, and when the ratio of the number of seeds and the number of neutrons approaches ~ 0.01, the strong r-process occurs (Woosley *et al.*, 2002; Woosley and Janka, 2005).

Neutron capture generates nuclei up to $A \geq 260$ situated along the "waiting-point" pathways (Fig. 6.1). These correspond to a quasi flow equilibrium, in which neutron capture and emission are balanced: (n, γ) $\leftrightarrow$ (γ, n). The high neutron fluence (generating similar waiting-point pathways in different SNe) and the fission of $A \sim 260$ nuclei (yielding similar seeds, i.e. the double-magic ^{132}Sn with 50 protons and 82 neutrons and neighbouring nuclides) are responsible for the remarkable uniformity of the r-process output of heavy nuclides with $A > 130$. Indeed, a comparison of heavy-element abundances in metal-poor stars with the non-s-process component of $A > 130$ in the solar system shows the universality of the heavy r-process element pattern (Cowan and Sneden, 2006).

As the material expands and cools rapidly, the flow equilibrium is quenched and the β-decay of n-capture nuclei populates the first stable isobar encountered for a given mass number A (Fig. 6.1, see also Section 1.2). The neutrino wind lasts several seconds, and the duration of the r-process within this interval is ~ 1 s (Woosley and Janka, 2005). Shorter time scales have been derived from specific r-process models: ~ 0.1 s (Farouqi *et al.*, 2005), and even less. A successful supernova produces about 10^{-5} M$_\odot$ of r-process nuclei with $A > 100$ and ejects them into the interstellar medium.

As mentioned earlier, the abundance patterns for the r-process elements with $A < 130$ observed in metal-poor stars are not fully consistent with solar system abundances. Also important is that s-process elements (e.g. Zr, see Figs. 3.1 and 5.3) are highly enriched in some metal-poor stars relative to their potential seeds, the Fe-peak nuclides (Fig. 5.2). To explain these and other observations, special

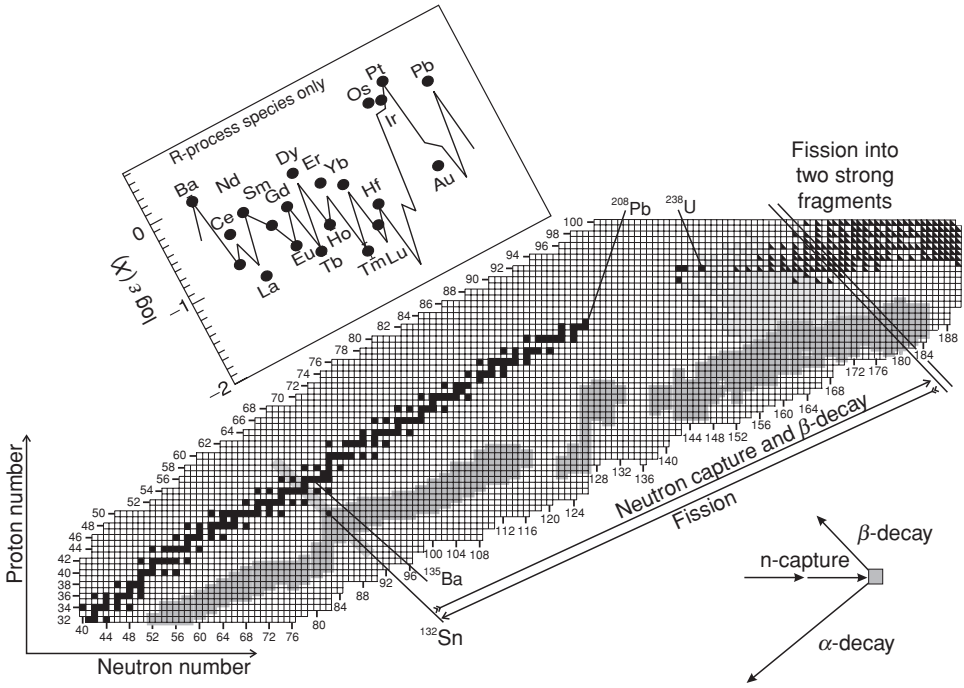

Fig. 6.1 Nuclide chart showing the β-stability valley (black squares) and the r-process-model waiting points (dark-grey areas). Several nuclides within the stability valley are labelled for better identification of the r-process elements seen in the inset (compiled from Fig. 3.1). The arrows in the right-hand bottom corner show the directions of n-capture, β-decay and α-decay paths. The light-grey shading at top right shows decay paths to yield U and Th. The small triangles show nuclei unstable to fission. Strong double-magic ^{132}Sn and other strong nuclei with $A = 132$ (the medium-grey rectangle crossing the ^{132}Sn point) are fragments expected from the fission of heavy nuclides ($A \sim 260$, on the right of the double line) that terminate the r-process waiting-point array. These fragments are considered as "uniform" seeds for the high-A r-process. From Schatz *et al*. (2002). Reproduced by permission of the American Astronomical Society.

environments and models have been suggested (e.g. Truran *et al.*, 2001; Pfeiffer *et al.*, 2001; Qian and Wasserburg, 2003).

In the expanding envelope, which is heated up to $\sim 5 \times 10^9$ K by the SNe shock, explosive nuclear burning according to

$$\begin{aligned} {}^{12}\mathrm{C} + {}^{12}\mathrm{C} &= {}^{20}\mathrm{Ne} + {}^{4}\mathrm{He}, \\ {}^{16}\mathrm{O} + {}^{16}\mathrm{O} &= {}^{28}\mathrm{Si} + {}^{4}\mathrm{He} \end{aligned} \tag{6.6}$$

etc., as well as explosive Si burning occurs. The burning of Si-rich material occurs via the disintegration of some ^{28}Si to α-particles and consequent (^{28}Si, α)

interactions (Eqns 6.4 and 6.5). The chief products of explosive Si burning are somewhat similar to stable burning; however, the temperature of explosive burning is high enough to establish so-called nuclear statistical equilibrium, which favours an enhanced abundance of the strong α-capture nuclei and, when cooling further, an "alpha-rich freeze-out". Abundant products of this process are ^{44}Ca (as ^{44}Ti, Fig. 3.5), ^{56,57}Fe (as ^{56,57}Ni) and other nuclides up to Zn.

The explosive burning of O and C takes place in a cooler region of supernovae at temperatures from 2 to 4 $\times$ 10^9 K. The products also resemble those of stable burning (Eqns 6.2, 6.3) but, because of the high temperature and abundance of α-particles, protons and neutrons are generated via (α, n) and (α, p), which leads to the synthesis of rare isotopes including ^{27}Al, ^{29,30}Si, ^{60}Fe and other n- and p-captured isotopes.

Summarizing, the ejected iron-group elements are mainly made explosively, but the intermediate-mass elements Si–Ca also have contributions from pre-explosion burning (Woosley *et al.*, 2002).

Associated p-, γ- *and* ν- *processes*

Some rare proton-rich isotopes cannot be produced by r- or s-processes because they are "shielded", i.e. the β-decay of n-capture nuclides produces other nuclides on the same isobar. Examples of such nuclides are ^{124,126}Xe and ^{130}Ba (compare the insets in Figs. 1.3 and 3.9). These require a special explanation. Under the extremely high temperatures of explosive burning, photons can dissociate nuclei and produce a proton-rich environment. As this cools, (p, γ) and (p, n) reactions can produce proton-rich nuclides (Wallerstein *et al.*, 1997). When the heavy nuclei generated by the p- and/or r- processes are available, (γ, n), (γ, p) and (γ, α) reactions can also generate proton-rich isotopes. For example, any sequence of photonuclear reactions that removed 14 neutrons and four protons from ^{208}Pb would produce the p nuclide ^{190}Pt (Wallerstein *et al.*, 1997). The time window for these reactions is however always short, up to a few seconds.

Neutrino capture, the ν-process, also plays a role in the r-process; neutrino capture produces light elements and some proton-rich nuclides during star explosions (Wilson *et al.*, 1986; Woosley *et al.*, 1990). The flux of neutrinos through the expanding envelope is so great that despite the small cross sections significant nuclear transmutations become possible. Neutrinos excite heavy nuclei to particle-unbound levels: the expulsion of a single neutron, proton or α-particle yields a new element:

$$\begin{aligned}(Z, A) + \nu \rightarrow (Z, A)^* + \nu' &\rightarrow (Z, A-1) + \mathrm{n} + \nu';\\ &\rightarrow (Z-1, A-1) + \mathrm{p} + \nu';\\ &\rightarrow (Z-2, A-4) + \alpha + \nu'. \qquad (6.7)\end{aligned}$$

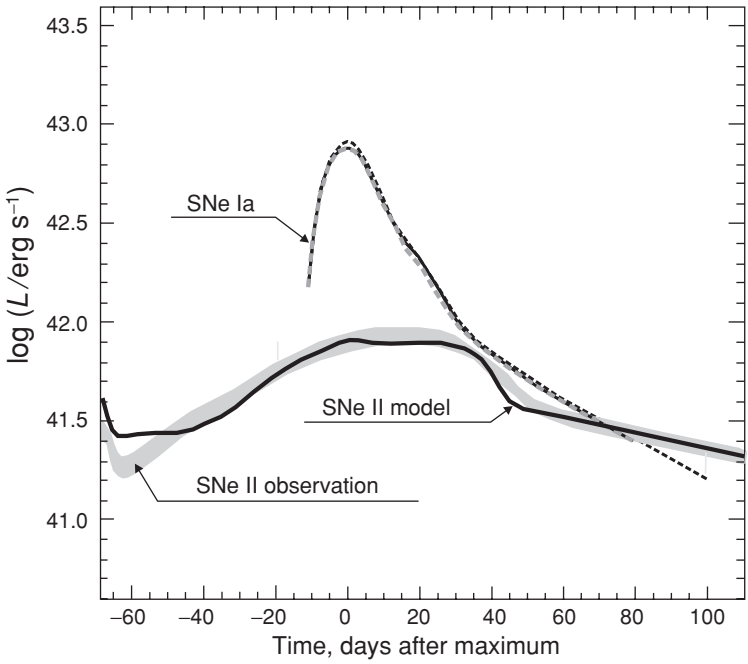

Fig. 6.2 Bolometric light curves of supernovae II and Ia. SNe II: measurements from two different observatories are included within the shaded band. The solid line is the SNe II model, envisaging the mixing of radioactive ^{56}Ni into the expanding outer envelope. SNe Ia: the bolometric curves from three SNe Ia are almost indistinguishable. After Wooden (1997) and Branch (1998).

These newly formed elements and the products of their decay significantly alter the outcome of traditional nucleosynthesis-model calculations. Heavy nuclei excitation by a neutrino, followed by fission, is also considered as a process capable of forming r-process nuclei with $A < 132$ such as Ru, Ag, Pd (Qian, 2002). Also, a large number of rare isotopes, including many odd-Z nuclei, from boron to copper owe much of their present abundance to this process. Specific nuclides produced almost entirely by the ν-process are ^{7}Li, ^{11}B, ^{19}F, ^{138}La and ^{180}Ta.

Special significance of ^{56}Ni and ^{44}Ti: bright isotopic candles

The first flash of a core-collapse supernova yields an effective temperature $T_{\rm e}$ as high as $\sim$ 500 000 K. This lasts only $\sim$ one day, and after this the decay of short-lived nuclides, shot into the H-envelope, powers the luminosity (Fig. 6.2). For the first $\sim$ three years the decay of a mass $\sim$ 0.07 $M_\odot$ (in some SNe up to 0.5 $M_\odot$, Sollerman, 2002) via $^{56}\mathrm{Ni} \rightarrow {}^{56}\mathrm{Co} \rightarrow {}^{56}\mathrm{Fe}$ dominates. The half-lives are 6.1 days and 77 days, respectively. After this, the β-decay chain $^{44}\mathrm{Ti} \rightarrow {}^{44}\mathrm{Sc} \rightarrow {}^{44}\mathrm{Ca}$ generates a roughly constant luminosity of the expanding ejecta for decades: the

half-life τ_{44} of ^{44}Ti is 60 yr, and this value is probably valid in the present context even though a highly ionized state is expected for the post-shock ejecta (Mochizuki, 2001; Laming, 2001).

All the above isotopes are generated in explosive nucleosynthesis within the internal shells of the supernova model. Both the shape of the light curve and hard X-rays and γ-rays from a supernova indicate a short time interval between the explosion and the appearance of the radioactive isotopes in the outer expanding H envelope. To fit this constraint, the internal matter containing these isotopes must have been shot at high velocities into the envelope and mixed there with unprocessed material (Wooden, 1997; Mitchell *et al.*, 2001).

The mixing was not perfect, however, and regions of the photosphere having high ^{56}Ni show up as hot Ni bubbles or plumes. Further, the observed ^{44}Ti/^{56}Ni ratios are enhanced relative to the model value. This, and the high and spotty abundances of the radioactive isotopes in the outer envelope, again indicate highly heterogeneous and asymmetrical explosions (Nagataki *et al.*, 1998; Cameron, 2001c; Vink, 2005).

6.4 SNe Ia: nucleosynthesis and luminosity

Supernovae of the class known as SNe Ia are frequently observed in elliptical galaxies having high metallicity and an enhanced population of small stars (Wallerstein *et al.*, 1997; Peacock, 1999). About 90% of SNe Ia are remarkably uniform in their properties. These include absolute peak magnitude, light curves showing that the luminosity is powered by the decay of ^{56}Ni and ^{56}Co (Fig. 6.2) and spectra showing Si, S, Ar and Ca lines, but no hydrogen. In the late nebular phase the spectra are dominated by iron features, thus indicating an abundance of iron-peak elements.

These observations suggest that SNe Ia originate from the thermonuclear disruption of a progenitor white dwarf, consisting mainly of products of He burning, i.e. C and O, that accretes material from a companion low-mass (1–3 $M_\odot$) star in a close binary system or via merging. The accretion ignites carbon burning deep in the stellar interior. Much uncertainty remains about what follows after the ignition (Hillebrandt and Niemeyr, 2000; Woosley, 2001). According to Woosley (2001) the central temperature increases in the course of C burning, thus stimulating convection which efficiently transfers hot material in runaway blobs. When the temperature approaches $\sim 7 \times 10^8$ K, explosive burning is initiated in the hottest individual regions of the inner core and the blobs. These regions then become more buoyant and transfer the fire throughout the stellar interior. This specific mechanism of burn propagation shortens the final stage of the explosion, with $T > 10^9$ K, down to milliseconds and this allows an enhanced yield of the α-capture nuclei ^{28}Si, ^{32}S, ^{36}Ar, ^{40}Ca (observed in the spectrum) and ^{56}Ni (which powers the luminosity) to be frozen out after the outburst. Modelling shows that such explosions can produce

solar abundances of ^{48}Ca, ^{50}Ti, ^{54}Cr and ^{70}Zn and also appreciable contributions to ^{66}Zn, ^{76}Ge, ^{82}Se and the short-lived ^{60}Fe. Type Ia supernovae are the most important source of these nuclei, especially ^{48}Ca (Woosley, 1997).

In the hydrogen-rich envelope accreting on the white dwarf, p-rich nuclei could also originate provided that the accretion rate and temperature are high enough to initiate rapid p-burning (rp-process, Wallerstein *et al.*, 1997). In this case (p, γ) reactions can yield the "waiting point" array of proton-rich short-lived radionuclides situated above the stability valley. The p-rich Te isotopes, which are very-short-lived α-emitters, terminate the array (Schatz *et al.*, 2001). The proton-rich radionuclides decay to populate the p-rich margin of the stability valley. The rp-process could be a source of heavy C and N, found in several presolar grains and characterized by very low ^{12}C/^{13}C (< 10) and ^{14}N/^{15}N (< 20) ratios respectively (Amari *et al.*, 2001b; see Fig. 3.3).

The great density of the progenitor ensures that the explosion energy is efficiently converted to kinetic energy of expansion, blowing all the material outwards. A luminous nebula results, and the star vanishes while giving birth to it.

The overall similarity of SNe Ia arises from the narrow range of the white dwarfs in mass, $\approx 0.6\ M_\odot$, and composition, mainly C and O (Matteucci and Recchi, 2001; Hansen and Liebert, 2003). Because of their remarkable uniformity and enormous luminosity, SNe Ia have presented a unique opportunity to obtain both redshifts and distances for distant galaxies from the comparison of the observable and model-derived spectra and luminosities, as discussed in Section 4.3. Importantly, these observations allow "normal" SNe Ia to be selected, which ensures correctness of the comparisons. For example, in normal SNe Ia the maximum luminosity and the shape of the light curve correlate. Anomalous events, not fitting this correlation, can be eliminated (Branch, 1998; Pinto *et al.*, 2001).

6.5 Summary

The evolution of massive stars ($M > 10\ M_\odot$) is fast (generally within 10 Myr) and complicated. Because of the higher temperatures, in their interior not only hydrogen and helium but also C, O and then Si can fuse, yielding elements up to $A \approx 60$. The star has an onion-like shell structure: the iron-group elements accumulate in the core and the outer shells have progressively lighter elements.

The iron-peak isotopes cannot yield fusion energy as their binding energy per nucleon already represents the maximum. This lack of available energy leads to core cooling and collapse. The collapse is destructive: the core heats up, Fe nuclei revert back to α-particles and then to neutrons and protons by photodissociation and the inner core approaches nuclear matter density. At the same time the enormous amount of energy from the infall of material onto the collapsed inner core is

transformed into heat. A sharp temperature upturn around the core generates the supernova shock. The inner core contracts, giving up binding energy (up to 10% of its rest mass or about 3×10^{53} erg): it then settles down into a neutron star and develops a gravity-powered neutrino explosion that (partially) blows away the overlying material. During this few-seconds-long pulse the SNe II neutrino luminosity can be brighter than all the stars in the observable Universe put together. Convection within the exploding envelope and other factors cause the explosion to be asymmetrical.

Further, r-, p-, γ-, ν- and explosive-burning nucleosynthetic processes are initiated within the expanding envelope, from the surface of the nascent neutron star outward to the O-rich or C-rich shells. These fast nucleosynthetic processes, which happen in the last seconds of the life of a massive star, yield many different elements. The explosive burning of C, O and Si favours the production of strong α-elements, terminating at ^{56}Ni. The r-process generates a great mass range of n-capture isotopes up to the heaviest radioactive ones. These are situated mainly along the lower margin of the stability valley. The r-process terminates at $A \sim 260$ because of fission of the super-heavy elements, and the fission products with $A \sim 130$ are its important seeds. The rp- and p- processes produce light p-nuclei (below $A \sim 130$) on the upper margin of the valley and also yield some low-abundance isotopes that cannot be produced by nucleus–neutron interactions.

Explosions also transfer heavy elements from the inner shells to the outer expanding envelope, which becomes a nebula in which the decay of heavy radioactive isotopes (^{56}Ni, ^{44}Ti) powers the luminosity (exceeding the luminosity of a whole galaxy!) for years. Owing to their short lifespan and the great quantity of freshly synthesized nuclides ejected, massive stars are the most important factories for the chemical evolution of interstellar matter and therefore for the Universe as a whole.

Supernovae events can also originate from low-mass progenitors such as white dwarfs (SNe Ia). In this case the explosion is ignited by the merging with, or accretion of, material from a neighbouring star. The similar masses and compositions of white dwarfs lead to a remarkable uniformity in the absolute peak magnitudes, light curves and spectra of SNe Ia. Because of these features SNe Ia present a unique opportunity to obtain both redshifts and distances for distant galaxies and thus allow precise determination of the Hubble parameter. They also generate appreciable amounts of nuclides up to the iron peak with an enhanced yield of the α-capture nuclei. SNe Ia events result in complete disruption, so that all elements generated are ejected into the interstellar medium.

7

Timing of stellar nucleosynthesis

7.1 Cosmochronology from long-lived radioactive elements

To understand the evolution of the elements related to stellar nucleosynthesis and their reservoirs, the galaxies, it is important to constrain the time when the elements heavier than helium were first generated and the rate of their generation. In principle, this time (or age) can be estimated from the decay of long-lived radioactive isotopes, e.g. Th and U, which both result from r-process nucleosynthesis. Thus, if the initial model-r-process-derived abundance ratios of ^{238}U and ^{232}Th are known (these are indicated by a subscript 0), their measured stellar abundances (indicated by a subscript 1) can yield the time difference between the nucleosynthetic event and the present via Eqn (10.11):

$$\Delta T_{0,1} = \frac{1}{\lambda_{238} - \lambda_{232}} \ln \frac{(^{238}\mathrm{U}/^{232}\mathrm{Th})_0}{(^{238}\mathrm{U}/^{232}\mathrm{Th})_1};$$

see Section 10.4 for a discussion of this equation. It is also possible to use the ratios of ^{232}Th or ^{238}U (or another radioactive isotope) and a stable r-process nuclide, for example Eu, in which case the first factor would be $1/\lambda_{232}$ or $1/\lambda_{238}$ respectively; the λ values are found in Table 28.1. However, attempts to use the Th/Eu ratio for this purpose have not given consistent results, as $(\mathrm{Th/Eu})_0$ is apparently variable (Cowan *et al.*, 1999; Qian, 2002; Honda *et al.*, 2004).

To avoid this problem, it has been suggested that one could use the abundances of a number of heavy r-process elements in a given star in order to provide a multi-element-consistent model and thus distinguish between the anomalous and normal yields of the species. Several metal-poor stars that pass such a test give a reasonable age interval, from 11 to 15 Gyr. The perspectives for radiometric stellar chronology of this kind include improvements in the accuracy of measurements, the further development of r-process models and the use of the less model-dependent U/Th and Th/Pb ratios (Cayrel *et al.*, 2001; Thielemann *et al.*, 2002; Schatz *et al.*, 2002; Cowan and Sneden, 2006).

7.2 The uranium isotopes: age and evolution of stellar nucleosynthesis

In the more common, higher-metallicity, case, where the observed abundances of radioactive isotopes are considered to result from continuous evolution, evolutionary models can be constructed. Such an approach can make use of the terrestrial $^{235}U/^{238}U$ and $^{232}Th/^{238}U$ ratios, which are very well known (Table 28.1). The principal unknown in these models, and an important parameter of galactic chemical evolution (GCE), is the rate of the preterrestrial contribution of r-process isotopes to the interstellar medium, $GCE(t)$, which should be added to Eqn (1.1):

$$dR/dt = -\lambda R + GCE(t). \tag{7.1}$$

The isotopes ^{235}U, ^{238}U and ^{232}Th are produced simultaneously, with model initial ratios $(^{235}U/^{238}U)_0 \approx 1.45$ and $(^{232}Th/^{238}U)_0 \approx 1.7$ (or slightly higher, ≈ 2.2, according to another r-process model; see Schatz *et al.*, 2002). These ratios should be compared with the solar system (SOS) present-day ratios recalculated to the time of solar system formation, 4.570 Gyr ago (Table 28.1); these SOS initial ratios are the principal constraints for modelling (Fig. 7.1).

For the simplest case, in which all these r-nuclides were produced in a single hypothetical nucleosynthetic event, $GCE(t) = 0$ and the rearrangement of Eqn (7.1) for the U-isotope ratio gives

$$^{U}R_0 = {}^{U}R_{SOLAR}[\exp(\lambda_{235}t)/\exp(\lambda_{238}t)] \tag{7.2}$$

and analogously for the $^{232}Th/^{238}U$ ratio. When the above ratio values are substituted into Eqn (7.2), the age of the event, T, is found to be 6.4 and 8 Gyr for the U/U and Th/U systematics respectively (Model I, Fig. 7.1). These values are much less than the Hubble time and the Th–Eu and Th–U estimates discussed above and are also significantly different from each other. As expected, the one-short-event model appears to be a gross oversimplification for high-metallicity systems.

A slightly more complicated model envisages the production of nuclides at a constant rate before they were isolated from the nucleosynthesis environment 4.57 Gyr ago: $GCE(t) =$ constant. The solution gives $T(U/U) = 14.5$ and $T(Th/U) = 12.5$ Gyr (Model II, Fig. 7.1). This opposite order of "nucleosynthesis ages" obtained for U/U and Th/U from the two above models implies that an intermediate scenario with a decreasing rate of nucleosynthesis would fit the data best. Indeed, an exponentially decreasing rate, by a factor ~ 2 per 10 Gyr (similar to the rate of supernovae nucleosynthesis, see the inset in Fig. 7.1), gives the same age, ~ 12 Gyr, for the beginning of nucleosynthesis of the heavy elements for both ratios. This value is in overall agreement with the Th–U chronology of metal-poor stars.

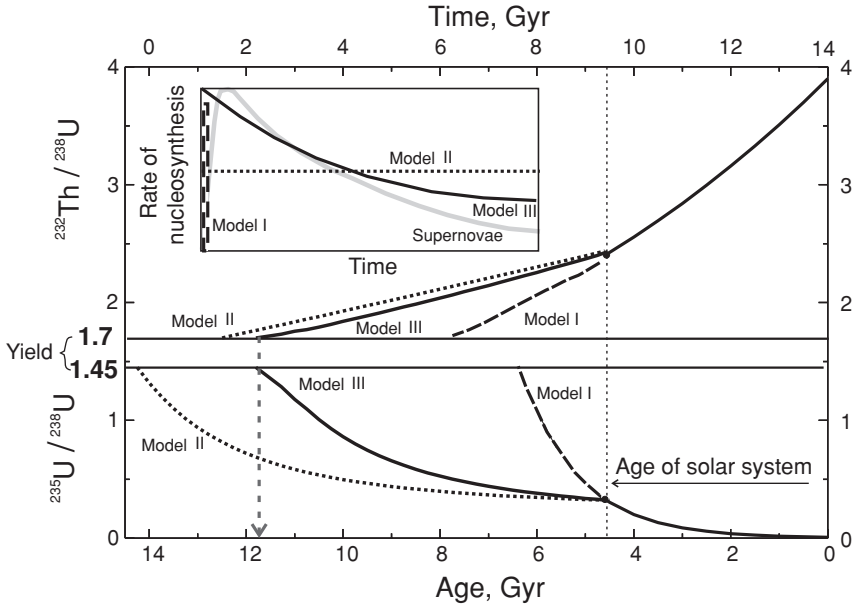

Fig. 7.1 Radiometric chronology of nucleosynthesis: the ^{238}U–^{235}U–^{232}Th systematics. Among three models of the rate of nucleosynthesis (see the inset: early short synthesis, Model I; continuous synthesis at a constant rate, Model II; exponentially decaying synthesis, Model III) only Model III gives a self-consistent solution (broken-line arrow), i.e. similar ages for the ^{235}U–^{238}U and ^{232}Th–^{238}U systematics at ~ 12 Gyr. For comparison, the rate of birth of supernovae, the major generators of these elements in the Galaxy, is also shown in the inset (grey line); the production rate in the early Galaxy (~ 13 Gyr ago) is estimated at ~ 30 stars per century. From Timmes *et al.* (1995). Reproduced by permission of the American Astronomical Society.

7.3 The age of stellar clusters: luminosity–temperature relationships

Beside the radioactive-isotope systematics there are several other methods of estimating the age T when nucleosynthesis started. Most of these methods employ so-called stellar isochrons (lines of equal age) within the luminosity–temperature H–R diagram. The luminosity L depends on the rate of energy production in the stellar interior. In a solar-like star this is proportional to the rate of hydrogen burning, $\psi(\mathrm{d}H/\mathrm{d}t)$, where ψ is the yield of nuclear energy per hydrogen atom (Shklovsky, 1977):

$$L = -\psi(\mathrm{d}H/\mathrm{d}t). \tag{7.3}$$

Approximating the solution of Eqn (7.3) allows us to estimate the age of a main-sequence star, T_{MS}:

$$T_{\mathrm{MS}} \approx \psi(H_0 - H_{\mathrm{MS}})/L. \tag{7.4}$$

Zero-age stars, for which $T = 0$, having an initial hydrogen abundance $H_0 \sim 10^{57}$ atoms for a solar-like star and the highest effective temperatures, are situated along the left-hand boundary of the main sequence (approximately along the left-hand edge of the shaded band in Fig. 5.1). This edge determines a zero isochron. As a star evolves it moves toward the right-hand edge of the main sequence; the rate and the trajectory of the movement depend on the stellar parameters. Figure 5.1 illustrates the trajectory for a solar-mass star. By the time such a star turns off the main sequence, its amount of hydrogen has dropped to 0.9 of the initial amount.

The energy produced by the fusion of each hydrogen atom is 1.12×10^{-5} erg (^{4}He being the final product, Section 1.2), whereas the solar luminosity is 3.86×10^{33} erg s^{-1}. Substituting the above values in Eqn (7.4) gives the age of a solar-like star situated on the right-hand edge of the main sequence, $T_{\rm MS} \sim 10$ Gyr.

Modelling gives the position of 10 Gyr stars for other masses, thus determining the 10 Gyr isochron within the H–R diagram. Clusters of "syngenetic" stars of different mass, generally formed almost simultaneously from the same cold molecular cloud complex, indeed define such isochrons (Peacock, 1999; Hartmann *et al.*, 2001). These cluster isochrons thus allow an age determination with more confidence than for individual stars, and values of 13 ± 1 Gyr were obtained for the two most ancient clusters (Salaris *et al.*, 1997).

Further, modelling of the evolution of very-low-mass main-sequence stars and white dwarf cooling rates gives ~ 12 Gyr and ~ 10 Gyr respectively (Peacock, 1999). Obviously these objects can only record the time that has passed since their formation and thus provide minimum estimates for the age of the earliest stars.

7.4 Summary

There are several independent methods of determining the time when the first stars appeared and stellar nucleosynthesis started. Each method is model dependent. The use of radioactive isotopes, e.g. ^{232}Th, ^{238}U and ^{235}U, relies on their initial abundances, obtained from models. Improvements in the accuracy of measurements and refinements of r-process models are "pathways" to a more reliable radiometric cosmochronology. Cluster isochrons in the H–R diagram rely on stellar models.

However, even though each method is far from perfect, the various independent approaches give a similar age for the earliest nucleosynthesis, $\sim$14 Gyr, which is indistinguishable from the Hubble time. There is little doubt that the galaxies, at least the Milky Way, and the earliest stars were formed very soon after cosmological nucleosynthesis, but the exact delay cannot be precisely quantified at present.

From self-consistent model estimates of the age of the most ancient r-elements an exponentially decreasing rate of production of these elements with time is derived. The exponent, ~ 2, agrees with models of galactic chemical evolution, to be discussed in the next chapter.

8

Chemical evolution of the Galaxy

8.1 Introduction: processes governing galactic chemical evolution

After the Big Bang, stellar nucleosynthesis became by far the major element-producing factory. During the mass-loss episodes experienced by most stars, newly produced elements are (partially) transferred to the interstellar medium (ISM), which thereby evolves chemically. The element yields and the transfer mechanisms are both dependent on stellar masses and evolution (Chapters 5 and 6).

The interstellar medium initially consisted almost exclusively of primordial H and He, and this low metallicity favoured the accretion of very massive stars, $\sim 30\ \mathrm{M}_{\odot} < M < \sim 300\ \mathrm{M}_{\odot}$. Even though adequate models of these stars have not yet been developed, they are considered to have a very short life. The total mass of the ejected heavy elements as well as their abundance pattern strongly depend on a stellar model, especially on the details of stellar death. In the case of a successful explosion, heavy r-process and Fe-peak elements are abundant in stellar ejecta whereas the inner core is converted into a neutron star. In the other case, only products of explosive burning in the outer shells are ejected; most material falls back onto the core to generate a massive black hole that could play an important role in the subsequent formation of a galaxy. In both cases the amount of material ejected into the interstellar medium could be enough to overcome the metallicity threshold in a stellar neighbourhood for the formation of low-mass stars, ${}^{\Sigma A}Z \sim -3$; therefore small low-metallicity long-lived stars could have sampled an array of elements generated by one or very few progenitor(s) (Silk and Bouwens, 2001; Bromm and Larson, 2004; Schneider, 2006; Cowan and Sneden, 2006).

In parallel with low-mass stars, massive stars, ~ 10 to $100\ \mathrm{M}_{\odot}$, continue to be formed even as the metallicity increases. After a rather short life (~ 10 Myr) these meet a dramatic death as SNe II, leaving behind a neutron star or black hole. There are ejecta, amounting (in the case of a successful explosion) to up to $\sim 90\%$ of the original stellar mass. Along with the initial constituents, the ejecta carry products

of burning, explosive burning and r-, p-, γ- and ν-nucleosynthesis. This material, ejected at high speed, not only contributes to the planetary nebulae and interstellar medium but also to the intergalactic matter (see Fig. 2.1). Because of their short lifetime and the large quantity of newly produced nuclides in the ejecta, massive stars dominate the chemical evolution of a galaxy.

Medium-sized stars (from 3 to 10 $M_\odot$) generate elements up to the iron peak and contribute most of the s-process elements and appreciable amounts of C and N to the interstellar medium. The degenerate core left behind develops into a white dwarf. In the case of a binary system, however, a white dwarf can accrete enough mass to initiate explosive burning as a SNe Ia. Strong α-nuclei up to the iron-peak elements are the major products of such events. It has also been proposed, however, that the accretion-induced collapse of a white dwarf into a neutron star may be associated with the production of heavy r-nuclei and may provide occasional coupling of high r-process and high s-process enrichments in the envelope of the surviving low-mass partner star (Qian and Wasserburg, 2003).

Small stars ($\sim M_\odot$) have such long lifetimes, up to the Hubble time, that they simply store the elements, both those initially available and those newly produced. If the ages of such stars are known, they can be used to trace the composition of the interstellar medium back to the time and place when and where they were formed. Even though the accumulation of dust in the interstellar medium favours the formation of small stars during late stages of galaxy evolution, in rare cases such stars were formed long ago: ultra-metal-poor stars present an example (Section 3.2).

The composition of the interstellar medium evolves through these varied stellar contributions, and new stars accreting from it inherit this evolving contribution and build further on it. In this chapter we examine this galactic evolution, mainly concentrating on the solar neighbourhood, for which most data are available. Spectroscopic observations on stars of various metallicities, as well as analytical data on presolar grains, will be reviewed and will form the basis for the models outlined at the end of the chapter. Modern models of chemical evolution treat the Galaxy as an open system, envisaging mass exchange with the intergalactic medium.

8.2 Milky Way evolution

The [Fe/H]–*age reference evolution*

The main result of accumulated stellar processing is an increase in the abundance of heavy elements in the interstellar (and intergalactic) medium through time. This measurable quantity justifies models of the chemical evolution of a galaxy.

Observations show that our Galaxy is a highly heterogeneous system, having reservoirs with different evolutions, compositions and ages. Pagel (1994, 2001),

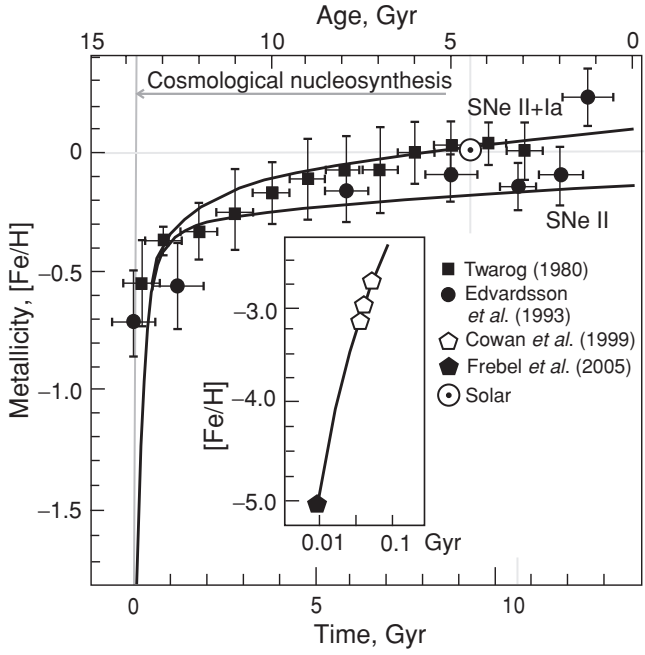

Fig. 8.1 Solar neighbourhood age–metallicity relationships. The metallicity is expressed as [Fe/H] (see the Glossary). The model curves show that the contribution from type Ia supernovae is important for reproducing the observed trend. The deviations observed are thought to originate from the heterogeneity of the Galaxy within the solar neighbourhood rather than from observational uncertainties. The solar age–metallicity data point is well within the trend, suggesting that the solar system element abundance indeed represents the relevant region of the solar neighbourhood. The inset shows the earliest part of the trend, the recent data for stars that have extremely low metallicity values. After Timmes *et al.* (1995), Cowan and Sneden (2006) and Frebel *et al.* (2005).

Timmes *et al.* (1995), McWilliam (1997), Clayton and Timmes (1997) and Chiappini and Matteucci (2001) have reviewed observations and models related to this complicated system.

Generally the relevant abundance trend of each isotope Z is expressed relative to iron, [Z/Fe], as a function of the iron-to-hydrogen ratio [Fe/H], because the latter is a relatively easy quantity to measure in stars. The calibration of the [Fe/H] ratio as a function of time is therefore the basis for the age–metallicity relationship for other elements.

The [Fe/H]–age relationship has several important features (Fig. 8.1). The ratio increases sharply during the early evolution of the Galaxy: its value is -3 about 10^7 yr after formation of the Galaxy, -2 at about 10^8 and -1 at about 10^9 yr. This early [Fe/H] evolution highlights the important contribution of short-lived SNe II

Table 8.1 *Compositions of SNe II and SNe Ia ejecta ($M/\mathrm{M}_\odot$)*

Supernovae II ($\sim 25\ \mathrm{M}_\odot$)			Supernovae Ia ($\sim 1\ \mathrm{M}_\odot$)[a]			
Isotope	Initial mass[b]	Final mass[c]	Isotope	Initial mass[b]	Isotope	Final mass[d]
^{1}H	17.7	9.4	^{1}H	0.71	Cr–Ni	0.86
^{4}He	6.9	8.7	^{4}He	0.28	^{54}Fe	0.14
^{16}O	0.24	3.24	^{16}O	0.01	^{56}Fe	0.61
^{12}C	0.08	0.41	^{12}C	0.003	^{32}S	0.16
^{20}Ne	0.04	0.65	^{20}Ne	0.002	^{28}Si	0.16
^{14}N	0.03	—	^{14}N	0.001	^{24}Mg	0.09
^{28}Si	0.016	0.29	^{28}Si	0.0007	^{58}Ni	0.06
^{56}Fe	0.029	0.24	^{56}Fe	0.0012	^{40}Ca	0.04
^{32}S	0.001	0.14	^{32}S	0.0004	^{36}Ar	0.02

[a] In the case of SNe Ia, the white dwarf (WD) composition (not shown, see Section 5.3) is considered as intermediate between the initial solar composition assumed for a parent star (fifth column) and the final composition (seventh column).
[b] The solar initial composition is used for the progenitor stars (Anders and Grevesse, 1989).
[c] The SNe II output composition is from Meyer (1997).
[d] The total final mass (seventh column) exceeds the initial mass of the progenitor (fifth column) because of the contribution of material from a WD companion, assumed to be a red-giant star (after Pagel, 1994). Note the dramatic difference between the initial and final compositions, especially in the case of SNe Ia.

(Table 8.1). After this time (~ 1 Gyr after BBN) the SNe Ia yield of iron-peak elements became important (Matteucci and Recchi, 2001). During the last roughly 7-Gyr-long interval the [Fe/H] ratio smoothly increased, implying a moderate contribution of metals compared with the amount already accumulated in the Galaxy. The [Fe/H] ratios for the solar neighbourhood are quite similar to the solar value itself. This justifies the comparison between the solar and local Galaxy element abundances (Section 3.4). As [Fe/H] can be readily measured and its relation to time is robust, this ratio is generally used instead of the age when the evolution of other elements is studied (Timmes *et al.*, 1995).

The CNO elements

The CNO triad are the most abundant elements after H and He. In ultra-metal-poor (UMP) stars, with [Fe/H] < -4 (Section 3.2), the enormously high abundances of these elements, especially C, indicate their specific early production. These high [CNO/Fe] ratios seen in the spectra of UMP stars and some other observations cannot be explained within the framework of standard SNe II models. Instead, "mixing–fallback" stellar models for the mass range $20-130\ \mathrm{M}_\odot$ appear to reproduce

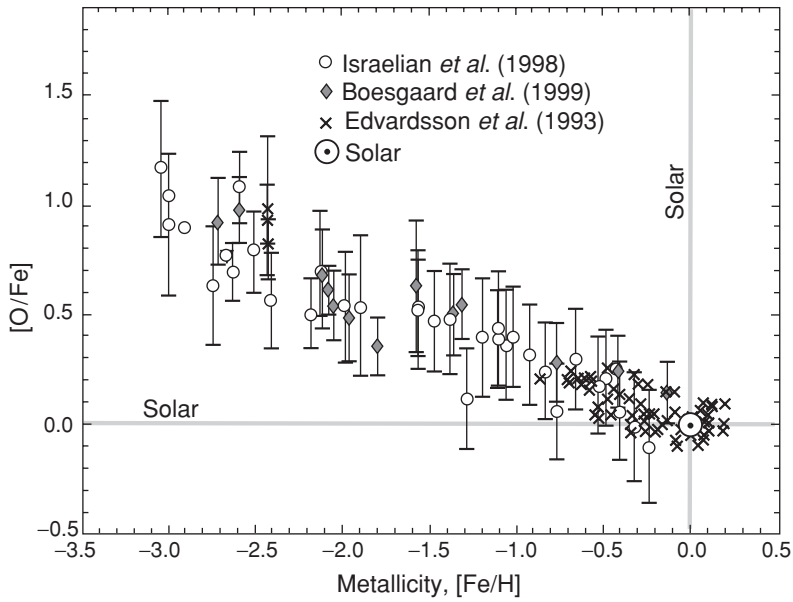

Fig. 8.2 Evolution of the oxygen-to-iron ratio as a function of [Fe/H]. The O-abundance is expressed as an [O/Fe] ratio (see the Glossary). The largest [O/Fe] and [CN/Fe] ratios are observed at low metallicities: the CNO elements in the very early Galaxy were probably generated by very massive stars. Then the SNe II take over, being the principal O-source in the Galaxy. Type Ia SNe begin to inject large amounts of Fe and negligible amounts of O into the interstellar medium $\sim$ 1 Gyr later, causing the observed downward trend. From Israelian *et al.* (2001). Reproduced by permission of the American Astronomical Society.

the observed [CNO/Fe] ratios: core collapse in these models is followed by mixing of the exploded material and fallback of most of it onto the core, resulting in a massive black hole (Section 6.3). The ejecta then transfer essentially α-products of explosive He burning in the outer shells, i.e. ^{12}C, ^{16}O and some N, into the interstellar medium, to be sampled in the formation of UMP stars. It is important that such SNe with very low ^{56}Ni and other Fe-peak elements in the ejecta have actually been observed. Other scenarios and stellar models have also been proposed to account for high [CNO/Fe] ratios, e.g. the contribution of matter ejected from a binary AGB (carbon) star onto the ultra-metal-poor star. These exciting topics were recently discussed in papers by Christlieb *et al.* (2004), and Frebel *et al.* (2005) and in a review by Beers and Christlieb (2005).

Later on, supernovae step forward as the major producers of heavy elements. Both SNe II and SNe Ia generate O (mainly ^{16}O) preferentially to C and N (Fig. 8.2, Table 8.1). Therefore the interstellar medium became relatively O-rich, and O-rich stars are considered "normal" in contrast with the "anomalous" C-rich

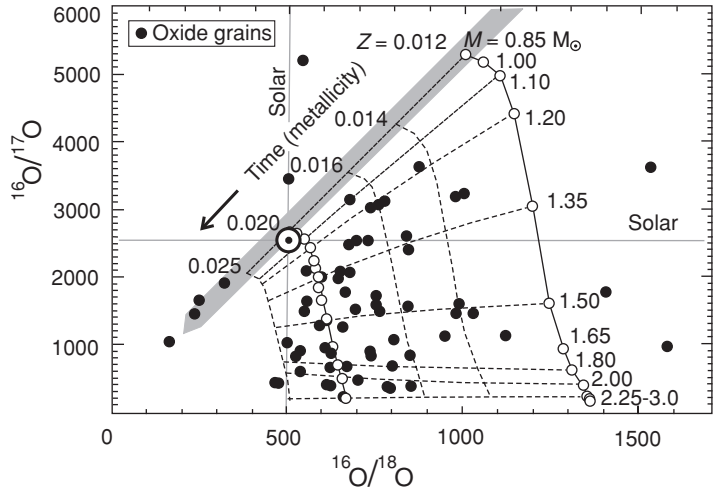

Fig. 8.3 Oxygen-isotope compositions observed in presolar oxide grains and those inferred from modelling. The shaded trend shows the postulated initial O-isotope ratios for an $M = 0.85\ M_\odot$ model and for various different metallicities Z; old stars, formed from low-Z material, show enhanced $^{16}O/^{17}O$ and $^{16}O/^{18}O$ ratios and vice versa. Each open circle corresponds to a prediction for a distinct stellar model depending on metallicity and mass, and the broken lines indicate interpolated values. The CNO cycle (Table 5.1) modifies the initial compositions by enriching ^{17}O and destroying ^{18}O. The mixing of this processed material with unprocessed subsurface material leads to deviation of the model data points from the initial compositions towards the bottom right. From Nittler (1997). Reproduced by permission, © 1997 American Institute of Physics.

stars (Wallerstein *et al.*, 1997). Also, n-capture r-process elements are yielded by core-collapse SNe II (Fig. 6.1).

Isotope compositions of CNO elements and Si: presolar grains and nucleosynthetic models

While SNe yield the α-O isotope ^{16}O, the major source of the "secondary" O isotope ^{17}O is partial H burning via the CNO cycles in the cores of low-mass stars ($0.8\ M_\odot < M < 3\ M_\odot$). Reaction 10 in Table 5.1 is slow and ^{17}O accumulates, thus decreasing the $^{16}O/^{17}O$ ratio with time. In the first dredge-up of the red-giant stage, the depth of convection depends on the stellar mass: the larger the stellar mass, the greater the depth of dredge-up and the more ^{17}O-enriched material is transferred into the envelope (Fig. 8.3). The isotope ^{18}O is produced by α-capture on ^{14}N during He burning. Thus even though the two secondary O isotopes originate in different processes, both depend directly on the initial CNO abundance: the $^{16}O/^{18}O$ and $^{16}O/^{17}O$ ratios are both predicted to be lower in young stars (which originate from

high-metallicity material), and presolar grains thus may reflect stellar sources of different age and mass (Fig. 8.3; Timmes *et al.*, 1995; Nittler, 1997).

During the AGB phase (Section 5.3), when the core is growing because of O and C accumulation from He burning in the shell, the burning is unstable and periodic He flashes initiate "third dredge-up" episodes. The third dredge-up of material consists mostly of ^{4}He and ^{12}C (the principal product of triple-α reactions), and its mixing into the surface envelope increases the C/O ratios. These then depend on the initial mass of the star, the mass loss caused by stellar winds during the first and second dredge-ups and the efficiency of the third dredge-up. Finally the C/O ratio may exceed unity: the star could develop into a carbon star, enabling SiC condensation (Lodders and Fegley, 1992; Nittler, 1997; Hoppe and Ott, 1997; Abia *et al.*, 2001). Infrared observations clearly show SiC formation in the circumstellar envelopes of low-mass C-rich stars (Gallino *et al.*, 1997). Also, the C-isotope ratios in these stars and those of SiC mainstream carbon are quite similar.

Indeed the distribution of the ^{12}C/^{13}C ratios of the mainstream SiC presolar grains is very similar to that of the atmospheres of carbon stars (Fig. 3.3). In both cases the ^{12}C/^{13}C ratios generally vary between 30 and 100, values of ~ 60 being the most common. Standard models assuming a solar initial composition (^{12}C/^{13}C = 89 and ^{14}N/^{15}N = 272) predict ^{12}C/^{13}C $\approx$ 20–30 and ^{14}N/^{15}N $\approx$ 600–2000 for the first and second dredge-ups, but a somewhat enhanced ^{12}C/^{13}C ratio $\approx$ 40–150 for the third dredge-up episode, the N-isotope ratios remaining the same. Mixing of the initial and processed materials explains the mainstream C- and most N-isotope compositions (Huss *et al.*, 1997).

Moreover, the isotopic compositions of some other elements, such as Al, Mg and the noble gases, are in agreement with this model. Therefore AGB stars are considered as the major source of carbon in the interstellar medium (Timmes *et al.*, 1995).

The extreme isotopic ratios seen in the grain population (Figs. 3.3, 3.4) require modifications of the standard models. One modification envisages nucleosynthesis as occurring during the mixing events themselves. Carbon rich in ^{13}C implies some circulation of matter between the base of the convective envelopes and regions close to the H-burning shell (Wasserburg *et al.*, 1995a). In this case the model third dredge-up material shows very low ^{12}C/^{13}C ≈ 3 and high ^{14}N/^{15}N ratios, $\sim 30\,000$ (Huss *et al.*, 1997). This fits the compositions situated in the top left corner of the N–C isotope plot (Fig. 3.3; Hoppe and Ott, 1997; Huss *et al.*, 1997; Amari *et al.*, 2001b). The compositions in the bottom left corner could have originated via the rp-process (Section 6.4). The anomalously high ^{12}C/^{13}C ratio and anomalously low ^{29}Si/^{28}Si and ^{30}Si/^{28}Si ratios in X-grains can be explained by the incorporation of supernova material: the trends seen in Figs. 3.3 and 3.4 indicate intensive mixing of nuclides generated in different stars (Zinner, 1998).

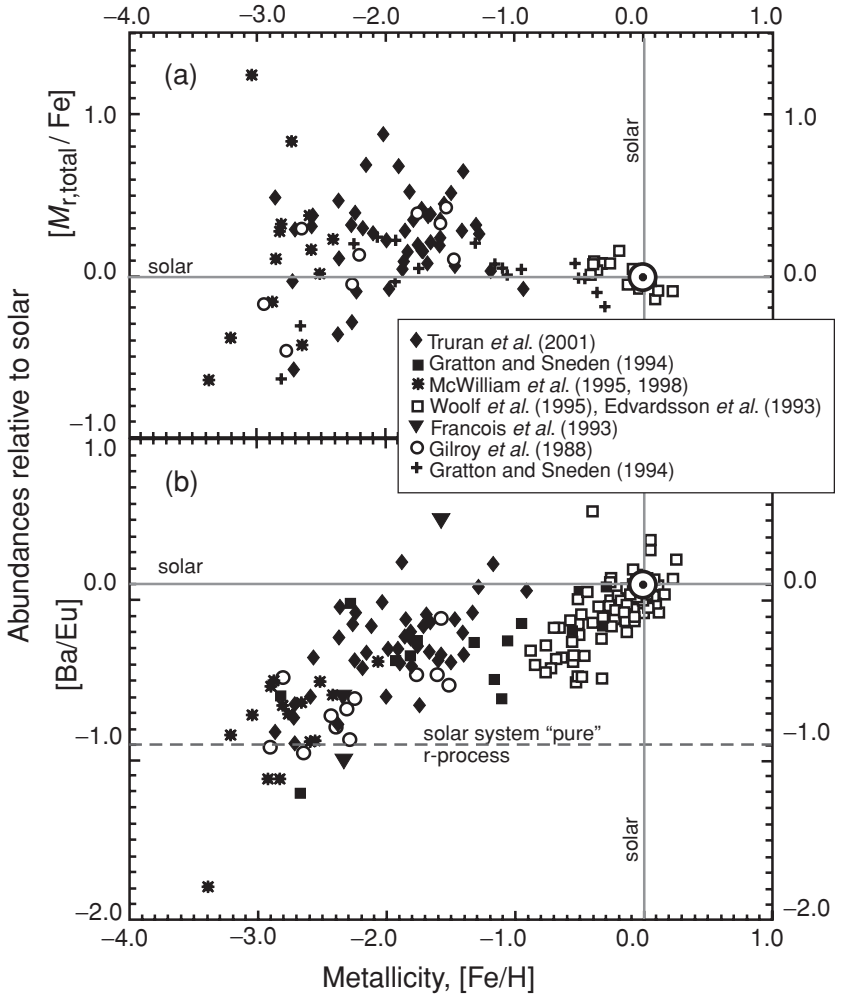

Fig. 8.4 Relationships between r- and s-process elements and metallicity. (a) The ratio of the abundances of r-process elements and of Fe (the total mass ratio) in stars and (b) the ratio of the abundances of s-process elements (Ba) and of the r-process elements (Eu), [Ba/Eu], vs. the stellar metallicity [Fe/H]. From Truran *et al.* (2001), © Elsevier Science 2001, reproduced by permission.

The covariant trend in $^{29}Si/^{28}Si$ and $^{30}Si/^{28}Si$ of "mainstream" silicon in SiC (Fig. 3.4) is still awaiting a plausible explanation.

Trace r- and s-process elements

Trace r-process elements display a large scatter of [Σ(r-process)/Fe] ratios, up to a factor ~ 300 at low metallicities, [Fe/H] < -2 (Fig. 8.4(a)). Above [Fe/H] ~ -1.5 the ratios are close to the solar value. Recalling that small metal-poor stars preserve

ancient material that does not evolve further in them, the scatter seen in Fig. 8.4 tells us: (1) there were several precursor stars to the metal-poor star population, and the rate of early nucleosynthesis and recycling exceeded the mixing rate; (2) the great age of the r-process elements means that the progenitor stars were short-lived and therefore massive; (3) different stars and stellar processes were responsible for the generation of the iron-peak and the r-process elements. The relative abundance of heavy r-process elements (Fig. 3.1) also emphasizes (4) the uniformity of the main r-process yield (Truran *et al.*, 2001).

Trace s-process elements show quite a different evolution. Figure 8.4 (lower panel) presents the evolution of the [Ba/Eu] ratio: Ba is mainly an s-process element and Eu an r-process product. At low metallicities, the [Ba/Eu] ratio is consistent with that for the pure r-process yield: in the early Galaxy r-process elements were much more abundant than s-process ones. Over time, the contribution of s-process species has smoothly increased relative to r-process species. The s-process elements were continuously generated in low-mass stars, which lived longer than massive stars; this explains the delayed input of s-process elements into the interstellar medium.

8.3 The sources of short-lived radionuclides

Along with the record of the evolution of stable and long-lived isotopes, matter from the interstellar medium and circumstellar disks has preserved vestiges of short-lived nuclides (Section 3.4). Recalling the ^{26}Al–^{26}Mg isotopic systematics, it has been shown that ^{26}Mg excesses correlate perfectly with the Al/Mg ratios in relevant meteoritic minerals, and therefore ^{26}Al was present in the early solar system (see Fig. 10.7).

Even though the history of short-lived isotopes is by definition short, it is in fact rather complicated because it includes the ejection of freshly synthesized nuclides from the stellar source(s), propagation of these nuclides in the interstellar medium, their mixing with relevant stable isotopes in the interstellar medium, their condensation or implantation in solid grains and mixing within the circumstellar disk. It is also possible that some of these nuclides may be (partially) generated directly in the interstellar medium (e.g. a presolar cloud) and/or in the planetary nebula itself. Identification of the process responsible for generating a given isotope is especially important in cases where the data could yield a chronological result.

Generation of short-lived radionuclides in the circumstellar disk

The interaction of energetic particles emitted by a young star with matter in the circumstellar disk could yield short-lived nuclides. In this regard the observation of decay products of the fragile ^{10}Be (Table 3.3) and especially of the very

short-lived ^{7}Be ($\tau_7 = 53$ days) is of extreme importance. The latter isotope could only be produced *in situ* in existing solid grains in the nebula. Chaussidon *et al.* (2006) investigated the systematics of ^{7}Be $\rightarrow$ e-capture $\rightarrow$ ^{7}Li (using ^{6}Li as a stable reference isotope) in high-temperature inclusions separated from the Allende chondrite and observed a weak ^{7}Li/^{6}Li versus ^{9}Be/^{6}Li correlation, which these authors interpreted as an indication of the *in situ* decay of ^{7}Be.

Gounelle *et al.* (2001, 2006) modelled the irradiation of early solar system rocks by intense solar radiation including impulsive and gradual components, and demonstrated that several short-lived nuclides could have been produced by *in situ* spallation reactions. The ^{7}Be/^{10}Be ratio observed in the inclusions is close to the production ratio modelled for spallation reactions between accelerated protons and O-atoms. Within the framework of such a model the canonical SOS ratios of ^{10}Be/^{9}Be, ^{26}Al/^{27}Al, ^{41}Ca/^{40}Ca and ^{53}Mn/^{55}Mn can be reproduced (Table 3.3). The compositions and energies of the irradiating fluxes used in the modelling are supported by observations of nascent stars. Modifications of these fluxes (mainly relating to gradual or impulsive events) might explain the observed decoupling between different short-lived families, such as the decay products of ^{10}Be and ^{26}Al (e.g. Marhas *et al.*, 2002).

The irradiation scenario was also developed by Leya *et al.* (2003). In order to explain the SOS "canonical" ratios, e.g. ^{26}Al/^{27}Al $\approx 5 \times 10^{-5}$, found in most samples (Fig. 10.7) it was suggested that the targets were gaseous (and therefore homogeneous) and were irradiated by similar fluxes. Young *et al.* (2005) presented new supporting evidence for this scenario: the earliest SOS rocks stay in a high-temperature environment for a relatively long time interval, comparable with the irradiation time scale, during which time the shortest-lived nuclides such as ^{41}Ca mainly decayed before the host object was "closed" (able to preserve both parent and daughter nuclides) while those having a somewhat longer life, e.g. ^{26}Al, survived until the closure time (Section 10.6). This removes an important argument against the irradiation scenario, namely that if ^{26}Al had been produced in the early solar nebula by the reaction ^{24}Mg(^{3}He, p)^{26}Al, the reaction ^{40}Ca(^{3}He, 2p)^{41}Ca would have vastly overproduced ^{41}Ca compared with observations (Sahijpal *et al.*, 1998; Srinivasan and Bischoff, 2001). The heavy O-isotope compositions in presolar grains (Fig. 3.2), which are not readily reproduced in stellar models, are also best explained by irradiation of the early solar nebular gas (O, Ne) by an impulsive solar flare (p, ^{3}He, ^{4}He) (Aleon *et al.*, 2005).

Even though there is thus strong evidence favouring the irradiation hypothesis, several radionuclides (e.g. ^{244}Pu, ^{182}Hf and even rather short-lived ^{60}Fe) can only be yielded by stellar nucleosynthesis, the contribution of which thus appears unavoidable.

Generation of short-lived radionuclides in interstellar clouds (cloud core)

Another scenario was suggested by Clayton and Jin (1995): the occurrence of ^{26}Al and several other short-lived radionuclides could be accounted for by bombardment of the proto-solar cloud with cosmic rays. Proposed mechanisms include: (1) the trapping of freshly synthesized particles (with ^{26}Al/^{27}Al ~ 0.01) accelerated from local SNe ejecta or by stellar wind; (2) the trapping of low-energy galactic cosmic rays with very high ^{26}Al/^{27}Al ~ 0.1; (3) the production of radionuclides within the cloud (cloud core) by the interaction of low-energy cosmic ray nuclei (O, Na, Mg, Si) with cloud constituents, e.g. ^{12}C(^{16}O, pn)^{26}Al. The discovery of the interaction of heavy cosmic ions with interstellar hydrogen supports the latter suggestion (Bloemen *et al.*, 1994). Clayton (1994) showed that the reactions ^{26}Mg(p, n)^{26}Al and ^{28}Si(p, ppn)^{26}Al could yield a ratio ^{26}Al/^{27}Al $\approx 2 \times 10^{-5}$, which is quite similar to the observed initial ratio in the solar nebula. Further, the reaction ^{38}Ar(α, n)^{41}Ca could yield ^{41}Ca. In such a scenario, the initially heterogeneous distribution of the short-lived species within the cloud or, later on, in the circumstellar disk could have resulted from the propagation of heavy ions through variable magnetic fields (Podosek and Cassen, 1994). However, very specific heavy-ion abundances and narrow limits for their energy are required to reproduce the observed abundances of several short-lived radionuclides.

Stellar sources for short-lived radionuclides

The third proposal envisages stellar production of the nuclides followed by ejection of stellar debris into the interstellar medium. Sources would be chiefly supernovae (SNe II) or low-mass AGB stars (Cameron *et al.*, 1995; Srinivasan *et al.*, 1996; Wasserburg *et al.*, 1994, 1995b; Woosley and Weaver, 1995). In this scenario, relatively long-lived species would have different histories from short-lived ones. The former (^{146}Sm, ^{244}Pu, ^{129}I and even ^{53}Mn) could have been produced by several generations of massive stars well before the formation of the solar system and stored in an interstellar cloud. The very short-lived nuclides (^{26}Al, ^{36}Cl, ^{41}Ca, ^{60}Fe, ^{182}Hf) would have to be synthesized and ejected into the interstellar medium not earlier than ~ 1 Myr prior to the formation of solid objects in the planetary nebula (Meyer and Clayton, 2000).

Models of low- to middle-mass stars allow quantitative estimates of the yield of ^{26}Al. Dredge-up is expected to bring ^{26}Al from the H-burning shell just outside the helium-exhausted core, where ^{26}Al is produced via ^{25}Mg(p, γ)^{26}Al, to the surface envelope of AGB stars. The ^{26}Al/^{27}Al ratios observed in presolar oxide grains are $\sim 10^{-2}$ to 10^{-4}, in agreement with those derived from AGB stellar

models. The oxygen-isotope composition of these grains also points to this source. The amount of ^{26}Al in the grains indicates the time interval between mass loss in AGB stars and grain formation (Nittler, 1997; Busso *et al.*, 1999).

An AGB source is, however, inconsistent with the observed initial solar system abundance of ^{182}Hf: the yield predicted by AGB models, ^{182}Hf/^{180}Hf $\sim 10^{-6}$, is a factor ~ 100 below the observed ratio listed in Table 3.3 (Wasserburg *et al.*, 1994; Arnould *et al.*, 1997). Also it is highly unlikely that AGB star wind and an SNe II would occur nearly simultaneously in the vicinity of a pre-collapse cloud.

Cameron (2001a, c) suggested that all extinct radionuclides except ^{7}Be could have been produced in SNe II explosive burning and the r-process (Section 6.3). Cameron's unifying approach envisages dominant production of the lighter species (^{26}Al to ^{60}Fe) in explosive nucleosynthesis, the medium species (^{107}Pd and ^{129}I) via the weak (low-*A*) r-process, and the heavy radionuclides (^{146}Sm, ^{182}Hf, ^{244}Pu) in the main (high-*A*) r-process. Cameron argued that even light fragile elements, e.g. ^{10}Be, could be synthesized in the expanding SNe envelope.

Summarizing, recent progress, particularly the identification of a ^{7}Li excess related to ^{7}Be decay and the development of adequate models, tilts the balance in favour of nebula irradiation, although this cannot be the sole producer of short-lived nuclides. Regardless of the precise model, however, it appears that in all cases these nuclides were produced early enough to allow a chronological interpretation of the observations (Sections 10.4, 11.6, 12.4).

8.4 Milky Way evolution: models and results

Introduction to modelling of galactic chemical evolution

The aim of galactic chemical evolution (GCE) models is to find the proportion of different types of model stars through time that reproduces the chemical evolution of stars and the interstellar medium (ISM) from primeval matter to its present-day composition. Such forward models incorporate the observations and results of models of the evolution of stars and their yield of matter. A solution is a set of parameters that leads to a good fit with observations.

The simplest model (see the contents of the braces in Eqn (8.1)) envisages a one-step formation of our Galaxy from homogeneous gas with the composition predicted by the cosmological nucleosynthesis (Pagel, 1994). More complicated and sophisticated models treat the Galaxy as an initially inhomogeneous, radially zoned, disk and include the time-dependent transfer of species to (inflow) and from (outflow, Eqn 8.1) a modelled reservoir, e.g. a halo, bulge or disk (Timmes *et al.*, 1995; Alibes *et al.*, 2001; Chiappini *et al.*, 2001; Pagel, 2001).

In the simplest model, the following processes control the abundance of isotope ${}^{i}Z$ in the ISM:

$$\mathrm{d}\,{}^{i}Z/\mathrm{d}t = \{-\text{birth} + \text{death} + \text{decay}\} + \text{inflow} - \text{outflow}. \tag{8.1}$$

Here the term "−birth" encompasses two parameters. One is the star-formation rate, quantifying the total amount of interstellar material consumed by stars in a given time interval and in a given region of the Galaxy; for example, a birth rate B proportional to the power n of the gas density $\rho(t)$,

$$B(t) = \rho(t)^{n}_{\mathrm{GAS}}, \tag{8.2}$$

allows solution of the GCE models for $n \sim 2$; the square of the surface gas density also does this (Schmidt, 1959; Timmes *et al.*, 1995). The second parameter, the initial mass function, gives the birth rate of stars as a function of their mass. This is important because both stellar lifetime and yield depend on stellar mass. The lifetimes decrease from $\sim 10\,000$ Myr for the lowest-mass stars of $\sim 1\ \mathrm{M}_{\odot}$ and less through ~ 100 Myr for stars of $5\ \mathrm{M}_{\odot}$ to ~ 10 Myr for stars of $\sim 30\ \mathrm{M}_{\odot}$ (Timmes *et al.*, 1995). The simplest assumption, that this mass–age relationship is independent of time, space and the composition of a star, allows the GCE models to be solved. An appropriate form of the initial mass function, $\phi(m) \propto \Delta N/\Delta m$, where ΔN is the number of stars having mass m (in $\mathrm{M}_{\odot}$) within the interval Δm, is given by

$$m\phi(m) = Am^{B}, \tag{8.3}$$

where A and B are constants. The simplest version of Eqn (8.3), which satisfies GCE models (including the present-day solar composition) reasonably well as well as being consistent with the present-day mass function for the solar neighbourhood, is known as the Salpeter law and has $A = 0.17$ and $B = -1.35$: the number of stars with mass within Δm decreases quasi-exponentially as m increases from ≥ 0.1 to ~ 100. A constant initial mass function over galactic time appears to be a reasonable approximation to this (McWilliam, 1997). Compositions of metal-poor stars, however, call for a more complicated function envisaging the preferential formation of extremely massive stars $\sim 100\ \mathrm{M}_{\odot}$, in accord with expectations for the zero-metallicity gas in the early Galaxy.

The term "death" in Eqn (8.1) is used to quantify the amount of initial material (from which a star was formed), plus the newly synthesized nuclides recycled back to the ISM, as well as the matter that remains locked up in the stellar remnant. As discussed already, stellar deaths are in fact responsible for the chemical evolution of the Galaxy. The "death" depends on the "birth" but it also has to include some stochastic components, e.g. that not every white dwarf develops into a type Ia supernova. This stochastic component of the models could be of prime importance

especially when the heterogeneity of the Galaxy is investigated (Travaglio *et al.*, 2001a, b).

The term "decay" takes into account the decay of radioactive nuclides and the accumulation of radiogenic nuclides in the ISM.

Some inferences from modelling

A dying star ejects a portion of initial and newly synthesized matter into the ISM, whereas another portion is sequestered in the stellar remnant. The full inventory of the elements existing at this stage is called the yield. Because the lifetimes of massive stars are orders of magnitude shorter than those of low-mass stars, tens of generations of massive stars can pass by in the lifetime of one low-mass star. In the early Galaxy the ejected elements (Table 8.1) as well as r-process elements (Figs. 3.1, 5.3) were abundant relative to the products of nucleosynthesis in lower-mass stars. In the course of an SNe II event, the r-elements and iron-peak nuclei are produced in different processes and sites; therefore the ratio of r-elements and iron depends on the mixing of stellar envelopes and is expected to be variable because of heterogeneous and asymmetrical explosions (Section 6.3). Also, the rate of ejection of the elements generated in the early stars could have exceeded the mixing rate, and thus varying [r-element/Fe] values were inherited by the early low-mass stars. Indeed, Fig. 8.4(a) illustrates the enormous variability of this ratio in the early Galaxy, as recorded by the very ancient stars (with [Fe/H] < -2).

The lower-mass stars started to supply their products to the ISM later: the lighter the star, the longer the delay. Type Ia supernovae present a good example. They have low-mass progenitors, living much longer than the massive stars. A dying SNe Ia is disrupted completely and the ejecta include mainly freshly synthesized nuclides: the iron-peak and lighter elements, products of explosive C and O burning (Table 8.1). The models and data in Fig. 8.1 show that, with the observed contribution of iron from SNe Ia, the stellar size and age distribution functions mentioned above are reconciled for the solar neighbourhood about 2 Gyr after nucleosynthesis started in the Galaxy. In fact this delay, often quoted as the SNe Ia time scale, is the time at which the Fe contribution from SNe Ia into the interstellar media starts to become important. In the Milky Way the rate of Fe input via SNe Ia approaches its maximal value even later, ~ 5 Gyr after the formation of the Galaxy (Matteucci and Recchi, 2001). Taking approximately two-thirds of the iron abundance as having been generated by supernovae type II events and one-third as having come from type Ia gives the best fit to the data, but an even higher contribution of SNe Ia is also possible (Timmes *et al.*, 1995; Alibes *et al.*, 2001).

The delay of the yield of elements generated in low-mass stars led to an increase in the relative contribution of these elements through time. A steeper slope of the

model [Fe/H] SNe Ia trend compared with SNe II (Fig. 8.1) indicates this "delayed" yield from the low"mass stars. A similar delay is seen for the supply to the ISM of s-process elements, also synthesized in relatively low-mass stars (bottom panel in Fig. 8.4).

8.5 Summary

A fundamental observation is that the abundance of heavy elements in the interstellar medium has increased through time. Generally astrophysicists use, as a proxy for time, the time-calibrated solar-normalized iron-to-hydrogen metallicity index [Fe/H], which is a relatively easy quantity to measure in stars. However, Fe is produced in different types of stars and its evolution is complicated. Another promising "chronometer" is [O/H], because O is the most abundant element produced in a galaxy and its chemical evolution is straightforward: except for the O-excess in the very early Galaxy, supernovae II are by far the most important source of oxygen.

The [CNO/Fe] abundance has its largest values at extremely low metallicities. These and some other observations point to early nucleosynthesis in supermassive stars with $M \geq 100\ \mathrm{M}_{\odot}$. Such stars have not yet been observed; modelling suggests that they could form at very low metallicities, would have a very short life span and could explode at an early stage, ejecting dominantly light (below Fe-peak) elements into the ISM.

Very high abundances of heavy r-process elements observed in ultra-metal-poor stars indicate an early contribution from supernovae II, the only sources of these elements. The pattern of $\sim$ 14-Gyr-old r-elements is indistinguishable from that in the solar system, suggesting a great uniformity of the r-process in different stars.

Trace s-process elements are underabundant at low metallicities; their abundance, along with the [s-process/r-process] value, increases smoothly with time. This is explained by the generation of s-process elements in low-mass stars, which live longer than massive stars.

Grains in the interstellar medium have preserved a high-resolution record of the evolution of stable isotopes as well as vestiges of the decay of short-lived nuclides. The stable isotopes provide constraints for models of red-giant, AGB and supernova nucleosynthesis processes. The radionuclides can potentially highlight details of galactic chemical evolution occurring on a short time scale, but interpretation of the data depends on the relevant nucleosynthetic processes, which are a subject of ongoing discussion.

Not only the evolution trends for the elements but also many other observations, such as the present-day mass of the Galaxy, the mass/gas ratio and the relative

abundance of stars of different masses, constitute the basis for galactic chemical evolution models. Such modelling allows some important parameters to be quantified. Thus, the formation rate of stars appears to be proportional to the square of the gas density in the Galaxy. Further, the number of stars being formed with mass m within an internal Δm decreases exponentially as m increases from ≥ 0.1 to ~ 100 $M_{\odot}$. A constant initial mass function over galactic time appears to be a reasonable approximation. Inflow and outflow are important for complicated models envisaging galaxy heterogeneity in space and time, which is indeed the case for our Galaxy.

Part II

Early solar system: nebula formation, evolution and lifetime

9

Introduction to the solar nebula

Now we narrow our view down to the solar system, which is a relatively young and small part of the Galaxy. For human beings, however, two objects of this system, the Sun and the Earth, are probably more important than all the vast outward Universe. Part II of the book describes the early solar system, focussing on the inner part of the solar circumstellar gas–dust disk (the solar nebula) where the terrestrial planets were formed (Fig. 9.1, also see Fig. 14.1). To form the planets, quite small particles, typically of the size of the grains constituting cold interstellar clouds ($\sim 10^{-4}$ cm or less, Section 10.1), ultimately assembled into bodies of size $\sim 10^8$ cm, a tremendous mass factor $\sim 10^{35}$. A long chain of complicated processes was involved in this growth. For the following simplified discussion, this chain is split into two time intervals: (1) dust accretion into planetesimals of the order of 10^6 cm in a gas-bearing nebula (this is considered in Part II) and (2) planetary accretion from planetesimals and planetary embryos (considered in Part III).

Most of the relevant processes are not observable and modelling appears to be the only way to study them. An exception is material from the accretion stage, which comes to Earth as meteorites and has helped a great deal to constrain the chemical evolution of the nebula and its time scale. There is a conventional so-called standard scenario describing the formation of the planetary system, different aspects of which have been discussed by Safronov (1969), Benz *et al.* (1986), Shu *et al.* (1987), Stevenson (1987), Vityazev *et al.* (1990), Wetherill (1990), Melosh *et al.* (1993), Cameron (1995), Canup (2004) and others. In the following chapters, discussions are given of the materials that originated or fractionated within each stage of the nebula evolution and the relevant processes.

Models for the formation of low-mass solar-like stars envisage an initially gradual and then rapid collapse of a cold molecular cloud (Section 5.2). Different mechanisms could have initiated the collapse (Cameron, 2001a). The occurrence of short-lived r-process radioactive nuclides in the post-collapse matter implies that

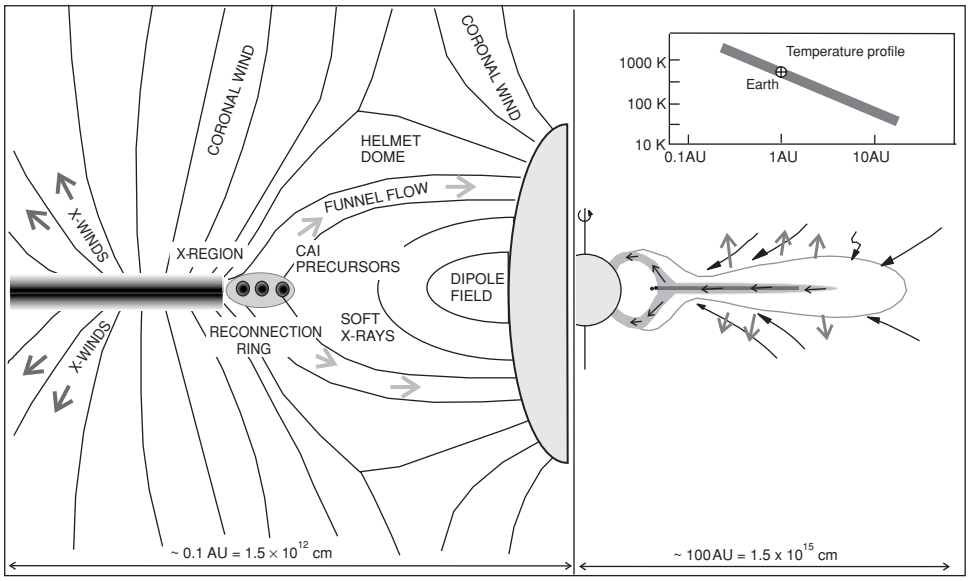

Fig. 9.1 Schematic presentation of the formation of the solar nebula and relevant processes. Right-hand panel, the major stage (1) of accretion: accretion flux onto the nebula (solid arrowheads), with mass transfer towards the growing Sun (momentum is transferred in the opposite direction) and radiation cooling of the nebula (open arrowheads). The inset shows the model temperature distribution in the central plane of the nebula during this stage. After Hartmann (2000). Left-hand panel, processes operating on the inner edge of the nebula at the end of stage (1). Calcium–aluminium-rich inclusions (CAIs) could have been formed in this environment and recycled back to the accretion disk by intense X-winds and/or turbulence. Solid particles became concentrated near the central plane of the nebula (black) and their vaporization within the reconnection ring could have produced a specific Si-vapour-rich gas reservoir, from which silicate melts could condense. After Shang *et al.* (2000).

a supernova explosion could be a likely mechanism for their delivery and also a trigger of the collapse.

As a by-product of collapse and stellar accretion, a circumstellar nebula may form and eventually develop into a planetary system. This is, however, not inevitable. Three scenarios are possible. Depending, among other factors, on the mass and density of the cloud, its initial rate of rotation and the turbulence within it, a binary or higher-order system, a star with a circumstellar nebula or a single star is formed. If a nebula is formed then the central nascent star consumes almost all the accreting mass, whereas a small mass fraction far from the star acquires almost all (98%) of the angular momentum. Such a configuration corresponds to the minimum energy of the system (Lynden-Bell and Pringle, 1974). The mechanism of momentum

transfer from the central body to the nebula (ultimately the planets) is a long-standing problem, still giving rise to lively discussion (see the review by Adams and Laughlin, 2000).

Within ~ 0.1 Myr after collapse started, the nebula that would produce the Sun had evolved from an initial post-fragmentation sphere-like shape into a flattened disk-like configuration with the nascent star in its centre. This development appears to be inevitable because the gravitational and centrifugal forces are not in general antiparallel, and the resulting force stimulates the compression of a cloud. Circumstellar accretion disks are often observed around bright pre-main-sequence solar-mass stars (Strom *et al.*, 1989; Beckwith *et al.*, 1990).

Three stages might be distinguished in the nebula's history (Cameron, 1995). During a short period (~ 1 Myr) of intense stellar accretion, termed the FU Orion stage, the nebula was at an approximate steady-state balance between fast infall from the cloud and accretion onto the Sun at a rate $\sim 10^{-6}$ $M_\odot$ yr^{-1} (stage 1). Highly refractory matter now found as inclusions in meteorites could have condensed or sublimated near the inner edge (bow) of the nebula at this stage (Chapter 10).

Later on, during the classical T Tauri stage (from 1 to 10 Myr), the Sun was slowly accreting by a residual mass flow (stage 2). The nebula disk was supported by centrifugal forces and by an increase in gas (H_2 and He) pressure towards the central plane of the disk and, along the plane, towards the central star. Because of the pressure support, the angular velocity of the gas molecules (atoms) was slightly lower than the Keplerian velocity. The solid particles were denser than the gas by orders of magnitude; therefore the particles had less pressure support and moved with variable, up to Keplerian velocity, depending on their size. This means that grains of different sizes would have differing velocities and, as a consequence, frequent collisions would occur between the grains. These collisions could result in the coagulation of grains. The rate of coagulation would depend on the relative velocities and masses of the interacting particles and their compositions and shapes. At this early stage the velocity differences were small, less than 100 m s^{-1}, thus favouring coagulation. For example, two quartz grains of size 0.1 μm can stick together on collision at this velocity (Chokshi *et al.*, 1993). The coagulation of icy grains is even more efficient.

Particles settled to the midplane of the nebula, and larger particles grew by trapping slower, smaller, particles. According to estimates by Cameron (2001b), the gravitational forces are greatest for grains entering the nebula boundary. These grains acquire the highest velocity, collide most frequently with smaller particles and therefore grow at the highest rate, giving rise to "fluffy" aggregates. While settling towards the midplane, these aggregates compress and merge with similar

ones, approaching ~ 100 m radius. For a Keplerian disk without turbulence and headwinds, the settling time scale for small particles (e.g. chondrules) is of order 10^3 yr, but "fluffy" aggregates, characterized by low density, could migrate for a longer time, giving rise to chondrite precursors with a "primary accretionary structure" (Metzler *et al.*, 1992).

Because of the general inward drift, most of the particles and bodies were finally vaporized near the inner bow of the nebula and then accreted onto the Sun (Fig. 9.1). The residence time of bodies in the nebula was dependent on their size. Large bodies ($\geq 10^6$ cm) experienced little gas drag and remained on Keplerian orbits, whereas very small particles ($\leq 10^{-1}$ cm) experienced little gravitational attraction and were supported by the gas pressure gradient. Both resided for a long time in the nebula; for the terrestrial region of the nebula their residence time is estimated at ~ 1 Myr or more. However, the nebula residence time for the intermediate bodies, $\sim 10^2$ cm, is expected to be as short as ~ 100 yr, because interactions with gas and dust efficiently slowed these bodies down. Consequently, their centrifugal speed decreased, allowing radial drift towards the central star (Cameron, 1995). Collisions of bodies of this and similar sizes could readily result in disruption rather than in agglomeration (Benz, 2000). These estimates show that, in order to pass this bottleneck, agglomeration of the bodies needs to be a fast process generally involving many collisions with smaller objects; otherwise they would not have survived in the nebula. In the inner region of the nebula, rocky planetesimals (e.g. chondrite parent bodies, Chapter 11) were formed at this stage.

The temperature and pressure conditions, important for the development of matter in the early solar nebula, were highly variable in space and time, especially within the relatively narrow inner zone where the terrestrial planets were formed. These parameters are discussed in Chapter 10 in the context of the earliest rocks of the solar system.

After planetesimals grew to $>10^6$ cm or $>10^{19}$ g, the accumulation and heat regimes changed. The decay of short-lived isotopes, first of all ^{26}Al, became a powerful heat source for the insulated interiors of these relatively large bodies, provided that their agglomeration occurred within 2–4 Myr after nebula formation. The decay of longer-lived isotopes, e.g. ^{40}K, which were more abundant than they are today, and energy released via the collision of large planetesimals could also have played a role.

After the termination of accretion of the central star (weak T Tauri, stage 3), the nebula was in a steady state with no significant dissipation or relative motions other than gas removal at the inner edge due to the T Tauri solar wind. Planetary embryos, of size 100 to 1000 km, and planetesimals still surviving now as meteorite parent

bodies in the asteroid belt, were formed during this stage; some of these underwent magmatic fractionation processes (Chapter 12).

The time interval between the start of the collapse and the accretion of large bodies in the inner nebula appears to be ~ 10 Myr, which is similar to that of the pre-main-sequence T Tauri stage of the evolution of solar-mass stars (Podosek and Cassen, 1994; Feigelson and Montmerle, 1999).

10

The primary solar system objects and related processes

10.1 Solar nebula: initial composition and early development

Initial composition

Initially gas and dust were the only constituents of the cold molecular interstellar cloud, the raw material for the solar nebula. Spectroscopic observations of dense interstellar clouds along with modelling indeed suggest that the difference between the local dust/gas ratio and that in other regions of the Galaxy can be attributed entirely to a difference in metallicity (Vuong *et al.*, 2003). According to the solar metallicity (Table 3.2), the bulk-mass dust/gas ratio in the presolar cloud was $\sim$ 1/100. The gas included highly volatile elements, first of all H_2, He, N_2, CH_4, CO, the noble gases etc. The dust grains, which were mineral or amorphous condensates, varied in composition from ices (H_2O, CO, CO_2, NH_3, C_2H_6) to refractory grains (e.g. Al_2O_3, SiC, graphite and diamond). The mean size of the dust grains was generally $\sim 10^{-4}$ cm but could vary from $\sim 10^{-8}$ cm up to 1 cm (Elmegreen, 1981).

The dust was chemically and isotopically heterogeneous (Section 3.3), implying a number of presolar sources of the raw material. More than 1000 stars might have contributed to the presolar cloud (Flam, 1991).

Early T Tauri stage: high-temperature processing

There are three approaches allowing *PT-t* parameters (i.e. pressure and temperature conditions varying in the course of time *t*), which govern the early evolution of matter of the solar nebula, to be estimated. One is "a view from outside" of the solar nebula via the observation of young stellar objects and circumstellar disks around them (e.g. Strom, 1985; Feigelson and Montmerle, 1999). Investigation of the nebula matter itself gives us a complementary, "inside", view (e.g. Wood, 1985, 1988; Wasson, 1985; Palme, 2000). Models of the disk undergoing accretion

from the infalling cloud envelope, based on observations from both "inside" and "outside", constitute the third source of relevant information.

These models predict a moderately warm (500–1500 K) inner disk, in good agreement with the observational constraints. The pressure in this region is expected to vary from $\sim 10^{-3}$ to $\sim 10^{-6}$ atm (Beckwith *et al.*, 1990; Makalkin and Dorofeeva, 1995). During early nebula evolution (stage 1), the high accretion rates yielded a high and variable input of accretion energy, whereas the limited optical depth controlled the energy loss. Variable input and loss would cause temperatures to vary in a non-monotonic way in the course of nebula evolution (Cassen, 1996).

The actual variability of the *PT-t* parameters in the nebula could well have exceeded that predicted by the smooth models. This follows from observations of the features of low-mass stars during their early evolution, i.e. enhanced bolometric luminosity, up to $\sim$ 10 $L_\odot$ (specifically, the X-ray emissions are up to 10^5 times solar), and transient highly elevated levels of magnetic activity, including strong fields and powerful magnetic reconnection flares, causing the bombardment of gas and dust by flare shocks and energetic particles. Young T Tauri stars can experience sharp episodic losses of the energy yielded by accretion via violent eruptions, strong gas ejections giving rise to intense supersonic stellar winds and large infrared excesses. The latter apparently come from the heating of the circumstellar dust by interaction with the expanding shell driven by the winds. The duration of these repeatable violent events varies from hours to hundreds of years; the temperature increase could be high enough to ensure partial or even total evaporation of the presolar grains in the inner region of the nebula (Hartmann and Kenyon, 1985; Rydgren and Cohen, 1985; Mundt *et al.*, 1985; Feigelson and Montmerle, 1999).

Condensation

As condensation appears to be the only way to produce solid materials from gas in interstellar and nebula environments it is expected to be a widespread process (e.g. Grossman, 1972). However, most early formed minerals appear to have crystallized from melts. To resolve this problem, Wood (1967) suggested that liquid condensates might also be stable under nebula pressures ($\sim 10^{-3}$ atm) in specific regions, where high abundances of heavy elements resulted from the vaporization of dust grains. The dust/gas mass ratio required for this would be $\sim$ 100–1000 times the average SOS value. Such a dust enrichment is expected in the vicinity of the nebula midplane, where dust is concentrated. Recent models involving the recondensation of gases produced by vaporization of dust-enriched systems yield condensation reactions and an evolution for the compositions of solid and liquid-solution phases that are in reasonable agreement with meteorite data (Yoneda and Grossman, 1995; Petaev and Wood, 1998; Ebel and Grossman, 2000).

10.2 Calcium–aluminium inclusions

Ca–Al-rich inclusions: introduction

Highly volatile-depleted calcium–aluminium-rich inclusions (hereafter CAIs) found in chondritic meteorites (some of which are volatile-rich) have preserved a record of early "hot" nebula processes. Texturally there are two types of CAI: aggregates and spherical, chondrule-like, objects. Aggregates are variable in shape and size, from quite small particles to those as large as ~ 1 cm. They incorporate complex mineral assemblages of contrasting refractory phases (e.g. spinel, hibonite) and alkali-rich phases (e.g. nepheline). The spherical objects range in diameter from 0.3 to 2 cm and contain crystals of sizes up to ~ 0.1 cm. Microspherules as small as ~ 0.01 cm are also observed in them. Occasionally coatings and rims are seen, implying a multistage formation. Some refractory inclusions also indicate local (re)condensation directly from a gas phase (e.g. Simon *et al.*, 2002). In total, CAIs constitute a small mass fraction of the host meteorites, within 1% to 6%.

The last episode in the formation of many spherical CAIs was progressive fractional crystallization from the rim inwards, suggesting the solidification of a droplet of melt. Some inclusions have preserved xenoliths, cores of pre-existing minerals, indicating reheating events intense enough to cause the melting, and possibly vaporization, of even these refractory assemblages. Modelling of such assemblages gives temperatures above ~ 2000 K under a pressure of $\sim 10^{-3}$ atm (Kerridge, 1993; Beckett and Stolper, 1994). Regarding the time scale, the internal texture indicates that cooling could not have been very fast, generally within 0.5 to 50 °C hr^{-1}, indicating a hot environment or a radiant heat source operating from tens of hours up to ~ 1 year (MacPherson *et al.*, 1989; Simon *et al.*, 1997; Russell *et al.*, 1998).

Ca–Al-rich inclusions: classification and compositions

Based on the mineral chemistry of CAIs in the Allende meteorite, Grossman (1975) suggested two types of CAI: type A with $\sim 20\%$ SiO_2, containing 80%–85% melilite, 15%–20% spinel and 1%–2% perovskite, and type B with $\sim 30\%$ SiO_2, containing 40%–60% clinopyroxene, 15%–30% spinel and only 5%–20% melilite (Table 10.1). Some further types of CAI have also been distinguished, for example hibonite-rich inclusions in CO3 meteorites (Russell *et al.*, 1998). All these compositions show an extremely low abundance of moderately volatile alkalis and other volatile elements (Table 10.1). The type A assemblage has a near-solar Ca/Al ratio and could have been formed from gas of solar composition under a pressure of $\sim 10^{-3}$ atm and at temperatures in the range 1475–1500 K. Hibonite should have

Table 10.1 *Chemical composition of calcium–aluminium-rich inclusions (CAIs): major elements (wt %)*[a]

Type	A				B					H			
Met.[b]	Col	Col	All		All	Col	Isna	All		Isna	Col	Isna	
Mineral	mel	spin	per	bulk[c]	cpx	spin	plag	mel	bulk[c]	hib	spin	ilm	bulk[c]
SiO_2	23.9	b.d.l.	n.d.	19.5	40.0	0.40	45.2	25.4	30.2	b.d.l.	b.d.l.	0.36	0.01
Al_2O_3	32.8	70.2	1.45	38.7	17.0	65.5	34.4	30.7	32.1	91.1	61.4	b.d.l.	78.6
FeO	b.d.l.[d]	0.50	0.07	0.09	0.27	0.39	0.48	0.05	0.30	0.39	26.8	44.3	9.18
MgO	1.2	28.3	0.23	5.8	10.3	26.9	0.44	2.47	11.5	0.04	9.60	1.60	2.94
CaO	41.1	b.d.l.	40.2	34.1	26.1	2.20	18.4	41.1	21.6	8.80	b.d.l.	0.26	6.62
Na_2O	b.d.l.	b.d.l.	n.d.	b.d.l.	0.02	b.d.l.	1.30	0.04	0.21	b.d.l.	b.d.l.	b.d.l.	0.00
K_2O	n.d.[e]	b.d.l.	n.d.	b.d.l.	0.02	b.d.l.	n.d.	n.d.	0.01	n.d.	b.d.l.	n.d.	0.00
TiO_2	b.d.l.	0.40	54.8	0.89	6.79	2.90	b.d.l.	0.04	4.04	0.07	b.d.l.	51.9	2.18
V_2O_3	n.d.	0.30	n.d.	0.05	n.d.	0.35	b.d.l.	n.d.	0.08	b.d.l.	b.d.l.	0.31	0.01
Cr_2O_3	n.d.	0.30	0.02	0.05	0.06	n.d.	n.d.	n.d.	0.03	b.d.l.	b.d.l.	n.d.	0.00
ZnO	n.d.	n.d.	n.d.	n.d.	n.d.	n.d.	n.d.	n.d.	n.d.	n.d.	1.90	n.d.	0.57
Total	99.0	100	96.8	99.1	100.6	98.6	100.2	99.6	100	100.4	99.7	98.7	100.1

[a] After Grossman (1975) and Russell *et al.* (1998), © Pergamon Press 1998, reproduced by permission from Elsevier Science.
[b] The abbreviations of meteorites are as in the List of meteorites.
[c] To calculate the bulk compositions (as examples and for comparison with compositions of meteorites and terrestrial rocks) the following relative abundances of mineral phases are used (also see the abbreviations). Type A: melilite (mel), 0.815; spinel (spin), 0.17; perovskite (per), 0.015. Type B: clinopyroxene (cpx), 0.5 (K_2O and Na_2O are from Colony pyroxene); spinel, 0.22; plagioclase (plag), 0.15; melilite, 0.13. Type H: hibonite (hib), 0.66; spinel, 0.3; perovskite, 0.02 (see the composition in type A inclusions); ilmenite (ilm), 0.02.
[d] Below the detection limit.
[e] Not determined.

condensed at an even higher temperature, ~ 1740 K (MacPherson and Davis, 1994). These high-temperature processes are best recorded by rare earth element (REE) abundance patterns.

REE and trace-element abundances in Ca–Al-rich inclusions

The rare earth elements (REEs) are important tracers of natural processes. For our purposes, we take the REEs to be the 15 elements from La to Lu in the Periodic Table (Sc and Y may also be included), which differ from each other only in the number of 4f electrons. Because these electrons do not readily participate in chemical bonding, the REEs show similar chemical behaviour, characterized by a 3+ valence (Table 10.2). Only the size of the atoms, decreasing monotonically with increasing atomic number, enables fractionation of the members of this conservative highly refractory family. Therefore the fractionation patterns are generally smooth functions of the atomic number. An exception occurs for Eu, which in some cases has a 2+ valence and then behaves differently from other REEs. It is convenient to normalize the REE abundances to the solar values or to C1 chondrites (Tables 3.2 and 11.2) and to plot the normalized value against the atomic number, i.e. against decreasing ionic radius.

Several typical REE patterns are observed in CAIs. One pattern is almost flat and shows a typical enrichment by a factor ~ 20, suggesting that the inclusions comprise ~ 5% of the most refractory material, in which the REEs are concentrated (group II in Fig. 10.1(a)). Another pattern is also flat except for deficiencies in Eu and Yb, which are the least refractory REEs. This suggests that the condensing mineral assemblage or melt was apparently formed from the nebula gas at a high temperature, when Yb and Eu were still partially in the gas phase (group III, Fig. 10.1(a)). The most complicated pattern, that for group I, corresponds to REE condensation from a residual gas after some portion of an earlier-condensed gas has been removed (Boynton, 1984, 1985).

Because the amount of REE-bearing material that solidified at such high temperatures must be small, the enrichment of REEs (except for Eu and Yb) is expected to be high. Indeed, REE abundances in the core of a hibonite-rich inclusion from the Murchison meteorite are as high as ~ 1000 times the C1 value, with strong negative Eu and Yb anomalies. This central part of the inclusion thus probably represents a very small fraction of the condensate (Fig. 10.1(b)). The rim of the same inclusion shows much weaker REE enrichment and smaller anomalies and may have formed from a larger-fraction condensate. Further specific features of REE patterns seen in CAIs, e.g. low overall concentrations in the corundum mantle, are expected from the unequal incorporation of the REEs in the coexisting minerals as they formed at ~ 1740–1725 K in equilibrium with a gas phase.

Table 10.2 *Trace elements in calcium–aluminium-rich inclusions (ppm)*

Meteorite CAI type	Allende CV A[a]	Efremovka CV A (per)[b]	Allende CV B[c]	Allende CV H[d]
Sc	96	854	127	236
Sr	153	201	121	70
Y	n.d.[e]	1790	n.d.	4
Zr	29	5430	57	23
Ba	44	9	42	7.49
La	3.3	326	6.3	13.1
Ce	8.8	908	18	0.062
Pr	n.d.	121	n.d.	3.28
Nd	n.d.	641	n.d.	16.9
Sm	2.3	203	4.1	3.49
Eu	1.3	8	1.03	0.99
Gd	n.d.	228	n.d.	2.8
Tb	0.34	43	0.87	0.28
Dy	2.7	333	6.2	1.47
Ho	n.d.	80	n.d.	0.26
Er	n.d.	204	n.d.	0.36
Tm	n.d.	34	n.d.	0.06
Yb	1.7	164	2.8	0.12
Lu	0.39	27	0.46	0.07
Hf	1.1	145	1.9	n.d.
Ta	0.2	n.d.	0.35	n.d.
U	0.1	n.d.	0.17	0.14

[a] Trace-element concentrations in bulk A-type inclusion from Grossman *et al*. (1977).
[b] The perovskite ($CaTiO_3$) that (partially) constitutes a rim of A-type CAI shows a great enrichment in REEs, Zr and some other trace elements (Fahey *et al*., 1987); the present authors' interpretation of this observation envisages the (re-)condensation of these involatile elements onto the inclusion, the core of which is mainly composed of melilite.
[c] From Grossman *et al*. (1977).
[d] From Hinton *et al*. (1988) with the U data added from Simon *et al*. (1997). Bulk trace element concentrations of A-, B- and H-type inclusions are not so different from those in specific minerals of CAIs.
[e] Not determined.

However, such evidence for the origin of CAI minerals as direct gas condensates is the exception rather than the rule, even for hibonite-bearing inclusions. For instance, hibonite microspherules from the Colony (CO3.0), from ALH 82101 (CO3.3) and from other meteorites display quite different REE patterns, with heavy-rare-earth-element (HREE) depletion relative to the light REEs (LREEs), which is readily explained by hibonite crystallization from a parent "fassaitic" melt (Russell *et al.*, 1998). The rare earth element patterns on the whole indicate that the melt–solid interaction appears to be typical for most CAIs. In some cases the

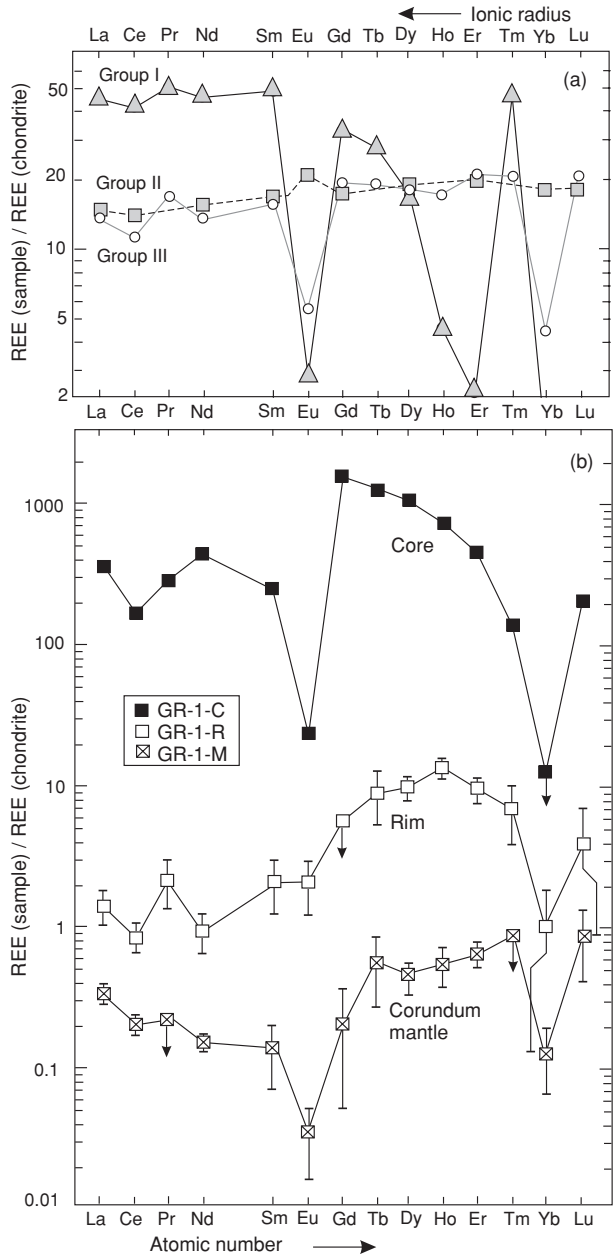

Fig. 10.1 Rare earth element abundances in Ca–Al-rich inclusions in meteorites. (a) Typical REE patterns for CAIs. Simplified after Boynton (1984). (b) REE abundances in a hibonite-rich CAI from Murchison carbonaceous chondrite: core and rim are separated by a corundum-bearing mantle. Note the complicated REE pattern and extremely high REE abundances in the core: less than 1% of the solar matter had been condensed when the inclusion was formed. Strong negative Eu and Yb anomalies reflect the somewhat greater volatility of these two elements. After Hinton *et al.* (1988), © Pergamon Press 1988, reproduced by permission from Elsevier Science.

indications are quite clear. Thus many unaltered type A CAIs show apparently flat patterns relative to C1, with overall REE concentrations exceeding those in C1 by a factor ~ 25. In an inclusion from the Kainsaz CO chondrite the melilite cores and diopside rims have complementary Eu abundances, indicating crystallization of the minerals from a single parent REE-enriched melt. Europium behaves anomalously in that it readily replaces Ca^{++} under reducing conditions, when most Eu is divalent. Therefore Eu readily partitions into melilite (having a high [Ca] value and being crystallized first), leaving behind a residual melt equally enriched in REEs but depleted in Eu. This complementary pattern then shows up in the later-crystallizing diopside (Kuehner *et al.*, 1989).

Thus, in nebula regions enriched in refractory elements transferred by dust under a total pressure of $\sim 10^{-3}$ atm, all three phase transitions were possible, vapour–solid, vapour–liquid and solid–liquid (Yoneda and Grossman, 1995). Where such transitions were incomplete, variations in the stable-isotope ratios may remain as traces of them.

Stable-isotope fractionation

Variations in stable-isotope ratios can record important features of physical and chemical processes. Given that isotope ratios of elements are primarily a function of nucleosynthetic processes in stars and are seen to vary immensely in presolar grains (Section 3.3), one obvious cause of isotopic variation could be incomplete mixing of the components of the solar nebula. Another cause could be mass-dependent or mass-independent isotope fractionation, generally resulting from a redistribution of isotopes between coexisting phases, e.g. between gas and liquid or between two neighbouring minerals.

There are two categories of mass-dependent isotope fractionation, kinetic and equilibrium fractionation.

Kinetic fractionation occurs along a transport pathway such as diffusion or evaporation, where the velocity differences between particles are relevant. At any given temperature the average kinetic energy of all types of molecule is the same, $E_k = mv^2/2$, so that the velocity v is proportional to $\sqrt{(1/m)}$. For two molecules with masses $m_1 < m_2$, $v_1/v_2 = \sqrt{(m_2/m_1)} > 1$; correspondingly, the lighter species has a higher migration rate, $\varphi_1 > \varphi_2$, related directly to its greater average velocity: $\varphi_1/\varphi_2 = A\sqrt{(m_2/m_1)}$, where A is a coefficient depending on the system. For the case of outward migration from a reservoir the lighter species becomes depleted in it relative to the heavier species: mass fractionation occurs. The more the element migrates out and the more the quotient m_2/m_1 deviates from unity, the stronger the fractionation becomes. In the case of an element with three isotopes with abundances N_1, N_2, N_3 and masses m_1, m_2, m_3, the fractionated

(subscript FRAC) isotope abundance ratios N_2/N_1 and N_3/N_1 are related by the same fractionation factor F, as follows:

$$(N_2/N_1)_{\mathrm{FRAC}} = (N_2/N_1)_0 \times (m_2/m_1)^F$$

and

$$(N_3/N_1)_{\mathrm{FRAC}} = (N_3/N_1)_0 \times (m_3/m_1)^F. \tag{10.1}$$

In practice, stable-isotope ratio measurements are compared with standard measurements to cancel out analytical bias. International standards are used, e.g. the standard mean ocean water (SMOW) value for oxygen and hydrogen. The fractionated isotope composition of a given element in a sample (SAM) is reported in terms of its deviation from a standard (STD) composition: it is expressed using δ with a mass (or mass ratio) as a superscripted index, and the standard reference as a subscripted index:

$$\delta^{m2}_{\mathrm{STD}}(‰) \equiv 1000 \left[\frac{(N_2/N_1)_{\mathrm{SAM}}}{(N_2/N_1)_{\mathrm{STD}}} - 1 \right]. \tag{10.2}$$

The factor 1000 in this expression "amplifies" the generally small differences found in stable-isotope compositions. For an element with three isotopes it is useful to plot δ values against each other, for instance $\delta^{29/28}$Si versus $\delta^{30/28}$Si as in Fig. 10.2. In mass-dependent fractionation, the δ values are predicted to correlate. Substitution of Eqn (10.1) into Eqn (10.2) with $(N_2/N_1)_{\mathrm{FRAC}} \equiv (N_2/N_1)_{\mathrm{SAM}}$ and $(N_2/N_1)_0 \equiv (N_2/N_1)_{\mathrm{STD}}$ etc. yields the relation

$$\frac{\delta^{m2}}{\delta^{m3}} = \frac{(m_2/m_1)^F - 1}{(m_3/m_1)^F - 1}. \tag{10.3a}$$

For example, substituting $F = 0.01$ and precise values of O-isotope masses into Eqn (10.3a) gives $\delta^{17}\mathrm{O} = 0.516 \times \delta^{16}\mathrm{O}$ (Section 10.5). In most cases F is indeed low and m_i/m_1 is close to unity; then Eqn (10.3a) may be approximated by

$$\frac{\delta^{m2}}{\delta^{m3}} \approx \frac{(m_2/m_1) - 1}{(m_3/m_1) - 1} \approx \frac{m_2 - m_1}{m_3 - m_1}, \tag{10.3b}$$

which gives $\delta^{17}\mathrm{O} \approx 0.5 \times \delta^{16}\mathrm{O}$. Relations (10.3a, b) enable one to test the hypothesis of mass-dependent fractionation for isotope ratios in a three-isotope plot.

Equilibrium stable-isotope fractionation envisages the redistribution of species among coexisting phases (gaseous, liquid or solid) governed by chemical bonds in a steady-state equilibrium. This redistribution is mass dependent and Eqns (10.1–10.3) apply to it. The steady-state and equilibrium conditions imply that, in contrast with kinetic fractionation, the effect is independent of pathways. Examples are plentiful and embrace different molecules in a gas or liquid mixture containing the same element and also coexisting minerals in metamorphic or magmatic rocks.

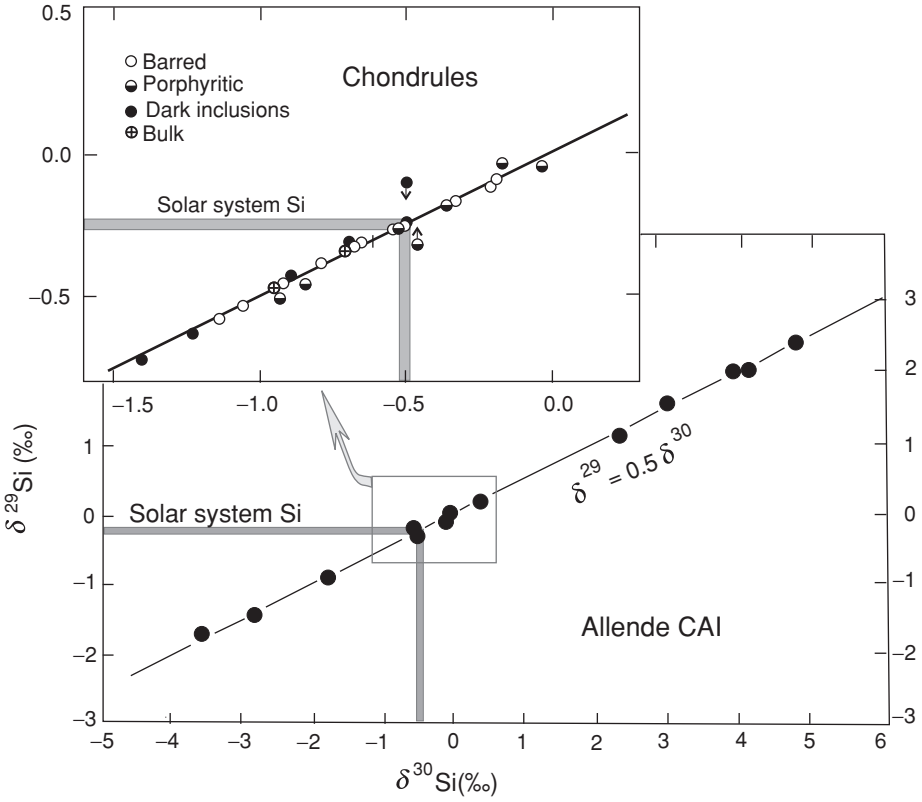

Fig. 10.2 Mass-dependent fractionation of Si isotopes in CAIs and chondrules. The isotopic ^{29}Si /^{28}Si and ^{30}Si/^{28}Si ratios are presented relative to the terrestrial standard NBS-28 as $\delta(^{30}\mathrm{Si})$ and $\delta(^{29}\mathrm{Si})$ (see Eqn 10.2 for the δ notation). Silicon is a slightly volatile element. Evaporation (leaving behind heavy Si) and recondensation affected its isotope compositions. On the basis of the analysis of a large number of stony meteorites, the average solar system $\delta(^{30}\mathrm{Si}) = -0.5\%$. All samples fall on the normal mass-dependent fractionation line, which passes through this value. After Clayton *et al.* (1985, 1988).

Phenomenologically, the equilibrium fractionation for isotopes 1 and 2 between two phases a and b is described by a fractionation factor α:

$$\alpha_{a-b} = (N_2/N_1)_a/(N_2/N_1)_b. \tag{10.4}$$

The factor α generally deviates further from unity with decreasing temperature, which leads to the important use of stable-isotope systematics as thermometers. The relation between α (Eqn 10.4) and δ (Eqn 10.2) is useful in practice. From Eqn (10.4),

$$\ln \alpha_{a-b} = \ln (N_2/N_1)_a - \ln (N_2/N_1)_b.$$

From the definition of δ, and bearing in mind that $\ln x \approx 1 + x$ if x is small, it follows that

$$1000 \ln \alpha_{a-b} \approx \delta_a - \delta_b.$$

Equilibrium isotope fractionation has its basis in quantum mechanics, which only allows specific energy levels for particles in atoms or molecules. Here we merely give a broad outline of the principle; the subject is treated in detail in a number of excellent reviews, e.g. O'Neil (1986) and Hoefs (2005).

In the case of the translational (straight) or rotational motion of a molecule or atom, the quantum energy levels are so close together that they effectively form a continuous range, and classical mechanics applies. However, for the vibrational motion relating to an elastic bond within a molecule or a crystal, the spacing between the energy levels is significant. Further, the allowed energy levels depend on the masses of the atoms or ions forming the bond. Heavier isotopes of the same element have a higher probability of lower energy levels of vibration. In other words, heavier isotopes form stronger bonds in the same crystal or molecule than lighter ones. Differences in this energy behaviour between different molecule or crystal species lead to the fractionation of stable-isotope ratios between them. At temperatures approaching absolute zero this effect is strongest. At high temperatures approaching 1000 K the relative difference between the energy levels is so small that there is generally no isotope fractionation. The temperature dependence is not a simple function. At temperatures higher than $\sim$ 300 K, $\ln \alpha$ varies approximately proportionally to $1/T^2$ for most substances, and at lower temperatures this changes gradually towards $1/T$. The differences in δ^{18}O values between silicate minerals reach 5‰ at 1000 K and 24‰ at 300 K, and although these differences are small they can be used to determine the temperatures of the respective chemical reactions, including metamorphism (Section 25.4). In three-isotope plots such as δ^{17}O versus δ^{18}O or δ^{29}Si versus δ^{30}Si, the calculated slope of a correlation line for equilibrium fractionation is exactly the same as that for a kinetic process (Eqn 10.3a).

In some cases the relationships (10.3) appear to be invalid, and it can be shown that this problem does not result from mixing. Then mass-independent fractionation (MIF) could be involved. Mass-independent fractionation can result from different processes. Thus, quantum-mechanical symmetry effects in molecules can be a reason (Thiemens, 1996). For instance, in reactions involving ozone, molecular symmetry kinetically favours the yield of $^{17}O^{16}O^{16}O$ and $^{18}O^{16}O^{16}O$ relative to $^{16}O^{16}O^{16}O$; therefore such reactions as $2O_3 \rightarrow 3O_2$ leave behind ^{16}O-depleted ozone O_3 and ^{16}O-enriched residual oxygen O_2. Also the non-symmetric molecules, e.g. ^{16}O–C–^{17}O or ^{16}O–Si–^{18}O, were found to be more stable than the corresponding symmetric ones, ^{16}O–C–^{16}O or ^{16}O–Si–^{16}O. In the δ^{17}O versus δ^{18}O plot, this

type of mechanism predicts a correlation with slope ≈ 1, in contrast with the value ≈ 0.5 that follows from Eqns (10.3a, b).

Another MIF mechanism envisages the isotope-dependent photodissociation of a chemical compound (e.g. an O-bearing or S-bearing compound, Sections 10.5 and 27.9 respectively; Farquhar *et al.*, 2001) and may be observed if the products of the dissociation have been preserved. The "pure" effect of MIF can be expressed as a difference between the observed fractionation and that predicted for the mass-dependent effect. For example, the MIF of the sulphur isotope ^{33}S is defined as $\Delta^{33}S \approx \delta^{33}S - 0.515 \times \delta^{34}S$ (Fig. 27.21).

Silica-isotope fractionation in CAI: a process of partial evaporation and recondensation

Silicon is on the verge between moderately volatile and refractory behaviour at the surmised high temperatures of CAI formation. Silicon-isotope ratios define a good correlation (Fig. 10.2) with a slope of 0.5, conforming to the relation of Eqn (10.3a, b) for the masses of Si isotopes. Compared with the average solar system ratios, heavy-isotope enrichment seems to dominate, but light-isotope-enriched Si is also seen. The fractionation line passes through the mean solar system Si ratios, which proves that the CAIs showing these effects are in fact fractionated products of the solar nebula (compare with Fig. 3.4). The inclusions enriched in heavy isotopes are generally coarse-grained and are probably residues of partial evaporation. The lighter isotopes would be preferentially lost during sublimation of the solid or evaporation from a liquid, possibly combined with diffusion. Those depleted in heavy isotopes are fine-grained and may represent condensates from a gas phase containing previously evaporated light Si.

10.3 An "absolute" age for the earliest solar system objects

General comments and requirements for absolute-age determinations

The absolute age of an object is defined as the time interval between the present, when it has an amount of a radioactive isotope ${}^{r}R_{FIN}$, and the time of its formation, when it had its initial amount, ${}^{r}R_{INI}$. These two quantities relate via Eqn (1.2): ${}^{r}R_{FIN} = {}^{r}R_{INI} \exp(-\lambda t)$, where t is the forward time. This relation cannot be used to determine ages, as ${}^{r}R_{INI}$ is itself a function of time. However, a radiogenic daughter isotope has accumulated over time, and the age can be obtained from its measurable present-day abundance ${}^{r}D^{*}_{FIN} \equiv {}^{r}R_{INI} - {}^{r}R_{FIN}$, provided that the object to be dated has always remained a closed system for the elements to which the parent and

daughter isotopes belong. Then the total amount of the daughter nuclide is

$$ {}^{\mathrm{r}}D_{\mathrm{FIN}} = {}^{\mathrm{r}}D_{\mathrm{INI}} + {}^{\mathrm{r}}D^{*}_{\mathrm{FIN}} = {}^{\mathrm{r}}D_{\mathrm{INI}} + {}^{\mathrm{r}}R_{\mathrm{FIN}}[\exp(\lambda T) - 1], \tag{10.5} $$

where ${}^{\mathrm{r}}D_{\mathrm{INI}}$ is the initial amount of the daughter nuclide and T is the age. Equation (10.5) is valid if all decays of one parent isotope produce the same daughter isotope, which can only be produced by that decay. There are three further possibilities. (1) A radioactive nuclide can decay in two ways, with a given decay in the proportion $B < 1$ (B is the branching ratio) of the total. Examples are ^{40}K, which decays to ^{40}Ca as well as to ^{40}Ar, and ^{238}U, which decays by both α-decay and (in a very small proportion) by spontaneous fission (Fig. 1.1). (2) A decay produces one of a number of possible daughter isotopes i, each with a yield fraction Y_i. An example is the production of ^{136}Xe by the spontaneous fission of ^{238}U, where only a fraction Y_{136} of fission events results in ^{136}Xe (see Fig. 1.1). (3) In some cases (e.g. ^{4}He) several parent isotopes (^{238}U, ^{235}U and ^{232}Th) produce the same daughter isotope (Fig. 24.6). Then the general form of Eqn (10.5) becomes:

$$ \begin{aligned} {}^{\mathrm{r}}D_{\mathrm{FIN}} &= {}^{\mathrm{r}}D_{\mathrm{INI}} + {}^{\mathrm{r}}D^{*}_{\mathrm{FIN}} \\ &= {}^{\mathrm{r}}D_{\mathrm{INI}} + \{B_i Y_i \, {}^{\mathrm{r}}R_{i,\mathrm{FIN}}[\exp(\lambda_i T) - 1]\} + \{\cdots\} + \cdots \end{aligned} \tag{10.6} $$

where the second term in braces would accommodate possibility (3). Note that the fission branching ratio for ^{238}U is very small, so that it can be disregarded in U–Pb systematics.

It is more convenient to study isotopic ratios than absolute concentrations. So, after dividing Eqn (10.6) by the abundance of a reference stable isotope ${}^{\mathrm{s}}D$ (relating to the daughter element D), the relation between the two measurable parameters $({}^{\mathrm{r}}D/{}^{\mathrm{s}}D)_{\mathrm{FIN}}$ and $({}^{\mathrm{r}}R/{}^{\mathrm{s}}D)_{\mathrm{FIN}}$ is given by

$$ \begin{aligned} ({}^{\mathrm{r}}D/{}^{\mathrm{s}}D)_{\mathrm{FIN}} = ({}^{\mathrm{r}}D/{}^{\mathrm{s}}D)_{\mathrm{INI}} &+ \{B_i Y_i ({}^{\mathrm{r}}R_i/{}^{\mathrm{s}}D)_{\mathrm{FIN}}[\exp(\lambda_i T) - 1]\} \\ &+ \{\cdots\} + \cdots \end{aligned} \tag{10.7a} $$

In the case where $({}^{\mathrm{r}}R/{}^{\mathrm{s}}D)_{\mathrm{INI}}$ is known rather than $({}^{\mathrm{r}}R/{}^{\mathrm{s}}D)_{\mathrm{FIN}}$, then we have

$$ \begin{aligned} ({}^{\mathrm{r}}D/{}^{\mathrm{s}}D)_{\mathrm{FIN}} = ({}^{\mathrm{r}}D/{}^{\mathrm{s}}D)_{\mathrm{INI}} &+ \{B_i Y_i ({}^{\mathrm{r}}R_i/{}^{\mathrm{s}}D)_{\mathrm{INI}}[1 - \exp(-\lambda_i T)]\} \\ &+ \{\cdots\} + \cdots \end{aligned} \tag{10.7b} $$

Apart from the closed-system requirement, it is necessary that $({}^{\mathrm{r}}D/{}^{\mathrm{s}}D)_{\mathrm{INI}}$ is known or can somehow be derived. Further, it is clear that the greater the present-day parent–daughter isotope ratio $({}^{\mathrm{r}}R/{}^{\mathrm{s}}D)_{\mathrm{FIN}}$, the greater the difference between $({}^{\mathrm{r}}D/{}^{\mathrm{s}}D)_{\mathrm{FIN}}$ and $({}^{\mathrm{r}}D/{}^{\mathrm{s}}D)_{\mathrm{INI}}$ for a given value of T and the more precise the age determination. Ideally, at least two objects should be available that were formed at the same time and with the same value of $({}^{\mathrm{r}}D/{}^{\mathrm{s}}D)_{\mathrm{INI}}$, of which one has a ratio $({}^{\mathrm{r}}R/{}^{\mathrm{s}}D)_{\mathrm{FIN}} \approx 0$, so that $({}^{\mathrm{r}}D/{}^{\mathrm{s}}D)_{\mathrm{INI}} \approx ({}^{\mathrm{r}}D/{}^{\mathrm{s}}D)_{\mathrm{FIN}}$ and can be directly measured,

and the other has a high value of $({}^{r}R/{}^{s}D)_{FIN}$, enabling dating. Failing such an ideal situation, good results can also be obtained if the cogenetic objects simply have different values of $({}^{r}R/{}^{s}D)_{FIN}$, so that an age can be obtained from the correlation of $({}^{r}D/{}^{s}D)_{FIN}$ and $({}^{r}R/{}^{s}D)_{FIN}$ in a so-called isochron, or evolution, diagram (e.g. Fig. 12.7). Variable values of $({}^{r}R/{}^{s}D)_{FIN}$ can result if the parent and daughter isotopes belong to elements with different characteristics, for instance, different volatilities or different affinities for given minerals and melts.

The Gerling–Houtermans equation and the related Pb–Pb isochron systematics

The U–Th–Pb systematics provide the most informative and at the same time the most complicated tool of isotope cosmo- and geochemistry and chronology. Three radioactive isotopes, ^{238}U ($\tau_{238} = 4468$ Myr), ^{235}U ($\tau_{235} = 704$ Myr) and ^{232}Th ($\tau_{232} = 14\,010$ Myr) decay to the stable isotopes ^{206}Pb, ^{207}Pb and ^{208}Pb respectively (Fig. 24.6). As Pb is a magic element, these three isotopes were relatively abundant in the initial solar nebula. A fourth Pb isotope, ^{204}Pb, is not produced by any radioactive decay and is therefore useful as a reference. The parent and daughter elements have very different behaviour in most astrophysical and terrestrial environments, as discussed below in Sections 11.6 and 12.4. With regard to CAI formation it is important that U is one of the most refractory and Pb one of the most volatile elements; therefore Pb is readily separated from U either during the condensation process or as a result of heating and partial vaporization. Moreover, U and Pb are concentrated in different minerals, owing to their different chemistry. As a result, strong U–Pb fractionation is expected for a number of objects.

Uranium–lead chronometry is unique because U has two live radioactive isotopes, ^{238}U and ^{235}U, which decay with different half-lives into the respective lead isotopes ^{206}Pb and ^{207}Pb. An object containing U therefore incorporates two clocks, which can be checked against each other. If in Eqn (10.7) we substitute ${}^{r}R = {}^{235}$U, ${}^{r}D = {}^{207}$Pb and ${}^{s}D = {}^{204}$Pb and then coupling this equation with the corresponding equation for the ^{238}U–^{206}Pb subsystem we obtain

$$\frac{({}^{207}\mathrm{Pb}/{}^{204}\mathrm{Pb})_{FIN} - ({}^{207}\mathrm{Pb}/{}^{204}\mathrm{Pb})_{INI}}{({}^{206}\mathrm{Pb}/{}^{204}\mathrm{Pb})_{FIN} - ({}^{206}\mathrm{Pb}/{}^{204}\mathrm{Pb})_{INI}} = \left(\frac{{}^{235}\mathrm{U}}{{}^{238}\mathrm{U}}\right)_{FIN} \frac{\exp(\lambda_{235}T) - 1}{\exp(\lambda_{238}T) - 1}. \qquad (10.8)$$

This is known as the Gerling–Houtermans equation. It is important that the present-day ^{235}U/^{238}U ratio in Eqn (10.8) is identical for all solar system materials and has been measured with a high accuracy (Chen and Wasserburg, 1981; Lugmair and Galer, 1992). The final Pb-isotope ratios can be measured directly. Therefore a unique advantage of the Gerling–Houtermans equation is that it allows an age to

be determined even if U or Pb have recently been partially lost. The parameters of Eqn (10.8) are, of course, not immune to Pb contamination, as this changes the Pb-isotope ratios. A further peculiarity of this dating method is that it is more precise for older ages than for young ones, because the $^{235}U/^{238}U$ ratio was ~ 50 times greater in the early solar system than today, so that the relative rate of ^{207}Pb accumulation was correspondingly higher.

Provided that the final ratios are measured in several samples, which originate from the same source material at the same time, then it follows from Eqn (10.8) that the measured ratios determine a straight line in a $^{207}Pb/^{204}Pb$ versus $^{206}Pb/^{204}Pb$ plot. This line, termed an isochron, passes through the point of the initial lead composition, and its slope gives the age for the U–Pb systematics as illustrated by the inset in Fig. 10.3. Many types of material with very high μ values (μ is the present-day $^{238}U/^{204}Pb$ ratio), such as e.g. CAIs (Fig. 10.3), have been dated by this method with high precision and accuracy.

The Pb/Pb age of Ca–Al-rich inclusions (CAIs)

Element abundances in CAIs are generally governed by volatility; therefore $^{238}U/^{204}Pb$ is high and varies widely in CAIs and their constituent minerals (up to ~ 5000, exceeding the SOS ratio by a factor ~ 1000). Correspondingly, the present-day Pb-isotope ratios in CAIs exceed the initial values by orders of magnitude, and uncertainties in the correction terms, e.g. $^{207}Pb/^{204}Pb_{INI}$, do not lead to major uncertainties in the age. The Pb/Pb age is the (almost) direct outcome from measured $^{207}Pb/^{206}Pb$ ratios (Chen and Wasserburg, 1981; Manhes *et al.*, 1984; Tilton, 1988; Allègre *et al.*, 1995a; Amelin *et al.*, 2002).

The Pb/Pb dating of Allende CAIs has yielded the oldest high-precision directly determined absolute age obtained so far for meteoritic constituents, 4566 ± 2 Myr (see the review by Allègre *et al.*, 1995a). Amelin and coworkers (Amelin *et al.*, 2002) derived the same age, but with a higher precision, for CAIs from the Efremovka CV chondrite, 4567.2 ± 0.6 Myr. A possibility that must be considered, however, is that during hydrous alteration in the host meteorite some early-formed radiogenic Pb could have been lost from the dated minerals; in this case the date of 4567 Myr would still have validity as a minimum age (Chapter 13).

10.4 Short-lived nuclides: further evidence for early CAI formation

Extinct nuclides and isochrons

Exciting knowledge on the formation and evolution of the solar nebula has been gained from the study of the decay products of extinct radioactive isotopes in nebula objects (Table 3.3). As outlined above, the nebula lifetime was probably

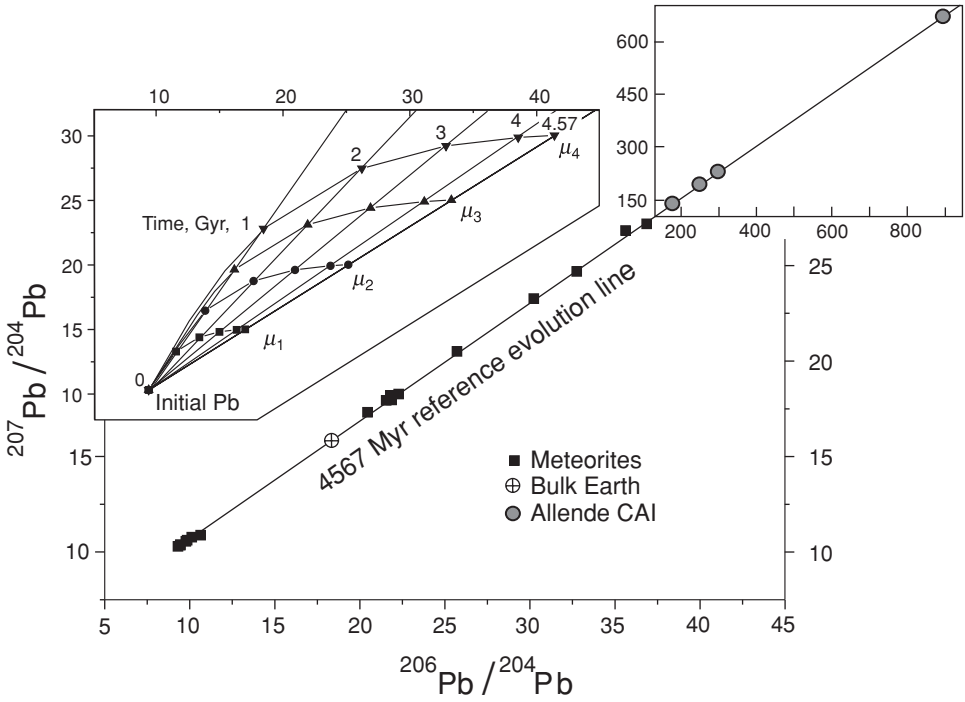

Fig. 10.3 The ratio ^{207}Pb/^{204}Pb vs. the ratio ^{206}Pb/^{204}Pb, for CAI-ALL and chondritic and achondritic meteorites. The left-hand inset shows the evolution of lead isotope ratios with time in samples having different ^{238}U/^{204}Pb $\equiv \mu$ ratios: $\mu_1 < \mu_2 < \mu_3 < \mu_4$. If all samples $\mu_1, \ldots, \mu_4$ had the same initial Pb-isotope composition and the system remained closed for U and Pb then at any given time (age) all these samples would lie on a straight line. The slope of this line yields the time (age) of closure of the U–Pb systematics in these samples. Indeed, the bulk meteorite data plot on or close to the 4567 Myr reference evolution line, which means that the ages of their parent bodies are close to this value. The bulk terrestrial Pb also plots close to this line. Refractory inclusions from the carbonaceous chondrite Allende (ALL, right-hand inset) show very high ^{206}Pb/^{204}Pb and ^{207}Pb/^{204}Pb ratios, so that the correction for common Pb does not introduce substantial errors. These samples determine the slope of the reference evolution line and give the most precise age, which appears to be the most ancient absolute age of any material found so far in the solar system. After Tilton (1973) and Allègre *et al*. (1995a).

short, ~ 10 Myr or less, and during this interval the nebula materials underwent dramatic evolution, from gas and dust to large differentiated planetary embryos. Chronometers based on short-lived radioactive nuclides allow a high time resolution and therefore enable one to discern milestones in the early solar system history.

The daughter products of the short-lived nuclides are visible as small isotope anomalies in minerals enriched in the parent isotope's element, which were formed

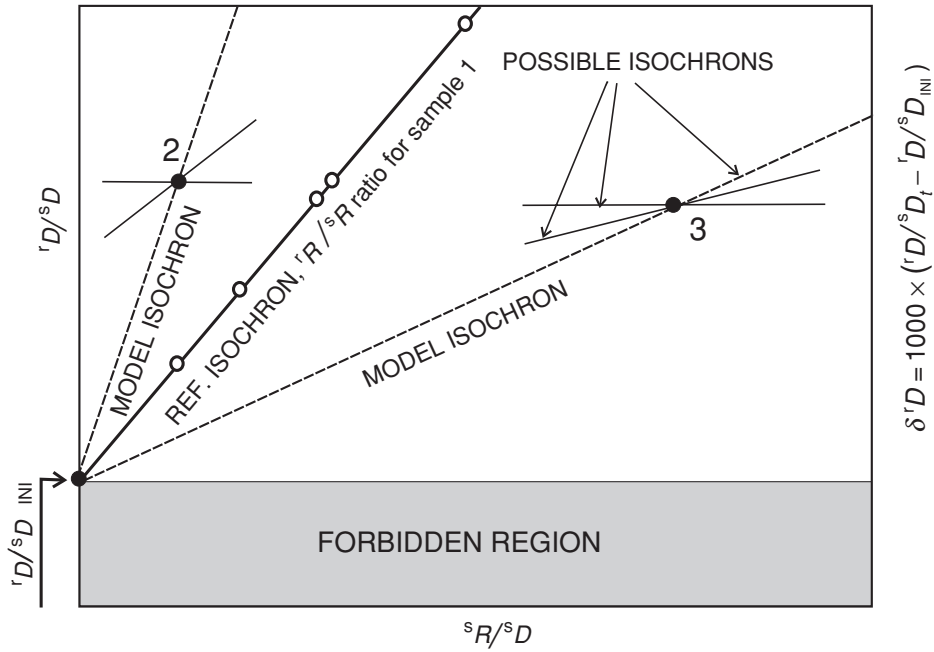

Fig. 10.4 Evolution diagram for extinct isotope systematics. The shaded area lies below the initial solar system ${}^{r}D/{}^{s}D_{\mathrm{INI}}$ ratio, therefore this is a forbidden region. To determine the relative formation interval, sample 1, having a well-defined isochron, is used as the reference. The slope of the reference isochron determines the ratio of ${}^{r}R/{}^{s}R_{\mathrm{INI}} \equiv {}^{r}D^{*}_{\infty}/{}^{s}R$ for sample 1 (Eqn 10.10). The parent materials for sample 2 (left of the reference isochron) and sample 3 (right) were formed earlier and later, respectively, than the reference sample. If no isochron is available for these samples, model ages can be derived by comparing the slopes of the model chords, as drawn, and the reference isochron (Eqn 10.11).

before the parent isotope had decayed and remained unaffected by the decay. These anomalies are revealed in diagrams in which the extinct radioactive isotope ${}^{r}R$ is represented by a stable "brother" ${}^{s}R$ on the horizontal axis, and ${}^{r}D$ on the vertical axis is in fact a proxy for the extinct ${}^{r}R$ (Fig. 10.4). If the data produce an isochron in this diagram, its slope yields directly not the age of the samples but the ratio ${}^{r}R/{}^{s}R$ at the time when the samples formed.

The evolution of a short-lived radioactive isotope ${}^{r}R$ with a stable brother ${}^{s}R$ can be discussed using two points in time. The first is $t = t_0$, when nucleosynthesis has ceased and the isotopes are ejected from the parent star into the interstellar medium with a ratio $({}^{r}R/{}^{s}R)_0$. The second is t_{INI}, when both the radioactive $({}^{r}R/{}^{s}R)_{\mathrm{INI}}$ and the daughter species $({}^{r}D/{}^{s}D)_{\mathrm{INI}}$ are incorporated into a host object. Ideally, the aim of a dating project would be to find the time difference $t_{\mathrm{INI}} - t_0$, known as the

formation interval ΔT. The amounts of the radioactive nuclide at t_{INI} and t_0 are related by

$$({}^{\mathrm{r}}R/{}^{\mathrm{s}}R)_{\mathrm{INI}} = ({}^{\mathrm{r}}R/{}^{\mathrm{s}}R)_0 \exp[-\lambda(t_{\mathrm{INI}} - t_0)]. \tag{10.9}$$

In the long time following t_{INI}, the radioactive nuclide decays completely within the object and the radiogenic addition to the daughter isotope species, ${}^{\mathrm{r}}D^* \equiv {}^{\mathrm{r}}R_{\mathrm{INI}}$, accumulates, provided that the closed-system assumption holds. Therefore, $({}^{\mathrm{r}}R/{}^{\mathrm{s}}R)_{\mathrm{INI}}$ can be obtained from present-day measurable parameters (subscripted MEAS). Referring to the isochron diagram (Fig. 10.4):

$$({}^{\mathrm{r}}R/{}^{\mathrm{s}}R)_{\mathrm{INI}} = \left[\frac{({}^{\mathrm{r}}D^*_{\infty}/{}^{\mathrm{s}}D)}{({}^{\mathrm{s}}R/{}^{\mathrm{s}}D)}\right]_{\mathrm{MEAS}} = \frac{({}^{\mathrm{r}}D/{}^{\mathrm{s}}D)_{\mathrm{MEAS}} - ({}^{\mathrm{r}}D/{}^{\mathrm{s}}D)_{\mathrm{INI}}}{({}^{\mathrm{s}}R/{}^{\mathrm{s}}D)_{\mathrm{MEAS}}}. \tag{10.10}$$

The value of ${}^{\mathrm{r}}D/{}^{\mathrm{s}}D_{\mathrm{INI}}$ can be determined in favourable cases from coexisting minerals with $({}^{\mathrm{s}}R/{}^{\mathrm{s}}D)_{\mathrm{MEAS}} \approx 0$ or, if an isochron is produced (Fig. 10.4), the values of $[({}^{\mathrm{r}}D^*/{}^{\mathrm{s}}D)/({}^{\mathrm{s}}R/{}^{\mathrm{s}}D)]_{\mathrm{MEAS}}$ and $({}^{\mathrm{r}}D/{}^{\mathrm{s}}D)_{\mathrm{INI}}$ may both be found by regression, as for an isochron in long-lived decay systematics. Equation (10.9) then yields the product $({}^{\mathrm{r}}R/{}^{\mathrm{s}}R)_0 \exp[-\lambda(t_{\mathrm{INI}} - t_0)]$.

Unfortunately even if the latter product can be quantified precisely enough, it contains two unknowns, the ratio $({}^{\mathrm{r}}R/{}^{\mathrm{s}}R)_0$, which is dependent on nucleosynthetic models, and the time difference $t_{\mathrm{INI}} - t_0$, or ΔT. However, the comparison of two different objects, 1 and 2 (e.g. two different inclusions or meteorites), allows the relative formation interval $\Delta T_{2,1}$ to be determined with a high accuracy. Assuming a uniform $({}^{\mathrm{r}}R/{}^{\mathrm{s}}R)_0$ at t_0 (i.e. one ${}^{\mathrm{r}}R$-producing event), then dividing Eqn (10.9) for sample 2 by the same equation for reference sample 1 and rearranging gives

$$\frac{1}{\lambda} \ln \frac{({}^{\mathrm{r}}R/{}^{\mathrm{s}}R)_{\mathrm{INI},2}}{({}^{\mathrm{r}}R/{}^{\mathrm{s}}R)_{\mathrm{INI},1}} = t_{\mathrm{INI},2} - t_{\mathrm{INI},1} = \Delta T_{2,1}, \tag{10.11}$$

which is the time interval between the formation of the two objects 1 and 2.

Generally an object yielding a well-defined isochron is used as the reference, 1, and then the relative formation interval can be derived for an object 2 for which the isochron is worse or even unavailable. In the latter case the assumption of closed-system evolution cannot be verified, ${}^{\mathrm{r}}D/{}^{\mathrm{s}}D_{\mathrm{INI},2}$ is usually assumed to be similar to ${}^{\mathrm{r}}D/{}^{\mathrm{s}}D_{\mathrm{INI},1}$ and a model age is obtained (samples 2 and 3 in Fig. 10.4). The $({}^{\mathrm{r}}D/{}^{\mathrm{s}}D)_{\mathrm{INI}}$ ratios bear evidence on the homogeneity of a source material and thus on the validity of chronological reconstructions (Lugmair and Shukoluykov, 1998).

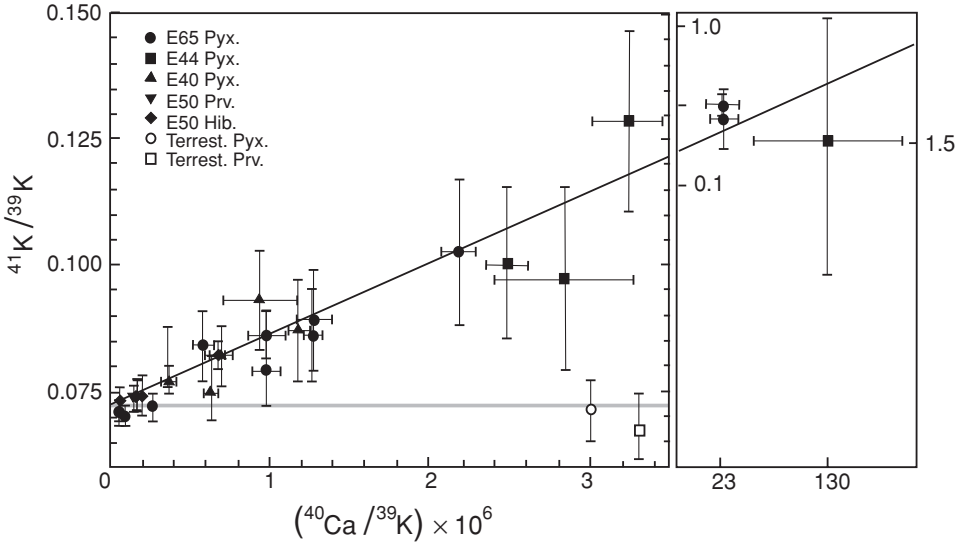

Fig. 10.5 The ^{41}Ca–^{41}K systematics in CAIs of the Efremovka meteorite. The samples are pyroxenes (Pyx.), hibonites (Hib.) and perovskite (Prv.). The right-hand panel shows the coordinates of three outliers. The data for terrestrial pyroxene and perovskite are shown for comparison. The slope of the regression line gives the Ca-isotope ratio at the time of CAI formation, $(^{41}Ca/^{40}Ca)_{INI} = (1.41 \pm 0.14) \times 10^{-8}$. The errors are $\pm 2\sigma$. From Srinivasan *et al.* (1996), © Elsevier Science 1996, reproduced by permission.

Extinct nuclides in CAIs: the earliest objects formed in the solar nebula

Calcium–aluminium-rich inclusions from the Efremovka chondrite show an extremely high ratio of involatile Ca over moderately volatile K and in these same inclusions traces of extinct ^{41}Ca have been discovered: the $^{41}K/^{39}K$ versus $^{40}Ca/^{39}K$ ratios in minerals separated from several CAI inclusions show a good correlation, as expected (according to Eqn 10.10) if excess ^{41}K has been produced *in situ* by the K-decay of radioactive ^{41}Ca ($\tau_{41} = 0.10$ Myr, Table 3.3, Fig. 10.5; Srinivasan *et al.*, 1996).

The correlation could have resulted from recent ^{41}Ca production and decay in the minerals while the meteorite travelled from the parent body to the Earth and was exposed to cosmic rays. The relevant nuclear reaction would be $^{40}Ca(n, \gamma)^{41}Ca$, the neutron fluence being from cosmic-ray-induced (p, n) and (α, n) reactions. However, the ^{41}Ca abundance in Efremovka would require a very dense neutron fluence, and other cosmogenic isotopes would have been greatly overproduced compared with the amounts observed in this meteorite. This allows the cosmogenic hypothesis to be eliminated in favour of the presence of live ^{41}Ca in the early solar system. Accordingly, CAIs must have been formed at a time when the relevant nucleogenic

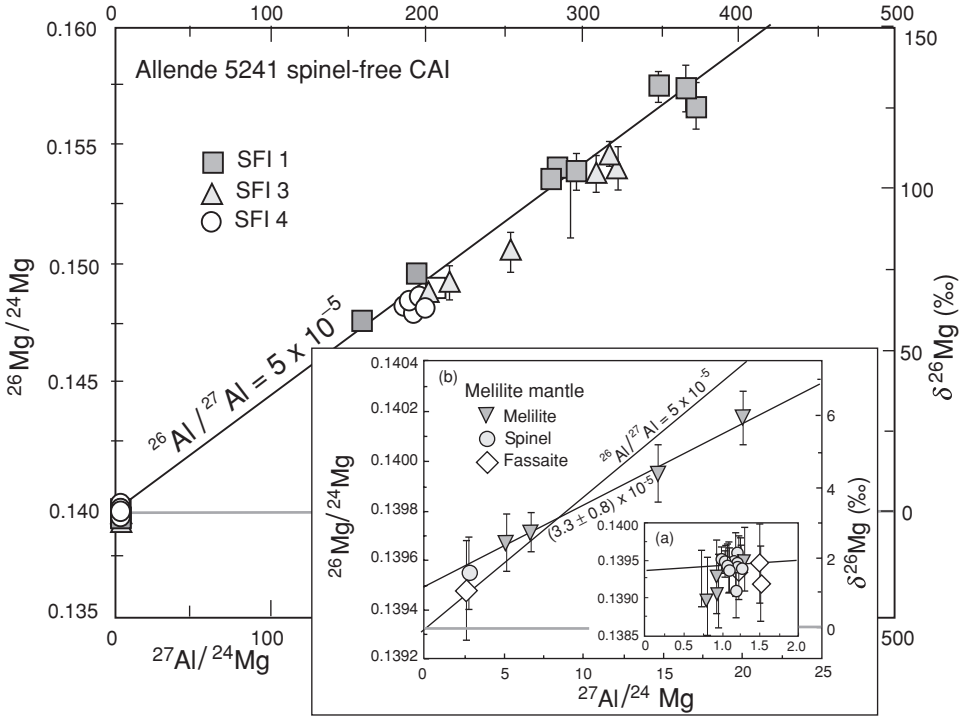

Fig. 10.6 The ^{26}Al–^{26}Mg systematics in CAIs from Allende C3V carbonaceous chondrite. The Mg-isotope composition is presented as the ratio ^{26}Mg /^{24}Mg (left-hand vertical axis) and also as δ^{26}Mg $= \{[(^{26}\text{Mg}/^{24}\text{Mg})_{\text{SAM}}/(^{26}\text{Mg}/^{24}\text{Mg})_{\text{STD}}] - 1\} \times 1000$ (right-hand vertical axis). The isochron gives the canonical solar nebula ratio of $^{26}\text{Al}/^{27}\text{Al} = 5 \times 10^{-5}$ (slope) and the daughter initial ratio of $^{26}\text{Mg}/^{24}\text{Mg} = 0.1393$ (intercept, Eqn 10.10) for spinel-free inclusions (SFIs). The inset shows (a) the data points with the lowest ratios and (b) the intercept and slope of the melilite mantle, which was formed by 0.4 Myr later. From Hsu *et al.* (2000), © Elsevier Science 2000, reproduced by permission.

process was still operating, or within several hundred thousand years after it had ceased, otherwise this nuclide would have decayed before it was incorporated in the inclusions.

Observations of traces of short-lived ^{41}Ca and especially ^{7}Be in CAIs put important constraints on the respective nucleosynthetic processes (Section 8.3); their very early formation supports the chronological interpretation of other systematics, first of all ^{26}Al–^{26}Mg.

Since the pioneer work by Lee *et al.* (1976) a perfect direct correlation between the ^{26}Mg/^{24}Mg and ^{27}Al/^{24}Mg ratios has been observed for many CAI minerals, indicating ^{26}Al decay as a source of excess ^{26}Mg*; generally the slope of the extinct isochron gives $^{26}\text{Mg}^*/^{27}\text{Al} \equiv (^{26}\text{Al}/^{27}\text{Al})_{\text{INI}} = 5.0 \times 10^{-5}$ (Figs. 10.6 and 10.7 and

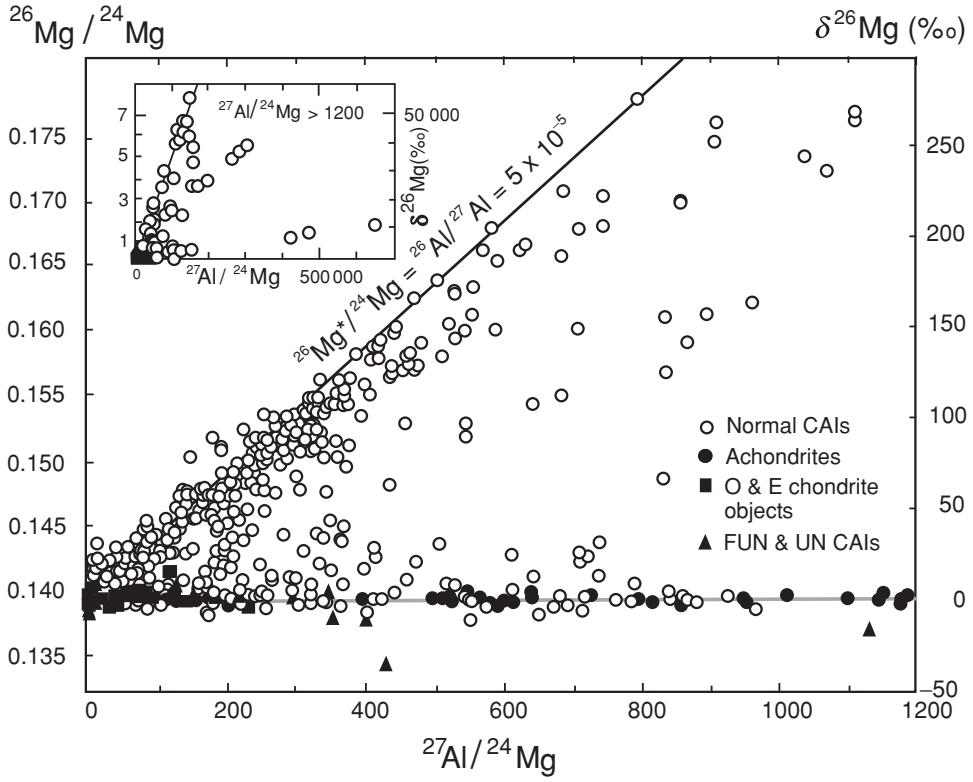

Fig. 10.7 The ^{26}Al–^{26}Mg systematics in CAI and other objects from various meteorites. The reference lines correspond to initial ratios $(^{26}Al/^{27}Al)_{INI}$ of 5×10^{-5} and 0 respectively. Most normal CAIs show $(^{26}Al/^{27}Al)_{INI}$ values similar to the canonical SOS ratio 5×10^{-5}. The inset shows the same evolution diagram but for very high $^{27}Al/^{24}Mg$ ratios. From MacPherson *et al.* (1995), © Meteoritical Society 1995, reproduced by permission.

Table 3.3). Somewhat higher initial ratios, up to 6×10^{-5}, were recently observed in the CAIs separated from several chondrites (Young *et al.*, 2005). According to Eqn (10.11), this corresponds to the formation of these inclusions ~ 0.25 Myr before the ^{26}Al–^{26}Mg systematics became closed for the majority of the inclusions. The authors consider that especially intense heating events during this interval reset the cosmochronometer, and the data on Mg diffusion rates in the CAIs validate this interpretation. In the following discussions we will use the "canonical" ratio, which fits the great majority of CAIs, as a time marker for the short-time-scale dating of other nebula objects.

It should be emphasized that Al is one of the most refractory elements and Mg is also not a volatile element (Table 3.1). Therefore the ^{26}Al–^{26}Mg chronometer works well for high-temperature objects such as CAIs and some chondrules, because only high-temperature condensation fractionates these elements, enhancing the Al/Mg

ratio in such minerals as hibonite (Table 10.1). Further, Al is immobile in aqueous metamorphic and alteration processes, although Mg can be mobilized. Some CAI minerals, such as hibonite, are highly resistant to alteration and therefore appear to be reliable carriers of fingerprints of *in situ* ^{26}Al decay. Because of these and other promising features of the ^{26}Al–^{26}Mg systematics, a large data base has been generated (Fig. 10.7). Inspection of this data base shows immediately that $(^{26}Al/^{27}Al)_{INI}$ ratios similar to those discovered in Allende are also observed in the great majority of CAIs from different carbonaceous and ordinary chondrites. Some samples, however, have lower values of $(^{26}Al/^{27}Al)_{INI}$ and some do not indicate the presence of live ^{26}Al at all.

The fact that these $(^{26}Al/^{27}Al)_{INI}$ ratios in the great majority of CAIs do approach the canonical value, $\sim 5 \times 10^{-5}$, leads to several important conclusions. (1) The nucleosynthetic and transport processes responsible for live ^{26}Al in the solar nebula must have yielded at least the above initial ratio. (2) Material with an initial ratio $\sim 5 \times 10^{-5}$ was abundant in the early solar nebula in the zone where CAIs were formed, and it originated within a short time scale of a few hundred thousand years. (3) If there was an initial ^{26}Al/^{27}Al heterogeneity in the solar nebula, this must have been small compared with the time-related isotope effect, so that a chronological interpretation of the ^{26}Al–^{26}Mg data is possible.

Correlated petrologic and isotopic studies show that the majority of canonical CAIs have almost never been disturbed by secondary processes. In contrast, samples in which $(^{26}Al/^{27}Al)_{INI}$ approaches zero demonstrate reheating or secondary alteration, which could have happened at any time after most ^{26}Al had decayed (MacPherson *et al.*, 1995; Swindle *et al.*, 1996; Huss *et al.*, 2001).

The $(^{26}Al/^{27}Al)_{INI}$ ratios can vary according to the distinct petrographic setting even within one inclusion: in late second-generation igneous phases and rims a ^{26}Mg/^{24}Mg anomaly may be absent (MacPherson and Davis, 1993). In some cases the high time resolution of the ^{26}Al chronometer allows the dating of multilayered CAIs. In one Allende CAI the spinel-free inclusions (within a spinel-rich core), which have an almost canonical $(^{26}Al/^{27}Al_{INI})$ value, $(5 \pm 0.1) \times 10^{-5}$, were formed first whereas the spinel core and the melilite-rich mantle show lower ratios $(4.3 \pm 0.1) \times 10^{-5}$ and $(3.3 \pm 0.8) \times 10^{-5}$ respectively (Fig. 10.6, inset). Substitution of these values into Eqn (10.11) using the inclusion as the reference sample gives the relative (post-inclusion) formation times for the core and the mantle as ~ 0.1 and ~ 0.4 Myr respectively. This shows that fractionation events, which occurred at least 4567 Myr ago, can be resolved on a scale of ~ 0.1 Myr and suggests that the high-temperature processes of CAI formation continued for as long as ~ 0.5 Myr (Hsu *et al.*, 2000). Chondrules in ordinary chondrites show lower $(^{26}Al/^{27}Al_{INI})$ ratios than those for CAIs, which means that chondrules (and chondrites) were formed 1 or 2 Myr later than CAIs; this follows, for example, from an elegant

investigation of a CAI core hosted by a chondrule rim (Krot *et al.*, 2006). The core and rim have different O-isotope compositions (used for the identification; see the next section) and the ^{26}Al–^{26}Mg systematics indicate formation of the rim at least 2 Myr later. The Pb/Pb chronology suggests a similar time difference (Fig. 11.6).

The interval between CAI and chondrite formation conflicts somewhat with model estimates of the residence time of CAI-like objects in the solar nebula, $\sim 10^5$ yr: during this time such an object would be expected to drift into the Sun (Cameron, 1995). A mechanism must have operated that prevented loss of the CAIs from the nebula for this relatively long interval, up to ~ 2 Myr, and this constrains models of CAI formation (Section 10.6).

10.5 Oxygen isotopes in nebula objects: the CAI array

Oxygen differs from other major elements in that it has two significant reservoirs in the solar nebula: a gaseous reservoir, CO and H_2O being the dominant constituents, and solid phases consisting of oxides and silicates. Exchange between these reservoirs, whether in kinetic or equilibrium situations, would be expected to involve isotope fractionation causing a substantial range of oxygen-isotope compositions in various objects of the nebula. As discussed above, kinetic as well as equilibrium chemical reactions yield mass-dependent oxygen-isotope fractionation, approximated by $\delta^{17}O \approx 0.516 \times \delta^{18}O$ for small fractionation factors (Eqn 10.3). Certainly such fractionation, within a few parts per million (ppm), is observed within given meteoritic groups, which define elongated clusters parallel to and, variably, slightly above or below the terrestrial fractionation line (Fig. 10.8).

The most important features of the oxygen-isotope systematics in the solar system, however, cannot be explained by mass-dependent fractionation. Within the three-isotope $\delta^{18}O$–$\delta^{17}O$ plots shown in Fig. 10.8(a), the CAIs lie along the reference mixing line characterized by $\delta^{17}O \approx \delta^{18}O$ and deviating from the carbonaceous chondrite whole-rock domain towards rather ^{16}O-enriched compositions, $\delta^{18}O \approx \delta^{17}O \approx -50‰$. This non-mass-dependent oxygen-isotope pattern in CAIs was first discovered by Clayton *et al.* (1973). Bulk meteorite and chondrule compositions reside at the heavy end of the CAI array, near to its intersection with the terrestrial fractionation line (Fig. 10.8).

Thus, the most striking features of solar nebular O-isotope abundances are: (1) the major CAI array with slope 1, where the O-isotope variation among the CAI minerals (melilite, spinel, fassaite deviating along this slope) indicates that crystallization of the CAIs started from ^{16}O-rich matter and that O-isotope exchange with the surrounding ^{16}O-poor nebular gas progressed throughout the crystallization (Yurimoto *et al.*, 1998); (2) a restricted compositional field for each meteoritic group; (3) a variable large difference between early-formed CAIs and later-formed

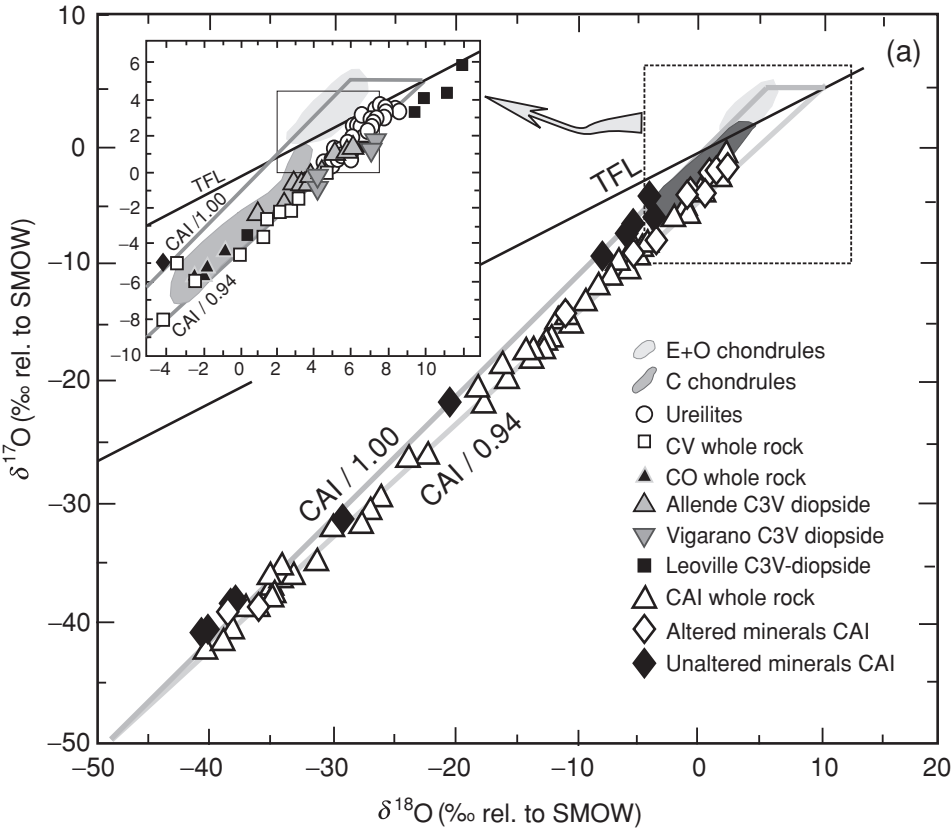

Fig. 10.8 (a) Oxygen-isotope compositions of meteorites. The terrestrial fractionation line (TFL), having a slope 0.516, corresponds to the mass-dependent fractionation of terrestrial matter (Eqn (10.2)). Calcium–aluminium-rich inclusions (CAIs), and minerals separated from them fall along the CAI lines. Note that unaltered minerals plot along a line with slope 1.00. Because of alteration and fractionation, altered minerals deviate from this line. Their regression yields a smaller slope, 0.94. The inset shows O-isotope compositions in bulk meteorites, mineral separates and chondrules (the axes of the inset are the same as those in the main figure). The chondrules generally overlap the compositions of the respective meteoritic groups: for example, CC chondrules overlap the compositions of the bulk CC meteorites.

whole-rock meteorite parent bodies (matrix + chondrules); (4) variable small differences between whole-rock and chondrule values within a given class of chondrites; (5) the similarity of highly processed stone and iron meteorites. Regarding the CAIs, the subject of this chapter, the most likely explanation of their slope-1 array envisages mass-independent O-isotope fractionation (MIF). This, rather than the mixing of two components, was originally proposed by Thiemens (1988) and an

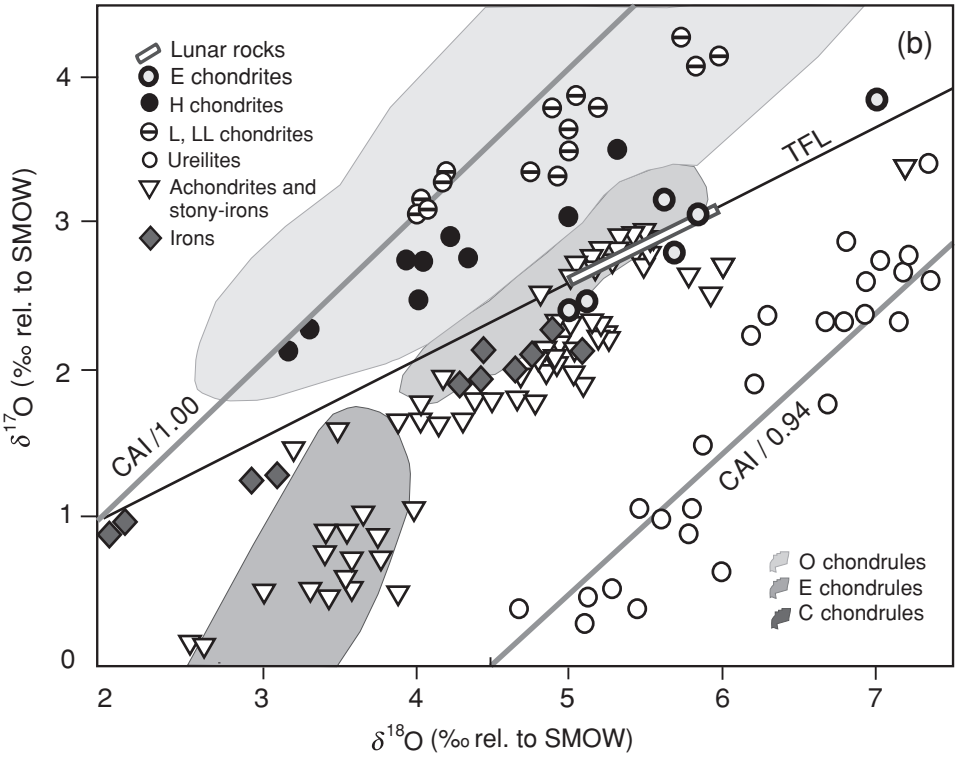

Fig. 10.8(b) Oxygen-isotopic compositions for ordinary and enstatite chondrites as well as for achondrites and iron meteorites. Chondrules from ordinary chondrites overlap both the H- and L-chondrite compositions. Some non-chondritic, stony-iron and iron meteorites show similar O-isotope compositions. Lunar-rock O-isotope compositions (open thin rectangle) are indistinguishable from the TFL. Modified from Clayton (1993, 2003), Clayton and Mayeda (1996), Wiens *et al.* (1999) and Wiechert *et al.* (2001).

astrophysically plausible hypothesis was suggested by Clayton (2002, 2003). A modification of this is discussed below.

In the presolar cold molecular cloud, CO is likely to have been one of the most abundant gaseous O-bearing molecules. It is chemically inert but can be dissociated by ultraviolet (UV) radiation. The wavelengths for the dissociation of CO with different C or O isotopes differ slightly from each other. Because of the dominance of ^{12}C and ^{16}O, UV light with a wavelength corresponding to the dissociation of $^{12}C^{16}O$ is attenuated at the radiating front of a gas–dust disk; $^{12}C^{16}O$ is thus relatively shielded further inside the disk, and CO molecules with ^{17}O or ^{18}O are dissociated preferentially. This in turn means that the ^{17}O and ^{18}O isotopes are both over-reactive and form solid condensates, mainly icy mantles on the surfaces

of silicate particles (Yurimoto and Kuramoto, 2004). By this mechanism, the isotopic effect seen in meteorites could be achieved within a short time interval, ~ 0.1 Myr.

In the very early, hot, highly turbulent nebula (within 0.5 Myr after collapse started) the icy material was vaporized and remixed with nebula gas to yield a mixture with an O-isotope composition close to the bulk solar value. Calcium–aluminium-rich inclusions could have inherited this bulk solar oxygen, possibly modified by an enhanced contribution of ^{16}O-rich oxygen vaporized from solid silicate grains in the innermost segment of the solar nebular midplane (Fig. 9.1). Later on (~ 1 or 2 Myr after the CAIs were formed), mixing within the nebula became less efficient. Therefore, while ice particles drifted along the central plane towards the Sun, crossed the snow line (at present at ~ 5 AU from the Sun) and eventually vaporized, the vapour gave rise to a specific ^{17}O- and ^{18}O-enriched "atmosphere" near the nebula midplane, where chondritic meteorites were formed. Oxygen-isotope exchange between silicate material and the ^{17}O- and ^{18}O-enriched gas then generated the observed O-isotope patterns in chondrites. It is also possible that ^{16}O-depleted ices were formed in the nebula itself, beyond the snow line. Various aspects of this UV-induced MIF were discussed by Yurimoto and Kuramoto (2004), Krot *et al.* (2005) and Lyons and Young (2005).

Clayton (2003) pointed out that, following this idea, the solar O-isotope composition should be close to the ^{16}O-rich end-member of the CAI array, so that the theory is testable. Unfortunately at present the O-isotope composition of the Sun is still highly uncertain. Solar-wind measurements (Collier *et al.*, 1998) give a δ^{18}O value equal to $+110 \pm 290$‰, whereas spectrometric measurements (Harris *et al.*, 1987) have yielded $+140 \pm 130$‰. Recent proposals have been made that the oxygen of relatively massive planets (such as the Earth) represents the solar oxygen best of all, whereas CAIs record some specific process that is not yet understood (e.g. Ozima *et al.*, 2007). These proposals are based primarily on mass balance rather than on a consideration of the fine structure of oxygen-isotope signals and possible processes.

10.6 CAI formation: concluding remarks

Before attempting to answer the three crucial questions of when, where and how the calcium–aluminium-rich inclusions (CAIs) were formed, it is worth summarizing their most important properties, which should be considered by any formation model.

These inclusions represent the most high-temperature material in the solar nebula. Petrological, chemical and isotopic signatures suggest that vaporization and recondensation (at up to 2000 K) and crystallization differentiation from specific

melts (which could itself originate from condensation in a gas or vapour atmosphere) are both important processes.

The highly conspicuous and heterogeneous isotopic fingerprints of presolar grains (Figs. 3.2–3.4), which are the starting solid-phase material of the Sun and solar nebula, are not observed in CAIs. This holds even for ~ 10 μm CAI minerals, which exceed the typical size of presolar grains only by a factor ~ 10 (e.g. Young and Russell, 1998; Fagan *et al.*, 2001).

The mechanism of CAI formation must allow for several consecutive events to occur since later, lower-temperature, minerals (mantles) often show ^{16}O-poorer compositions than the high-temperature cores.

The CAI-forming process appears to have been short, < 0.5 Myr, but CAIs must have resided somewhere in the nebula for ~ 1–2 Myr until the time when they were incorporated in meteorite parent bodies.

Thanks to the high-precision U–Pb and short-life chronometers, in particular ^{26}Al–^{26}Mg, the answer to the first question appears to be the most straightforward: CAIs are the first objects that originated in the solar nebula and were formed at least 4569 Myr ago within a short time interval of ~ 0.3 Myr (Young *et al.*, 2005). Because of the clear record of high-temperature processing, CAI formation could have been related to the maximum energy dissipating from the accreting Sun, which was mostly transferred into heat. According to the models, this energy peaked sharply at ~ 0.5 Myr after infall started (Wood, 2000). According to the available data, other high-temperature materials, first of all Al-rich chondrules, were formed ~ 1–3 Myr later (Fig. 11.7), and the Pb/Pb systematics in high-μ minerals of chondritic meteorites were closed ~ 3 Myr after CAI formation (Figs. 11.6, 13.1).

To answer the second question, where were the CAIs formed, it should be recalled that they have passed through more furious events than other objects of the solar nebula. For example, some hibonite grains record temperatures as high as ~ 1800 K (MacPherson *et al.*, 1983; Hinton *et al.*, 1988; Simon *et al.*, 1997). In fact, peak temperatures above 2000 K were almost certainly reached (Hsu *et al.*, 2000). No presolar grains, not even diamonds, survived these events. The Sun-facing edge of the early nebula disk appears to be the most plausible environment (Section 10.1, Fig. 9.1).

Regarding the third question, in this environment the total evaporation of the dust moving towards the Sun is postulated, with two consequences: (1) a well-mixed Si-rich gas with Si/H ratios in the nebular midplane region ~ 100 to 1000 times the solar value (Wood, 1981); (2) a ^{16}O-rich O-isotope composition. Powerful X-winds could have transported this Si- and ^{16}O-rich gas (or possibly plasma) back into less heated and less ^{16}O-enriched regions of the planetary nebula (Shu *et al.*, 2001; Shang *et al.*, 2000). In the course of cooling, CAIs were formed by condensation (mainly

to a melt phase), revaporization, recondensation and crystallization-differentiation processes. These are recorded by the high abundance of high-temperature mineral phases, by anomalies in the REE abundance patterns and by mass-dependent Si-isotope fractionation (Grossman *et al.*, 2000, 2002; Alexander, 2004). Such CAI formation processes would have operated ~ 0.3 Myr during the late FU Orion stage and ceased along with the anomalous activity of the early Sun.

As follows from models of a weakly turbulent nebula (Cuzzi *et al.*, 2003), some CAIs could have travelled inside the nebula, against the gas-drag-induced drift towards the Sun. Some could have made another loop and acquired specific later-formed mantle(s), as shown in Fig. 10.6. Others could have been trapped by growing agglomerates of chondritic material. This scenario also explains the overall independence of the O-isotope compositions of CAI from the host meteorite class (Huss *et al.*, 2001).

Chondritic material was accreted ~ 1 to 3 Myr after the CAIs were formed, when icy bodies (enriched in ^{17}O and ^{18}O, Section 10.5) drifted from outside the snow line toward the Sun, evaporated after crossing this line and generated an atmosphere depleted in ^{16}O near the nebula midplane. Depending on the *PT-t* conditions, some minerals with CAIs could have acquired this heavy oxygen, and some new CAI-minerals could have been formed in equilibrium with this gas phase, thus providing CAI shift along the line of slope 1 on the O-isotope plot (Fig. 10.8(a)).

11

Chondritic meteorites

11.1 Introduction to chondritic meteorites: compositions and taxonomy

The most primitive meteorites are aggregates consisting of a fine-grained heterogeneous matrix, in which are embedded small (generally from 0.2 to 1.0 mm) droplet-like silicate particles termed chondrules, which have given the name to this meteorite class, chondrites. The chondrules and the matrix comprise distinct and different assemblies of chemical elements, e.g. volatile-depleted chondrules coexist with a volatile-enriched matrix. Some chondrites also contain metal grains. The third component of chondrites, Ca–Al-rich inclusions, was discussed in Chapter 10.

Chondrites preserve a unique record of processes and conditions in the early nebula. Although never molten after their agglomeration, chondrites have variably undergone metamorphism that has in some cases altered their mineralogy and composition. The relative abundances of involatile major and trace elements in bulk chondrites are generally similar to the solar abundances (see Section 3.4). However, in sharp contrast with the solar composition, only four elements, oxygen, silicon, magnesium and iron, are the major chondritic components, contributing almost 90% by mass, and these same four are also the major constituents of the terrestrial planets (Tables 11.1 and 17.1). There are clear reasons for the high contributions of these elements to the meteoritic and planetary compositions. First of all, the most abundant isotopes of O, Mg and Si are the so-called α- or primary isotopes (^{16}O, ^{24}Mg and ^{28}Si), characterized by a high binding energy per nucleon (Chapter 1). Therefore these isotopes are produced preferentially to other nuclides in explosive SNe II nucleosynthesis, which is the dominant source of heavier-than-carbon elements in the Galaxy (Chapter 8). Iron-peak elements having the highest binding energy per nucleon are the final products of nuclear fusion and are abundant in both SNe II and SNe I ejecta (Table 8.1). Another important reason for the exceptionally high abundances of these four elements is that the oxides of these

Table 11.1 *Abundances of major elements in chondrite groups (the abundance ratios are in atomic %, excepting the last column, which is in mol %)*[a]

Clan	Group	Si, wt %	Al/Si	Ca/Si	Mg/Si	Fe/Si	Fe(met)/Si	FeO/(FeO+MgO)
refractory-rich	CV[b]	15.6	11.6	8.4	108	76	0.6–19	35
mini-chondrule	CO[c]	15.9	9.3	6.9	91	78	2.3–15	35
	CM[d]	12.9	9.7	6.8	91	80	0.1–0.5	43
volatile-rich	C1[e]	10.6	8.6	6.2	92	86	< 0.1	45
ordinary	LL[f]	18.9	6.5	4.7	81	53	2.7–22	27
	L[g]	18.5	6.6	4.7	80	57	17–22	22
	H[h]	16.9	6.8	4.9	83	80	46–52	17
enstatite	EL[i]	18.6	5.4	3.6	76	65	47–57	0.05
	EH[j]	16.7	5.1	3.6	63	97	68–72	0.05

[a] After Kallemeyn and Wasson (1981), Wasson (1985), Wasson and Kallemeyn (1988), Rubin (1997).
[b] CV, large-chondrule-bearing, abundant CAIs, volatile-poor (relative to other groups), partially aqueously altered.
[c] CO, mini-chondrule-bearing, metal-bearing.
[d] CM, mini-chondrule-bearing, aqueously altered.
[e] C1, chondrule-free, volatile-rich, aqueously altered.
[f] LL, low total iron, low metallic iron.
[g] L, low total iron.
[h] H, high total iron.
[i] EL, low total iron, highly reduced, moderately sized chondrules.
[j] EH, high total iron, highly reduced, mini-chondrule-bearing.

metals as well as of metallic iron are involatile and condense at high temperatures between 1300 and 1600 K, thus forming solid grains.

On the basis of textural, chemical and mineralogical criteria, three major classes of chondritic meteorites are distinguished: carbonaceous (CC), enstatite (EC) and ordinary (OC) chondrites, which are in turn subdivided into subgroups (Table 11.1). Carbonaceous chondrites are so named because they contain organic matter; these meteorites constitute the least metamorphosed group even though most underwent hydrous alteration (Kallemeyn and Wasson, 1981). They play a central role in understanding the early evolution of the solar system and are therefore the focus of our discussion. Ordinary chondrites are the most common "falls" and "finds". However, spectral analysis of the light reflected by objects in the asteroid belt shows that the majority of these resemble carbonaceous chondrites (Meibom and Clark, 1999).

Abundances of the major elements vary slightly from one group of chondrite meteorites to another and also within a group, giving rise to a more detailed classification. Thus, the total Fe/Si ratio is highest in carbonaceous C1 chondrites,

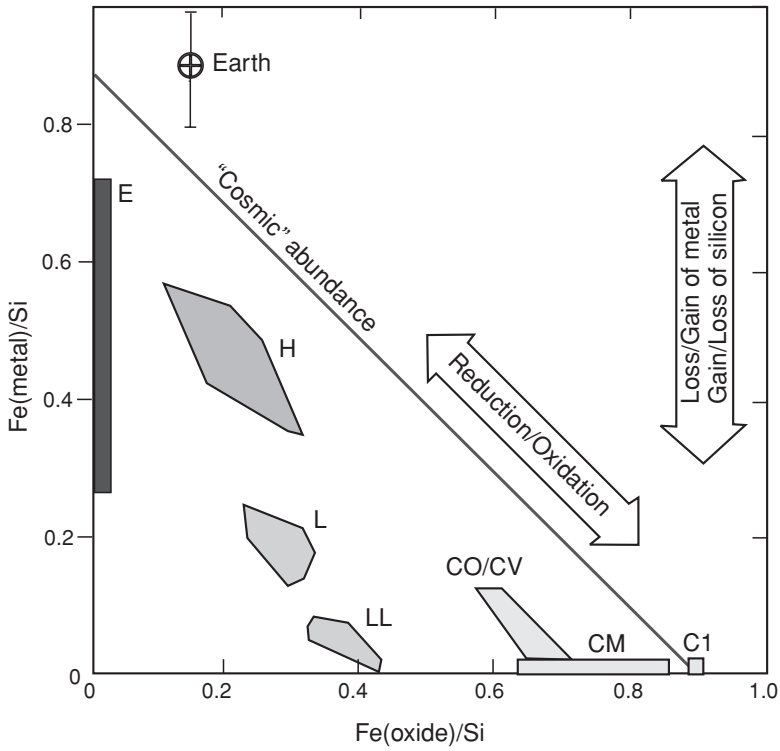

Fig. 11.1 Atomic Fe/Si ratios in meteorite classes depending on oxidized/redox states of iron. After Kerridge (1993) and McDonough and Sun (1995).

intermediate in high-metal (H) and low-metal (L) chondrites and lowest in the very-low-metal chondrites LL (Table 11.1, Fig. 11.1). The proportion of metallic to total [Fe] also varies, increasing from ~ 0 in the highly oxidized C1 (all the Fe is present as oxide or silicate minerals) to ~ 1.0 in the highly reduced EH (almost all the Fe is present as metal).

Refractory lithophile-element abundances in chondrites clearly show flat patterns when normalized to C1, exceeding the C1 abundances by $\sim 15\%$ for the CM and CO groups and by as much as $\sim 30\%$ for the CV groups. These differences are for the most part due to a variable depletion in the volatile elements and the proportion of major refractory compounds.

Even though carbonaceous chondrites are considered the most primitive group, there are substantial differences between them, related to formation processes, aqueous alteration and the extent of parent body metamorphism. Compared with C1, moderately volatile elements are depleted in other CC groups in order of decreasing condensation temperature (Fig. 11.2, Table 11.2). This pattern is even more pronounced for ordinary chondrites, so that OC/C1 abundance ratios are below

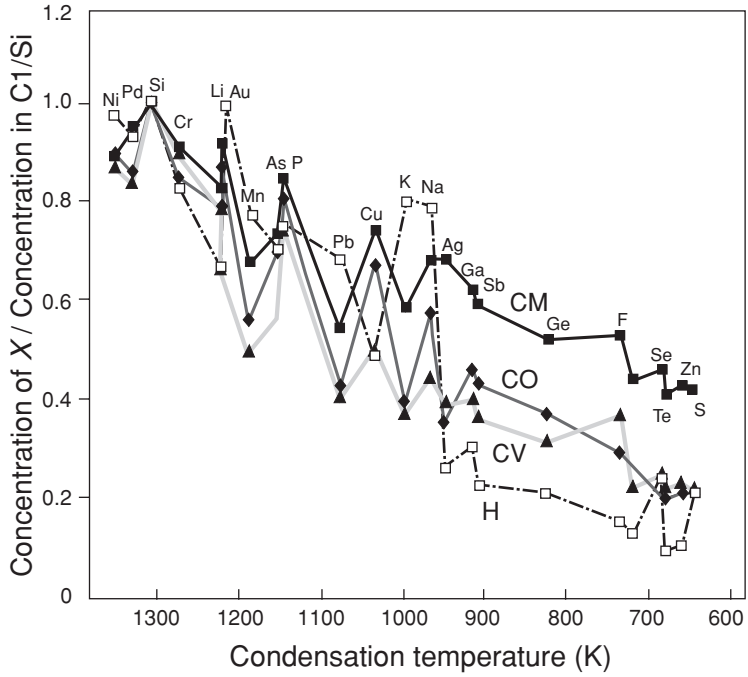

Fig. 11.2 Abundances of major and trace elements in chondrite meteorites. Plotted is the ratio for a given class of meteorite of the average concentration of element X and the average concentration of Si, divided by the same ratio for C1 meteorites, as a function of condensation temperature. From Cassen (1996), © Meteoritical Society 1996, reproduced by permission.

~ 0.1 for Tl, Bi, Pb and several other highly volatile elements (Wasson and Kallemeyn, 1988). The abundance patterns seen in Fig. 11.2 emphasize specific features of the loss process and the environment in which it occurred, e.g. enhanced abundances of K and Na in H-chondrites most probably reflect highly reduced conditions, at which alkali metals are less volatile.

The matrix and chondrules of meteorites record nebula conditions and their interrelationships are of prime importance for understanding nebula processes.

11.2 Chondrules and matrix

Chondrules and matrix: phenomenology

Depending on the conditions governing the formation of a meteorite, the matrix-to-chondrule mass ratios vary from ~ 0.8 to ~ 0.2, and the C1 group contain almost no chondrules. The matrix of chondritic meteorites consists in most cases of three major components: broken chondrules, relatively coarse-grained high-temperature material and fine-grained material, including carbonaceous organic matter.

Table 11.2 *Average trace-element abundances in chondritic meteorite groups. From Wasson and Kallemeyn, (1988), © The Royal Society 1988, reproduced by permission.*

Element		C1	CM	CO	CV	H	L	LL	EH	EL
Li	ppm	1.5	1.36	1.2	1.24	1.7	1.8	2.1	2.1	0.58
C	%	3.2	2.2	0.45	0.56	0.11	0.09	0.12	0.4	0.36
N	ppm	1500	1520	90	80	48	43	70	n.d.[a]	n.d.
Na		5000	4100	4100	3300	6400	7000	7000	6800	5800
K		558	400	345	310	780	825	790	800	735
Ca		9280	12 700	15 800	19 000	12 500	13 100	13 000	8500	10 100
Ti		436	580	780	980	600	630	620	450	580
V		56.5	75	92	96	74	77	75	54	60
Cr		2660	3050	3550	3600	3660	3880	3740	3150	3050
Mn		1990	1700	1650	1450	2320	2570	2620	2200	1630
Co		502	575	688	655	810	590	490	840	670
Ni	%	1.1	1.2	1.4	1.34	1.6	1.2	1.02	1.75	1.3
Rb	ppm	2.3	1.7	1.45	1.25	2.9	3.1	3.1	2.6	2.5
Sr		7.8	10.1	12.7	15.3	10	11.1	11.1	7.2	8.2
Y		1.56	2	2.4	2.4	2.2	2.1	2	1.3	n.d.
Zr		3.94	8	7.8	8.3	6.3	5.9	5.9	4.9	5.2
Nb	ppb	246	370	450	540	360	390	370	250	n.d.
Mo		928	1500	1900	2100	1700	1300	1100	n.d.	n.d.
Pd		560	640	703	705	870	560	530	885	690
Ag		199	157	97	107	45	65	72	236	23
I		433	425	200	188	68	53	n.d.	150	53
Ba		2340	3300	4290	4900	4200	3700	4800	2600	n.d.
La		234.7	317	387	486	295	310	315	235	190
Ce		603	838	1200	1290	830	900	907	660	300
Pr		89	129	157	200	123	132	122	94	n.d.
Nd		452	631	772	990	628	682	659	460	233
Sm		147	200	240	295	185	195	200	140	135
Eu		56	76	94	113	73	78	76	54	54
Gd		197	276	337	415	299	310	303	214	107
Tb		36	47	57	65	53	57	48	35	n.d.
Dy		243	330	404	475	343	366	351	240	139
Ho		56	77	94	110	73	81	77	50	n.d.
Er		160	218	266	315	226	248	234	166	97
Tu		24	33	40	45	39	39	34	25	n.d.
Yb		163	222	270	322	205	220	220	160	165
Lu		24	33	40	48	31	33	33	24	24
Hf		104	186	178	194	180	170	150	140	150
W		93	140	160	190	160	110	n.d.	n.d.	n.d.
Re		36.5	46	55	65	70	40	33	52	47
Os		486	640	790	825	820	515	400	654	589
Ir		481	595	735	760	760	490	360	565	525
Pt		990	1100	1200	1250	1400	1050	850	1200	n.d.
Au		140	165	184	144	215	162	140	330	225
Pb		2470	1700	2200	1400	240	370	n.d.	1100	n.d.
Th		29.4	40	45	60	42	43	43	30	35
U		8.1	11	13	17	12	13	13	9	10

[a] Not determined.

Even though C1 chondrites show a uniform bulk composition, their matrix is quite heterogeneous on a small scale, down to ~ 100 μm and even less: the FeO and SiO_2 concentrations vary from 10 to 40 wt %, and the REE concentrations in some grains approach ~ 150 times the bulk C1 value, much exceeding the variations in the bulk concentrations (Tables 11.1 and 11.2). This heterogeneity results from variable amounts of different minerals, most of which indicate aqueous alteration: phyllosilicates, iron-bearing phases such as magnetite and ferrihydrite, sulphates, phosphates and others (Brearley, 2003; Morlok *et al.*, 2006). The least altered crystalline grains (found in a few meteorites) are those of forsterite and enstatite. The compositional and structural features of these minerals suggest that they formed as condensates that cooled below 1300 K at a rate ~ 1000 K hr^{-1}. From these observations it appears that precursor grains, formed and modified at high temperatures, are part of the matrix of chondritic meteorites. The latter should then be considered as a complicated mixture of diverse high-, intermediate- and low-temperature components and products of their interactions (Scott and Krott, 2005).

Chondrules also show a great variety of structures, textures and compositions. Some chondrules include xenoliths of precursor rocks or metal cores; some are covered by rims of microchondrules or more volatile-rich minerals or thin dust layers; some present examples of the "frozen" collisions of two or more droplets. Porphyritic textures are common, suggesting the presence of mineral dust in the chondrule-forming environment, which might have collided with molten droplets (Grossman *et al.*, 1988; Connolly and Hewins, 1995). In some cases the dusty rims include presolar grains.

The principal minerals in chondrules are olivine and orthopyroxene, which occur in a glassy-to-microcrystalline groundmass or mesostasis with variable minor amounts of Ca-rich pyroxene, Fe-rich metal, FeS and spinel (Grossman, 1988; Hewins *et al.*, 1996). Variable Fe/Mg ratios point to different redox conditions during the formation of these minerals. Indeed, in a compositional classification two major groups of chondrules (and about eight subgroups) are distinguished: chondrules belonging to group A are more reduced and have a higher abundance of refractory lithophile elements than those of group B. For both groups, oxidized chondrules are generally larger than reduced ones (Sears *et al.*, 1992; Kerridge, 1993; Sears *et al.*, 1996).

From the general petrography and modelling it can be concluded that chondrules experienced flash-heating events up to ~ 2000 K for a duration ranging from tens of seconds to several minutes. These flash events were followed by cooling at a rate between 400 and 2000 K hr^{-1} down to a near-solidus temperature ~ 1500 K (Hewins, 1988; Connolly and Love, 1998). Often two or more flash events are recorded by one chondrule (Wasson, 1996; Rubin and Krot, 1996; Rubin, 2000).

Small unmelted grains and grain aggregates coexisted with molten chondrules; the temperature differences between coexisting μm-size grains and mm-size chondrules may have exceeded several hundred K. Further, even though chondrules were formed in a high-temperature event (or events) capable of vaporizing refractory minerals, they are not severely depleted in moderately volatile elements. This implies that their precursor was volatile-rich (Kong and Palme, 1999) or that they could have acquired volatile elements from a gas phase (Bridges *et al.*, 1998).

Chondrules and matrix: products from the same nebula region

Generally there are relationships between the compositions of meteoritic chondrules and the whole rock, or matrix. Thus, in the O-isotope plot the field of chondrules from ordinary chondrites broadly overlaps with that for ordinary chondrite whole-rock compositions, although there is no precise correspondence between a given class of ordinary chondrites and the O-isotope signature of chondrules (Fig. 10.8(b)). Similar O-isotope compositions were measured on bulk unequilibrated ordinary chondrites and their chondrules (Bridges *et al.*, 1999). This means that, within a given meteorite class, chondrules and matrix were formed at the same time and broadly within the same region. However, the three main classes, ordinary chondrites, enstatite chondrites and carbonaceous chondrites, occupy distinct fields, indicating that each assemblage of chondrites + chondrules was formed in a different environment.

Besides O-isotope compositions, the chemical compositions of chondrules, metal and matrix also indicate a genetic association of these constituents, at least for some chondrite groups (Wood, 1988; Bridges *et al.*, 1998, 1999; Kong and Palme, 1999; Kong *et al.*, 1999). Regarding the major elements, Murchison (C2) presents a good example. The Fe/Si (atomic) ratio in its matrix is 1.23 and that in its chondrules is ~ 0.2. The observed chondrules/matrix mass ratio is 0.4, which gives a calculated bulk Fe/Si value ~ 0.8 (close to C1). This ratio has actually been found for bulk Murchison samples. Further, in CR carbonaceous chondrites the moderately volatile lithophile elements (e.g. K and Na), which are depleted in the chondrules, are enriched in the matrix, the K/Mg and Na/Mg ratios exceeding the solar values (Kong and Palme, 1999).

Generally chondrules are somewhat depleted in metal and the missing metal and sulphide is present in the matrix, mainly as small grains. The complementary pattern is readily seen in the distribution of moderately volatile siderophile trace elements. This is illustrated by the siderophile-element abundances in the metal fraction and in the matrix of the CR chondrites (Fig. 11.3). It is important that the volatility of these elements, but not their siderophile nature, controls the abundance pattern seen in Fig. 11.3: the depletion of moderately volatile siderophile elements in the

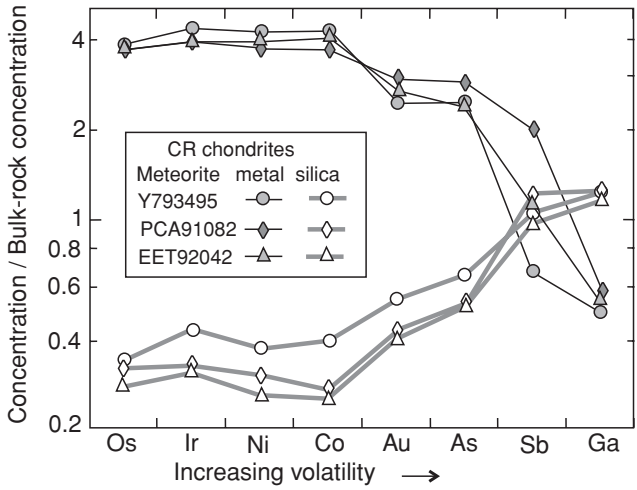

Fig. 11.3 Distribution of siderophile elements between the metallic and non-metallic fractions of CR chondrites. The normalized abundances of the siderophile elements show complementary patterns controlled by the volatility of the elements but not by their siderophile behaviour. From Kong *et al.* (1999), © Elsevier Science 1999, reproduced by permission.

metal fraction is compensated by the appreciable enrichment of these elements in the silicate fraction of the meteorites.

The third actor: precursor material

The complementary patterns not only reveal genetic relationships between chondrules and matrix but also indicate the presence of a third actor, the progenitor material, which appears to be similar to C1 in composition. The flat C1-normalized abundance patterns of the involatile siderophile elements Os, Ir, Ni, Co are seen both in the metal and the matrix and are independent of the metal–silicate partition coefficients (Fig. 11.3). This pattern could be readily established within the framework of the following scenario (Kong *et al.*, 1999). (1) A precursor material is characterized by uniform C1-like concentrations of the siderophile elements. To avoid the partitioning of these highly siderophile elements in the metal phase of the material (after which they could hardly be extracted), the precursor material needs to contain little metallic iron. Therefore the Fe should be mainly oxidized, thus pointing to a C1-like major-element composition (see Fig. 11.1). (2) Some portion of this material was melted, forming chondrules under highly reducing conditions. Thereby the volatile elements, including volatile siderophiles, partly evaporated. (3) Melting caused segregation, and involatile siderophiles were quantitatively partitioned into the metal phase, leaving behind the siderophile-element-free silicate portion

of chondrules. (4) The volatile siderophiles recondensed and were incorporated in the non-melted silicate matter (the matrix).

An oxidized fine-grained precursor must be invoked to ensure near-solar abundances of the major elements forming different minerals (Alexander, 1994). Otherwise such ratios as Ca/Al or Ti/Al, which vary in major mineral phases, e.g. pyroxene and plagioclase, could not have had the consistently near-solar values observed in chondrules. From investigations of agglomeratic chondrules, a grain size $\sim$1–5 μm has been derived for the precursor (Weisberg and Prinz, 1996).

A wide range of Fe/Mg ratios is observed among chondrules in a given chondrite, and this can be ascribed to variable partial equilibration with the gas phase during one or more heating events (Wood, 1985). In a gas of solar composition with reducing hydrogen as its major constituent (see Table 3.2), olivine would contain only $\sim$0.001 mol % of Fe_2SiO_4 and Fe would almost exclusively appear as a metallic alloy; this has never been observed. A much higher contribution of Fe_2SiO_4 (from 0.05 to 50 mol %) typical of chondrule olivine (of any chondrite class) could have originated during chondrule formation by the melting of a highly oxidized precursor material (which would have had Fe-rich olivine) in a reducing environment. The melted droplets would have cooled and solidified before they had time to equilibrate fully with this environment, giving rise to the observed heterogeneity in the Fe/Mg ratios. A clear indication of exchange between chondrule melts and the ambient gas, corroborating the evidence from the volatile siderophile elements, comes from Si-isotope data. Figure 10.2 illustrates mass-dependent Si fractionation in chondrules, presumably due to partial evaporative loss and recondensation of silicate matter in the course of chondrule-forming events.

11.3 Metamorphism and equilibration in chondrites

Evidence of variable heating in chondrites after their agglomeration is found from mineral reactions and recrystallization and from O-isotope thermometry (Sections 10.2 and 25.4). At high temperatures, hydrous clay minerals and organic matter become unstable and react to other minerals, whereby volatiles are released. The original chaotic matrix texture and even chondrule boundaries are obliterated as progressively more coarse-grained aggregates are formed. Temperatures obtained from oxygen isotopes approach $\sim$1000 °C for highly recrystallized meteorites (Clayton, 1993; Clayton and Mayeda, 1999; Choi *et al.*, 2000). Mineral chemistry, applied to recrystallized chondrites, defines a range from $\sim$350 °C to $\sim$1000 °C (Olsen and Bunch, 1984; Zhang *et al.*, 1996). Shock metamorphism, which causes localised melting and structural changes in minerals, is also very commonly seen in chondrites.

With the exception of shock metamorphism, in many cases it is not clear which process caused the high temperatures, the formation itself or later heating, e.g. by the decay of radioactive isotopes or by collisions. Therefore the more neutral term "equilibration" is used, referring to the type of texture and to the mineral and oxygen-isotope equilibria alike. Greater equilibration corresponds to petrographic types ranging from 1 to 6 in order of increasing apparent temperature.

For equilibrated ordinary chondrites some problems arise if metamorphism is seen as resulting from reheating within the parent body after its formation. First, when compared with terrestrial rocks that have undergone metamorphism at similar temperatures, the textures are still remarkably pristine. For instance, in high-grade ("granulite") metamorphism on Earth, complete recrystallization occurs at a temperature $\sim 850\ ^{\circ}C$, leading to a coarse-grained texture even in the absence of aqueous fluid. In contrast the chondrite Allegan, for which O-isotope temperatures $\sim 1000\ ^{\circ}C$ have been measured, has clearly defined chondrules and a fine-grained matrix, with no evidence of reactions between chondrules and matrix as would have been expected in a high-grade metamorphic rock. Second, even in a chondrite that has been heated to a high temperature, the observed O-isotope equilibration is spatially limited to a path length of a few millimetres (Olsen *et al.*, 1981). This implies an exchange process of short duration, which is difficult to envisage for metamorphism within a proto-planetary body. Third, strongly and moderately volatile elements are generally more depleted in equilibrated than in unequilibrated types of chondrites. Fourth, the relatively short time span recorded by the I–Xe ages of chondritic meteorites of various classes argues against a long-lasting heating (see Fig. 11.9).

Observations on the metal fraction of chondrites show that high-temperature equilibration did not occur within the meteorite parent body but happened prior to or during its accretion, the exchange and equilibration being mediated by a vapour phase (Kong and Ebihara, 1997). This notion is attractive as it would allow one to explain all the above points. The observed O-isotope and petrographic temperatures would in this case be the temperatures of accretion upon the parent body, the relatively rapid cooling preventing O-isotope exchange over long path lengths and coarse-grained recrystallization. This concept requires a vapour phase to be present during chondrite agglomeration.

However, some reactions clearly occurred in the matrix after chondrite formation; Hanowski and Brearley (2000) described mm-scale Fe-enriched haloes, formed as outward-moving reaction fronts, around altered metal grains in the matrix of CM chondrites. Further, many carbonaceous chondrites have veins with minerals (e.g. calcite) that apparently crystallized from aqueous fluids, demonstrating hydrothermal activity. Water was probably incorporated in the parent body as it accreted, and hydration reactions and hydrothermal processes, even if secondary, may have

occurred as part of the consolidation process after agglomeration. Some carbonaceous chondrites show true thermal metamorphism superimposed on their low-temperature hydrous mineralogy. For instance, metamorphic dehydration reactions are seen in several C1 meteorites (Hiroi *et al.*, 1993).

In summary, the somewhat loose concept of "chondrite metamorphism" embraces many different processes, of which some (e.g. the equilibration of ordinary chondrites) are probably related to the accretion of the parent body itself, leaving only a few processes (shock metamorphism and the dehydration of some carbonaceous chondrites) as "true" metamorphic processes in the sense that they evidently post-date the formation of the parent body.

11.4 Highly volatile elements: hydrogen, carbon and nitrogen

The three major highly volatile elements reside in different phases in chondrites. Hydrogen is hosted primarily in hydrous silicate minerals, and to some extent in organic matter. Carbon is situated in organic matter, graphite and carbonate and nitrogen in organic matter. Presolar grains also contribute small variable amounts of C and N (Fig. 3.3). Among carbonaceous chondrites C1 have the highest content of these elements, and CV and CO the lowest.

Ordinary chondrites have a highly variable D/H ratio, from $\sim 1 \times 10^{-4}$, typical of chondrules, up to $\sim 7 \times 10^{-4}$ in phyllosilicates (Fig. 11.4); this may result from equilibrium fractionation, with an additional kinetic effect during water loss in dehydration reactions (see Section 11.3). In all chondrite types, however, the D/H ratio is significantly (by a factor > 6) above the probable initial bulk value of the solar system: the D/H ratio in interstellar hydrogen is $\sim 2.6 \times 10^{-5}$ (Section 3.1), and data on the Jupiter atmosphere show that this probably corresponds to the solar neighbourhood hydrogen 4.5 Gyr ago (Mahaffy *et al.*, 1998).

Variations in δ^{13}C values among the groups are small compared with the D/H variations, but nevertheless significant. For carbon, this cannot be readily explained by processing within the solar nebula and therefore probably reflects a primary heterogeneity. The solar value (confirmed by measurements on Jupiter, Owen and Encrenaz, 2003) is within the range defined by the chondrites (Fig. 11.4).

The δ^{15}N values are much more variable among the meteoritic classes, deviating by up to $\pm 40‰$ from the terrestrial standard (i.e. atmospheric nitrogen, $\delta^{15}N_{ATM} \equiv 0.0‰$) and do not correlate with C-isotope compositions. Carbonaceous chondrites contain both heavy (C1, C2) and light (C3) nitrogen. Moreover, as in the case of the D/H ratio, there is a large difference from the solar-neighbourhood value, assumed to be equal to that of Jupiter's atmosphere ($\delta^{15}N \approx -400‰$).

For the D/H ratios and δ^{15}N values, the striking differences between the chondritic and solar-neighbourhood values can be explained if it is assumed that the

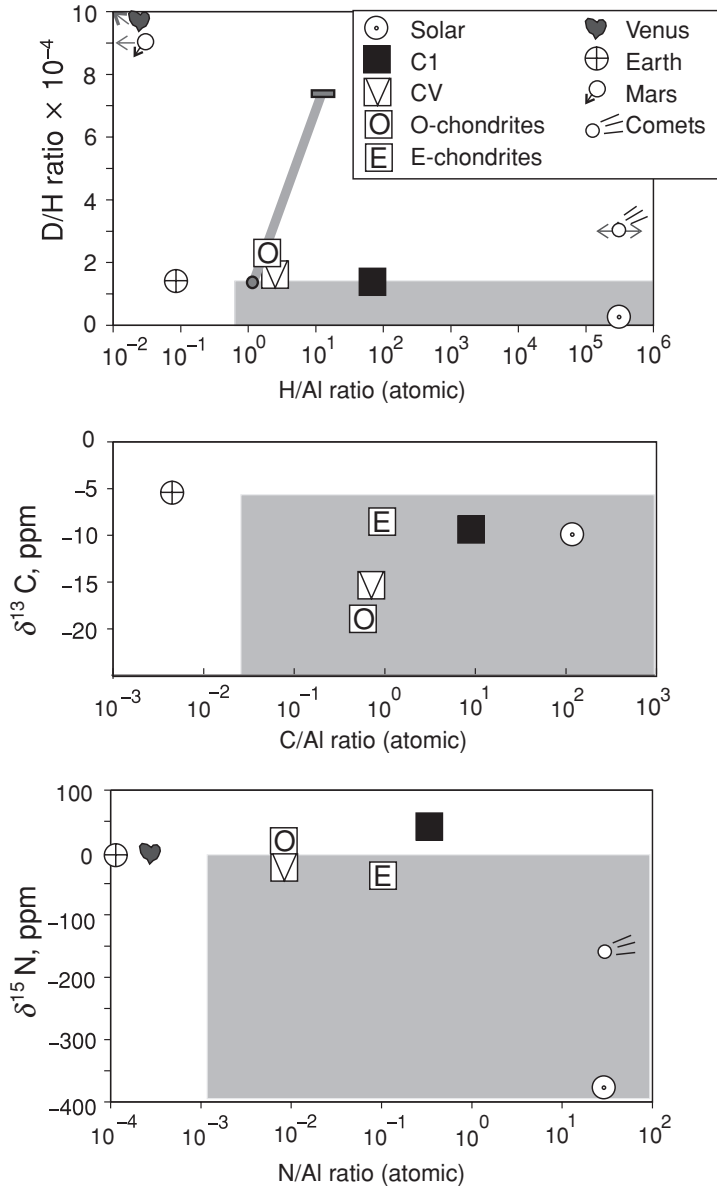

Fig. 11.4 Elemental and isotopic abundances of major atmophile species in meteorites, comets and planets. Abundances are normalized to the highly refractory lithophile Al. Planetary inventories are presented for comparison. Possible sources of terrestrial atmophile elements are expected to lie within the shaded areas (Section 20.4; note that, in the case of delivery of most of the atmophile elements after the giant impact, the source-isotope compositions should more closely match the terrestrial values). Top: hydrogen. The D/H ratio in C1 is not homogeneous: the H related to organic molecules is heavy, whereas the H in clay minerals is light and similar to terrestrial hydrogen. This is also valid for ordinary chondrites: water in

H and N incorporated in chondrite parent bodies were derived from solid presolar grains, while the solar value represents the (dominant) gas in the solar neighbourhood. For example, in a presolar molecular cloud the H-isotope fractionation between gaseous, liquid and solid phases via the exchange of neutral species and ion–molecule reactions under low-*PT* conditions would result in a D enrichment in grains, i.e. ices, clay minerals and organic molecules (Millar *et al.*, 1989; Drouart *et al.*, 1999; Robert *et al.*, 2000; Robert, 2001). The D/H ratio in water vapour in a "hot" nebula during chondrite agglomeration is therefore expected to be $\sim 1 \times 10^{-4}$, which is a factor ~ 3 to 4 above the solar-neighbourhood composition. Nebular cooling and ice formation would have caused further D enrichment in ices, D/H $\sim$ (1.3–1.8) $\times 10^{-4}$, if the equilibrium temperature had been ~ 160 K. The predicted D/H ratios in these ices are thus indistinguishable from those observed in C1 chondrites (Lecluse and Robert, 1994).

Apart from shedding light on the mode of delivery of the volatile elements to chondrite parent bodies, these isotope data are also highly valuable in assessing possible sources of matter for terrestrial accretion, as discussed in Section 20.4.

11.5 Highly volatile elements: noble gases

Introduction to the noble-gas family

The noble gases present a unique isotopic family for several reasons. After nucleosynthesis and ejection in an interstellar medium, the primordial noble gases mainly reside in the gas phase and thus are always greatly underabundant in the complementary solids including meteoritic materials. Against the generally low background of trapped components, the products of radioactive decay and nuclear reactions, even in cases of exceedingly low yield, are therefore readily observable. Further, complicated chemical processes in extraterrestrial and planetary reservoirs affect

←

Fig. 11.4 (*cont.*) chondrules and in metal- and C-rich parts of the matrix ($\sim 1 \times 10^{-4}$, solid circle) is light, whereas phyllosilicates show a high abundance of D-rich water (solid rectangle); the thick line shows the mixing trend of these end-member compositions. The martian atmosphere has D/H $= 8.1 \times 10^{-4}$ and the value for the martian mantle is 3×10^{-4}, both well above the Earth's ratio. The comet values are from Oort cloud comets (see Fig. 14.1); the Al/H ratio in comets is not well constrained.
Middle: chondrite-like material could be a plausible source of terrestrial carbon.
Bottom: N-isotope compositions in meteorites vary in a wider range compared with carbon. The CV carbonaceous chondrite, E-chondrite and comet-type material could have supplied both Earth and Venus with nitrogen. After Deloule and Robert (1995), Deloule *et al.* (1998), Robert (2001, 2003), Owen and Bar-Nun (2001) and Grady and Wright (2003).

these records much less than those for chemically active systematics; therefore more straightforward and simple interpretations are possible.

A simplified classification of extraterrestrial noble-gas components, established on the basis of their elemental and isotopic patterns, includes solar, nuclear (spallogenic, radiogenic), meteoritic or Q, subsolar and "exotic" components (Ozima *et al.*, 1998).

Solar noble gases and their occurrence in meteorites

Solar gases, first discovered in the non-chondritic meteorite Pesyanoe by Gerling and Levsky (1956), are generally used as a reference composition even though a truly representative sample of them has not yet been found. The elemental and isotopic patterns of solar corpuscular emissions, i.e. solar-wind emissions (SW, Table 11.3) can deviate from the true present-day solar ratio as a result of chemical (ionization-potential) and mass-dependent effects.

Among solar noble gases ^{4}He is mainly of primordial origin. According to the standard model of the Sun, H-only burning affects the He abundances within the Sun's core, which does not yet exchange matter with the outer convecting zone. Also, the solar initial (mass) ratio of He/H = 0.275 (Grevesse and Sauval, 1998) is close to the BBN production ratio (Fig. 4.3). Helium-3 in solar emissions is a mixture of primordial ^{3}He and (mainly) that yielded by D burning in the young Sun during its pre-main-sequence stage (Sections 3.1 and 5.3); other noble gases are the products of presolar stellar nucleosynthesis and galactic evolution.

Solar-type noble gases have been detected in carbonaceous and ordinary chondrites, mainly in brecciated samples. The relation between the trapped-solar-wind content and the degree of brecciation suggests that the solar noble gases were implanted in the clastic matrix, which had been exposed on the surface of the asteroid (Metzler *et al.*, 1992). In some meteorites (e.g. CM chondrites, Nakamura *et al.*, 1999a, b), initially implanted SW gases were then partially released and fractionated; in general, heavy isotopes were somewhat better retained in solids and this retained component is known as fractionated solar-wind (FSW) gases. This retention effect is also sometimes observed in the lunar regolith (Table 11.3).

The heavy-noble-gas-enriched meteoritic component Q

The most abundant noble-gas component observed in chondritic meteorites is known as the "planetary", "P" or "Q" component ("Q" means "quintessential",

Table 11.3 *Solar light-noble-gas abundances in solar wind (SW), fractionated solar gases (FSW; values in brackets) and in the solar system (SOS)*

Ratio	SW (FSW) Acfer[a]	SW Apollo foils[b]	SW (FSW) lunar ilmenite, young[c]	SW (FSW) lunar ilmenite, old[d]	SOS[e]
$^4He/^3He$	2310 ± 90 (4420 ± 150)	2350 ± 120	2190 ± 40 (4610 ± 100)	2230 ± 80 (4200 ± 400)	6020
$^4He/^{20}Ne$	612 ± 10*	550 ± 50	—	—	850
$^{20}Ne/^{22}Ne$	—	13.3 ± 0.3	13.8 ± 0.1 (11.2 ± 0.2)	13.4 ± 0.1 (11.2 ± 0.2)	13.7
$^{21}Ne/^{22}Ne$	0.036	0.033 ± 0.004	0.0328 ± 0.0005	—	0.033
$^{20}Ne/^{36}Ar$	41 ± 3	48.4 ± 7	—	—	37
$^{36}Ar/^{38}Ar$	5.15 ± 0.20*	—	5.48 ± 0.05	5.42 ± 0.05	5.33

[a] Data from Acfer111 H3-6 chondrite: concentrations vary depending on grain size, $[^4He] \sim 1 \times 10^{-2}$ cm^3 STP g^{-1}; for the $^{21}Ne/^{22}Ne$ ratio the lowest value measured in metal grains is shown, with the least contribution of spallogenic ^{21}Ne; $^4He/^{20}Ne$ and $^{36}Ar/^{38}Ar$ ratios are those measured in metal grains and corrected for spallation component (Pedroni and Begemann, 1994).

[b] From the Apollo foil-collection experiments (Geiss and Reeves, 1972; Bochsler, 1987).

[c,d] Lunar ilmenite young (irradiated during last ~ 100 Myr), $[^4He] \sim 0.1$ cm^3 STP g^{-1}; lunar ilmenite old (irradiated ~ 1 Gyr ago), $[^4He] \sim 0.8$ cm^3 STP g^{-1} (Benkert *et al.*, 1993).

[e] These ratios and also $^{36}Ar/^{84}Kr = 3320$ and $^{84}Kr/^{132}Xe = 20.6$ are accepted for the solar system (Anders and Grevesse, 1989). $^4He/^3He$ ratio as measured in the Jupiter atmosphere; this value is considered as representative for the initial He-isotope composition in the solar system (Mahaffy *et al.*, 1998). Deuterium burning during pre-main-sequence evolution substantially increased this ratio in the early Sun (Section 3.1).

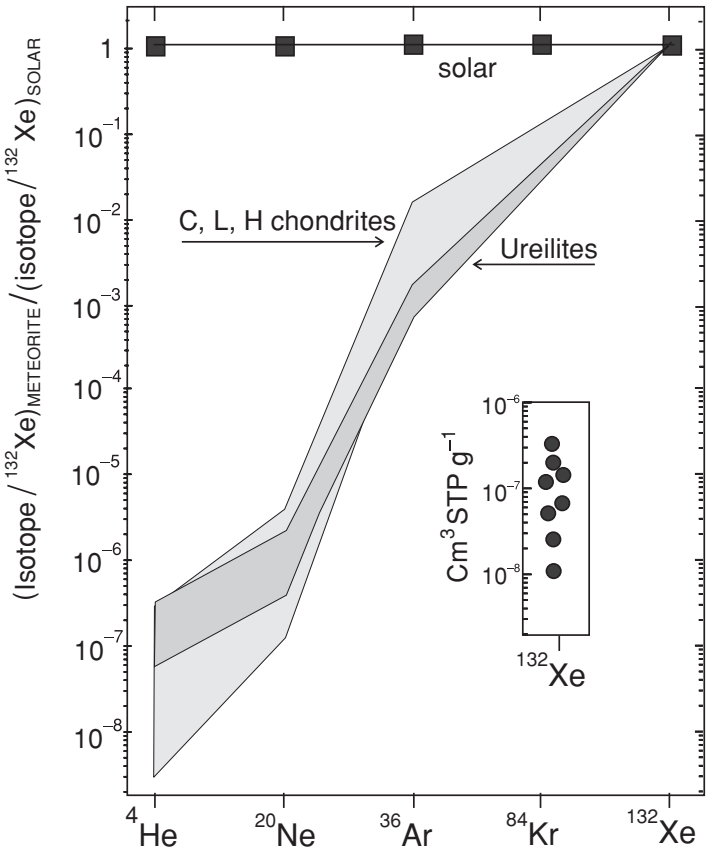

Fig. 11.5 Elemental pattern of Q noble gases relative to the solar composition. The inset shows [^{132}Xe] in HF- and HCl-resistant residues, in which the Q gas carrier is enriched relative to the bulk meteorite. The bulk [^{132}Xe] values in carbonaceous chondrites are a factor $\sim$ 100 lower than those shown in the inset; Table 28.3 presents a comparison with the model-derived Earth mantle concentration. From Busemann *et al.* (2000), © Meteoritical Society 2000, reproduced by permission.

highlighting the importance of this component, Lewis *et al.*, 1975). The Q elemental pattern is relatively well defined and is similar in different chondrite classes, the heavy gases being extremely abundant compared with the light ones (Fig. 11.5). The isotopic compositions of the heavier gases in Q are similar to the solar compositions (Table 11.4). The Ne-isotope pattern indicates some contribution of exotic neon (Ne-E), ^{22}Ne, which most probably originated from ^{22}Na decay. Regarding helium, the Q ^{4}He/^{3}He ratio, $\sim$7100 (Busemann *et al.*, 2000), is not very different from the presolar value as measured in the Jupiter atmosphere (Table 11.3).

Even though the Q gas carrier has not yet been firmly identified, there is little doubt that these gases were concentrated in a carbon-bearing phase. There are several lines of evidence supporting this. (1) The host phase of Q is soluble in

Table 11.4 *Isotopic compositions of Xe in several important reservoirs* ($100 \times {}^{i}\mathrm{Xe}/{}^{130}\mathrm{Xe}$)[a]

Reservoir	^{124}Xe	^{126}Xe	^{128}Xe	^{129}Xe	^{131}Xe	^{132}Xe	^{134}Xe	^{136}Xe
SW (Lun)[b]	2.94(7)	2.55(8)	51.0(5)	627(4)	498(2)	602(3)	221(1)	179.7(6)
SW (Pes)[b]	2.8(1)	2.59(7)	51.2(4)	634(4)	497(3)	606(4)	222(1)	179(1)
FSW[c]	—	—	46(1)	661(8)	519(9)	637(6)	241(3)	199(3)
Q-Xe[d]	2.81(2)	2.50(2)	50.7(2)	643(2)	505(1)	618(1)	233(1)	195(1)
U-Xe[e]	2.95	2.54	50.8	628.7	499.6	604.8	212.9	166.3
Mars atm.[f]	2.3(3)	2.1(3)	47.3(1.3)	1556(8)	518(3)	653(4)	258(2)	227(2)
Earth atm.[g]	2.337(7)	2.18(1)	47.15(5)	649.6(6)	521.3(6)	660.7(5)	256.3(4)	217.6(2)
Earth atm.[h]	2.337(7)	2.18(11)	47.15(5)	605(3)	518.7(7)	651.8(13)	247.0(13)	207.5(13)

[a] The values in brackets are the error limits for the last digit (95% confidence limits).
[b] SW, lunar ilmenite 71501 (Wieler and Baur, 1994) and aubrite Pesyanoe (Kim and Marti, 1992); hereafter accepted as solar system $\mathrm{Xe_{SOS}}$.
[c] FSW, lunar ilmenite 79035 (Wieler and Baur, 1994).
[d] Q-Xe after Busemann *et al.*, (2000); abundances of non-radiogenic isotopes in Q-Xe are indistinguishable from those in SW xenon. Concentrations of ^{130}Xe in lunar ilmenites (implanted SW-Xe) and in bulk carbonaceous chondrites (trapped Q-Xe) approach $\sim 5 \times 10^{-10}$ cm^3 STP g^{-1} (Wieler and Baur, 1994; Busemann *et al.*, 2000).
[e] U-Xe is a model-derived composition, which after being fractionated fits to atmospheric xenon (Pepin and Phinney, 1978); this composition has never been observed in natural materials.
[f] Martian atmosphere from Mathew *et al.* (1998) and Mathew and Marti (2002).
[g] Earth's atmosphere from Basford *et al.* (1973), $^{130}\mathrm{Xe_{ATM}} = 1.40 \times 10^{16}$ cm^3 STP.
[h] Earth's atmosphere without the radiogenic or fissiogenic component; from Pepin (1991).

oxidants, such as HNO_3, while it is resistant when non-oxidizing solvents are used (HF or HCl; Wieler *et al.*, 1991). (2) The extraction patterns for carbon and heavy primordial gases in combustion experiments are similar (Ott *et al.*, 1984). (3) The carbon-rich low-density phase of a meteorite contains more than 99% of the "Q" component (Frick and Chang, 1978; Verchovsky *et al.*, 2002). *In situ* analyses have shown that the Q component is enriched in fine-grained rims around chondrules and also in particles termed the primary accretionary rock (Nakamura *et al.*, 1999a, b). The highly unequilibrated assemblage of the rims and rim–core relationships imply the accretion of rim material, together with the C-rich carrier of Q and interstellar diamonds, to the surfaces of chondrules. The isotopic composition of helium definitely shows that the trapping mechanism operated in an environment shielded from post-D-burning solar corpuscular radiation: no traces of SW, FSW or spallogenic noble gases have been found in the Q host materials. However, the exotic component is sometimes observed together with Q.

The heavy-noble-gas-enriched component, Q: a key to the pre-nebula environment?

The specific features of Q described above imply that the heavy noble gases were adsorbed onto a C-rich carrier that could have occurred in either of two environments: a dense cold interstellar cloud, from which the Sun and the nebula were formed later, or in the solar nebula. The first environment is more likely, because homogeneous gas compositions and low temperatures are expected within the cloud. The mean mixing time in a dense molecular cloud core is ~ 1 Myr, whereas the cloud lifetime is generally ≥ 10 Myr (Elmegreen, 1985). Temperatures in the clouds are quite low, < 100 K (Section 5.2), so that the sorption should be efficient.

The following mechanism is envisaged as generating a Q-bearing phase (Huss *et al.*, 1996). In a cold presolar molecular cloud with a well-mixed noble-gas content, heavy-noble-gas atoms could be adsorbed onto the surfaces of carbon-rich grains accreting from organic molecules. The heavier the gas, the more efficient the sorption and the higher the concentration. Non-absorbable He and Ne would be trapped in the porous accreting matter in much lower abundance and without substantial fractionation between the two gases. Such a mechanism would be able to produce the uniformly fractionated heavy-noble-gas pattern and the high concentrations of heavy gases as observed in the Q carrier. The exotic component, i.e. s-process Kr and Xe and radioactive ^{22}Na (which decays to Ne-E), could be contributed from grains that had condensed in stellar ejecta. A correlation between Q-gas abundances and the contribution of presolar grains validates this mechanism further.

These indications for a presolar host of Q gases strengthen the case made in Section 11.4 for a similar presolar origin of the carriers of meteoritic H, C and N.

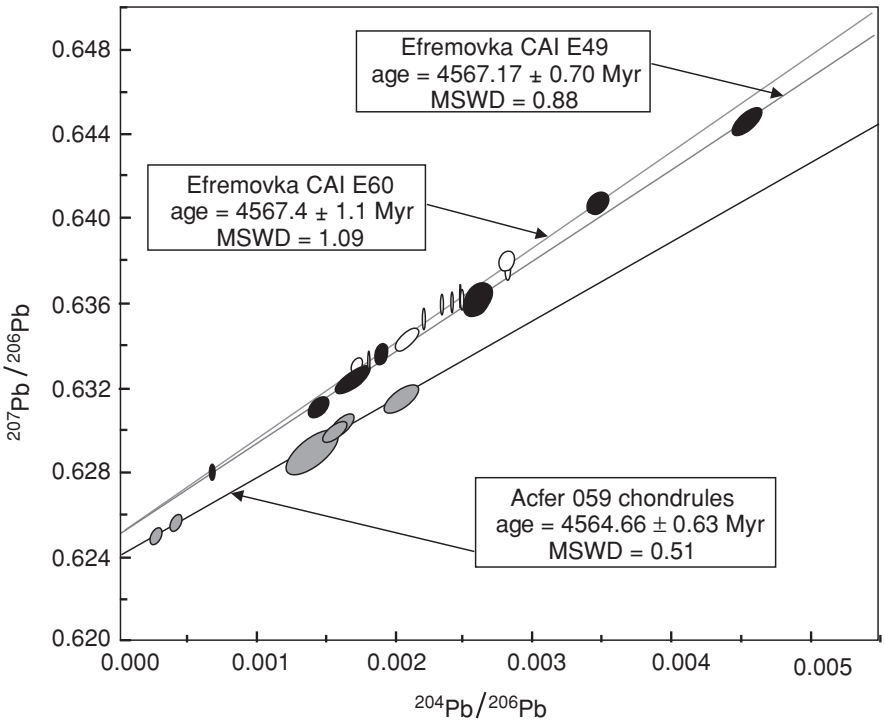

Fig. 11.6 The Pb/Pb isochron ages for CAIs from Efremovka (CV) and for chondrules from Acfer (CR) chondrites. From Amelin *et al.* (2002). Reproduced with permission from AAAS.

11.6 Chondritic meteorites: time scales

Formation time scales

The oldest date on chondritic material other than CAIs, 4564.7 ± 0.6 Myr, was obtained on chondrules from the Acfer CR chondrite (Fig. 11.6) using the Pb/Pb method, which is the most precise absolute chronometer applicable to the early solar system (Section 10.3). Dating of the Ste Marguerite (H4) phosphates resulted in a similar age, 4563.0 ± 0.6 Myr, even though the phosphates are secondary minerals (Fig. 13.1). According to these data, chondrules and chondrites were formed simultaneously within a short time interval of ~1 Myr, and they are ~2 Myr younger than calcium–aluminium-rich inclusions (CAIs). A number of Pb/Pb dates on (secondary) phosphate minerals in equilibrated L and H chondrites have yielded much younger ages, but these probably correspond to later events that affected chondrite parent bodies (Rubin, 1995).

As in the case of CAIs (Section 10.4), a fairly complete relative chronology can be pieced together for the formation and early history of chondrite parent bodies from short-lived-nuclide decay systematics (^{26}Al–^{26}Mg, ^{53}Mn–^{53}Cr and ^{129}I–^{129}Xe;

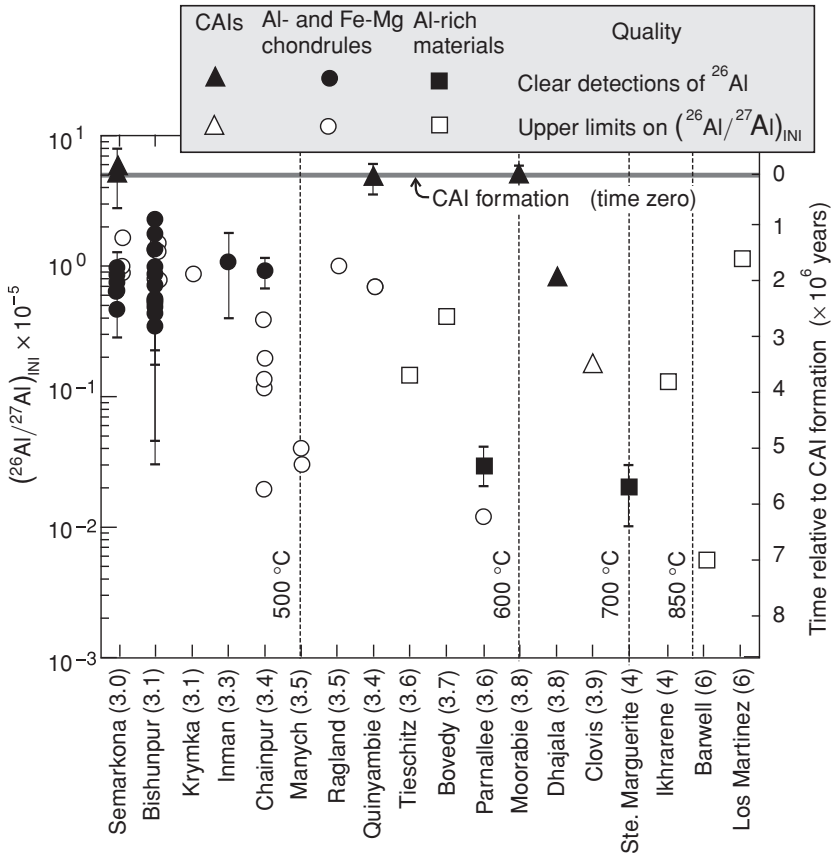

Fig. 11.7 Initial $^{26}Al/^{27}Al$ ratios in CAIs and chondrules from ordinary chondrites and the corresponding time intervals. From Huss *et al.* (2001), © Meteoritical Society 2001, reproduced by permission.

Table 3.3). Aluminium-rich chondrules in ordinary chondrites have been found that contain excess $^{26}Mg^*$ corresponding to the initial ratios $^{26}Al/^{27}Al_{INI} \sim 1 \times 10^{-5}$ (Russell *et al.*, 1996; Huss *et al.*, 2001). Substitution of this and the "canonical" CAI ratio $^{26}Al/^{27}Al_{SOS,INI} = 5 \times 10^{-5}$ into Eqn (10.11) gives a relative formation age ≈ 2 Myr after CAI formation; this value is indistinguishable from the Pb/Pb age differences (Figs. 11.6, 11.7, 13.1). Somewhat younger ages, mainly from chondrites with higher equilibration temperatures, imply metamorphic processes that might have caused the resetting and later closure of the ^{26}Al–^{26}Mg systematics.

However, in rare cases chondrules show high $^{26}Al/^{27}Al_{INI}$ ratios up to $(5.66 \pm 0.8) \times 10^{-5}$, thus indicating formation contemporaneously with CAIs; several chondrules in the Allende chondrite present an example (Bizzarro *et al.*, 2004).

A further important chronometer comprises the extinct parent ^{182}Hf and its daughter ^{182}W (Table 3.3). Both Hf and W are involatile elements, but Hf is

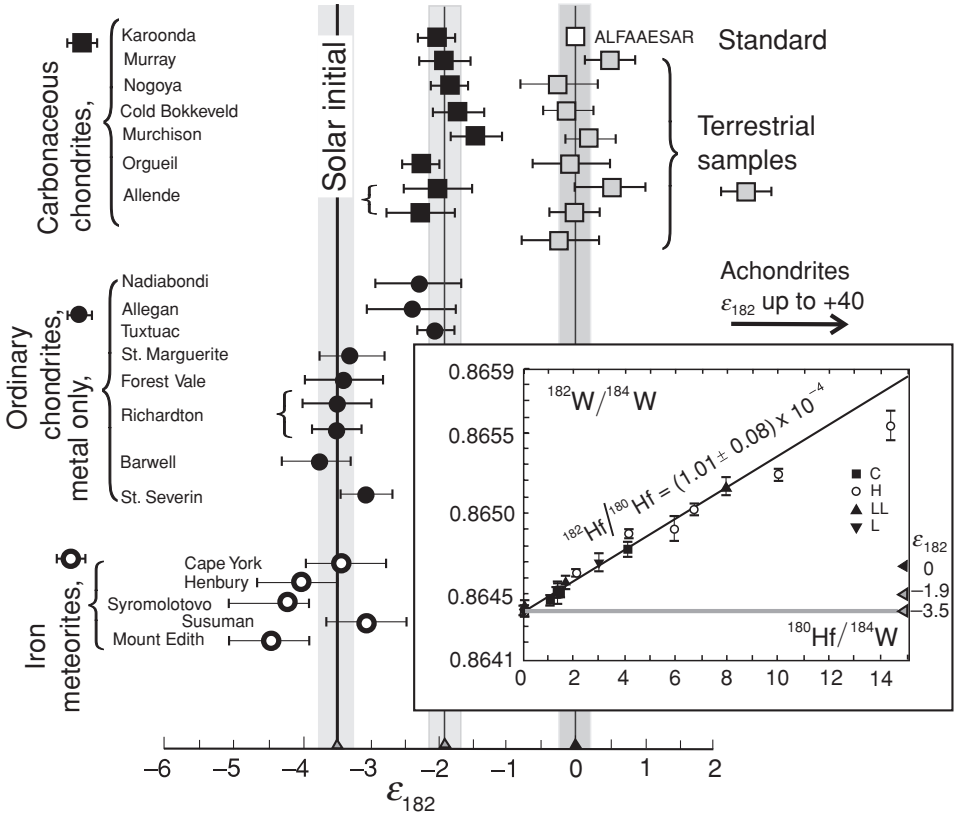

Fig. 11.8 The systematics of $^{182}Hf - ^{182}W$ in solar system materials. The daughter-isotope ratios, $^{182}W/^{184}W$, are expressed as ε_{182} deviations from the terrestrial W value (Eqn 19.1b) with $(^{182}W/^{184}W)_{BSE} \equiv \varepsilon_{182} = 0.864\,78 \pm 0.000\,04$, which is 3.5 ε_{182} units above the inferred SOS initial value seen in metal objects, $(^{182}W/^{184}W)_{SOS,INI} = 0.864\,481\,2 \pm 0.000\,017$. Carbonaceous chondrites show an intermediate deviation of -1.9 ε_{182} or $(^{182}W/^{184}W)_{SOS,NOW} = 0.864\,524\,9 \pm 0.000\,017$. For achondrites the high ε_{182} values are typical, thus indicating their early metal–silicate differentiation (Section 12.4). The inset shows a $^{182}W/^{184}W$ vs. $^{180}Hf/^{184}W$ isochron plot for chondrites. The inferred initial $^{182}Hf/^{180}Hf_{SOS,INI} = 1.01 \times 10^{-4}$ together with $^{180}Hf/^{184}W_{SOS}$ (Table 3.3) and $(^{182}W/^{184}W)_{SOS,INI}$ (as above) determine the chondritic ^{182}Hf–^{182}W systematics. After Halliday *et al.* (2000) and Jacobsen (2005).

lithophile and W is moderately siderophile, particularly under reducing conditions (Table 18.1). In the equilibrium partitioning of these elements between metal and silicate matter, the silicate fraction acquires a high Hf/W ratio, accumulates radiogenic $^{182}W^*$ and hence shows a high $^{182}W/^{184}W$. Complementarily low ratios are expected for the metal fractions.

Some iron meteorites and metal particles in chondrites show low contributions of radiogenic $^{182}W^{*}$. The least radiogenic $^{182}W/^{184}W$ ratio, $\varepsilon_{182} = -3.5$, corresponds to the initial isotope composition of W defined by a meteoritic isochron (Fig. 11.8, inset). The above value is accepted as the SOS initial; most metal particles (meteorites) vary within ± 0.25 ε_{182} units (the leftmost grey band in Fig. 11.8), corresponding to a formation time interval of ± 2 Myr. The meteoritic isochron also defines $^{182}Hf/^{180}Hf_{SOS,INI} = 1.01 \times 10^{-4}$. Substitution of this value and that derived from the internal isochron of the Ste Marguerite H4 chondrite, 0.85×10^{-4}, into Eqn (10.11) gives 2.2 Myr, which corresponds exactly to the difference between the Pb/Pb ages of Ste Marguerite phosphates and of chondrules from the Acfer meteorite (above). Besides engendering a great confidence in this relative dating method, this indicates a later closure of the phosphates for both isotopic systematics.

Processing time scales

To constrain the relative chronology of processes, parent–daughter pairs are useful in which the parent is strongly enriched in a newly formed phase or the element containing the daughter isotope is strongly depleted. The ^{26}Al–^{26}Mg and ^{53}Mn–^{53}Cr chronometers are examples of the first case and the ^{129}I–^{129}Xe clock an example of the second. Aluminium and magnesium were separated not only by their different volatilities but also by specific mineralogy. Thus, the ^{26}Al–^{26}Mg clock can date the formation of Al-rich Mg-poor minerals such as feldspars. Feldspars formed by post-accretion processes in the Ste Marguerite chondrite (H4) have an initial $^{26}Al/^{27}Al$ ratio of $(2.0 \pm 0.6) \times 10^{-7}$ and were thus formed ~ 5.6 Myr after the Allende CAIs (Fig. 11.7; Zinner and Goepel, 1992).

In the case of the ^{53}Mn–^{53}Cr clock (Table 3.3), high Mn/Cr ratios may occur in carbonate minerals generated by the hydrous alteration of chondritic meteorites. Endress and Bischoff (1996) obtained a $^{53}Cr/^{52}Cr$ versus $^{55}Mn/^{52}Cr$ isochron with $^{53}Mn/^{55}Mn = 1.8 \times 10^{-6}$ for carbonate vein samples from the Orgeuil and Ivuna C1-type carbonaceous chondrites. Assuming a solar system initial $^{53}Mn/^{55}Mn$ ratio, 8.5×10^{-6} (Table 3.3), and substituting these values into Eqn (10.11) gives the vein formation at ~ 8.3 Myr after SOS formation and shows that carbonaceous chondrite parent bodies cooled very early in solar system history.

The ^{244}Pu–^{238}U–^{129}I–Xe^{*} isotope systematics, termed xenology (by J. Reynolds), is unique in that three radioactive precursors with very different half-lives produce radiogenic (fission) Xe-isotopes (Table 3.3). Therefore Xe-isotope abundances can shed light on the fractionation of meteoritic and planetary materials, first of all on the volatile transfer that occurred on three rather different time scales, from tens of millions of years to gigayears. Extinct ^{244}Pu decayed

slower than other isotopes listed in Table 3.3, so that the chronology of ^{244}Pu fission to $^{136-131}$Xe(Pu) can hardly be applied to problems of solar nebula evolution, although it is important for understanding the early history of the terrestrial planets.

The ^{129}I–^{129}Xe subsystem involves two highly volatile as well as water-soluble elements. Iodine-129 lived long enough to be homogeneously distributed in the solar nebula. This favours a chronological interpretation of the ^{129}I–^{129}Xe data (Swindle and Podosek, 1988; Swindle *et al.*, 1991; Swindle, 1998; Brazzle *et al.*, 1999; Gilmour *et al.*, 2000). Provided that meteoritic objects retained both stable ^{127}I and ^{129}I-produced ^{129}Xe(I) since their closure to Xe loss, the equality

$$\frac{^{129}\mathrm{Xe}(^{129}\mathrm{I})}{^{127}\mathrm{I}} \equiv \left(\frac{^{129}\mathrm{I}}{^{127}\mathrm{I}}\right)_{\mathrm{INI}}$$

is readily translated into time intervals (Eqn 10.11).

As shown in Fig. 11.9, about 85% of analysed objects have ^{129}I/^{127}I$_{\mathrm{INI}}$ ratios in the range (0.7–1.4) $\times$ 10^{-4}, which corresponds to a $\sim$ 14 Myr time interval. It is clear that the time that elapsed before rock units in chondrite parent bodies were able to retain Xe and I must have been significantly longer than the time scales of chondrite parent-body formation given by the relative ^{26}Al–^{26}Mg chronology (2 Myr) and W-isotopes in metal in chondrites (3 Myr). The ^{129}I–^{129}Xe relative age is similar to the ^{53}Mn–^{53}Cr relative age obtained for chondritic carbonates. Because of the great water solubility of both the parent element I and the daughter element Xe, it is reasonable to relate closure (the setting of the clock) to the cessation of hydrothermal activity in the parent bodies.

In the Allende meteorite, the matrix contains iodine with higher initial ^{129}I/^{127}I values than both the Ca–Al-rich inclusions, considered as the most ancient objects formed in the solar nebula, and chondrules and thus appears to predate both of these, in contrast with the data of e.g. the ^{26}Al–^{26}Mg systematics (Fig. 11.7). This apparent discrepancy results from the resetting of the I–Xe clock in CAIs and chondrules by hydrous-alteration processes in a meteorite parent body. Indeed, the secondary mineral sodalite (a typical product of alteration) is the principal carrier of ^{129}Xe(I) in CAIs (Kirschbaum, 1987). In some Allende CAIs almost all the iodine is ^{129}Xe*-correlated (Zaikowski, 1980), indicating early pre-^{129}I-decay alteration, the subsequent closure of ^{129}I–^{129}Xe(I) systematics and, therefore, an early relatively cool environment.

For special cases where non-primary minerals were formed in discrete events, the Pb/Pb chronometer offers an opportunity to calibrate the relative I–Xe clock. Indeed, for several chondrites a good correlation has been found between the Pb/Pb dates on phosphates and the I–Xe relative ages for both phosphates and feldspars (Fig. 11.10). This correlation strengthens the confidence in both types of age dates, particularly as the parent–daughter pairs of the two clocks are chemically so different.

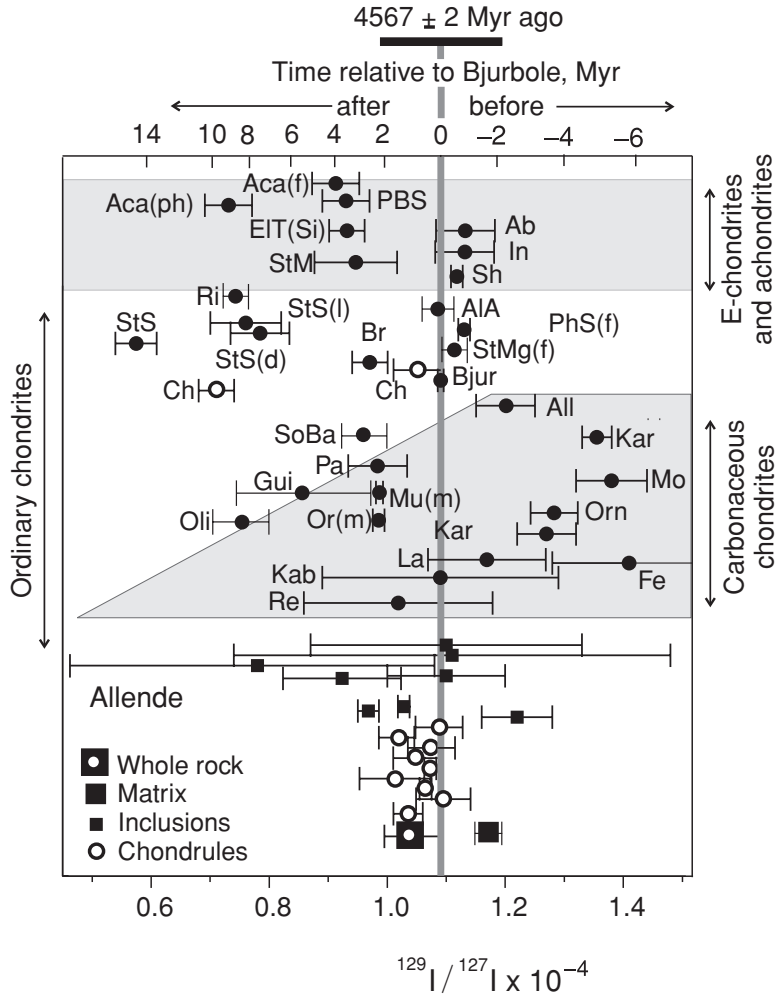

Fig. 11.9 The I–Xe systematics in meteorites. The time intervals are derived relative to the best-determined $^{129}I/^{127}I$ values for the Bjurbole (L4) chondrite, for which the Pb/Pb model age is shown at the top. Almost all meteorites and inclusions were able to retain $^{129}Xe(I)$ within ±8 Myr. This interval is long relative to that inferred from the ^{26}Al–^{26}Mg systematics and the Pb/Pb ages (Section 11.7). The few exceptions (data plotting to the left of this plot and not shown here) most probably relate to late metamorphic processes. Precise Pb/Pb ages are available for some of these meteorites (Fig. 11.10). For all meteorites but Allende the solid circles denote the matrix or (if mentioned within parentheses) mineral separates, and the open circles denote chondrules; for the data and legend for Allende see the bottom part of the figure. The fractions analysed are: f, feldspar separates; ph, phosphate separates; m, magnetite; d, dark fraction; l, light fraction; see the List of meteorites. Sources of data: Podosek (1970), Herzog *et al.* (1973), Lewis and Anders (1975), Drozd and Podosek (1976), Hohenberg *et al.* (1981), Crabb *et al.* (1982), Swindle *et al.* (1983, 1988), Bernatowicz *et al.* (1988) and Brazzle *et al.* (1999).

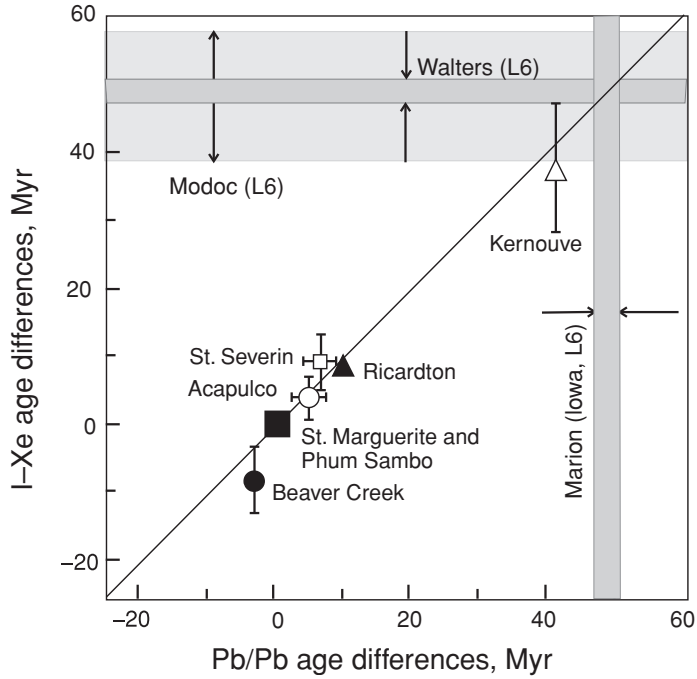

Fig. 11.10 The I–Xe and Pb/Pb age differences of phosphates and feldspars from ordinary chondrites and achondrites (relative to St Marguerite and Phum Sambo, both H4 chondrites). The I–Xe ages are available for two L6 chondrites (overlapping horizontal light-grey bands) as well as the Pb/Pb age for the third meteorite of the same subclass (vertical grey band): their crossing gives the consistent I–Xe and Pb/Pb relative ages (black line). After Göpel *et al.* (1994) and Brazzle *et al.* (1999).

In summary, the short-lived nuclide chronometers suggest chondrite parent-body formation within 2–3 Myr, and certainly less than 4 Myr after the formation of the earliest rocks in the solar nebula. Further, in parent bodies that had trapped water, hydrous alteration under relatively cool conditions apparently lasted up to ~ 10 Myr after their accretion. Relative ages up to ~ 60 Myr younger, which may relate to discrete events such as collisions, are also recorded by the I–Xe and Pb/Pb systematics.

11.7 Chondritic meteorites: formation processes

A possible nebula environment for chondrite-forming processes

Several convincing observations favour local heating events (causing partial vaporization and recondensation of particles) in a dusty nebula as the most likely mechanism and environment for the formation of the chondrite parent bodies. The

key observation is the preservation of presolar grains in the matrixes of chondrites and in the chondrule rims (Alexander *et al.*, 1990a, b; Huss, 1990; Nittler *et al.*, 1994). Further, most probably the components carrying heavy hydrogen and Q-type noble gases were formed in a presolar molecular cloud and were preserved in the matrixes of chondritic meteorites. Also, the O-isotope compositions of chondrules and matrix (Fig. 10.8(b)) indicate their formation from somewhat different materials that had not become equilibrated. Therefore only the "dusty-nebula" scenario is discussed below; more comprehensive discussions are found in the book edited by Hewins *et al.* (1996) and also in papers by Wood (1996), Liffman and Toscano (2000), Hood and Ceisla (2001) and Cuzzi *et al.* (2003).

In addition to the observations mentioned above, a chondrite-forming mechanism must explain or include

- iterative local vaporization, i.e. recondensation events recorded e.g. by the Si-isotope compositions of chondrules. These events must also have caused the loss of moderately and highly volatile elements from the bulk material (Fig. 11.2) and led to complementary abundance patterns between chondrules (volatile-depleted) and matrix (volatile-enriched; Fig. 11.3; Sears *et al.*, 1996; Alexander, 1996);
- the fragmentation of chondrules, and how the fragments became incorporated in the matrix (Section 11.2);
- the presence of different oxygen fugacities, ideally leading to oxidation–reduction heterogeneity (Section 11.2);
- the formation of chondrules and matrix in the close neighbourhood of the solar nebula, in contrast with the "alien" nature of the CAIs in the matrix, for example, how ordinary chondrite chondrules (even those with almost the same O-isotope composition) could have been incorporated into H, L or LL chondrites (see Fig. 10.8(b)).

Even though there is some consensus on this local-neighbourhood scenario (Taylor *et al.*, 1983; Grossman *et al.*, 1988; Hewins *et al.*, 1996), a chondrule-heating mechanism, capable of operating locally and repeatedly in a dusty nebula, has not been firmly identified so far. Only two classes of mechanisms appear to be consistent with these general requirements: electrostatic discharges (lightning) and gas-dynamic shock waves. Both classes are still characterized by large uncertainties but the shock model has reached the point at which quantitative tests of its validity are beginning to be possible, and so only this model is outlined below (Boss and Graham, 1993; Hood and Kring, 1996; Connolly and Love, 1998).

Formation of chondrites: shock waves in a dusty nebula

A shock wave is a sharp discontinuity between hot compressed high-speed gas (moving faster than the local speed of sound) and cooler, less dense, slower-moving gas (Connolly and Love, 1998). Gas overrun by a shock wave is abruptly

compressed, heated and accelerated. The temperature and density increase moderately behind the shock wave, whereas the pressure increases much more strongly. Solid particles are also affected by the shock wave: they suddenly find themselves in a blast of wind moving at several kilometres per second and thus, behind the shock, particles are accelerated. Friction as well as thermal irradiation from gas heat the particles, and they lose heat by radiation and evaporation. Frictional heating ends when a particle attains the speed of the gas, which occurs when it has encountered a mass of gas comparable with its own mass. At nebula conditions a micrometre-sized particle attains the gas velocity within a few hundred metres of the shock wave, whereas a millimetre-sized particle falls hundreds of kilometres behind the shock wave before matching the speed with the post-shock gas. The distance determines the time of the heat pulse, varying from ~ 10 ms to ~ 100 s for the above two particles, respectively (Connolly and Love, 1998).

The difference in the velocity–distance–time sets inferred from the shock-wave mechanism for chondrules of different sizes readily explains several features of meteoritic chondrules. Thus, larger chondrules are generally found to be more heated than smaller ones or fine grains or dust. Within the framework of the above trio of parameters the time of heating is much longer and the net adsorption of energy is more efficient for larger grains or aggregates, which would thus be more likely to melt and turn into chondrules. Because of the different braking distances, large relative velocities between massive chondrules and fine grains are expected and hence numerous collisions between the two. Fine-grained dust rims should appear on the surface of chondrules, which is in accord with observations. The rotation of chondrules is almost inevitable as a result of asymmetric collisions and would ensure a roughly concentric build-up of dust material during their flight through the dusty nebula. The larger the chondrule, the more numerous collisions with dust particles would be and the thicker the rim. This also fits with observed relationships. Numerical modelling shows that the observed direct proportion between the rim thickness and the chondrule radius can be reproduced by the hypersonic interaction between a chondrule and a mixture of gas and dust (Liffman and Toscano, 2000). The velocities of already solidified chondrules are still high enough to cause braking and abrasion via collisions with other previously formed chondrules, which leads to chondrule recycling and to chondrule fragments in the matrix.

Modelling shows that nebula shock waves could heat an initially cold chondrule precursor to melting temperatures during time intervals consistent with those determined experimentally (Hood and Horanyi, 1993; Hood and Kring, 1996). Molten chondrules are unstable and can evaporate under canonical solar nebula ambient pressures (Section 10.1). However, (1) the shock-wave mechanism increases the pressure in the post-shock region more than the temperature, thus counteracting evaporation. Even though the maximum temperatures recorded by chondrules,

$\sim$2200 K, could lead to (2) hydrogen dissociation and (3) silicate evaporation, these processes consume orders of magnitude more energy than collision or radiation heating can produce. The three processes would have a feedback function, constraining the degree of vaporization and leading to the moderate volatile loss indicated by chondrules.

The required cooling rates could also be provided by the shock-wave mechanism. The relatively rapid heating and slow cooling rates experienced by chondrules constrain their formation to locally hot nebula regions $\sim$100 km or less in thickness (Connolly and Love, 1998). Shock-wave propagation on the above distance scale allows the duration of the model-derived particle heat pulse to be reconciled with observational data. The turbulent concentration of aerodynamically size-sorted particles would allow chondrule-sized particles to be concentrated in a chondrule-forming region by a factor up to 10^5 (Cuzzi *et al.*, 1996). This phenomenon could be responsible for several features of ordinary chondrites. Thus, the average chondrule size increases from H through L to LL chondrites, along with an increase in the oxidation rate and a decrease in the metal concentrations. The proposal that larger chondrules were formed in a region more enriched in dust and therefore having a higher O/H ratio appears quite reasonable (Clayton, 1993). These chondrules would contain iron in oxidized form whereas previously formed small reduced chondrules and small droplets of metal would be lost from the L and LL formation region.

The mechanism causing the required shock wave would have to be astrophysically realistic and have a high probability of occurring in nebula formation, so that it could happen repeatedly. Four potential mechanisms have been proposed. These are: (1) the irregular (clumpy) accretion of interstellar gas onto the proto-planetary nebula (Boss and Graham, 1993; Boss, 1996; Hood and Kring, 1996; Morfill *et al.*, 1993); (2) outbursts from the young Sun (Boss, 1996); (3) spiral-arm instabilities in the disk (Boss, 1996; Morfill *et al.*, 1993); (4) eccentric planetesimals moving at hypersonic speeds through the proto-planetary disk (Hood, 1998). At present, nebula-formation models are insufficiently detailed to exclude any of these.

11.8 Summary: chondritic meteorites and early evolution of the solar nebula

The constituents of chondritic meteorites record some major processes that governed the evolution of matter in the solar nebula. The most ancient constituent is presolar grains, which indicate great heterogeneity of their source, a cold interstellar molecular cloud that collapsed and gave rise to the solar system. The second-oldest constituent, Ca–Al-rich inclusions, were formed in the nebula itself

at least 4567 Myr ago and record early high-temperature processes in the innermost nebula region, where solid matter was vaporized, mixed and then recondensed.

The most abundant components of chondritic meteorites, the matrix and chondrules, were formed within a short time interval, mainly between 1 and 3 Myr after the CAIs, in the presence of nebular gas and dust heated by short local events. The most probable heating mechanism, the propagation of shock waves, caused size-dependent heating in such an environment, because behind the shock front the gas was accelerated to a higher speed than the particles. The heavier a particle, the more it would have been heated by friction and collisions, and temperatures could have reached ~ 2200 K in the case of a ~ 1 mm particle. This important feature of the shock-wave heating mechanism along with relatively fast subsequent cooling readily explains the principal record of chondritic meteorites: the coexistence in a close neighbourhood of highly processed (even partially vaporized) silicate droplets and unprocessed or moderately processed (presolar and other) small grains. During these events volatile elements were partially lost from the bulk material and partially redistributed between volatile-depleted chondrules and (relatively) volatile-enriched matrix, which also included chondrule fragments. Matrix and chondrule rims, even though showing substantial mixing and equilibration with gas-phase components (e.g. with oxygen), both preserve presolar and highly heterogeneous μm-size grains and, in less processed chondrites, carbonaceous matter enriched in the heavy noble gases and heavy hydrogen and nitrogen.

The mass-dependent relative velocities of chondritic agglomerates stimulated their fast growth so that large bodies, chondritic planetesimals ($\sim 10^{20}$ g), were formed 2 to 3 Myr after the CAIs (Fig. 13.1). Central parts of the larger planetesimals, insulated from fast heat loss, were heated (probably by the decay of the short-lived nuclides ^{26}Al and ^{60}Fe). This and collisional heating caused mineral reactions and the redistribution of volatile elements; these late metamorphic processes operated on a time scale of ~ 10 Myr.

A more severe heating caused the partial melting of chondritic planetesimals, the segregation of metal and the fractionation of silicates and their degassing. Non-chondritic stony-iron and iron meteorites, discussed in Chapter 12, record these processes.

12

Highly processed meteorites

12.1 Introduction: non-chondritic meteorites and their relationships

The two main groups of meteorites other than chondrites are achondrites and iron meteorites (Wasson, 1985). Meteorites from the first group consist essentially of silicate minerals and are distinct from the chondrites both in their compositions and internal rock textures (the intergrowths of minerals), which indicate that they crystallized from a silicate melt or, at least, equilibrated extensively with such a melt. The second group comprises iron meteorites consisting chiefly of metal, frequently with sulphide and occasionally silicate inclusions. They tend to be coarse-grained (up to cm-size grains) and, by etching of a polished surface, the crystalline structure of the metal is made visible in the so-called Widmanstatten structures so often admired in museum collections.

There are ample arguments that both these meteorite types are products of the thermal processing of a chondritic precursor. These are, for example, the identical oxygen-isotopic compositions of some chondrites, achondrites and irons; the complementary chemical compositions of achondrites and iron meteorites: the mineralogy of silicate inclusions in stone-irons; the similar densities of processed asteroids and chondritic meteorites and of the unprocessed clasts of chondritic material often seen in non-chondritic meteorites (Zolensky *et al*., 1996; Meibom and Clark, 1999).

Oxygen isotopes appear to be a powerful tool for tracing the relations between primitive and processed meteorites. Enstatite chondrites, enstatite achondrites and aubrites have O-isotopic compositions close to the terrestrial fractionation line. The so-called HED meteorites, constituting the largest suite of achondrites and discussed in some detail below, stony-irons (mesosiderites and the main group of pallasites) and magmatic iron meteorites (IIIAB) all fall on a mass-dependent fractionation trend slightly below the terrestrial fractionation line, implying derivation from a single reservoir (Fig. 10.8(b)).

Chemically, magmatic iron and non-chondritic silicate meteorites could be complementary to each other; iron meteorites are enriched in siderophile trace elements and achondrites are depleted in them whereas with lithophile elements it is naturally the reverse. By combining appropriate amounts of iron meteorites and achondrites, a chondritic precursor can be reconstructed. V. M. Goldschmidt was first to notice this and he coined the terms "siderophile" and "lithophile" on this basis. For the severe processing of chondritic matter, a heat source is required. Radioactive heat produced by short-lived nuclides, e.g. ^{26}Al, ^{60}Fe (Ghosh and McSween, 1998; Mostefaoui *et al*., 2004), by long-lived nuclides (Haack *et al*., 1990) or by collisions of meteorite parent bodies (Vityazev *et al*., 1990; Rubin, 1995) have all been proposed and it is likely that all three mechanisms played a role.

Different initial compositions and masses of the parent bodies, as well as the highly variable *PT* conditions in them, caused a great diversity in the final products. For detailed discussions of the relevant topics the reader is referred to the monograph by Wasson (1985) and reviews by Hewins and Newsom (1988) and Mittlefehldt *et al*. (1998). Here we merely present a record of the magmatic silicate rocks and irons, which were probably delivered from the asteroid Vesta and its neighbourhood, as an illustration of the very early igneous activity in the solar nebula.

12.2 Magmatic fractionation and trace-element partitioning

Magmatic fractionation

In melting processes within multicomponent systems such as planetesimals, fractionation occurs both for major and for trace elements. These do, however, follow different principles and laws. The concentrations of major elements determine which phases are formed under given conditions, whereas the trace elements are not present in sufficient abundance to determine the physical state of the system and have to be accommodated somehow in given minerals, melts, fluids or vapour phases.

In the igneous differentiation of planetesimals three main types of process play a part. The first process is the segregation of the metal phase as a separate melt, which is a direct consequence of the insolubility of reduced metals in silicate lattices and melts, and this may form a core. The major elements dictating the state of the system are the iron-peak elements Fe and Ni, and the trace elements are partitioned between the silicate and metal phases, essentially following their siderophile or lithophile character. It is important to note that the actual segregation of a metallic melt from a silicate matrix can only proceed in an extensively melted environment, e.g. 40% or even 70% melt (Stevenson, 1990; Taylor *et al*., 1993). The reason for this is

the high interface energy between metallic melts and solid silicates. As a result a metallic melt does not "wet" silicate grain surfaces but forms separate droplets, which can percolate only when they are large enough. A further requirement for the segregation of a metallic melt into a core is, of course, sufficient gravity on the planetesimal where it is formed.

The second process is the redistribution of trace siderophile elements in the course of solidification of the core due to their different partitioning between liquid and solid metal. Diffusion and convection of the liquid phase are also important in determining the final "frozen" compositions.

The third process is the redistribution of the elements within the silicate portion in the course of its partial melting and melt–solid separation. Generally the silicate matter constitutes a multicomponent system for which there is a melting temperature interval when solid and liquid silicates occur together, bracketed by the solidus and the liquidus curves. The solidus temperature is always lower than the melting points of any of the constituent minerals on their own: melting is in fact a set of chemical reactions between different phases. The melt produced at the solidus temperature of a multiphase assembly is saturated in all components making up the phase assemblage; it is termed the eutectic melt. The chemical composition of this melt is firmly determined by which phases are present but is independent of their relative abundance. Therefore a rock consisting of e.g. 90% olivine, 5% clinopyroxene and 5% spinel produces the same eutectic melt as one with 33.3% of each phase. The eutectic melt of a chondrite-like assemblage of olivines, pyroxenes and spinel is close to basaltic in composition, i.e. it contains considerably more Al, Si and Ca and has a higher Fe/Mg ratio than the rock from which it was produced (Yoder and Tilley, 1962). Hence, igneous fractionation of the silicate portion of a chondritic precursor leads to differentiation into two complementary reservoirs, basaltic crust and ultramafic mantle.

Magmatic fractionation: trace elements

The trace elements, essentially the n-capture elements and Li, Be and B, are orders of magnitude less abundant than the major elements making up a crystal lattice, and whether they can be accommodated in that lattice depends on their similarity to those major elements in effective ionic radius and charge. That similarity, or lack thereof, governs the partitioning of the trace elements between coexisting phases, e.g. silicate and/or metallic melts, metallic and silicate solids, solid and vapour.

Defining $C_{i,2}$ and $C_{i,1}$ as the concentrations of a trace element i in phases 2 and 1, which are in equilibrium, the concentration ratio $C_{i,2}/C_{i,1} \equiv D_{i,2/1}$ is the Henry's law partition coefficient, which is generally known from both experimental and theoretical data (Kuehner *et al.*, 1989; Johnson, 1998; Allan *et al.*, 2003; McDade

et al., 2003; Table 24.2). This definition implies equilibrium partitioning occurring when the coexisting phases 2 and 1 are in contact long enough for diffusion to have taken place. The coefficient D_i for most elements depends on *P, T* and chemical parameters such as the oxygen fugacity and the major-element concentrations, which vary in the course of fractionation. For example, in the case of inner-core solidification, D_i depends on the concentrations of S, P and C in the melt (Mittlefehldt *et al*., 1998). In some cases the assumption of constant partition coefficients appears to be a useful simplification.

If two phases, 1 and 2, are present in mass fractions $F_1 + F_2 \equiv 1$ then the mass balance of element *i* can be written as

$$C_{i,1}F_1 + C_{i,2}F_2 = C_{i,0}(F_1 + F_2) = C_{i0}, \tag{12.1}$$

where $C_{i,0}$ is the bulk concentration of species *i* in the total system (if phases 1 and 2 were fully remixed). Substituting $D_{i,2/1}$ and F_2 into Eqn (12.1) gives

$$C_{i,1}F_1 + C_{i,1}D_{i,2/1}(1 - F_1) = C_{i0} \tag{12.2}$$

or

$$C_{i,1}[F_1 + D_{i,2/1}(1 - F_1)] = C_{i0}. \tag{12.3}$$

Thus the concentration of element *i* in phase 1 is given by

$$C_{i,1} = C_{i,0}/[F_1 + D_{i,2/1}(1 - F_1)]. \tag{12.4}$$

This is an equation for the distribution of a trace element between any two coexisting phases. If phase 1 is a melt and 2 a solid, the equation describes melting equilibrium; if $D_{i,2/1} > 1$ then element *i* is more compatible in the solid than in the melt, and if $D_{i,2/1} < 1$ then vice versa. These cases are normally simply referred to as those of "compatible" and "incompatible" elements respectively.

For the case where more than two phases, such as different silicate or metallic solid phases and melts, are in equilibrium with each other then Eqn (12.4) can be extended to *n* phases:

$$C_{i,1} = C_{i,0}/(F_1 + D_{i,2/1}F_2 + D_{i,3/1}F_3 + \cdots + D_{i,n/1}F_n) \tag{12.5}$$

where $F_1 + F_2 + F_3 + \cdots + F_n = 1$.

Equations (12.4), (12.5) describe "batch" melting, in which the melt remains in contact with the solid during the complete melting process. In contrast with this, "fractional" melting refers to the case in which consecutive small fractions of melt are produced in equilibrium with the solid matrix and then removed from it, to accumulate elsewhere. For this and the more complicated case of time-dependent $D_{i,j}$ and F_j parameters, the element transfer needs to be described by a system

of differential transport equations, which then can be integrated numerically or, providing the system is simple enough, analytically (Shaw, 1970).

For fractional melting the concentration of an element i in each elementary melt fraction F_1 (separated continuously from a host matrix) is given by the Rayleigh equation

$$C_{i1} = C_{i0}(1/D_{i,2/1})(1 - F_1)^{1/D_{i,2/1}-1}. \tag{12.6}$$

If $F_1 \to 0$ and element i is incompatible ($D_{i,2/1} < 1$), its concentration in the melt C_{i1} approaches a maximum value, as follows from both Eqns (12.4) and (12.7) below.

The concentration C^*_{i1} in the aggregate liquid, where the fraction F^* is the sum of the individual melt fractions, is

$$C^*_{i,1} = (C_0/F^*)[1 - (1 - F^*)^{1/D_{i,2/1}}]. \tag{12.7}$$

Substituting 0.1 for the aggregate melt fraction (this is similar to the value for many basalt melts extracted from peridotite on Earth) and 0.01 for the partition coefficient (this is similar to the value for the light rare Earth elements) into Eqns (12.4) for batch melting and (12.7) for fractional melting gives values for the C_{i1}/C_{i0} and C^*_{i1}/C_{i0} ratios equal to 9.174 and 9.9997 respectively; the corresponding relative concentrations in the solid residuals are 0.092 for batch melting and 3×10^{-5} for fractional melting. This comparison clearly shows that the final distribution of the elements in coexisting phases strongly depends on the mechanism of the fractionation process. Iwamori (1994) presented a general equation for trace-element partitioning between the melt and the residual assemblage for a combination of fractional and batch melting mechanisms.

For some situations, such as a solidifying inner core, the solid phase is formed in small portions that are separated from the melt immediately after they crystallize. This case of "fractional crystallization" is the opposite of fractional melting, and the concentration $C_{i,2}$ in each portion of newly formed (solid) phase 2 depends on the fraction F_2 as follows:

$$C_{i,2} = D_{i,2/1}C_{i,0}(1 - F_2)^{D_{i,2/1}-1}. \tag{12.8}$$

Here $D_{i,2/1} \equiv C_{i,2}/C_{i,1} \equiv$ constant and $C_{i,0}$ and $C_{i,1}$ are the initial bulk concentration and the concentration in melt phase 1 respectively. It is assumed that material of phase 2 with "frozen" $C_{i,2}$ is being removed from the reacting zone. Note that for two elements i, j the track of successive fractions of phase 2 is a straight line on a plot of log $C_{i,2}$ versus log $C_{j,2}$ with slope $(D_{i,2/1} - 1)/(D_{j,2/1} - 1)$. Figure 12.5 presents an example of such a partitioning.

Thus, modelling of the abundances of compatible and incompatible trace elements in fractionated systems allows the identification of many features of the fractionation and transfer mechanisms that have occurred. This is also very important in lunar and terrestrial melting events (Chapters 18, 21, 24, 25).

12.3 Major and trace elements in non-chondritic meteorites

Magmatic stony and iron meteorites from Vesta and its vicinity

Among a great variety of highly processed non-chondritic stone meteorites, the howardites, eucrites and diogenites (HED) constitute the largest interrelated suite. Very similar O-isotope compositions and complementary abundances of incompatible trace elements imply their origin in a restricted region of the nebula or perhaps within one parent body. There is convincing evidence that these meteorites could have come from the asteroid 4 Vesta, a 510-km-size body at a heliocentric distance of 2.36 AU. The reflectance spectrum of Vesta is very similar to those characteristic of HED (Binzel *et al*., 1997), and a huge impact crater near the south pole of Vesta indicates that some material may have been ejected. Indeed small "Vestoids", showing similar characteristics and therefore considered as ejecta from this crater, were found at 2.5 AU in orbits for which scattering into the inner solar system to cross the Earth's orbit is predicted. The complementary magmatic metal meteorites, a suitable proxy for the core of Vesta, also constitute a large group, $\sim$ 30% of all iron meteorites, and could represent cores of similar asteroids that were fragmented in collisions (Drake, 2001).

Howardites, eucrites and diogenites: major and trace elements

Diogenites are coarse-grained orthopyroxenites consisting mainly ($\sim$ 85%–100%) of orthopyroxene, with chromite and olivine as common minor minerals constituting 0%–5% each (Mittlefehldt *et al*., 1998). Accessory minerals include diopside, troilite, metal and a silica phase. Diogenites are very uniform in bulk major and trace-element compositions (Tables 12.1 and 12.2).

Eucrites constitute two groups. Pigeonite–plagioclase fine-to-medium-grained rocks with minor and accessory tridymite, quartz, chromite, ilmenite, metal, troilite, whitlockite, apatite, olivine and rare zircon form the (main) basaltic group. Basaltic eucrites are very uniform in composition and petrographically similar to terrestrial and especially lunar basalts. The second group, cumulate eucrites, are coarse-grained gabbros composed principally of low-Ca pyroxene and calcic plagioclase with minor chromites and accessory silica, phosphate, ilmenite, metal and troilite. These rocks show a wider compositional range, being somehow intermediate between basaltic eucrites and howardites.

Table 12.1 *Major-element compositions (wt %) of diogenites, eucrites and howardites. From Mittlefehldt et al. (1998). Reproduced by permission of the Mineralogical Society of America*

					Eucrites (main group)				
	Diogenites		Cumulate eucrites		Stannern trend	Nuevo Laredo trend		Howardites	
Oxide	Johnstown	Shalka	Moama	Serra de Mage	Stannern	Juvinas	Nuevo Laredo	Kapoeta	Y-7308
SiO_2	52.5	51.6	48.6	48.5	49.7	49.2	49.5	50.3	50.8
TiO_2	0.10	0.06	0.22	0.13	0.98	0.63	0.83	0.30	0.23
Al_2O_3	1.50	0.60	13.70	14.80	12.30	13.00	12.20	8.30	4.27
Cr_2O_3	0.82	2.41	0.61	0.63	0.34	0.31	0.28	0.69	1.02
FeO	15.9	16.3	14.8	14.4	17.8	18.7	19.6	17.5	16.7
MnO	0.48	0.55	0.50	0.48	0.53	0.52	0.58	0.50	0.52
MgO	25.5	25.8	11.9	10.7	6.97	6.60	5.55	15.8	21.4
CaO	1.83	0.73	9.47	9.75	10.70	11.00	10.30	5.20	3.83
Na_2O	0.02	0.04	0.22	0.25	0.62	0.38	0.51	0.28	0.13
K_2O	0.00	0.00	0.01	0.01	0.07	0.03	0.05	0.02	0.01
P_2O_5	0.04	0.00	n.d.	0.03	0.10	n.d.	n.d.	n.d.	n.d.
S	0.22	n.d.	n.d.[a]	0.15	n.d.	n.d.	n.d.	n.d.	0.11
Total	98.9	98.1	100.0	99.8	100.1	100.4	99.4	98. 9	99.0

[a] Not determined.

Table 12.2 *Trace-element compositions of diogenites, eucrites and howardites*[a] *from Mittlefehldt et al. (1998). Reproduced by permission of the Mineralogical Society of America*

	Diogenite (typical)		Cumulate eucrites		Eucrites, main group			Howardite	
					Stannern trend	Nuevo Laredo trend			
	Johnstown	Shalka	Moama	Serra de Mage	Stannern	Juvinas	Nuevo Laredo	Kapoeta	Y-7308
Element	1	2	3	4	5	6	7	8	9
Sc, ppm	15.8	9.9	23.4	22.1	30.6	28.5	33.3	20.7	18.1
V	115	n.d.	114	111	n.d.	n.d.	61	n.d.	124
Co	38.1	18	8.6	9.5	7.18	5.8	2.15	28	20.5
Ni	150	n.d.	n.d.	n.d.	n.d.	n.d.	2.9	410	
Ga	0.18	n.d.	n.d.	n.d.	2.17	2.16	1.2	1.04	0.51
Ba	n.d.[b]	n.d.	n.d.	n.d.	53	n.d.	39	n.d.	8.25
La	0.063	0.009	0.18	0.58	5.08	2.58	3.83	1.39	0.68
Ce	n.d.	n.d.	n.d.	n.d.	13.7	n.d.	9.9	n.d.	1.67
Sm	0.059	0.004	0.16	0.35	3.15	1.48	2.32	0.54	0.42
Eu	0.011	0.002	0.36	0.33	0.782	0.61	0.71	0.32	0.17
Gd	0.24	n.d.	n.d.	n.d.	n.d.	2.3	n.d.	1.25	0.54
Tb	n.d.	n.d.	n.d.	0.07	0.73	0.6	0.54	0.29	0.1
Dy	0.21	n.d.	n.d.	0.6	5.05	3.2	3.7	1.26	0.66
Ho	0.059	n.d.	n.d.	n.d.	1.13	0.42	n.d.	0.23	0.16
Yb	0.17	0.03	0.42	0.39	2.9	1.72	2.4	0.89	0.49
Lu	0.027	0.006	0.075	0.066	0.4	0.28	0.35	0.14	0.073
Hf	n.d.	n.d.	n.d.	0.14	2.34	1.3	1.61	0.6	0.33
Ta, ppb	n.d.	n.d.	n.d.	80	500	120	181	100	42
Ir	6.4	n.d.	n.d.	n.d.	n.d.	27	0.083	20	n.d.
Au	1.7	n.d.	n.d.	n.d.	n.d.	7.9	1.5	6.8	0.45
Th	n.d.	n.d.	n.d.	n.d.	600	n.d.	440	n.d.	n.d.
U	2.8	n.d.	n.d.	n.d.	160	89	140	51	22

[a] In ppm from Sc downwards, and in ppb from Ta downwards.
[b] Not determined.

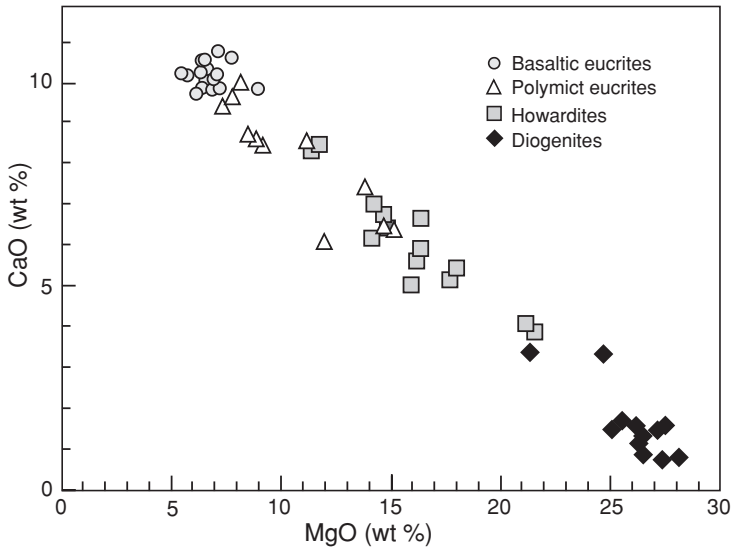

Fig. 12.1 Plot of percentages by weight of CaO vs. MgO for HED meteorites. All three types of rock belong to one family, the differences being generated by partial melting and fractional crystallization; howardites can be seen as mixtures between the end-members. From Mittlefehldt *et al.* (1998), Reproduced by permission of the Mineralogical Society of America.

Howardites are polymict breccias composed of diverse mineral and lithic clasts set in a fine-grained matrix; they often contain glassy spheres and irregularly shaped particles. Howardites are highly heterogeneous in both major- and minor-element composition. These rocks are intermediate between diogenites and eucrites and may represent impact breccias. Figure 12.1 shows that all three groups belong to one family in which magmatic differentiation probably defines the relationship between basaltic eucrites (the ultimate melt product) and diogenites (the residue), with cumulate eucrites as intermediate members and howardites as a mixing product (Mittlefehldt *et al*., 1998).

The abundances of involatile incompatible lithophile trace elements in HEDs vary within a great range, showing, however, a systematic pattern related to the rock types: the concentrations of the REE trio Sm, Eu and La increase in the sequence from diogenites through cumulate eucrites (and howardites) to basaltic eucrites (Fig. 12.2(a), (b)). The complementarity relative to the initial chondrite-like composition is also readily seen in Fig. 12.2(a), (b). The Sm/La ratio, inferred from the slope of the correlation, is indistinguishable from the chondritic value, indicating a chondrite-like precursor. A small fraction of melt emerges as the carrier (and controlling factor) of the high concentrations of these elements in basaltic eucrites, as seen from Eqns (12.4) and (12.7).

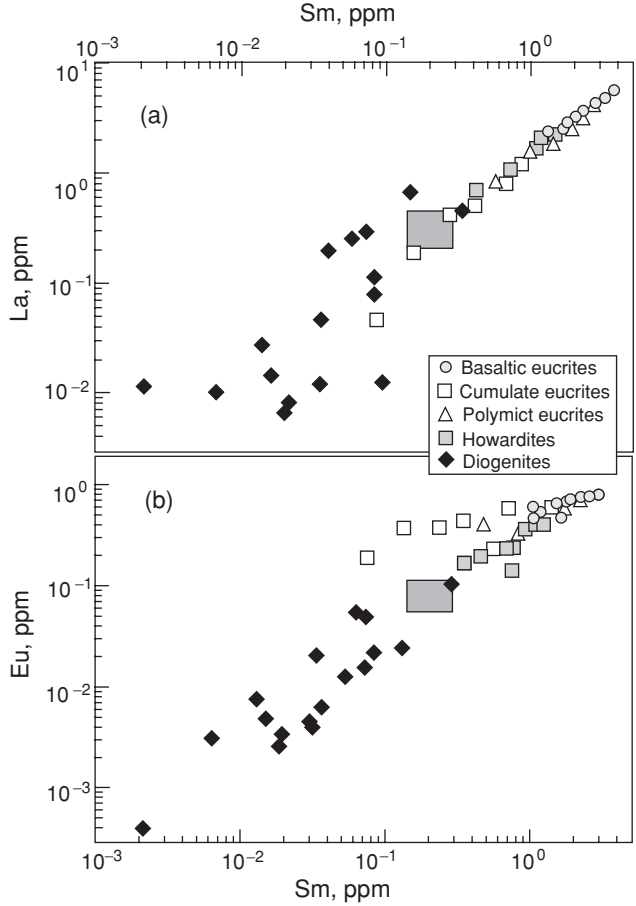

Fig. 12.2 (a), (b) Abundances of Sm, Eu and La in HED meteorites. Concentrations of highly incompatible REEs vary in a wide range in HED meteorites, both above and below the chondritic values (large grey rectangles). The concentrations increase in the sequence diogenites, howardites, cumulate eucrites and basaltic eucrites. The scatter in REE abundance in diogenites and cumulate eucrites is due to a trapped melt component. The "flattened" Eu–Sm trend between the cumulate and basaltic eucrites occurs because Eu becomes more compatible once plagioclase becomes a liquidus phase (see Fig. 12.3). From Mittlefehldt *et al*. (1998). Reproduced by permission of the Mineralogical Society of America.

The decoupling of the Eu abundances from the rest of the REE patterns is due to the specific partitioning of Eu in Ca-bearing minerals, e.g. in plagioclase: unlike other REEs this element occurs partly in the divalent state and then has an ion radius similar to that of Ca and readily substitutes for this element. Cumulate eucrites (e.g. Serra de Mage, Fig. 12.3) were formed by the partial crystallization of a melt, and plagioclase, an abundant component of these rocks, consumed Eu. Other REEs stayed in the melt and their concentrations, except for Eu, increased in the course of progressive crystallization. The final products, represented by the

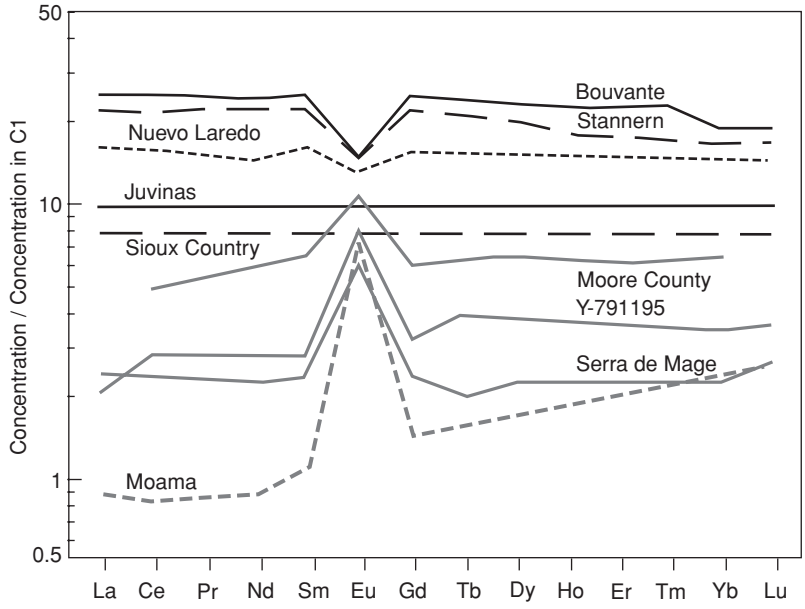

Fig. 12.3 Rare earth elements in basaltic and cumulate eucrites. Cumulate eucrites contain the Ca-bearing feldspar plagioclase. Basaltic eucrites crystallized later from Eu-depleted melts. From Treimann (1997; see the references to the original data there), © Meteoritical Society 1997, reproduced by permission.

basaltic eucrites (e.g. Stannern), show high REE concentrations and a negative Eu anomaly.

The HED meteorites are highly depleted in volatile lithophile trace elements. For example the Rb/Sr ratios, although fractionated in the cumulate-to-basaltic eucrites, are all extremely low, on average almost a factor 100 lower than those in C1 chondrites (compare Figs. 12.7 and 12.8). This is due to the low abundance of Rb, which is depleted along with other volatile elements in HED meteorites, while the refractory Sr has close to chondritic abundances. The consistency of the Rb/Sr ratios for cumulate and basaltic eucrite types shows convincingly that the depletion of Rb in the parent body occurred before magmatic fractionation.

Important is that the alkali metal losses appear to increase not in accordance with their volatility but inversely with the solid–melt partition coefficients. Thus, the more incompatible Rb has a lower volatility but shows higher depletion than K (see Fig. 17.2); similar relationships hold true for Na (Fig. 17.3). This points to a loss mechanism via the vaporization of alkali metals from differentiated melts on the asteroid surface.

In contrast with the involatile lithophiles, the involatile siderophile elements are greatly depleted in HEDs and most other processed stony meteorites. For example, the concentrations of moderately siderophile compatible Co in eucrites (the basaltic

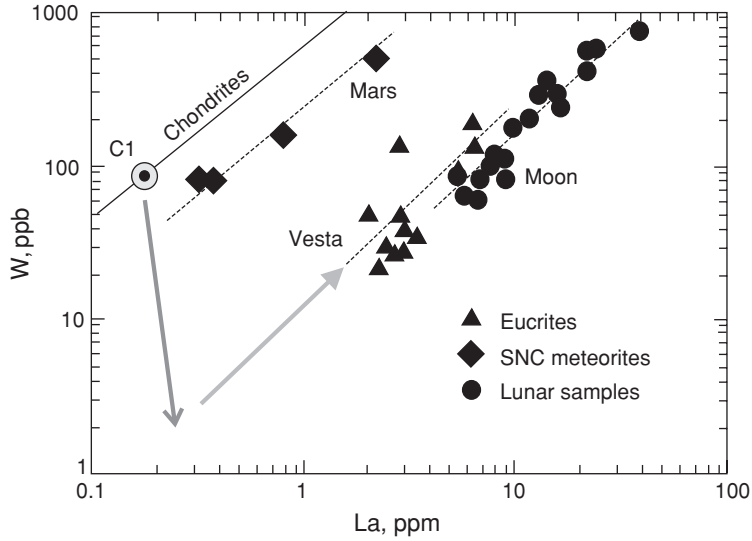

Fig. 12.4 Tungsten vs. lanthanum concentrations in chondrites and basaltic rocks from the Moon and Vesta. Black arrow: when the core is segregating, siderophile W is partitioned into the core and its abundance in silicate matter decreases, whereas the abundance of lithophile La is almost constant (it increases slightly because of the removal of metal). During the subsequent fractionation of silicate matter, [La] and [W], having similar solid/melt partition coefficients, are proportionally increasing in the melts (grey arrow), which then crystallize, giving rise to the lunar and HED crusts. After Drake (2001), © Meteoritical Society 2001, reproduced by permission.

crust of Vesta) and diogenites (the mantle) are ~ 5 and ~ 25 μg g^{-1} respectively (Table 12.2). The latter concentration is thus representative for the bulk silicate shell of Vesta, and it is a factor ~ 20 below the chondritic [Co] value (Table 11.2). In the case of an incompatible siderophile element, e.g. W, the concentration in the silicate part of the parent body needs to be reconstructed. In Fig. 12.4 this is achieved via the correlation with an equally incompatible lithophile element, La, for which the concentration in the silicate matter of the asteroid did not change much during core segregation and therefore is expected to be similar to the precursor chondritic concentration. Extrapolation to the chondritic [La] value ≈ 0.25 ppm gives $[W]_{VESTA} \approx 2$ ppb, which is a factor 50–100 below the chondritic [W] value (Table 11.2).

The segregation of metal in a meteorite parent body and the corresponding redistribution of siderophile elements between the metal and silicate phases clearly emerges as the process responsible for the depletion of the involatile siderophile elements in stony meteorites.

Magmatic iron meteorites

Iron meteorites are greatly enriched in involatile trace siderophile elements in comparison with chondrites but especially relative to processed stony meteorites (Table 12.3). For example, the average [Co] value $\approx 0.5\%$ in IIIAB irons, the largest chemical group, comprising $\sim$ one-third of the iron meteorites; this value exceeds the abundance observed in diogenites by a factor 200. The coefficient is even larger, > 1000, for highly siderophile noble metals, e.g. iridium. Hence even a small liquid metal core, a few per cent of the total mass of a meteorite parent body, could have served as a major reservoir bearing siderophile elements.

Specific abundance trends within the magmatic IIIAB irons (Fig. 12.5) and some other groups of iron meteorites also favour liquid–metal segregation as a process that differentiated parent asteroids (Scott, 1972). The progressive solidification of a segregated initially molten iron reservoir, during which siderophile elements were partitioned between the liquid and solid metal (Eqn 12.8), appears to be the most probable cause of these trends. The almost perfect correlation between Au and As (Fig. 12.5(a)) could arise from their similar behaviour in a solid-metal–liquid-metal system: both elements are equally incompatible, $D_{\mathrm{Au}} \approx D_{\mathrm{As}} \approx 0.4$, in low-sulphur metal magmas. Iridium, in contrast with gold, is a highly solid-compatible element and the difference between the concentrations of these two elements in the melt increases as crystallization proceeds. Droplets of melt trapped by crystallizing solids could then produce the substantial scatter seen in the Ir–Au plot (Fig. 12.5(b)).

Most iron meteorites show a great loss of volatile siderophile elements. This is indicated, for example, by the abundances of siderophile Ag and Ni in iron meteorites. Silver is a moderately volatile element whereas Ni is involatile. Figure 12.6 shows that the Ag/Ni ratio varies within an enormous range, $\sim$ four orders of magnitude, almost all ratios being at least a factor 100 below the solar value (Fig. 12.6). This enormous loss of the highly siderophile Ag could hardly have occurred after it had been partitioned into the metal and thus it appears that it must have happened very early in the history of these meteorites, before the segregation of the metal core of the parent body.

12.4 The chronology of planetesimal processing

The cosmochronology of Rb–Sr and the initial $^{87}Sr/^{86}Sr$ ratios

As briefly discussed in Section 10.3, the most common isochron dating methods use measurements of the parameters of Eqn (10.7a) for several different samples that originated (according to *a priori* data) simultaneously and from the same material. If the samples have remained closed systems, Eqn (10.7a) is valid for each sample,

Table 12.3 *Average compositions of iron-meteorite chemical groups. From Mittlefehldt et al. (1998). Reproduced by permission of the Mineralogical Society of America*

	Ni	S	P	Co	Ga	Ge	Cr	Cu	Mo	Ir	W	Pd	Au	As	Sb
Group	wt %				ppm										ppb
IAB	16	n.d.[a]	0.21	0.46	96	400	16	130	8.2	2.7	1.6	3.5	1.5	11	270
IC	7.1	n.d.	0.43	0.46	52	230	70	160	7.7	0.38	1.3	3.5	1.1	11	98
IIAB	6.1	0.2	0.6	0.53	58	170	38	130	6.9	10	2.1	2.6	1.1	9.9	200
IIC	11	n.d.	0.53	0.65	37	95	87	260	8.4	6.4	n.d.	6	1.1	8.2	150
IID	11	n.d.	0.98	0.47	76	87	31	280	9.4	9.9	2.4	5.3	1.1	10	220
IIIAB	8.5	1.4	0.56	0.5	20	39	40	160	7.2	4.1	1	3.5	1.2	10	265
IIIF	8	n.d.	0.22	0.36	6.8	0.91	210	170	7.2	3.2	1.2	4.4	0.91	11	86
IVA	8	0.8	0.09	0.4	2.2	0.12	140	150	5.9	1.9	0.6	4.6	1.5	7.6	9
IVB	17	0.03	0.1	0.74	0.22	0.05	88	12	27	22	3	12	0.15	1.1	1.5

[a] Not determined.

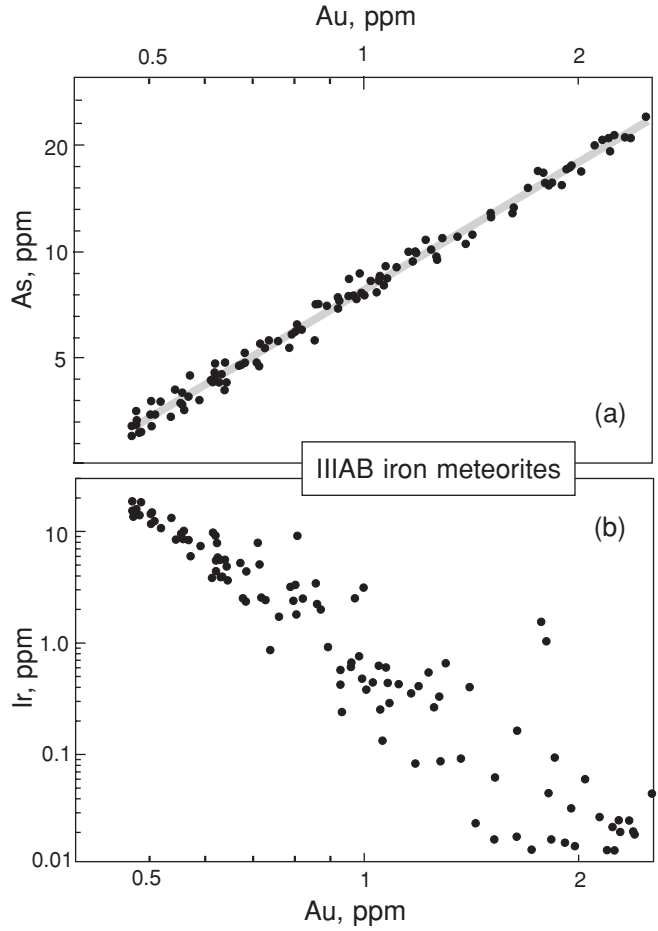

Fig. 12.5 (a), (b) Fractionation of Au, As and Ir in magmatic IIIAB irons. The clear trends reflect the partitioning of the elements between solid and liquid metal in the course of solidification of the metallic cores of meteorite parent bodies. From Wasson (1999), © Elsevier Science 1999, reproduced by permission.

and therefore a set of these equations is available. The factors $({}^{r}D/{}^{s}D)_{INI}$ $(\equiv a)$ and $[\exp(\lambda T) - 1]$ $(\equiv b)$ are expected to be constants for this given set. Therefore the evolution of $({}^{r}D/{}^{s}D)_t$ $(\equiv y)$ as a function of $({}^{r}R/{}^{s}D)_t$ $(\equiv x)$ is expressed by the straight line $y = a + bx$ (an isochron) on a y versus x plot (see the inset in Fig. 12.7), yielding both the age and the initial ratio of the suite of samples.

The method further provides a test for the integrity of the systematics in a sample suite. If the measured $({}^{r}D/{}^{s}D)_t$ and $({}^{r}R/{}^{s}D)_t$ ratios in several different samples constitute a straight line then it can be concluded that (1) the samples originated simultaneously and the regression slope b gives their age; (2) the parent material

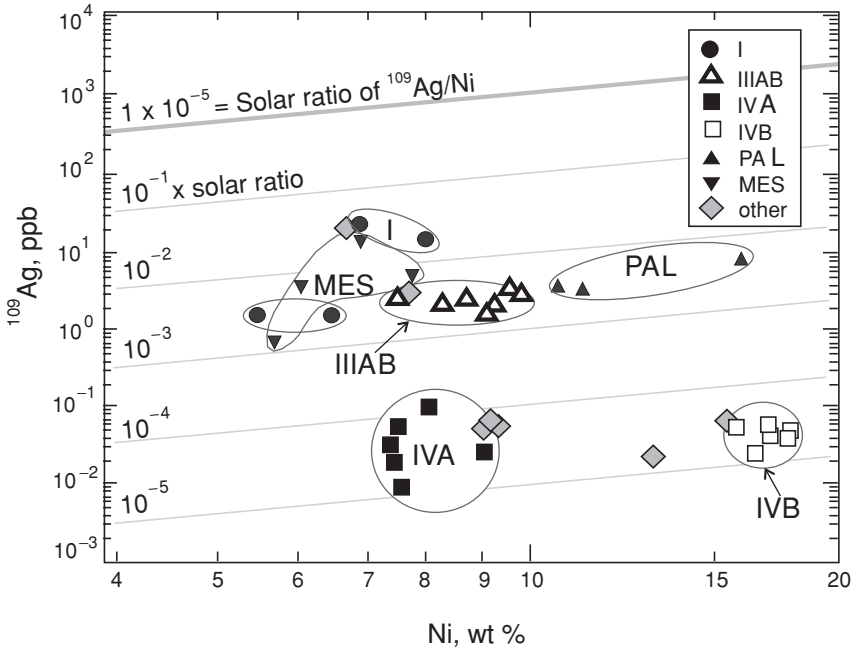

Fig. 12.6 Silver depletion in iron, pallasite and mesosiderite meteorites: Ag shows a strong depletion in a number of iron meteorites, down to 10^{-5} relative to the solar abundance. After Chen and Wasserburg (1996), © 1996 American Geophysical Union, modified by permission.

was homogeneous with the (initial) ratio $({}^{r}D/{}^{s}D)_{INI}$ fixed by the intercept a; and (3) the samples have not experienced loss or gain of the species relevant to Eqn (10.7a).

Figure 12.7 illustrates the results of the Rb–Sr isochron dating of a large number of chondritic and achondritic meteorites: radioactive ^{87}Rb β-decays to ^{87}Sr, and ^{86}Sr is the reference stable isotope. Rubidium is a highly volatile element whereas Sr is refractory (Table 3.1). The proximity of all the data points to a straight line indicates that all these meteorites were formed from the same well-mixed initial material. The age fits (to within the uncertainty limits) with the Pb/Pb ages. The far lower precision of the Rb–Sr isochron compared to the Pb/Pb isochron is a result of the much longer half-life of ^{87}Rb, and, further, it must be noted that there is still a $\sim 1\%$ uncertainty associated with the ^{87}Rb half-life.

Non-chondritic meteorites show extreme Rb depletion, and the range of ^{87}Rb/^{86}Sr ratios in eucrites (Fig. 12.8) corresponds to the extreme left of Fig. 12.7. The age derived from the isochron plot in Fig. 12.8 agrees with other results, indicating that the rocks have remained closed systems for Rb and Sr. Although this age is not highly significant owing to its large error, a precise initial ratio can be obtained.

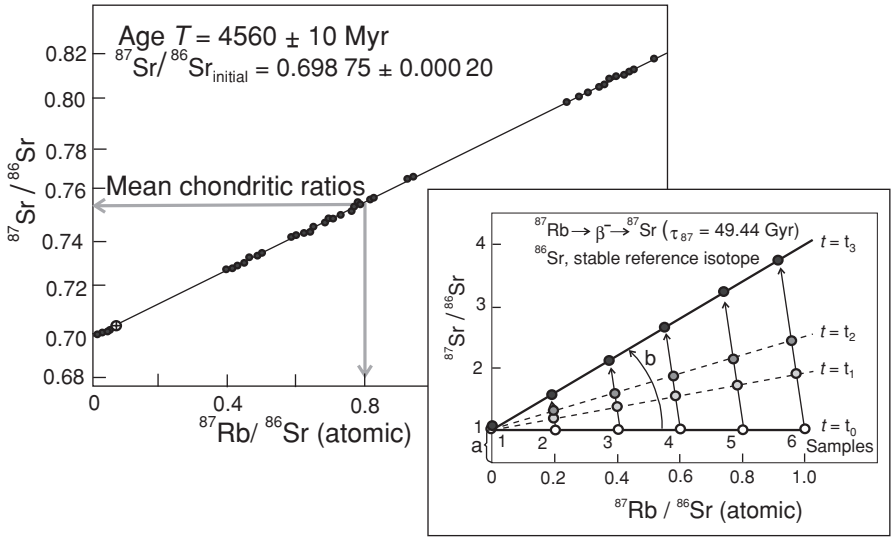

Fig. 12.7 Isochron dating: Rb–Sr systematics in meteorites. The inset at lower right shows the principles of the isochron-dating technique (Section 10.3). The Rb–Sr meteoritic isochron indicates the simultaneous formation of a number of meteorites, the inferred age is similar to the Pb/Pb age but much less precise. After Minster *et al.* (1982).

Further such results for the Lewis Cliff (LEW), Angra dos Reis (ADOR) and Moore County angrites are indistinguishable from each other: $^{87}Sr/^{86}Sr_{INI} = 0.698\,970 \pm 0.000\,015$ (Lugmair and Galer, 1992). Calcium–aluminium-rich intrusions (CAIs), which also have extremely low Rb/Sr ratios, have lower values of $^{87}Sr/^{86}Sr_{INI} = 0.698\,80 \pm 0.000\,03$ in accord with their greater age. Assuming that the achondrite precursors evolved with a Rb/Sr_{SOS} ratio ~ 0.3 since the time of CAI formation would give a reasonable (model-dependent) 10–15 Myr time difference between CAI formation and the achondrites (Papanastassiou and Wasserburg, 1969; Gray *et al.*, 1973; Birck and Allègre, 1978).

The Pb/Pb chronometry of processed meteorites

Lead is a volatile element and is in addition chalcophile and slightly siderophile, while U is a lithophile refractory element. Therefore U–Pb and Pb/Pb systematics provide a suitable chronometer for the events that generated the parent bodies of non-chondritic meteorites generally indicating metal (and probably sulphide) fractionation as well as the loss of volatile elements.

Again, as in the case of CAI dating (Section 10.3), high-μ minerals are most appropriate for Pb/Pb dating. However, because of the extreme Pb loss from achondrite parent bodies, not only phosphates such as whitlockite but also common

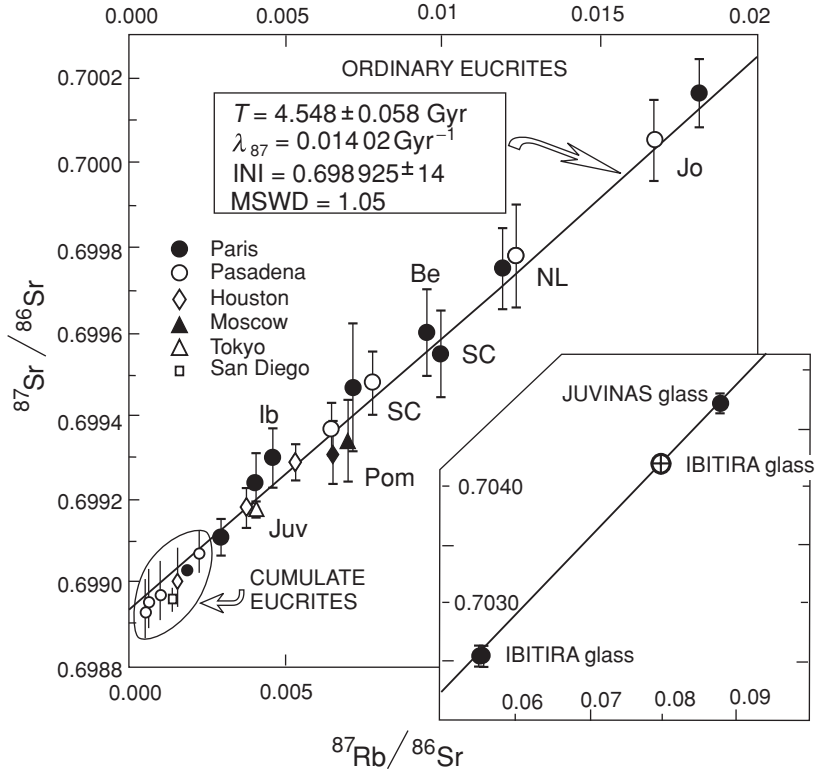

Fig. 12.8 The Rb–Sr systematics of eucrites. Ordinary eucrites show rather low present-day $^{87}Sr/^{86}Sr$ ratios, corresponding to time-integrated Rb/Sr ratios a factor almost 100 lower than the chondritic values (~ 0.85) on average. Even lower ratios are typical for cumulate eucrites. These meteorites exhibit a great loss of volatile Rb early in the history of their parent body. From Smoliar (1993, see references on original contributions there), © Meteoritical Society 1993, reproduced by permission.

silicate minerals such as pyroxenes have high μ values. There are three high-quality Pb/Pb ages for non-chondritic meteorites.

Whole-rock samples of the angrites SAH99555 and NWA1296 show extremely high μ values up to ~ 3000; these samples along with mineral separates and leachates from them yield a Pb/Pb isochron in the $^{207}Pb/^{206}Pb$ versus $^{204}Pb/^{206}Pb$ diagram giving an age of 4566.2 ± 0.1 Myr, which is the most precise absolute date of any early solar system object (Baker *et al.*, 2005). This age is very similar to the chondrite-formation age and both are only ~ 3 Myr younger than the earliest objects of the solar system, CAIs (Fig. 11.6).

Pyroxenes from LEW 86010 and Angra dos Reis also show μ values up to ~ 5500; in this case Pb/Pb dating yields identical ages of 4557.8 ± 0.5 and 4557.8 ± 0.4 Myr respectively for the two meteorites (Lugmair and Galer,

1992; see Fig. 13.1). The dated minerals are not secondary but are direct products of melt crystallization. They do not show signs of later disturbance and therefore yield an age for the magmatic differentiation. The Acapulco meteorite also contains primary magmatic phosphate, which has yielded a Pb/Pb age of 4557 ± 2 Myr, indistinguishable from those obtained for LEW 86010 and Angra dos Reis (Göpel *et al*., 1994).

The difference of almost 10 Myr between two very well-defined and robust dates on similar achondrite parent bodies is surprising. While the older set could record a ^{26}Al heating effect, this is not possible for the younger set, which therefore more probably reflects collision heating. Independently of their precise interpretation, however, these Pb/Pb dates provide reliable absolute-age markers for early solar system history, and have been used to construct combined time scales (Chapter 13; Lugmair and Shukolyukov, 2001; Baker *et al*., 2005).

The Pd–Ag and Hf–W isotopic systematics in irons and achondrites

The extreme depletion of iron meteorites in moderately volatile Ag (Fig. 12.6) and the correspondingly high Pd/Ag ratios allow the measurement of radiogenic ^{107}Ag* and thus the use of the Pd–Ag chronometer for iron meteorites, even though ^{107}Ag is the most abundant isotope of silver. The ^{107}Pd–^{107}Ag systematics (half-life 6.5 Myr; Table 3.3) present an important constraint on the timing of the devolatilization of iron meteorites and associated processes. The best (reference) Pd–Ag evolution diagram was obtained for the Gibeon metal meteorite (Fig. 12.9). The diagram implies closed-system evolution, therefore the slope of the regression line gives the ^{107}Pd/^{108}Pd ratio at the time of the loss of moderately volatile Ag (Eqn 10.10): $^{107}\mathrm{Ag}^*/^{108}\mathrm{Pd} \equiv {}^{107}\mathrm{Pd}/^{108}\mathrm{Pd}_{\mathrm{INI}} = (2.40 \pm 0.05) \times 10^{-5}$. The Canyon Diablo IA iron shows a similar value (Carlson and Hauri, 2001).

High-quality Gibeon-like isochrons are not available for other iron meteorites. However, reasonable assumptions allow the relative chronology of volatile loss events. These assumptions are: (1) the solar nebula was homogeneous with respect to the initial ^{107}Ag/^{109}Ag ratio; (2) a meteorite exhibited a simple two-stage evolution, with solar values of the ratios $^{109}\mathrm{Ag}/^{108}\mathrm{Pd}_{\mathrm{SOS}}$ and $^{107}\mathrm{Ag}/^{109}\mathrm{Ag}_{\mathrm{SOS}}$ before the loss event. Then the measured ratios on a single sample suffice to determine the $^{107}\mathrm{Pd}/^{108}\mathrm{Pd}_{\mathrm{INI}}$ ratio at the time of the event:

$$^{107}\mathrm{Pd}/^{108}\mathrm{Pd}_{\mathrm{INI}} = \left(^{107}\mathrm{Ag}/^{109}\mathrm{Ag}_{\mathrm{MET}} - {}^{107}\mathrm{Ag}/^{109}\mathrm{Ag}_{\mathrm{SOS}}\right) \times {}^{109}\mathrm{Ag}/^{108}\mathrm{Pd}_{\mathrm{MET}}.$$

Substitution of the $^{107}\mathrm{Pd}/^{108}\mathrm{Pd}_{\mathrm{INI}}$ ratios for the meteorite and for Gibeon in Eqn (10.11) gives the age of the loss event relative to the Gibeon age: most meteorites were formed within ∼ 10 Myr after Gibeon (Fig. 12.10).

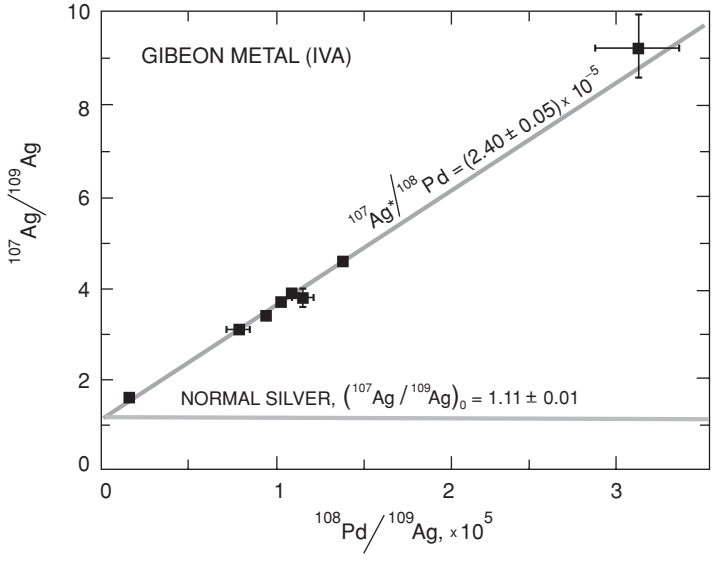

Fig. 12.9 The Pd–Ag evolution diagram for Gibeon metal. The great depletion of Ag makes it possible to measure the excess of $^{107}Ag^{*}$, the product of extinct radioactive ^{107}Pd. From Chen and Wasserburg (1996), © 1996 American Geophysical Union, modified by permission.

The ^{182}Hf–^{182}W systematics are useful for providing time constraints on metal–silicate melt segregation (Section 11.6). Iron meteorites have essentially zero Hf/W ratios and thus record the relative time of metal formation from the nebula, or the last equilibration of metallic melt with silicate melt. The range of ε_{182} in iron meteorites, which is $\pm 0.5\varepsilon_{182}$ relative to the assumed SOS value, along with the respective solar system ratios (Fig. 11.8, Table 3.3) yield model ages within an interval of ~ 8 Myr, again similar to the age ranges discussed above.

It must, however, be noted that a large population of iron meteorite samples plot close to the least radiogenic value. This means either that these highly processed iron meteorites were formed at the same time as the earliest metal particles in chondrites or that they inherited unradiogenic W from their precursors, these same metal particles. The first possibility is unlikely in view of the Pd/Ag chronological evidence and the age relationships between chondritic and non-chondritic meteorites discussed above. The second possibility implies that the assumption of complete isotopic resetting does not hold for the W systematics in iron meteorites; the W-isotopic ratios are more a tracer than a chronometer for these meteorites.

As well as in metal–silicate segregation, Hf/W ratios are fractionated in silicate melting and crystallization processes. Quitté *et al*. (2000) found a large range of Hf/W ratios in eucrites and inferred a time of formation of the eucrite parent body

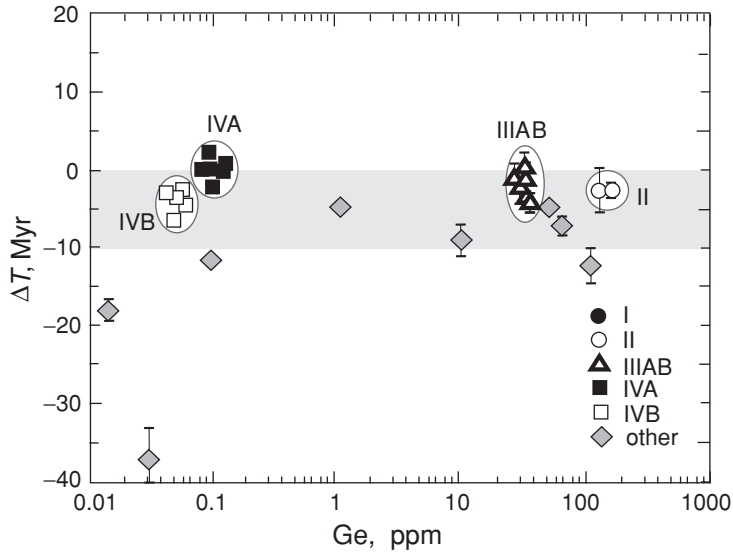

Fig. 12.10 Relative ages for iron, pallasite and mesosiderite meteorites inferred from the ^{107}Pd–^{107}Ag systematics, plotted against Ge content as a measure of volatile depletion. Groups IVA and IVB irons are highly depleted in volatile elements and therefore these meteorites could have originated as metal condensates; correspondingly, the ^{107}Ar*/^{108}Pd = ^{107}Pd/^{108}Pd ratio inferred from the Gibeon isochron is expected to be close to the SOS initial value. Note the short formation interval, within 10 Myr (grey band), for all but two meteorites. This is in agreement with the Sr initial ratio systematics and with the Pb/Pb ages of angrites (Fig. 13.1). After Chen and Wasserburg (1996), © 1996 American Geophysical Union, modified by permission.

shortly (less than 1 Myr) after the Ste Marguerite chondrite; this follows from substitution of the respective initial ^{182}Hf/^{180}Hf$_{INI}$ ratios (Fig. 12.11 and the inset in Fig. 11.8) into Eqn (10.11). A similar time scale follows from a simple two-stage model for the metal–silicate differentiation in Vesta: assuming the SOS abundances of the species of interest during the first stage (Table 3.3), a post-differentiation ^{180}Hf/^{184}W$_{VESTA,MANTLE}$ ratio ≈ 21 and the present-day $\varepsilon_{182} \approx 17$ (Jacobsen, 2005) and substituting these values into Eqn (18.2) gives 2.5 Myr (after SOS formation). Thus core segregation on Vesta occurred very early, at about the same time as the SAH 99555 and NWA 1296 angrite parent body was being formed. The early differentiation of Vesta is further confirmed by the Mn–Cr chronometer.

The ^{53}Mn–^{53}Cr isotope systematics in achondrites

We have encountered the ^{53}Mn–^{53}Cr chronometer in the context of secondary carbonate in a chondrite (Section 11.6). In the course of the processing of asteroid-like

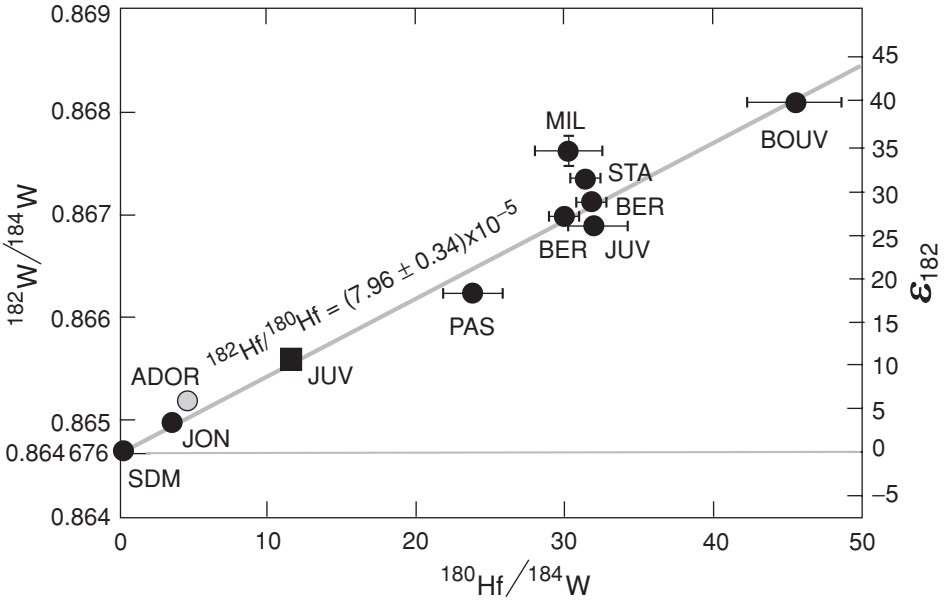

Fig. 12.11 The ^{182}Hf–^{182}W systematics of eucrite meteorites. The best-fit line was calculated without Millbillillie (MIL) and the duplicate for Bereba (BER). See Eqn (19.1b) for the ε notation. Substituting the initial $^{182}Hf/^{180}Hf_{SOS} = 1.01 \times 10^{-4}$ and the inferred $^{182}Hf/^{180}Hf_{INI} = 7.96 \times 10^{-5}$ into Eqn (10.11) gives a ~ 3.1 Myr time interval between the formation of chondrites and silicate fractionation of the eucrite parent body. For meteorite names and classes, see the List of meteorites. After Quitté *et al.* (2000) and Jacobsen (2005).

bodies, both Mn and Cr behave as lithophiles. They are fractionated in silicate melting and crystallization, Cr and Mn entering spinel and Ca-bearing minerals respectively. Therefore the silicate magmatic activity on achondrite parent bodies has led to differences in the Mn/Cr ratio both between batches of magma, which are now individual stony meteorites, and between minerals that crystallized in equilibrium with each other within a single meteorite. The ^{53}Mn–^{53}Cr systematics among minerals of the LEW 86010 and Angra dos Reis meteorites indicate a ^{53}Mn/^{55}Mn ratio equal to $(1.25 \pm 0.07) \times 10^{-6}$ at the time of their crystallization at 4557.8 $\pm$ 0.4 Myr (Lugmair and Shukolyukov, 1998). Thereby the relative ^{53}Mn–^{53}Cr time scale is now also calibrated to an absolute age.

The steepest Mn–Cr isochron found is that yielded by whole-rock howardites, eucrites and diogenites (Fig. 12.12), which gives a ^{53}Mn/^{55}Mn ratio equal to $(4.7 \pm 0.5) \times 10^{-6}$. The HED parent body therefore was likely to have been differentiated 7.1 $\pm$ 0.8 Myr before the 4557.8 $\pm$ 0.5 Myr Pb/Pb age obtained for LEW and ADOR, i.e. at 4564.9 $\pm$ 1 Myr, which is the same time as that when, according to Pb/Pb-isochron age measurements, chondrules (Fig. 11.6) and some highly

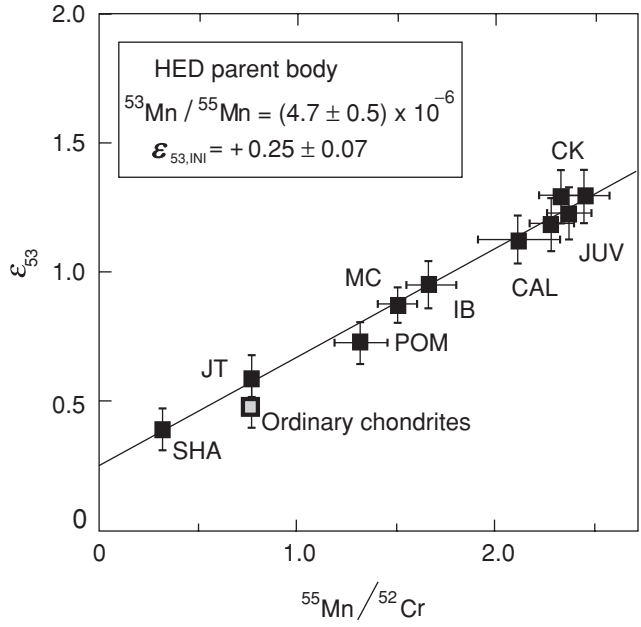

Fig. 12.12 The Mn–Cr isochron for whole-rock samples of the howardites, eucrites and diogenites (HED). The average ordinary-chondrite data point is shown for comparison. The slope of the isochron gives a common $^{53}Mn/^{55}Mn$ ratio for all meteorites separated presumably from a common 4565-Myr-old parent body (see the main text). At that time the precursor material had already evolved to 0.25 ε units (Eqn 19.1b) above the present day terrestrial value. From Lugmair and Shukolyukov (1998), © Elsevier Science 1998, reproduced by permission.

processed meteorites were formed. This shows that the differentiation of asteroids and the formation of parent bodies of non-chondritic meteorites started almost simultaneously with chondrite formation.

Relationships between extinct and live chronometers

In addition to its Pb/Pb age of 4557 ± 2 Myr, phosphate from the Acapulco meteorite has yielded a highly precise ^{129}I–^{129}Xe relative age, 9.26 ± 0.25 Myr younger than that of the Bjurböle chondrite (Brazzle *et al.*, 1999), and this now allows us to assign an age of 4566.3 ± 2 Myr to Bjurböle, whereby the I–Xe relative time scale of Fig. 11.9 is calibrated with much greater precision and confidence than if only chondritic ages were used.

The two calibrations obtained (1) via Acapulco and ^{129}I–^{129}Xe systematics and (2) via angrite ^{53}Mn–^{53}Cr systematics can be compared, as they have independently yielded ages for the feldspar of the Ste Marguerite H4 chondrite. Using I–Xe

systematics and the Acapulco calibration, the feldspar has an apparent absolute age of 4567 ± 2 Myr (Brazzle *et al*., 1999). Using the angrite calibration, a Mn–Cr age of 4565 ± 0.7 Myr results (Lugmair and Shukolyukov, 2001). The second, more precise, result is within experimental error of the first, and the confidence in both approaches is very high. In Chapter 13 these results are considered further and combined with ^{26}Al–^{26}Mg systematics to provide a more complete overview of early solar system chronology.

12.5 Formation of non-chondritic stony and iron meteorites: processes and time scales

Unprocessed clasts in stony meteorites, the mineralogy of silicate inclusions in stony irons, oxygen-isotopery, chronology and other approaches allow a chondrite-like precursor for non-chondritic meteorite parent bodies to be convincingly identified. To develop this precursor into stony, iron and stony-iron meteorites with the major-element compositions and trace-element and isotope abundances discussed in Sections 12.3 and 12.4, four principal processes must operate: the loss of volatile species, the segregation of metal, the fractionation of silicate mantle and the fractional crystallization of metal cores.

Loss of volatile species

Having obtained the depletion factors and time scales from three different isotopic systems involving a volatile and an involatile element, it is important to outline possible processes. The great depletion in Ag and Rb observed in iron meteorites and achondrites cannot have resulted from any equilibrium process such as metal–silicate, metal–vapour or silicate–vapour partitioning. It could only have been caused by the different behaviour of the volatile (Ag, Rb, Pb) and refractory (Pd, Sr, U) elements during a process involving extensive vaporization and recondensation (Chen and Wasserburg, 1996). Iron–nickel alloy is formed first, at 1375 K, and slightly below this temperature Pd is condensed and added to the Fe–Ni alloy. The temperature of Ag metal condensation is substantially, ∼ 300 K, lower. If the metal phase and the vapour phase were separated while the system's temperature was in this intermediate range, this could explain the Ag depletion. The equivalent process involving silicate melt and vapour might also explain the Rb and Pb depletions, for which the condensation temperatures are below 1200 K and 550 K respectively.

One adequate scenario would envisage the formation of a chondrite-like precursor parent body from the nebula gas and dust shortly before (or almost simultaneously with) its magmatic processing, 3–4 Myr after CAI formation. In this case

volatile species, including Ag, Pb and Rb, could be lost in a hot nebula environment during the formation of the parent body. The loss of lithophile elements (especially efficient for incompatible volatile species, e.g. Rb and Pb, which are abundant in the basaltic crust of a differentiated asteroid) could also continue during later post-core-segregation evolution. Within the framework of this early-processing scenario the decay of short-lived nuclides, e.g. ^{26}Al, could serve as a source of heat required for planetary differentiation and volatile loss (Ghosh and McSween, 1998). The cooling of an asteroid at depth could be slow, as shown by Widmanstatten figures in iron meteorites ($\sim 10\ ^{\circ}$C Myr^{-1}) and therefore the younger ages of LEW 86010 and Angra dos Reis could reflect a late magmatic event. Late impact and the related heating is another possible mechanism that would produce these younger ages.

Core segregation

The great depletion of all silicate rocks in involatile siderophiles suggests that the metal separation from silicates was mainly completed by the time the silicate fraction was crystallized. Assuming that small droplets of metal (inherited from a chondritic precursor) were in apparent equilibrium with a silicate melt, then the mass balance of siderophile elements allows both the fraction of metal melt and the apparent partition coefficient to be estimated.

The redistribution of two involatile siderophile elements, Co and W, between metal and silicate phases presents an example. The post-segregation abundances of these elements in the silicate shell of Vesta and in magmatic irons are well constrained, and the chondritic initial concentrations are also known (Tables 12.2, 12.3 and 11.2). Substituting the initial concentrations into Eqn (12.4) and varying the metal/silicate mass ratio and the apparent metal/silicate partition coefficient in order to reconcile the calculated and observed concentrations both in metal and silicate fractions allows the partition coefficients $D(\mathrm{Co})_{\mathrm{LM/LS}}$ and $D(\mathrm{W})_{\mathrm{LM/LS}}$ and the mass fraction F_{MET} to be constrained (Table 12.4).

The inferred fraction of metal, ~ 0.2, suggests a relatively small core on Vesta, and this is in accord with the results of more comprehensive modelling (Righter and Drake, 1996, 1997) and also with estimates of the mantle composition and mean density of the asteroid (Dreibus *et al*., 1997). Metal–silicate partition coefficients vary depending on the O-fugacity, the composition of the metal and silicate fractions and the pressure, temperature and some other parameters. The apparent value obtained from the illustrative calculations above is within the known range (Righter and Drake, 1997). Thus, equilibrium partitioning of involatile siderophile elements between silicate and metal during partial melting of the chondritic precursor emerges as a reasonable approximation to the natural processes.

Table 12.4 *Concentrations in g g^{-1} of the involatile siderophile elements Co and W in precursor material,[a] silicate shell[b] and core of the asteroid Vesta*

Parameters	Co	W
Initial: input concentrations (H-chondrite precursor, Table 11.2)	8.1×10^{-4}	1.6×10^{-7}
Observed: asteroid Vesta (silicate shell)	2.4×10^{-5}	6.4×10^{-9}
Observed: proxy for asteroid Vesta core (IIIAB, Table 12.3)	5×10^{-3}	1×10^{-6}
Inferred: partition coefficients $D_{LM/LS}$	45	35
Inferred: metal/silicate ratio F_{MET}	0.25	

[a] Precursor material of mainly-H-chondrite type was postulated for the asteroid Vesta by e.g. Boesenberg and Delaney (1997), Ghosh and McSween (1998).
[b] The value used for post-segregation [Co] in the silicate shell of Vesta is the mean one for diogenites (Mittlefehldt *et al.*, 1998), and is very similar to other estimates, e.g. Righter and Drake (1996); [W] is from Mittlefehldt *et al.* (1998).

Fractionation of silicate mantle and metal core

Following a concept originally introduced by Mason (1962), a chondrite-like asteroid already depleted in volatiles (particularly in Na) was completely melted; a metallic core segregated and the silicate melt assembled in a magma ocean that engulfed the planetesimal and solidified via fractional crystallization. Within the frame of such a model a vigorous post-core-formation convection of the Vesta magma ocean is postulated, so that crystals would largely remain entrained in a magma flow. Then the crystallization process would follow equilibrium crystallization (Righter and Drake, 1996, 1997). When a substantial portion of silicate matter ($\sim 80\%$ of the total silicate matter) had been crystallized, the convection slowed down, the remaining melt ($\sim 20\%$) was squeezed out of the matrix and floated upwards and erupted to form the eucritic crust.

Taking into account volatile loss and metal removal into the core as discussed above, 80% of equilibrium crystallization yields an olivine–spinel–orthopyroxene assemblage and then a mainly orthopyroxene composition similar to that observed in diogenites. The composition of the partial melt still present would be quite similar to that observed for the main group of eucrites (Table 12.1), the REE abundance exceeding C1 by a factor ~ 10 and showing a slightly fractionated pattern, as observed e.g. for Nuevo Laredo (Fig. 12.3). The compositions of the typical cumulate eucrites (for example, Serra de Mage) can be reproduced adequately by a simple model that considers the rock as a mixture of crystals and intercumulus magma,

providing that there is equilibrium between the growing crystals and magma and chemical closure after accumulation ceases. Early cumulate with an enhanced abundance of Eu-attractive plagioclase would show a Serra-de-Mage-like REE pattern, whereas main-group eucrites, crystallized from a small residual portion of melt, could display the REE abundance pattern observed in Stannern (see Stolper, 1977, and Jurewicz *et al.*, 1993, 1995, for a partial-melting model of the silicate mantle on Vesta).

Along with the fractionation of the silicate materials, siderophile elements within the liquid iron–nickel core were also redistributed between the liquid and crystallizing metal. In the course of fractional crystallization of metal from the metal melt, incompatible siderophile elements, having a solid/liquid partition coefficient $D < 1$, accumulated in the liquid fraction. As crystallization proceeded, their concentrations in the melt increased. Correspondingly, the concentrations in later-crystallized solid portions increased as well. Assuming that post-crystallization redistribution of the elements between the solid portions was negligible, this trend could be "frozen" in the iron meteorites. Other (compatible) elements with $D > 1$ were depleted in melts and, correspondingly, in progressively crystallized solids (Fig. 12.5). These trends indeed confirm fractional crystallization as the principal process forming the solid core (Scott, 1972; Wasson, 1999) and thus convincingly point to substantial melting, the segregation of metal melt and the formation of metal pools within the meteorite parent bodies. The relatively heavy metal melts tended to sink to the central part of a meteorite parent body, where the cooling rates could be slow ($\sim 10\,^{\circ}$C per Myr for IIIAB irons); again this is consistent with the observed equilibrium partitioning, which is generally a slow process.

12.6 Summary: late nebular processes as recorded by non-chondritic meteorites

Non-chondritic silicate and iron generally show a great depletion in moderately volatile lithophile and siderophile elements. The details of this are not well understood, but at the present state of the art it appears that volatile loss started before the differentiation of a parent asteroid and segregation of the metal core (almost simultaneously with, or even in the course of, the accretion of an asteroid) and continued during post-core-segregation evolution.

Among the non-chondritic stony meteorites that originated from magmatic processing, the howardites, eucrites and diogenites (HED), thought to have originated from the asteroid Vesta, provide an example of a complete cogenetic silicate differentiation suite. Magmatic iron meteorites of the group IIIAB complement this by presenting evidence of core segregation followed by cooling and crystallization of the core. Further, both groups of meteorites plot on a single

fractionation trend in the $\delta^{17}O$ versus $\delta^{18}O$ plot. A depletion of the HED group in involatile siderophile trace elements is complemented by their enrichment in the iron meteorites.

The mantle of an asteroid is represented by the orthopyroxenitic diogenites, which are chemically homogeneous, tempting the conclusion that they crystallized from a magma ocean. The cumulate variety of eucrites is coarse-grained and consists of minerals crystallized from this melt, whereas the basaltic type represents the final product of fractionation. Incompatible lithophile trace-element fractionation trends and REE patterns showing positive Eu anomalies in the cumulates and negative ones in the most evolved basalts confirm this cogenetic relationship. Howardites are brecciated, strongly heterogeneous and probably impact-related. Group IIIAB iron meteorites show correlations between trace siderophile elements that indicate a gradual crystallization of the core in their parent asteroid.

Radiometric dating with Pb/Pb and the extinct Mn–Cr and Hf–W chronometers has yielded robust chronologies for the HED suite and some other achondrite families. The HED parent body differentiated $\sim$ 3–4 Myr after CAI formation, almost simultaneously with chondrite formation (or $\sim$ 1 Myr later). The Pb/Pb dating of angrites yields two highly precise dates, 4566.2 $\pm$ 0.1 Myr (the same as for HED meteorites) and 4557.8 $\pm$ 0.5 Myr, $\sim$ 8 Myr later. The formation of differentiated meteorite parent bodies thus starts $\sim$ 3 Myr and extends to $\sim$ 10 Myr after CAI formation. A more complete framework is presented in Chapter 13.

The decay of radioactive isotopes is considered as the most likely heat source for early melting enabling the differentiation of the asteroids, but for later melting events, several Myr or more after the first of such events, an alternate source of heat, e.g. collisions, must be invoked.

13

A summary of early solar system chronology

In Sections 10.3, 10.4, 11.6 and 12.4 the results of dating with various relative and absolute chronometers were reviewed, and time scales for the formation of different solar nebula bodies emerged. In the present brief chapter we attempt to present an overview by combining the results of highly precise and robust Pb/Pb dating with the time differences obtained from extinct-nuclide chronometry for different types of material.

Of the absolute-age determination methods applicable to early solar system history only Pb/Pb dating has so far demonstrated a precision of ± 1 Myr or better, which is comparable with the short-lived nuclide chronometers, and it is the only option for calibrating these chronometers to an absolute time scale. It would be tempting to use Pb/Pb ages on CAIs for this. However, the individual Pb/Pb ages of CAI fragments from the Efremovka meteorite range from 4566 to 4569 Myr, scattering outside the analytical error (Amelin *et al.*, 2002) and in contrast with the consistency of the $(^{26}Al/^{27}Al)_{INI}$ ratios. Further, CAIs, the most ancient solid objects to have been generated in the solar system, have I–Xe relative ages younger than some chondrite matrix samples and this indicates clearly that after their formation, their chemistry was affected to some extent by hydrothermal alteration, which is prevalent in carbonaceous chondrites and appears to have persisted for ~ 10 Myr (Section 11.6). This means that in these inclusions Pb/Pb chronometers may have been affected by subtle alteration: Pb is relatively mobile in hydrothermal systems. Therefore, in spite of the great analytical quality and precision of the Pb/Pb ages of CAIs, they may in fact constitute minimum ages for the actual crystallization process. A better approach to dating this process is a combination of the highly refractory relative Al–Mg chronometer (Section 10.4) and the Pb/Pb-isochron absolute clock applied to non-chondritic meteorites (Section 12.4).

It appears that Pb/Pb dates on magmatic minerals in achondrites are the most reliable absolute ages for meteoritic material and that these should be used for the calibration of short-lived nuclide chronometers (Lugmair and Galer, 1992; Baker

et al., 2005). The most ancient and hitherto most precise Pb/Pb-isochron age of the angrites SAH 99555 and NWA 1296, 4566.2 ± 0.1 Myr, is at present the best of these time markers. The whole-rock-model Al–Mg ages of the above duo are 3.5 ± 0.2 Myr younger than CAI formation, resulting in an absolute age 4569.7 ± 0.3 Myr for these most ancient rocks. In the light of the above discussion, this age appears to be more reliable than the directly measured Pb/Pb-isochron CAI age, 4567 Myr. Another avenue leads from the Pb/Pb age, 4557.8 ± 0.5 Myr, for the angrites LEW 86010 and ADOR via $^{53}Mn/^{53}Cr$ to Ste Marguerite (H4) feldspars and from there via $^{26}Al/^{26}Mg$ systematics to the CAIs. This gives a CAI age equal to 4570.6 ± 0.8 Myr (Lugmair and Shukolyukov, 2001). The error overlaps that of the CAI age found via SAH 99555 and NWA 1296 (Fig. 13.1).

A rounded value of 4570.0 Myr is used hereafter as the absolute age of CAI formation and the solar system (SOS). The similarity of the ages obtained for CAIs using this bridging approach and using angrite sets having two very different ages engenders great confidence in this result. Starting from this age, the early chronology may be quantified using relative and absolute chronometers (Figs. 13.1, 13.2).

(1) According to the $^{26}Al/^{26}Mg$ chronometer, the formation of chondrules (and chondrite parent bodies) occurred 2 ± 1 Myr after SOS (Fig. 11.7); the corresponding absolute age is thus 4568 Myr, preceding the closure of U–Pb systematics in Acfer chondrules, 4565 Myr, obtained by Pb/Pb isochron dating (Fig. 11.6). Another similar age discrepancy is found for minerals in the Ste Marguerite chondrite. Its feldspars were dated by two independent approaches: first via I–Xe systematics and a calibration against Acapulco (4567 ± 2 Myr, Brazzle *et al.*, 1999) and second using the absolute Pb/Pb age of LEW 86010 and ADOR and ^{53}Mn–^{53}Cr systematics (4565.0 ± 1 Myr). However, this age is ∼ 2 Myr older than the Pb/Pb age of the phosphates from this meteorite, 4562.7 ± 0.6 Myr (Lugmair and Shukolyukov, 2001).

Such discrepancies between the robust combined-approach dates and the Pb/Pb ages on mineral phases and chondrules thus appear to be the rule rather than the exception, and we consider it most likely that, as suggested above, the Pb/Pb ages on chondrules and CAIs have been affected by hydrous activity in the parent body. The Pb/Pb ages obtained on phosphate minerals record later events. For instance, the age difference of ∼ 2 Myr between the phosphate Pb/Pb age and the feldspar (Mn–Cr + Pb/Pb) age for Ste Marguerite is not inconsistent with later reheating that produced the minerals in succession.

(2) Volatile loss and the magmatic differentiation of chondrite parent bodies started not later than 4 Myr after SOS or 4566 Myr ago (immediately after or even simultaneously with the formation of chondrites), as is directly constrained from the ages of the most ancient products of these processes, the angrites SAH 99555 and NWA 1296. Using the Pb/Pb model ages of Angra dos Reis and Lewis Cliff 86010,

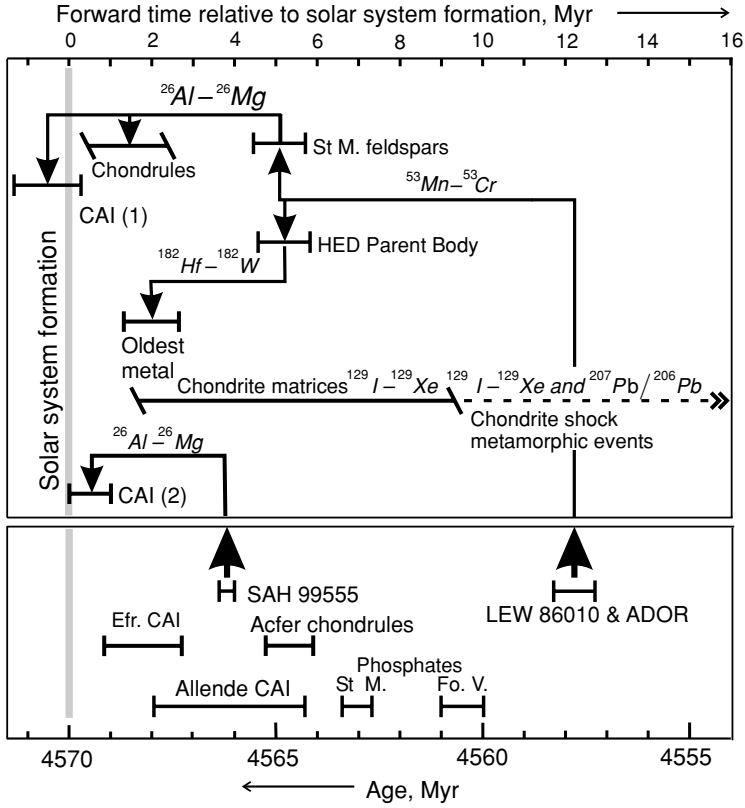

Fig. 13.1 Relative early solar system time scale calibrated to $^{207}Pb/^{206}Pb$ dates on achondrites. The short horizontal lines with vertical terminations indicate error bars and those with oblique terminations indicate ranges. The lower panel gives absolute ages; all the dates shown are $^{207}Pb/^{206}Pb$ ages. St M., Ste Marguerite phosphates (not identical in age to feldspars, see Section 11.6); Fo.V., Forest Vale phosphates; Efr. CAI, Efremovka CAI. The large arrows show the main calibration points: 4566.2 ± 0.2 Myr for SAH 99555 and 4557.8 ± 0.5 Myr for Angra dos Reis and LEW 86010 (Section 12.4). The upper panel shows relative time lines (the horizontal "bridges"); the decay systems determining the time differences are indicated above them. The arrowheads indicate calibrations. CAI (1) and CAI (2), Allende CAI, calibrated via Angra dos Reis/LEW 86010 and SAH 99555 respectively. The vertical grey interrupted line illustrates the calibration of the zero point on the relative time scale to 4570 Gyr, based on the excellent agreement of both "bridged" CAIs obtained via achondrite dates. Note the discrepancy with the $^{207}Pb/^{206}Pb$ ages (lower panel) for both CAIs and chondrules. After Gray *et al.* (1973); Lugmair and Galer (1992); Göpel *et al.* (1994); Allègre *et al.* (1995a); Lugmair and Shukolyukov (1998, 2001); Quitté *et al.* (2000); Amelin *et al.* (2002); Baker *et al*. (2005).

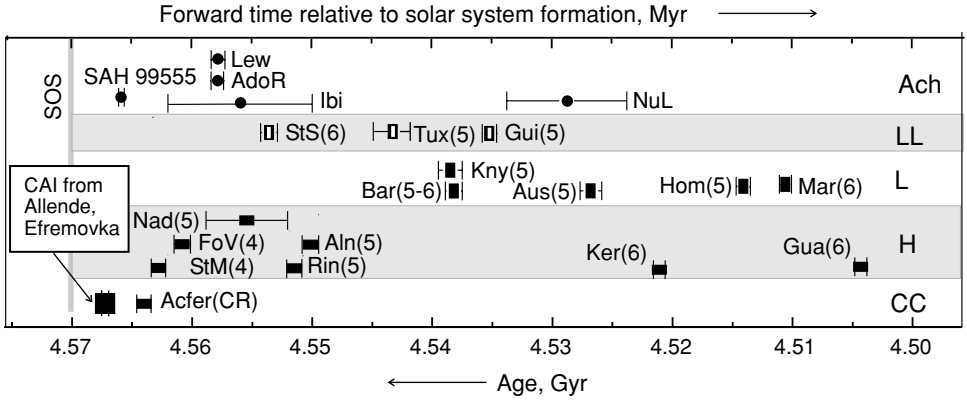

Fig. 13.2 The plot shows Pb/Pb ages for chondritic meteorite parent bodies with, for comparison, those for CAI and processed meteorites. The Efremovka and Allende CAIs show the most ancient Pb/Pb ages (the error bars lie within the symbol). Phosphates in ordinary chondrites were formed ~3 Myr after the CAIs (e.g. Ste Marguerite H4 chondrite). The younger ages of equilibrated chondrites correspond to late (probably collision-related) metamorphic events. The younger ages obtained for some meteorites also probably date post-nebula processes. The chondrite meteorite classes are as in Table 11.1. "Ach" indicates non-chondritic meteorites. See the data sources in the caption to Fig. 13.1.

4557.8 ± 0.5 Myr, and the time difference between formation of these angrites and HED meteorites inferred from ^{53}Mn–^{53}Cr systematics, 7.1 ± 0.8 Myr, gives 4565 ± 1 Myr for HED differentiation, which is indistinguishable from the above age of the early angrites. The decay of radioactive isotopes, in particular ^{26}Al, is thus a realistic source of heat for the early differentiation processes. The somewhat younger ages of such non-chondritic meteorites as Angra dos Reis and Lewis Cliff 86010, given the sharpness of the isochronism and the consistency of their Pb/Pb and Mn–Cr systematics, may be explained by later magmatic events due to slow cooling of the parent body at depth or by collisions.

The ^{182}Hf/^{182}W time constraints can also be coupled with this construct. If the Mn–Cr formation age for the eucrite parent body (4564.9 ± 1 Myr) is considered as given then the time interval, 3.1 ± 0.3 Myr, between the isolation of the least radiogenic W in metal (both in metal particles in chondrites and in iron meteorites) and the differentiation of eucrites (Quitté *et al.*, 2000; Jacobsen, 2005) places the formation of this metal at 4568 ± 1.3 Myr, which is contemporaneous with chondrule formation, as indicated by the LEW 86010 and ADOR age and ^{53}Mn–^{53}Cr and ^{26}Al–^{26}Mg calibration.

From these results, the most refractory matter in the solar nebula, the CAIs, were formed during a short time interval 4570 Myr ago. The formation of chondrite parent

bodies and their magmatic development started ∼2 and ∼ 4 Myr later respectively, with late magmatic events lasting up to ∼10 Myr after SOS formation. Metamorphic events occurred until long afterwards, as recorded by e.g. U–Pb and I–Xe isotopic systematics (Figs. 11.10 and 13.2). Therefore highly differentiated embryos having metal cores and silicate mantle and crust are considered as major building blocks of terrestrial planets, as discussed in Part III of the book.

Part III

Accretion of the Earth

14

Introduction to the planetary system, Earth and Moon

14.1 The solar system: the planets and satellites

The formation of the planets and their satellites is the subject of planetary cosmogony. This is a multidisciplinary field, whose general aim is to understand the origin and evolution of planetary systems, making use of the laws of physics and chemistry, and constrained by the presently observed parameters. Mass and its distribution are indeed important: the planets all together have acquired slightly more than 0.001 of the solar mass (Fig. 14.1). However, these "small" planets are a factor of 10^7 to 10^{10} heavier than their building bricks, the planetesimals, which originated in the solar nebula in the presence of nebular gas (Part II) and are still observable on the margins of the planetary system (Jewitt *et al.*, 1998). From this comparison it is clear that mechanisms allowing the growth of large bodies by the consumption of millions of smaller ones must have operated in the early history of the solar system.

The planets are orbiting the Sun, and the circle-like orbits are all within the same equatorial plane. Almost all the planets rotate relatively rapidly around their own axis and in the prograde direction, i.e. following the rotation of the Sun; Safronov (1966) proposed that the observed spins resulted from stochastic impacts of growing planets with large planetary embryos at a late stage of accretion. From the spin characteristics, impactors would have ranged in mass from 0.01 to 0.1 of the growing planets, except in the cases of Mercury and Venus (Lissauer and Safronov, 1991).

The orbits are remarkably orderly: the ratios between the orbit radii R of two neighbouring planets n and $n+1$ vary within a narrow range, $R_{n+1}/R_n \approx 1.4$–2. This relationship is known as the Titius–Bode law (Vityazev *et al.*, 1990; Ragnarsson, 1995). It is not clear, however, whether this law allows any relevant constraint on planetary formation models to be set or is an implicit outcome of gravitational instability in any flat rotating disk (Graner and Dubrulle, 1994).

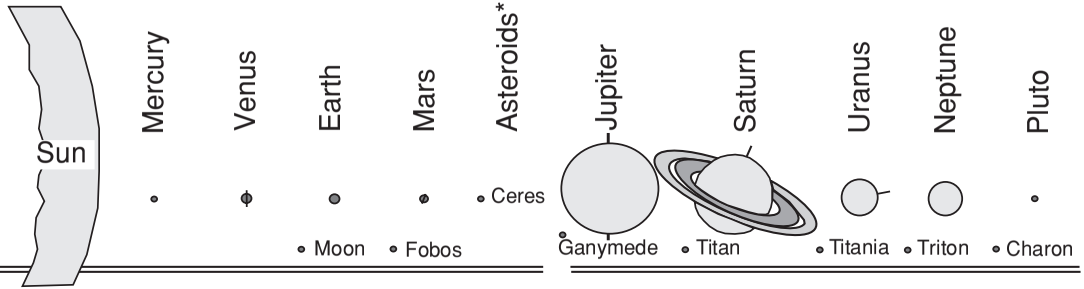

Characteristics	Terrestrial planets[a]						Giant planets[a]				
Distance from Sun (10^6 km):	—	58	108	150	228	415	778	1430	2870	4580	5900
Mass ($M_\oplus = 1$)	3.3×10^5	0.055	0.815	1	0.107	10^{-4}	318	95	14.5	17.1	0.002
Mean density (g cm^{-3})	1.4	5.4	5.2	5.5	3.9	2.7	1.3	0.69	1.26	1.64	2.3
Radius (10^3 km)	696	2.44	6.05	6.37	3.39	0.46	69.95	58.30	25.90	24.76	1.12
Revolution around the Sun (terrestrial years)	—	0.24	0.62	1	1.88	—	11.9	29.5	84	165	249
Revolution around own axis (terrestrial days)	25	58	243R[b]	1	1.03	0.38	0.41	0.44	0.71[c]	0.67	6.4[c]
Eccentricity of the orbit	—	0.2	0.007	0.017	0.093	—	0.043	0.056	0.047	0.01	0.25
Number of known satellites	9	0	0	1	2	5000	16	18	15	8[d]	1
Major constituents of atmosphere	H, He	none	CO_2	N_2, O_2	CO_2	none	H_2, He, CH_4	H_2, He, CH_4	H_2, He CH_4	H_2, He CH_4	Trace CH_4

[a] Only the name of the largest satellite (if any) in a planetary system is given.
[b] Slow retrograde motion.
[c] Retrograde motion
[d] Besides Neptune, millions of comets (planetesimals) constitute the Kuiper belt, typical size ~100 km, total mass ~ $0.1 \times M_\oplus$ and at 50000 AU billions of comets constitute the Oort cloud.

Fig. 14.1 The present-day solar system and its important parameters. After Brown and Mussett (1981).

There are two groups of planets. Closest to the Sun, the internal or terrestrial planets, Mercury, Venus, Earth and Mars are small, dense and spin slowly. In contrast the external or giant planets, Jupiter, Saturn, Uranus and Neptune are massive but less dense and spin faster (Fig. 14.1).

These physical aspects of planetary cosmogony have attracted the attention of generations of scientists, and as a result an accretionary model (also termed the standard model) has emerged that is physically realistic and predicts observations, at least for the terrestrial planets. A detailed discussion of the model is beyond the framework of this book; instead we only briefly introduce it with regard to Earth and Moon formation (Chapter 15) and in its energetic aspects, which are important for the early development of their matter (Chapter 16). For the detailed study of Earth and planetary accretion we refer to the books by Safronov (1969), Vityazev *et al.* (1990), Canup and Righter (eds.) (2000) and Lewis (2004), the review articles by Wetherill (1990), Ahrens (1990) and Weidenschilling (2000) as well as original contributions (Chambers and Wetherill, 1998, 2001; Agnor *et al.*, 1999; Wetherill and Inaba, 2000; Canup, 2004).

In order to understand the evolution of matter in the course of planetary accretion, it is useful to compare the post-accretion composition of a planet with the potential proto-planetary materials inferred from observations on meteorites, comets, planetary satellites etc. as well as from models of the early solar nebula. It is difficult to reconstruct the bulk compositions of present-day differentiated planets, and therefore such comparisons might be far from straightforward. Isotopic arguments, however, leading to constraints on source materials, processes and time scales, appear to be especially valuable.

14.2 A first look at the post-accretion Earth and Moon

Physical aspects of the early Earth–Moon system

What did the post-accretion Earth–Moon system look like? Let us first discuss our home planet, the Earth. The Earth is one of the four rocky planets formed in the inner nebula of the Sun (Fig. 14.1). While the densities of these planets vary in a modest range, implying that they consist of similar material, the "twin" planets Earth and Venus acquired more than 90% of the mass, leaving only $< 10\%$ for Mars and Mercury. Even though very similar in mass and density, the "twins" had a different infancy, shown by a tremendous contrast in their spins. These not only differ by a factor of ~ 250 (!) but also show opposite directions of rotation: prograde for the Earth and very slow and retrograde for Venus. The eccentricity of the Earth's orbit is a factor 2.5 larger than that of Venus. The Earth has a satellite, the Moon, in contrast to its childless sister. So terrestrial planets are not at all a uniform

family, contrary to what might be expected from a possible similarity of the starting material.

Returning to the Earth, it should be emphasized that independently of how we observe the planet, whether by looking at it from space or by travelling with seismic waves in the deep planetary interior, we arrive at the conclusion that the mass is heterogeneously distributed: at least two very distinct large reservoirs must exist. For instance, the moment-of-inertia factor for a homogeneous Earth with mass $M_\oplus = 1\ \mathrm{M}_\oplus$ and equatorial radius a would be $C/(M_\oplus\, a^2) = 0.4$, where C is the moment of inertia of this homogeneous sphere. The value 0.33 obtained from the observational data, e.g. from satellite trajectories (Lewis, 2004), is well below this estimate, indicating that some heavy material is concentrated close to the Earth's centre.

This heavy material is almost certainly metal: the mean density of the Earth is 5.5 g cm^{-3} and its uncompressed bulk density, 4 g cm^{-3}, is too high for silicate minerals and is similar to the density of primitive ordinary chondrites containing $\sim 30\%$ iron (Fig. 14.2, see also Fig. 11.1). Assuming that Fe (with some alloyed elements, e.g. Ni but also some lighter elements, Section 18.1) has been segregated into a metal core ($\rho_{\mathrm{COR}} \sim 12$ g cm^{-3}) covered by a silicate mantle ($\rho_{\mathrm{BSE}} \sim 4.4$ g cm^{-3}, where the subscript BSE means bulk silicate Earth), such a configuration gives about the right values for the mean Earth density (5.5 g cm^{-3}) and for the observed moment of inertia factor (0.33). Indeed the geophysical data, first of all seismology, have provided a detailed picture of a deep Earth having a metal core surrounded by a silicate mantle (Fig. 14.3). There is little doubt that the gravitational segregation of the core was related to the process of Earth accretion and that the core had already been almost completely formed at the time of our inventory, 4.45 Gyr ago (Chapter 18).

The Moon, even though it has only 1.23% of the Earth's mass, should not be considered as a small satellite: the total mass of Jupiter's satellites constitutes a much smaller part of the host planet, and this holds for other planets with satellites except for the Pluto–Charon duo (Lewis, 2004). The Moon is a less dense body than the Earth: its uncompressed density is $\rho_{\mathrm{LUN}} = 3.34$ g cm^{-3}, which is also below the density of ordinary chondrites (Fig. 14.2).

The Moon, gravitationally bound to the Earth, raises tides in the Earth, and the frictional dissipation of energy by tidal motions has slowed down the Earth's rotation from an initial value of about 5 hours to 24 hours per revolution (e.g. Pritchard and Stevenson, 2000). However, the Earth–Moon angular momentum, $L_{\mathrm{EM}} = 3.5 \times 10^{41}$ g cm^2 s^{-1}, remains unchanged since the formation of the duo and, correspondingly, the Moon is slowly spiralling away from the Earth. This large angular momentum provides an important physical constraint on the accretion process (Stevenson, 1987). A further important feature of the Earth–Moon system

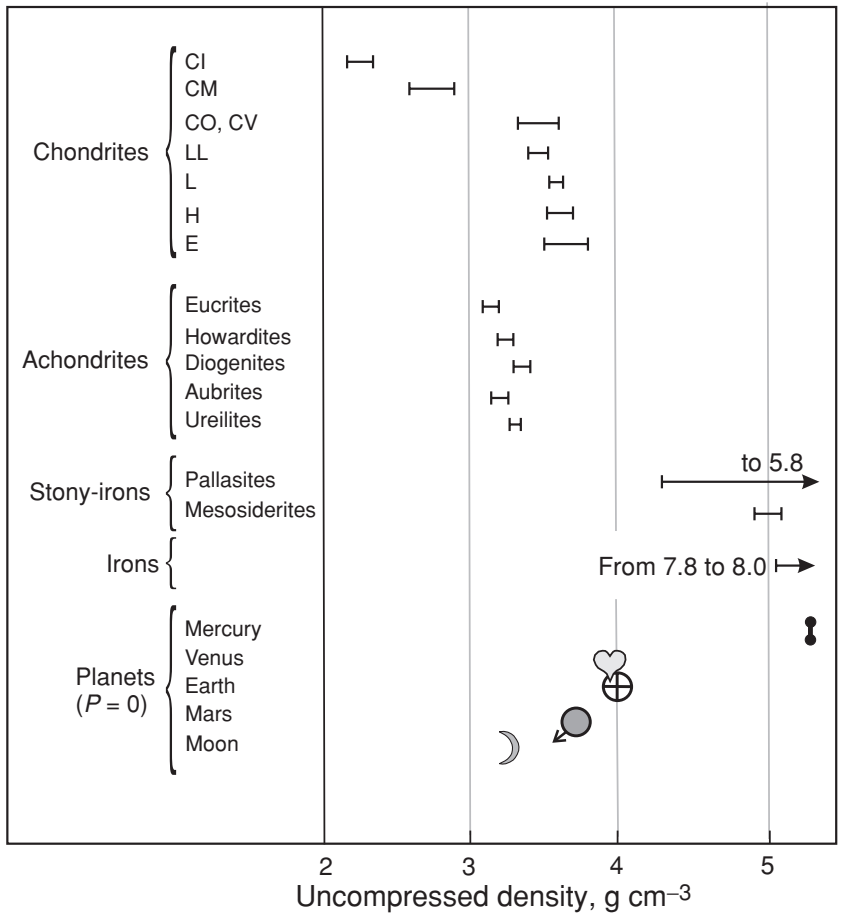

Fig. 14.2 Uncompressed (zero-pressure) densities of meteorites and rocky planets. The densities of the planets (except Mercury) are only slightly above those inferred for ordinary chondrites. After Lewis (2004).

is that the ellipse-like lunar orbit is inclined at 5.1° to the plane of the ecliptic, whereas the axial plane of the Earth is inclined at 23.4°. These parameters of the Earth–Moon system point to a giant impact at a time when the Earth was already a large planet.

Chemical aspects

Specific features of planetary accretion have left imprints in (and can therefore be reconstructed from) the major- and trace-element compositions and isotopic data. Of the major elements, O, Mg, Si and Fe are by far the most abundant in the Earth,

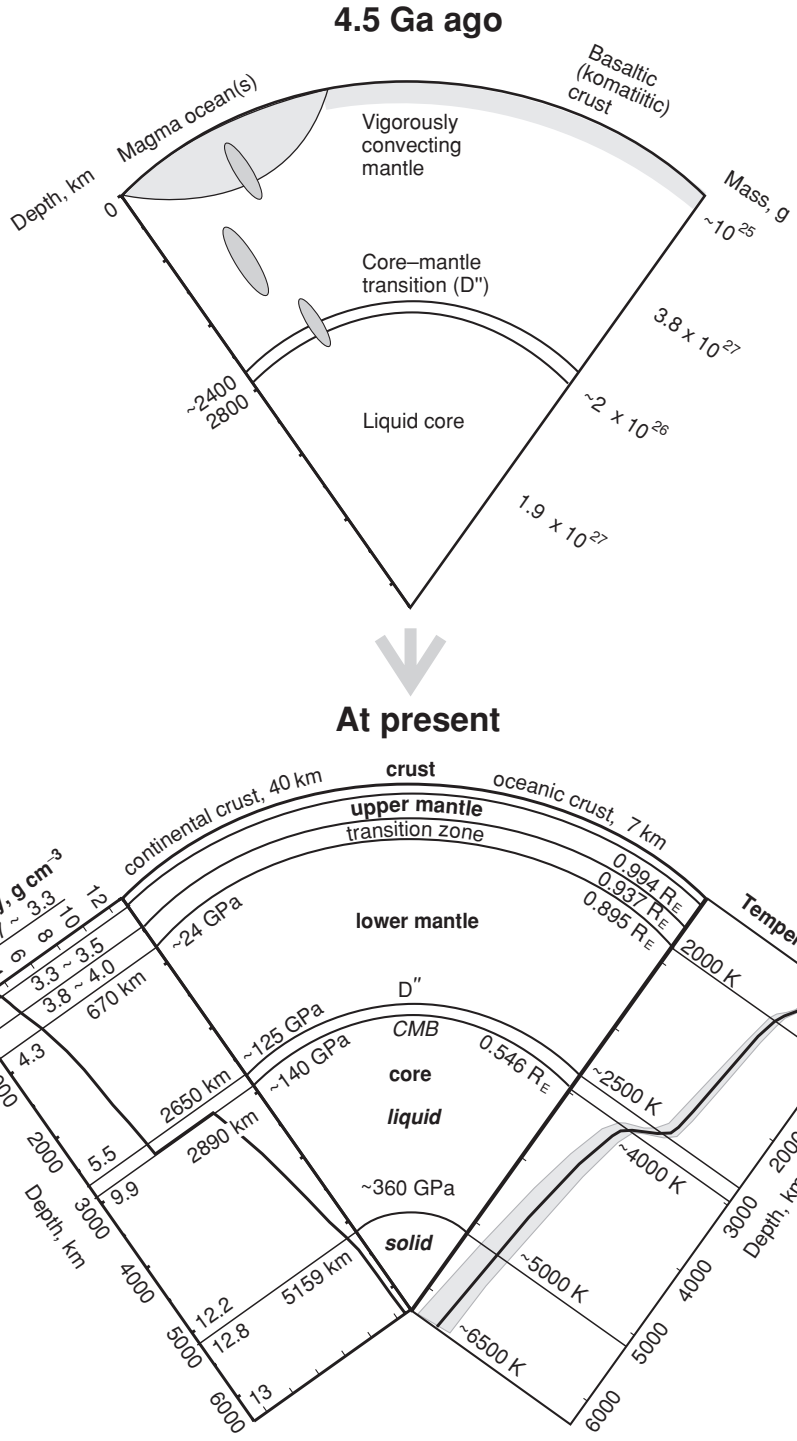
4.5 Ga ago
Basaltic (komatiitic) crust
Magma ocean(s)
Vigorously convecting mantle
Depth, km
0
Mass, g
~10^25
Core–mantle transition (D")
3.8 x 10^27
~2400
2800
Liquid core
~2 x 10^26
1.9 x 10^27
At present
crust
continental crust, 40 km
oceanic crust, 7 km
upper mantle
transition zone
0.994 R_E
0.937 R_E
0.895 R_E
lower mantle
~24 GPa
Density, g cm^-3
2.7 ~ 3.3
3.3 ~ 3.5
3.8 ~ 4.0
670 km
D″
~125 GPa
CMB
~140 GPa
0.546 R_E
core
liquid
2650 km
2890 km
~360 GPa
solid
5159 km
4.3
5.5
9.9
12.2
12.8
13
Depth, km
Temperature, K
2000 K
~2500 K
~4000 K
~5000 K
~6500 K

Moon and terrestrial planets (Section 11.1). The distribution of iron between the core ($\sim 80\%$) and silicate Earth ($\sim 20\%$) is one of the most important features relevant to the conditions during accretion, which must have been highly reducing otherwise most iron would occur in an oxidized form, as in e.g. the C or L chondrite parent bodies (Fig. 11.1). The uncompressed density of the Moon is much lower (Fig. 14.2). This is due to a much lower abundance of metal in the Moon than in the Earth, a difference that is an important constraint on Moon-origin models.

Moderately volatile elements are also considered to be sensitive tracers of accretionary processes. The K/U ratio presents a unique opportunity to compare the volatile-element depletion of terrestrial and lunar materials. Both elements are lithophile and differences in the metal abundance do not affect them: they are readily concentrated in planetary silicate mantle and crust. Their geochemical behaviour is also similar: they generally partition in a melt without substantial relative fractionation and independently of melt composition. Therefore K/U abundance ratios reflect the compositions of presumably large homogenized source reservoirs. The principal difference is that K is a moderately volatile element, whereas U is refractory (Table 3.1). Both elements are radioactive and their abundances can be investigated using satellites or aeroplanes, so K/U ratios of planetary surfaces are better known than for most other elements. Another suitable ratio of a volatile and an involatile element, Rb/Sr, can be derived from the respective isotopic systematics, and Fig. 14.4 presents both ratios for meteorites and the planets. Because of the fully identical O-isotope composition of the Earth and Moon (Fig. 10.8(b)), we may assume a common starting material and examine the K/U and Rb/Sr ratios, as differences in these would be the result of processing of this starting material in the course of accretion.

The Earth's relative K and Rb depletion, a factor ~ 3 larger than that in primitive meteorites, could have occurred very early, during the formation of "terrestrial chondrite" matter (using a term suggested by M. Drake) in the Earth's feeding zone. This was closer to the Sun than the asteroid belt (Fig. 14.1), and agglomeration of its chondrite-type parent bodies probably happened at a higher temperature than

←

Fig. 14.3 A primitive proto-Earth at the end of accretion ~ 4.5 Gyr ago (top) and the present-day differentiated planet (bottom). The top panel presents the principal terrestrial reservoirs that continued to grow slowly as late accretion proceeded; the dark blobs are metal downwelling diapirs. Bottom panel: the central segment shows the structure of the deep Earth; the numbers are pressures and fractions of the Earth's radius R_E. The left-hand segment shows a smoothed density profile; the numbers are the depths of the principal transition zones and densities. The right-hand segment shows the temperature profile; the numbers are the temperatures of the principal transition zones. After Lowrie (1997) in accordance with Boehler (1996) and Taylor (2001).

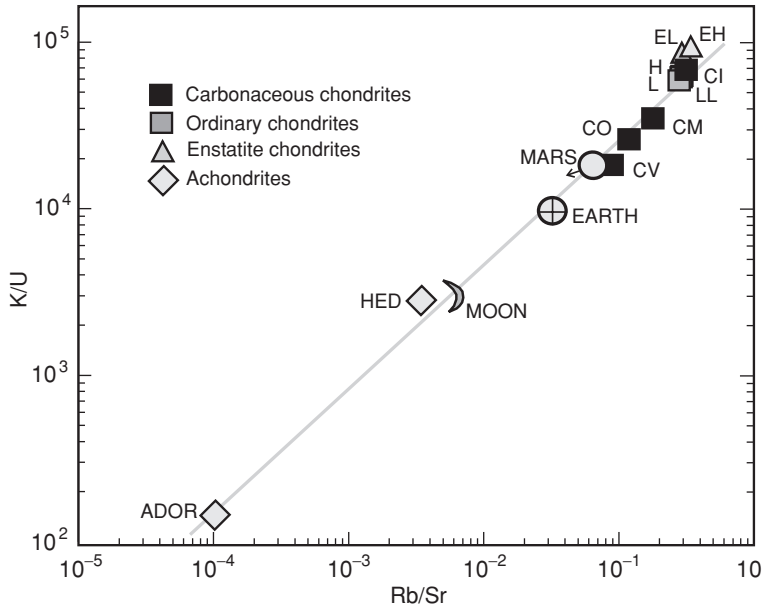

Fig. 14.4 The K/U and Rb/Sr (weight) ratios for meteorites and planets. Note the good correlation, implying the coherent behaviour of the alkali metals in the course of loss of these moderately volatile elements. The Moon and meteorites from the asteroid Vesta (HED) show a similar depletion in alkali metals, as do Mars and the CV carbonaceous chondrites. From Allègre *et al.* (2001), © Elsevier Science 2001, reproduced by permission.

that shown by chondritic meteorites (Fig. 9.1). The K/U and Rb/Sr ratios of lunar rocks are a factor ~ 3.5 below those for the silicate Earth and at least a factor ~ 10 below those for chondritic meteorites. The proto-Moon material was formed in the same feeding zone as the Earth, and therefore the differences in the K/U and Rb/Sr ratios between the Earth and Moon need a special explanation. A further constraint is that the loss of moderately volatile elements (e.g. K, Rb) was not accompanied by measurable isotope fractionation. Some authors (e.g. Halliday and Porcelli, 2001) have considered that the additional loss of moderately volatile elements from the Moon could be linked to a process of Moon formation, involving a giant impact. However, eucrites, magmatically processed meteorites from Vesta, are in many aspects almost indistinguishable from lunar basalts and also show a strong depletion in volatile elements (Figs. 14.4, 17.2(a), (b)). Therefore other authors (e.g. Ruzicka *et al.* 2001) have argued that this aspect of lunar chemistry could be inherited from a proto-planetary stage. This problem is discussed further in Section 21.2.

Summarizing, the spins and orbiting parameters of the terrestrial planets are very different, implying an important role for stochastic factors in the course of accretion. The large angular momentum of the Earth–Moon system is an important

constraint for any adequate model of its formation. Further, the clear differences in the post-accretion chemistry of the Earth and Moon, outlined above, must have resulted from differences in their accretion histories.

A Moon-formation model that explains all these observations would naturally be favoured. Such a model would be instructive about the process of planetary accretion as a whole.

15

Introduction to planetary accretion

15.1 Orderly growth

As mentioned earlier, the planets are heavier than planetesimals by many orders of magnitude, and collisional accretion emerges as the only adequate process for their formation. The implicit energetics of such accretion could affect the final composition, structure and orbital parameters of the planets and satellites. Therefore in this and Chapter 16 we will discuss some physical aspects of accretion, highlighting those aspects responsible for the compositional development of proto-planetary materials.

As planetesimals accreted into larger bodies, e.g. planetary embryos ($\sim 10^{25}$ g) and terrestrial planets ($\sim 10^{27}$ g), gravitational interactions became significant. Perturbations by close encounters caused random velocities of the bodies orbiting the Sun within a given feeding zone. The magnitude of the disturbance depends on the sizes involved. The collision rate, which affects the size distribution, is in turn strongly dependent on the relative velocities. Therefore the sizes and velocities and as a consequence the eccentricities and inclinations of the bodies evolve together, and the details of their interdependence determine the outcome of the evolution.

The collisional cross section θ of a planetesimal with mass m and radius r approached by a potential impactor is

$$\theta = \pi r^2 \left(1 + V_{\mathrm{ESC}}^2 / V_{\mathrm{REL}}^2\right) \tag{15.1}$$

where $V_{\mathrm{ESC}} = (2Gm/r)^{1/2}$ is the escape velocity from the surface of the planetesimal and V_{REL} is the relative velocity of the impactor (e.g. Weidenschilling, 2000). The planetesimal gains mass at a rate $\mathrm{d}m/\mathrm{d}t$ proportional to the cross section θ, the amount of potentially available material (expressed as a space density δ) and the relative velocity V_{REL}:

$$\mathrm{d}m/\mathrm{d}t = \delta V_{\mathrm{REL}}\, \theta. \tag{15.2}$$

Initially the disturbed orbits and the small masses of the bodies ensure that $V_{REL} \gg V_{ESC}$. Therefore (other things being equal) $dm/dt \propto r^2$ and the growth rate becomes

$$(1/m)\, dm/dt \propto 1/r, \tag{15.3}$$

which means the relatively faster growth of a smaller body in the "swarm" of objects orbiting the Sun. This stage is generally referred to as "orderly growth" (Safronov, 1969; Wetherill and Stewart, 1993; Kortenkamp *et al.*, 2000).

15.2 Runaway growth

As accretion proceeds, collisions evolve towards both an increase in the relative velocities V_{REL} (especially of the lighter bodies) and the equipartition of energies, so that more massive bodies are damped to lower velocities (Wetherill, 1990; Kortenkamp *et al.*, 2000). Meanwhile V_{ESC} grows monotonically with the mass of the growing planetesimals, and at some stage of the accretion the inequality $V_{ESC} > V_{REL}$ is achieved, at least for the more massive bodies. Then $dm/dt \sim r^4$ and

$$(1/m)\, dm/dt \propto r, \tag{15.4}$$

showing that the growth rate of larger bodies, the embryos of future planets, is favoured at that stage. This is termed "runaway growth" (Weidenschilling, 2000).

Runaway growth within the swarm of objects orbiting the Sun is restricted to a feeding zone $a \pm \Delta a$ (a is the distance from the Sun), from which a growing planetary embryo with mass m is able to consume smaller planetesimals; the half-width of this zone Δa is given by

$$\Delta a = K R_H. \tag{15.5}$$

Here the Hill radius $R_H = a(m/3M)^{1/3}$, where M is the mass of the Sun, and $K \sim 2 \times (3)^{1/2}$ for close-to-circular orbits (Wetherill, 1990; Weidenschilling, 2000). After the embryo has consumed all the smaller bodies within $\pm \Delta a$, its mass is

$$m_{MAX} = 2\pi a \Delta a\, \sigma \tag{15.6}$$

where σ is the surface density of the feeding zone. Assuming that the mass of the solid matter between 0.5 and 1.5 AU is $\sim 2\ M_\oplus$ (Fig. 14.1) and that it is homogeneously distributed within this interval, then substitution of the above values in Eqns (15.5) and (15.6) gives $\Delta a \sim 0.025$ AU at $a = 1$ AU and a maximum mass $m_{MAX} \sim 0.05\ M_\oplus$.

According to these estimates, runaway growth occurs more or less independently in each interval Δa and as a result ~ 40 closely spaced mini-planets are produced instead of four terrestrial planets, two of which contain almost all the matter in their

combined feeding zones. The time scale inferred from the modelling of runaway growth is estimated at ~ 0.1 to 1 Myr (Vityazev *et al.*, 1990; Wetherill, 1990; Weidenschilling, 2000).

15.3 Planet formation

The modelling of the final stage of planetary accretion starts from an array of a few tens of mini-planets (Chambers and Wetherill, 1998). Their initially circular orbits are gradually altered by gravitational perturbations until they are no longer isolated from each other. Then close encounters occur and further increase their orbital eccentricities, so that many orbits soon cross those of neighbouring bodies. The system becomes chaotic, allowing collisions causing the merging or fragmentation of planetary embryos and the efficient mixing of proto-planetary matter ("homogeneous accretion"). Gravity plays a dominant role in determining the outcome of collisions. The mean ejecta speeds resulting from large-body collisions do not generally exceed the escape velocities (Benz *et al.*, 1994; Benz and Asphaug, 1999). It thus appears that fragmentation has only a modest effect on the accretion rate. The largest bodies are predicted to experience one to several giant impacts late in their growth, and the present-day spin and eccentricities of the terrestrial planets reflect these stochastic events. Also, these highly energetic impacts affected the chemical composition of the planets (Chapter 16). Eventually the remaining planets were so few and widely spaced that their orbits no longer crossed or influenced each other and the system became stable.

The time scale for the formation of terrestrial planets and the establishment of stable orbits as modelled by numerical simulations is between a few tens of Myr and ~ 100 Myr (Chambers and Wetherill, 1998; Chambers, 2004).

The succession of orderly growth, runaway growth and planet formation as outlined above is known as the standard model of planetary accretion.

16

Earth accretion: the giant impact(s)

16.1 Giant impacts: impactor mass and energy deposited

Giant collisions and the merging of massive bodies, $\sim 10^{27}$ g, during the late stages of planetary accretion are a straightforward prediction of the standard model (Wetherill, 1990). Probably the Moon was formed by the giant impact of the proto-Earth with an approximately Mars-sized proto-planet. Modelling, both analytical (Vityazev *et al.*, 1990) and numerical (Benz *et al.*, 1986, 1987) predicts that impacts between planet-sized bodies must be far from elastic and that most of the energy released must be deposited within the growing planet.

For the Earth–Moon system, the impactor mass $m_{\rm IMP}$, its velocity $v_{\rm IMP}$ and the "off-centre" or impact parameter $b_{\rm IMP}$ together determined the system's total angular momentum $L_{\rm EM} = m_{\rm IMP} v_{\rm IMP} b_{\rm IMP} = 3.5 \times 10^{41}$ g cm^2 s^{-1}, provided that $L_{\rm EM}$ resulted only from the impact (Melosh *et al.*, 1993). The value of each individual quantity is uncertain; nevertheless reasonable estimates are possible. High-resolution numerical modelling of the giant impact suggests a proto-Earth mass at the time of collision of equal to 0.8 to 0.85 $M_\oplus$ (Canup, 2004). The escape velocity $v_{\rm ESC}$ from such a body is $\sim 10^6$ cm s^{-1} (see Eqn 15.1), and this equals the lowest possible relative velocity of the impactor; $v_{\rm IMP} \geq v_{\rm ESC}$. For the off-centre parameter $b_{\rm IMP}$, a value $\sim 5 \times 10^8$ cm (the centre of the impactor grazes the surface of the proto-Earth) would result in the observed high angular momentum of the post-impact Earth–Moon system. The three values $L_{\rm EM}$, $v_{\rm IMP}$ and $b_{\rm IMP}$ then give an impactor mass $m_{\rm IMP} \sim 10^{27}$ g, which exceeds the mass of Mars.

The energy released in such a collision is the sum of the kinetic and gravitational energies and could reach $\sim 5 \times 10^{38}$ erg or $\sim 10^{11}$ erg g^{-1} (Melosh *et al.*, 1993). This energy and the mean silicate heat capacity ($\sim 10^7$ erg g^{-1} K^{-1}) would give a mean temperature of the proto-Earth of $\sim$10 000 K, exceeding the vaporization temperature of any terrestrial matter. Although melting and vaporization are endothermic, and the heat may have been very unevenly distributed, this

simple estimate nevertheless illustrates that a giant collision is expected to result in widespread melting and some vaporization.

16.2 The post-impact Earth model

Modelling shows that the giant impact had a major effect on the evolution of the planet. It is expected that the distribution of the impact energy was highly heterogeneous in space and time. The sizes of the target and the impactor imply that both already had iron cores (Section 12.5). The energy released in this process heated the impactor core up to many thousands of degrees, causing it to melt and partially evaporate (the latter process is the most heat consuming) and the temperature of the Earth's mantle could have risen to more than 3000 K, which is above the melting temperature of silicate rocks even at high pressures. Models of this complicated process and their results have been discussed in the scientific literature for more than 20 years (Benz *et al.*, 1986, 1987, 1989; Stevenson, 1987; Cameron, 2000, 2001b; Canup and Asphaug, 2001; Canup, 2004).

Furthermore, the modelling tells us that a huge crater, almost covering the facing overheated hemisphere, would be formed and rocky material thrown out to form a disk around the proto-Earth (Melosh *et al.*, 1993). Part of the ejected material, mainly the silicate mantle of the trailing hemisphere of the impactor, would have escaped beyond the Roche limit mostly as partially molten clumps. The Moon would have been formed from these bodies soon afterwards, probably within ~ 1000 years (Pritchard and Stevenson, 2000).

Vaporization, causing the severe loss of volatile elements, occurred at the ejection stage, when a layer of hot, mainly silicate, vapour flowed around the proto-Earth and covered it. This dense, hot, thick atmosphere also received energy from the re-accretion of ejected material. The temperature increased with height, thus preventing convective cooling and extending the lifetime of the silicate atmosphere. Before the silicate component of this atmosphere condensed and fell back to Earth, the high temperatures in its upper reaches would have promoted the thermal escape of even the heavy elements (Benz and Cameron, 1990; Cameron and Benz, 1991).

The fate of the initial atmosphere during the giant impact is not clear (Melosh, 2003). Some models envisage its almost total loss by escape of the impact plume, antipodal shock or thermal (and hydrodynamic) escape (Cameron, 1983; Cameron and Benz, 1991; Ahrens, 1993; Chen and Ahrens, 1997). Genda and Abe (2003) revised the antipodal-shock escape model of Chen and Ahrens and concluded that this is not an efficient mechanism for escape. Thermal and hydrodynamic outflow during the hot stage of the atmosphere remains likely, however. Below are several observations pointing to extensive loss of the early terrestrial atmosphere, some of which are discussed in more detail in Chapter 20.

(1) The noble-gas abundances of the Venusian atmosphere exceed the terrestrial abundances by a factor ~ 100 (Fig. 20.1). The deficit of non-radiogenic noble gases (e.g. ^{36}Ar) in the Earth is recorded by the ^{40}Ar/^{36}Ar ratio, which equals 295.5 in the Earth's atmosphere and only ~ 1 in the Venusian atmosphere (Istomin *et al.*, 1983). Even though the K abundance in Venus is considered to be somewhat lower than that in Earth (by a factor ~ 2) and degassing models for Venus predict better retention of ^{40}Ar (again by a factor ~ 2; e.g. Kaula, 1999), the low ^{40}Ar/^{36}Ar ratio still indicates a roughly one-hundred-fold deficit of terrestrial ^{36}Ar. The simplest interpretation of this discrepancy is that in the course of accretion the twin planets acquired similar amounts of noble gases. However, the Earth lost its initial atmosphere mainly during the giant impact and (partially) retained a post-impact supply only, whereas Venus, which most probably did not suffer a giant collision (as deduced from e.g. its slow rotation and the absence of a satellite, Fig. 14.1), has better preserved its noble gases. Following this interpretation, the similarity of the abundances of major volatile species, e.g. N_2 or CO_2, in the Earth and Venus can be explained by late (post-impact) delivery of a major part of the atmophile species to both planets (Section 20.4).

(2) The inventory of radiogenic xenon isotopes, e.g. ^{129}Xe(I), definitely shows that more than 90% (probably $\sim 99\%$) of the total amount generated in the Earth via the decay of extinct ^{129}I has been lost from the Earth-atmosphere system. Xenon loss from the atmosphere is also recorded by the ^{244} Pu–^{136}Xe(Pu) systematics. The xenon loss could have been partially caused by the impact. Correspondingly, the loss of all lighter gases from the atmosphere appears to have been inevitable (Chapter 20).

(3) After the giant impact, it is thought that the lower mantle solidified on the short time scale of $\sim 10^3$ yr, but a transient ~ 500-km-thick magma ocean could have survived for a longer time. This depends crucially on the rate of heat loss from the Earth. A thick early atmosphere would retard heat loss and slow down convection (Section 17.5). It has been argued that this negative feedback could extend the lifetime of a magma ocean up to $\sim 10^8$ yr and even longer without any heat supply (Abe, 1993; Solomatov, 2000). An irreversible fractionation of the magma ocean and the formation of a thick buoyant crust would appear to be inevitable consequences of such a development. If the giant impact caused the loss of the early atmosphere, then vigorous convection (Section 17.5) could have prevented mantle fractionation and formation of the crust and would also have led to fast mantle cooling and magma-ocean solidification within $\sim 10^6$ yr or less (Tonks and Melosh, 1990). The Earth's mantle and crustal compositions suggest that this is a much more likely scenario (Chapter 17).

Post-giant-collision accretion proceeded via interactions of the Earth and small bodies, which served to reduce the planet's eccentricity and spin rate (Agnor *et al.*, 1999). Metal–silicate fractionation in transient magma seas, induced by these impacts, could have caused the final stages of core formation, characterized by low metal–silicate ratios in the mantle. Therefore it is expected that moderately siderophile elements would have been left in the silicate fraction (Azbel *et al.*, 1993; Kramers, 1998). Even though such late impacts contributed additional energy they also stripped the outer boundary layer, allowing melts to reach the planetary surface and thus enhancing heat dissipation and enabling cooling of the planetary interior (Pritchard and Stevenson, 2000).

17

The post-accretion silicate Earth: comparison with meteorites

17.1 Introduction: principal reservoirs of the post-accretion Earth

Modelling of the compositional development of the Earth in the course of the giant Moon-forming impact predicts the loss of a minor fraction of the material of the merged bodies, within a few per cent of the total mass (Cameron, 2001b). This means that the terrestrial abundances of most elements were not substantially affected. However, the great amount of energy deposited by this and preceding impacts triggered two fundamental irreversible processes, which changed the chemistry of our planet. These were the segregation of the metal core (Chapter 18) and the loss of much of the primary content of atmophile species (Chapter 20).

After the giant impact, the enormous amount of heat generated by the impact itself and by the sinking of metal through the mantle would have led to a global magma ocean. However, in contrast with the Moon (Chapter 21), the Earth shows no chemical and isotopic evidence of fractionation such as would be expected if a magma ocean had existed. The answer to this problem lies in the nature of convection in the terrestrial magma ocean; this is discussed in Section 17.5.

The mixing of late-accreting chondritic matter (with a higher Fe-content, and thus higher density, than terrestrial silicate rocks) with post-segregation metal-free silicates in the mantle or protocrust could have generated material with an intermediate density. Owing to the intrinsic density contrast, such material could have descended to the core–mantle boundary and accumulated there, thus constituting a separate reservoir at the base of the mantle (Chapter 19). Indeed seismic studies reveal a $\sim$300-km-thick core–mantle transition zone termed D$''$, overlying the metallic core (Fig. 14.3).

Mantle degassing associated with impacts and convection supplied gases to the atmosphere. The mantle thus participated in some way in the formation of all other reservoirs. Also, it is important that the mantle is the only directly observable early reservoir, even though it has been modified in the course of Earth

history. Therefore the abundances of major and trace elements in the mantle are discussed first, except for the siderophile (Chapter 18) and atmophile (Chapter 20) elements.

17.2 The silicate Earth: ways of reconstruction

There are several approaches that allow us to trace the way back to the composition of the silicate Earth about 4.5 Gyr ago. Each of these approaches addresses a specific aspect but as they are combined the results converge.

The assumption that the starting material in the terrestrial feeding zone was primitive and chondrite-like directly constrains the terrestrial abundances of the major and trace involatile elements, although this material must have originated under enhanced temperatures compared with the asteroid belt (Fig. 14.1). This is a forward model. In a complementary, inverse, approach the presently observed differentiated silicate reservoirs, the mantle and continental crust, which are respectively depleted and enriched in incompatible elements, can be recombined into a hypothetical bulk silicate Earth (BSE). The ratios of elements with similar chemical behaviour, e.g. K/U as discussed earlier (see Fig. 14.4 and the related text), allow the abundances of some volatile elements (e.g. K, Rb) to be quantified using involatile ones (U).

Isotopic systematics give time-integrated elemental (parent/daughter) ratios even for reservoirs inaccessible to direct sampling, and they are therefore especially important for such an inverse approach. Below, the direct and inverse approaches are discussed mainly via examples illustrating the "restoration techniques" for the case of selected elements. The terrestrial inventories of all elements can be found in e.g. Rudnick and Gao (2003), Veizer and Mackenzie (2003) and Palme and O'Neill (2003) and in scientific contributions by Ringwood (1975), Morgan and Anders (1980), Hart and Zindler (1986), Hofmann (1988), McDonough and Sun (1995), Allègre *et al*. (1995b, 2001).

Observational and experimental petrology give the pressure and temperature conditions under which melting would occur and geochemistry sheds light on the partitioning of elements between melts and residues. Together, these disciplines help us to understand the numerous and, in part, huge deviations from chondritic compositions that are seen in subsystems of the silicate Earth and to interpret them in terms of fractionation processes.

Seismology and other geophysical observations related to the physical properties of terrestrial materials under different conditions, first of all temperature and pressure, allow the composition and state of matter, even at great depths, to be evaluated.

17.3 Major elements

Fertile peridotites

The four major components of chondritic meteorites, O, Si, Mg and Fe, are also the major components of terrestrial rocks. As the continental crust is a relatively small reservoir it follows that the mantle is, for the abundance of these major elements, approximately representative for the whole silicate Earth. This is also true for the less dominant major elements Al, Ca, Ti. However, the mantle is heterogeneous (although less so than the continental crust), and it is still a problem to derive its average primitive composition as it was before fractionation processes affected it.

The composition of so-called "fertile peridotites" (i.e. those not depleted by melting events) is considered to portray the silicate mantle best of all (e.g. Jagoutz *et al*., 1979; McDonough and Sun, 1995). Peridotites, consisting mainly of olivine and orthopyroxene with minor amounts of clinopyroxene and garnet or spinel (depending on the depth of origin) occur in the mantle above a depth of ~ 670 km (where a phase transition takes place). These rock-forming minerals could only equilibrate at high pressures and temperatures, indicating their mantle source. Fragments of these rocks (xenoliths) were brought up by volcanic eruptions, and whole provinces of them (massifs) have been exposed at the surface as a result of mountain-building episodes. A detailed discussion of peridotites from both settings can be found in the compilations by Pearson *et al.* (2003) and by Bodinier and Godard (2003). As the partial melting of a peridotite reduces the Fe and Al content of the residue, it can be chemically assessed if a given peridotite is a residual rock depleted by a melt extracted from it or is undepleted or "fertile". Even though fertile peridotites cannot *a priori* be considered as pristine never-fractionated rocks, and in fact most of them have passed through melt extraction–refertilization processes (Section 27.7), they are still reasonably good proxies for the pristine mantle. The physical properties of peridotites, such as their density and seismic-wave propagation characteristics, match the geophysical constraints on the mantle.

As mentioned in the previous section, another, "inverse" way to reconstruct a fertile model mantle rock is to start with the composition of basalts, typical products of mantle magmatism, and then obtain the initial (fertile) and residual (depleted) compositions on the basis of data from melting experiments. Such a widely used fertile model rock is the "pyrolite" of Green and Ringwood (1963, 1967). It is important that both ways of reconstruction should give a very similar initial BSE composition. Even though both approaches are based on samples and processes occurring at shallow depths in the Earth, the inferred composition is most probably valid for the whole mantle: mantle convection, especially vigorous in the early Earth (Section 17.5), probably prevented the preservation of large-scale chemical heterogeneities in the mantle (van Keken *et al*., 2003).

Peridotites and meteorites: a comparison

Figure 17.1 presents for comparison the abundances of the three major elements in chondritic meteorites and peridotitic rocks (Jagoutz *et al*., 1979; Jones and Palme, 2000). With regard to nebular processes, the meteoritic trend convincingly shows a substantial deviation of the major-element abundances (even within the carbonaceous chondrite class) from the most primitive C1 composition. Taking into account that the formation of proto-terrestrial materials occurred closer to the Sun and in a higher-temperature environment, it cannot be excluded that differences between the terrestrial abundances and the chondritic ones resulted from nebular rather than planetary processes.

The peridotitic trend reflects variable partial melting of the samples. Both the most fertile peridotites analysed and the model "pyrolites" have low Mg and high Al abundances. The intersection of the two trends, almost within the CV compositional field, directly relates the chondritic and terrestrial compositions. This highlights the primitive character of peridotites and militates against global-scale differentiation of the silicate Earth. Several more or less similar model BSE compositions have been suggested that lie close to this intersection.

The similarity in the major-element abundances is further confirmed by isotopic data. The Earth, Moon, Mars and differentiated asteroids share common Mg- and Si-isotope compositions: the terrestrial planets appear to have formed from the same nebular reservoir, which was homogeneous with respect to the isotope compositions of these two abundant elements (Norman *et al*., 2006).

The absolute concentrations of the major elements can be derived from the accepted ratios. Thus, melt extraction has little effect on the Si concentration of the residue. Therefore taking [Si] $\approx$ 21 (wt %) in these primitive rocks, along with the Mg/Si and Al/Si ratios (Fig. 17.1), readily gives [Mg] and [Al]. A good inverse correlation between CaO and MgO in peridotite xenoliths and massifs allows [Ca] in the bulk Earth to be constrained, and the inferred Ca/Mg ratio is similar to that of C1 (McDonough and Sun, 1995). The abundances of the other major elements are fixed in a similar way (Table 17.1). In essence, the model-mantle compositions derived by different authors are quite similar (Newsom, 1995; Palme and O'Neil, 2003).

In the Fe/Si ratios there is a conspicuous difference between the bulk Earth and chondrites: iron is more abundant in the Earth than in any chondritic meteorites (Fig. 11.1). This effect, on the one hand, could have been merely apparent: the Si concentration in the Earth could have been underestimated because a portion of Si could be sequestered in the core (Section 18.1). Conversely, the Fe concentration in the core might be less ($\approx$ 79%, Allègre *et al*., 2001) than the previously accepted value ($\approx$ 88%, e.g. Morgan and Anders, 1980). However, the difference between the

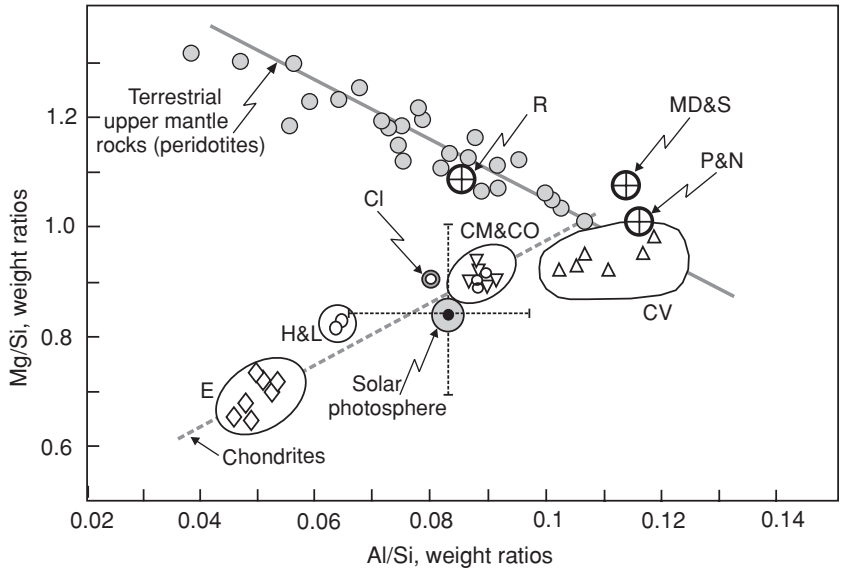

Fig. 17.1 Abundances of the major elements in meteorites and in mantle rocks (grey circles). The compositions of fertile peridotites and chondritic meteorites follow distinct trends; the intersection of these trends gives Al/Si $\sim$ 0.11, Mg/Si $\sim$ 1, which are considered as the most plausible values for the bulk silicate Earth (BSE). Model BSE compositions: R, "pyrolite", Ringwood (1979); MD&S, McDonough and Sun (1995); P&N, Palme and Nickel (1985). From Palme (2000, Fig. 2), © Kluwer Academic Publishers 2000. Reproduced with kind permission of Springer Science and Business Media.

chondritic and terrestrial Fe/Si ratios could also be a consequence of the formation of the "terrestrial chondrites" at higher temperature and lower O-fugacity than those in the asteroid belt, and these factors could be responsible for the enhanced abundance of Fe in the Earth. Finally, it is also possible that the Earth or its precursors underwent several giant impacts, as a result of which parts of the silicate mantles of both the Earth and the projectiles were lost whereas the metal cores merged.

17.4 Trace elements

Refractory trace elements

Chondritic meteorites, even though quite different from each other in the concentrations of volatile elements, have very similar relative abundances of refractory lithophile elements (Chapter 11). The concept of chondrite-like relative abundances of these elements, e.g. the REEs, in the silicate Earth, relies heavily on the assumption that involatile elements should behave similarly during planetary accretion, as is the case in nebula evolution.

Table 17.1 *Compositions of the bulk silicate Earth (BSE) with for comparison those of the depleted MORB-source mantle (DMM, Chapter 24) and the continental crust (CCR, Chapter 26)*

Compound or element	BSE[a]	DMM[b]	CCR[c]
SiO_2, wt%	45.4	44.9	60.6
TiO_2	0.21	0.133	0.72
Al_2O_3	4.49	4.28	15.9
FeO	8.1	8.07	6.71
MnO	0.135	0.135	0.1
MgO	36.7	38.22	4.66
CaO	3.65	3.5	6.41
Na_2O	0.349	0.29	3.07
K_2O	0.031	0.007	1.81
mg#	0.89	0.89	0.55
Li, ppm	1.6	0.7	16
Be	0.07	0.025	1.9
B	0.26	0.06	11
C	100	14	n.d.
N	2	0.02	56
F	25	11	553
P	86	41	n.d.
S	200	119	404
Cl	30	0.51	244
Sc	16.5	16.3	21.9
V	86	79	138
Cr	2520	2500	135
Co	102	106	26.6
Ni	1860	1960	59
Cu	20	30	27
Zn	53.5	56	72
Ga	4.4	3.2	16
Ge	1.2	1	1.3
As	0.066	0.0074	2.5
Se	0.079	0.072	0.13
Br	0.075	n.d.[d]	0.88
Rb	0.605	0.088	49
Sr	20.3	9.8	320
Y	4.37	4.07	19
Zr	10.81	7.94	132
Nb, ppb	588	210	8000
Mo	39	25	800
Ru	4.55	5.7	0.57
Rh	0.93	1	n.d.
Pd	3.27	5.2	1.5
Ag	4	6	56
Cd	64	14	80
In	13	12.2	52

(*cont.*)

Table 17.1 (*cont.*)

Compound or element	BSE[a]	DMM[b]	CCR[c]
Sn	138	100	1700
Sb	12	2.6	200
Te	8	15.1	n.d.
I	7	n.d.	710
Cs	18	1.32	2000
Ba	6750	1200	456 000
La	680	234	20 000
Ce	1786	772	43 000
Pr	270	131	4900
Nd	1327	713	20 000
Sm	431	270	3900
Eu	162	107	1100
Gd	571	395	3700
Tb	105	75	600
Dy	711	531	3600
Ho	159	122	770
Er	465	371	2100
Tm	71.7	60	280
Yb	462	401	1900
Lu	71.1	63	300
Hf	280	199	3700
Ta	40	13.8	700
W	16	3.5	1000
Re	0.32	0.157	0.19
Os	3.4	2.99	0.041
Ir	3.2	2.9	0.037
Pt	6.6	6.2	1.5
Au	0.88	1	1.3
Hg	6	10	30
Tl	3	0.38	500
Pb	146	40	11 000
Bi	5	0.39	180
Th	72	18	5600
U	19	7.2	1300

[a] BSE after Palme and O'Neill (2003) with the following modifications: U concentration as suggested by Rocholl and Jochum (1993); Th/U = 3.9 as in Kramers and Tolstikhin (1997); K/U = 12 000 as in Jochum *et al.* (1983).

[b] DMM after Salters and Stracke (2004) and U, Th, Pb from Kramers and Tolstikhin (1997). The DMM has had large amounts of melt extracted from it in multiple episodes. For compatible elements there is in general a good agreement between BSE and DMM values (the largest difference is a factor 2 for Te). As expected, the incompatible elements are very strongly depleted in the DMM.

[c] CCR after Rudnick and Gao (2003).

[d] Not determined.

In some fertile peridotitic rocks and xenoliths, the REE concentrations display chondrite-like patterns. They have been interpreted as representing primitive mantle material. However, such flat chondrite-like patterns can also result from the "refertilization" (Section 27.7) of previously depleted material and therefore their pristine nature is often in doubt. Nevertheless there is various indirect evidence that the planetary precursor was chondrite-like. An example is the Ca/Yb ratio, which increases in a mantle rock with progressive melt extraction. The lowest Ca/Yb ratios, found in fertile peridotites, approach the chondritic value, $\approx 5.65 \times 10^4$. This ratio and $[Ca]_{BSE} = 2.6\%$ translate into $[Yb]_{BSE} = 460$ ppb. Chondrite-like relative abundances for the REEs in the BSE are derived from the REE abundance patterns and Sm–Nd isotope systematics of the present-day mantle and crust, to be discussed in Chapter 27. Therefore $[Yb]_{BSE}$ constrains the BSE abundances of all the REE, including $[La]_{BSE} = 680$ ppb (Table 17.1).

Among the other refractory elements, U, Th and Sr are important because they are members of the isotopic U–Th–Pb and Rb–Sr families, and also key elements to the alkali metals K (via the K/U ratio) and Rb (via the Rb/Sr and K/Rb ratios). For instance, as Th and La are both strongly incompatible, their ratio in mantle-derived volcanics is uniform, Th/La ≈ 0.12 (Kelemen *et al.*, 2003), and the above $[La]_{BSE}$ gives $[Th]_{BSE} = 82$ ppb. With terrestrial Th/U $\equiv \kappa = 3.9$ (derived from the U–Th–Pb isotope systematics, Chapter 27) this gives $[U]_{BSE} = 21$ ppb, similar to that measured in fertile mantle peridotites (Drake, 1986). A comparison with chondritic meteorites (Rocholl and Jochum, 1993) gives a slightly lower $[U]_{BSE}$ value, 19 ppb (Table 17.1).

Similar abundances of these involatile key elements in the bulk silicate Earth have been obtained from the element/Si ratios in chondritic meteorites, thus supporting a "chondritic" Earth model. On the basis of such a model, the abundances of other involatile lithophile elements are constrained, and then tested using results obtained for the most suitable terrestrial samples and by modelling the terrestrial inventories.

Moderately volatile elements

There is no uniform way to make an inventory of the moderately and highly volatile trace elements and an individual approach has to be found for each element. Here, we illustrate some of the approaches for deriving the concentrations used in the following sections.

Pairs of elements that have different volatilities but similar geochemical behaviour allow us to assess the volatility-related element depletion. As discussed in Section 14.2, the terrestrial Rb/U ratio varies in a narrow range, Rb/U ≈ 30 (Fig. 17.2(a)). The value for $[U]_{BSE} = 0.019$ ppm then yields $[Rb]_{BSE} = 0.6$ ppm. Similarly, K/U $\approx 10\,000$ gives $[K]_{BSE} \approx 10\,000 \times [U]_{BSE} \approx 200$ ppm. This is well

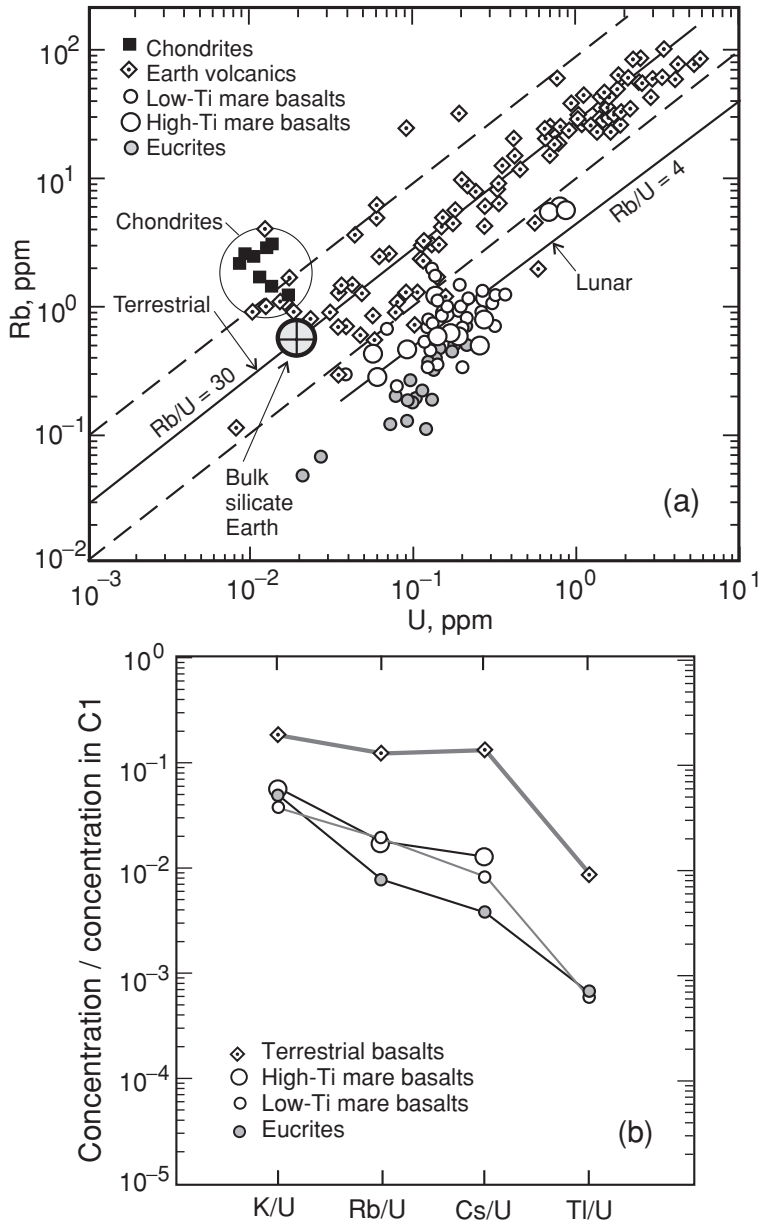

Fig. 17.2 The ratios Rb/U and K/U in terrestrial rocks and other materials. (a) The abundances of Rb and U in carbonaceous chondrites, terrestrial volcanic rocks, lunar mare basalts and eucrites. Note the lower abundances of Rb relative to U in lunar rocks as compared with the terrestrial abundances. (b) Ratios of volatile elements and U in differentiated materials. Note the similarity between lunar mare basalts and eucrites. After Ruzicka *et al.* (2001), © Elsevier Science 2001, reproduced by permission.

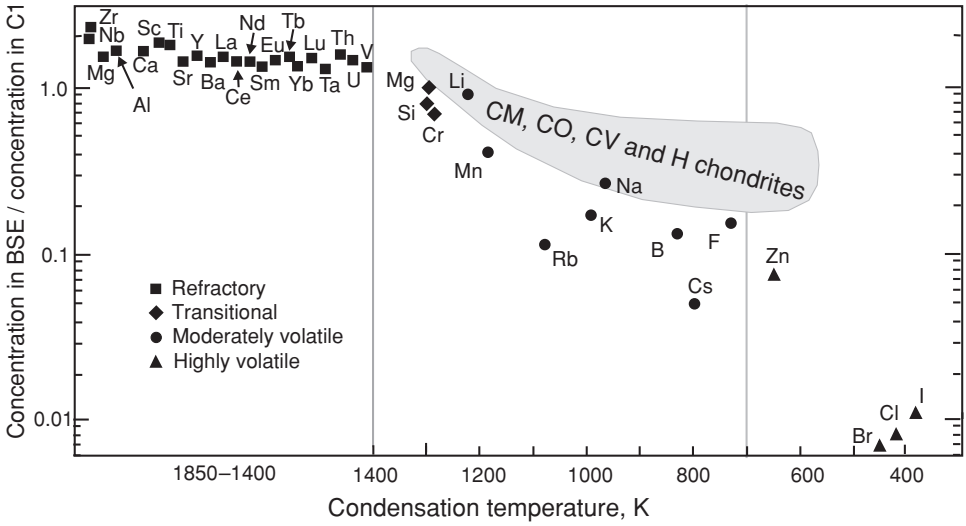

Fig. 17.3 Volatile-element depletions of the BSE. The condensation temperatures shown correspond to a pressure 10^{-4} atm. The Earth is more depleted in volatile lithophile elements than chondritic meteorites, owing to either formation of the precursor materials under higher temperatures (closer to the Sun) or to impact-related losses at later stages of accretion. The chondrite-like volatile-element pattern is shown for comparison (grey shading). Data from McDonough and Sun (1995) and Cassen (1996).

above the minimal value of 120 ppm necessary for all the atmospheric ^{40}Ar to have been produced by ^{40}K decay in the silicate Earth if the latter had been completely degassed (e.g. Hurley, 1968; Gast, 1968).

The BSE Rb concentration is found via Rb–Sr isotope systematics. The inventory of Sr-isotope abundances in terrestrial reservoirs gives $^{87}Sr/^{86}Sr_{BSE} \approx 0.7045$ (see Chapter 27 for the details). This yields a time-integrated $(Rb/Sr)_{BSE}$ value of about 0.03. This ratio and $[Sr]_{BSE}$ then allow an independent estimate of the abundance of the moderately volatile Rb: $[Rb]_{BSE} = 0.6$ ppm. The above concentrations of K and Rb correspond to K/Rb $\sim$ 330, in accord with the K/Rb ratios actually observed in terrestrial rocks.

On the whole the terrestrial abundances of major lithophile elements and moderately volatile trace elements are not dramatically different from the chondritic pattern (Fig. 17.3, compare with Fig. 11.2). Therefore it is not necessary to invoke processes that would fractionate these elements during the accretion of large bodies. Nebula processes, similar to those that produced primitive meteorites, could also have formed chondrite-like proto-terrestrial material in the Earth's feeding zone (e.g. Humayun and Cassen, 2000; Ruzicka *et al*., 2001).

Highly volatile elements

The most difficult problem is to constrain the concentrations of the highly volatile trace elements in the Earth. In this case the isotopic approach is especially promising. For instance, the Pb-isotope compositions in terrestrial rocks and ores allow a reliable determination of the BSE abundance of this element, which is not only highly volatile but also siderophile. Because the half-life of ^{238}U is almost equal to the age of the solar system, 4570 Myr, half its initial amount, 40 ppb, has decayed during Earth's evolution, yielding $[^{206}Pb^{*}]_{BSE} = 20$ ppb. The observed present-day $^{206}Pb/^{204}Pb_{EAR}$ varies mainly from 17 to 19 (Chapter 27), thus giving $^{206}Pb/^{204}Pb_{BSE} \approx 18$, and the initial ratio is known from studies on iron meteorites: $^{206}Pb/^{204}Pb_{INI} = 9.308$. From this, the bulk silicate Earth abundance of ^{204}Pb is

$$[^{204}Pb]_{BSE} = \frac{[^{206}Pb^{*}]_{BSE}}{^{206}Pb/^{204}Pb_{BSE} - {}^{206}Pb/^{204}Pb_{INI}} \approx 2.3\,\text{ppb}.$$

and the mean present-day lead-isotope composition gives $[Pb]_{BSE} = 150 \pm 30$ ppb (Table 17.1).

For most volatile elements it is not possible to derive terrestrial abundances via such useful radioactive family relations. This is the case for iodine, which is of special importance as its terrestrial abundance sheds light on the evolution of Earth's early reservoirs. Iodine is an extremely incompatible element and this property allows (once again) the use of the ratio of a volatile element (iodine) and a refractory element with similar incompatibility. Involatile and highly incompatible Th may play the role of reference element. The average [I] and [Th] in mantle-derived mid-ocean ridge basalts (MORBs) are 8.5 ppb and 190 ppb respectively. This gives $(I/Th)_{BSE} \equiv (I/Th)_{MORB} = 0.045$ and hence $[I]_{BSE} = 3.9$ ppb (Muramatsu and Wedepohl, 1998).

At present the major portion of iodine resides in the crust. An inventory of the crustal rocks yields a total crustal amount of iodine of $\sim 8.6 \times 10^{18}$ g (Muramatsu and Wedepohl, 1998). The crust contains about half the BSE inventory of highly incompatible lithophile elements. Correspondingly $[I]_{BSE} = 4.3$ ppb, in reasonable agreement with the above estimate via thorium. These two values are relatively robust estimates of the I_{BSE} abundance even though they are a factor ~ 2.5 lower than the "canonical" $[I]_{BSE} = 10$ ppb typical of fertile peridotitic rocks (Deruelle *et al.*, 1992). The I_{BSE} abundance is considered further in Section 20.2 in connection with early degassing time scales. There we use the range from 3 to 10 ppb, with some preference for the lower value.

Even for elements that are both volatile and siderophile, abundances in the bulk silicate Earth may be reconstructed via ratios of these elements and involatile lithophile species with similar incompatibilities. For example, Jochum *et al.* (1993) studied the mantle abundances of Sn, which is a highly volatile and siderophile

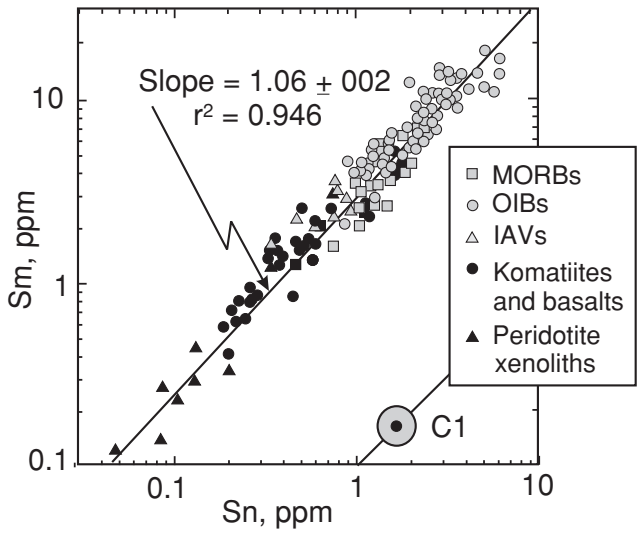

Fig. 17.4 The Sm–Sn correlation in terrestrial rocks. After Jochum *et al.* (1993), © Pergamon Press 1993, reproduced by permission from Elsevier.

element, and found an excellent correlation between Sn and the involatile REE Sm with an average Sn/Sm ratio 0.34 ± 0.01 (Fig. 17.4). This value translates into $[Sn]_{BSE} = 138$ ppb. The correlation is valid for volcanic rocks with both shallow- and deep-mantle sources as well as for ancient mantle rocks. It thus precludes siderophile-element removal from deep plume sources into the core and indicates that metal segregation and core formation only occurred early in Earth history.

17.5 Concept of a terrestrial magma ocean: the role of convection

Terrestrial magma ocean: apparent contradiction of observations and models

As discussed above, on the one hand neither the representative mantle rocks, peridotites, nor the chemical BSE reconstructions or radiogenic isotope systematics indicate any traces of global chemical differentiation of the mantle. On the other hand, recent Earth-accretion models with one or more giant impacts on the almost fully grown Earth make the robust prediction of (almost) planetary-scale melting (Chapter 16). Crystallization differentiation of a terrestrial magma ocean, involving high-pressure minerals such as majorite garnet and Mg-perovskite silicate, would cause a strong fractionation of some element ratios that would leave traces in the isotope systematics, for instance, in Lu/Hf (Kato *et al.*, 1988; Ringwood, 1990).

Geochemical arguments cannot of course exclude the possibility that the mantle was once (partially) fractionated in some way but became thoroughly mixed again

afterwards. A promising way to look for such mixing is to search in very ancient minerals and rocks for preserved isotope anomalies that could have resulted from fractionation in a magma ocean. There are indications of very early terrestrial fractionation, such as the excess of the terrestrial $^{142}Nd/^{144}Nd$ ratio over the chondritic value and a small excess of the $^{142}Nd/^{144}Nd$ ratio over the average terrestrial value in 3.8-Gyr-old metamorphic rocks in West Greenland (Fig. 27.16) and the variable time-integrated $^{176}Hf/^{177}Hf$ ratios in zircons up to 4.4 Gyr old from Western Australia, indicating the occurrence of ancient enriched and depleted sources (Fig. 27.17). These data thus show that some magmatic fractionation occurred in the early Earth, but they do not suggest the strong and uniform effect that is expected from fractionation in a mantle-wide magma ocean: other interpretations of these observations are favoured (Section 27.8). This apparent discrepancy between observations and the predictions of Earth-accretion and Moon-formation models can be resolved in an elegant way: vigorous convection in the post-impact molten mantle could have prevented substantial early differentiation of the silicate Earth. Convection plays a major role in Earth's evolution and is therefore discussed in some detail below.

Convection in the present-day Earth's mantle

Convection is the movement of viscous matter caused by temperature-induced density differences in a gravitational field g. A straightforward example is a liquid layer. If no heat is transferred into the layer from below or released from the top, the relationships between the temperature $T_0(l)$ (l is the distance from the upper cold boundary of the layer) and the density $\rho_0(l)$ will be adiabatic; then no convection would be possible. It is different when the layer is heated at the bottom (with relevant heat inflow f_0) and/or contains elements producing heat dispersed within the layer (f_D) and it is cooled at the top. Then the total heat outflow is $\Phi = f_0 + f_D$ (assuming a steady-state condition) and the superadiabatic temperature contrast between the bottom and top boundaries of the layer is ΔT. To develop convection, the thickness d of layer should be sufficient (otherwise the heat could only be transferred by conduction). In this simple but still relevant case, a temperature upturn within some confined parcel of chemically homogeneous matter causes its expansion (with coefficient α), decreases the density $\rho = \rho_0(1 - \alpha\Delta T)$ and develops a buoyancy force $F_B = \alpha\rho_0\Delta T\, g$, which pushes the parcel up into the cooler environment above it. However, as the parcel enters this cooler environment, its temperature decreases owing to thermal conduction (with, say, coefficient χ), thus decreasing its buoyancy and retarding further movement. Also, the buoyancy force may not be able to overcome the viscous resistance of the matter: the higher the viscosity η (or the kinematic viscosity $\nu = \eta\rho_0$), the stronger the resistance. The

Table 17.2 *Parameters determining the rate of mantle convection (after Zharkov, 1983)*

Parameter	Symbol	Units	Value
thermal expansion	α	K^{-1}	2×10^{-5}
depth	d	cm	3×10^{8}
thermal conductivity	χ	$cm^2\ s^{-1}$	3×10^{-2}
gravity acceleration	g	$cm\ s^{-2}$	10^3
density	ρ	$g\ cm^{-3}$	4.5
kinematic viscosity (at present)	ν	$cm^2\ s^{-1}$	3×10^{22}
kinematic viscosity (silicate melts)	ν	$cm^2\ s^{-1}$	1×10^{2}
heat outflow	Φ	$erg\ cm^{-2}\ s^{-1}$	60
specific heat	c_p	$erg\ g^{-1}\ K^{-1}$	1.2×10^{7}
temperature contrast	Δ	K	1000

dimensionless Rayleigh number R_Φ is the ratio of the factors promoting convection and those inhibiting it:

$$R_\Phi \equiv \alpha g \Phi d^3/(\rho c_P \chi^2 \nu). \tag{17.1}$$

Convection proceeds if R_Φ exceeds a critical value, $R_\Phi \geq R_C$; the latter is close to $\sim 10^3$ for the simple model outlined above.

The silicate mantle of the Earth is heated from below and, in addition, by heat-producing elements distributed within it, and it is cooled at the top (resembling the above model). Estimates of all parameters entering Eqn (17.1) for the present-day mantle are available from measurements and are presented in Table 17.2 (Zharkov, 1983). Substitution into Eqn (17.1) gives $R_\Phi \approx 6.7 \times 10^6$, which exceeds R_C by a factor > 1000, implying that convection must develop in the mantle. Relevant observations indicate that this indeed is the case: a solid mantle behaves as a convecting viscous fluid (Turcotte and Schubert, 1982; Zharkov, 1983; Puster and Jordan, 1997).

The Rayleigh number determines the vigour of the convection. At the Rayleigh numbers typical of the present-day mantle, about 10^6 to 10^7, the viscous forces greatly exceed the inertial forces: the ratio of these forces is expressed as the dimensionless Prandtl number

$$Pr = \nu/\chi. \tag{17.2}$$

Substitution of the mantle parameters into Eqn (17.2) gives an almost infinite Pr, $\approx 10^{24}$, indicating a slow laminar type of convection. At such large Pr values several

important physical characteristics of convection relate directly to the Rayleigh number, including the velocity of convection u_R (Zharkov, 1983):

$$u_R \approx R_\Phi^{2/5} \times (\chi/d). \tag{17.3}$$

Using parameters from Table 17.2 gives $u_R \sim 2$ cm yr^{-1}. However, even at this slow rate convection is by far the most efficient mechanism of heat transfer to the Earth's surface. This follows from another dimensionless parameter, the Nusselt number

$$Nu \approx (R_\Phi/R_C)^{1/3} \approx 30; \tag{17.4}$$

the Nusselt number is the ratio of the efficiencies of the convective ($R_\Phi \gg R_C$) and conductive ($R_\Phi \sim R_C$) transfer of heat.

Regarding the present-day style of mantle convection, there is growing confidence that convective flow involves the whole mantle. The images of seismic velocities inferred from seismic tomography show little evidence for mantle layering but instead give strong indications of the very deep penetration of cold subsurface material (Chapter 25) as well as ascending hot mantle flows from (almost) the core–mantle boundary to the lower boundary of the lithospheric mantle (Section 27.3). These ascending flows clearly penetrate through a phase transition at depth ~ 670 km even though the penetrating material cools down owing to the endothermic chemical reactions that change mineral phases at these depths. Seismic tomography (Grand, 1994; Nataf, 2000; Nolet *et al*., 2006), the combination of seismic and geodynamic data (Simmons *et al*., 2006) and mantle dynamic models (Christensen, 1995; Puster and Jordan, 1997; van Keken *et al*., 2002) all favour whole-mantle convection, and this model is adopted hereafter in our text (Chapters 19 and 28).

Convection in the post-impact Earth

In the present-day Earth a liquid phase may appear only in the uppermost ~ 100 km of the mantle, where fractionation then occurs via solid–melt partitioning and melt migration away from the residue (Chapter 24). When the melt constitutes the major phase of a convecting system, the situation is dramatically different. Magnesium–silicate melts have a low viscosity ν, of order ~ 1 to 100 cm^2 s^{-1} (Tonks and Melosh, 1990; Solomatov and Stevenson, 1993a). Also, it is thought that the heat flux (Φ in Eqn 17.1) generated after the giant Moon-forming impact was extremely high: the total energy transferred into the post-impact Earth was of order $\sim 5 \times 10^{38}$ erg (Chapter 16). Modelling of the evolution of such a magma ocean using different scenarios has yielded cooling times ranging from $\sim 10^4$ to $\sim 10^8$ yr (Tonks and Melosh, 1990; Solomatov, 2000). For an intermediate value, $\sim 10^6$ yr, the resulting flux from the magma ocean would be $\Phi \approx 6 \times 10^6$ erg cm^{-2} s^{-1}, in accord with a

more detailed estimate by Solomatov and Stevenson (1993b). Substitution of this value and $\nu \sim 100\,\mathrm{cm^2\,s^{-1}}$ into Eqn (17.1) with the other parameters as in Table 17.2 gives $R_\Phi \approx 2.6 \times 10^{31}$ and a convection velocity $u_\mathrm{R} \sim 250$ cm s^{-1} or ~ 6400 km (the Earth's radius) per month, exceeding the present-day velocity by $\sim$ nine orders of magnitude. This convective flow must have become turbulent (Tonks and Melosh, 1990; Solomatov and Stevenson, 1993b).

Crystallized minerals settle out of a magma by gravity, with a velocity of settling v_S following Stokes' law. However, in a turbulent flow with an effective friction velocity u_F (proportional to u_R), settling is inhibited and crystals tend to remain suspended. The fate of crystals in a magma ocean is determined by the $v_\mathrm{S}/u_\mathrm{F}$ ratio, known as the dimensionless Rouse number S:

$$S \equiv v_\mathrm{S}/u_\mathrm{F} \approx \text{constant} \times a^2 \Delta\rho/\nu^{8/9}. \tag{17.5}$$

If $S \leq 1$ then the convective flow is able to keep crystals suspended; if $S > 1$ then settling proceeds. Equation (17.5) is a simplified version of Eqn (20) in Tonks and Melosh (1990), in which the three most important parameters are the size of the crystals a, the density contrast between melt and crystal, $\Delta\rho$, and the kinematic viscosity ν; other parameters relevant to the mantle-deep magma ocean are as discussed above and, for simplicity, they are here hidden in the constant, which is ≈ 4. Assuming quite large crystals, $a \sim 1$ cm, a large density contrast $\Delta\rho \sim 0.2$ g cm^3 and the lowest possible $\nu \sim 1$ cm^2 s^{-1}, we get a threshold regime $S \sim 1$ for the magma ocean.

However, for such vigorous convection much smaller crystals are expected, $<$ 0.01 cm, because the magma circulation rate is very high. At different pressures different mineral phases are in stable equilibrium with the melt and, as the magma moves up or down, crystals form and are resorbed at phase boundaries. A melt parcel crosses the whole mantle in ~ 1 month. Therefore the residence time of the parcel in the depth range where a specific mineral phase is stable would be much shorter than a month. Settling of the small crystals would appear to be hardly possible, and entrained crystals that nucleated in a high-pressure layer will disappear again at lower pressures: the nucleation becomes cyclic. Thus, in the post-impact terrestrial magma ocean, crystal fractionation is highly unlikely.

In the course of cooling of the magma ocean crystallization proceeds and, as the fraction f, $0 < f \leq 0.5$, of suspended crystals grows, the effective viscosity ν_EFF increases exponentially:

$$\nu_\mathrm{EFF} \approx \nu_\mathrm{LIQ} \exp(23 f), \tag{17.6}$$

thus dramatically decreasing the Rouse number. When f approaches ~ 0.5 the melt–solid mixture "locks up" and begins to behave like solid mantle matter. Only within the top ~ 100 km can melt penetrate through the porous mush and accumulate in

magma chambers, leading to melt–residue fractionation and the formation of an oceanic-like crust and a depleted mantle lithosphere. The entrainment of these two reservoirs in downward convection and subsequent mixing would tend to stir the products of this top-level fractionation, thus keeping the post-giant-impact silicate Earth in a relatively homogeneous state.

17.6 Summary

Direct investigations of fertile mantle rocks, along with comparisons with chondritic meteorites, allow the terrestrial abundances of major and trace involatile lithophile elements to be reconstructed. It is important that the two independent approaches, one based on chondritic abundances and the other on terrestrial rock data, have been found to agree well, thus validating the chondrite Earth model and instilling confidence in the inferred model composition, even though no single class of meteorites fits the bulk Earth composition precisely. The abundances of volatile elements are derived more or less individually for each element, from comparisons of involatile and volatile species that behave similarly in major terrestrial fractionation processes, from relevant isotopic systematics and from mass-balance considerations.

The principal conclusion from the reconstructed inventory is that the chemical composition of matter in the silicate Earth was largely inherited from the nebula stage of its development in the Earth's feeding zone. It is possible that for the terrestrial chondrites this early vaporization–condensation–agglomeration stage differed from that recorded by primitive meteorites from the asteroid belt, because higher temperatures and thus more severe processing are expected. The late accretion stages of the Earth did not bring dramatic changes in its composition, except for the possible loss of highly volatile elements and the dramatic loss of gaseous species. This conclusion is consistent with the standard accretion models, suggesting that the merging of colliding bodies is the principal process. Another inference from the accretion models, the formation of a global magma ocean after a giant impact, may be reconciled with the inferred mantle composition by postulating that intense convection within such a magma ocean prevented the early irreversible differentiation of the silicate Earth. In contrast with the different species of silicate material, the metal could readily segregate because of the large density contrast; it follows that turbulent convection did not inhibit the segregation of the Earth's core (Chapter 18).

18

Core segregation

18.1 Introduction: siderophile elements in the silicate mantle and light elements in the core

Siderophile-element abundance pattern in the Earth's mantle

As discussed above, it is an important feature of the silicate Earth that its refractory-lithophile-element abundances are like those of chondrites, thus documenting a relation between the Earth and chondritic matter. In contrast, the siderophile elements are depleted in the silicate Earth, almost certainly because of their segregation into the metallic core. Their relative depletion pattern provides important clues on the core-segregation process (Wänke *et al*., 1984; Ringwood, 1984; Jones and Drake, 1986; Newsom, 1990; O'Neill, 1991a, b).

Transitional, moderately and highly siderophile elements constitute three groups that are progressively depleted, thus pointing to metal–silicate fractionation having played an important role in core formation (Fig. 18.1). However, (1) within each group the observed chondrite-normalized abundance pattern is almost flat and contrasts with the variable abundances predicted from metal–silicate equilibrium fractionation. Also (2) for strongly siderophile and for most moderately siderophile elements, the observed abundances greatly exceed those predicted from equilibrium fractionation, while for W and the transition elements they are lower.

Becker *et al*. (2006) recently reported new data for highly siderophile element (HSE) concentrations in the mantle. Their best estimate, [Ir] = 3.5 ppb, is indistinguishable from the previous average value suggested by Morgan *et al*. (2001), and the C1-normalized HSE pattern is flat except for a small enhancement of [Ru] (by a factor 1.4) that is not revealed by previous data sets. This deviation is below the accuracy of core-formation models and for the sake of simplicity we will consider the relative HSE abundance pattern to be close to chondritic.

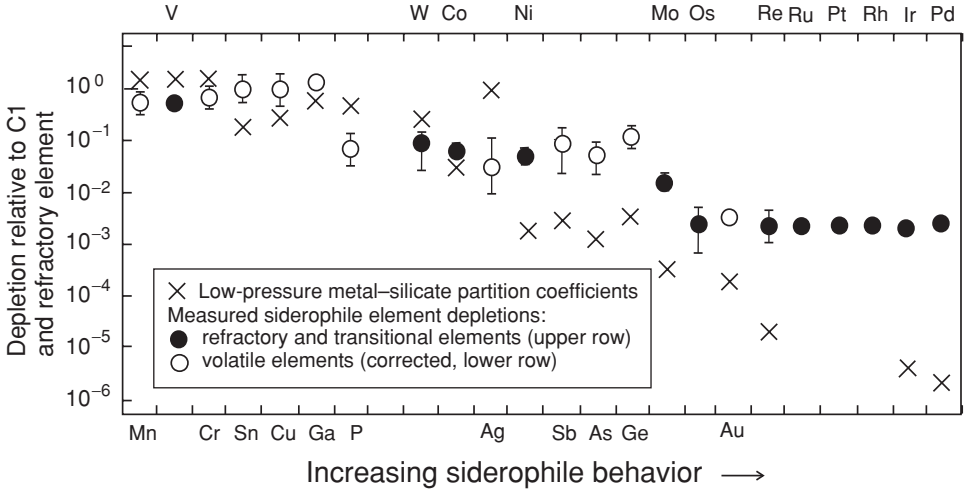

Fig. 18.1 Normalized abundances of trace siderophile elements in the Earth's mantle. The depletion for element i is calculated as $([^iC]/[\mathrm{Al}])_{\mathrm{BSE}}/([^iC]/[\mathrm{Al}])_{\mathrm{C1}}$. Shown are elements ranging from transitional (between siderophile and lithophile) V to highly siderophile Ir and Pd. The depletion factors of volatile siderophile elements are corrected for their volatility. For compatible involatile elements, e.g. Co and Ni, the depletion factors are reliably known, to within $\sim 10\%$: their mantle abundances are not complicated by crust formation, and efficient mantle mixing has led to their uniform concentrations in mantle rocks (Newsom and Sims, 1991). Note the rather similar depletion factors of moderately siderophile elements (from P to Mo) and highly siderophile elements (from Os to Pd), in contrast with expectations from the rather variable partition coefficients. After Righter and Drake (2000) and Borisov *et al.* (1994).

The simplest approach: a single-stage equilibrium model

Both features highlighted above are very different from the predicted outcome of a single-stage metal–silicate equilibrium process. Assuming that a fully accreted (but undifferentiated) Earth with concentration ${}^iC_0$ of element i fractionates into liquid metal (subscript LIM) and liquid silicate (subscript LIS) and that the liquid silicates present the post-segregation silicate Earth concentrations (${}^iC_{\mathrm{LIS}} \equiv {}^iC_{\mathrm{BSE}}$), then the depletion factor for species i predicted from one-step-equilibrium partitioning is given by (Eqn 12.4)

$$\text{depletion factor} \equiv \frac{{}^iC_{\mathrm{BSE}}}{{}^iC_0} = \frac{1}{{}^iD_{\mathrm{LIM}}F_{\mathrm{LIM}} + F_{\mathrm{LIS}}}. \tag{18.1}$$

As the bulk-Earth-like metal–silicate fractions are $F_{\mathrm{LIM}} \approx 0.3$, $F_{\mathrm{LIS}} \approx 0.7$ and ${}^iD_{\mathrm{LIM}} \equiv {}^iC_{\mathrm{LIM}}/{}^iC_{\mathrm{LIS}} \gg 1$ for moderately and highly siderophile elements (Table 18.1), the depletion factors ${}^iC_{\mathrm{BSE}}/{}^iC_0 \approx 1/{}^iD_{\mathrm{LIM}}$ should be highly variable, in accordance with the variable partition coefficients, and generally well below those

Table 18.1 *Metal–silicate partition coefficients*[a] *for the dynamic core-formation model (after Kramers, 1998)*

	Early core formation		Late core formation	
Element	LIM/LIS[b]	SOM/LIS[c]	LIM/LIS[b]	SOM/LIS[c]
V	3.25	0.23	0.06	0.005
W	2000	200	3.2	0.6
Mo	8×10^4	6.5×10^5	90	900
Co	500	400	40	30
Ni	1600	1500	130	210
Au	2×10^4	2.5×10^4	1×10^4	1.3×10^4
Re	2.5×10^4	4×10^4	6500	9000
Ir	4×10^4	3.5×10^6	2×10^4	1.6×10^6

[a] Righter *et al.* (1997) investigated the relationship between the partition coefficients and temperature, pressure, melt composition and oxygen fugacity, the last being one of the most important: an increase in oxygen fugacity in the course of accretion causes a dramatic decrease in the partition coefficients for moderately siderophile elements.
[b] LIM/LIS: the liquid-metal–liquid-silicate value.
[c] SOM/LIS: the solid-metal–liquid-silicate value.

observed. Figure 18.1 illustrates the disagreement between the observed depletion pattern (solid and open circles) and the values predicted by the one-step-equilibrium model (crosses). It is not possible to obtain a better fit even by considering other phases, such as solid metal and/or solid silicate, and varying their proportions.

However, the partition coefficient for each siderophile element depends on the parameters of the segregation (the temperature, pressure, melt composition etc.). Righter *et al*. (1997) and Righter and Drake (1999) suggested that it might be possible to find a set of these parameters (and corresponding partition coefficients) that would allow the observed abundances (Fig. 18.1) to be reconciled with those calculated via Eqn (18.1). These authors investigated the partitioning of moderately siderophile Ni, Co, Mo and W between metal and silicate melts and obtained a good reconciliation providing that core segregation occurred at the base of a deep ($\sim$1000 km, $\sim$2500 K) hydrous magma ocean. For some other elements, other authors have also found agreement between one-step high-pressure partitioning models and the data, although these models in part require very specific conditions (Ohtani *et al*., 1997; Murthy and Karato, 1997; Ruzicka *et al*., 2001). Jana and Walker (1997a, b) highlighted the influence of sulphur concentrations and silicate compositions on the partitioning of siderophile elements and concluded that core formation was more complex and intricate than an equilibrium segregation, whatever its parameters.

Indeed, the observed BSE concentrations of the highly siderophile elements can be explained by such a model only if their metal–silicate partition coefficients at high pressures and temperatures are orders of magnitude lower than those determined experimentally at a pressure of 1 bar, and all have approximately the same value. Neither criterion is fulfilled. The metal–silicate partition coefficients for Ir, Pd and Pt do not decrease significantly with pressure, at least down to ~ 500 km depth (Borisov and Palme, 1997; Holzheid *et al*., 2000). For Re and Os, Fortenfant *et al*. (2003) found that, although both partition coefficients decrease with pressure, they remain very different throughout the 5–10 GPa range. However, the Re/Os ratios (Fig. 18.1) and the Os-isotope compositions of mantle peridotites (Meisel *et al*., 2001) are both close to chondritic. Consequently the observed abundances of Pd, Ir, Pt, Rh and Os in the upper mantle are inconsistent with those derived from a simple one-stage-equilibrium model regardless of P, T or the composition of melts.

Moreover, the abundances of siderophile elements in non-cumulate eucrites are quite low, implying that metal–silicate fractionation occurred in the asteroid Vesta (Section 12.3). The chronology of the differentiated meteorites shows that core-forming metal–silicate fractionation occurred very early in meteorite parent bodies, within < 10 Myr after SOS formation (Section 12.4). Therefore most of the Earth's embryos had initially been fractionated at low pressures, owing to the much lower mass of these objects, before they impacted the growing Earth. After each collision the metal cores of impactor and target could have been partially re-equilibrated with the silicate mantle and partially merged without re-equilibration (Karato and Murthy, 1997).

The one-step equilibrium partitioning of siderophile elements between metal and silicate melts thus appears to be an oversimplified scenario, irrespective of pressure. It is in contradiction with the standard model of planetary accretion (Chapter 15), and its inability to reproduce the observed abundances of at least some involatile siderophile elements is therefore not surprising.

A portion of proto-terrestrial chondrite-like material (e.g. relatively small planetesimals, fragments or particles) could have escaped metal–silicate fractionation, preserving the chondritic siderophile-element abundances, and then have been mixed with the already fractionated silicate mantle of a growing planet. This mixing of unfractionated and fractionated materials appears to be compatible with the standard model of planetary accretion (see also Chapter 19). This late accretion or "late veneer" has been explored as a potential explanation for the discrepancies between the observed abundances and those expected from a single-step fractionation and core-formation process (e.g. Morgan *et al*., 2001). As can be readily seen from Fig. 18.1, this concept allows the observed BSE abundances of the noble metals to be reconciled by the addition of $\sim 0.3\%$ of chondrite-type undifferentiated matter to the mantle. To reconcile Ni and Co, however, requires about 8% addition.

Therefore the "late veneer" model on its own is also unable to reproduce the observations self-consistently.

A light element in the core

Beside the siderophile elements, the partitioning of other species into the Earth's core must also be considered. Seismological observations demonstrate that the outer liquid core density is about 8–12 wt % below that of an Fe–Ni alloy under the prevailing pressures and temperatures. A smaller core density deficit of ~ 5 wt % has also been suggested (Anderson and Isaak, 2002). In either case this reservoir should include some proportion of one or more abundant elements lighter than iron. Even though the solid inner core is 0.55 g cm^{-3} denser, a smaller but still appreciable fraction of light elements is expected there as well. Following the classical paper by Birch (1952) and later proposals by many authors, H, C, O, Si and S (or a combination of these elements) could have partitioned into the core, thus accounting for the above density deficit.

The composition of this light-element admixture may have had a bearing on the core-segregation process and the development of the core, on the subsequent mass transfer between the mantle and core and, naturally, on the overall bulk composition of the Earth. Even though this important problem is widely debated in the literature, it is still far from being solved (e.g. Poirier, 1994; O'Neill *et al*., 1998). For example, Kilburn and Wood (1997) and Gessmann *et al*. (2001) suggested that the BSE depletion in Si relative to the C1 chondrites and the core-density deficit could both be explained if Si was alloyed with Fe–Ni during core segregation under high-*PT* conditions and very low O-fugacity (e.g. at the bottom of a magma ocean following the giant impact). Lin *et al*. (2002, 2003) investigated Fe–Si alloys and considered that ~ 10 and $\sim$4 wt % of Si in the outer and inner core, respectively, would satisfy the seismological constraints. However, Williams and Knittle (1997) found that the alloying of Si in the core would be unable to satisfy the observed variation of seismic velocity with depth in the core, and therefore Si could not be the primary light element of the outer core. Jones (1996) arrived at the same conclusion from cosmogeochemical considerations. Li and Agee (2001) investigated the partitioning of S, O and Si between liquid Fe–Ni alloy and liquid silicate and concluded that sulphur is the most plausible principal light element in the core. Alfe *et al*. (2000), in contrast, concluded from chemical-potential calculations that the outer core could not be a binary iron–sulphur mixture. Instead, they suggested that the presence of oxygen in the core is essential to account for the seismic measurements. Okuchi (1997) determined the metal–silicate melt partition coefficient of hydrogen as a function of temperature for high pressures (7.5 GPa) and suggested that about 60 per cent of the core-density deficit could be accounted for by hydrogen, provided that the core

formed in equilibrium with a hydrous-silicate magma ocean. Williams and Hemley (2001) reviewed the possibility of hydrogen as the light constituent of the core and considered that the core could be the largest potential hydrogen-bearing reservoir in the Earth. However, as discussed in Section 20.4, it is in any case difficult to find a proper source for the terrestrial hydrogen from which the Earth's hydrosphere was supplied, and an additional H-bearing reservoir increases this difficulty.

In summary, the observed core-density deficit remains unexplained and therefore cannot be used to constrain the core-segregation process. The mantle abundances of siderophile elements appear to be much more informative and allow core-formation processes to be understood in the framework of the standard planetary-accretion model, as discussed below.

18.2 Successful core-formation models

Constraints from physical models

Models of metal–silicate differentiation include the following possibilities: large masses of solid metal sink through solid silicate matter or liquid metal percolates through a solid matrix or rains out from a liquid metal–silicate emulsion. The last was found to be the most effective segregation mechanism (Stevenson, 1990). This mechanism is also compatible with a scenario of Earth accretion via impacts of relatively large, $\sim$ 100 to 1000 km, planetary embryos. The mean initial (post-collision) size of metal melt drops is predicted to be much less than 1 cm (Stevenson, 1990). Because of the rather fast diffusion of siderophile elements in liquid iron, equilibrium partitioning is expected for such droplets and for smaller ones. For instance, Dobson (2000) estimated the Co diffusivity in a liquid Fe–FeS eutectic to be $\sim 1 \times 10^{-4}$ cm^2 s^{-1} at $T = 1100$ °C, $P = 2$–5 GPa. For metal drops of size 1 cm this corresponds to an equilibration time scale $\sim 10^{-4}$ yr. Even though the mean residence time of a metal droplet in a silicate magma ocean is short, of order $\sim 10^2$ yr (Karato and Murthy, 1997), equilibrium could thus readily be accomplished. It should also be noted that, unlike silicate grains, metal droplets could segregate from turbulent silicate magma as the density contrast is much greater and the stability of metal is not pressure dependent. In the molten mantles of small planetesimals, convection is weaker and settling is slower owing to the lower gravity, so that metal–silicate equilibration is especially favoured. Generally, metal segregation from melts could proceed even after the metal fraction in the mantle has become very small, down to $\sim 10^{-4}$, which will be important in our later discussion (see the end of this Section).

In the event of whole-mantle melting, the iron could have settled directly onto the core as relatively small blobs. Even if, at late stages of accretion, blobs

accumulated onto mantle rheological boundaries (e.g. between a molten upper and a solid lower mantle), the metal should have sunk to the core via catastrophic overturns or diapirs (Karato and Murthy, 1997). Physical models thus predict a geologically short residence time for metal in a (partially) molten mantle. A substantial delay in core formation (such as a few hundred million years after the termination of accretion) appears to be out of the question.

Dynamic chemical model of the core-segregation process

The standard model of planetary accretion and the above results from physical modelling provide a clear framework for models of core-segregation processes. This includes the start of metal segregation and core formation in planetesimals at an early, preterrestrial, stage of accretion, at which equilibrium between metal and silicates is expected, and the merging of cores without significant metal–silicate equilibration at later stages. In this framework the dynamical geochemical models of Azbel *et al*. (1993), Kramers (1998) and to some extent the contributions by Karato and Murthy (1997) and Murthy and Karato (1997), can be accommodated. These models envisage Earth growth via a mass flux from a reservoir of undifferentiated proto-terrestrial material into an outer silicate shell (Fig. 18.2), which can be seen as the collective mantle of planetesimals. Melting in this shell enables metal–silicate equilibrium and the segregation of metal into the (collective) core. Core formation produces internal heat (Davies, 1990; Stevenson, 1990; Vityazev *et al*., 1990) and, once triggered, its rate is then limited by the addition of matter supplying new metal to the mantles.

The concept of a collective core and mantle from many planetesimals implies that in collisions of previously differentiated bodies their cores would simply merge without equilibrating further with the silicate matter. This is one end-member scenario. However, in highly energetic impacts cores may be dispersed. This appears to have happened to at least part of the impactor's core in the Moon-forming giant impact (Canup, 2004), and further depletion of the silicate mantle in siderophile elements probably occurred in the magma ocean owing to a transient increase in its metal content, as will be discussed further below. After accretion has ceased, core formation will continue as long as localized mantle melting occurs and the metal content in a mantle fractionation zone is high enough to allow metal segregation and settling.

The model envisages that metal-bearing accreting material is mixed with the metal-depleted mantle material on arrival (by explosions, vigorous convection etc.). Then fractionation occurs in a mantle fractionation zone, melted either locally as a result of impact or through decompression resulting from convection. Trace

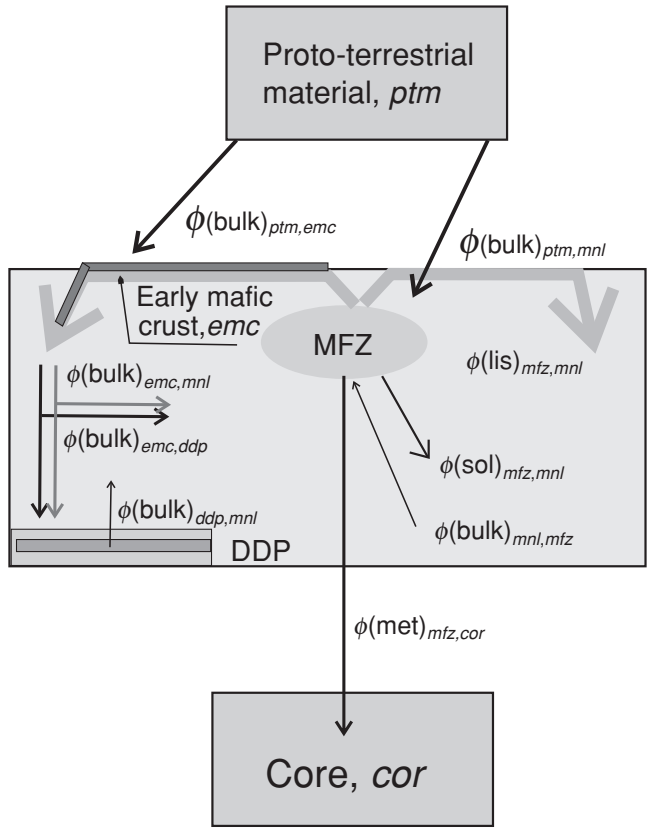

Fig. 18.2 Schematic presentation of chemical transport model for homogeneous Earth accretion and the formation of the core and core–mantle transition-zone (D′′ or DDP) reservoirs. Reservoirs: *ptm*, proto-terrestrial materials; *mnl*, mantle; *mfz*, mantle fractionation zone; *cor*, core; *ddp*, core–mantle transition zone; *emc*, early mafic crust. Materials constituting the fluxes: bulk, bulk undifferentiated material; lis, liquid silicates; sol, solid silicates; met, metal. For example, the mass flux from the early oceanic crust into the DDP is expressed as $\phi(\text{bulk})_{emc,ddp}$; the flux is shown by two perpendicular arrows indicating contributions of two different materials in it (proto-terrestrial + early mafic crustal rocks). The flux of the same material, $\phi(\text{bulk})_{emc,mnl}$, if entrained by a convective mantle flow delivers siderophile elements to the mantle (the "late veneer"). From Tolstikhin *et al.* (2006), © Elsevier Science 2006, reproduced by permission.

siderophile elements are partitioned in equilibrium between liquid and solid metal and silicate minerals and melt (Eqn 12.5).

The metal is concentrated by segregation followed by the merging and settling of droplets; this process can ultimately form large enough blobs to sink through the mantle and join the core. The metal fraction of the mantle is controlled by the feeding flux carrying a given metal content, by the mantle mass and by the mantle–core flux removing metal from the mantle reservoir. Obviously the metal fraction

decreases from $F_{\mathrm{LIM}} \sim 0.3$ at the start of core segregation to very low values during the late stages of the process.

The solid silicates are returned to the mantle reservoir. The silicate melt could form a primitive crust and then also be remixed with the mantle. Both fluxes are highly depleted in siderophile elements and thus dilute the siderophile-element content of the mantle. At a late, terrestrial, stage such early crust may be loaded with chondritic matter (a terrestrial regolith) and sink to the core–mantle boundary, where it is envisaged to form the D″ (DDP) reservoir (Chapter 19).

The partition coefficients

A straightforward outcome of the continuous-core-formation model is that the metal fraction in the mantle decreases in the course of core segregation. Further, as Fe-rich metal is removed to the core, the Fe content in both the metal and the silicate phases in the mantle decreases: the molar ratio $mg\# = \mathrm{Mg}/(\mathrm{Mg} + \mathrm{Fe}^{2+})$, known as the Mg number, of molten and solid silicates increases along with the Ni content of the metal fraction (Schmitt *et al*., 1989; Arculus *et al*., 1990). A more Ni-rich metal phase buffers the oxygen fugacity at higher values, and the mantle becomes progressively less reducing. This causes a decrease in the metal–silicate partition coefficients of transitional and some moderately siderophile elements, including W. To handle this decrease, two "end-member" sets of partition coefficients are defined (Table 18.1). The first corresponds to the strongly reducing conditions in the initial Earth, with a 33% iron-rich metallic phase, whereas the second reflects the limiting case when the metal is just used up, having been presumably Ni- and S-rich (Kramers, 1998). The values of the effective partition coefficients for any intermediate situation are found from the metal content in the mantle by interpolation.

Siderophile elements in the mantle during core segregation

The model solution reveals that the depletion of the mantle in siderophile elements happens in three distinct stages (Fig. 18.3). During the first major stage two competing processes govern their abundance: the addition of undifferentiated chondrite-like material, which adds the siderophile elements to the (collective) mantle, and the partitioning of these elements into a metal phase, followed by their removal to the (collective) core. Because a relatively large fraction of metal is still available, all siderophile elements are strongly partitioned into the metal, and the similarity of the abundances for high and moderate siderophiles simply reflects the mixing of processed metal-free and newly arrived metal-bearing matter. The transition element V becomes lithophile at a very early stage.

The giant impact and its effects constitute the second stage. A mantle depleted in metal and siderophile elements is inherited from the first stage.

Whole-mantle melting leads to a very high fractionation rate and thus very rapid further depletion. In the version shown in Fig. 18.3 the dispersion of the impactor's core and its re-equilibration with the Earth's mantle is complete, and this gives the strongest depletion of moderately siderophile elements possible in this event, as the Earth's core is not dispersed (Canup, 2004).

During the third stage, late accretion builds up metal and siderophile elements in the mantle again, as well as its metal fraction, so that the metal flux into the core resumes at some stage. As accretion slows down and ceases, the metal fraction in the mantle fractionation zone decreases. Therefore the moderately siderophile elements are fixed in the mantle and only the highly siderophile elements will be further depleted.

The late influx of material with a chondritic siderophile-element pattern and the transfer of this material from the Earth's surface into the mantle are indeed unavoidable, according to recent data showing (1) a chondrite-like relative pattern of highly siderophile elements (Becker *et al*., 2006), and (2) a chondrite-like evolution of the Re–Pt–Os isotopic systematics in the mantle (Brandon *et al*., 2006). After the metal content in the mantle has become so low that no further segregation can take place, this final influx sets the highly siderophile elements in chondritic relative abundances.

18.3 Time constraints on terrestrial core segregation

A time constraint on the core-segregation process follows from the ^{182}Hf–^{182}W isotope systematics, as applied to achondritic meteorites (Section 12.4). The simplest way to this constraint uses the assumption that the Earth's core was formed in a single event of metal–silicate fractionation from chondrite-like material: this implies total re-equilibration between metal and silicate at the time t_{GIP} when the giant impact happened. During re-equilibration (the partitioning of W and Hf between the metal core and silicate mantle), the $(^{180}\mathrm{Hf}/^{184}\mathrm{W})_{\mathrm{SOS}}$ ratio (1.325, Table 28.1) changed to the BSE value (17.28, Table 17.1). This assumption relates the present-day $(^{182}\mathrm{W}/^{184}\mathrm{W})_{\mathrm{BSE}} = 0.864\,78$ and the time of the giant impact via a combination of Eqns (10.7b) and (10.9):

$$\begin{aligned}\left(\frac{^{182}\mathrm{W}}{^{184}\mathrm{W}}\right)_{\mathrm{BSE}} = &\left(\frac{^{182}\mathrm{W}}{^{184}\mathrm{W}}\right)_{\mathrm{SOS,INI}} \\ &+ \left(\frac{^{182}\mathrm{Hf}}{^{180}\mathrm{Hf}}\right)_{\mathrm{SOS,INI}} \left(\frac{^{180}\mathrm{Hf}}{^{184}\mathrm{W}}\right)_{\mathrm{SOS}} [1 - \exp(-\lambda_{182} t_{\mathrm{GIM}})] \\ &+ \left(\frac{^{182}\mathrm{Hf}}{^{180}\mathrm{Hf}}\right)_{\mathrm{SOS,INI}} \left(\frac{^{180}\mathrm{Hf}}{^{184}\mathrm{W}}\right)_{\mathrm{BSE}} \exp(-\lambda_{182} t_{\mathrm{GIM}}), \qquad (18.2)\end{aligned}$$

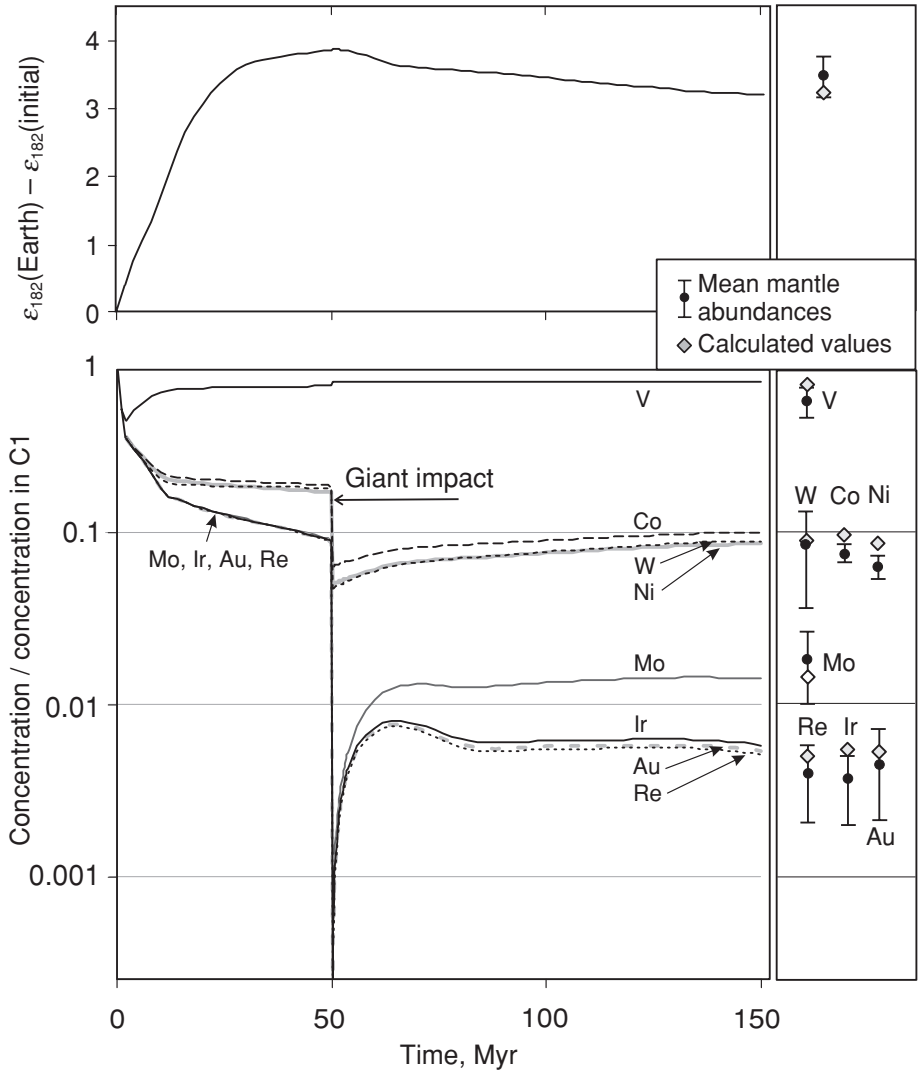

Fig. 18.3 Bottom panel: evolution of the siderophile elements in the Earth's mantle. Moderately siderophile elements were set in the mantle after the giant impact during slow post-impact accretion, when the fraction of metal had become smaller than their silicate–metal partition coefficients. Highly siderophile elements that could be scavenged by very small fractions of metal were further depleted and were not set until after core segregation ceased. Top panel: evolution of ε_{182} for the collective planetesimal mantles (early times) and the Earth's mantle (late times) during core-segregation processes. Note that the giant impact is modelled at 50 Myr after SOS formation; in the range between 30 and 60 Myr after SOS its timing is not critical for the outcome, either for siderophile-element abundances or for the W-isotope systematics.

Right-hand panel: the data and the model results for comparison. The data are as in Fig. 18.1 (element abundances) and Fig. 11.8 (ε_{182}). The model results (diamonds) were calculated after Kramers (1998), using the data of Tables 18.1 and 3.3.

where the second term expresses the contribution of radiogenic $^{182}W^{*}$ during the pre-impact evolution of proto-terrestrial materials and the last term defines the post-impact addition of $^{182}W^{*}$ to the silicate Earth. Substitution of the above values and those from Table 3.3 gives $t_{GIM} = 29.5$ Myr (Kleine *et al.*, 2002). This time scale also fits the lunar ^{182}Hf–^{182}W systematics (Jacobsen, 2005).

However, the validity of the assumption behind this approach and therefore the above time scale are in question. The giant impact probably only partially rehomogenized the bulk Earth + impactor metal and silicate reservoirs. Modelling of the giant impact shows that the Earth's core, the major metal-bearing reservoir at the time of the impact, would have remained in place during this event, although the impactor's core might have been partially or completely dispersed (see above). Thus the Earth–impactor system might have been only partially rehomogenized (Canup, 2004). Further, the $^{182}W/^{184}W$ ratios of iron meteorites, including those considered as cores of differentiated planetesimals (the IIIAB group) are all very primitive (generally even lower than those of metal particles in chondrites, Fig. 11.8) and thus no late re-equilibration events are reflected in them.

Therefore the present-day $(^{182}W/^{184}W)_{BSE}$ ratios could result from incomplete Hf–W re-equilibration of the proto-Earth and impactor materials, in which case the ^{182}Hf–^{182}W systematics would give only a minimum value for the time of the giant impact; longer time scales are also possible. This is illustrated in Fig. 18.3, which depicts a giant impact at 50 Myr after SOS, yielding a difference between the initial-SOS and terrestrial ε_{182} values within the error limits of the data (Fig. 11.8). Further slow accretion and core formation could have lasted long after the giant impact without significant effect on the Hf–W chronology. The reason is that no significant Hf/W fractionation occurred, owing to the low metal content of the mantle. The hafnium-182 had decayed, and all that then happened was a gradual lowering of the ε_{182} value of the Earth's mantle in the course of time as it was mixed with late-accreted chondrite-type matter, further invalidating oversimplified chronological interpretations of the Hf–W systematics for planetary accretion.

19

Heavy "crust" on the top of the core

19.1 Introduction: geochemical indicators for the occurrence of an early-formed apparently isolated reservoir

There is diverse evidence that the core is not the only deep, isolated, geochemically important terrestrial reservoir. This evidence comes not only from studies of the geological record of the differentiated Earth but also from seismology. Of the geochemical data, the isotopic signatures of noble gases in the mantle are especially important and convincing. This is so because of the very low noble-gas abundances in meteoritic and potential proto-terrestrial materials, an effect that is a direct consequence of their "nobility". Consequently, noble-gas isotopic anomalies are readily seen above the background of their terrestrial deficit, which is many orders of magnitude relative to the solar abundance (Fig. 20.1).

(1) Terrestrial xenology and its constraints on the time scales of the early Earth present a paradox (Chapter 27). In a simple, one-reservoir, two-stage degassing model of the mantle, with complete degassing of Xe isotopes during the first stage and complete retention afterwards, the observed abundances of different radiogenic nuclides in mantle and atmospheric Xe require quite different, and therefore inconsistent, degassing time scales: ~ 100 and ~ 500 Myr (Kunz *et al*., 1998). The traditional interpretation of the mantle xenon paradox (since the early inspiring paper by Butler *et al*., 1963) envisages an apparently isolated reservoir, formed ~ 100 Myr after SOS formation, which acts as a source of ^{129}Xe(I) and ^{136}Xe(Pu), from which these species are transferred into the convecting continuously degassing mantle.

(2) The ^{4}He/^{3}He and ^{21}Ne/^{22}Ne ratios in some mantle-derived volcanic rocks can be reproduced neither by a single-mantle-reservoir degassing model nor by the mixing of crustal and mantle materials; thus at least one additional source reservoir with much lower time-integrated (U,Th)/^{3}He and (U,Th)/^{22}Ne ratios than those in the bulk mantle is required (Section 27.4). Further, O'Nions and Oxburgh (1983)

pointed out that heat and He fluxes from the Earth's mantle are "most readily compatible with a convecting upper mantle, which loses its radiogenic heat and He efficiently but which is isolated from a lower mantle reservoir"; this lower mantle reservoir generates a significant portion of the terrestrial radiogenic heat. Van Keken *et al*. (2001) reviewed and confirmed this conclusion.

(3) Notwithstanding the strong overall evidence for the chondritic relative abundances of refractory non-siderophile elements in the bulk silicate Earth (BSE), it is difficult to reconcile their inventories in the present-day continental crust (CCR, which is enriched) and mantle (DMM, which is depleted) with an overall chondritic BSE inventory without invoking some further reservoir.

This is best illustrated by the Sm–Nd systematics (introduced in Section 21.3; see also Chapter 27). For the concentrations of radiogenic $^{143}Nd^*$ in the mantle, $[^{143}Nd^*]_{DMM}$, and in the continental crust, $[^{143}Nd^*]_{CCR}$, the mass balance dictates (e.g. Allègre, 1997):

$$M_{CCR}[^{143}Nd^*]_{CCR} + M_{DMM}[^{143}Nd^*]_{DMM} = (M_{CCR} + M_{DMM})[^{143}Nd^*]_{BSE}. \tag{19.1a}$$

The expression

$$\varepsilon_{143,i} \equiv 10\,000 \times \left[\frac{(^{143}Nd/^{144}Nd)_{RES}}{(^{143}Nd/^{144}Nd)_{BSE}} - 1\right], \tag{19.1b}$$

normalizes the Nd-isotope composition in a given reservoir or sample i to that in the BSE. Substituting this quantity into Eqn (19.1a) gives

$$\begin{aligned} &M_{CCR}[Nd]_{CCR}\varepsilon_{143,CCR} + M_{DMM}[Nd]_{DMM}\varepsilon_{143,DMM} \\ &= (M_{CCR} + M_{DMM})\varepsilon_{143,BSE}\,. \end{aligned} \tag{19.2}$$

The Earth is assumed to be of chondritic composition in respect of the REEs; hence $\varepsilon_{143,BSE} \equiv 0$ and

$$M_{DMM} = -\frac{M_{CCR}[Nd]_{CCR}\varepsilon_{143,CCR}}{[Nd]_{DMM}\varepsilon_{143,DMM}}. \tag{19.3}$$

Substituting into the right-hand side of Eqn (19.3) values from Table 28.2 gives the mass of the depleted mantle as $M_{DMM} \approx 0.3\ M_{BSE}$, whereas the mass of the total mantle today is $\sim 0.995\ M_{BSE}$. Thus a (large) primitive or (smaller) enriched reservoir is required to store a considerable portion of Sm and Nd (as well as all other refractory lithophile trace elements).

(4) A coherent ε(Hf) versus ε(Nd) terrestrial array shows that the regression line ε(Hf) lies about +3 units above the chondritic BSE value (Fig. 27.13). This discrepancy might be explained if the superchondritic Lu/Hf ratios revealed in the outer shells of the Earth were balanced by subchondritic values in a hidden

fractionated early-formed reservoir (e.g. Chase and Patchett, 1988; Blichert-Toft and Arndt, 1999).

(5) Apart from the small anomaly in the 3.8 Gyr West Greenland province (Fig. 27.16(a)), the silicate Earth is highly homogeneous with respect to its $^{142}Nd/^{144}Nd$ ratio. The terrestrial ratio has, however, been found to be ~ 20 ppm higher than that in chondritic meteorites (Fig. 27.16(b), Boyet *et al.*, 2003). Within the framework of a chondritic Earth model (supported, among other evidence, by a chondritic $^{142}Nd/^{144}Nd$ ratio in the lunar mantle; Rankenburg *et al.*, 2006, Chapter 21) this could be interpreted as evidence of an early-formed enriched reservoir separated from the silicate Earth, which became apparently isolated, leaving the remaining mantle somewhat depleted.

(6) Almost all terrestrial magmatic, metamorphic and sedimentary rocks show a relative deficit of Nb (an involatile and incompatible element) and corresponding subchondritic Nb/La ratios. Refractory rutile-bearing eclogite presents the exception because Nb is readily partitioned into rutile, thus providing the complementary superchondritic Nb/La. The problem of the Nb deficit may then be resolved if Nb-bearing eclogite had been transferred, at some stage of the Earth's evolution, into a silicate reservoir that subsequently remained isolated from the convecting mantle (Rudnick *et al.*, 2000).

To explain these observations several proposals have been put forward, most of which are deficient in some way: (i) most proposals consider only some of the observations (e.g. mantle noble gases, Porcelli and Halliday, 2001; Trieloff and Kunz, 2005); (ii) the reservoir proposed is very large and has not been seen by seismic tomography (e.g. Kellogg *et al.*, 1999); (iii) no suggestion has been made of when and how a long-lived distinct mantle reservoir could have been formed and stabilized (e.g. van Keken *et al.*, 2002; Samuel and Farnetani, 2003).

Tolstikhin and Hofmann (2005) proposed that the core–mantle transition zone, termed D″ (hereafter the abbreviation DDP is also used for this zone), could be a distinct geochemically important reservoir; this can be readily understood in terms of the standard model of Earth accretion.

19.2 Present-day status: the core–mantle transition zone

Seismological investigations of the deep mantle have revealed a ~ 300-km-thick zone at the core–mantle boundary, characterized by strong lateral variations of S- and P-wave velocities that indicate a heterogeneous structure of this most dramatic boundary layer inside the Earth. The D″ density, ~ 5.7 g cm^{-3}, exceeds the density of the overlying lower mantle. Its present-day mass is estimated at $\sim 2 \times 10^{26}$ g. The two-fold density contrast between the core and D″ greatly exceeds the overall density difference, $\sim 20\%$, between the two most distinct complementary silicate

reservoirs, the continental crust and upper mantle. The temperature drop across D″ is at least ∼700 °C, whereas the total temperature drop through the almost ∼3000-km-thick overlying mantle is only about twice this value (Fig. 14.3).

Because of the enormous temperature gradient, the viscosity within the D″ zone changes by many orders of magnitude. The flow velocity in the outer core is estimated at $\sim 10^6$ cm yr^{-1} whereas the velocity of convection of the overlying mantle is less than 10 cm yr^{-1} (Section 17.5). The material of D″ appears to be highly heterogeneous on a scale of tens to thousands of kilometres, including velocity anomalies deviating up to 3.5% relative to the standard Earth models (Knittle and Jeanloz, 1991; Weber *et al.*, 1996). The early origin and long-term stability of D″ have been suggested by, among others, Hansen and Yuen (1988) and Wen *et al.* (2001).

19.3 Early formation of the core–mantle transition

Solidification of a post-giant-impact magma ocean must have involved the formation of a vast basaltic to ultramafic crust. This crust must have been bombarded and loaded, both by late accretion and by re-accreting matter ejected by collisions. The modelling of late accretion shows that planetary embryos could have remained dynamically coupled to a low-mass planetesimal swarm (e.g. Agnor *et al.*, 1999). Some of these planetesimals could have crossed the Earth's orbit, accreted and supplied the crust with chondrite-like material. Larger differentiated impactors would produce ejecta and vapour plumes; much of the processed silicates and metal (from the impactors' cores) would have fallen back onto the crust (Canup, 2004). Thus a terrestrial regolith would have been formed.

The chondrite-like and metal components of crust loading would have both enhanced the density of the basalt + regolith cake and enriched it in siderophile elements. Traces of such a component have been found in some of the earliest terrestrial sediments (Fig. 19.1) and on the lunar surface (e.g. Dikov *et al.*, 2002; Day *et al.*, 2006). Along with the siderophile elements, the chondritic component of this terrestrial regolith would also be expected to carry Q noble gases with an enhanced abundance of the heavy species Kr and Xe (Sections 11.5 and 28.3).

Further, because the solar nebula was already transparent at that time, the surfaces of these planetesimals, fragments and grains would have been exposed to the solar wind while in space, and they would thus have accumulated appreciable amounts of implanted solar gases. Even at the present intensity of solar radiation, an exposure time of ∼100 yr is enough to implant $[^4\mathrm{He}] \sim 1 \times 10^{-2}$ cm^3 STP g^{-1} in a radiation-accessible surface layer, and this concentration is similar to those observed in noble-gas-rich meteorites and the lunar regolith (Section 11.5). It is thought that 4.5 Gyr ago the solar wind was at least a factor ∼100 to 1000 more intense than

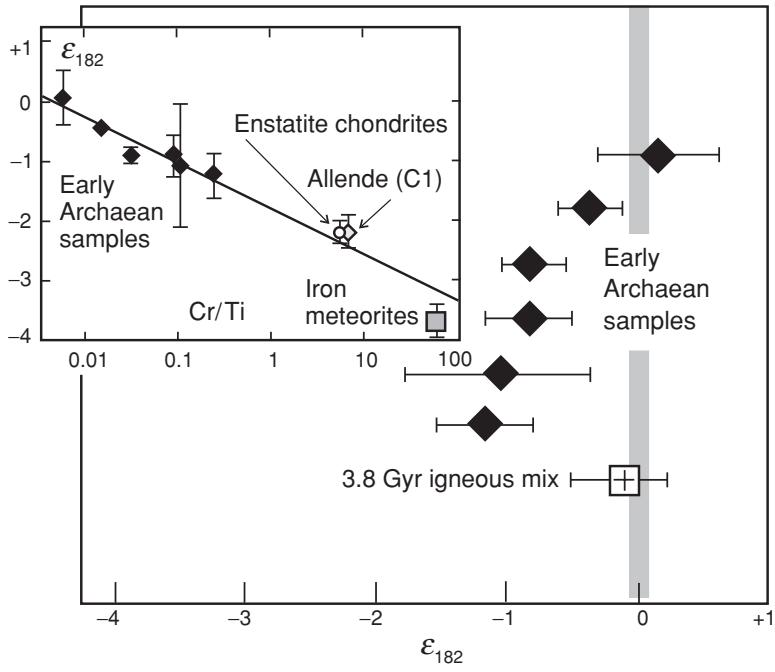

Fig. 19.1 Tungsten-isotope composition in metamorphosed sedimentary rocks from the Isua greenstone belt, West Greenland. The ε_{182} values deviate from terrestrial tungsten, shown as the grey band, and correlate inversely with the Cr/Ti ratios (inset), for which high values are typical of meteorites. These data imply the occurrence of a chondrite-like material on the surface of ancient (3.8-Gyr-old) crust. After Schoenberg *et al.* (2002).

today (Wood *et al.*, 2002). Therefore intense implantation must have occurred on a much shorter time scale. As collision fragments and ejecta resided in space up to millions of years before re-impacting (Melosh and Tonks, 1993), their surfaces would have been fully saturated with implanted gases, a considerable portion of which is expected to have been preserved after accretion of this material onto the crust, as follows from investigations of meteorites (Section 11.5). On the whole the terrestrial regolith thus contained a combination of Q and solar noble gases similar to the "subsolar component" observed in E-chondrites.

As a basaltic-to-ultramafic crust becomes loaded with such a terrestrial regolith its density increases; it becomes gravitationally unstable and tends to sink. The sinking of ocean-crust slabs today is accompanied by extensive dehydration, which would have entailed loss of the noble gases. However, as the giant impact is likely to have caused dissipation of the atmosphere (Section 16.2), this earliest crust could have been essentially dry and thus have sunk without dehydration and consequently without noble-gas loss. Further, the hydration of any silicate rock lowers its solidus.

An unhydrated mafic crust is less likely to undergo partial melting on sinking into a hot mantle; its metal content could thus have been retained. This appears to be the only feasible way that matter could have been transferred into the deep Earth while retaining both noble gases and a metal phase. Metal and chondrite-like material have uncompressed densities $\rho \approx 7.5$ g cm^{-3} and $\rho \approx 4$ g cm^{-3}, respectively, both exceeding the density of the almost metal-free silicate mantle, $\rho \approx 3$ g cm^{-3}. Therefore fragments of this crust, if sufficiently loaded with mixed regolith material, would have a chance of (1) sinking to its base and remaining as a long-lived reservoir, stabilized and isolated from both core and mantle by its intermediate density, and/or (2) being entrained by mantle convection flow and mixed within the mantle, thus delivering late-veneer siderophile elements directly into it.

The requirement of dryness means that this mechanism could only have operated before liquid water became abundant on the Earth's surface. On the one hand, some of the most ancient zircons, up to 4.4 Gyr old, have enhanced δ^{18}O values (Peck *et al.*, 2001; Wilde *et al.*, 2001), apparently indicating some interaction of the magma from which they crystallized with surface water. On the other hand, the most pristine grains do not show such enhanced δ^{18}O (Nemchin *et al.*, 2006). Even if the evidence for interaction with surface water is upheld, this still leaves a perhaps 4.5 to 4.4 Gyr dry interval, which is in reasonable agreement with the mantle xenon-isotope systematics (Section 27.5) and the ^{142}Nd/^{144}Nd data (Section 27.8).

19.4 Summary: geochemical importance of the core–mantle transition zone

Several independent lines of evidence point to the occurrence of an early formed terrestrial reservoir, chemically complementary to the convecting mantle and apparently separated from it. Even though each piece of evidence on its own does not constitute proof, their combination warrants research. A proposal by Tolstikhin and Hofmann (2005) is that the subduction of dry mafic crust loaded with a chondrite-like solar-particle-irradiated regolith could have formed a reservoir that has the required characteristics. The sunk dry crust–regolith mixture could either have been entrained by a convective flow and then mixed within the mantle, as the geochemical model of core segregation envisages (Chapter 18), or it could have sunk further to the mantle–core boundary and resided there, owing to an intrinsic density excess. A discrete layer ~ 300 km thick at the core–mantle transition, D″, is indeed recorded by seismic tomography.

The geochemical consequences of such a reservoir are further elaborated in Chapter 28. Briefly, it would readily enable one to resolve the xenon radiogenic-isotope paradox; such a reservoir could also accommodate extraterrestrial noble

gases. These features, along with the enhanced abundances of incompatible trace elements (including heat-generating ones; e.g. Coltice and Ricard, 1999) in this reservoir and its apparent isolation from the overlying mantle, allow a chemical Earth model with a wholly convecting mantle. Such a model is investigated further in Chapter 28.

20

The early atmo-hydrosphere

20.1 Introduction

The major elements in the Earth's atmosphere and hydrosphere, H, N, C and O, are highly reactive and also play major roles in solid-Earth evolution. Thus the noble gases are the most suitable tracers for early atmo-hydrosphere processes.

The sources of non-radiogenic noble gases in the Earth's interior are reasonably well understood: these include the accreting bodies of chondritic composition that delivered "subsolar" noble gases to the Earth–atmosphere system (in abundances similar to those in E-chondrites), and/or mixed materials such as C1 chondrite-type matter bearing Q gases along with grains containing implanted solar noble gases (Chapter 28).

The present-day abundance of noble-gas isotopes in the atmosphere could have developed via (1) fractionation of the initial composition during early loss event(s) and (2) the addition of radiogenic or fissiogenic isotopes, transferred to the atmosphere from the planetary interior. Comparison of the subsolar noble-gas isotope pattern, seen in the Earth's mantle and postulated as the initial one for the atmosphere, with the present-day atmospheric abundances of unradiogenic isotopes reveals an elemental and mass-dependent isotopic fractionation of the atmospheric gases. Therefore adequate models of atmosphere-loss mechanisms must account for these features (Section 20.3).

The inventory of radiogenic noble-gas isotopes, first of all the ^{129}I–^{129}Xe(I) and ^{136}Xe(Pu)–^{244}Pu systematics, indicates a major loss of atmophile elements, even as heavy as xenon, from the Earth's and the martian atmospheres and also presents rough estimates of the relevant time scales (Section 20.2).

The sources and processing of the major volatiles then may be considered in the context of constraints imposed by noble-gas observations and modelling, as in the fundamental contribution by R. Pepin (1991). Regarding the sources of the "major" atmophile elements, the solar-implanted component does not fit at all to the

atmospheric abundances. For example, assuming that terrestrial ^{14}N and ^{36}Ar are mainly concentrated in the atmosphere, then $(^{14}N/^{36}Ar)_{AIR} = 4.95 \times 10^4$ applies to the Earth as a whole. For the small fraction in the solid Earth a higher value of the ratio $^{14}N/^{36}Ar$ is expected, because N is a main constituent of several minerals, e.g. nitrates, whereas non-radiogenic ^{36}Ar is mainly degassed. The atmospheric ratio exceeds the solar value, $(^{14}N/^{36}Ar)_{SOS} \approx 37$, by a factor ~ 1000, indicating a negligible contribution of solar-wind-implanted nitrogen in the terrestrial budget (Anders and Grevesse, 1989; Wieler *et al.*, 1999). This is also true for the martian nitrogen–noble-gas relationships (Bogard *et al.*, 2001). A similar comparison can be made for $H/^{36}Ar$ in the terrestrial atmo-hydrosphere, giving a relative enrichment factor ~ 100 for terrestrial hydrogen compared with the solar atmosphere. These comparisons provide firm evidence of the pre-accretion decoupling of at least the light noble gases and major volatiles (see an alternative approach in Owen and Bar-Nun, 2001, and references therein).

Comets, carbonaceous, ordinary or enstatite chondrite-like materials, specific proto-terrestrial matter ("terrestrial chondrites" formed in the inner-planet feeding zone) or a combination of these sources could have supplied the post-giant-impact Earth with the major volatiles, H, C and N (Section 20.4). The variable isotopic abundances of these elements in the solar nebula do not allow a single source to be identified. Also, modifications of the elemental and isotopic abundances in the course of volatile-loss events complicate the understanding of pre-loss isotopic compositions and the search for the gas sources. The rates of loss and fractionation depend on the nature of the loss process and its environment and time scales, and all these issues are poorly understood at present. Selected data on the isotope inventory of highly volatile elements on Mars allow some constraint of these complicated issues and are therefore included in this chapter; reliable data on isotope abundances of the martian atmospheric species are available from studies of martian meteorites and the martian atmosphere by satellites (Swindle and Jones, 1997; Bogard *et al.*, 2001).

20.2 Noble-gas inventories and constraints on atmosphere evolution

Light-noble-gas abundances: solar, mantle and atmospheric

There are convincing arguments for the occurrence of solar-like noble gases in the Earth's interior. In the least-air-contaminated mantle-derived samples, the non-radiogenic He and Ne are found to occur in solar-like relative abundances (Chapter 27). Modelling of the evolution of light noble gases in the Earth's mantle also predicts their solar-like initial abundances (Chapter 28). Because mantle degassing transfers atmophile elements to the atmosphere, the solar composition may be used as an initial reference for the light atmospheric noble gases.

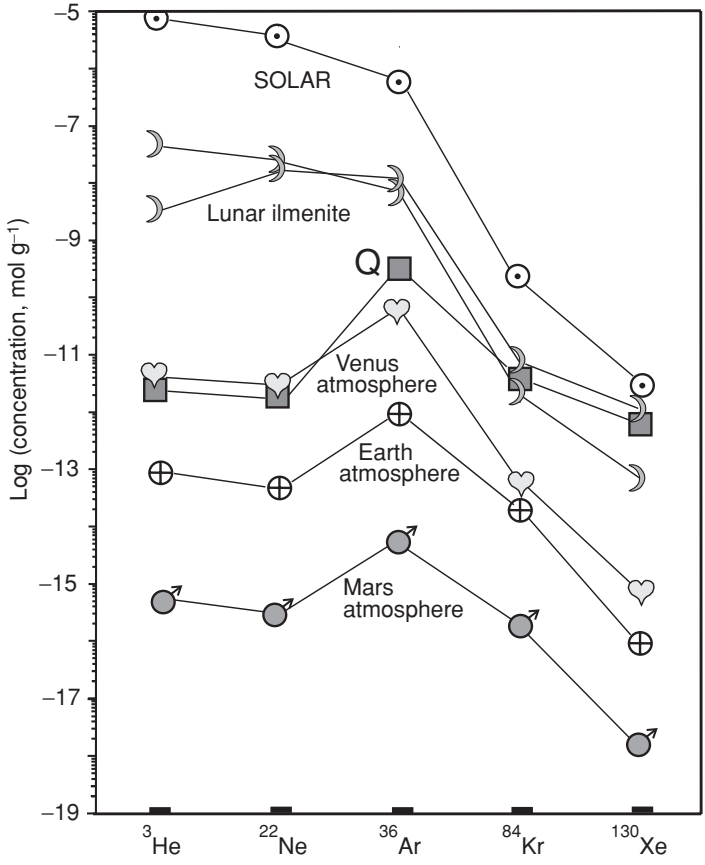

Fig. 20.1 Noble-gas abundances in planetary atmospheres, with solar abundances and those of other reservoirs for comparison. Assuming that planetary atmospheres are the principal noble-gas-bearing reservoirs, then the Earth is depleted from five (Xe or Kr) to eight (Ne) orders of magnitude compared with the solar abundances. Mars shows even more extreme depletion. The ^{3}He abundances correspond to "non-dissipated" atmospheres. From Tolstikhin and O'Nions (1996), © Elsevier Science 1996, reproduced by permission.

A comparison of the initial and present-day atmospheric compositions might give clues on processes that played a part in the development of the atmosphere. The atmospheric noble gases are depleted to different degrees relative to solar abundances (Fig. 20.1). Neon, argon and krypton display a single trend: the lighter the gas, the more it is depleted. Xenon is an important exception, discussed below in Section 20.3.

The atmospheric noble gases, if fractionated, are always depleted in the lighter isotopes. Neon presents a straightforward example: atmospheric Ne is "heavy", i.e. both the ^{20}Ne/^{22}Ne and the ^{21}Ne/^{22}Ne ratios are well below the solar values (Table

11.3). The observed degree of fractionation, f, derived from the differences between the solar ratio $(^{20}Ne/^{22}Ne)_{SOS} = 13.7$ and the atmospheric ratio $(^{20}Ne/^{22}Ne)_{ATM} = 9.80$ and from the mass difference $\Delta = 2$ amu between the two isotopes i, j is given by

$$f \equiv 100\left(\frac{1}{\Delta}\right)\left[\frac{(N_i/N_j)_{ATM}}{(N_i/N_j)_{SOS}} - 1\right] = -14.2\% \text{ per amu.}$$

Neon is a chemically inert element; therefore this fractionation could only be a kinetic effect. Substituting the isotopic and atomic mass ratios for ^{20}Ne and ^{22}Ne into Eqn (10.1) gives an exponent $F = 3.51$; F is the fractionation factor. Applying this value and the respective ratios for ^{21}Ne and ^{22}Ne to Eqn (10.1) again gives $(^{21}Ne/^{22}Ne)_{ATM} = 0.0280$ for fractionated Ne_{ATM}, in good agreement with the present-day atmospheric value, 0.0290. The small difference is probably due to the contribution of nucleogenic $^{21}Ne^*$ to the atmosphere (via the degassing of the solid Earth, e.g. Porcelli and Ballentine, 2002).

Initial and present-day Kr and Xe in the terrestrial and martian atmospheres

To estimate the rate of fractionation and derive the initial composition of a noble gas, the uncertainties related to the addition of radiogenic nuclides should be minimized. A suitable noble gas should have several stable isotopes with a minimal contribution of radiogenic nuclides and be heavier than the major atmospheric constituents. Krypton has five stable isotopes and a minor contribution of fissiogenic Kr isotopes and therefore it fits these requirements better than any other noble gas.

The isotope composition of Kr in the martian atmosphere is indistinguishable from the solar one, and the Kr in Earth's air could have originated from a solar-like precursor via subtle mass fractionation (Fig. 20.2). Thus solar Kr is a likely precursor for Kr in the planetary atmospheres and thus also for planetary interiors. The minor-isotope fractionation of Kr contrasts with the much more severe fractionation of Ne in the martian and terrestrial atmospheres.

Along with solar Kr, solar Xe appears to be a perfect precursor for martian Xe: after subtraction of the contributions of radiogenic and fissiogenic isotopes, a striking similarity is observed between fractionated Xe_{SOS} and Xe in the martian atmosphere (Fig. 20.3). The stronger isotope fractionation of Xe_{ATM}, compared with that for the lighter Kr_{ATM}, which is observed in both the martian and terrestrial atmospheres, presents a fundamental problem (Section 20.3).

In contrast with martian xenology, the precursor of the terrestrial atmospheric Xe has not been properly defined yet: the isotope composition of fractionated Xe_{SOS} does not fit the terrestrial-air Xe (Fig. 20.4). From correlations of

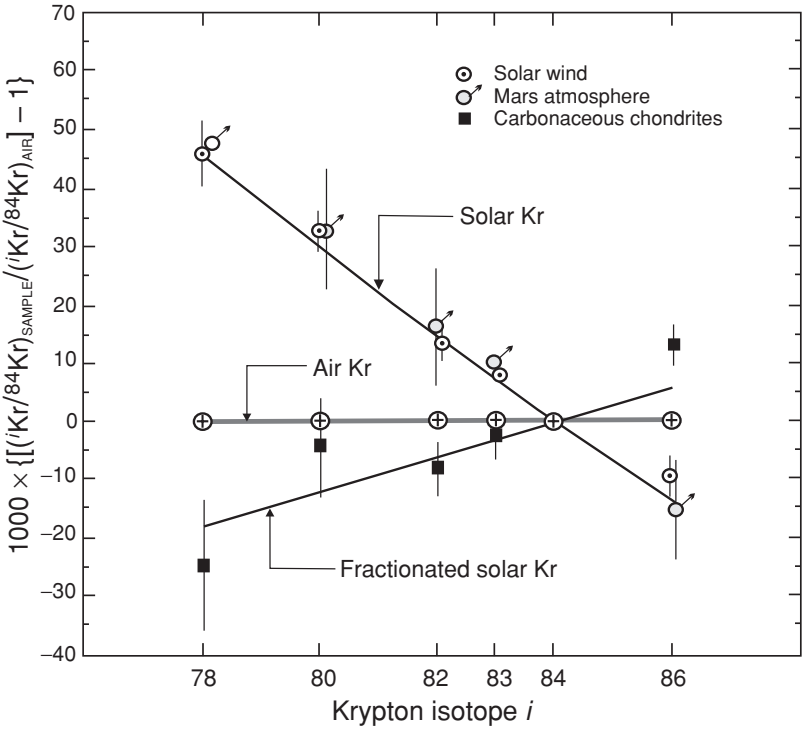

Fig. 20.2 Krypton-isotope abundance δ in solar-wind, martian and terrestrial atmospheres. A modest fractionation of solar Kr, 0.8% per amu, could yield terrestrial atmospheric Kr (the exponential fractionation factor $F = 0.61$; see Eqn (10.1)). From Pepin and Porcelli (2002). Reproduced by permission of the Mineralogical Society of America.

trapped-Xe-isotope abundances in meteorites, Takaoka (1972) and Pepin and Phinney (1978) deduced a specific heavy-isotope-depleted composition, loosely termed "U-Xe" (Table 11.4). Fractionation of this hypothetical U-Xe would yield a composition, that fits the non-radiogenic-isotope abundance of Xe_{ATM}, and therefore U-Xe has been mostly used for modelling the terrestrial ^{244}Pu–$^{136}Xe(Pu)$ systematics (Pepin, 1991; Azbel and Tolstikhin, 1993). Unfortunately, U-Xe has never been observed in any natural environment in spite of a long and extensive search (e.g. Busemann and Eugster, 2002, and references therein).

It appears a promising approach to consider a combination of different atmospheric loss and fractionation mechanisms that start from a solar-wind (SW) Xe composition and result in doubly fractionated SW-Xe that resembles air Xe, leaving some room for a fissiogenic contribution (Fig. 20.4). This is discussed further in Section 20.3.

In summary, both SW-Xe and SW-Kr could be precursors for the martian xenon and krypton, as well as SW-Kr for terrestrial krypton. In contrast, neither solar

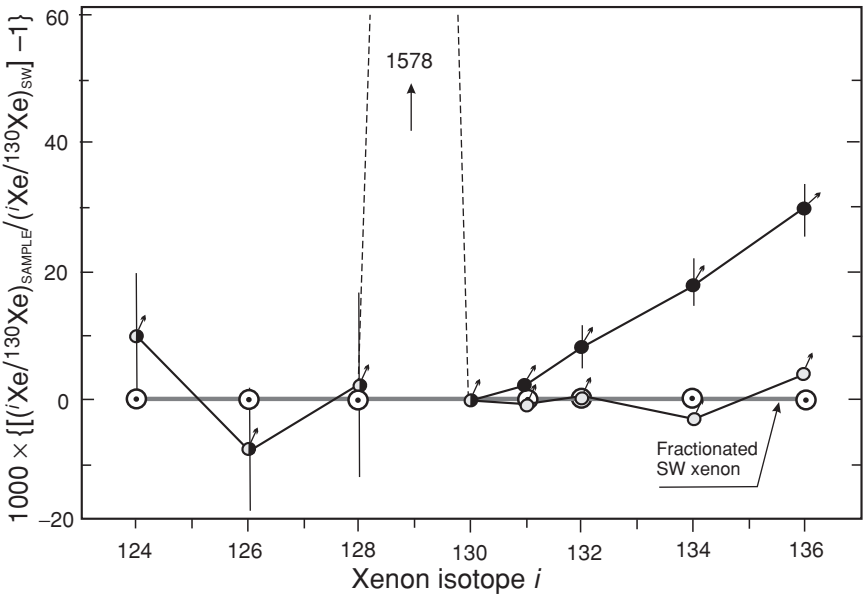

Fig. 20.3 The isotopic abundances δ of solar Xe and of the Xe in the martian atmosphere (black circles). After the fissiogenic $^{131–136}$Xe(^{244}Pu) has been subtracted from the observed martian-atmospheric Xe composition, the result (light grey circles) is indistinguishable from fractionated solar-wind Xe (fractionation factor $f = 3.77\%$ per amu, exponential fractionation factor $F = 4.8$). Some of the original data points are not changed by the fission correction (half-black circles). Note the large excess of ^{129}Xe(I) in the martian atmosphere. From Mathew *et al.* (1998), © Meteoritical Society 1998, reproduced by permission.

Xe nor the very similar Q-Xe can be reconciled to terrestrial atmospheric xenon. Only doubly fractionated SW-Xe may hold some promise for this. The subtraction of initial abundances from those presently observed allows the contributions of radiogenic or fissiogenic Xe isotopes in the Xe of Mars and Earth, and the respective time scales, to be estimated.

Rates and time scales of Xe loss from the Earth-atmosphere system

The uniquely informative value of xenology arises from the fact that radiogenic Xe isotopes have three radioactive precursors with very different half-lives: ^{129}I, ^{244}Pu and ^{238}U (Table 28.1). The ratios of radiogenic (or fissiogenic) Xe isotopes, which record parent–daughter fractionations, thus relate to both relatively short time scales (tens of millions of years, comparable with the ^{129}I lifetime) and rather long time scales (hundreds of millions of years, similar to the ^{244}Pu lifetime). These time scales are long enough for the parent isotopes to decay into the daughters

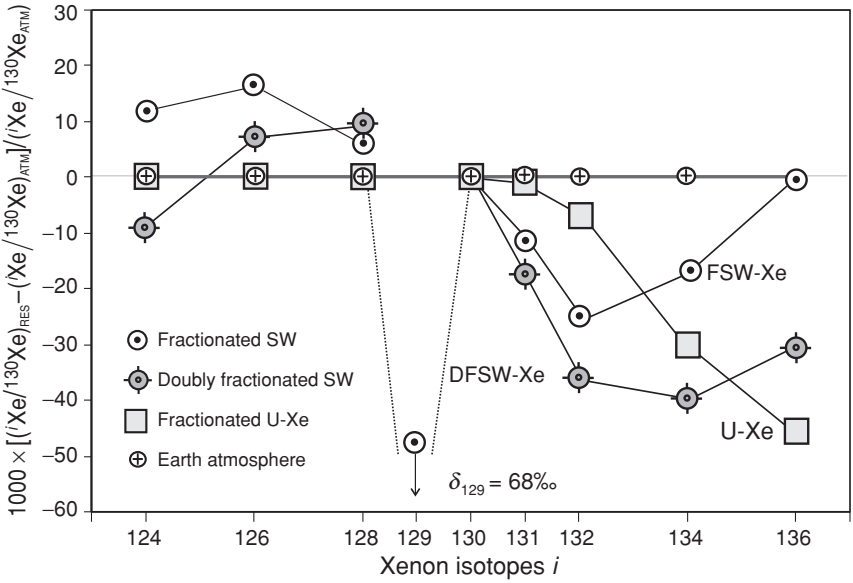

Fig. 20.4 Fractionated solar-wind Xe, U-Xe and air Xe, shown together for comparison. The presently observed composition of atmospheric Xe is used as the reference composition. Fractionated SW-Xe differs from the Earth-atmospheric Xe; ^{132}Xe exhibits the largest deviation at 25‰. The pattern for DFSW-Xe (doubly fractionated solar-wind xenon) shows the results of preliminary modelling starting from an SW composition. A small amount of loss by Jeans escape (at 16 000 K) is combined with a large loss by a dynamic drag escape mechanism (see Section 20.3) and the later admixture of an unfractionated SW component. The total amount of loss is ∼ 96% (all compositions are from Table 11.4). The total contribution of fissiogenic isotopes to the terrestrial atmosphere is $\sim 0.045 \times {}^{136}\mathrm{Xe}_{\mathrm{ATM}}$ if U–Xe is the precursor of the air Xe. Doubly fractionated solar-wind Xe similarly leaves room for fissiogenic Xe isotopes in the atmosphere. Sources of data: Wieler and Baur (1994) and Pepin (1991).

$^{129,131–136}$Xe during Earth accretion and post-accretion evolution. Therefore knowledge of the initial abundances of the parent nuclides in proto-terrestrial matter (Table 28.1) along with the present-day terrestrial abundances of the daughter isotopes (derived below) allows a better understanding of the early evolution of our planet.

As seen in Fig. 20.4, U–Xe leaves room by ∼ 4.5% for the fissiogenic $^{136}\mathrm{Xe(Pu,U)}_{\mathrm{ATM}}$; this corresponds to $^{136}\mathrm{Xe(Pu)}_{\mathrm{ATM}} \approx 0.04 \times {}^{136}\mathrm{Xe}_{\mathrm{ATM}} = 3.3 \times 10^{34}$ atoms. This estimate is highly dependent on the initial Xe-isotope composition, which is poorly understood at present.

In contrast with the uncertain abundances of the heavy Xe isotopes, the initial atmospheric ratio $^{129}\mathrm{Xe}/^{130}\mathrm{Xe}_{\mathrm{INI}}$ is reliably obtained from meteoritic data by interpolation between the two stable neighbouring isotopes ^{128}Xe and ^{130}Xe (Table 11.4). The contribution of radiogenic ^{129}Xe(I) is then readily estimated as

$\delta_{129} = 68‰$ (Fig. 20.4), and this allows a precise estimate of $^{129}Xe(I)_{ATM} = \delta_{129} \times {}^{129}Xe_{ATM} = 1.7 \times 10^{35}$ atoms, where $^{129}Xe_{ATM}$ is the total amount of ^{129}Xe in the Earth's atmosphere; $^{129}Xe_{ATM} = 2.45 \times 10^{36}$ atoms.

Because of the severe degassing of the mantle and crust (Section 27.5), the Earth's atmosphere contains by far the major portion of $^{129}Xe(I)$ available in Earth's accessible reservoirs. However, this is much less than the total amount of $^{129}Xe(I)$ that has been generated in the Earth. For $[^{127}I]_{BSE} = 10$ ppb (Section 17.4) and $(^{129}I/^{127}I)_{INI} = 1 \times 10^{-4}$ (Fig. 11.9), $^{129}I_{BSE,INI} \equiv {}^{129}Xe(I)_{BSE} = 1.93 \times 10^{37}$ atoms. This gives a depletion factor for $^{129}Xe(I)$ of about 0.01. Taking into account a model-derived portion of $^{129}Xe(I)_{DDP}$ still present in the D″ transition zone (Section 28.3) and a possibly lower abundance of ^{127}I in the Earth (Section 17.4), then the depletion factor may increase to ≈ 0.05, but this does not change the important conclusion that not less than 95% of $^{129}Xe(I)$ has been lost from the Earth-atmosphere system. An even more severe depletion of $^{129}Xe(I)$, ~ 0.001, is expected for Mars (Pepin, 1991, 1994; Marty and Marti, 2002). These estimates leave little doubt that both planetary-atmosphere systems lost major portions of their heaviest constituent, Xe, which implies a corresponding loss of all other atmospheric species.

The simplest loss model, i.e. that all the Xe was lost from the Earth-atmosphere system before a time t_{LOSS} and all the $^{129}Xe(I)$ generated after this time has been preserved, allows t_{LOSS} to be derived from the above estimates. Assuming as above that

$$\begin{aligned} {}^{129}I_{BSE}(t_{LOSS})/{}^{129}I_{BSE,INI} &\equiv {}^{129}Xe(I)_{ATM+DDP}/{}^{129}Xe(I)_{BSE} \\ &\equiv \text{depletion factor} = 0.05 \end{aligned}$$

and applying Eqn (1.2), then the equality $\exp(-\lambda_{129} t_{LOSS}) = 0.05$ (λ_{129} is taken from Table 28.1) gives $t_{LOSS} = 70$ Myr, which is the minimum time interval between SOS formation and the loss event. Within the framework of a more complicated model with later loss episodes (as follows e.g. from the Ne-isotope abundances in air) the main event could have happened somewhat earlier, e.g. 50 or 60 Myr after SOS.

The ^{129}I–^{129}Xe systematics alone give only a minimum time scale because the atmospheric $(^{129}Xe/^{130}Xe)_{ATM}$ ratio could have developed from the initial value of 6.05 to the observed 6.496 early in Earth history. The atmospheric xenon, with $^{129}Xe(I)$ already "frozen" into it, could then have escaped from the atmosphere much later. In order to obtain both the loss rate and time scale, the ^{129}I–$^{129}Xe(I)$ and ^{244}Pu–$^{136}Xe(Pu)$ duo is required.

Plutonium is a highly refractory lithophile element, and the initial abundance of ^{244}Pu in the bulk silicate Earth can therefore be reconstructed from the meteoritic $^{244}Pu/^{238}U$ ratio, 0.01 ± 0.005, and from $[U]_{BSE} = 19$ ppb. The occurrence of ^{244}Pu

in the early Earth has been demonstrated by the presence of ^{136}Xe(Pu) in ancient zircons (Turner *et al.*, 2004a). Therefore the total amount of ^{136}Xe(Pu) produced in proto-terrestrial materials and then in the early Earth is reasonably well known, to within a factor ~ 2. Unfortunately the present-day inventory of ^{136}Xe(Pu) retained in the solid Earth + atmosphere system is poorly known, mainly because of the question of the initial Xe-isotope composition (Fig. 20.4).

Applying the same reasoning to the ^{244}Pu–^{136}Xe(Pu) systematics as that discussed above for ^{129}I–^{129}Xe(I) indicates that the time of the ^{136}Xe(Pu) loss is also within the range 60 Myr $\leq t_{\mathrm{LOSS}} \leq$ 250 Myr after SOS formation, for two end-member sets of parameters. Both sets envisage U–Xe as the precursor of air Xe. The shortest time interval is inferred for $(^{244}\mathrm{Pu}/^{238}\mathrm{U})_{\mathrm{INI}} = 0.005$ and the present-day terrestrial $^{136}\mathrm{Xe(Pu)}_{\mathrm{EARTH}} = {}^{136}\mathrm{Xe(Pu)}_{\mathrm{ATM}} + {}^{136}\mathrm{Xe(Pu)}_{\mathrm{DDP}}$ (Table 28.3), and it is similar to that derived for the ^{129}Xe–^{129}I systematics. The longest interval is obtained for $(^{244}\mathrm{Pu}/^{238}\mathrm{U})_{\mathrm{INI}} = 0.01$ and $^{136}\mathrm{Xe(Pu)}_{\mathrm{EARTH}} = {}^{136}\mathrm{Xe(Pu)}_{\mathrm{ATM}}$, the latter quantity being the most poorly known at the present state of the art; both the precursor compositions of air Xe, i.e. SW-Xe and U–Xe, are model dependent and both allow (after adequate fractionation, see Fig. 20.4) a similar amount of Xe(Pu) in the Earth's atmosphere. Also, if more than one loss event occurred then some Xe(I, Pu) must have been lost at later stages, and the time of the first loss of radiogenic Xe isotopes therefore could have occurred earlier, ~ 50 Myr after SOS formation.

An interesting combination of time scales now arises. The Hf–W systematics give a robust minimum time scale of ~ 30 Myr after SOS for Earth accretion, including the giant impact (Section 18.3). The time of the major atmosphere-loss (and Xe fractionation) event is ~ 50 to 70 Myr. The most robust oldest age of a lunar rock obtained by the Sm–Nd method is 4.456 ± 0.040 Gyr (Norman *et al.*, 2003), ~ 100 Myr after SOS.

These dates are therefore in accord with a giant-impact event occurring ~ 50 or 60 Myr after SOS formation almost finalizing core segregation and causing a huge atmosphere loss in which even Xe isotopes, the heaviest atmospheric constituents, were mainly lost (see the next section), leaving behind only a fractionated residual portion of xenon.

20.3 Mechanisms for the loss of volatile elements from the planetary atmospheres

Escape mechanisms

Several loss mechanisms have been suggested, most of which were important at some time in various planetary environments. In this section two mechanisms,

(1) and (2), are considered in some detail; other mechanisms, (3)–(5), are mentioned for completeness.

(1) Thermal (Jeans) escape occurs when the upward velocity of molecules with mass m due to thermal kinetic energy at the exosphere, $v = \sqrt{2E/m}$, exceeds the escape velocity $v_{ESC} = \sqrt{2GM/r}$. Here G is the gravitational constant, M is the mass of the planet and r is the radius of the exosphere. Helium dissipation from the present terrestrial atmosphere is an example (Nicolet, 1957; Pudovkin *et al*., 1981). The velocity of molecules at a given temperature is not uniform but follows a Maxwell distribution. Individual molecules can have velocities that are orders of magnitude above the mean value but with progressively smaller probability. Therefore Jeans escape causes very strong mass fractionation. The escape rate is proportional to $\exp(-GMm/kTr)$, where k is Boltzmann's constant and T is the temperature of the exosphere. Jeans escape is particularly applicable to a superheated post-impact plume or atmosphere. The thermal-loss mechanism is also partly responsible for ongoing hydrogen escape from the atmosphere. The major H loss, however, is non-thermal: H atoms are removed from the exosphere by charge-exchange processes, where an ion with excess energy is converted into a neutral atom with excess energy, i.e. $H + H^{+*} \rightarrow H^{+} + H^{*}$ (an asterisk denotes excess kinetic energy). Ion escape is prevented by the Earth's magnetic field, but neutralized ions are free to escape.

(2) Hydrodynamic escape is related to Jeans escape: an upward flux of a light atmospheric constituent (governed by Jeans escape or the above charge-exchange process) drags heavier species out of the atmosphere. Hydrogen appears to be the most suitable (light and abundant) carrier, and indeed the only one at low temperatures. At very high exosphere temperatures ($\sim 16\,000$ K) such as may have reigned after the giant impact, vaporized silicate matter may have been important (Benz and Cameron, 1990). The resulting hydrodynamic escape would have caused isotopic and elemental fractionation, but less extreme than that due to Jeans escape. The escape rate is approximately proportional to $1/m$ (Zahnle and Kasting, 1986; Hunten *et al*., 1987; Pepin, 1991).

A combination of a small amount of Jeans escape from such a very hot atmosphere (causing strong non-linear Xe-isotope fractionation) with a much more extensive loss by dynamic drag escape appears to yield an atmosphere-like Xe-isotope pattern without the fissiogenic isotopes, as shown in Fig. 20.4. Another possibility envisages the double fractionation of SW-implanted Xe: the isotopically light Xe component was released (from accretion materials) into the early atmosphere (e.g. via ablation) and then fractionated again during Xe loss, whereas the complementary heavy component (FSW-Xe in Table 11.4) resided in the terrestrial regolith and was then subducted to form D″(Section 19.3). These very preliminary considerations appear to hold promise for a solution of the Xe-isotope problem.

(3) Sputtering, i.e. the ejecting of atoms from the exosphere to space via the ionization and acceleration of ions by the SW electric field, is important for atmospheres unprotected by a magnetic field, e.g. for those of Mercury, Mars and the Moon (Jakosky *et al*., 1994; Stern, 1999).

(4) If a dust particle enters into a planetary atmosphere under a small impact angle, $\sim 10^{\circ}$, with an entry velocity equal to or exceeding the escape velocity then the elastic collision of an atom with the dust particle and subsequent collision(s) with major constituents of the upper atmosphere could yield an "upwind" velocity $> V_{ESC}$ and dissipation of the atom (Pavlov and Pavlov, 1997–1998). The dust influx could also deliver solar-like noble gases into the atmosphere, so within the framework of this model both the input of the solar-like noble gases and their fractionation via loss from the atmosphere could be explained.

(5) Impact erosion occurs due to the direct acceleration of the atmosphere (or part of it) by an impact-related shock wave (Ahrens, 1993; Newman *et al*., 1999; Genda and Abe, 2003).

Gas loss from the atmosphere: reservoirs and processes involved

As outlined in the above discussion, Xe and all lighter constituents escaped from the early atmosphere. The escape mechanism caused the thorough fractionation of some elements (e.g. Ne and Xe) while leaving others only slightly fractionated (Ar and Kr in the Earth's atmosphere) or even unfractionated (Kr in the martian atmosphere). A further important feature of atmospheric noble gases is that the $^{84}Kr/^{130}Xe$ ratio in the Earth's atmosphere is ~ 2 and ~ 10 times higher than those in SW and in Q gases respectively. Tolstikhin and O'Nions (1994) suggested an explanation of these observations envisaging a combination of two reservoirs, i.e. the mantle and atmosphere, and two processes, i.e. mantle ingassing or degassing and gas loss from the atmosphere, as follows.

(1) The first process is a fractional solubility-controlled degassing or ingassing of silicate magmas: the heavier the gas, the less soluble it is in silicate melts, Xe being the least soluble (e.g. Lux, 1987). These processes favour the preferential accumulation of Xe in a "gas phase", the atmosphere, whereas a comparatively larger fraction of the lighter noble gases remains in the magma. Here element fractionation but no isotope fractionation is expected.

(2) The complementary process, gas loss from an early atmosphere, favours the opposite trend (better retention of the heavier species). Here both elemental and isotope fractionation are expected.

The first process leads to a higher relative concentration of the heavier noble gases in an atmosphere in equilibrium with a magma ocean, or a more rapid mantle degassing rate in the case of volcanism. In either case, a situation is possible where the amount of Xe left in the mantle was well below that in the present-day atmosphere whereas the mantle abundances of Kr and the lighter noble gases were not less than those in the atmosphere. Modelling predicts upper-atmosphere temperatures up to $\sim 16\,000$ K after the giant impact (Benz and Cameron, 1990), and at this temperature Xe could be lost to a small extent by Jeans escape and further by a process, similar to hydrodynamic escape, driven by dissipation fluxes of both major volatiles and silicate vapour. According to preliminary modelling, these processes could have caused the isotope fractionation of initially SW-like Xe, producing an air-like pattern, whereby Kr and certainly the lighter gases would be blown away from the atmosphere in quantity.

The mixing of this fractionated Xe with unfractionated Xe and Kr, degassed later from the mantle, could have resulted in the isotopic abundances and the Xe/Kr ratio presently observed in the atmosphere.

Further degassing would have replenished the atmosphere with (unfractionated) lighter noble gases, and (impact-induced) events of hydrodynamic escape could then have caused the loss and fractionation of Ne, accompanied by the much less intense loss of the heavier gases with little or no isotope fractionation. After these loss events, the fluxes of unfractionated noble gases from the mantle into the atmosphere would not have been intense enough to overshadow the fractionated-noble-gas pattern that had been set earlier (Tolstikhin and O'Nions, 1994; Tolstikhin and Marty, 1998).

20.4 Major volatile species: inventories and sources

Initial inventories

To identify the sources of the major volatiles and trace their early evolution, the presently observed planetary inventories must be established. The next step is to reconstruct their initial inventories, taking into account possible sinks of atmophile elements into the solid Earth and losses from the Earth-atmosphere system (e.g. Pepin, 1991; Sano and Williams, 1996; Kuramoto, 1997). As follows from the noble-gas data, lighter species are lost from planetary atmospheres preferentially to heavier ones (Sections 20.2 and 20.3). Therefore the relative abundances of light isotopes in any plausible source must have been higher than (or at least equal to) those in the present-day Earth's accessible reservoirs (EARs), which include the atmosphere, continental crust and convecting degassing mantle.

The reconstructed initial terrestrial inventories can then be compared with the contents of the potential sources, the solar nebular gas or volatile-rich chondrite- or cometary-type matter. Thus the early evolution of the solar nebula must be considered, as well as the subsequent evolution of source(s) during about 4500 Myr. Also important is the potential of the sources' orbits to intersect those of the terrestrial planets and the specific behaviour of the elements during or after impact on a host planet. As explained in Chapter 16, the primordial early atmosphere was blown away and the post-giant-impact Earth was a volatile-poor planet. The major atmophile elements were delivered mainly at the later stages of accretion.

The concentrations of these elements in potential carriers must be high enough to supply the bulk terrestrial inventories by the addition of material comprising a relatively small fraction of the Earth's mass, also taking into account the gas-loss events discussed above.

Abundances of atmophile elements in the Earth's accessible reservoirs (EARs)

Hydrogen

There are two major terrestrial reservoirs of water, the hydrosphere and the mantle. The amount of hydrogen in the hydrosphere is well known, since there are 1.4×10^{24} grams of water, including oceans, freshwater and groundwater, and the bulk D/H ratio of this water is 1.557×10^{-4} (Lecuyer *et al.*, 1998). The depleted mantle appears to have an H_2O content between 100 and 500 ppm, the lower value being preferable (Sobolev and Chaussidon, 1996; Workman and Hart, 2005). This range is consistent with the amount of OH detected in nominally anhydrous minerals in mantle-derived xenoliths (Bell and Rossman, 1992) and corresponds to (0.4–2) $\times 10^{24}$ grams of water, with hydrogen that is 4%–8% lighter than ocean-water hydrogen. Thus the bulk present-day water amounts to 2.6×10^{24} g with D/H = 1.50×10^{-4} (Fig. 11.4, Robert *et al.*, 2000).

Carbon

Three reservoirs are important for the terrestrial carbon inventory. Chemical sediments and metasediments contain in total 3.5×10^{22} g of carbon in the form of carbonates (Ronov and Yaroshevsky, 1976; Wedepohl, 1995). In addition the continental crust contains $\sim 0.9 \times 10^{22}$ g of organic carbon (coaly matter and hydrocarbons); other crustal sources are insignificant (Lecuyer *et al.*, 2000).

The mantle component of carbon appears also to be important in the terrestrial inventory. The ^{3}He concentration in the mantle and the $CO_2/^3$He ratio in mantle melts give 37 ppm of carbon (Marty and Tolstikhin, 1998). This value is consistent

with the lower end of the plausible range of carbon concentrations (40–80 ppm) obtained for the upper mantle from thermodynamic modelling (Holloway, 1998). The total amount of carbon in the mantle is thus $\sim 1.4 \times 10^{23}$ g.

Carbon in the mantle is characterized by $\delta^{13}C \approx -5.2‰$ (relative to the PDB standard). This $\delta^{13}C$ value (corresponding to $^{13}C/^{12}C = 0.011\,18$) is generally considered to characterize the total EAR reservoir of $\sim 1.8 \times 10^{23}$ g of carbon (Fig. 11.4, Marty and Zimmerman, 1999). Note, however, that this is not firmly established, as organic carbon is biologically fractionated to light values ($\delta^{13}C \sim -10$ to -35) and its total amount (see above) is in fact estimated from an isotope mass balance, assuming that $\delta^{13}C \approx -5.2‰$ for the sum of the carbonate and organic carbon. Light carbon with $\delta^{13}C$ values down to $-25‰$ has been reported for diamonds; these values, however, have been attributed to subducted organic carbon or, alternatively, to fractionation (Cartigny *et al.*, 2001). The light carbon in the mantle probably does not constitute a significant reservoir and is not considered in the terrestrial inventory.

Nitrogen

The atmosphere is the largest N reservoir, $N = 3.87 \times 10^{21}$ g. Studies of mantle-derived rocks have allowed the C/N ratio of the upper mantle to be constrained at 530 ± 230 (Marty and Tolstikhin, 1998), assuming incompatible behaviour of N in mantle melting (but see Javoy, 1998; Cartigny *et al.*, 2001 for an alternative view). This indicates a low amount of N in the mantle, a factor ~ 10 less than the total atmospheric abundance.

Considerable N-isotope heterogeneity is observed in mantle-derived volcanics, with $\delta^{15}N$ (relative to the atmosphere) dropping as low as $-10‰$, the average value being $-3.3‰$ (Marty and Zimmermann, 1999). Diamonds also record heterogeneous $\delta^{15}N$ values varying between $-10‰$ and $+5‰$, with a few values down to $-25‰$ whereas the main population clusters around $-5‰$. This probably reflects the mixing of a crustal component and an atmospheric component recycled into the mantle with isotopically lighter primeval N inherited from proto-terrestrial material.

Crustal rocks contain a somewhat greater amount of N than the mantle, but show positive $\delta^{15}N$ values from about 2‰ to 5‰. This inventory gives a bulk value of $\delta^{15}N_{EAR} \sim 0$ and a N_{EAR} value $\approx 5 \times 10^{21}$ g (Fig. 11.4).

These estimates of the bulk EAR inventories of the major volatiles are summarized, normalized to Al and solar abundances, in Fig. 20.5. The bulk "initial" inventories of major volatile elements that would have been observed if no loss from the EARs had occurred are even more poorly known than these. The modelling of a hydrogen-driven hydrodynamic escape mechanism predicts pre-escape abundances of H, C and N a factor 10 to 100 above the present-day values. If the

giant impact caused a major loss of atmophile elements, and only $\sim 10\%$ of the total mass of the planet was added afterwards (as follows from the terrestrial inventory of siderophile elements, Chapter 18), the concentrations of the atmophile elements (or atmophile-element/Al ratios as in Figs. 11.4 and 20.5) in their potential sources would therefore have been at least a factor 100 to 1000 above the present-day abundances in EARs.

Sources of major atmophile elements and relevant processes

Among proposed mechanisms for the formation of the Earth's atmosphere, the direct gravitational capture of nebular gas by a sufficiently massive planet (Hayashi *et al*., 1979) appears to be the least plausible hypothesis, as it is in conflict with the inferred inventories of the atmophile elements, the relevant time scales and the generally accepted hypothesis of Moon formation via a giant impact.

A very early massive atmosphere delivered by accreting planetesimals (e.g. Matsui and Abe, 1986) requires volatile-rich carriers. In contrast with this, the proto-terrestrial material was formed relatively close to the Sun and therefore is expected to be volatile-poor (Fig. 14.4). Further, this hypothesis encounters the same problem with the giant impact as that of a captured nebular atmosphere. For these and other reasons we do not consider this scenario here (see Genda and Abe, 2003, and references therein).

Late delivery of the major atmophile elements appears to be the most plausible concept at the present time, although it is not simple or well understood. In the asteroid belt, beyond ~ 2.5 AU, a relatively cool environment enabled volatile-rich planetesimals, such as the carbonaceous chondrite parent bodies, to accrete. Disturbance of their orbits by Jupiter and Saturn is thought to have caused collisions and scattering and, as a result of this, many objects from the asteroid belt could have impacted on the terrestrial planets. Depending on the original orbits of Jupiter and Saturn, it is possible that this could have occurred at a time when the Earth was almost fully accreted (Morbidelli *et al*., 2000; Chambers and Wetherill, 2001).

If the compositions of these bodies were similar to carbonaceous chondrites, they could have supplied the terrestrial planets with adequate amounts of volatile elements in relative abundances broadly similar to those of the EARs (Fig. 20.5), and a 10% post-giant-impact accretion of this nature would have supplied sufficient quantities to allow for hydrodynamic escape, as discussed above.

On the one hand, the C1 chondrites contain slightly heavier nitrogen, with $\delta^{15}\mathrm{N} \approx +40‰$ relative to the terrestrial value, $\sim 0‰$. Material similar to e.g. CV carbonaceous chondrites could have supplied the Earth with isotopically appropriate nitrogen and carbon. The average water concentration in these meteorites is

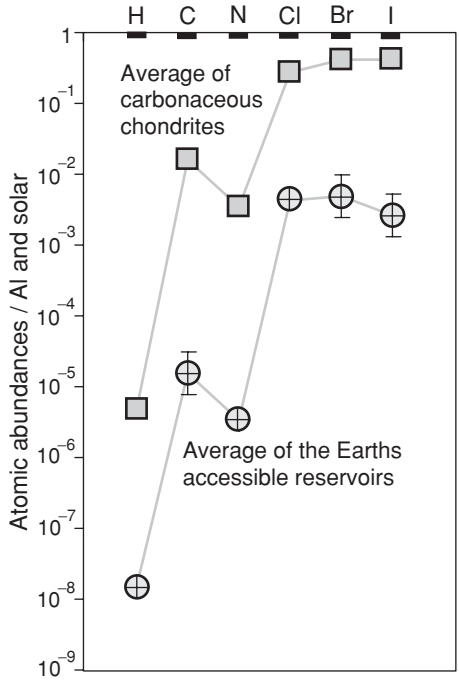

Fig. 20.5 Abundances of highly volatile elements in average carbonaceous chondrites and the Earth's accessible reservoirs (EARs). After Kramers (2003).

somewhat low and the water is slightly D-enriched compared with what is needed to reproduce the terrestrial value (Fig. 11.4); however, several CV chondrites show an enhanced H_2O content and D/H ratios below the terrestrial value. On the other hand, both C1 and CV chondrites contain Q noble gases with $^{130}Xe/^{84}Kr$ ratios exceeding the terrestrial value by a factor > 10. This complicates the solution of the "missing Xe" problem (Section 20.3).

Ordinary chondrites have a relatively low abundance of water with variable D/H ratios (Section 11.4). Also, the N in O-chondrites is somewhat heavier than the terrestrial N. For the C–N duo, enstatite chondrite material appears to be a good candidate. These meteorites incorporate appreciable amounts of relatively light C and N (Fig. 11.4) and subsolar noble gases, which would also fit terrestrial initial values. Also important is that their O-isotope composition is identical to the terrestrial value (Fig. 10.8(b)); therefore the formation of E-chondrites could have taken place not far from the terrestrial feeding zone. However, water is virtually absent in E-chondrites.

Thus the above speculations merely indicate that a volatile-rich chondrite-type source for major atmosphere components is realistic. This is not in conflict with a solar-implanted origin for light noble gases in the mantle: as discussed in Section

20.1 an amount of SW implantation that had only a negligible effect on the terrestrial major-volatile-element inventory could still deliver a major contribution of the light noble gases.

20.5 Summary

Noble gases appear to be the best tracers of processes in the early history of the Earth's atmosphere. Strong isotope fractionation of the heaviest noble gas, Xe, the high Kr/Xe ratio in the Earth's (and the martian) atmosphere and a great deficit in radiogenic and fissiogenic early-generated Xe isotopes indicate a severe loss of Xe very early in Earth history, and it is speculated that this was associated with the giant impact that formed the Moon. The strong fractionation of Xe points to Jeans escape and dynamic-drag escape mechanisms at extremely high temperatures, which would have caused the complete loss of the lighter atmospheric constituents. However, Kr and the lighter noble gases are more soluble in silicate magma than Xe, and therefore a larger proportion of their terrestrial inventory would have been hidden in the magma ocean while the major loss of the primordial atmosphere occurred. The subsequent degassing (of unfractionated Xe, Kr and lighter gases) and mixing set the atmospheric Xe-isotope abundances and Kr/Xe ratio, and neither changed substantially during the later evolution of the atmosphere.

The major constituents of the Earth's secondary atmo-hydrosphere, N, C and H, were delivered to the Earth in solid form, essentially at the post-giant-impact accretion stage. Chondrite-like material, particularly of (relatively water-rich) CV-type, or E-chondritic bodies and icy planetesimals, could be likely sources both from the abundance and the isotopic perspective.

Light noble gases (presently seen in the mantle) were transferred by solar-particle-irradiated material. This is quantitatively modelled in Chapter 28.

The strong isotope fractionation of air Ne can be explained by post-giant-impact episodes of partial atmospheric loss. Hydrodynamic escape appears to be an adequate loss mechanism, in which the heavier species were also partially lost but without significant isotope fractionation.

21

Light from the Moon . . .

21.1 Introduction

As seen in the preceding chapters, the giant impact fundamentally affected the history of the Earth. This event has been postulated to explain the existence of the Moon, and the parameters for modelling it have been tuned to produce a Moon with the right mass and metal/silicate ratio, and the right angular momentum for the Earth–Moon system.

One of the impressive results of the Luna and Apollo missions is a chronology of the magmatic evolution of the Moon: major planetary-scale differentiation occurred $\sim$4.45 Gyr, followed by mare basaltic magmatism within $\sim$ 4.0 to 3.0 Gyr ago. Unlike terrestrial materials, the ancient rocks of the Moon have preserved a record of its very early evolution.

Within the framework of this book, it would have been attractive to exploit this record in order to understand the early history of our planet better. However, from the following sections we shall see that, although the existence of the Moon is essential evidence for the standard model of planetary accretion and although there is an underlying partial similarity of chondrite-like volatile-depleted initial matter to that of the Earth (Section 21.2), the Moon's evolution was fundamentally different from what happened on the early Earth. An exception is the record of frequent impacts on the Moon with a late heavy bombardment lasting up to $\sim$ 3.8 Gyr ago, which therefore must also have occurred on Earth. Apart from this, we could almost say that we study the Moon in order to understand what *has not happened* on Earth.

The Moon's story nevertheless yields important perspectives on non-terrestrial planetary processes and their consequences but, because it sheds only a little light on the early development of the matter of our planet, only a brief discussion of lunar composition, structure and the corresponding processes is given in this chapter. We recommend the monographs edited by Hartmann *et al*. (1984), Canup and Righter

(2000), and Jolliff *et al*. (2006), the review by Warren (2003) and the discussion of unresolved lunar issues by the Taylor trio (2006) for detailed presentations of major aspects of the Moon's composition, origin and evolution.

21.2 Bulk composition and formation of the Moon

Moon composition: important similarities to that of the Earth

The Moon is almost completely covered by regolith material. A reconstruction of the composition of the lunar interior is complicated because all lunar rock samples came from this regolith and thus can never fully represent the outcrop material belonging to a given intrusive body, magmatic province etc. Therefore lunologists must collect evidence on the lunar compositions by grains, in the literal meaning of this word. Because of this fundamental feature of lunar samples, isotopic records, which allow the chemistry of inaccessible reservoirs to be reconstructed, appear to be the most reliable.

In this regard oxygen, the most abundant element of rocky planets, but with isotopic compositions that vary substantially between the different solar system bodies, is of prime importance. The compositions of the Moon's and the Earth's oxygen lie exactly on the same terrestrial fractionation line (Fig. 10.8(b), Wiechert *et al*., 2001; Spicuzza *et al*., 2007). Samples from the Moon and the Earth also have indistinguishable $^{53}Cr/^{52}Cr$ ratios, suggesting that their source materials had similar Mn/Cr and initial $^{53}Mn/^{55}Mn$ ratios at the time they formed as closed systems for Mn and Cr. In contrast, Mars and the chondrites show different initial $^{53}Cr/^{52}Cr$ ratios, indicating that the Earth, Mars and the chondrite parent bodies had separate feeding zones, isolated from each other (Lugmair and Shukolyukov, 1998; Carlson and Lugmair, 2000). Also, Mn is a moderately volatile lithophile element (Table 3.1) and the FeO/MnO ratio inferred for the bulk Moon composition is very similar to the terrestrial value, in agreement with the above isotopic constraints (Warren, 2005).

From these isotopic and chemical criteria, the proto-Earth and proto-lunar matter could have originated in a close neighbourhood; the high degree of similarity (especially indicated by O-isotope compositions) favours this conclusion even though it is not a unique one as discussed by Taylor *et al*. (2006).

The ^{182}Hf–^{182}W chronometer gives $\sim$ 30 Myr as a minimum time interval between solar system formation and the giant Moon-forming impact (Section 18.3). This is consistent with the most reliable estimate of the ancient lunar crust age, 4.456 ± 0.040 Gyr (Norman *et al*., 2003). Thus no contradiction to the giant-impact hypothesis arises from the available time constraints, and the proto-Moon and proto-Earth could indeed share an overall similar early accretion history.

Moon and Earth compositions: differences?

There are important differences between the bulk compositions of the Earth and Moon. The (uncompressed) density of the Moon (3.34 g cm^{-3}) is much less than the Earth's density (4.45 g cm^{-3}), indicating a heavy-element deficit; only Fe is heavy and abundant enough to make this difference. Geophysical investigations of the Moon can be reconciled with a lunar model having a small metallic core, $\sim$ 1%–3% of the lunar mass, at least an order of magnitude less than that of the Earth (Hood and Zuber, 2000). Even though this interpretation is not unique (Jolliff *et al*., 2006), the uncompressed density contrast between the Earth and Moon is indeed unarguable.

The abundances of the involatile moderately siderophile elements (e.g. Co and W) in lunar rocks are broadly similar to the terrestrial values; however, the highly siderophile elements in the lunar mantle are depleted by at least a factor 10 compared with the Earth's mantle, and they do not show a chondritic relative abundance pattern. These features have been used to argue that the mantles of the Moon and Earth are too different to have a common source (Wolf and Anders, 1980; Newsom and Taylor, 1989). This could, however, have originated from highly-siderophile-element (HSE) partitioning into the lunar core in the course of its segregation (Kramers, 1998; Righter, 2002) and therefore may shed no light on compositional similarities or dissimilarities to the Earth.

Regarding major lithophile-element abundances, two different models of the bulk silicate Moon are at present still being considered: one is quite similar to the BSE model (Warren, 2005) and the other postulates enhanced abundances, by a factor $\sim$ 1.5, of the most refractory elements, such as Al, Ca, Ti and including heat-producing U and Th (Taylor *et al*., 2006).

An important difference between the Moon and Earth is the greater depletion of lunar rocks in some volatile elements, first of all the alkali metals, compared with terrestrial rocks. For example, the K/U and Rb/Sr ratios are a factor $\sim$ 4 below the terrestrial values (see Fig. 14.4). Isotopic data corroborate this more severe depletion of the Moon in volatile elements. The U–Th–Pb isotope systematics indicate two major source regions for lunar rocks, both with time-integrated μ values exceeding the bulk silicate Earth $\mu \approx 8$. Many lunar crustal rocks were derived from an extremely high-μ source, with $\mu > 500$. Lead-isotope ratios in lunar meteorites point to a less extreme source with μ between 10 and 50 but still generally above the terrestrial value (Premo *et al*., 1999; Snyder *et al*., 2000).

In the ^{87}Rb–^{87}Sr isotope systematics, the very low initial $^{87}Sr/^{86}Sr$ ratios of lunar rocks indicate that the loss of volatile Rb occurred from proto-lunar materials before the giant impact, within $\sim$ 15 Myr after the formation of the solar system. Such an early depletion in volatile elements is, however, not a unique feature of lunar rocks,

which are almost indistinguishable from a highly differentiated meteorite species, the eucrites. Another type of differentiated meteorites, the angrites, shows an even more extreme depletion (see Fig. 14.4).

The $^{142}Nd/^{144}Nd$ ratios measured in lunar basalts by Rankenburg *et al*. (2006) appear to be indistinguishable from chondritic matter, in contrast with those in terrestrial mantle and crustal rocks (Fig. 27.16(b)). This apparent discrepancy between the Moon and Earth may in fact underline the initial similarity of the Sm- and Nd-isotope abundances in the Earth, Moon and chondrites; whereby in the Earth a somewhat enriched reservoir, the D″ layer, was isolated at some time after the giant impact (as proposed in Chapter 19).

It should be noted, however, that ^{142}Nd was produced in an s-process whereas ^{144}Nd was yielded by both s- and r- processes; therefore the mixing of the two could have been incomplete, and more detailed studies of the Nd-isotope composition in chondritic meteorites are needed. Andreasen and Sharma (2006) showed that the excess observed in terrestrial rocks is not the effect of any nucleosynthesis presolar anomaly. The lunar $^{142}Nd/^{144}Nd$ ratios strengthen the case made by these authors that the chondritic ^{146}Sm–^{142}Nd systematics indeed provide a reference for the planets.

The giant-impact hypothesis and peculiarities of lunar composition

The giant-impact hypothesis (Chapter 16) allows some of the compositional differences between the Earth and the Moon to be understood. The Mars-sized impactor had already been differentiated into metal core and silicate mantle. High-resolution simulations of the giant impact (Canup, 2004) show that the impactor's iron core was eventually in the main combined with the proto-Earth core, whereas material derived from the far-side mantle of the impactor was blown away, together with a small portion of its metal, beyond the Roche limit. From this already metal-poor material the Moon was formed $\sim$ 10 years after the impact (Pritchard and Stevenson, 2000). Thus, an impact-related mechanism of Moon formation can readily explain the depletion of the lunar material in metal, even if the impactor itself had an Earth-like bulk-metal/silicate ratio.

Regarding the lunar siderophile-element abundances, several authors have suggested that the Moon inherited siderophile elements from the mantle of the impactor, and afterwards further depletion occurred during equilibrium core formation (Newsom and Taylor, 1989; Jones and Hood, 1990; Righter and Drake, 1996). Because of the one-stage segregation process on the Moon and the small fraction of metal available, only highly siderophile elements were partitioned into the lunar core, thus

leaving behind a lunar mantle further depleted in accordance with the respective partition coefficients (Kramers, 1998).

The lunar material could have lost volatile elements at the nebula stage, in the course of formation of the Mars-sized impacting body (Ruzicka *et al.*, 2001), and/or during the post-giant-impact vaporization of volatiles (Pritchard and Stevenson, 2000). The Sr-isotope evidence cited above favours the first two scenarios.

21.3 Early lunar crust and mantle

Lunar mountains: the ancient crust

On the Moon there are two major landforms that can be clearly distinguished even with the naked eye: relatively dark plains and light-coloured highlands. The plains are composed of lunar basalts, covering $\sim$ 17% of the lunar surface but constituting only $\sim$ 1% of the lunar crustal mass. The lunar crust, 83% of the lunar surface, forms the highlands. We always see the same side of the Moon because its centre of mass lies $\sim$ 2 km closer to the Earth than its geometrical centre. The conventional explanation of this offset is that the light highland crust is more abundant on the far side of the Moon. The total mass of the lunar crust corresponds to at least $\sim$ 6% of the Moon, which is much higher than the Earth's crust/mantle ratio (Taylor, 2001; Warren, 2003).

The lunar crustal rocks can be subdivided into three major groups and one minor group, using mineralogical and chemical criteria, e.g. the Ca/(Ca + Na) ratio in plagioclase versus the magnesium number in associated mafic minerals (Warren and Kallemeyen, 1993; Shearer and Papike, 2005), as follows. (1) The most abundant rocks are rich in plagioclase feldspar and belong to the ferroan anorthosite suite (FAS); these rocks constitute 70% to 80% of the crust. (2) Magnesium-rich basalt-like rocks (the high-magnesium suite or HMS) belong to the second group, making up about 20% of the crust. (3) The high-alkali suite (HAS) is relatively rare and comprises various rock types, including granites, that are extremely enriched in alkali metals. Also important are (4) basalts enriched in K, Rb, the REEs and P (KREEP). These unique rocks, not observed on Earth or in meteorite parent bodies, are not very abundant on the lunar surface, but they could represent an important ancient complementary reservoir still preserved at some depths in the Moon.

Ferroan anorthosites differ strongly from all other magmatic lunar rocks (Fig. 21.1, Table 21.1). The anorthosites generally consist to more than 90% of an extremely calcic plagioclase, anorthite, and therefore show a high [Al_2O_3] value, $\sim$ 25%. The associated mafic minerals ($\leq$ 10%) are primary high-Ca pyroxene, subordinate low-Ca pyroxene and rare olivine. These are quite iron-rich, with *mg*#

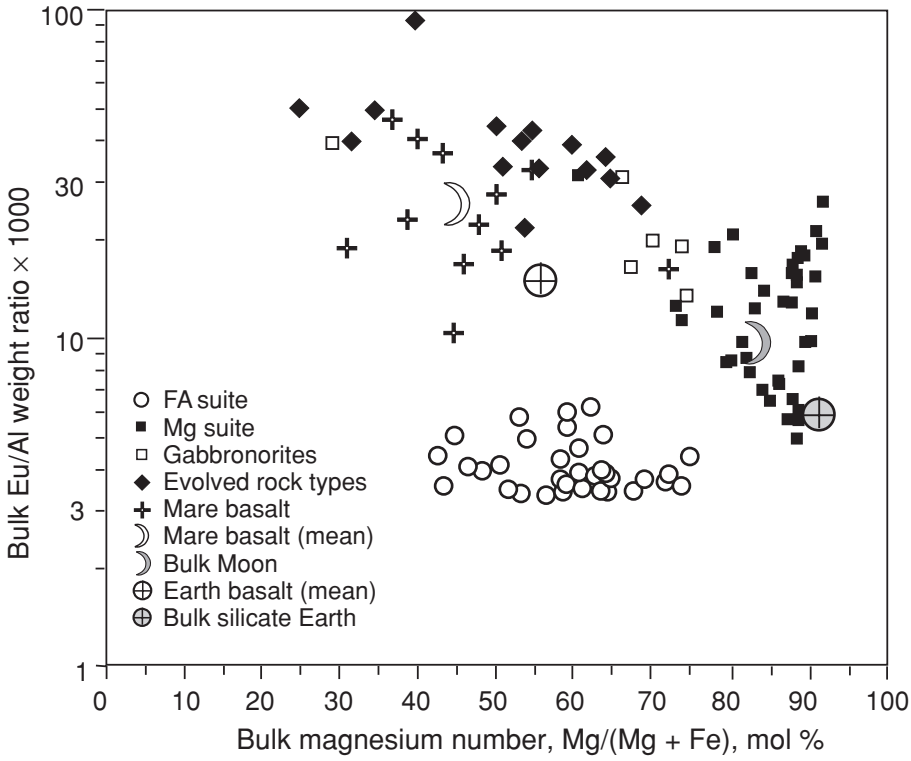

Fig. 21.1 The plot shows Eu/Al vs. Mg/(Mg + Fe), illustrating the bimodality of lunar rocks. After Warren (2003); bulk Moon composition from Newsom (1995); bulk silicate Earth and mean Earth basalt compositions from Tables 17.1 and 24.1.

values ~ 50 to 70, which is much lower than the model value for the bulk silicate Moon.

The REE patterns in FAS are approximately flat or slightly LREE-enriched with abundances similar to or slightly higher than the chondritic abundances but generally lower than in other lunar rocks; in Fig. 21.2 a pronounced excess of Eu is clearly seen; Eu readily replaces the Ca in Ca-rich plagioclase, as also seen in cumulate eucrites (Fig. 12.3). Within ferroan anorthosite rocks, plagioclase and pyroxene show complementary REE patterns that are broadly consistent with equilibrium partitioning during crystallization from a parental melt (Fig. 21.3).

The high-magnesium suite (HMS) comprises mainly dunites, troctolites, norites and gabbros, i.e. rocks consisting of, or rich in, high-Mg phases. In their mineralogy and major-element composition, HMS rocks resemble the products of fractional crystallization, i.e. cumulates, of basaltic melts (Table 21.1). They have *mg*# values up to 90 but show some incompatible-element enrichment relative to chondrites. Their REE abundances are generally higher than in FAS with variable positive Eu

Table 21.1 *Chemical composition of the major types of lunar rock (major-element oxides in wt %, trace elements in ppm)*[a]

	Highland crust	KREEP	High-Ti basalts	Low-Ti basalts	All basalts
SiO_2	45	50	38.9	48.2	44.6
TiO_2	0.56	2	12.1	0.7	4.7
Al_2O_3	24.6	15.1	8.9	10.4	10.6
FeO	6.6	10.3	18.9	18.3	19.1
MnO	0.072	0.14	0.29	0.25	0.27
MgO	6.8	8.3	8.4	12.5	9.4
CaO	15.8	9.8	10.5	9.4	10.6
Na_2O	0.45	1.2	0.39	0.15	0.35
K_2O	0.075	1.1	0.06	0.02	0.11
Cr_2O_3	0.1	0.17	0.39	0.26	0.32
Sc	10	23	80	47	58
V	21	40	92	165	140
Co	20.6	25	20.3	46	34
Ni	250	n.d.[b]	12	51	36
Rb	1.7	22	2	1.05	4
Sr	120	200	173	103	170
Zr	63	1400	216	50	219
Ba	66	1300	166	62	158
La	5.3	110	11.6	6.8	9.5
Sm	2	48	8.3	8.8	8.2
Eu	1	3.3	1.75	1.81	1.6
Tb	0.35	10	2.19	2.24	1.9
Lu	0.21	5	1.16	1.23	0.96
Hf	1.4	38	7.5	8	5.4
Th	0.9	22	0.26	0.4	1.1

[a] The all-basalts composition has been derived from a large sample set whereas the high-Ti and low-Ti sets represent end-member compositions. From Warren (2003) and Ruzicka *et al*. (2001).
[b] Not determined.

anomalies (Fig. 21.2). They may show enhanced REE abundances and negative Eu anomalies, indicating a contribution of KREEP material (Snyder *et al*., 1995; Shearer and Papike, 2005).

The high-alkali suite comprises rocks with extremely high alkali-element content, elevated incompatible-lithophile-element abundances and generally evolved chemical signatures. This suite includes anorthosites and gabbros as well as lunar monzodiorites and granites.

The KREEP basalts, showing a very high enrichment in incompatible elements, appear to represent an extreme case of magmatic fractionation. The REE concentrations in KREEP basalts can reach 700 times the chondritic values with a minor

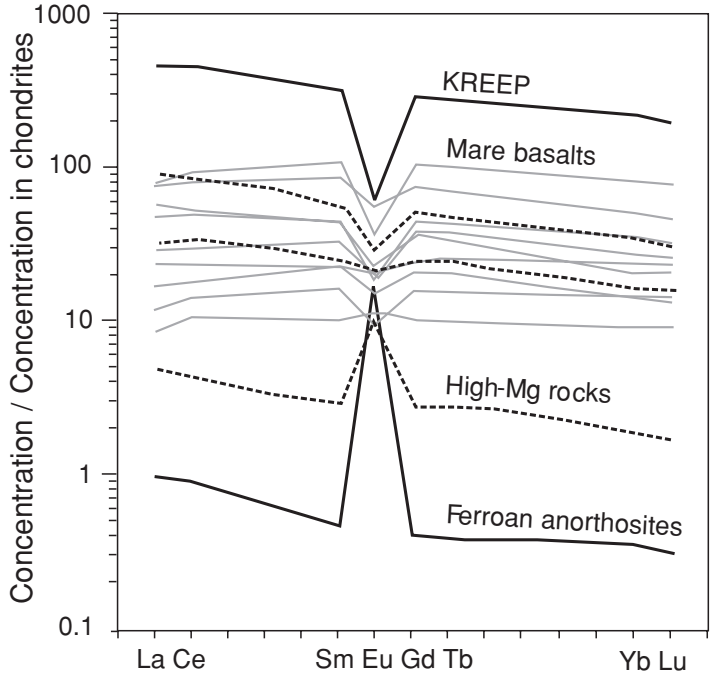

Fig. 21.2 Chondrite-normalized REE concentrations in ferroan anorthosites, Mg suite rocks, KREEP and mare basalts. Note the low abundances and pronounced positive Eu anomaly in ferroan anorthosites, owing to the compatibility of Eu^{2+} in Ca sites of plagioclase, and complementary signatures in KREEP; the La/Sm ratios in mare basalts are lower (even subchondritic in most Ti-rich basalts) than in KREEP; both rock types show negative Eu anomalies. After Warren (2003) and Shearer and Papike (2005).

LREE enrichment relative to the HREEs and with a large negative Eu anomaly (Fig. 21.2). KREEP appears to be heterogeneously distributed below the lunar crust; using enhanced [Th] (which is detectable by satellite-borne γ-ray spectrometry) as a KREEP tracer, the highest contribution of this unusual material is observed in the regolith of the most ancient lunar basin, Procellarum, with [Th] $\approx$ 4.6 ppm, whereas concentrations four times lower are inferred for the regolith of the relatively young South Pole Aitken basin (Warren, 2005).

Late mare magmatism: composition of the post-crust-extraction lunar mantle

Lunar mare basalts (LMBs) differ in mineralogical and chemical composition from their terrestrial analogues. They are more picritic in composition, i.e. far richer in mafic silicates and poorer in feldspar. They show a strong depletion of volatile

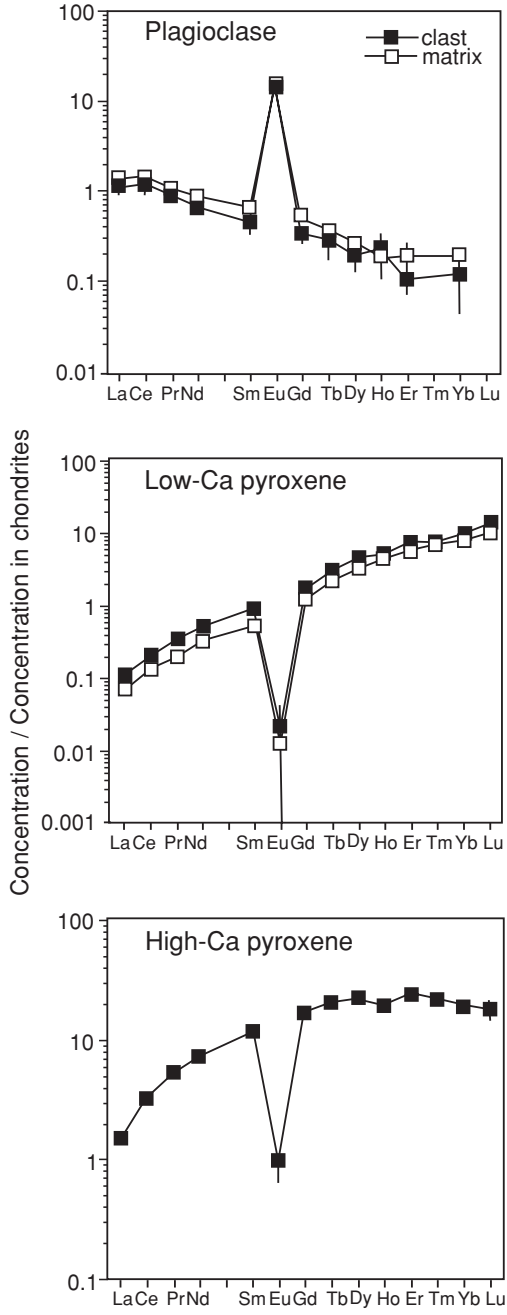

Fig. 21.3 The plots show C1 chondrite-normalized REE patterns for minerals from lunar ferroan anorthosites. The complementary abundance patterns in plagioclase and pyroxenes from ferroan anorthosites indicate that the minerals crystallized from the same evolving parental magma. From Floss *et al.* (1998), © Elsevier Science 1998, reproduced by permission.

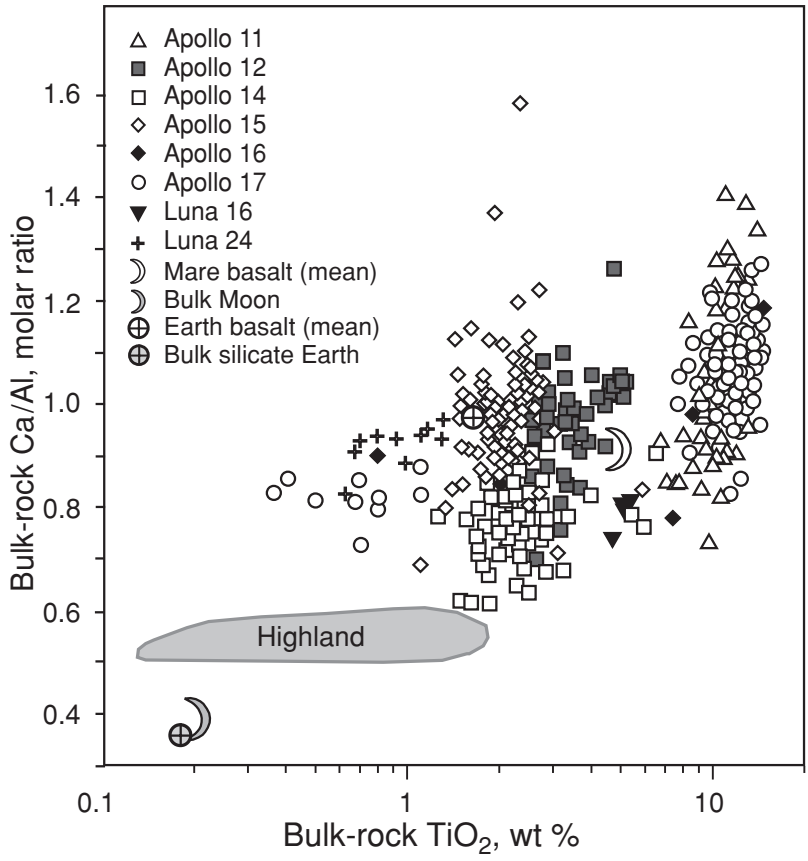

Fig. 21.4 The apparent bimodal distribution of TiO_2 in mare basalts. High-Ti basalts show somewhat enhanced Ca and reduced Al (compared with lower-Ti ones, Table 21.1) and therefore have generally enhanced Ca/Al ratios. Modified after Warren (2003); the bulk Moon composition is from Newsom (1995); bulk silicate Earth and Earth basalt compositions are from Tables 24.1 and 17.1.

elements (Fig. 14.4), and the presence of Fe metal and of reduced valence states for Fe, Ti and Cr reflect O-fugacities much below those typical of the Earth's mantle. Further, they show a spectacular range in TiO_2 concentrations, from 0.2% to 17%. Traditionally, low-Ti and high-Ti LMBs were distinguished (Fig. 21.4); however, remote sensing data indicate a high abundance of intermediate-Ti rocks, so that the Ti-concentration range is wide and probably not strictly bimodal (Warren, 2003). In any case ilmenite, the major concentrator of Ti, appears to be an important constituent of the upper lunar mantle, the LMB source. Lunar mare basalts contain typically $\sim$ 8%–10% Al_2O_3, indicating an appreciable amount of Al in the mantle even after the differentiation that produced the Al-rich lunar crust.

The concentrations of rare Earth elements in LMBs are within 10 to 100 times [C1], enhanced values being typical for the high-Ti rocks. The REE patterns are flat with well-defined negative Eu anomalies in almost all samples (Fig. 21.2), which is reminiscent of basaltic eucrites (Fig. 12.3). This feature of mare basalts indicates that a large portion of the lunar mantle underwent plagioclase fractionation and removal before mare magmatism.

Introduction to Sm–Nd and Lu–Hf systematics

Of all long-lived decay systems, the Sm–Nd and Lu–Hf isotope systematics have proved most suitable for both the age determination of lunar rocks and the identification of their source reservoirs. There are several reasons for this. All four elements are refractory, lithophile and moderately incompatible, and three of the four belong to the REEs, for which the behaviour is better understood than that of most other trace elements (Section 10.2). In both cases, the daughter elements are somewhat more incompatible than the parents in the course of partial melting. Therefore the parent/daughter ratios (and the rate of accumulation of radiogenic isotopes) decrease in magmas and the corresponding magmatic rocks, whereas the residual assemblages follow an opposite trend (Figs. 27.13 and 27.18). Also, the Sm/Nd ratios are strongly fractionated between pyroxenes and feldspars, both major constituents of gabbroic to anorthositic rocks (Fig. 21.3). For the Lu–Hf systematics, the strong preferential partitioning of Lu in garnet is an important feature, so that a garnet-bearing assemblage in equilibrium with a melt acquires an enhanced Lu/Hf ratio. The opposite, a low Lu/Hf ratio, is found in ilmenite-bearing rocks in equilibrium with melts (Beard *et al.*, 1998). Furthermore, Hf behaves as a chemical twin of Zr and therefore is built into zircons up to a few per cent, reliably preserving its isotopic signature in these resistant minerals (Section 27.8).

The Sm–Nd pair comprises two decay systems: long-lived ^{147}Sm–^{143}Nd (α-decay, $\tau_{147} = 106$ Gyr) and short-lived extinct ^{146}Sm–^{142}Nd (Table 3.3). Lutetium-176 undergoes β-decay, $\tau_{176} = 37.17$ Gyr. The long half-lives of ^{147}Sm and ^{176}Lu mean that the radiogenic contribution to ^{143}Nd and ^{176}Hf is always relatively small, and the ε-notation (Eqn 19.1b) is therefore generally used to highlight small deviations of a given sample or reservoir from the chondritic evolution line. The relevant parameters of these systematics are presented in Tables 3.3 and 28.1.

In the case of the Earth, numerous measurements of the ^{147}Sm/^{144}Nd and ^{143}Nd/^{144}Nd ratios allow Nd model ages to be estimated (Fig. 21.5); these are used in turn to obtain the crustal-age distribution function (Section 26.5) and to constrain models of crustal growth and recycling (Chapter 28). In contrast, the lunar-mantle sources appear to be highly heterogeneous, and an average mantle ε_{143} could hardly be derived from the mare basalt data, as discussed below.

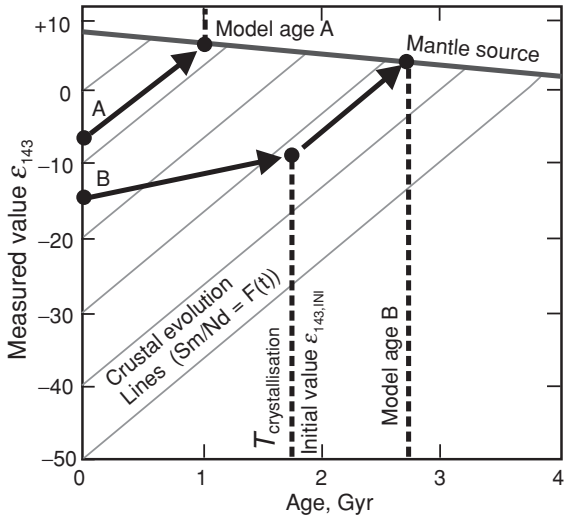

Fig. 21.5 The Nd model-age concept. Because of the relatively simple behaviour of REEs, an Nd model age can be derived for a single sample, and such ages can be used to understand and model the evolution of crustal reservoirs on Earth (Section 26.5). Sample A is of mantle origin; its model age is indistinguishable from the crystallization age. Sample B is of crustal origin; substituting measured values of $^{147}Sm/^{144}Nd$ and $^{143}Nd/^{144}Nd$ (or ε_{143}) and the crystallization age into Eqn (10.7a) gives the initial $^{143}Nd/^{144}Nd$ (or $\varepsilon_{143,INI}$). Substituting this initial value and a model crustal $^{147}Sm/^{144}Nd$ ratio into the same equation and varying the age T until ε_{143} converges with that of the mantle source evolution line gives the model T_{143}.

The Sm–Nd and Lu–Hf lunar chronology: ancient age of the lunar crust

Mineral isochrons for $^{147}Sm/^{144}Nd$ versus $^{143}Nd/^{144}Nd$ obtained on four individual FAS samples gave 4.56 ± 0.07, 4.44 ± 0.02, 4.29 ± 0.03 and 4.40 ± 0.11 Gyr (Carlson and Lugmair, 1988; Alibert *et al*., 1994; Borg *et al*., 1999). Norman *et al*. (2003) noted that in the feldspars of FAS some disturbance of Sm–Nd systems might have occurred due to impacting. They obtained a Sm–Nd date of 4.456 ± 0.040 Gyr from just the pyroxene fractions of these four FAS samples and considered this to be the most robust estimate for the age of the suite. High-magnesium-suite magmatism immediately followed, or could have been contemporaneous with, FAS formation and extended over a period from 4.45 to 4.0 Gyr ago. The initial Sr-isotope ratios of HMS rocks are higher than those of FAS, indicating that they originated from a somewhat Rb-enriched reservoir.

All the FAS and HMS samples seen in Fig. 21.6 display slightly positive initial ε_{143} values ∼ 0.8, indicating an LREE-depleted source. Carlson and Lugmair (1988) inferred a source for the Moon with $\varepsilon_{143,INI} \approx +1$. This is still within the

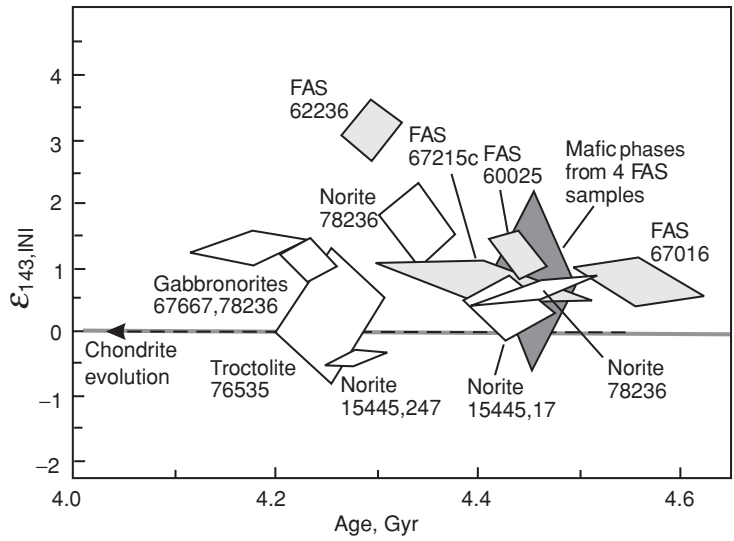

Fig. 21.6 Initial $^{143}Nd/^{144}Nd$ ($\varepsilon_{143,INI}$) values in lunar rocks belonging to the ferroan anorthosite suite (FAS) and high-magnesium suite (HMS). Note the grouping of initial Nd compositions in lunar-rock sources around an $\varepsilon_{143,INI}$ value $\sim +0.8$ without a visible trend, in accord with the close-to-chondritic Sm/Nd ratios inferred for the lunar magma ocean. Carlson and Lugmair (1988) suggested a slightly depleted source for the Moon with $\varepsilon_{143} = +1$. The black diamond (mafic phases) presents the most reliable FAS age and respective $\varepsilon_{143,INI}$. After Borg *et al.* (1999) and Norman *et al.* (2003).

possible range of chondritic meteorites, taking into account the variations in these (Jacobsen and Wasserburg, 1984) and a possible analytical bias caused by different measurement methods (Nägler and Kramers, 1998).

According to lunar chronology, KREEP magmatism was most active between 4.2 and 3.8 Gyr ago; KREEP basalts show slightly negative initial ε_{Nd} values, indicating an LREE-enriched source with a $^{147}Sm/^{144}Nd$ ratio equal to 0.17, only slightly below the chondritic value (0.196).

The Sm–Nd chronometer gives ages for mare basalts ranging from 4 to 3 Gyr (Warren, 2003). In view of these much younger ages, basaltic magmatism is generally considered to be unrelated to the processes that formed the lunar crust but to have been caused by large impacts, although this is still being debated. Lunar basalts have positive and highly variable $\varepsilon_{143,INI}$ values, indicating an LREE-depleted heterogeneous mantle source (Fig. 21.7). The observed $\varepsilon_{143,INI}$ values can only partially be due to differences in age: the variations within individual landing sites (comprising basalts of presumably similar ages) are also very large (e.g. A12 in Fig. 21.7) showing that basalts have indeed sampled a highly heterogeneous mantle source,

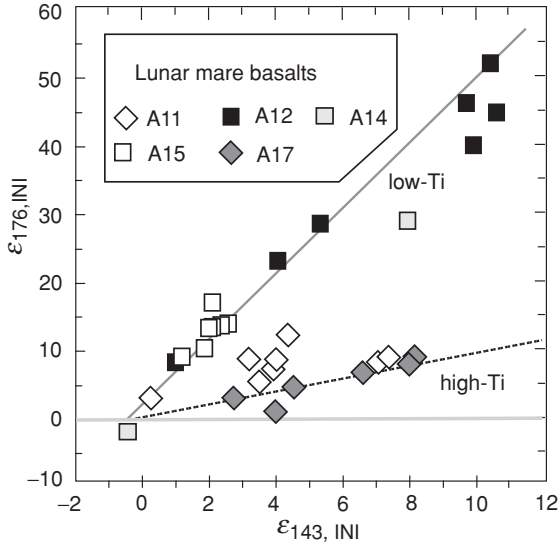

Fig. 21.7 Chondrite-normalized initial Hf- and Nd-isotope compositions in lunar mare basalts. The compositions display two distinct trends (both differ from the terrestrial array, Fig. 27.13). Also, the samples from one landing site (A12) show rather variable $\varepsilon_{143,INI}$ and $\varepsilon_{176,INI}$ values, indicating source heterogeneity. The Lu/Hf and Sm/Nd ratios in all the lunar basalts are nevertheless similar, contrasting with what would be expected from the heterogeneity of the sources. An explanation of these puzzling features is proposed in Section 21.4 and Fig. 21.9. After Beard *et al.* (1998), © Elsevier Science 1998, reproduced by permission.

$0.2 < {}^{147}Sm/{}^{144}Nd < 0.3$, compared with the SOS ratio, 0.196; this ratio governed the development of $\varepsilon_{143,INI}$ from an almost chondritic value to up to +10 in the time interval between lunar magma ocean (LMO, see the next section) crystallization ($\sim$ 4.45 Gyr ago) and lunar mare magmatism (between 4 and 3 Gyr).

The variation in $\varepsilon_{176,INI}$ is even larger, and indicates ${}^{176}Lu/{}^{177}Hf$ ratios of ~ 0.13 and ~ 0.10 for the highest $\varepsilon_{176,INI}$ values in the A14 and A12 basalts respectively, exceeding the SOS value (0.036) by almost a factor 4, much larger than for the Sm/Nd ratio. A further striking feature is that in the low-Ti basalts, the $\varepsilon_{176,INI}$ values correlate very differently with the $\varepsilon_{143,INI}$ values than in the high-Ti ones, where the variation in $\varepsilon_{176,INI}$ is quite small.

In view of the great heterogeneity portrayed for mantle sources by these isotopic fingerprints, the elemental Sm/Nd and Lu/Hf ratios of mare basalts themselves are surprisingly uniform. The Sm/Nd ratio is close to the chondritic value, as seen from the REE patterns (Fig. 21.2), and Lu/Hf is about 0.6 times chondritic, independently of the Ti content. The paradox cannot be resolved by invoking mixing, as this would

obliterate the isotope signatures. A unifying hypothesis for lunar mantle evolution is briefly reviewed below.

21.4 Early evolution of the lunar mantle and crust

The global lunar differentiation: a mass-balance approach

There are several independent lines of evidence that a large and probably even major part of the Moon was involved in early planetary-scale magmatic differentiation. From the point of view of the major-element chemistry, high concentrations of Al_2O_3 in ferroan anorthosites, which are the most abundant crustal rocks, require Al extraction from a major part of the Moon. If it is assumed that (1) the $[Al_2O_3]$ values in the silicate Earth and Moon are similar, $\sim 4\%$ (chondritic, enhanced by core extraction, Table 17.1), (2) the average $[Al_2O_3]$ value in the lunar crust is $\sim 25\%$ (Table 21.1) and (3) the minimal crust/mantle ratio is ~ 0.06, then it would take $\sim 40\%$ of the Moon to supply Al to the crust (Warren and Kallemeyen, 1993). Meanwhile the chemical compositions of lunar mare basalts (LMBs) indicate that the lunar mantle still contains an appreciable amount of Al: a comparison with terrestrial basalts gives [Al] in the LMB source as ∼two-thirds of the initial abundance. This and the above estimate imply that crustal Al was extracted from the whole mantle.

Regarding the trace-element chemistry, the negative Eu anomalies, seen in almost all LMBs and picritic glasses, indicate widespread fractionation of the mantle before the onset of basaltic magmatism, i.e. earlier than ~ 4 Gyr ago. Also, the extremely high concentrations of incompatible elements in the KREEP basalt source imply that this source was extracted from a substantial portion of the Moon.

Concept of a lunar magma ocean: simplest model

The mass-balance considerations cannot be satisfied by petrological models based on partial melting (as generally applied to the terrestrial mantle): this mechanism would allow the plagioclase content of the lunar crust to be at most ~ 50 wt %, well below the observed concentrations, which average $\sim 75\%$ and range up to 90%. As a way out of this contradiction the concept of a lunar magma ocean (LMO) was proposed. It was suggested that the highly anorthositic rocks of the lunar crust were formed via plagioclase crystallization and flotation in this LMO (see Warren, 2003, and references therein).

However, plagioclase can only crystallize from a high-aluminium parental magma with $Al_2O_3 \geq 15\%$ and under the moderate-*PT* conditions found at depths

of $\sim$ 200 km or less in the lunar mantle (e.g. Ringwood, 1979; Warren and Kallemeyen, 1993). Therefore, again assuming that the bulk Moon [Al] value is similar to that of the silicate Earth, an approximately four-fold pre-enrichment in Al of the plagioclase-sourced LMO portion is required. Further, a massive anorthositic crust with low *mg*# values (see Fig. 21.1) could not have been produced directly from a lunar mantle if this had had an ultramafic composition with *mg*# $\sim$ 90.

These problems are solved by the LMO model, which conforms to magmatic petrology. First, mafic minerals denser than the melt i.e. olivine and then olivine + pyroxene, segregated, sank and settled at the base of the LMO. The deeper the settled layer, the higher the olivine contribution, so that the lowermost mantle would consist of dunite (Fig. 21.8). The concentrations of Al and incompatible elements would thus increase and the *mg*# index in the remaining LMO magma would decrease, raising its density. Then, after $\sim$ 75% equilibrium crystallization of olivine and pyroxene, the plagioclase would become a liquidus phase and its segregation and flotation would start. Plagioclase scavenges Eu but not the other REEs and so the residual melt would develop enhanced REE concentrations with a significant negative Eu anomaly: the more plagioclase is extracted, the more pronounced the Eu anomaly in the remaining melt becomes (see the right-hand panel in Fig. 21.8). The plagioclase crust and the complementary melts are both slightly LREE enriched, owing to the segregation of LREE-depleted Ol + Px in the underlying mantle (Shearer and Floss, 2000). Iron and titanium are excluded from the plagioclase cumulates and are further enriched in the melt. The continued accumulation of Fe and Ti then leads to ilmenite becoming a liquidus phase in the late shallow LMO and to the formation of a Ti-rich reservoir in the upper mantle (e.g. Beard *et al*., 1998, and references therein).

The LMO becomes progressively enriched in incompatible elements. Late intrusions of magmas from this reservoir into the anorthosite crust could have produced cumulates of the HMS and evolved magmas of the high-alkali suite; finally, extremely fractionated melts in the solidifying magma ocean could have been the source of KREEP basalts (Warren, 2003).

The LMO concept implies convection of the lunar mantle. As discussed in Section 17.5, vigorous convection of the terrestrial magma ocean prevented crystal settling and Earth-mantle differentiation. The very low viscosity of an ultramafic silicate melt would have allowed intense convection in the LMO. The principal difference between the lunar and terrestrial magma-ocean conditions lies in the low lunar gravity: the pressure in the Moon increases only slowly with depth. Therefore on the Moon the depth interval for crystallization of a given mineral phase is much greater than on the Earth, and crystals can grow large while they are still within the interval. Then these large crystals can settle down or float up (Eqn 17.5; Melosh *et al*., 1993). The total LMO duration is constrained by the time interval between

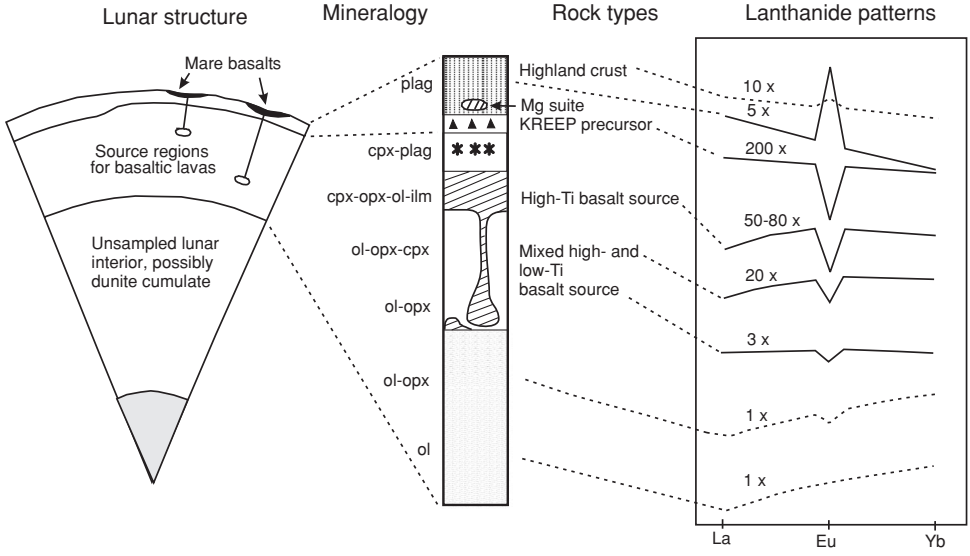

Fig. 21.8 Simplified lunar cross section, mantle rock types and REE patterns in different lunar rocks: plag, plagioclase; cpx, clinopyroxene; opx, orthopyroxene; ol, olivine; ilm, ilmenite. KREEP appears to be the reservoir complementary to the (mainly ferroan anorthositic) crust, i.e. it represents the residual melt after plagioclase extraction. Note the very high abundances of REEs in KREEP, in some samples exceeding the chondritic abundances by a factor ~ 1000, without relative fractionation among the REE. After Taylor and McLennan (1988), © Elsevier Science 1988, reproduced by permission.

the giant impact, $\sim$ 30 to 60 Myr after SOS, and lunar-crust formation, $\sim$ 100 Myr after SOS.

Lunar mare basalts and the lunar magma-ocean model

The mare basalts were extracted from the lunar mantle and reflect aspects of its structure and chemistry. Their origin has been modelled as due to the partial melting of cumulates of the LMO (e.g. Warren, 2003). In these models, the low-Ti basalts would have resulted from the remelting of cumulates from an earlier stage of LMO crystallization, still ilmenite-free and moderately enriched in incompatible elements. The high-Ti basalts would have been derived from rocks that formed at a late stage of LMO development, when the magma ocean had become extremely rich in incompatible elements and crystallized ilmenite.

Not only the general chemical features of mare basalts but also their Nd- and Hf-isotope characteristics (Fig. 21.7) call for the LMO model. First, the two correlations of initial ε_{176} with ε_{143} for low-Ti and high-Ti basalts would follow from the

presence or absence of ilmenite in their mantle source. A low Lu/Hf ratio is expected in ilmenite-rich cumulates that have formed in equilibrium with a melt, since Lu is strongly incompatible in ilmenite whereas Hf is only slightly incompatible; correspondingly, low time-integrated $^{176}Hf/^{177}Hf$ (and ε_{176}) values, should characterize an ilmenite-rich source. In an ultramafic cumulate containing no ilmenite, the inventory of Lu and Hf is dominated by clinopyroxene, which has a Lu/Hf ratio about twice that of the melt and therefore high $^{176}Hf/^{177}Hf$ (and ε_{176}) values. For the Sm/Nd ratios, the presence of ilmenite has no effect as both elements are strongly incompatible in it.

Second, the root cause of the very great heterogeneity of both ε_{143} and ε_{176}, i.e. their spread along the separate trends in Fig. 21.7, can be understood by viewing cumulates as variable mixtures of minerals and a small amount of trapped melt, which later solidifies *in situ*. The trace-element concentrations (and their ratios) of a cumulate rock would be the weighted averages of those of the minerals and the trapped melt. For instance, a rock with much pyroxene and/or little trapped melt would evolve to high ε_{143} and ε_{176} values, see Fig. 21.7, and vice versa. While this works in principle, it remains difficult to explain the large variation in the amount of trapped melt.

Third, the uniformity in the Sm/Nd and Lu/Hf ratios of the mare basalts themselves also follows from the LMO concept. Upon partial melting of a cumulate, the assemblage formed from the trapped melt would be consumed first. Then, as long as significant amounts of all mineral phases are left in the residue, the trace-element concentrations in the melt are determined by those in these minerals and by the partition coefficients. The equilibrium between melt and mineral phases in partial melting is no different from that in fractional crystallization, and thus a mare basalt liquid formed by a relatively small fraction of partial melting from a cumulate could have very similar trace-element ratios to the melt that initially crystallized that cumulate. However, in equilibrium the melts that form will also inherit the different isotope compositions that have evolved in their different source rocks. This explains why mare basalts all have similar REE abundance patterns but different source isotopic fingerprints.

Problems with a layered lunar mantle: the overturn model

The lunar mantle structure inferred from the LMO model is apparently layered, as indicated in Fig. 21.8. Experimental work on mare basalts to determine the pressure of melting initially appeared to confirm this layered-mantle concept, in which high-Ti basalts originate at $\sim$ 0.6 GPa ($\sim$ 180 km depth) and low-Ti basalts at $\sim$ 1.2–2.0 GPa ($\sim$ 200–400 km). There are, however, important observations that do not follow from this model. First, high melting pressures were found for

some Ti-rich basalts (Walker *et al.*, 1975). Second, the compatible elements Ni and Co, which should be depleted in the source of Ti-rich basalts, are, in some cases actually enriched in such basalts (Ringwood, 1979). Third, the negative Eu anomalies, which should have developed in the LMO only at a late stage (when the anorthositic crust was segregated), are also found in deep-seated low-Ti basalts from mantle sources that were formed at an early stage of the magma ocean. Fourth, the trapped melt component in the mantle source rocks of the basalts, postulated to explain the Nd- and Hf-isotope systematics, would have to have been distributed in a highly heterogeneous way.

The above observations can be reconciled by invoking some amount of overturn in the lunar mantle (Ringwood, 1979). Along with the progressive extraction of lunar crust and solidification of the mantle, Fe accumulated in the residual melt as well as Ti, and the density of the melt increased. Gravitational instabilities relative to the underlying mantle are then expected. Dense minerals that crystallized in this layer, e.g. ilmenite, could have caused inverted diapirs of it to sink into the cumulate in overturns of differing scales, and to different depths. Such sinking matter could have been composed of the crystallized minerals and also trapped melt, already evolving to a KREEP-like composition. Shearing in the course of the sinking of this mixture would cause a more heterogeneous distribution of the trapped melts, as is commonly observed in deformation processes on Earth.

Such overturns would lead to a highly heterogeneous mantle, in which cumulates from early crystallization stages of the LMO could coexist at the same depth as those from the KREEP stage. This would naturally account for the evidence of high-Ti matter with negative Eu anomalies in the deep mantle and the high Co and Ni content in Ti-rich basalts. By entailing a heterogeneous distribution of trapped melt, the overturn concept also helps to explain the extreme heterogeneity reflected both in the ε_{143} and the ε_{176} initial values. In addition, a dense mixture of late-stage cumulate and melt could have had high concentrations of the heat-producing elements U and Th, and its transfer to deeper levels could thus have facilitated partial melting in the lunar mantle.

The Hf–Nd isotope evolution in high- and low-Ti basalts illustrates the consequences of the LMO overturn model (Fig. 21.9). Some of the highly heterogeneous sources are the "overturned" high-Ti and low Lu/Hf rocks in which Hf isotopes slowly evolved to low $^{176}Hf/^{177}Hf$ ratios (and ε_{176} values). In other, non-overturned, sources clinopyroxenes ensure high Lu/Hf ratios (as well as $^{176}Hf/^{177}Hf$ and ε_{176} values). Upon partial melting of a low-Ti source the Lu/Hf fractionation between melt and residue was stronger, leading to a much lower Lu/Hf ratio in the melt, similar to that for a high-Ti source. The initial Hf-isotope compositions were, however, inherited. Afterwards, Hf isotopes in the two basalt types evolved in parallel with each other, because of the similar Lu/Hf ratios (Beard *et al.*, 1998).

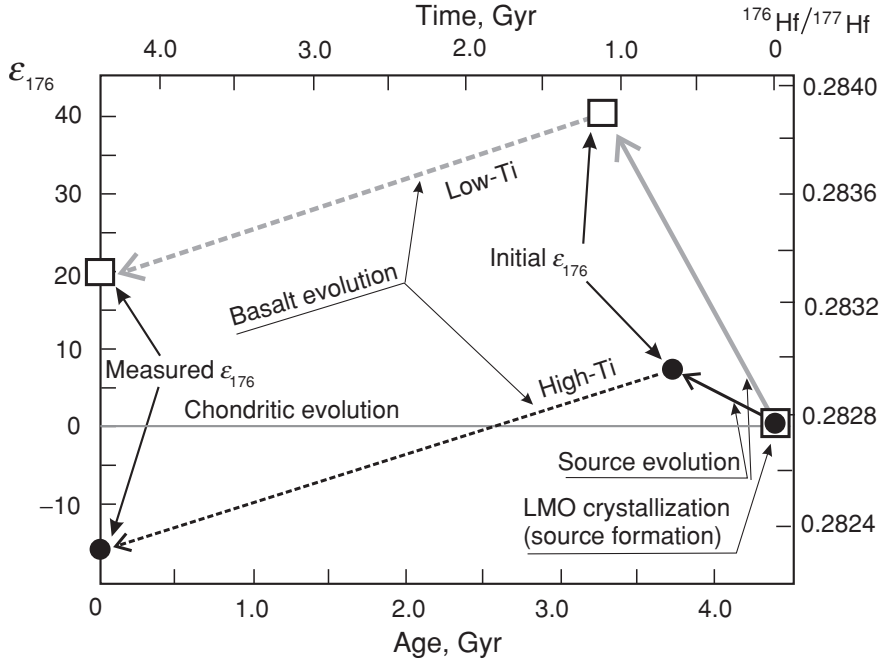

Fig. 21.9 The Hf-isotope evolution trends for low-Ti and high-Ti lunar basalts. Source evolution: cumulates of different composition were formed during LMO crystallization ~ 4.4 Gyr ago. The Lu/Hf ratios of the cumulates are dependent on the relative abundances of minerals. In ilmenite-free cumulate (a low-Ti source) a high Lu/Hf ratio is set by clinopyroxene: therefore the subsequent ingrowth of radiogenic $^{176}Hf^*$ (expressed as ε_{176}) is fast. The ilmenite-rich cumulate (a high-Ti source) has a low Lu/Hf ratio, as Hf is almost compatible in ilmenite (the ingrowth of radiogenic $^{176}Hf^*$ is slow). On melt formation in a low-Ti cumulate, the Lu/Hf fractionation between melt and residue is also stronger, leading to a melt Lu/Hf ratio similar to that of the high-Ti basalt. The different initial ε_{176} values are, however, inherited. Afterwards, Hf isotopes in the two basalt types evolve parallel to each other, because of these similar Lu/Hf ratios. Simplified from Beard *et al.* (1998), © Elsevier Science 1998, reproduced by permission.

21.5 Summary

The evolution of the Moon differed radically from that of the Earth. Early lunar magmatism caused irreversible differentiation of the silicate Moon into a light plagioclase-rich crust, a dense olivine-rich mantle and a reservoir highly enriched in incompatible elements that is complementary to these two. The lunar crust/mantle mass ratio exceeds the terrestrial value by at least an order of magnitude. A predominance of plagioclase in the lunar highland crust precludes partial melting as the principal mechanism of crust formation (also in contrast with the Earth; see Chapters 24 and 25). Instead, plagioclase segregation and flotation from a lunar

magma ocean is envisaged, after magmas evolved to a high Al_2O_3 content by Ol + Pyx fractional crystallization and the removal and accumulation of these mafic minerals in a deep dunite layer, the lower lunar mantle. In the course of such differentiation some major elements (Ti, Fe) and trace elements (incompatible in plagioclase) were concentrated further in the melt, the last remnants of which solidified into a reservoir that sourced basalts enormously enriched in K, REE, P, Rb, U and Th, termed KREEP, and never seen in other objects of the solar system. Removal to the crust of elements compatible in plagioclase left specific fingerprints for KREEP, e.g. a negative Eu anomaly. The limited chronological data show that the early crust segregated from the lunar magma ocean 4.45 Gyr ago. The duration of this stage of lunar magmatism was about 100 Myr.

Later on, bombardment of the Moon by accreting planetesimals occurred and was especially intense $\sim$ 3.9 Gyr ago (Elkins-Tanton *et al*., 2004), indicating that a similar bombardment must have occurred on Earth. Between 4 and 3 Gyr, partial melting of the lunar mantle formed the lunar maria. The compositional features of lunar basalts, e.g. a bimodal Ti distribution, negative Eu anomalies and specific relationships between the Nd- and Hf-isotope compositions, point to sources at different depths in a broadly stratified mantle, which was modified by (partial) overturns causing long-term heterogeneities. KREEP-type matter brought down to the deep mantle in this way could have been a cause of the mare volcanism via radioactive heating; impacts were probably also a trigger.

Since $\sim$ 3 Gyr ago the Moon has been stagnant: only tides, rare impacts and solar wind have affected its history, again in contrast with the still tectonically active Earth. While lunar rocks, interesting and exciting in themselves, provide little knowledge about the structure, composition or evolution of our planet, their study has introduced an invaluable alternative perspective on planetary development.

Part IV

Global evolution of the Earth

22

First look at the Earth

In Part IV we distinguish and characterize the principal reservoirs of the present-day highly differentiated planet and the most important processes by which matter is transferred between them; as we saw in Parts I–III, the crucial tools are the abundances of the major and trace elements as well as the relevant isotopic systematics. We will trace these processes and reservoirs into the geological past in order to arrive at the post-accretion Earth of ~ 4.5 Gyr ago (Part III), which consisted of a metal core, a core–mantle transition zone, a vigorously convecting silicate mantle, a comparatively short-lived basaltic crust and an early, still dissipating, atmosphere. As in Parts I–III, we present the observational data first and then consider the corresponding processes and models.

To understand our dynamic planet, a multidisciplinary approach is needed. First, the geological aspect involves studying terrestrial materials and deducing the processes that have created them and brought them to where they are now. Second is the physical approach, geophysics, probing the depths of the Earth. The theoretical investigation and modelling of natural materials and processes constitute the third approach.

Such a multidisciplinary approach allows an in-depth interpretation of the observational data and more reliable constraints on specific processes and materials. The rewards are a better understanding of the evolution and present-day state of the Earth: the plate-tectonic model of the present-day Earth presents an impressive example (e.g. Brown *et al.*, 1992a).

The modern plate-tectonic concept (Le Pichon, 1968; McKenzie, 1968; Morgan, 1968) is used here as a framework to describe the present-day Earth. According to this concept the Earth's surface is covered by relatively rigid lithospheric plates that overlie a solid but mobile "asthenospheric" mantle. Even though plate tectonics is caused by heat-driven mantle convection, the principal feature of our planet, it is the sinking of old, cold and dense plate sections that forms the main driving force for plates to move and interact. Magmatic, metamorphic, degassing and other

processes, operating as a result of these interactions, play a key role in the evolution of terrestrial matter.

The order of presentation is chosen to fit the plate-tectonic framework. In Chapter 23 we introduce the major geotectonic units and give a classification of plates, plate boundaries and the respective reservoirs. This introduction is mainly derived from what is directly observable, so that the reader approaches the plate-tectonic concept by looking at the Earth's surface. We present the most powerful plate-producing and plate-interacting processes, consider plate development, via rifting or orogeny, intraplate magmatism, sedimentation and metamorphism, and complete our discussion by considering plate destruction and recycling: these are in fact the major processes by which the Earth's matter is developed.

In Chapters 24, 25 and 26 the major reservoirs of matter in and on the present-day Earth and the processes taking place in them and transfers between them are discussed in some detail, including the major- and trace-element data. Chapter 27 presents the most informative isotopic systematics: the compositional and isotopic evolutionary trends starting from a primitive bulk silicate Earth 4.5 Gyr ago and leading to the present-day masses and compositions of the differentiated terrestrial reservoirs. A self-consistent geochemical model (Chapter 28) presents a possible evolution path for the major terrestrial reservoirs, the mantle, crust and atmo-hydrosphere.

23

The plate-tectonic concept: some phenomenology

23.1 Major geotectonic units: the plates

Let us imagine that we observe the Earth from a remote point, for example from a satellite, and that the atmosphere and oceans are transparent and therefore we can see the whole solid surface of the planet (Fig. 23.1(a), (b)). The most intriguing features of this surface are long narrow zones or cuts, characterized by enhanced seismicity and heat flow and also by intense volcanic activity: volcanic exhalations are easily seen from our satellite. These narrow zones outline much "quieter" (aseismic and non-volcanic) regions, which cover most of the surface. Within the plate-tectonic concept the stable regions of the Earth surface are termed lithospheric plates and the active zones are plate boundaries (e.g. van Andel, 1992). Using the satellite-positioning system, we can observe that the plates move with relative velocities between 1 and 10 cm yr^{-1}. The active zones separate plates that are moving in different directions. As discussed in Section 17.5, the largest terrestrial reservoir, the mantle, consists of solid silicate material convecting at the rate of a few cm yr^{-1}. This is similar to the observed plate velocities, and the similarity implies that there is some relationship between the motion of the plates and the convection of the underlying mantle: the plates form the lid of the mantle.

The plates vary greatly in size (and therefore in the lengths of their boundaries), from $\sim$ 1000 km or less (Cocos, Corda, Fig. 23.1(b)) to more than 10 000 kilometres (Pacific, Antarctic, Eurasia). Continents, large regions of high surface elevation (e.g. Africa), occur "frozen" onto otherwise low-lying, oceanic plates. The phenomenon of continents appears to be unique to the Earth (Section 26.1). The structures and compositions of the plates depend strongly upon the processes operating at the plate boundaries, discussed in the next section.

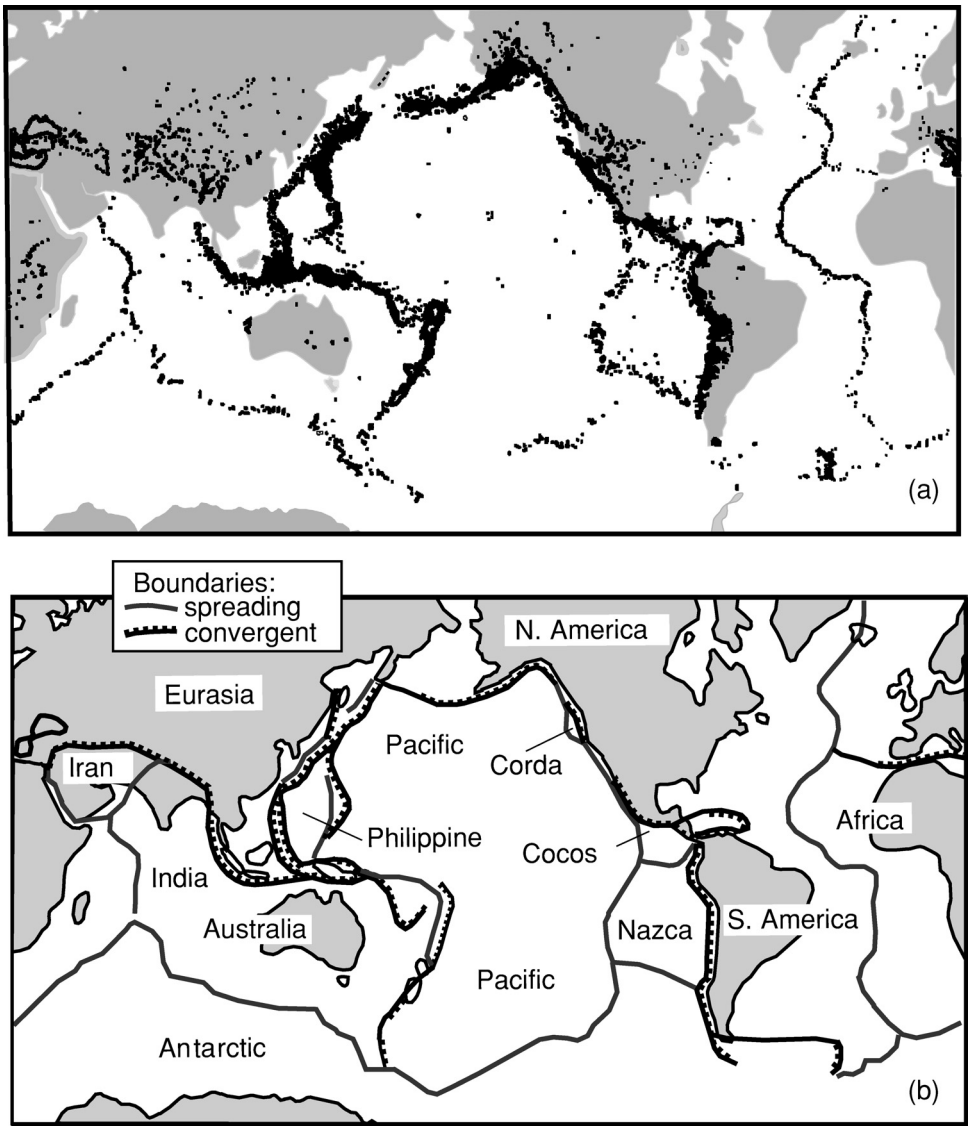

Fig. 23.1 Tectonically active zones, continents and plates. (a) The black dots show manifestations of intense tectonics and magmatism. (b) The thick lines are plate boundaries; the names of plates are shown. Modified after van Andel (1992).

23.2 Plate motions: processes on the plate boundaries

Divergent (spreading) boundaries

A plate can move relative to another in three different ways (Fig. 23.2). Two plates may separate across a divergent or spreading boundary, where the gap is

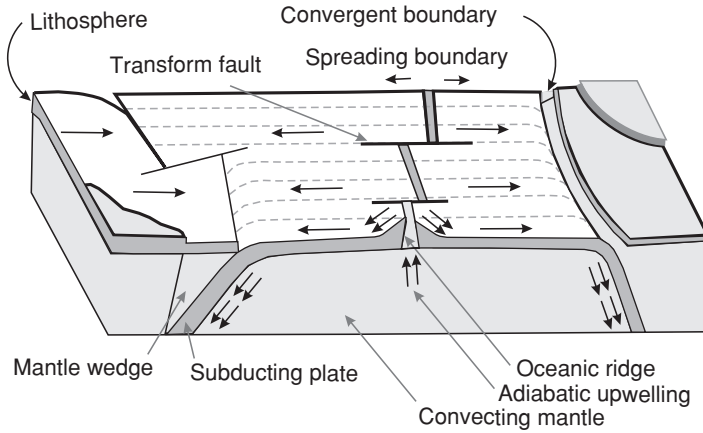

Fig. 23.2 The three principal plate interactions and the moving forces. The single arrows show the direction of plate movement, and the double arrows indicate the plate movements and forces related to the sliding of the plate away from the ridge and its sinking into the mantle. At a spreading boundary the plate movement is in opposite directions; at a convergent boundary or subduction zone, one plate moves below another; at a transform fault, slipping (thick line segments) occurs as one plate moves parallel to another. As a plate ages and cools, the thickness of the cold lithosphere increases, thus increasing the gravitational force on the plate segment as it sinks through the mantle. After van Andel (1992).

continuously being filled by upwelling material. The present-day spreading boundaries are generally those between oceanic segments of the plates, and they appear as long, uniformly high, ridges (Fig. 23.1). A closer look (through our hypothetical "transparent" ocean) reveals the "filling" process, which takes place in a narrow valley (termed a rift valley) along the uppermost ridge. The depth of the valley varies inversely to the spreading rate, from 0.1 km at a spreading rate ~ 10 cm yr^{-1} to ~ 1 km at ~ 1 cm yr^{-1}. One or several fissures occur in the floor of the valley and erupt basaltic lava at a rate that is much higher in fast-spreading rifts than in slow ones. The thickness of the layer newly formed from solidified magmas, the basaltic oceanic crust, varies from 1 to ~ 10 km, with a mean value close to 7 km (Humler *et al.*, 1999).

The basaltic magmas are generated by the partial melting of "fertile" peridotite, the dominant rock type of the mantle discussed in Chapter 17. The melting occurs, without heating, through decompression as hot mantle rock rises below the ridge and crosses its solidus. Harzburgitic (or "depleted" peridotitic) rocks, which are residues of this partial melting, underlie the basaltic crust and constitute a suboceanic lithosphere up to ~ 100 km thick.

The depth of the ocean floor increases, along with the age of the crust, away from the ridge axis. This is due to cooling both of the oceanic crust as it ages and

of the suboceanic lithosphere underlying it, so that they become denser. Fine silt is sedimented onto the basaltic crust. Naturally, the thickness of this sediment cover increases away from the ridge.

Although we see from our virtual satellite that at present the divergent boundaries are generally between oceanic segments of the plates (Fig. 23.1), rifting could start not only via the spreading of an oceanic floor (e.g. the west boundary of Nazca) but also as continental break-up. Thus, the fit of the shapes of some opposing continental coastlines and their geological structure and other features, e.g. S. America and Africa, led Wegener (1915) to propose the drift of these continents away from each other.

The mean speed of a plate's motion (e.g. $\sim$ 1 cm yr^{-1}) and its size ($\sim 10^8$ cm, both in principle measurable from our satellite) allow the age of the oceanic crust to be estimated at an average $\sim$ 100 Myr. This age, the thickness of the oceanic basaltic crust ($\sim$ 7 km), its density ($\sim$ 3 g cm^{-3}) and its total surface area, $\sim 2.9 \times 10^{18}$ cm^2 (about two-thirds of the total surface of the oceans) together give the present-day rate of ridge magmatism, 6×10^{16} g yr^{-1}. This is by far the most productive magmatic process on Earth (Chapter 24).

Convergent boundaries

The spreading of the plates on the Earth's spherical surface inevitably causes collisions, and the plate boundaries where this occurs are termed colliding or convergent (Fig. 23.2). The colliding plates may interact in two different ways.

In the course of collision one plate can turn downwards and sink back (be subducted) into the mantle; this generally takes place if another colliding plate is thicker and stronger, for example in the collision of oceanic and continental plates (e.g. the oceanic Pacific and continental Eurasian plates). Subduction, however, also takes place when two oceanic plates collide (e.g. in the south-western Pacific Ocean). Subduction consumes most of the oceanic crust and lithosphere that originated at the spreading boundary, along with its sediments. Some of this highly diverse material is released from the subducting slab as fluids and/or melts, which enter the overlying mantle and stimulate its partial melting. The resulting magmas mainly erupt in volcanic arcs, chains of volcanoes parallel to the subduction zone, but can also evolve to silica-rich compositions and ultimately form continental crust. The arc volcanic chains are clearly visible from our satellite; the circum-Pacific volcanic belt presents an example. Finally the remaining slab sinks deep into the mantle, introducing chemical and isotopic heterogeneities in this otherwise relatively homogeneous reservoir; a "mantle wedge" develops between the two plates (Fig. 23.2).

Continued convergence of the oceanic lithosphere can culminate in the collision of two continental masses. As this material has lower density than the oceanic crust and mantle, such a collision cannot be accommodated by subduction. Compression results in local thickening of the crust via intense rock deformation and faulting. This in turn leads to isostatic uplift: orogeny, or the building of mountain chains. An example, the Himalayan chain, also visible from our satellite, is a direct consequence of the collision of the Indian and Eurasian plates.

Continental crustal matter is further evolved by three major processes that operate in and below these mountain chains. First, the high heat flow and deep fluid circulation in this thickened crust can lead to melting, producing granitic magmas that intrude into higher crustal levels, thus augmenting the upper crust. Second, the destruction of the mountains by weathering and erosion is another important process leading to the formation of sedimentary rocks. Third, crustal rocks, whether originally magmatic or sedimentary, that are subjected to heating and high pressures within mountain belts undergo changes in their mineral composition known as metamorphism. Apart from normally involving the loss of a hydrous component (which escapes as fluid), this process is largely isochemical, but it can drastically change the mechanical properties of rocks and their density, both of which affect continental tectonic processes. All these features are clearly seen in the Himalayan chain.

Transform boundaries

A transform boundary occurs when two plates move approximately parallel to each other but in different directions, or in the same direction but with different velocities. In either case the plates slip past each other with relatively weak interaction (Fig. 23.2). Also, different segments of a given plate may move relative to each other, for example owing to a uniform rate of spreading on the spherical Earth, and the separation between such segments is termed a transform fault. They are perpendicular to oceanic ridges, often offsetting the ridge itself. Transform boundaries and faults process matter in a very minor way compared with spreading ridges and subduction zones and are therefore not discussed further here.

23.3 Intraplate magmatism: plumes

A more careful look from our satellite at oceanic segments of plates reveals tens of thousands of small isolated volcanic seamounts (Batiza, 1982; Wessel and Lyons, 1997), but also, within the plates, large volcanoes, volcanic islands and even chains of volcanoes and volcanic islands. A classical example is the $\sim$ 5000-km-long Hawaiian-Emperor chain on the Pacific plate. The Meiji seamount, at the extreme north-western end of this chain and about to descend into the Aleutian subduction

zone, is 85 Myr old, and at its south-eastern end the Hawaiian islands have highly active present-day volcanism. Between these extremes, the intermediate ages correlate with the distance from Hawaii. If the track of this chain (from older to younger) is compared with the direction of motion of the Pacific plate (to the north-west), the first impression is that the plate has been persistently punctured by silicate magma as it moved over a stationary "plume" of hot material upwelling from the mantle. Even though seismological observations show that some plumes are not stationary, their displacement is much slower and the tracks are shorter than those typical of plate motion (e.g. Molnar and Stock, 1987; Steinberger and O'Connell, 1998).

Because their sizes, structures and compositions are variable, plumes are thought to originate at different depths in the mantle and from different source materials. Moreover, there is no strict definition of what constitutes a plume, and therefore no consensus on their total number; estimates vary from ~ 10 to ~ 100 (e.g. Malamud and Turcotte, 1999). The highest-temperature Hawaiian, Tahiti and Iceland plumes, for instance, are derived from great depth: their roots are detected well below ~ 600 km (Section 24.6). Their upwelling velocities reach ~ 300 km Myr^{-1} in relatively narrow jets, so they are able to cross the mantle in geologically short times ~ 10 Myr (Larsen *et al.*, 1999). In contrast, the Azores plume relates to a shallow (possibly crustal) source. At present the total rate of magma generation by plumes is a factor ~ 10 less than the MOR rate (Crisp, 1984); however, plume materials bear important signatures of deep-mantle sources and their origin and evolution. Moreover, in earlier geological epochs plumes may have played a major role in both tectonics and magmatism, and have been powerful triggers for the rifting of plates and the break-up of large continents as well as possibly playing a role in the generation of the continental crust and subcontinental lithosphere.

23.4 The moving forces of plate tectonics

As mentioned above, mantle convection could, directly or indirectly, drive plate motion. In either case, the amount of heat energy carried by convection to the Earth's surface would probably be greater than that required by plate tectonics. The total observed heat flux released by the Earth from its surface per time unit is ~ 44 TW (Pollack *et al.*, 1993). The total radioactive heat production of the BSE, calculated from K, U and Th in Table 17.1, is ~ 16 TW, of which the present-day continental crust with a mean U concentration of 1.3 ppm and the canonical ratios Th/U ≈ 4 and K/U $\approx 10\,000$ (Table 26.3) produces ~ 6.5 TW. The mantle and D$''$ thus produce ~ 9.5 TW of radioactive heat, and the source of the remainder could be the core. The Nusselt number for the mantle is ~ 20 (Section 17.5), which indicates that moving mantle matter, e.g. plumes and rising branches of convective cells, is by far the major carrier of this heat from the Earth's interior to the surface.

Hewitt *et al*. (1975) showed that ∼ one-sixth of the convection-delivered mantle heat, ∼ 6 TW, is converted into mechanical power that could drive plate tectonics.

By comparison, the observed amount of energy actually released in plate tectonics is quite small: ∼ 0.03 TW is released in earthquakes, 0.08 TW by volcanic activity and 0.2 TW by orogenesis. This is in total ∼ 0.3 TW, a factor 20 less than the total supply available. Hence, mantle convection carries more than enough power to enable plate tectonics (see Zharkov, 1983 and references therein; Tackley, 2000).

The processes directly responsible for the movement of plates are the gravitational sliding of segments away from an oceanic ridge, which pushes a plate, and the sinking of cool dense lithosphere at a subduction zone, which pulls it. The second factor appears to be by far the more important. For example, plates having very extensive subduction zones, e.g. Nazca, Cocos and Pacific, generally move faster than others (Forsyth and Uyeda, 1975). These mechanical forces have played a prime role in plate tectonics, at least during the second half of Earth's history. However, the power that plate movements consume appears to be of second order in importance compared with the total energy delivered to the crust and uppermost mantle by convection, which is dissipated as heat.

Continents, even though covering only a third of the Earth's surface, are especially important actors in the plate-tectonic movie. They are thick, (generally) cool and have high viscosity; only conductive heat transfer, which is slow, is possible through them. A domain of the convecting mantle underneath a large stagnant (super)continent gradually heats up under this insulating lid, and becomes less dense. A swell can thus develop beneath the continent on a time scale of ∼ 300 Myr. A plume from the deeper mantle can add to this effect and impel continental rifting. The results of recent seismic studies support the magma-assisted rifting of initially thick and strong continental lithosphere (Kendall *et al*., 2005). Break-up and divergence of the two or more resulting subcontinents could follow, accompanied by the formation of oceanic plates behind them.

In this way a giant plume separated the supercontinent Gondwana into several pieces between 200 and 150 Myr ago. Ultimately, the collisions of continents and their welding together in orogenic belts will lead to the formation of a new supercontinent (Trubitsyn, 2000).

Summarizing, there is little doubt that heat delivered by mantle convection to the Earth's tectonosphere is the major factor ultimately driving plate tectonics: the Earth is a geologically living planet owing to this phenomenon. However, this does not mean that there are simple straightforward relationships between the configuration of convective cells in the mantle and the position of oceanic ridges or subduction zones: after the latter are born, they develop further on their own (e.g. McKenzie and Bickle, 1988).

23.5 Summary: the major terrestrial factories reworking matter

Several major processes are involved in the formation and evolution of the principal terrestrial reservoirs and the exchange of matter between them. All these processes are direct or indirect consequences of mantle convection.

Processes involving the partial melting of silicate rocks play a key role in the evolution of matter in the Earth. Among them mid-ocean-ridge magmatism is by far the most productive factory, reworking fertile peridotitic mantle rocks and generating the relatively short-lived and small but important basaltic oceanic crust and the complementary depleted suboceanic lithospheric mantle (Chapter 24). Another process, plume-related melting and mantle fractionation, appears to be less prolific at present. However, plume magmas, gases and rocks, brought up from the deep Earth, can yield unique evidence on the composition and structure of the Earth's interior. Moreover, plume magmatism could have been of greater importance in the geological past. Both processes have in common that melting results from the decompression of ascending, hot and relatively dry mantle materials. Magma degassing and hydrothermal processes operating on the oceanic plates change the composition of the terrestrial atmo-hydrosphere.

While ridge and plume magmatism originate from upwelling mantle matter, the sinking of oceanic plates back into the mantle, subduction, serves as an opposite, downwelling, branch of the major terrestrial matter-evolving conveyor. Dehydration of the "wet" subducting ocean crust slab plays a role in subduction-related magmatism and the associated fractionation. Ascending magmas erupt at arc volcanoes and add matter to the continents.

Heat, supplied by arc and intraplate mantle melts or resulting from continental collisions, can cause metamorphism and intracrustal melting; magmatic fractionation can then lead to the formation of the most evolved magmatic rocks, granites (Chapter 26).

The above summary shows that magmatism plays an extraordinary role in generating compositional diversity within and on the Earth; therefore its various manifestations are discussed in some detail in Chapters 24 and 25 and Section 26.7.

Volcanic activity on the continental margins and within the continents, the post-glaciation uplift of crustal blocks and, in particular, continental collisions generate mountains and mountain chains, which are particularly susceptible to weathering and erosion. The resulting sedimentary rocks constitute a distinct small but important reservoir (Section 26.3). Chemical compounds and organic debris that originated mainly in oceans, seas and lakes also contribute to this reservoir. The accumulation of sediments onto oceanic crust, followed by their subduction into the mantle, can replenish the mantle with volatile and incompatible elements.

24

Ocean-ridge and island magmatism

24.1 Introduction to anhydrous mantle melting

It has long been known that the ascent and therefore decompression of hot mantle material is the major cause of both ridge- and plume-related magmatism. The rate of ascent v predicted by mantle convection and plate motion is of order 1 to 10 cm yr^{-1}, and similar values are in fact observed in the ascent of thick lithosphere (characterized by thickness $L \sim 100$ km and thermal diffusion coefficient $k \approx 2.5$ mm^2 s^{-1}, Gibert *et al*., 2003). For rates of this order, advective heat transfer (along with the ascending material) prevails over conduction (through the material towards a cold upper boundary) as follows from the high value of the ratio of advective and conductive heat transport, which is known as the Peclet number Pe:

$$Pe = vL/k \sim 30. \tag{24.1}$$

This greatly exceeds $Pe = 1$, at which value conductive heat transfer is important. Therefore the pressure P decreases faster than the temperature T. For the dry-peridotite solidus these two parameters approximately relate as (Takahashi and Kushiro, 1983):

$$T_0 \approx 1150\ ^\circ\text{C} + (120\ ^\circ\text{C/GPa})P_0. \tag{24.2}$$

As hot upwelling mantle material crosses the solidus (Fig. 24.1), partial melting starts. After melts separate from the matrix and ascend they generally do not erupt directly onto the ocean floor but collect in elongated magma-mush chambers, usually several kilometres deep and wide, underneath the rift. Here the magma evolves somewhat by crystal fractionation, producing layered gabbros. From the chambers, magma intrudes into fissures as they open above it. As magma approaches the ridge surface, a fluid phase exsolves (separates); gas bubbles rising to the surface enable devolatilization of the magma and this is also the major degassing process on Earth.

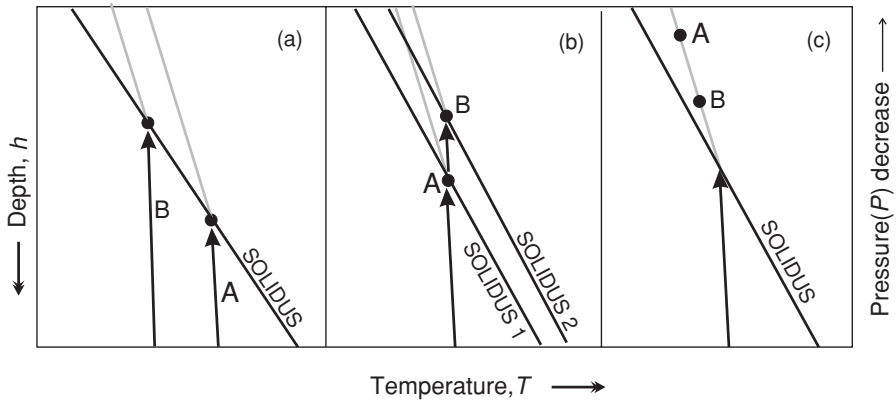

Fig. 24.1 Schematic profiles of depth (i.e. pressure) vs. temperature: A and B represent the paths followed that generate magmas erupting along shallow or deep ridges respectively. (a) Different mantle domains have different temperature gradients, therefore melting starts at different depths. (b) Mantle compositions beneath different ridges are also different; for a more fertile mantle (A) melting starts deeper than for a more depleted mantle (B). (c) The solidus is intersected at the same pressure, but the magmas segregate at different depths and therefore the extent of melting is different. Note that when melting starts, some heat is consumed by the melting process and the gradient is different, because the fraction of melt and the amount of heat consumed are both increasing. This is why the temperature drops faster after the solidus is crossed. After Klein and Langmuir (1987), © 1987 American Geophysical Union, modified by permission.

The oceanic crust thus consists of gabbro at the base (i.e. cumulate), fissure-filling basalts (i.e. dykes) in the middle and degassed erupted lava at the top.

Basaltic crystalline rocks and glasses can be studied at the surface, whereas cumulate rocks formed by crystal fractionation, e.g. gabbros, are found in drill cores and in so-called ophiolite complexes; these are segments of oceanic crust that have been transported onto continents by tectonic processes. There is, however, no direct way to study the partial melting of silicate rocks and melt migration in the mantle, and so to understand these processes all available data must be considered. Experiments at high temperature and pressure yield physical aspects of the rock–melt system and the redistribution of major and trace elements between the source rock and melt, while chemical and isotopic data obtained for natural materials reveal much about the mantle sources, melting and transport processes.

The major-element composition of a melt is governed by thermodynamic equilibria with solid phases, which depend on pressure, temperature and the composition of the parent rocks. The melt composition varies as melting proceeds, because the solid phases also change in the course of melting and, in addition, some major elements, e.g. sodium, are incompatible. Furthermore, minor rock-forming minerals can be used up in large melt fractions.

If the melt constitutes only a small fraction then it does not change the physical characteristics of the melting environment and, within the melt as well as the solid residue, the major-element compositions are not highly dependent on the degree of melting. However, incompatible trace elements are partitioned preferentially into the melt even if its fraction is quite small. The rare earth elements, which are all chemically similar but variably incompatible, are especially important for understanding the melting and differentiation of matter (see Figs. 12.2 and 12.3 and the related text). The abundances of trace elements in rocks that formed from melts, residual rocks, minerals or melt inclusions record subtle features of the partial melting process, and such data are important for modelling both the processes and the source materials involved.

Powerful tools for the reconstruction of melting and fractionation processes are radioactive isotopes that decay on time scales comparable with the duration of magmatism (Section 24.4). The isotopes belong to elements that are partitioned differently among the residual minerals, melt and gas phases and record important features of partial melting and associated processes, such as (1) the degree of melting, (2) the rate of melt generation and (3) the style and time scales of the separation of melt from the host rocks, its transfer to the surface and its subsequent degassing. Several daughter isotopes of the ^{238,235}U and ^{232}Th decay series are used, from ^{234}U with a relatively long half-life, $\tau_{234} = 2.45 \times 10^5$ yr, to short-lived ^{222}Rn ($\tau_{222} = 3.8$ days).

In contrast, the study of long-lived isotopic systematics is important for understanding the composition and evolution of magma source reservoirs in the mantle (Chapter 27).

24.2 Tholeiitic basalts: major products of ocean-ridge magmatism

As discussed in Section 12.2, basalts are products of the partial melting of peridotitic rocks. The highest rate of generation of basaltic crust occurs at ridges, amounting to $(6.7 \pm 0.3) \times 10^{16}$ g yr^{-1} and contributing more than 70% to the total present-day terrestrial melt production (Crisp, 1984).

Mid-ocean ridge magmatism belongs to the tholeiitic suite, i.e. the primary magmas are characterized by being relatively poor in Ca, Na and K, and evolve by the fractional crystallization of first olivine and orthopyroxene and then plagioclase feldspar, as represented by the layered sequences of gabbros occurring in ophiolite complexes. The resulting basaltic melts crystallize at the surface and yield terrestrial tholeiitic basalts composed of orthopyroxene, clinopyroxene and plagioclase with minor contributions of olivine or quartz and rare K-feldspar (Yoder and Tilley, 1962).

Table 24.1 illustrates the average composition of mid-ocean ridge basalts (MORBs). For comparison, it also shows other mantle-derived magma types and

Table 24.1 *Composition (wt %) and trace-element abundances (ppm) of depleted mantle (DMM), mid-ocean ridge basalts (MORBs), ocean-island basalts (OIBs), the global average composition of subducted sediments (GLOSS) and primitive arc basalts and andesites*

Compound or element	DMM[a]	All-MORB[b]	OIBs[c]	GLOSS[d]	Arc basalts[e]	Arc andesites[e]
SiO_2	44.9	50.6	50.33	58.5	51.3	58.0
TiO_2	0.133	1.45	2.42	0.62	0.98	0.79
Al_2O_3	4.28	15.4	13.3	11.9	15.7	15.9
FeO	8.07	9.98	11.4	5.21	8.72	6.14
MnO	0.135	n.d.[f]	0.18	0.32	0.17	0.12
MgO	38.22	7.95	8.45	2.48	9.48	6.56
CaO	3.5	11.5	11	5.95	9.93	7.2
Na_2O	0.29	2.71	2.25	2.43	2.61	3.31
K_2O	0.007	0.183	0.44	2.04	0.88	1.67
P_2O_5	0.009	0.15	0.18	0.19	0.22	0.22
Total	99.54	100.01	99.98	89.72	100.02	100.02
mg#	0.89	0.58	0.57	0.46	0.65	0.65
Li	0.7	n.d.	5.60	n.d.	n.d.	6.73
Be	0.025	n.d.	n.d.	n.d.	n.d.	0.87
Sc	16.3	n.d.	n.d.	13.1	32.5	20.9
V	79	n.d.	n.d.	110	246	158
Cr	2500	n.d.	n.d.	78.9	397	326
Co	106	n.d.	n.d.	21.9	41.2	31.4
Ni	1960	n.d.	n.d.	70.5	158	137
Cu	30	n.d.	n.d.	75	91.9	91.7
Zn	56	n.d.	n.d.	86.4	81.3	74.4
Rb	0.088	3.1	31.0	57.2	18.6	45.6
Sr	9.8	130	660	327	425	586
Y	4.07	32.1	29.0	29.80	18.7	17.1
Zr	7.94	97.4	280	130	92.7	137
Nb	0.21	5.02	48.0	8.94	6.23	7.94
Cs	0.001 32	n.d.	0.39	3.48	0.71	2.27
Ba	1.2	36.2	350	776	295	501
La	0.234	4.81	37	28.8	11.8	18.9
Ce	0.772	13.3	80	57.3	25.8	37.4
Pr	0.131	1.92	9.7	n.d.	2.85	5.38
Nd	0.713	10.4	38.5	27.0	14.9	20.9
Sm	0.27	3.42	10	5.78	3.43	3.92
Eu	0.107	1.23	3	1.31	1.07	1.08
Gd	0.395	4.3	7.62	5.26	3.55	3.92
Tb	0.075	0.82	1.05	n.d.	0.51	0.51
Dy	0.531	5.24	5.60	4.99	3.32	3.09
Ho	0.122	1.15	1.06	n.d.	0.68	0.55
Er	0.371	3.29	2.62	2.92	1.95	1.63
Yb	0.401	3.19	2.16	2.76	1.82	1.54

Table 24.1 *(cont.)*

Compound or element	DMM[a]	All-MORB[b]	OIBs[c]	GLOSS[d]	Arc basalts[e]	Arc andesites[e]
Lu	0.063	0.48	0.30	0.41	0.28	0.23
Hf	0.199	2.48	7.8	4.06	2.14	3.56
Ta	0.0138	n.d.	2.7	0.63	0.45	0.85
Pb	0.040	0.59	3.2	19.9	3.36	8.45
Th	0.0180	0.42	4	6.91	2.03	4.51
U	0.0072	0.11	1.02	1.68	0.53	1.57

[a] DMM composition from Table 17.1.
[b] All-MORB composition from Su (2002). The mean U, Th, Pb abundances are calculated from Nb, Ba, Ce in the column and the constant MORB ratios Nb/U = 45.74, Ba/Th = 86.04 and Ce/Pb = 22.36.
[c] OIBs from Sun and McDonough (1989).
[d] GLOSS from Plank and Langmuir (1998); enhanced concentrations of $CO_2 = 3.01\%$ and $H_2O = 7.29\%$ together with the total shown in the Table give a more consistent sum, 100.02%.
[e] Primitive arc basalt and andesite compositions from Kelemen *et al*. (2003). Because of possible contamination by continental materials and crystallization differentiation in intracrustal magma chambers only high-Mg samples (with $mg\# > 60$) were used to obtain the mean values.
[f] Not determined.

average subducted sediments, all of which will be discussed in later sections. In terms of their major-element composition and concentrations of moderately incompatible and compatible trace elements, MORBs can be considered to be relatively uniform compared with, for example, oceanic island basalts or crustal rocks.

24.3 Mid-ocean ridge magmatism: evidence from stable trace elements

Trace-element abundances in mid-ocean ridge basalts and residual peridotites

To understand and model the compositions of melt sources and the partial-melting–fractionation processes, it is essential that the abundances of trace elements with a large range of mineral–melt partition coefficients (Table 24.2) are considered for all matter associated with the process: fertile peridotites, basalts, basalt glasses, melt inclusions in minerals and finally the residual rocks.

First, a representative MORB sample set from the southern mid-Atlantic ridge shows that the normalized concentrations of the most incompatible elements, e.g. Rb, vary by almost two orders of magnitude, from values below the bulk silicate

Table 24.2 *Partition coefficients[a] for minerals in equilibrium with mafic melts. From Salters and Stracke (2004). Copyright (2004) American Geophysical Union. Modified by permission of the American Geophysical Union*

	3 GPa				2 GPa		
	Olivine	Opx	Cpx	Garnet	Olivine	Opx	Cpx
Cs	0	0	0	0	0	0	0
Rb	0.0003	0.0002	0.0004	0.0002	0.0003	0.0002	0.0004
Ba	0.000 005	0.000 006	0.0004	0.000 07	0.000 005	0.000 006	0.0004
Th	0.000 05	0.002	0.005 66	0.009	0.000 05	0.002	0.0059
Pb	0.003	0.009	0.009	0.005	0.003	0.009	0.012
U	0.000 38	0.002	0.0113	0.028	0.000 38	0.002	0.0094
K	0.000 02	0.0001	0.001	0.013	0.000 02	0.0001	0.001
Ta	0.0005	0.004	0.01	0.015	0.0005	0.004	0.015
Nb	0.0005	0.004	0.01	0.015	0.0005	0.004	0.015
La	0.0005	0.004	0.015	0.0007	0.0005	0.0031	0.03
Ce	0.0005	0.004	0.038	0.017	0.0005	0.004	0.08
Sr	0.000 04	0.0007	0.091	0.0007	0.000 04	0.0007	0.091
Nd	0.000 42	0.012	0.0884	0.064	0.000 42	0.012	0.088
Hf	0.0011	0.024	0.14	0.4	0.0022	0.03	0.2835
Sm	0.0011	0.02	0.1509	0.23	0.0011	0.02	0.299
Ti	0.015	0.086	0.14	0.6	0.015	0.086	0.35
Gd	0.0011	0.065	0.16	1.2	0.0011	0.0065	0.35
Dy	0.0027	0.065	0.17	2	0.0027	0.011	0.4
Er	0.013	0.065	0.18	3	0.013	0.045	0.42
Yb	0.02	0.08	0.25	5.5	0.02	0.08	0.45
Lu	0.02	0.12	0.276	7	0.02	0.12	0.511

[a] Values for spinel are not listed as they are insignificantly small. Generally the partition coefficients depend on several parameters of the melting processes, such as pressure, temperature, chemical compositions, oxygen fugacity and fluid abundance, and the values given in the table could vary somewhat. For example, Su (2002) presented an opx–melt partition coefficient of 0.007 for Nd that was the same as that used by McKenzie and O'Nions (1991) in their inversion model, but a factor 1.7 below the value presented in this table. After Salters and Stracke (2004).

Earth (BSE) to 30 times above it (Fig. 24.2). Also, the mean MORB concentrations of these elements are a factor 30 above those obtained for the MORB-source mantle, thus requiring a contribution of highly enriched melts in the bulk MORB magmas. According to Eqn (12.4) such melts must be segregated in (and then removed from) the melting environment at low melt/solid ratios. The REE elements show a smooth pattern and, in accordance with their range in incompatibility, the light rare Earth elements (LREEs) are more variable than the less incompatible heavy rare Earths (HREEs).

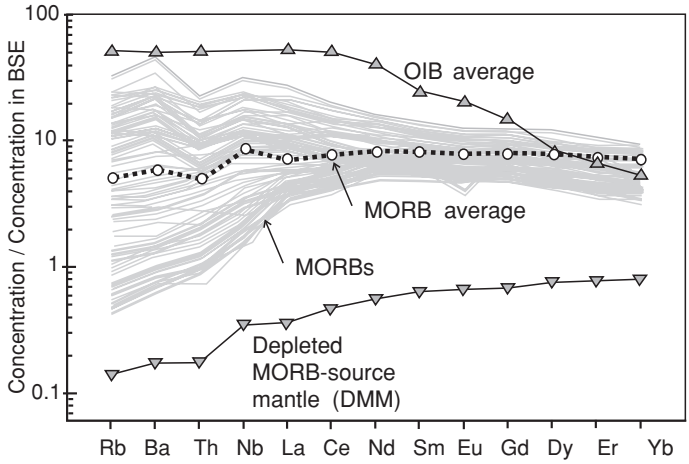

Fig. 24.2 Trace elements in mid-ocean ridge basalt (MORB) samples. The average MORB abundances (using all available MORB data), the model abundances in MORB-source mantle and the average abundances in oceanic island basalts (OIBs) are shown for comparison. The bulk silicate Earth (BSE) composition is used for normalization (Tables 17.1 and 24.1). From Hofmann (2003), © Elsevier Science 2003, reproduced by permission.

This variability in incompatible elements, including the LREEs, has led to a traditional subdivision of MORBs into three groups, the predominant "normal" (or depleted) N-MORBs, the less common "enriched" E-MORBs, and the "transitional" T-MORBs (Fig. 24.3). The latter have a quite similar composition to that of "all-MORBs", i.e. an average MORB (Table 24.1). From these data alone, however, it is difficult to identify precisely the causes of the variability, which could be mantle-source heterogeneity or differences in the partial melting and fractionation processes.

Second, to shed more light on these processes, trace-element data on melt inclusions have been shown to be of extreme importance. A small amount of melt can be trapped before extensive mixing occurs and can thus preserve compositions resulting from early stages of partial melting (Sobolev, 1996; Shimizu, 1998; Slater *et al*., 2001). The most surprising feature of melt inclusions is that their compositions are so variable. For example, several olivine-hosted melt inclusions in a single olivine grain from the Atlantic MORBs show LREE patterns that are more depleted than the whole-rock value and thus reveal the initial heterogeneity of the melts (Fig. 24.4).

Trace-element abundances in mantle peridotites are the third important source of relevant information. These rocks, termed abyssal peridotites, are obtained from mid-ocean ridges by dredging and drilling. In general, the sampling of such rocks

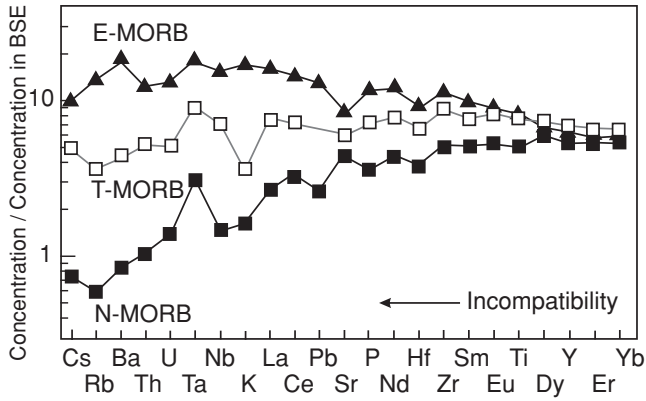

Fig. 24.3 Average trace-element abundances in mid-ocean ridge basalts (MORBs). The bulk silicate Earth (BSE) composition is taken from Table 17.1. From Klein (2003), © Elsevier Science 2003, reproduced by permission.

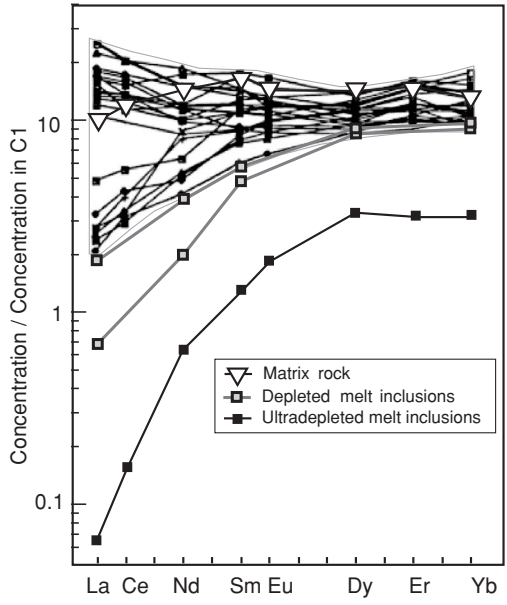

Fig. 24.4 Rare earth elements in olivine-hosted melt inclusions from the mid-Atlantic ridge. One melt inclusion shows an extreme depletion, in contrast with the host matrix (light shading), while two others are less depleted. This example illustrates the progressive mixing of small melt fractions with the host melt, which is itself a mixture of previous such contributions. The C1 composition is taken from Table 11.2. After Sobolev and Shimizu (1993) and Sobolev (1996).

from modern ridges is rare and limited to the uppermost mantle. However, ophiolites expose large mantle sections as well as the mantle–crust interface. One of the best-preserved sections of oceanic lithosphere is the Semail ophiolite complex in Oman. Like most abyssal peridotites, the rocks in this complex are strongly depleted in LREEs and other highly incompatible elements (Fig. 24.5). The La concentrations are typically within 0.005–0.05 of the chondritic values, and the LREE/HREE (normalized) ratios are low; $(La/Yb)_N \sim 1/30$. The REE pattern of these rocks is smooth, indicating fractionation of all the elements: the lighter the element, the more severe its depletion. The depletion of the most incompatible elements is truly impressive, e.g. [Th] $\approx$ 1 ppb or $\sim$ 0.013 times the BSE value. Uranium is slightly less depleted, so that U/Th $\sim$ 1 (Godard *et al*., 2000).

A comparison of the REE patterns from the Semail harzburgites and dunites (Fig. 24.5) with those of the depleted MORB-source mantle (DMM) model (Fig. 24.2) reveals differences that are fundamental to understanding the cause of DMM depletion. Not only are the Semail patterns much more strongly depleted, but they also have a different shape: a convex-up shape for LREEs and an almost flat pattern with modest depletion for HREEs are typical of the DMM, while the Semail rock patterns are concave-up, with $(Gd/Yb)_N$ down to 0.1 and $(La/Gd)_N$ mostly around 0.4. The difference is readily explained: the Semail harzburgites and dunites represent the residue after MORB extraction, whereas the model MORB mantle patterns are those of the source rock before the melt was extracted from it.

This observation allows us to conclude that the incompatible-element depletion in the normal MORB-source mantle is not the result of MORB melt extraction (if it were then the mantle pattern would resemble that of the Semail rocks in shape). This conclusion is of course entirely logical: MORB is recycled into the mantle at subduction zones (Chapter 25), whereas the incompatible-element depletion in the mantle results largely from the long-term extraction of matter that formed the continental crust (Chapter 26). It should also be noted here that the depletion pattern is associated with isotope fingerprints. For instance, the high $^{147}Sm/^{144}Nd$ and $^{176}Lu/^{177}Hf$ ratios of the depleted MORB-source mantle have engendered high $^{143}Nd/^{144}Nd$ and $^{176}Hf/^{177}Hf$ ratios, which show that the depletion of the mantle has occurred on a time scale of billions of years, in sharp contrast with the short lifetime of MORBs but in agreement with the great average age of the continental crust. This will be discussed further in Chapters 27 and 28.

While the depletion of source rocks is a principal outcome of partial melting, melts ascending through depleted residues can also cause enrichment, or refertilization, by solidifying there and thus producing the quasi-"primitive" REE patterns occasionally observed in peridotites. The isotopic data, however, may reveal a far-from-primitive evolution of such samples (Section 27.7).

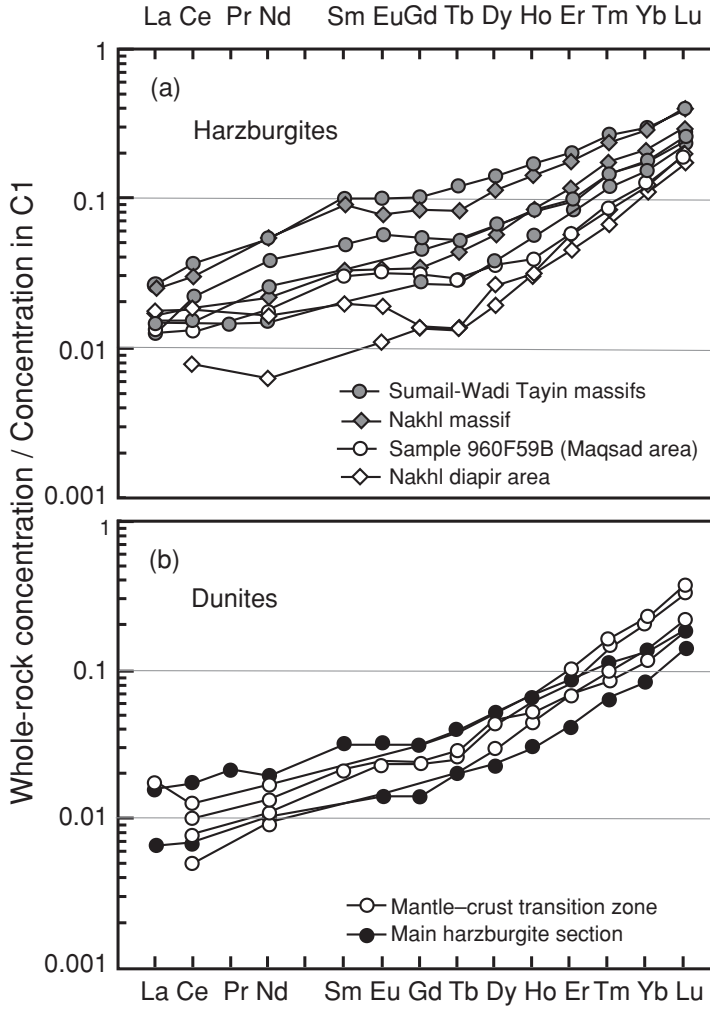

Fig. 24.5 Rare earth elements in ophiolitic peridotites from Oman. Note the strong depletion of LREEs, both absolute and relative to the HREEs, and the aberrant pattern compared with the depleted MORB-source mantle (DMM) model; see Fig. 24.2. The C1 composition is taken from Table 11.2. After Godard *et al.* (2000), © Elsevier Science 2000, reproduced by permission.

24.4 Mid-ocean ridge magmatism: evidence from radioactive trace elements

Constraints on melt generation and transport from radioactive trace elements: introduction to disequilibrium

While long-lived radioactive isotope systematics are useful for dating and for tracing the long-term histories of mantle sources, processes such as melting and the

ascent of magmas occur on time scales comparable with the half-lives of some naturally occurring short-lived nuclides: ^{234}U (half-life $\tau_{234} = 2.45 \times 10^5$ yr), ^{230}Th ($\tau_{230} = 7.74 \times 10^4$ yr), ^{231}Pa ($\tau_{231} = 3.25 \times 10^4$ yr), ^{226}Ra ($\tau_{226} = 1.6 \times 10^3$ yr) and ^{210}Pb ($\tau_{210} = 22.6$ yr).

Short-lived isotope-system studies on mantle melts have contributed greatly to our understanding of melting processes. Figure 24.6 shows the decay chains for three long-lived radioactive isotopes, ^{238}U, ^{235}U and ^{232}Th, ultimately decaying into ^{206}Pb, ^{207}Pb, and ^{208}Pb respectively. In particular the intermediate daughters ^{234}U, ^{230}Th and ^{226}Ra in the chain of ^{238}U, but also others, are used as radioactive clocks embedded in the natural fluxes of melts (McKenzie, 2000), waters (e.g. Chabaux *et al*., 2003; Tricca *et al*., 2001) and gases (e.g. Lehmann *et al*., 1999).

A comparison of the half-lives shows that the three parent isotopes of the chains decay orders of magnitude more slowly than all the daughters. Thus on a time scale $t \sim 5$ Myr the abundances of the chain parents may be considered as constants. Assuming a closed-system evolution of the ^{238}U chain (no losses and gains during $t \sim 5$ Myr) and applying the equations of radioactive decay (see Eqns 1.1, 1.2 and the related text), then, as before letting the nuclide symbol represent the atomic concentration, $\Delta^{238}\mathrm{U}/\Delta t \approx 0$ and the number of ^{238}U decays per unit time is constant:

$$\lambda_{238}{}^{238}\mathrm{U} \approx RE. \tag{24.3}$$

Here *RE* denotes the corresponding radioactive equilibrium constant. Under the above assumptions the evolution of each radioactive isotope within the chain, e.g. ^{234}Th, is given by

$$\mathrm{d}^{234}\mathrm{Th}/\mathrm{d}t = -\lambda_{234}{}^{234}\mathrm{Th} + \lambda_{238}{}^{238}\mathrm{U} = -\lambda_{234}{}^{234}\mathrm{Th} + RE, \tag{24.4}$$

for which the solution is

$$^{234}\mathrm{Th}(t) = (RE/\lambda_{234})[1 - \exp(-\lambda_{234}t)] \tag{24.5}$$

or, for the concentration $^{i}C(t)$ of any isotope i within the chain,

$$^{i}C(t) = (RE/\lambda_i)[1 - \exp(-\lambda_i t)]. \tag{24.6}$$

In view of the above time scale, $t \sim 5$ Myr $\gg 1/\lambda_i$, then $\exp(-\lambda_i t) \approx 0$ for all intermediate daughter isotopes including ^{234}U, the longest lived one, and $^{i}C(t) \approx$ constant. This state is termed radioactive or secular equilibrium: each nuclide within the chain decays at exactly its rate of production, and its abundance is therefore constant. Correspondingly, the radioactive equilibrium concentration ratio (*ECR*) of any two nuclides, parent j and daughter i, is also constant:

$$\lambda_j{}^{j}C = \lambda_i{}^{i}C \qquad \text{and} \qquad ECR \equiv {}^{i}C/{}^{j}C = \lambda_j/\lambda_i = \tau_i/\tau_j. \tag{24.7a}$$

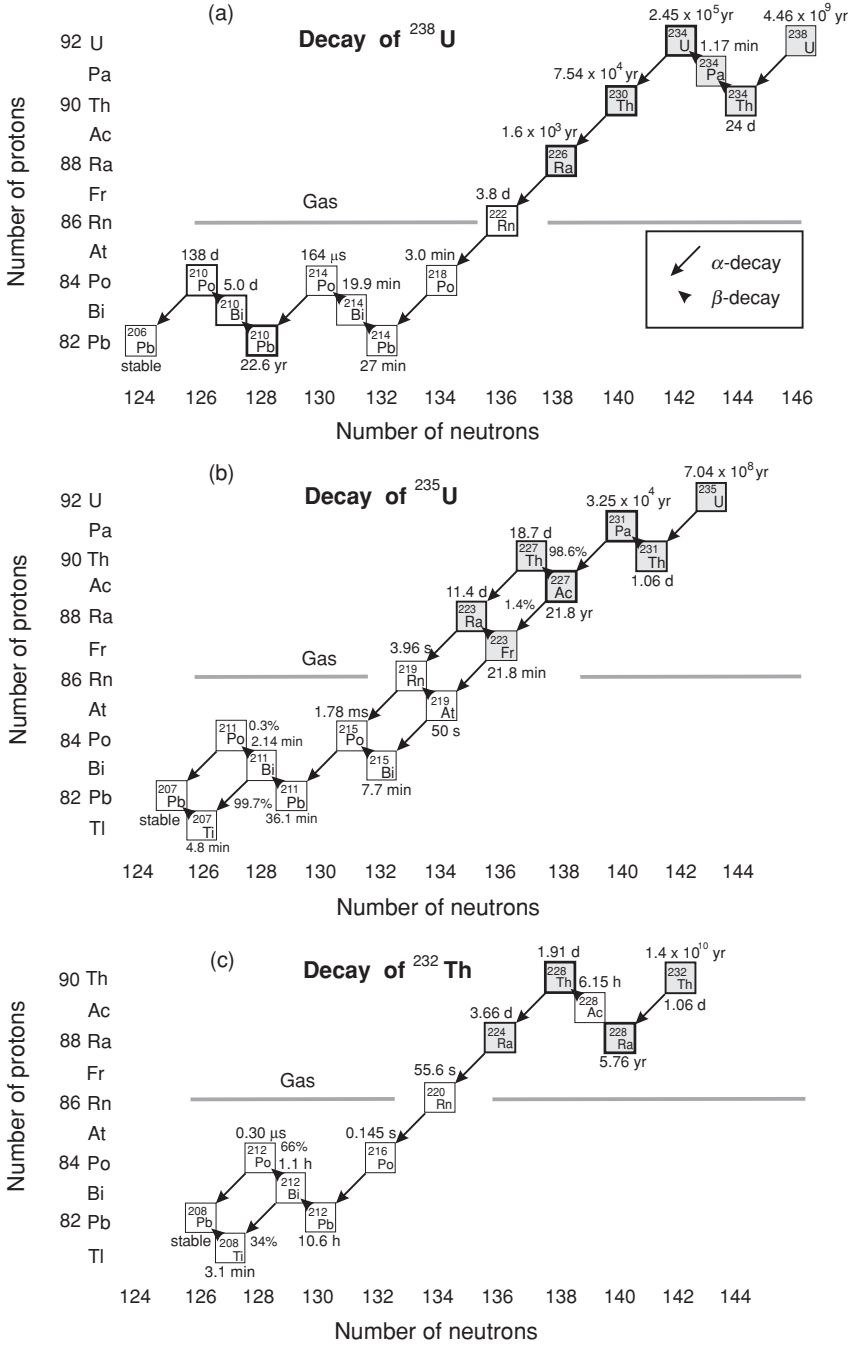

Fig. 24.6 (a), (b), (c) Radioactive decay chains. Note the highly variable half-lives of isotopes in the chains, allowing the measurement of different time scales. As ^{238}U, ^{235}U, ^{232}Th and the respective short-life isotopes of the chains decay into stable ^{206,207,208}Pb, they emit eight, seven and six α-particles (He-atoms) respectively (Eqn 10.7). After McKenzie (2000), © Elsevier Science 2000, reproduced by permission.

In a state of secular radioactive equilibrium, as seen in Eqn (24.7a) the number of decays per time unit is equal for all nuclides in the chain. The ratio $(\lambda_i{}^iC)/(\lambda_j{}^jC)$, the activity ratio *ECR*, is often indicated in the literature simply by the use of parentheses, e.g.

$$(^{230}\mathrm{Th}/^{234}\mathrm{U}) \equiv (\lambda_{230}{}^{230}\mathrm{Th})/\,(\lambda_{234}{}^{234}\mathrm{U}). \tag{24.7b}$$

In the case of partial melting the equilibrium of the melt and residue will be disturbed if the parent and daughter of a decay pair are different elements and thus have different mineral–melt partition coefficients. When the melt (fraction F) and solid (fraction $1 - F$) are in equilibrium in the source, combining the mass balance in Eqn (12.1) with Eqn (24.7a) gives for the parent and daughter isotopes in the melt (liquid silicate, LIS) and the solid (SOL)

$$\lambda_j[F\,{}^jC_{\mathrm{LIS}} + (1 - F)\,{}^jC_{\mathrm{SOL}}] = \lambda_i\,[F\,{}^iC_{\mathrm{LIS}} + (1 - F)\,{}^iC_{\mathrm{SOL}}], \tag{24.8}$$

because in radioactive and chemical equilibrium the total activities in melt + solid must be the same. Taking into account that $C_{\mathrm{SOL}}/C_{\mathrm{LIS}} \equiv D$, the partition coefficient (Section 12.2), Eqn (24.8) then gives the activity ratio in the melt:

$$\begin{aligned} ECR_{\mathrm{LIS}} &\equiv (\lambda_i\,{}^iC_{\mathrm{LIS}})/(\lambda_j\,{}^jC_{\mathrm{LIS}}) \\ &= [F + {}^jD(1 - F)]/[F + {}^iD(1 - F)]. \end{aligned} \tag{24.9}$$

If the magma separates from its source region and ascends, erupts and solidifies on a short time scale compared with the half-lives of daughter nuclides, and is rapidly sampled and analysed, the melt fraction can be derived using Eqn (24.9), provided that both partition coefficients are known (Table 24.2).

After a fractionation event such as partial melting, portions of the chain return to equilibrium on time scales $\sim 1/\lambda_i$ for the various daughter isotopes i in the volcanic rock that has been produced. If equilibrium has not been achieved for any pair j, i measured in a volcanic rock, the time scale of magma fractionation or the parameters governing melting, melt segregation and uplift can be estimated from the activity ratios. The ^{238}U chain has a number of parent–daughter pairs with highly differing daughter half-lives that are useful for this (Fig. 24.6); such a pair can also be constituted by two isotopes that are separated by a chain of very short-lived ones, e.g. ^{210}Pb and ^{226}Ra constitute a pair, applicable on time scales up to $\sim$100 yr. The others are ^{226}Ra, ^{230}Th (up to $\sim$ 6000 yr) and ^{230}Th, ^{234}U (up to $\sim$ 300 000 yr). The longest lived pair, ^{234}U, ^{238}U, cannot be used for magmatic systems as it is not fractionated (in surface processes and sedimentology, however, there is fractionation). The ^{235}U chain has one useful pair, ^{231}Pa, ^{235}U (up to $\sim$120 000 yr). In the ^{232}Th chain, the pair ^{228}Ra, ^{232}Th is useful for extremely rapid processes up to $\sim$ 30 yr.

The degree of initial disequilibrium of a magmatic rock depends on several factors, such as the source composition, the mechanisms and rates of melt segregation and ascent, the degree of fractionation in subsurface magma chambers and the contamination of the magmas. A detailed discussion of these processes and the corresponding models can be found in McKenzie (1985, 2000); Spiegelman and Elliott (1993); Iwamori (1994); Bourdon *et al*. (1996a); Sims *et al*. (2002); Jull *et al*. (2002); Rubin *et al*. (2005).

Constraints on melt generation and transport from the activity ratios in MORBs

Rubin *et al*. (2005) found (^{210}Pb/^{226}Ra) activity ratios down to 0.85 in unaltered N-MORB samples collected from the Juan de Fuca and East Pacific Rises (Fig. 24.7(a), (b)). As Ra is much more incompatible than Pb in mantle melting, a lower initial (^{210}Pb/^{226}Ra) value (equal to 0.2–0.4, depending on the melting rate) is expected for the initial melt. Therefore the time scale for magma ascent indicated by samples with (^{210}Pb/^{226}Ra) $\sim$ 0.85 is just over two half-lives of ^{210}Pb, $\sim$ 50 years. Assuming some average depth of partial melting beneath ridges, at $\sim$ 50 km (McKenzie and O'Nions, 1991), the rate of melt ascent appears to be as high as $\sim$ 1000 m yr^{-1}.

In the light of this extremely short time scale of melt transport, any disequilibria found in MORBs for pairs with longer-lived daughter isotopes in the chain, e.g. ^{226}Ra, ^{230}Th and ^{230}Th, ^{234}U, have no age significance but reflect the conditions of melting and fractional crystallization. Thus, Th is more incompatible than U for melting at great depths ($P > \sim 2$ GPa, or depths > 60 km), in the garnet peridotite stability field, whereas at shallower depths the U and Th partition coefficients are similar. Indeed, a (^{230}Th/^{234}U) value up to 1.4 was found in MORBs: a high-^{230}Th signal indicates first that fractionation happened at a great depth and second that the melt ascended without significant equilibration with the wall rocks (Bourdon *et al*., 1996b).

This interpretation allows the melt fraction in the deepest part of the melt column to be estimated. Assuming that D(Th) is $\sim$ 3 times lower than D(U) (which is $\sim$ 0.001; Iwamori, 1994) and a typical activity ratio (^{230}Th/^{238}U) = 1.15, then Eqn (24.9) gives $F = 0.004$, indicating a very low degree of melting.

24.5 Main features of a MORB melting model: evidence from trace elements and radioactive nuclides

The mechanisms of melt generation and extraction are described by a dynamic melting model. According to this model, melt produced in the upwelling mantle

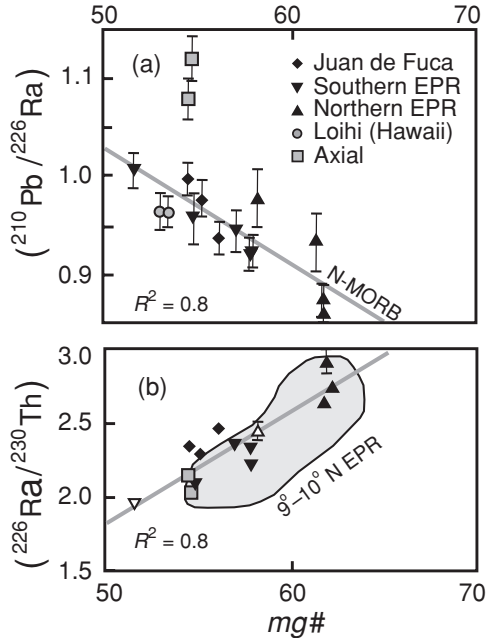

Fig. 24.7 The $^{210}Pb/^{226}Ra$ and $^{226}Ra/^{230}Th$ systematics in MORB and OIB magmas. The black, grey and open symbols in plots (a) and (b) are N-MORB, seamount, and older N-MORB lava flows respectively. (a) Note that the largest ^{210}Pb–^{226}Ra–^{230}Th disequilibria occur in the most magnesium-rich (the least fractionated or non-fractionated) lavas. Residence of a further $\sim$ 60 years in a fractionating magma chamber would have obliterated the ($^{210}Pb/^{226}Ra$) deficit. Furthermore, this could also have been diminished in the magma chamber by the preferential incorporation of ^{226}Ra in crystallizing plagioclase, as suggested by the inverse correlation between ($^{210}Pb/^{226}Ra$) and ($^{226}Ra/^{230}Th$). (b) Values of ($^{226}Ra/^{230}Th$) up to 3 are commonly observed in MORBs and are readily explained, as Ra is more incompatible than Th at any depth of melting (Sims *et al.*, 2002). After Rubin *et al.* (2005).

remains in equilibrium with the solid residue until a critical threshold melt fraction is reached. The threshold value is small, of the order of 0.005 or less. Any melt produced in excess of this threshold escapes through compaction of the source rock (McKenzie, 1984, 1985; Salters *et al*., 2001).

Compositions of some "deep" melt inclusions and special signatures such as ($^{230}Th/^{238}U$) show that melting starts at substantial depths (somewhat below 100 km) in the garnet stability field. In order for the high-pressure chemical signatures to be preserved, the melts generated at deep levels must ascend rapidly and without much interaction with the mantle-wall rocks at higher levels. Such a great speed of ascent is indeed documented by the ($^{210}Pb/^{226}Ra$) disequilibrium (Fig. 24.7). In the

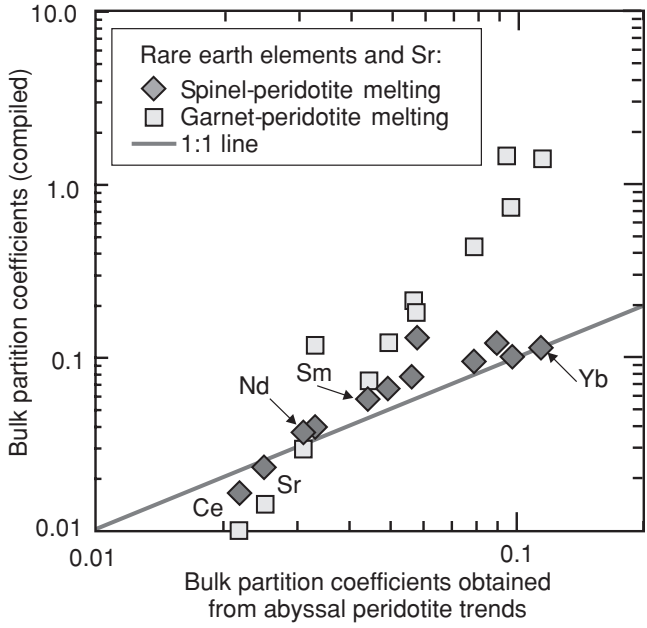

Fig. 24.8 Values for the bulk REE and Sr partition coefficients plotted against those obtained by regression of the abundances in abyssal peridotite of both spinel and garnet facies. The regression-based D values are calculated assuming that $D(\mathrm{Nd}) = 0.031$. It is clear that the slope of the D values indicates that melting has occurred more in the spinel facies than in the garnet facies. Choosing another value for D(Nd) will change the absolute values but not the slopes of the arrays. After Workman and Hart (2005), © Elsevier Science 2005, reproduced by permission.

course of ascent these deep melts could have been partially mixed and then trapped by phenocrysts formed at ≤ 40 km depth.

The bulk trace-element partition coefficients recorded by the depletion of abyssal peridotites correspond to those of spinel peridotites (Fig. 24.8), i.e. a depth shallower than ~ 60 km. In consequence, for most trace elements the high-pressure signal would be overshadowed by the predominantly low-pressure melt products. These shallower melts also result from fractional melting, melt separation, ascent (without equilibration with the rocks) and mixing, and they contain progressively lower abundances of incompatible trace elements (already extracted by the deeper melts): the shallower the melting, the more the melts are depleted (Fig. 24.4).

The total fraction of melts increases, via the mixing of small melt batches, upwards to the ~ 30 km level, where now efficient mixing occurs and the MORB primary melt composition is finalized. The aggregate melt fraction found to fit the DMM and primary MORB melt trace-element concentrations is $\sim 6\%$ (Workman and Hart, 2005). This melt fraction, smaller than the values derived from

experiments, may be due to slight hydration of the DMM ($\sim$ 100 ppm water). This would also explain the greater depth of incipient melting as water depresses the solidus (see Chapter 25). Modelling based on REE abundances in N-MORBs and E-MORBs has given a somewhat higher aggregate melt fraction, $\sim$ 8% for N-MORBs and twice this value for E-MORBs (McKenzie and O'Nions, 1991).

An observed disequilibrium between MORB melts and the plagioclase peridotites that constitute the uppermost section of the mantle column (Godard *et al*., 2000) requires a fast melt-flow regime. In the Semail ophiolite, dunitic diapirs have been identified as a likely locus for this. A diapir initially formed by the percolation of a large melt fraction works afterwards as a porous channel that controls the flow of ascending melts. From fluid-dynamic considerations, McKenzie (2000) suggested that melt transport through high-porosity channels could be very fast, up to 0.1 m s^{-1}.

In large-scale seismic mantle tomography, no thermal anomaly is usually visible underneath mid-ocean ridges (e.g. Zhao, 2004), which is in stark contrast with plumes (see below). This is instructive in terms of the mechanism that drives MORB generation. Although the melting itself is a result of decompression, this decompression is not the result of large-scale mantle upwelling. The alternative is that it must be driven by the localized removal of a top layer, i.e. by the plate-spreading process itself. This again highlights the point that plate-tectonic processes (although driven by internal heat) are largely mechanically decoupled from mantle convection, rather than being its surface expression.

24.6 Features specific to ocean-island basaltic magmatism

Because ridge and ocean-island basaltic magmatism both originate via the rise and decompression of hot mantle material, the mechanisms of melt generation, segregation and ascent for ocean-island basalts (OIBs) are similar, in several important respects, to those outlined above for MORBs. Therefore in this Section we discuss only the specific features of melt production beneath islands that contrast with MORBs. To highlight the difference, we concentrate on oceanic islands related to hot mantle plumes upwelling from a great depth (in contrast with a shallow MORB-source mantle): as deduced from seismic tomography, the Iceland plume and several others come from below the 670 km transition (Nataf, 2000; Nolet *et al*., 2006, and references therein). The worldwide production rate of melt by hot oceanic plumes is $\sim 1.2 \times 10^{15}$ g yr^{-1} (only $\sim$ 2% of the MORB production rate), so this process is not very important in the sense of global present-day development of the Earth. However, plume magmas and the volcanic rocks and gases derived from them carry chemical and, of particular importance, isotopic signatures that yield information about matter and processes deep in the mantle: they are unique

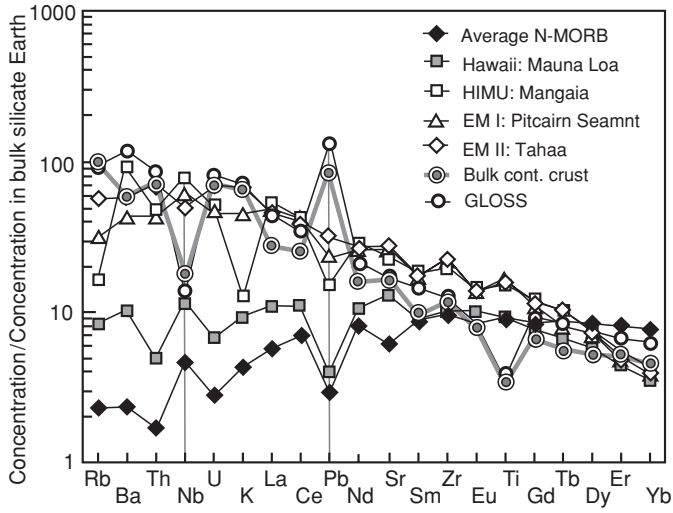

Fig. 24.9 Trace elements in oceanic island basalts (OIBs). Note the large differences in concentration of the most incompatible elements in different OIBs. Abundances in the bulk continental crust and in oceanic sediments (GLOSS) are added for comparison; the MORB and OIB magmas never show the crust-like abundances of some elements with anomalous behaviour (Pb and Nb). The crustal composition, GLOSS and BSE values are from Tables 26.3, 24.1 and 17.1 respectively. After Hofmann (2003), © Elsevier Science 2003, reproduced by permission.

windows into the deep Earth. Moreover, plumes probably were more productive in the geological past than at present.

Ocean-island basalts vary in their compositions from tholeiitic to alkali basaltic rocks, with a high potassium content, the average $[K]_{OIB}$ value being about $2.5 \times [K]_{MORB}$, and also enhanced $[TiO_2]$ (Table 24.1). The concentrations of incompatible trace elements in OIBs can exceed those in the DMM and MORBs by factors ~ 300 and ~ 10 respectively (compare Figs. 24.2, 24.9). Large plumes (Hawaii) show some similarity to MORBs in their trace-element signature, whereas small plumes often present peculiar and anomalous compositions, e.g. depletion in Pb and the alkali metals K and Rb (e.g. the Mangaia OIBs, discussed further in Section 27.3).

The modelled REE abundances in OIBs can be reconciled with the observed values (Fig. 24.9) if it is assumed that the parental melts were generated within the garnet–spinel transition zone (McKenzie and O'Nions, 1998). In many cases, however, the observed trace-element concentrations exceed even the maximum values that could be derived from the MORB-source mantle. Then a source enriched in incompatible elements must be postulated. Such mantle enrichment might have resulted, for instance, from a premelting "metasomatic" enrichment or the

refertilization of a DMM domain (Section 27.7), or they might have another source, such as subducted sediments.

The isotope disequilibrium data, i.e. the enhanced (^{230}Th/^{238}U) ratios, require that melting starts deep in the mantle and that fractional melting with a small melt fraction is a principal process, in overall agreement with the REE record (Sims *et al*., 1999). The deep source and fast uplift leads to anomalously high temperatures of plume material, up to $\sim 300\ ^{\circ}$C above the surrounding mantle at depths of a few hundred kilometres, as indicated by seismic tomography (Nataf, 2000). Thus the peridotite solidus can be crossed at much greater depths than in the case of MORBs (Sims *et al*., 1999; McKenzie, 2000).

Summarizing, both geochemical and geophysical data indicate the beginning of partial melting within typical plumes at depths below 150 km, under higher pressures and temperatures than those of the MORB factory (see Fig. 24.1(a)). The exciting problems of the mantle heterogeneities recorded by OIB magmas and their possible causes are discussed in Chapter 27.

24.7 Summary

Mid-ocean ridge magmatism, the major magmatic process on Earth, results from the decompression melting of dry mantle peridotitic rocks ascending (at a rate of 1 to 10 cm yr^{-1}) and filling the gap between spreading plates. Melting starts in the garnet-peridotite stability field ($\sim$ 100 km depth, $\sim 1400\ ^{\circ}$C) and continues within the spinel-peridotite depth interval (30–70 km), where the major portion of the melt is produced. This is followed by a final mixing of different batches of magma from different melting domains and differentiation in magma chambers at $\sim$ 30 km depth. Magma flows upward from these, through faults and fissures, to erupt into a rift valley ($\sim$ 3 km below the ocean surface). Thus tholeiitic basaltic (MORB) crust, highly variable and on average 7 km in thickness, is continuously generated. This overlies gabbros and a depleted mantle lithosphere consisting mainly of harzburgites and dunites.

The partial-melting mechanism at ridges is envisaged as being polybaric fractional melting, starting with small melt fractions, $F \sim 0.005$ or less. Any melt produced in excess of such a threshold escapes from source rocks. Melt batches ascend through the overlying mantle lithosphere without substantial re-equilibration with the wall rocks and then mix, providing relatively high concentrations of incompatible trace elements in the final basaltic magmas, on average $\sim$ 20 times the concentration in the depleted MORB-source mantle (DMM), as well as a complementary severe depletion of residual rocks in these elements ($\sim$ 0.01 times the concentration in DMM). Depending on the mantle's temperature, composition and ascending rate, the depth of the melting column, the bulk melt fractions and the

enrichment factors (for most incompatible elements) could be large, $\sim$ 130 km, $\sim$ 0.15 and $\sim$ 100 respectively, in which case enriched or E-MORBs would be generated, or as small as $\sim$ 80 km, $\sim$ 0.07 and $\sim$ 5, in which case N-MORBs would be generated.

Radioactive-isotope disequilibria in recent MORB volcanics indicate a very short time scale, $\sim$ 50 yr, for the sum total of these processes. If it is assumed that ascent is the most time consuming of these processes, then its velocity may reach ~ 1 km yr^{-1}.

Immediately after the oceanic crust is formed, enormous hydrothermal activity sets in, removing water-soluble elements into the ocean and thus changing the water chemistry on an ocean-wide scale (Fig. 27.20) and precipitating other elements into newly forming metamorphic minerals. Fluid release from the hydrated crust and underlying lithosphere plays a crucial role during subduction, the next stage of evolution of the oceanic crust + lithosphere (Chapter 25).

In the case of ocean-island magmatism, the underlying plume ascends faster, $\sim$ 100 cm yr^{-1}, and from greater depths than the shallow mantle below the ocean ridges; therefore it is hotter and crosses the solidus at depths well in excess of 100 km. The principal features of the melting process are similar to those for MORBs, but in some cases the observed concentrations of incompatible elements are too high to have been generated by the melting of MORB-source mantle. Therefore premelting metasomatic enrichment (refertilization) of rocks (Fig. 27.14(a), (b)) or enriched sources (Fig. 27.4) are postulated. These are best traced by isotopic systematics, as discussed further in Chapter 27.

25

Subduction and island-arc magmatism

25.1 Introduction: subduction, associated processes and the crucial role of water

The subduction factory reworks a huge amount of material, similar to that involved in ridge magmatism, and it redistributes trace elements in uniquely fractionated relative abundances between three principal terrestrial reservoirs, the mantle, the continental crust and the oceans.

The bulk present-day mass flux of subducted material is impressive, $\sim 10^{18}$ g yr^{-1}, of which sedimentary (mainly terrigenous) and basaltic subfluxes contribute 1.3×10^{15} g yr^{-1} and 6.7×10^{16} g yr^{-1} respectively and the remainder is material of the subcrustal lithospheric mantle (Crisp, 1984; Veizer and Jansen, 1985; Rea and Ruff, 1996; Plank and Langmuir, 1998).

On its way to a convergent boundary, the oceanic plate is cooled and becomes thicker as the lithosphere freezes onto its base. The pre-subducted oceanic plate thus consists of several rock types: sediments highly enriched in certain trace elements, basaltic crust, gabbros and peridotites. The intense water flux through the ocean floor ($\sim 10^{17}$ g yr^{-1}) alters all these rocks (particularly the basalts), which then carry specific ocean-related chemical and isotopic signatures, and it also changes the sea-water chemistry via the delivery of mantle-derived elements into the ocean (Fig. 27.20; Staudigel, 2003).

Subduction occurs at the convergent boundaries where plates collide (Fig. 23.2). When approaching the collision zone, the stresses applied to the cold rigid plate cause its faulting and bending and its movement downward, generating a deep trench between the subducting and overriding plates. Compression of the hydrated and therefore plastic sediments in this trench (partially) scrapes them off and squeezes them out, thus producing an intensely folded mountainous zone known as an accretionary prism. A portion of the sediments remains attached to the slab, which, because of its bulk negative buoyancy, sinks down into the mantle.

Table 25.1 *Computed densities of major rock types transformed to ultra-high-pressure metamorphic mineral assemblages. After Ernst (2001), © Elsevier Science 2001, reproduced by permission*

Rock type (density, g cm^{-3})	Mineral	Mineral density (g cm^{-3})	Mode (vol. %)
Garnet lherzolite (3.24)	Enstatite	3.21	30
	Diopside	3.25	15
	Olivine	3.22	50
	Pyrope garnet	3.67	5
Basaltic eclogite (3.68)	Omphacite	3.34	60
	Garnet	4.17	35
	Rutile	4.25	5
Granitic gneiss (3.03)	Jadeite	3.28	40
	Coesite	3.01	35
	K-feldspar	2.56	15
	Muscovite	2.85	10

This sinking of slabs is promoted by an important positive-feedback process. When the slab material reaches depths of several tens of kilometres, its temperature and pressure increase enough to initiate metamorphism, i.e. the formation of new mineral assemblages via a series of solid-state chemical reactions. Similar processes operate in the middle and lower crust, which consist largely of metamorphic rocks (Section 26.4); a very important transition, occurring at about 100 km depth, is that from basalt to a rather dense eclogite (Table 25.1). This helps to explain why plate movement appears to be primarily driven by the sinking of slabs, as mentioned in Section 23.4 (Forsyth and Uyeda, 1975).

The importance of slab sinking as a plate-tectonic locomotive is further illustrated by the development of so-called back-arc basins, several hundreds of kilometres beyond the trenches in the direction of subduction (Fig. 25.6). These basins are extensional and may have volcanism and spreading ridges. It is generally thought that the extension is driven by the sinking slab. Moreover, even continent break-up could result from this process.

Metamorphic transitions in a sinking slab do not occur in a fully closed system. With increasing temperature and pressure, the progressive dehydration of water-bearing minerals generates a hydrous mobile phase, which can escape from the slab. Temperatures can also rise so high that altered sedimentary and basaltic rocks can be partially molten and then magmas (also water-saturated) serve as the mobile phase. A large temperature gradient across the slab (which is still cold inside but hot close to the contacts with the mantle) allows different fluids to be released simultaneously and in close proximity.

The hydrous fluid phases released from the slab carry into the overlying rock units soluble and (in the case of fluid-saturated melts) incompatible elements causing metasomatism and triggering partial melting; the resulting magmas can contribute to the growth of continents. Volcanism in this tectonic setting constitutes $\sim 15\%$ of the total global amount (Crisp, 1984). In contrast with the MORB environment (Chapter 24), a continental-crust province can overlie the melting zone and the compositions of magmas can evolve by interactions with crustal rocks as well as by fractional crystallization, often in combination (Kelemen *et al.*, 2003; Schmidt and Poli, 2003).

Finally, the residual slab rocks will have become dehydrated or may even have lost a partial melt fraction; therefore their solidus temperature is raised, so the slab can sink further down into the mantle without melting. When these rocks, with their particular trace-element and isotopic signatures, are introduced into the mantle, this leads to elemental and isotopic heterogeneity.

In the following sections we will discuss the concentrations of major elements (Section 25.2) and trace elements in arc magmas, highlight the importance of the $^{10}Be/^{9}Be$ and B/Be record of sediment recycling (Section 25.3) and then outline the relevant processes (Sections 25.4–25.6). Chapter 27 presents isotopic evidence pointing to the source of the matter that is processed in slab dehydration (and melting). Detailed reviews of subduction and associated processes have been presented by e.g. Martin (1999), Turner *et al.* (2003) and Kelemen *et al.* (2003).

25.2 Major-element chemistry of arc magmatic rocks

As could be expected from the heterogeneity of the matter in the descending slab and surrounding mantle region and the complexity of the processes occurring there, subduction-related magmatism generates a great variety of different rock types, including basalts (some of which are indistinguishable from MORBs), rocks of broadly granitic composition (typical of continental crust) and a variety of rocks of intermediate compositions. Volumetrically, basalts (with $SiO_2 < 54\%$) are the most abundant rocks, followed by andesites (with $SiO_2 > 54\%$). Below only primitive basalts and andesites are discussed, i.e. those with magnesium index $mg\# > 60$. The magnesium index generally decreases as a melt evolves, and the most primitive rock types come closest to the primary-melt composition (Kelemen *et al.*, 2003).

Table 24.1 shows that the SiO_2 content of arc basalts is indistinguishable from that typical of MORBs, and other oxide contents are similar, except for a somewhat higher K_2O content.

Primitive andesites are found almost exclusively in arcs (both continental and oceanic), and they are particularly frequent in arcs situated above young, slow-subducting, plates. Therefore they are indicative of "fossil arcs" in older geological

provinces (Gill, 1981). Primitive andesites, besides having (by definition) an enhanced SiO_2 content relative to basalts, also show substantially higher concentrations of the alkali metals K and Na but are underabundant in CaO, MgO and FeO (Table 24.1). Therefore in K_2O–Na_2O, FeO–Na_2O and CaO–Na_2O concentration plots, the fields of basalts and andesites overlap only slightly (see the corresponding figures in Kelemen *et al.*, 2003).

The concentrations of major elements in andesites and in the mean continental crust are similar, implying that potentially these rocks could be important as crustal precursors. Even though they appear not to be abundant enough at the surface (at least at present) to represent a principal component of crustal growth, a considerable portion of andesitic magma could have solidified deeper in the continental crust. These magmas are more viscous than basaltic magmas; they are also less hot and can "freeze" in the crust as hydrous fluid exsolves and escapes, increasing the solidus temperature (Kelemen *et al.*, 2003).

25.3 Trace-element chemistry of primitive arc volcanics

Trace elements in arc volcanics: comparison with oceanic basalts

The trace-element abundance patterns of primitive arc volcanics highlight first the overall difference between arc rocks and MORBs and second the similarity of different arc rocks to each other in respect of some particular trace-element features (Fig. 25.1). Arc rocks display spectacular enrichments in the large-ion lithophile elements (LILEs) Rb, Ba, K and also Pb and Sr. A common property of these elements is that they are highly soluble in aqueous fluids, and therefore this general feature of the arc trace-element patterns is in full accord with the hypothesis that fluid advection plays an important role in arc magmatism. On the one hand, Th and U, which are abundant in sediments, are also enriched compared with MORBs (Table 24.1); these enrichments, however, are not enough to supply the continental crust with these elements. On the other hand, all arc magmatic rock types are depleted in high-field-strength elements (HFSEs) such as Ta, Nb and Ti.

The rare earth elements also show a very specific abundance pattern. The LREEs are slightly more concentrated than in N-MORBs, whereas the rare Earth elements heavier than Sm are all relatively depleted in both basalts and andesites (Table 24.1) and show a concave-up distribution. Such a pattern is typical for melts that have equilibrated with amphibole, in which the HREEs are all only slightly incompatible; generally the $D(\text{mineral/melt})_{\text{HREE}}$ values are within 0.3 to 1 (Dalpe and Baker, 2000). In the hydrated mantle wedge this hydrous silicate has a very large field of stability at pressures between $\sim$ 0.2 and 3 GPa (i.e. at almost 100 km depth, Niida and Green, 1999).

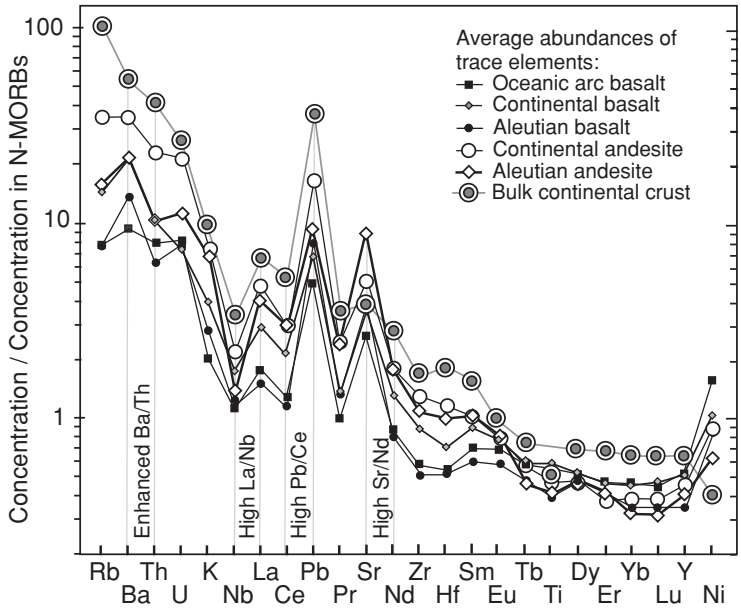

Fig. 25.1 Trace-element abundances in primitive arc volcanics and continental rocks. Crustal composition from Rudnick and Fountain (1995). Be, B, Nb and Ta abundances from McLennan (2001), N-MORB composition used for normalization from Sun and McDonough (1989). After Kelemen *et al.* (2003), © Elsevier Science 2003, reproduced by permission.

The depletion of Nb relative to La and MORBs (Fig. 25.1), also a fingerprint common to all arc magmatic rocks, is a further pointer to subduction-zone processes. The high La/Nb ratios of arc rocks exceed the ratios in primitive mantle, MORB-source mantle and all known mantle derivatives, which reflect the similar incompatibilities of La and Nb in common mantle minerals (Fig. 26.6). As the concentration of La fits with that of the other LREEs, it must be Nb that is behaving in an anomalous manner. Further, the negative Nb anomaly cannot be attributed to the fluid insolubility of Nb, as the LREEs are also not transported by fluids. A possible solution is that arc magmas are generated in equilibrium with a mineral or assemblage in which Nb is less incompatible than the LREEs, or even compatible. As Ti is also depleted in arc magmas (Table 24.1) and Nb is compatible in rutile (TiO_2), this is the phase that is widely thought to cause the Nb anomaly (Kelemen *et al.*, 2003). However, Foley *et al.* (2002) carried out experimental studies on the rutile–melt and amphibole–melt partitioning of Nb, La and Ta and found that amphibole also lowers the Nb/La ratio in the melt: the partition coefficient ratio D_{Nb}/D_{La} is ≈ 2. Equilibration with amphibole would produce a low Nb/Ta ratio in the melt, as is indeed observed in many arc magmas and in the continental crust. This indicates that in the formation of arc basalts (and continental crust), the equilibration

of melt with amphibole-bearing assemblages was probably an important factor, whether this took the form of the partial melting of amphibolite or the fractional crystallization of an amphibole-rich cumulate. A further examination of the abundance patterns reveals differences between basalts and andesites: the latter show the greatest enrichments in the LILEs as well as in U and Th. This is also true for basalts and andesites from the Aleutian arc, where no continental crust is present. These trace-element characteristics shed light on the complicated combination of fluid-releasing and partial-melting processes in subduction zones. It is particularly useful to compare the behaviour of fluid-insoluble elements with that of soluble elements.

Thorium is a suitable element for such a comparison (Straub *et al.*, 2004). Experimental studies of eclogite–aqueous-fluid and peridotite–aqueous-fluid partitioning show that Th is poorly soluble. However, Th is highly incompatible during partial melting. Another highly incompatible element, Ba, is much more readily partitioned into a fluid phase than Th, and therefore the Ba/Th ratio of volcanics is predicted to be enhanced and variable if a fluid phase is involved in magma genesis. The Ba/Th ratios in arc volcanics are indeed variable by a factor of up to 100, reaching values as high as $\sim$ 1000 (Fig. 25.2). For comparison, the average Ba/Th value inferred for MORBs is $\sim$ 70 (Hofmann, 1988), for OIBs it is $\sim$ 80 (see Sun and McDonough, 1989) and for the global average of subducted sediments (GLOSS) it is $\sim$ 100 (Plank and Langmuir, 1998), and these values are much less variable.

The highest Ba/Th ratios are found in arc rocks with relatively low [Th] values and $^{143}Nd/^{144}Nd$ ratios similar to those in MORBs (Fig. 27.2(a)). Most arc volcanics show enhanced Th concentrations, resulting in lower Ba/Th ratios (but still higher than those of MORBs, OIBs and GLOSS). With increasing Th content their $^{143}Nd/^{144}Nd$ ratios approach those of GLOSS (Fig. 25.2), which indicates a large contribution from subducted sediments. As Nd is also insoluble in fluids, this combined trend indicates that the sediment contribution to these Th-rich arc volcanics resulted from partial melting of the sediments rather than their dehydration.

Uranium–thorium fractionation also occurs during slab dehydration: arc volcanics generally have higher U/Th ratios than both MORBs and sediments. This feature has also generally been considered as the result of preferential U transfer by fluids from the subducting slab into the mantle wedge; fluid-insensitive Th remained in the slab rocks, at least as long as these did not melt. According to the available fluid–mineral partition coefficients, U/Th ratios as high as $\sim$ 40 are expected in slab-derived fluids, much exceeding those observed in any mantle and crustal rocks (Table 24.1, Turner *et al.*, 2003). Addition of such a fluid should indeed increase the U/Th ratio in any reservoir.

The observed abundances of fluid-soluble trace elements in arc volcanics, along with estimates of the rates of volcanism in given arc segments, allow the fluxes of

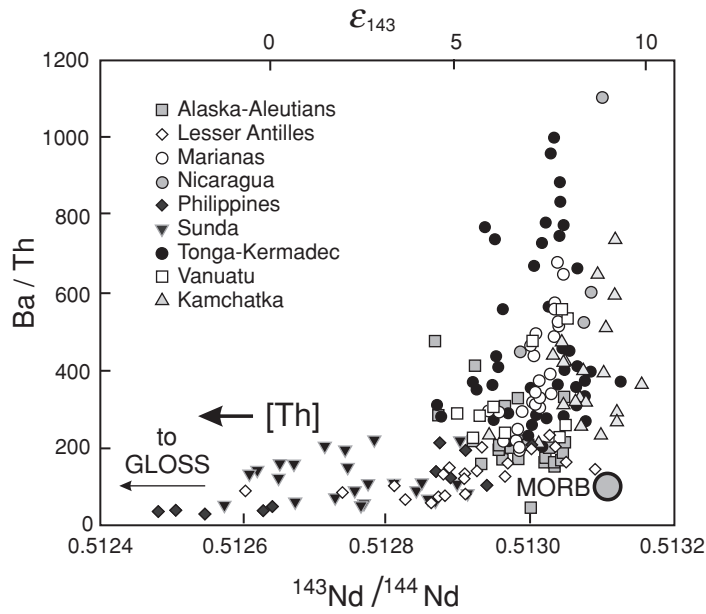

Fig. 25.2 Thorium and barium abundances vs. Nd-isotopic compositions in arc volcanics. The arrow and [Th] show an increase in Th concentrations from the $\sim$ 0.4 ppm typical of MORBs (Table 24.1) up to 15 ppm in the samples with the lowest ^{143}Nd/^{144}Nd ratios. Arc lavas with the high [Th] values and low Ba/Th and ^{143}Nd/^{144}Nd ratios typical of continental crust indicate the contribution of a "mobile phase" (partial melts or supercritical fluids) from slab sediments into the source of arc magmas. From Turner *et al.* (2003). Reproduced by permission of the Mineralogical Society of America.

matter out of subducting slabs to be quantified. The ^{10}Be and B systematics are especially important in this respect.

Subduction of sediments: the special significance of ^{10}Be and B

The contribution of a mobile phase, which separated from sediments and altered basaltic crust in the course of subduction and was then transferred into the overlying mantle wedge, is reliably indicated by the ^{10}Be/^{9}Be and B/Be systematics (Table 3.3). Beryllium-10 is mainly generated in the Earth's atmosphere by spallation reactions on O and N nuclei. In the atmosphere, ^{10}Be atoms readily attach to solid and liquid particles, which rain out. Eolian dust is considered as the most significant source of ^{9}Be to the oceans. Thus, the sources and input mechanisms of Be isotopes into the oceans are different. In sea water Be is "particle-reactive"; its residence time in the oceans varies from 100 to 1000 yr (Morris *et al.*, 2002). Because of this short residence time and their different sources, the concentrations of the two Be

isotopes and their ratios vary by a factor ~ 3 in sea water and in young oceanic sediments (von Blanckenburg *et al.*, 1996), with an average ratio of $^{10}Be/^{9}Be = (8.0 \pm 2.5) \times 10^{-8}$ (Brown *et al.*, 1992b) and a Be concentration in non-carbonate ("undiluted") sediments ≈ 1 ppm (Reagan *et al.*, 1994).

Also, the concentration of short-lived ^{10}Be decreases downwards in the sediment column (as the sediments age) and it is generally undetectable below a few hundred metres (Morris *et al.*, 2002). Finally it should be noted that ^{10}Be is mainly attached to leachable phases of ocean sediments, whereas ^{9}Be is incorporated in resistant minerals. Therefore an early dehydration process would extract Be with an enhanced $^{10}Be/^{9}Be$ ratio, and this ratio would generally (but not always) decrease in residual rocks and late-derived fluids (Bourles *et al.*, 1992).

Boron is highly soluble in sea water, where its residence time is close to 10 Myr. In pelagic (non-carbonate) sediments [B] values vary within a factor ~ 5, from 30 to 150 ppm with a mean value ≈ 70 ppm. The altered oceanic crust is also an important reservoir of B, with [B] ≈ 25 ppm, whereas the model DMM and BSE concentrations are quite low, well below 1 ppm (Table 17.1). The above estimates give a mean "initial" ratio of B/Be ~ 70 in subducting sediments (Fig. 25.3).

If sediments are attached to a hydrous subducting slab, dehydration is inevitable as the temperature and pressure increase. Boron is highly soluble in hydrous fluids whereas Be is relatively immobile. Therefore the B/Be ratios are expected to be fractionated in the course of subduction, being higher in fluid phases and lower in residual phases. This tendency is similar to the evolution expected for the $^{10}Be/^{9}Be$ ratio. Apart from the labile (surface) siting of ^{10}Be in sediments, another factor in the $^{10}Be/^{9}Be$ evolution in arcs is dilution, as mantle rocks contain ^{9}Be but no ^{10}Be.

In accord with the above predictions, the $^{10}Be/^{9}Be$ and B/Be ratios generally correlate and decrease from higher values in fore-arc volcanoes towards the lower values typical for back-arc volcanoes (Fig. 25.3) even though exceptions, e.g. a sharp increase in $^{10}Be/^{9}Be$ in back-arc volcanics, are also known (Morris *et al.*, 2002). The correlation seen in Fig. 25.3 is interpreted as a mixing trend between two principal end-members (Tera *et al.*, 1986; Reagan *et al.*, 1994). One of these is similar to MORBs or OIBs, with low $^{10}Be/^{9}Be$ ($\approx 3.5 \times 10^{-11}$) and B/Be ratios. The other end-member is derived by extrapolation using regression and the average $^{10}Be/^{9}Be$ value obtained for the bulk pre-subducted sedimentary column. In the case of the Cocos plate the average $^{10}Be/^{9}Be$ ratio of the "sedimentary end-member" is 460×10^{-11}, and the observed regression (Fig. 25.3) gives B/Be in the slab-derived fluid as ≈ 1000, exceeding the mean B/Be ratio in subducting rocks (~ 70) by a factor > 10. The high B/Be ratio thus indicates that the fluid participated in partial melting in the mantle wedge and the generation of arc magmas. Moreover, co-variations of $^{10}Be/^{9}Be$ with the activity ratio ($^{230}Th/^{232}Th$) and the $^{87}Sr/^{86}Sr$ ratio, and also mass-balance considerations, imply the subduction of almost all the

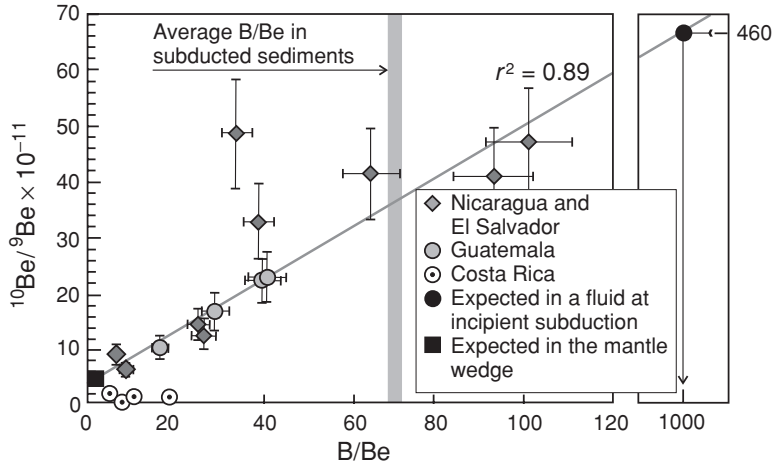

Fig. 25.3 Beryllium–boron isotopic systematics in Central American arcs (the Cocos plate). The regression indicates mixing between two end-members, an overlying mantle peridotite with quite low $^{10}Be/^{9}Be$ and B/Be ratios and a slab-derived fluid for which a B/Be ratio, $\sim$ 1000 is obtained via extrapolation of the regression to the bulk ratio $^{10}Be/^{9}Be \approx 460$ estimated for the sedimentary column on the Cocos plate (right-hand plot). The convergence rates in arc systems are generally known from geophysical observations and usually give a few millions of years for the time that elapses from incipient subduction to fluid release from the slab. This allows the amount of ^{10}Be decayed during subduction to be corrected. The decay-corrected input–output inventories of ^{10}Be suggest that the whole sedimentary column is subducted beneath the Central American arcs. After Reagan *et al.* (1994), © Elsevier Science 1994, reproduced by permission.

$\sim$ 500-m-thick sedimentary column overlying the basaltic crust of the Cocos plate (Fig. 23.1), also pointing to the validity of a sedimentary end-member.

Summarizing, the ^{10}Be, ^{9}Be and B family presents strong evidence not only of slab dehydration and element transfer by a fluid phase but also of the scale of sediment subduction.

Radioactive disequilibria caused by subduction processes

Because ^{10}Be signals trace the expulsion of a mobile fluid phase from young sediments, a comparison of the $^{10}Be/^{9}Be$ ratios with the U–Th series disequilibria should allow us to determine whether these disequilibria originated by element fractionation in the same fluid segregation; this fractionation could then be dated. An excellent correlation between the $^{10}Be/^{9}Be$ and $^{226}Ra/^{230}Th$ ratios was observed for historic lavas from the southern volcanic zone in Chile, where the Nazca plate is subducting beneath the Andes (Fig. 25.4 and 23.1). Radium, whose closest chemical analogue is Ba, readily partitions into a fluid phase while Th is insoluble. Because

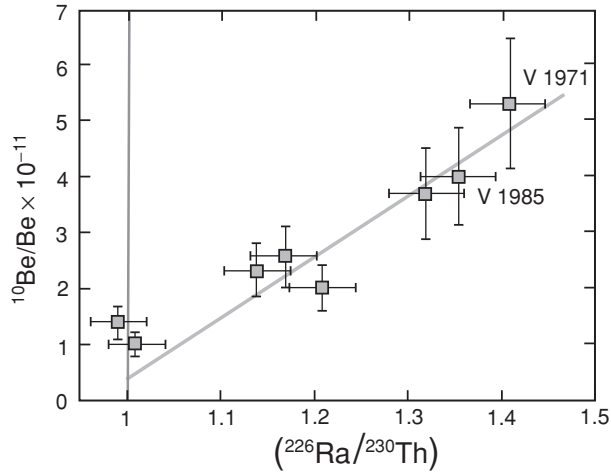

Fig. 25.4 The ^{226}Ra–^{230}Th–^{10}Be systematics in recent lavas from southern Chile volcanoes. Generally (^{226}Ra/^{230}Th) is not well correlated with ^{10}Be/^{9}Be owing to decoupling between the sediment and fluid signatures but the good correlation here should be considered as "a present from Nature showing how it works": the correlation results from the variable contributions of a slab-derived mobile phase (high ratios) into the mantle wedge, the source of arc melts (low ratios). Similar relationships can also be seen in Fig. 25.5. From Sigmarsson *et al.* (2002), © Elsevier Science 2002, reproduced by permission.

the ^{10}Be is sourced in subducting sediments, the correlated ^{226}Ra most probably originated from the same source. Also, a shift of ^{10}Be/^{9}Be towards 0 is the signature of mantle melts, for which a (^{226}Ra/^{230}Th) activity ratio ~ 1 (secular equilibrium) is expected and is actually observed (Fig. 25.4), thus validating the parameters for the mantle end-member used in the previous section.

The Chilean volcanics further show a good correlation between the activity ratios (^{226}Ra/^{230}Th) and (^{238}U/^{230}Th) (Fig. 25.5), and similar trends are also observed in several other arcs. This is expected for fluid segregation under oxidizing conditions, because U is highly fluid-soluble in the hexavalent state. Note that if the oxygen fugacity were to vary significantly between or within subduction zones this could have a major effect on U-series fractionation. Most observations, however, indicate that fluid phase transport causes fractionation of the Ra–Th–U trio, whereby the fluid carries Ra and U preferentially to Th from the downgoing slab into the overlying mantle.

The observed disequilibrium between ^{226}Ra and ^{230}Th gives an upper time limit for the combined process of mobile phase transfer from a source-slab segment to the melting zone in the mantle wedge followed by melt transport to the Earth's surface. As $\tau_{226} = 1.6 \times 10^3$ yr (Fig. 24.6), these two species equilibrate after about 8×10^3 yrs, and so the transfer time scale must be shorter than this value. If the slab is assumed to be at about 80–100 km depth below the volcanic front, the

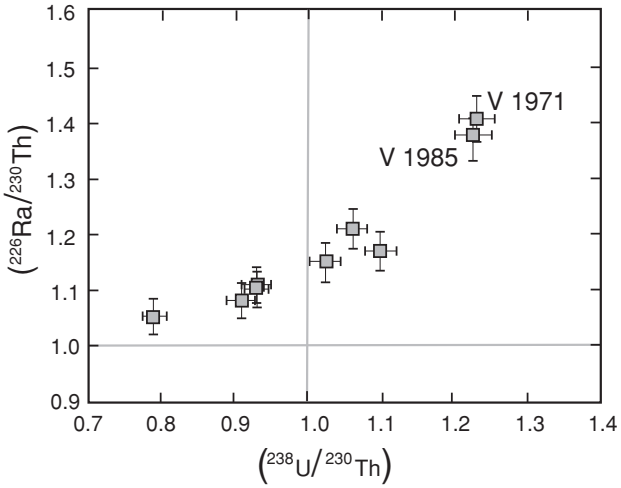

Fig. 25.5 The ^{238}U–^{230}Th–^{226}Ra systematics in recent lavas from southern Chile volcanoes. Correlations between ^{226}Ra/^{230}Th and U/Th, two fluid-indicative indices, are common for arc volcanics, indicating recent fluid addition into the arc melt source. After Sigmarsson *et al.* (2002), © Elsevier Science 2002, reproduced by permission.

above time scale gives a minimum average ascent velocity of ~ 10 m yr^{-1} for fluid and melt (Sigmarsson *et al.*, 2002).

A lower time limit for the fluid + magma segregation and ascent is given by the ^{228}Ra–^{232}Th systematics ($\tau_{228} = 6$ yr). Even in very young arc lavas this ratio is in secular equilibrium, indicating that ^{226}Ra – ^{230}Th fractionation occurred at least 30 years ago, which is comparable with the value of ~ 50 years derived for mid-ocean ridge magmatism from (^{210}Pb/^{226}Ra) disequilibria (Fig. 24.7(a)). The 30 yr lower time limit gives a maximum average ascent velocity of ~ 2000 m yr^{-1} (Turner *et al.*, 2004b).

In contrast with the enhanced abundance of fluid-sensitive isotopes discussed above (Fig. 25.5), ^{235}U is less abundant than its fluid-insensitive daughter, ^{231}Pa. Therefore (^{231}Pa/^{235}U) > 1 indicates that not only fluid-related fractionation processes operate in arc magmatism (see Section 25.7 below).

25.4 Development of slab rocks during subduction: introduction to metamorphism

Processes that occur as pressure and temperature increase

As discussed above, arc magmatic rocks contain enhanced abundances of fluid-soluble (e.g. Rb, K, Ba, Pb, Sr) and sediment-sourced (B, Th, ^{10}Be) elements and isotopes. These observations, along with some revealing isotopic systematics (^{10}Be/^{9}Be, Section 25.3) and "input–output" correlations (i.e. between the abundances of these species in the slab and those transferred by arc magmas to the

Earth's surface) show convincingly that a mobile hydrous phase, expelled from the slab, was by far the most important vehicle for transporting these trace elements into the overlying mantle wedge, even though some matter (sediments in particular) could have been added to the mantle wedge by bulk mixing (Turner *et al.*, 2003). At high-*PT* conditions the partial melting of slab rocks could also cause fractionation and transport of the elements, as will be discussed in Sections 25.5 and 25.6.

The questions now to be addressed are, why and how is such a fluid phase generated in the subducting slab? To answer these questions it is necessary to review some aspects of metamorphism, which is the solid-state change in mineral composition of a rock in response to changes in temperature and pressure. Metamorphism that occurs with increasing P and T (such as in a subducting slab) is termed prograde, and the reverse is retrograde.

Metamorphic chemical reactions produce a new equilibrium mineral assemblage that has the lowest free energy under the modified *PT* conditions. The highest-*PT* assemblage, formed during peak metamorphism, could be reset during a retrograde path to a lower-*PT* assemblage. In some cases, however, the peak-*PT* conditions can be preserved, especially in "dry" conditions.

In prograde metamorphism, hydrous minerals (which have OH-groups built in as part of their crystal structure, e.g. chlorites or amphiboles) are progressively replaced by anhydrous ones having an otherwise similar chemical composition (e.g. pyroxenes), and hydrous fluid is set free. Interactions of this fluid with the mineral assemblage present and its subsequent escape cause fractionation of fluid-soluble trace elements (e.g. the removal of Rb and K from residual rocks). Under extreme conditions even the least movable elements, such as the rare Earths, can be fractionated.

The reverse mineral reactions, which characterize retrograde metamorphism, require the input of a hydrous fluid, and therefore a dry environment allows the peak-*PT* signatures to be preserved. Under wet conditions, such as in the ocean floor underneath oceanic ridges, where heated ocean water circulates through the rock, retrograde reactions can transform the anhydrous magmatic minerals of basalts (e.g. pyroxene, plagioclase and olivine) to hydrous minerals that are stable at lower temperatures (e.g. chlorite, serpentine).

Pressure–temperature records: introduction to thermobarometry

The simplest examples of metamorphic reactions are isochemical phase transitions in single minerals. One such phase transition, allowing a high pressure to be detected, is

$$\begin{matrix} \mathrm{SiO_2} = \mathrm{SiO_2} \\ \text{(quartz)} \quad \text{(coesite)}. \end{matrix} \tag{25.1}$$

The transition from quartz to the denser coesite occurs at pressures of $\sim$ 3 GPa ($\sim$ 90 km depth). Other simple reactions are also used in thermobarometry.

Much more commonly used, however, are changes in mineral association, or parageneses, where minerals react with each other to form new assemblages. Depending on the *PT* conditions, several so-called metamorphic facies are distinguished, which are defined by specific parageneses. Those with the highest T and P (before melting occurs) are the granulite and eclogite facies ($P \sim 3$ GPa, $T \sim 800 \pm 100\,^{\circ}$C). Two typical mineral reactions are

$$\text{anorthite} + \text{olivine} \rightarrow \text{pyrope} + \text{grossular garnet} \tag{25.2}$$

and

$$\text{labradorite} + \text{olivine} + \text{diopside} \rightarrow \text{garnet} + \text{omphacite} + \text{quartz}. \tag{25.3}$$

The right-hand side of Eqn (25.3) represents the high-density rock type eclogite (Table 25.1), which sinks into the mantle and is therefore an important motor for plate tectonics, as discussed above.

While phase transitions in single minerals or in equilibrium mineral assemblages are useful to constrain an area in *PT*-space, reliable *PT* measurements can be made via exchange reactions that modify the major-element chemical composition of coexisting minerals. Widely used reactions of this kind are the exchange of Mg and Fe^{2+}, for instance between garnet and pyroxene:

$$\begin{array}{ccccccc} \frac{1}{3}Mg_3Al_2Si_3O_{12} & + & CaFeSi_2O_6 & \leftrightarrow & \frac{1}{3}Fe_3Al_2Si_3O_{12} & + & CaMgSi_2O_6 \\ \text{pyrope (prp)} & & \text{hedenbergite (hd)} & & \text{almandine (alm)} & & \text{diopside (di)} \\ \text{(garnet)} & & \text{(clinopyroxene)} & & \text{(garnet)} & & \text{(clinopyroxene)} \end{array} \tag{25.4}$$

According to Nernst's law, the equilibrium constant K for a given assemblage of mineral phases is derived from the activities γ and molar fractions X (Essene, 1989):

$$\begin{aligned} K &= \frac{\gamma(\text{Mg, prp})X(\text{Mg, prp}) \times \gamma(\text{Fe, hd})X(\text{Fe, hd})}{\gamma(\text{Mg, di}) \times (\text{Mg, di}) \times \ \gamma(\text{Fe, alm})X(\text{Fe, alm})} \\ &= \frac{\gamma(\text{Mg, prp})\gamma(\text{Fe, hd})}{\gamma(\text{Mg, di})\gamma(\text{Fe, alm})} \times \frac{X(\text{Mg, prp})X(\text{Fe, hd})}{X(\text{Mg, di})X(\text{Fe, alm})} \\ &= [K(\gamma)] \times [K_{\text{D}}] \end{aligned} \tag{25.5}$$

where $[K_{\text{D}}]$ is the factor relating to dispersion. Further, the equilibrium constant K relates to the extensive parameters enthalpy, H, and entropy, S, as follows:

$$\ln K \approx -\Delta H(0, T)/RT + \Delta S(0, T)/R - P(\Delta V)/RT. \tag{25.6}$$

The thermodynamic parameters $K(\gamma)$, ΔH and ΔS can be obtained from experimental and theoretical approaches. Therefore a measurement of K_D from the chemical compositions can be used to obtain a relationship between the unknowns P and T, i.e. a curve in PT-space. The intersection of several such curves, representing different mineral reactions, then yields reliable values for the P and T values of the metamorphism. Regarding reaction (25.4), the partition coefficient

$$K_D = \frac{(Fe/Mg)_{Cpx}}{(Fe/Mg)_{Grt}}$$

has been shown to vary considerably and to be strongly temperature dependent, in the geothermometer function

$$T(K) \approx \frac{3686 + 283.5P(GPa)}{-\ln K_D + 2.33}, \tag{25.7}$$

as initially suggested by Raheim and Green (1974). Later on, relationship (25.7) was improved to be in accord with the *mg*# value of the system, rates of migration of the elements in the minerals etc. (e.g. Lee and Ganguly, 1988; Pattison and Newton, 1989; Bejina *et al.*, 2003). Other exchange reactions constrain the pressures (Essene, 1989).

Trace-element partitioning between coexisting minerals also depends on the pressure and temperature. Some of these elements are resistant to diffusive re-equilibration and are therefore convenient for the determination of peak-PT conditions. For example, the equilibrium distribution of yttrium between Y-bearing monazite (xenotime) and garnet depends on temperature (Pyle and Spear, 2000). Calibration of the relationship $[Y]_{garnet} = f(T)$ using other thermobarometers, e.g. garnet–biotite thermometry and garnet–plagioclase barometry, then allows $[Y]_{garnet}$ (ppm) to be translated into a temperature T (in K):

$$\ln [Y_{garnet}] = (16031 \pm 862)/T - (13.25 \pm 1.12). \tag{25.8}$$

This is especially temperature-sensitive within the range 450 to 550 °C. Similarly, the Zr content in rutiles correlates with the metamorphic grade of Zr and thus allows the temperature of metamorphism to be quantified (Zack *et al.*, 2004).

The oxygen-isotopic compositions of coexisting minerals also appear to be a powerful tool in estimating the PT conditions of metamorphism. Since the fundamental contribution of Urey (1947) it is known that O-isotope compositions of minerals (equilibrated within a given mineral assemblage) depend on the temperature. If this dependence is calibrated experimentally and/or theoretically, the temperatures of metamorphism can be derived from them. The O-isotopic compositions δ_i, δ_j (ppm) of minerals i and j depend on temperature as follows (e.g.

Farquhar *et al.*, 1996):

$$T(\mathrm{K}) = \left\{ \frac{10^6 A_{ij}}{1000 \ln(1000 + \delta_i)/(1000 + \delta_j)]} \right\}^{1/2} \tag{25.9}$$

where A_{ij} is the temperature coefficient, known from experimental and theoretical data. For a pair of a metamorphic mineral and quartz this coefficient varies between 0.9‰ and 6.3‰ (see Table 1 in Farquhar *et al.*, 1996). Recent studies have shown that it is possible to correct the observed distribution of O-isotopes for isotope exchange during retrogression; therefore O-isotope thermometry can be applied even to ultra-high-grade metamorphic rocks, which have cooled slowly from high temperatures (Farquhar *et al.*, 1993; Moecher and Sharp, 1999; Vannay *et al.*, 1999). To prove the preservation of the peak-*PT* values, several geobarometers and geothermometers are generally applied. If the resulting *PT* conditions are in agreement, this provides confidence that they represent the true parameters of the peak of metamorphism.

25.5 Metamorphism in the slab: fluid production and release

Low-PT metamorphism, high dehydration-fluid production rates

At the beginning of subduction an oceanic plate contains pore water as well as about 20 mineral species, which include hydroxyl groups or H_2O molecules as structural components. Some minerals contain more than 10 wt % water, e.g. chlorite (which is present in various hydrated rocks: pelites, basalts, gabbro, peridotites), clay minerals, serpentine (the major component of retrogressed peridotites, i.e. serpentinites) and others. In total, a slab fluid is a composite of fluids derived from metasediment ($\sim 5\%$) and metabasalt ($\sim 95\%$, Straub *et al.*, 2004). Carbon-dioxide-bearing minerals also play a role, even though the bulk CO_2 concentration in altered oceanic crust is substantially lower than the water content.

Devolatilization starts with incipient subduction, when pore fluids are expelled owing to compaction of the sediments. The inventory of ^{10}Be shows that in some ^{10}Be-rich volcanic arcs almost all sediments present in the fore-arc crust are subducted down to the melting region (e.g. the Aleutian arc). Other arcs, even those with a presumed ^{10}Be input and moderate or fast subduction rates, show a low ^{10}Be abundance (Costa Rica); underplating and/or subduction erosion of the slab are suggested to explain this discrepancy. Generally the estimates of sediment contribution into a subducting slab from the ^{10}Be data agree with the geophysical observations (Morris and Rayan, 2003).

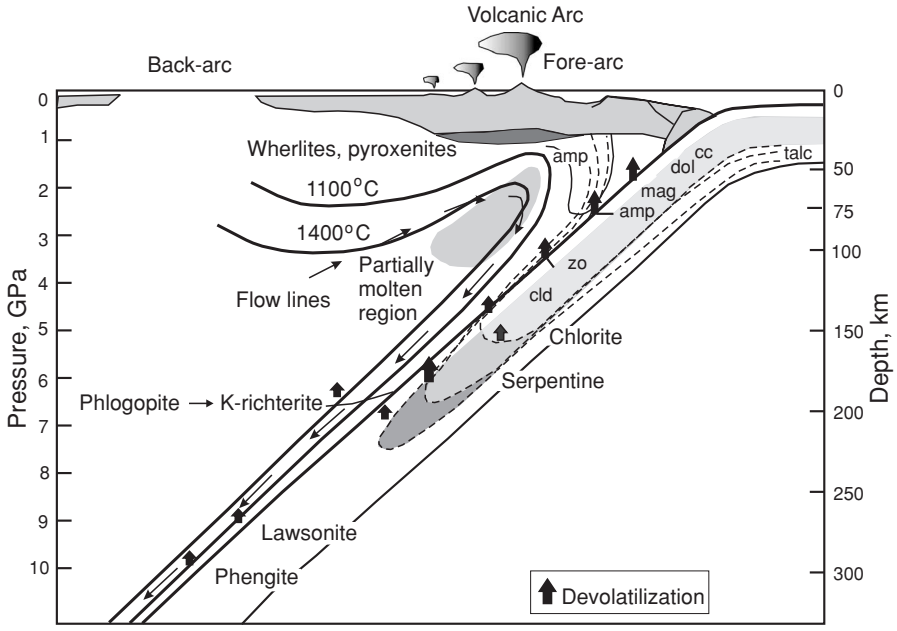

Fig. 25.6 Subduction: a schematic presentation of materials and processes. Abbreviations: cc, calcite; dol, dolomite; mag, magnesite; amp, amphibole (other than high-pressure amphiboles such as richterite and glaucophane); zo, zoisite; cld, chloritoid. The thick upward arrows signify fluid release. After Schmidt and Poli (2003), © Elsevier Science 2003, reproduced by permission.

As the temperature and pressure increase, both metasediments and metabasalts in the slab release fluid: metamorphic chemical reactions, determined by the *PT* conditions and the chemistry of a reservoir, destroy hydrous minerals one after another, releasing water from their mineral lattice to produce parageneses that are stable at enhanced *P* and *T*.

Three major regimes of metamorphic devolatilization may be readily distinguished (Fig. 25.6, Schmidt and Poli, 2003): the low-grade stage, the stage of eclogite facies metamorphism and the melting stage. Here we consider the first of these, which occurs below $\sim 600\ ^{\circ}C$ and ~ 2.4 GPa. Dehydration is caused by the breakdown of water-bearing minerals such as chlorites, amphiboles etc. Altered MORBs, gabbros and peridotites are the most important sources of aqueous fluid at this stage. Because of the short duration of the fractionation and transfer processes (Section 25.3) and the relatively low temperatures, diffusion and trace-element exchange between the fluids and minerals are not important and the mobilized elements are generally those hosted in minerals that have broken down (Schmidt and Poli, 2003).

In the course of slab devolatilization, amphiboles play a role as they are important carriers of both volatile and trace elements (e.g. Rb, Cs, water-sensitive B and

water-insensitive Be). Minerals of this group are abundant in the basaltic rocks and gabbros that were hydrated in the ocean floor. Amphiboles are progressively modified with increasing *PT* in the depth range ~ 40 to ~ 70 km; they release hydrous fluid and ultimately break down to form omphacite and garnet (see below). The residual low-grade metamorphic rocks and the complementary fluids released at fore-arcs both indicate the efficient transfer of Rb, Cs, B, as well as As, Sb, Pb and some other elements, during "early" subduction. For example, B begins to leave the slab at relatively low temperatures, in contrast with Be, and the B/Be ratios in fore-arc materials are generally high. This ratio decreases with increasing metamorphic grade, and in back-arc magmas it is indistinguishable from that observed in MORB/OIB magmas, as illustrated by Fig. 25.3.

High-PT metamorphism, low dehydration rates and little fluid production

Above 2.5 GPa (from ~ 2.5 to ~ 4 GPa, i.e. 80–120 km depth, 500–800 °C) the subducting slab contains less than 2 wt % water. At this stage, metamorphosed sediments (metapelites) are an important source of hydrous fluids; among the mineral phases, lawsonite and phengite are of prime importance. Lawsonite contains up to 12 wt % of water and may host about half the total water present in the slab crustal segment. Phengite, mainly abundant in sediments, is formed from clay minerals during low-grade metamorphism in early subduction. It is the principal host of K, Ba, Rb, and some other trace elements (e.g. Be, including ^{10}Be). The breakdown of phengite at high-*PT* conditions liberates Be with high ^{10}Be/^{9}Be ratios, whereas B has already been washed out; this results in the low B/Be ratio of deep back-arc fluids and melts (Morris *et al.*, 2002).

During this second stage continuous reactions dominate and therefore fluid and accompanying trace elements are released from the slab continuously as well, but it is possible that the two principal minerals partially survive down to the melting regime (see below). Fluid-insensitive elements such as Th and the REEs show no evidence of significant losses: 80%–90% of their initial abundance survives this stage.

This important feature of slab development, i.e. the extraction and removal of given elements owing to the breakdown of the host mineral, provides an explanation for the great variability of the respective trace elements in arc magmas in space and time: the same element can be liberated from minerals in the slab at different *PT* conditions and be transferred by different mobile-phase fluxes.

At depths of ~ 100 km and temperatures of ~ 700 °C the former basaltic part of the oceanic crust loses all hydrous phases and turns into a dry eclogite, a metamorphic rock with major-element abundances similar to MORBs but including high-*PT* dense minerals such as garnet, omphacitic clinopyroxene, titanite and rutile

(Table 25.1). In eclogites that have been brought to the surface ("exhumed") by tectonic processes or by deep-sourced volcanic rocks, specific "barometer" minerals, e.g. coesite (see above) and microdiamond, which are stable only at very great depths (> 90 km and > 120 km respectively), are sometimes found as inclusions in major minerals that are stable over a wider pressure interval, such as garnet. The host mineral serves as a high-pressure vessel, allowing the high-pressure mineral inclusions to survive exhumation and provide direct evidence of the conditions reached in eclogite metamorphism (e.g. Stachel *et al.*, 2004).

Eclogites show strong depletions of K, Rb and Ba relative to Th when compared with unaltered and altered MORBs or ocean-island basalts; however, the largest fraction of these elements appears to be lost by temperatures ~ 600 °C or less. Fluid-immobile Th, Ti, Zr and the REEs show no evidence of significant losses (any such losses are $< 10\%$–20%). These data indicate that Th in typical arc magmas was mainly transferred from sediments (Becker *et al.*, 2000). Under certain circumstances, open-system behaviour may have occurred so that even the REEs fractionated, e.g. through the breakdown of some LREE-rich accessory minerals (Bernard-Griffiths *et al.*, 1991).

25.6 Melting of subducting slab: supercritical liquids

In cases where arc magmas have high abundances of slab-related trace elements considered as fluid-immobile (at moderate *PT* conditions), such as Th and the REEs, and enhanced Th/La ratios identical to those in the subducting sediment column, this points to the mobilization and transfer of the elements into the mantle wedge by partial melts or supercritical fluids ($800\ ^\circ\text{C} < T < 1200\ ^\circ\text{C}$ and $4\ \text{GPa} < P < 6\ \text{GPa}$). In some arc magmas, however, high [Th] concentrations, ~ 1 ppm, are accompanied by low $^{87}Sr/^{86}Sr$ and high $^{143}Nd/^{144}Nd$ ratios (< 0.7030 and > 0.5130, respectively), which are characteristic of MORBs rather than sediments, implying the partial melting of subducting basaltic crust. If a hydrous fluid is present, the melting temperatures for metapelites and metabasalts are similar. At the above *PT* conditions both fluid-saturated, or "flush", melting and solid–fluid interactions significantly increase the mobilities for most elements, even those that are fluid-insensitive at moderate conditions (including Th and the LREEs). Therefore a large fraction of Be, B, Rb, Cs, Sr, Ba, the LREEs, Pb, Th and U could be removed effectively from the metasediments and metabasalts by fluid-saturated melts and/or supercritical fluids (Kelemen *et al.*, 2003; Schmidt *et al.*, 2004; Kessel *et al.*, 2005).

Such slab processing is made possible by the thermal gradients that are established in slabs as they sink into a hotter mantle: the middle part is heated up less fast than the boundaries. Modelling predicts up to 400 °C differences in temperature

between the slab–mantle-wedge interface and the base of the oceanic basaltic crust (Peacock *et al.*, 2005). Thus fluids arising from dehydration within the relatively cold segment in the middle of the slab can develop the hotter domain close to the upper boundary. In some cases the residual eclogitic assemblages indicate the involvement of a large amount of fluid phase in their development (John *et al.*, 2004). Under enhanced P and T, the processing of outer segments of the slab by these deeply sourced fluids could initiate fluid-saturated or flush melting or generate supercritical fluids. In most cases the ratios of incompatible trace elements in the resulting arc melts (such as Th/La in the above example) are similar to those inferred for the basaltic or sedimentary sources, which points to large melt/solid and fluid/solid ratios.

At higher pressures ($\sim$ 6.5 GPa), melting in the strict sense does not take place. Instead, the amount of H_2O still present in the slab is apparently sufficient to dissolve phengite entirely, near 1050 °C. Extraction of these supercritical solute-rich melts, which could contain about 30%–40% H_2O, leaves an anhydrous garnet + clinopyroxene $\pm$ coesite $\pm$ kyanite $\pm$ rutile residue (Schmidt *et al.*, 2004). This fluid–melt phase transfers almost all K (and most B, Be, Rb, Ba and other phengite-hosted trace elements) into the mantle wedge without substantial fractionation. Thus the concepts of dehydration and partial melting are no longer separate: solid assemblages progressively dissolve in a non-solid phase that is initially volatile-rich and becomes more like a silicate melt with increasing temperature.

25.7 Melting in the mantle wedge

Compared with the relatively simple spectacle of MORB magmatism, the melting drama in arc tectonic settings is highly complicated. Partial melting, melt segregation and uplift in the mantle wedges are controlled by a number of different processes and parameters: the fluid and melt transfer from the subducting slab (in turn depending on slab composition, age, subduction velocity and angle); the composition of a given wedge and its dynamics and thermal structure; the thickness and composition of the overlying continental plate; the crystallization differentiation in crustal magma chambers. Because of these complexities a standard model of melt generation beneath a "standard arc" has not yet been put forward. The great variation in the data probably reflects the fact that processes are affected by many parameters that are independent of each other. Sets of observations and related models are reviewed by Ulmer (2001), Turner *et al.* (2003), Schmidt and Poli (2003) and Kelemen *et al.* (2003). Below we recall some principal observations (mainly already discussed in this chapter) and qualitatively outline major points of a scenario for the generation of arc magmas that take these observations into account. Radioactive isotope tracers are particularly important in this.

Three different processes are generally recorded by arc magmas: (1) the transfer of a mobile phase that originated in the slab under high-*PT* conditions; (2) the addition of "normal" fluids, derived from the slab at moderate *PT*, to an arc-melt source within the mantle wedge; (3) the partial melting of this metasomatized hybrid source. We now discuss these in turn.

(1) In arc magmas, Th and ^{10}Be are the best tracers of high-temperature fluids from sediments (Plank and Langmuir, 1993). Also, Ce anomalies inherited from the sedimentary environment indicate the addition of slab melts (or supercritical fluids, Kessel *et al.*, 2005) into the arc magma source (Section 25.6). In the course of slab dehydration and melting processes, the U/Th ratio is expected to be fractionated, causing a deviation of the (^{230}Th/^{234}U) activity ratios from secular equilibrium. However, in contrast with this expectation, the values of these activity ratios in arc volcanics are commonly $\sim$ 0.95, deviating only slightly from equilibrium. The time scale for ^{230}Th equilibration is relatively long, $\sim$ 300 kyr (Elliott *et al.*, 1997; Turner *et al.*, 2003).

(2) The addition of "normal" slab-derived fluids to arc magma sources is clearly shown by e.g. the correlations seen in Figs. 25.3–25.5. The injection of a slab-derived fluid with a high ^{238}U/^{232}Th ratio into an arc magma source and the subsequent ingrowth of ^{230}Th should generate an inclined array in the ^{230}Th / ^{232}Th versus ^{238}U / ^{232}Th isotope plot, with a slope < 1. This is indeed observed in several arcs. The chronological interpretation of such arrays gives ingrowth time scales of $\sim$ 30 kyr or longer (Elliott *et al.*, 1997; Turner *et al.*, 2003). However, the departure of the (^{226}Ra / ^{230}Th) ratio from equilibrium (Fig. 25.5) dictates much shorter time intervals, less than 10 kyr, between the separation of a fluid (the carrier of hydrophilic ^{226}Ra and ^{238}U) from the downgoing slab and the eruption of arc lavas. A way to resolve this contradiction between robust data is to propose that the subduction-related modification of the mantle wedge, adding slab-derived elements such as Th, Sr and Be and various intermediate decay products of the U chains, happened in diachronous stages (Morris and Rayan, 2003).

(3) The value of (^{231}Pa/^{235}U) > 1 observed in arc volcanics also departs from equilibrium but cannot be explained by fluid addition to an arc magma source: Pa is not a hydrophilic element and the addition of U would have yielded (^{231}Pa/^{235}U) < 1 instead. Protactinium is an extremely incompatible element, with D(solid/melt) $\sim 10^{-5}$. Therefore an increase in the activity ratio could result from partial melting and melt–solid fractionation. This indicates a small melt fraction, $\sim$ 0.001, during arc magma generation as U is also a highly incompatible element (Bourdon *et al.*, 2003; Turner *et al.*, 2003).

Traditionally, arc melting is considered to result chiefly from the lowering of the solidus of rocks in the mantle wedge by the introduction of hydrous fluids. This would not be readily compatible, however, with the extremely small partial-melt fraction reflected by (3) above. A scenario envisaging (i) slab melting and melt migration into a slowly upwelling hot peridotitic diapir, within the mantle wedge at some distance above the subducting slab, (ii) further metasomatic development of the diapir with slab-derived fluids and (iii) its decompression fractional

melting in the upper region of the wedge has therefore been suggested (see Conder *et al.*, 2002; Kohut *et al.*, 2006, and references therein). As the rocks in a diapir approach the depth of slab melting ($\sim$ 150 to 200 km), enriched hydrous melts or/and supercritical liquids from the slab metasomatize rock units in the wedge, thus increasing [Th] and fractionating the U/Th and (^{230}Th/^{238}U) ratios. As ascent proceeds, ^{230}Th approaches secular equilibrium (Elliott *et al.*, 1997). The rate of ascent estimated from the equilibration time scale is of order $\sim$ 10 cm yr^{-1}.

At somewhat lower depths, slab-derived fluids may interact with the diapir, yielding an enrichment in fluid-sensitive elements. The observed chemistry of arc rocks belonging to the calc-alkaline to tholeiitic compositions requires a small amount of water in the mantle source, of order 0.1%–0.5% (Ulmer, 2001). The arc lava O-isotope inventory also suggests a low bulk contribution of slab derivatives (melts, fluids), generally $<$ 1% (Eiler *et al.*, 2000). To reconcile the time scales dictated by ^{230}Th and ^{226}Ra disequilibrium, two or more subsequent fluid-injection events are postulated (Bourdon *et al.*, 2003).

As ascending material reaches the solidus, the partial melting of metasomatized peridotite starts. Initially the melt fraction remains small (and increases slowly) because of the postulated slow uplift of the diapir and the higher viscosity of hybrid melts compared with MORBs; the small melt fractions lead to preferential partitioning of Pa into the melt compared with U, and the time scale for ^{231}Pa equilibration is a few tens of kyr (Bourdon *et al.*, 2003). Through mixing, the aggregate melt fraction could become quite large, approaching the value $\sim$ 10% generally accepted from major- and moderately-incompatible-element data.

The data indicate a close temporal and spatial link between the final addition(s) of ^{226}Ra-bearing fluid(s) and the segregation and removal of magmas with fast ascent velocities, $\sim$10 to 100 m yr^{-1} (Turner *et al.*, 2000, 2003).

Generally melting and melt segregation proceeds at depth and temperature intervals within 120 to 30 km and 1450 to 1200 °C, respectively (Conder *et al.*, 2002; Kohut *et al.*, 2006). For example, in the case of the Japan arcs the seismological data indicate melt generation at 90 km depth (or somewhat below this depth if initially small melt fractions are postulated), efficient melt segregation and transfer through dykes and cracks at 65 km depth and melt accumulation below the base of the crust (Nakajima *et al.*, 2005).

25.8 Summary

The sources of arc volcanics could include: (1) fluids derived by the dehydration of subducting metabasalt and/or metasediment, (2) magmas (and/or supercritical fluids) derived from subducting metabasalt and/or metasediment, (3) fertile mantle peridotite similar to the MORB source, (4) mantle peridotite depleted by magma

extraction beneath a mid-ocean ridge and/or a back-arc basin and (5) an enriched mantle similar to the source of OIBs (Kelemen *et al.*, 2003). The primitive parental magmas are generally developed further by crystallization differentiation within or below the overlying crustal plate. All these complexities lead to highly variable compositions and volumes of arc magmas.

The fundamental difference between ridge and arc magmatism is in that, in arcs, fluxes of a mobile phase from the subducting slab metasomatize the overlying mantle wedge and thus modify its composition and the conditions of its partial melting (Fig. 25.6). Even though the bulk contribution of this phase is generally small, $\sim 1\%$ or less (Eiler *et al.*, 2000), the mobile phase delivers most fluid-soluble elements, trace-incompatible elements and those that are specifically enriched in sediments in arc-melt sources within the mantle wedge.

Details of the complicated melting mechanisms in the mantle wedge are not well understood yet. Some data imply the decompressional fractional melting of metasomatized initially depleted peridotite. However, an enhanced contribution of a slab-derived mobile phase could initiate other mechanisms, such as flush melting.

From the trace-element evidence, both primitive andesites and basalts originate from partial melting within the mantle wedge: the difference between the rocks arises from different amounts of slab derivatives. The production of andesites requires a higher contribution of slab components than arc basalts. The andesite major-element chemistry results from the presence of a hydrous mobile phase rich in K_2O (from the melting of phengite), and Na_2O, which enables a high SiO_2 (andesitic) melt to exist in equilibrium with mantle olivine at moderate pressures, ~ 1 GPa. Further, the solidus temperature becomes progressively lower as the H_2O content increases. The fact that andesites are frequently observed above "young" slowly sinking plates can thus be understood: in such a case the slab is hotter at a given pressure than a cold fast-sinking slab, and a higher production of slab-related mobile phase is expected. Arc basalts are produced in a similar setting but with smaller mobile-phase input: the lower abundances of specific slab-derived elements in these rocks are clearly seen in Fig. 25.1.

In general, the contribution of fluids and melts from the downgoing slab into the overlying mantle wedge allows the major-element and trace-element chemistry of the primitive arc rocks to be explained. Large-ion lithophile elements (LILEs), specifically sediment-related elements such as Th, Ba, Pb and the LREEs come from the slab and introduce the fingerprints of arc-related magmas such as high La/Nb, Sr/Nd and Pb/La ratios. A substantial portion of the middle and heavy REEs and the HFSEs appears to be mainly derived from the mantle wedge. An underabundance of HREEs, with their characteristic concave-up abundance-pattern shape, is due to the partitioning of the HREEs in amphibole. Garnet may play a part, reducing the HREE contents further.

The specific geochemical signatures of slab dehydration and magmatic processes in both slab and wedge, as outlined above, are imprinted in the trace-element concentrations and ratios of the arc volcanics and are also generally seen in rocks of the continental crust. In that context they are regarded as reliable indicators of the major role of subduction-related processes in the generation of the continental crust, which is discussed in Chapter 26.

26

Composition of the continental crust: magmatic, metamorphic and sedimentary processes

26.1 Introduction: the continental crust

If we look, as in Section 23.1, from a satellite at our blue planet, we see that its surface elevation is bimodal: about 40% (or 210×10^6 km^2) is on average ~ 5 km higher than the rest. Typically the elevated areas are large, often many hundreds of kilometres across, and are termed continents. A major part of the continents, $\sim$ 70%, rises above the ocean water level, whereas $\sim$ 30% is shallowly submerged. A remote observer would be unable to see the deep structure of the continents, but several physical methods help. In particular, measurements of travel times of seismic waves reveal a sharp downward increase in seismic wave velocity, known as the Mohorovičić discontinuity, at an average depth of $\sim$ 40 km underneath the continents. The layer between this boundary and the surface is termed the continental crust, and the above parameters show that the continental crust is a small reservoir, $\sim$ 0.8% of the Earth's volume. Assuming that both continental and oceanic lithospheres are in isostatic equilibrium with the underlying viscous mantle (DMM) then it follows that the crust (CCR) should consist of a relatively light material. A simple estimate of the density can be made using the $\sim$ 40 km depth of the Mohorovičić discontinuity, the $\sim$ 5 km surface elevation difference and the ocean-water column, which is on average 4 km thick:

$$40\ \rho_{\mathrm{CCR}} = 35\ \rho_{(\mathrm{DMM+OC})} + 4.$$

If the average density of the uppermost mantle + oceanic crust is assumed to be 3.2 g cm^{-3}, an average continental crust density of 2.9 g cm^{-3} results, which is only slightly above the measured densities of the rock types making up the continental crust (with average density 2.8 g cm^{-3}; Rudnick and Fountain, 1995).

Owing to this lower density, the subduction of large blocks of continental crust into the mantle is impossible. Further, older continental masses in particular are underlain by an up to 250-km-thick subcontinental lithospheric mantle keel

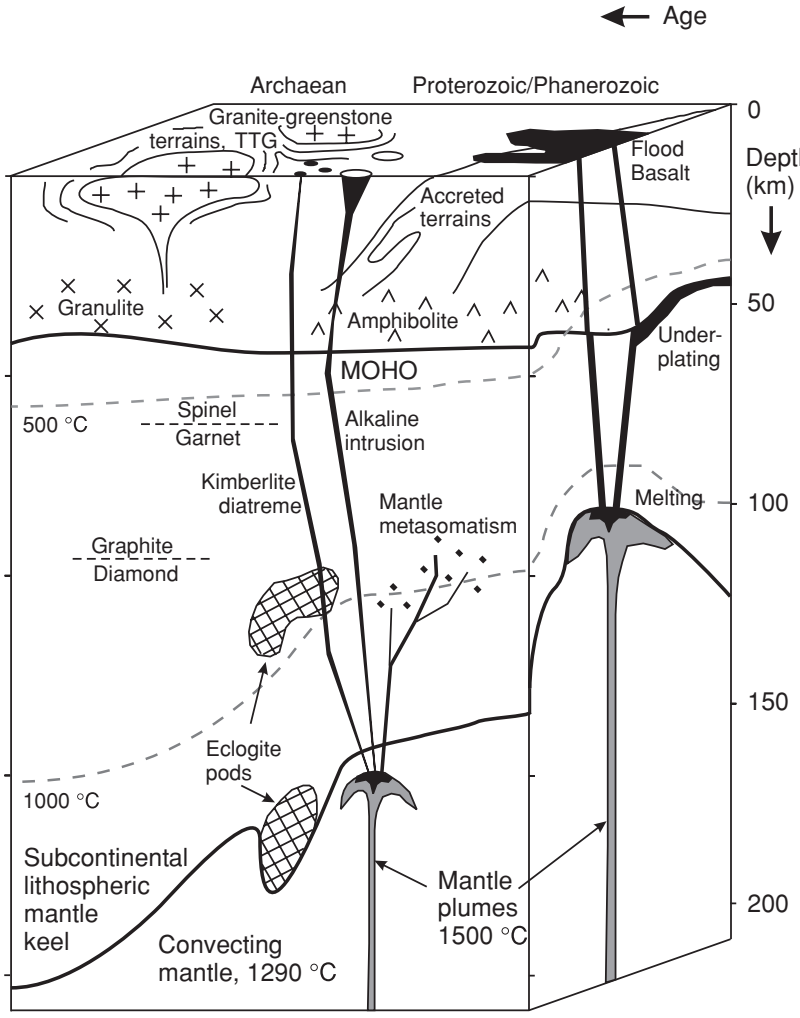

Fig. 26.1 The continental crust, the bottom of which is defined by the moho (upper solid line), the subcontinental lithospheric mantle keel (between the upper and lower solid lines) and the underlying convecting mantle. The character of the Archaean and Proterozoic–Phanerozoic crustal architecture and the thickness of the subcontinental lithosphere are strongly generalized, as are potential sources of continental magmatism. The spinel–garnet and graphite–diamond phase boundaries are approximate, as they depend on the geothermal gradient.

(Fig. 26.1), which is less hot than the convecting mantle and therefore more rigid, and this further stabilizes the continents (Carlson *et al.*, 2005). For these reasons the continental crust has preserved a varied and detailed record of the geological past of the planet. This is one reason why the continental crust is so important for understanding the evolution of the silicate Earth. Not less important is that the crust,

even though small, is the major store of lithophile incompatible elements, which have been transferred from the mantle and become concentrated in it as it formed over geological history (Gast, 1968). These include the heat-producing elements U, Th and K; their concentration in a "surface" reservoir changes the dynamics of the planet. Also, the Earth's crust is our home, which we must understand and protect.

The continental crust is a highly heterogeneous reservoir, not only in terms of its age but also its chemistry. In the latter sense it appears to have a broadly layered structure and can be subdivided into an upper and a lower crust, discussed in Sections 26.2–26.4. The complex processes that have caused the great heterogeneity of the continental crust are summarized in Section 26.7.

26.2 The upper continental crust: magmatic rocks

The lateral heterogeneity of the upper crust can be seen from space by the naked eye. The rocks exposed at the Earth surface may be readily classified into four major types.

(1) *Magmatic rocks that formed via partial melting of mantle rocks or oceanic crust*. These feed the continental crust: the arc-like volcanic chains along the convergent margins of the continents, such as those making up the circum-Pacific belt, bear witness to the major contribution of subduction-zone magmatism in the generation of the continental crust, at least at the present time (Fig. 23.1, Chapter 25). Volcanic rocks represent only a small portion of the magma produced at continental arcs. Much of it crystallizes at various levels in the crust, forming so-called plutonic igneous rocks, ranging in composition from gabbros to granites (i.e. with SiO_2 contents from 55% to 75%). These are visible in deeply incised valleys and uplifted, eroded, areas, for instance in the southern Andes. Away from the young accreting margins, erosion has removed the volcanic arc rocks and exposed the underlying plutonic rocks. Granites, granodiorites and tonalites, often summarized under the term granitoids, make up by far the most abundant single constituent of the upper crust, $\sim$ 50% (Wedepohl, 1995). Although, being in the interior of continents, they are not geographically associated with modern arcs, they mostly show all the geochemical characteristics of arc magmatism and thus represent products of past subduction. Their common mineralogical features are large contents of variably Ca-, Na- and K-rich feldspars and the presence of quartz and of micas and/or amphiboles hosting the relatively small amounts of Fe and Mg. Compared with the DMM, granitoids show very high concentrations of incompatible trace elements, e.g. Rb, Th, U and K.

(2) *Magmatic rocks that are not related to subduction zones, past or present*. Among these are basalts, which can constitute large igneous provinces of

continental crust (see Coffin and Eldholm, 1994, and Jerram and Widdowson, 2005, for comprehensive reviews). Further, deeper-level equivalents of such provinces are seen, mainly in older continental regions. These are huge intrusions of (mainly) primarily basaltic magma that underwent progressive differentiation by fractional crystallization, leading to layered complexes with peridotites at the base and feldspar-rich gabbros at the top, often rhythmically repeated. Many such complexes are resources for Cr and for Pt-group elements.

The non-subduction-zone magmatic rocks also include granitoids, some of which appear to be the products of remelting continental crust at depth. Others, particularly alkali-rich granites and syenites (silica-poor alkali-rich rocks) are associated with small amounts of melting at the top of mantle plumes. Some rare volcanic rocks, such as lamprophyres and nepheline basalts, are in many cases associated with these.

Other very rare rocks, carbonatites and kimberlites, probably belong to the same general geotectonic setting. Carbonatites are magmatic carbonate rocks, and their enrichment in incompatible elements is so huge that they can constitute valuable deposits of P and various metals, including the REEs. Kimberlites are strongly hydrous, mixed carbon- and silica-rich subvolcanic rocks mostly occurring in explosively formed channels or pipes. They are in many cases mined for diamonds, and this attests to rapid extrusion from a depth in excess of 120 km. These rocks carry important records of their mantle protolith compositions and the fractionating mechanisms that operate in the subcontinental mantle lithosphere and the underlying convecting mantle (Carlson *et al.*, 2005). Mantle rocks themselves are also seen in the upper crust, occurring in mountain belts as massifs uplifted by tectonic processes. The most spectacular of these are the ophiolite complexes, which may contain a complete oceanic plate section, from peridotitic upper mantle to basaltic oceanic crust, e.g. in Cyprus and Oman. These have yielded invaluable information on the structure and formation of the oceanic crust (Section 24.3) as well as on the nature of the upper mantle. The other mantle rocks found in the upper crust are fragments entrained by ascending magmas, which are known as xenoliths. These are a direct source of data relating to the composition of the subcontinental lithospheric mantle and the lower crust (Section 26.4).

(3) *Sedimentary rocks* contribute $\sim$ 15% to the continental rock budget (Wedepohl, 1995; Veizer and Mackenzie, 2003). These consist of matter settled after transport by water or, more rarely, by wind and solidified by a process called diagenesis, whereby, for instance, sand grains become cemented together to form a sandstone or soft mud hardens to mudstones and shales. Their compositions and structures show enormous diversity. For example, the compositions of so-called detrital sediments (consisting of transported grains) are similar to those of the eroded precursor bedrocks whereas chemical sediments, e.g. carbonates or evaporites, reflect their precursor natural solutes. Organogenic sediments have in part inherited the

composition of organisms, e.g. plants (Morse, 2003). Sediments deposited on continental crust bear witness to periods of submergence; these rocks mainly record shallow-water environments and may be rich in fossil life as a result. These fossils and their depositional environment provided the main record of Earth history in classical geological terms. However, sediment material derived from the continents is also deposited in the seas and oceans. This deposition is the major process whereby the upper crust is gradually destroyed and the ocean water modified. Finally, sediment subduction affects the composition of the mantle (Chapter 27).

(4) The next major group comprises *crustal metamorphic rocks*, gneisses, schists etc., which contribute $\sim 30\%$ to the upper crustal budget. These rocks result from mineralogical changes in response to increases in P and T, usually associated with mountain-building episodes.

The age range of upper crustal rocks and/or minerals covers almost the whole of Earth history, down to 4.4-Gyr-old detrital zircons (Wilde *et al.*, 2001) and 3.79-Gyr-old metamorphic sediments and volcanics (Nutman *et al.*, 1997; Bolhar *et al.*, 2004, 2005). Crustal domains of different ages have preserved a record of changing conditions of crustal growth, sedimentation and recycling; they also bear evidence on mantle and atmospheric compositions through time and are therefore of prime importance in reconstructing the global evolution of the Earth (Chapters 27 and 28).

Granitoids: major constituents of the upper crust

Granitoids and their deformed equivalents (gneisses) represent the end product of the magmatic evolution of terrestrial silicate matter. Even though these rocks are accessible at the Earth's surface and their investigation has a very long history, many questions related to their source materials and formation mechanisms are still open (Clarke, 1996). This is mainly due to the great diversity of their protoliths, their highly variable *PT-t* conditions of formation and the fact that granitoids can be formed by many different processes (see Barbarin, 1999 for a discussion of granite classification problems).

The simplest compositional classification, the alumina saturation index *ASI* (Table 26.1), allows three major granite types to be distinguished. These generally occur in specific tectonic settings: peraluminous granites are typical for orogenic belts formed by the collision of continental crustal plates, in which the lower crust is heated and partially melted; metaluminous granites are often associated with subduction zones (calc-alkaline granitoids) and/or are related to the magmatic underplating, thinning and rifting of the pre-existing crust; peralkaline granites are mostly extreme fractionation products of magmas that originated from the mantle. An attempt at a comprehensive treatment of the complicated and controversial problems of granitoid formation is beyond the scope of this book, and in the

Table 26.1 *Classification of granitic rocks*[a] *according to the alumina saturation index: molar ratio* $ASI = [Al_2O_3/(CaO + Na_2O + K_2O)]$

Category	Chemical definition	Diagnostic mineralogy
peraluminous	$ASI > 1.0$	aluminous biotite ± muscovite, cordierite, garnet, Al-silicate
metaluminous	$ASI < 1$	subaluminous biotite ± hornblende, clinopyroxene, accessory allanite, titanite, epidote
peralkaline	$ASI \ll 1$ Al/(Na + K) < 1	sodic pyroxene (aegirine) or amphibole

[a] After Kemp and Hawkesworth (2003), © Elsevier Science 2003, reproduced by permission. See also the discussion of the granite classification problem by Barbarin (1999) and related references therein.

subsections below we merely present several examples that illustrate how varied the processes and geotectonic settings can be in which granitoids are formed.

Peraluminous granitoids: high Himalaya

High Himalayan peraluminous granites constitute ∼ 15 plutons and a great number of dykes and veins that intruded (∼ 20 Myr ago) into the ∼ 1500-km-long sublatitude zone of gneisses and sedimentary rocks that form the high Himalaya. The exposed area of each pluton varies from several hundreds to ∼ 1000 km^2. The rocks are generally fine-grained and fairly homogeneous in their major-element compositions. The rock-forming minerals are quartz, K-feldspar, plagioclase, muscovite and biotite; the last is either intergrown with muscovite or is replaced by tourmaline, giving rise to two subgroups, two-mica and tourmaline granites. The accessory minerals are apatite, zircon, ore minerals, monazite, uraninite and, in rare cases, fluorite (Le Fort *et al.*, 1987).

The two-mica leucogranites of the Makalu pluton, situated 20 km south-east of Mt Everest, are characterized by $ASI \sim 1.2 \pm 0.1$ and a *mg*# value ∼ 0.24. The latter is well below the value typical of the bulk continental crust (compare Tables 26.2 and 26.3). The REE abundances are low, the patterns are fractionated with strong HREE depletion and there is a consistent negative Eu anomaly (Eu/Eu* = 0.17–0.21, Fig. 26.2). The concentrations of specific incompatible trace elements such as Li, Rb, Pb and U are high, greatly in excess of the mean crustal values, whereas Sr is less abundant. Extremely radiogenic initial Sr-isotope compositions, with $^{87}Sr/^{86}Sr \sim 0.75$ (to be compared with $^{87}Sr/^{86}Sr \sim 0.716$ for the mean upper crust), point to a crustal protolith with a high time-integrated Rb/Sr ratio, typical of mica schists. A low $\varepsilon_{143,INI}$ value (–15 ± 2) indicates that the protolith had an average crustal residence time of at least ∼ 1 Gyr.

Table 26.2 *Abundances of major (wt %) and trace (ppm) elements in granitoids*

Element	HLG[a]	FRG(W)[b]	KAG[c]	CAR[d]	TTG[e]
SiO_2	73.5	69.9	75.94	64.6	69.7
TiO_2	0.12	0.42	0.23	0.65	0.34
Al_2O_3	14.8	13.4	10.76	15.9	15.5
FeO_T	1.13	3.80	2.8	4.27	2.81
MnO	0.03	0.06	0.044	0.08	0.05
MgO	0.20	0.35	0.076	2.15	1.18
CaO	0.78	2.16	0.39	5.10	3.19
Na_2O	3.82	3.09	3.56	3.62	4.88
K_2O	4.54	5.46	4.97	1.95	1.76
Total	99.0	98.7	98.77	98.3	99.5
ASI	1.18	0.90	0.90	0.92	0.99
mg#	0.24	0.16	0.046	0.47	0.43
Li	103	n.d.[f]	72	n.d.	22.3
Be	11.5	5.00	n.d.	n.d.	2.32
B	140	n.d.	10.9	n.d.	n.d.
F	5090	2400	1240	n.d.	n.d.
Sc	2.50	8.00	3.1	14.0	4.70
V	11.1	n.d.	19	85	35
Cr	25.9	n.d.	109	47	29
Co	1.50	n.d.	3.6	n.d.	23.6
Ni	5.73	n.d.	11.3	13.0	14.0
Cu	14.1	n.d.	16.6	10.0	19.5
Zn	73.4	125	88.2	76.0	70.9
Rb	260	271	295	60.0	55.0
Sr	112	155	40	375	454
Y	11.1	63.0	71	19.0	7.50
Zr	50.0	459	815	139	152
Nb	10.5	26.4	47	6.70	6.40
Ba	257	1140	150	641	690
La	13.9	95.9	134	16.0	32.0
Ce	29.2	182	263	35.0	56.0
Pr	4.81	21.5	n.d.	n.d.	n.d.
Nd	12.8	80.6	102	14.0	21.4
Sm	3.42	14.6	18	n.d.	3.30
Eu	0.69	2.56	1.11	n.d.	0.92
Gd	3.69	12.6	19.1	n.d.	2.20
Tb	0.57	2.14	2.36	n.d.	0.31
Dy	3.06	12.70	19.6	n.d.	1.16
Ho	0.55	2.67	n.d.	n.d.	0.39
Er	1.17	7.26	12.7	n.d.	0.59
Tm	0.16	1.07	n.d.	n.d.	0.12
Yb	1.20	7.31	10.06	n.d.	0.55
Lu	0.17	1.05	1.39	n.d.	0.12
Hf	n.d.	12.7	18.8	n.d.	4.50

Table 26.2 *(cont.)*

Element	HLG[a]	FRG(W)[b]	KAG[c]	CAR[d]	TTG[e]
Pb	75.6	38.0	40	10.0	13.28
Th	14.2	24.7	30	7.20	6.90
U	13.9	8.08	5.5	1.50	1.60

[a] HLG, peraluminous Himalayan leucogranites, from Visona and Lombardo (2002).
[b] FRG(W), metaluminous Finnish Rapakivi granite (Wiborgite), from Haapala *et al.* (2005).
[c] KAG, Kola alkaline granites, from Vetrin *et al.* (1999).
[d] CAR, continental arc granitic rocks, from Kemp and Hawkesworth (2003).
[e] TTG, average for tonalite–trondhjemite–granodiorite rocks (a suite typical of > 2.5-Gyr-old crust provinces), from Kemp and Hawkesworth (2003) and Kamber *et al.* (2002).
[f] Not determined.

Table 26.3 *Chemical composition of the continental crust: major (wt %) and trace (ppm) elements. After Rudnick and Gao (2003), © Elsevier Science 2003, reproduced by permission*

Element	Upper crust	Middle crust	Lower crust	Total crust
SiO_2	66.6	63.5	53.4	60.6
TiO_2	0.64	0.69	0.82	0.72
Al_2O_3	15.4	15	16.9	15.9
FeO_T	5.04	6.02	8.57	6.71
MnO	0.1	0.1	0.1	0.1
MgO	2.48	3.59	7.24	4.66
CaO	3.59	5.25	9.59	6.41
Na_2O	3.27	3.39	2.65	3.07
K_2O	2.8	2.3	0.61	1.81
P_2O_5	0.15	0.15	0.1	0.13
Sum	100.05	100	100	100.12
mg#	0.47	0.52	0.60	0.55
Li	24	12	13	16
Be	2.1	2.3	1.4	1.9
B	17	17	2	11
N	83	n.d.	34	56
F	557	524	570	553
S	621	249	345	404
Cl	294	182	250	244
Sc	14	19	31	21.9
V	97	107	196	138
Cr	92	76	215	135
Co	17.3	22	38	26.6
Ni	47	33.5	88	59
Cu	28	26	26	27
Zn	67	69.5	78	72
Ga	17.5	17.5	13	16
Ge	1.4	1.1	1.3	1.3
As	4.8	3.1	0.2	2.5

(*cont.*)

Table 26.3 *(cont.)*

Element	Upper crust	Middle crust	Lower crust	Total crust
Se	0.09	0.064	0.2	0.13
Br	1.6	n.d.	0.3	0.88
Rb	82	65	11	49
Sr	320	282	348	320
Y	21	20	16	19
Zr	193	149	68	132
Nb	12	10	5	8
Mo	1.1	0.6	0.6	0.8
Ru	0.34	n.d.	0.75	0.57
Pd	0.52	0.76	2.8	1.5
Ag	53	48	65	56
Cd	0.09	0.061	0.1	0.08
In	0.056	n.d.	0.05	0.052
Sn	2.1	1.3	1.7	1.7
Sb	0.4	0.28	0.1	0.2
I	1.4	n.d.	0.14	0.71
Cs	4.9	2.2	0.3	2
Ba	628	532	259	456
La	31	24	8	20
Ce	63	53	20	43
Pr	7.1	5.8	2.4	4.9
Nd	27	25	11	20
Sm	4.7	4.6	2.8	3.9
Eu	1	1.4	1.1	1.1
Gd	4	4	3.1	3.7
Tb	0.7	0.7	0.48	0.6
Dy	3.9	3.8	3.1	3.6
Ho	0.83	0.82	0.68	0.77
Er	2.3	2.3	1.9	2.1
Tm	0.3	0.32	0.24	0.28
Yb	2	2.2	1.5	1.9
Lu	0.31	0.4	0.25	0.3
Hf	5.3	4.4	1.9	3.7
Ta	0.9	0.6	0.6	0.7
W	1.9	0.6	0.6	1
Re	0.198	n.d.	0.18	0.188
Os	0.031	n.d.	0.05	0.041
Ir	0.022	n.d.	0.05	0.037
Pt	0.5	0.85	2.7	1.5
Au	1.5	0.66	1.6	1.3
Hg	0.05	0.0079	0.014	0.03
Tl	0.9	0.27	0.32	0.5
Pb	17	15.2	4	11
Bi	0.16	0.17	0.2	0.18
Th	10.5	6.5	1.2	5.6
U	2.7	1.3	0.2	1.3

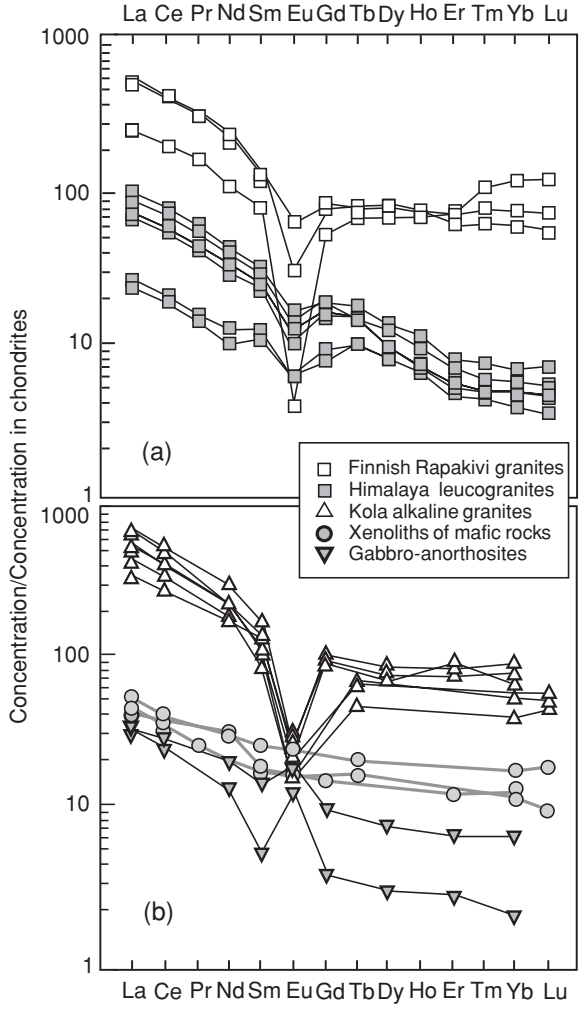

Fig. 26.2 Rare earth elements in granitic and associated rocks. (a) The Rapakivi granites show much higher abundances of REEs, flat HREE patterns and deeper Eu anomalies than the Himalayan leucogranites. After Haapala *et al.* (2005) and Visona and Lombardo (2002). (b) Note the complementary REE patterns in the Kola alkaline granites and associated anorthosites and compare these with the basalt-like patterns of the mafic xenoliths. According to this signature the latter could represent a protolith that partially melted to form anorthositic rocks (cumulates) and granites (late-crystallized melts). After Vetrin *et al.* (1999) and Balashov (2004).

From these diverse geochemical data, the most plausible source rocks for these granites are the quartz-rich metapelites that are abundant in the underlying Tibetan slab and would fit all the geochemical and isotopic requirements (Le Fort *et al.*, 1987). Most peraluminous granites are considered to result from the partial melting of sediments and are therefore also referred to as S-type granites.

Metaluminous granitoids: western American batholiths

Very large composite granitoid intrusions known as batholiths are found along subduction zones, spatially associated with coeval arc volcanic rocks, in many regions of the world (CAR in Table 26.2). Prime examples are the Sierra Nevada batholith in California and the coastal batholiths of Peru and Chile, where subduction zones have been active for > 300 Myr. All are dominated by amphibole-bearing tonalitic to granodioritic rocks containing gabbroic to dioritic (and in some cases ultramafic) xenoliths. Mafic intrusions are also part of the associations.

The Peruvian and Chilean batholiths both extend for ~ 1600 km along the Pacific coast, reaching 50–100 km inland. The Chilean batholith consists of complexes that range in age from 290 Myr (Carboniferous) to 90 Myr (Cretaceous), in which the younger intrusions are found further inland (see Parada *et al.*, 1999, and references therein). The Peruvian batholith is mainly Cretaceous, and gravity work has shown it to be a high-level sheet-like intrusion, not thicker than 3 km in most places (Haederle and Atherton, 2002).

In the Chilean batholith, the REE patterns of both granitoids and associated mafic rocks are very similar to those typical of the arc volcanic rocks shown in Fig. 25.1, with La_N/Lu_N ratios between 5 and 10, MORB-like HREE abundances and negative Eu anomalies. They also mostly have an Nb deficit, with La/Nb ratios generally > 3 (Fig. 26.6). In addition to these features, the initial ε_{143} values and Sr-isotope ratios for granitoids and the associated mafic suites are similar within each age range, showing clearly that the rock units are related to each other in a magmatic differentiation sequence. The mafic rocks are regarded as cumulates and/or as the crystallization products of primary and intermediate magmas (Parada *et al.*, 1999). From 290 to 90 Myr, the $\varepsilon_{143,INI}$ values increase from ~ –3 to ~ +5, showing a contribution from ancient crustal matter to the magmas that decreases through time. Such a contamination could be caused by sediments in the slab or by partial melting of the lower crust as the magma ascended.

The Sierra Nevada batholith is about 600 km long and 100 km wide, situated roughly 200 km inland and elongated parallel to the Pacific coast. Its individual intrusions range in age from 220 Myr (Triassic) to 80 Myr (Cretaceous), the 125–85 Myr age range being predominant (Ducea and Saleeby, 1998, and references therein). The currently exposed levels correspond to an emplacement depth range of ~ 30 km, the shallow levels showing a direct connection with volcanism. The batholith consists of numerous plutons ranging in size from less than 1 km^2 to over 100 km^2, with compositions that are mainly tonalitic to granodioritic and with well-preserved igneous textures.

The granitoids of the Sierra Nevada batholith have more fractionated REE patterns (La_N/Lu_N =10–15) than those of Chile, with small Eu anomalies. Apart from the deeper levels of emplacement found here, this batholith is characterized by

mafic xenoliths consisting of garnet and clinopyroxene (eclogites), which formed at depths between 35 and 100 km, and these have Sm–Nd mineral ages between 120 and 80 Myr, similar to the age range of the host rocks. They also have initial ε_{143} values within the same range as the granitoids themselves (-8 to 1.8) and are regarded as representing deep-level cumulates and/or residues. Thus a very thick cumulate/residual mafic counterpart to the granitoids is thought to underlie much of the Sierra Nevada batholith (Ducea and Saleeby, 1998). The more strongly fractionated REE patterns of its granitoids, compared with those of the Chilean batholith, are entirely expected if the evolving melts equilibrated with garnet at depth.

Apart from the low and variable initial ε_{143} values seen in the Sierra Nevada rocks, old "inherited" U–Pb ages in the cores of zircon grains and high $\delta^{18}O$ values in zircons crystallized from the magma also indicate a significant contribution by older continental crust to the batholith (Lackey *et al.*, 2005). Their messages are different: the high $\delta^{18}O$ values indicate sea-water alteration in slab rocks, whereas the Nd and U–Pb data indicate contamination by ancient crustal matter. The latter could have been introduced via clastic sediments subducted with the slab. However, the remelting of pre-existing crust is documented near batholith rocks at deep levels (Zeng *et al.*, 2005).

These are but a few examples. Generally, despite a great variety in their mode of intrusion, the giant subduction-related batholiths in continental margins have many features in common: (1) a calc-alkaline metaluminous slightly hydrous magma composition, leading to the prevalence of amphibole; (2) an association with arc volcanic rocks; (3) similar trace-element abundances to the latter; (4) proof of extensive magmatic differentiation involving mafic cumulates and/or residues; (5) repeated intrusions of a large age range (corresponding more or less with the time over which subduction occurred); and (6) an involvement of older crustally derived matter in their origin.

Metaluminous granitoids: Rapakivi, Baltic shield

A different class of metaluminous granitoids is represented by the Rapakivi granites. These have been particularly well studied (for over more than 300 years!). They are metaluminous to slightly peraluminous rocks ($ASI = 0.9$) and belong to the ferroan calc alkaline suite. The largest Rapakivi granite province is that of Fennoscandia, covering an area of $\sim$ 500 000 km^2 around the eastern Baltic sea, the Gulf of Bothnia and the Gulf of Finland (Haapala and Ramo, 1999). Within this province several Rapakivi plutons, ranging from 1670 to 1470 Myr (Andersson *et al.*, 2002) occur as intrusions in Proterozoic to Archaean crust. The magmatic association is bimodal: the granites represent the felsic (SiO_2-rich) end-member and are associated with a mafic (MgO-rich, Fe_2O_3-rich) suite of tholeiitic diabases, gabbroids and

anorthosites. The rocks of the different Rapakivi massifs vary somewhat, but they share common distinctive features, which are most pronounced in the granites of the large Wiborg batholith. These are coarse-grained porphyritic rocks, with large (3–4 cm diameter) rounded ovoids of alkali feldspar, most of which are mantled by 1–3 mm Na-rich plagioclase rims. Other major phases are quartz, amphibole and biotite, and the accessory minerals are zircon, fluorite, apatite, ilmenite and magnetite (Elliott, 2001). Their major-element composition (Table 26.2) is quite similar to the mean metaluminous granite composition compiled by Whalen *et al.* (1987).

Rapakivi granites are characterized by enrichment in the incompatible elements K, F, Rb, Zr, U and Th and also by enhanced Fe/Mg ratios and Sr depletion. They have very high REE abundances with particular enrichment in the LREEs, negative Eu anomalies, flat HREE patterns and also relatively high Nb concentrations setting them apart from arc-related magmatic rocks (Figs. 26.2 and 26.6).

The initial Nd-isotopic compositions of the different Rapakivi granite plutons and the associated mafic rocks have $\varepsilon_{143,\mathrm{INI}}$ values that vary between –1 and –10, indicating the mixing of mantle and crustal materials. From these data it has been concluded that a mantle-derived melt, which gave rise to the Rapakivi granites by differentiation, had assimilated between 20% and 40% of the Archaean crust (Andersson *et al.*, 2002). Further, the mantle-derived magmas were not arc-related, as seen from the elevated Nb content, but were instead most likely associated with a plume.

Peralkaline granitoids

The granite province in the central and eastern parts of the Kola Peninsula, north-east of the Baltic shield, constitutes one of the largest and most ancient manifestations of alkaline magmatism. The province occupies an area $\sim$ 3000 km^2 and includes several massifs 2.60 to 2.75 Gyr old that are spatially associated with gabbro-anorthosite complexes of similar age (Zozulya *et al.*, 2005).

The medium-grained to porphyritic granites consist of quartz, albite and microcline, with less abundant aegirine and alkali amphibole and with significant accessory titanite, zircon, magnetite, ilmenite, fluorite, monazite, apatite and britholite (Vetrin *et al.*, 1999). They have peralkaline chemistry (Table 26.2) with high [K] and [Na], so that the molar Al/(K + Na) ratio is less than 1, and low [CaO] and [MgO] with quite a low *mg*# value, 0.046. Among the trace elements, Li, Zr, Nb, Y, Th, U and the REEs are abundant, with La/Nb = 2.8 (slightly above the crustal mean, Fig. 26.6), MORB-normalized $\mathrm{La_N/Yb_N} = 5.3$ (slightly below the crustal mean, $\sim$ 10), a flat HREE pattern and a pronounced negative Eu anomaly,

$Eu/Eu^* \sim 0.2$ (Fig. 26.2). The Ba concentration is curiously low, with $Ba_N/Th_N = 0.05$ (a factor 20 below the crustal mean).

The alkali granites contain xenoliths of mafic rocks, gabbros, gabbro-diabases and gabbro-norites; these consist of clinopyroxene, hypersthene and plagioclase. They have smooth whole-rock REE patterns, with slightly enhanced LREE values ($La_N/Yb_N \approx 3$), that are almost indistinguishable from Archaean basalts.

The major constituents of the associated gabbro-anorthosite bodies are plagioclase, olivine, titanomagnetite, clinopyroxene and hypersthene. In these rocks the REEs are much less abundant and show a positive Eu anomaly, features that are in some ways complementary to those in the granites (Balashov, 2004).

The Sm–Nd isotope systematics indicate a common source for all these rocks, granites, xenoliths and anorthosites (Balashov, 2004): they define a single evolution line in a $^{147}Sm/^{144}Nd$ versus $^{143}Nd/^{144}Nd$ isochron plot. The slope and intercept of this line correspond to a 2735 ± 68 Myr age and to $\varepsilon_{143,INI} \approx 1.7$, pointing to a contribution of mantle material: at that time the model-derived DMM value was $\varepsilon_{143} \approx +4$ (Fig. 27.18).

These data can be reconciled by a model involving the fractionation of an enriched basaltic melt, forming plagioclase-rich cumulates, after which the granites crystallized from REE-enriched but Eu-depleted melts. The xenoliths may represent compositions close to that of the primary melt, which is considered to be related to a late-Archaean mantle plume beneath the eastern Kola domain (Vetrin *et al.*, 1999; Balashov, 2004; Zozulya *et al.*, 2005).

Metaluminous and peralkaline granitoids, whether from plumes or arc-related, that apparently formed from the differentiation of mafic melts rather than from crustal melting are also known as I-type granitoids as distinct from the S-type granitoids discussed above.

Archaean and post-Archaean upper continental crust: a comparison

There are almost 40 exposed Archaean terrains covering in total $\sim 10\%$ of the continents and a much larger portion is underlain by Archaean rocks (Martin, 1994). The full data set of Nd model ages on continental crust indicates that about 40% of the presently existing crust had been formed by ~ 2.5 Gyr, at the end of the Archaean era (Chapter 27). A comparison of the chemical compositions of crustal domains having different ages is a unique approach to Earth evolution and is also important in determining the bulk composition of the continental crust.

It has been known for a long time that there is a significant difference between the compositions of the Archaean and post-Archaean rocks of the continental crust. The dominant Archaean granitoids are rocks of tonalite–trondhjemite–granodiorite (TTG) composition.

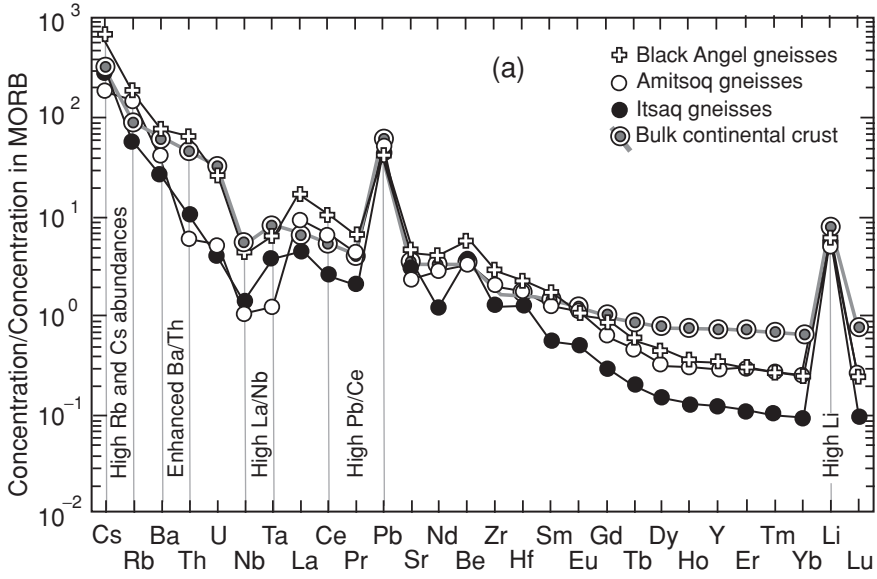

Fig. 26.3 Trace-element abundances of Archaean tonalite–trondhjemite–granodiorite gneisses (TTGs) and those for the bulk continental crust. (a) The elements are arranged in order of decreasing compatibility for MORB-source melting. The thickest line shows the bulk crust abundances. All three types of ancient TTGs show strong enrichment in Pb, Li and Be and subchondritic Nb/La ratios, signatures typical of the continental crust (Figs. 26.6 and 26.7). The TTGs also display strong LREE/HREE fractionation. The value of $mg\# = \mathrm{Mg}/(\mathrm{Mg} + \mathrm{Fe})$ for TTGs is 0.43. Normalization values from Sun and McDonough (1989); concentrations in the bulk crust from Rudnick and Fountain (1995). After Kamber *et al.* (2002). (b) Chondrite-normalized La_N/Yb_N ratios vs. Yb_N abundances in TTGs; $La_N \equiv La_{SAMPLE}/La_{BSE}$ and the same holds for Yb. A substantial difference in the REE abundances for Archaean and post-Archaean rocks indicates a major break in the mode of evolution of the continental crust at $\sim$ 2.5 Gyr ago: the heavy rare earth elements (e.g. Yb) are strongly depleted in the ancient crust. (c), (d) The insets show typical REE patterns, with a specifically low abundance of Yb and a concave form at the HREE end (c), pointing to a specific (HREE-consuming) residue assemblage in the Archaean (Section 26.7). After Martin (1994), © Elsevier Science 1994, reproduced by permission.

The most typical mineral associations of TTG rocks are sodic plagioclase, quartz and biotite, with less abundant K-feldspar, epidote, hornblende and titanite accompanied by accessory apatite, zircon, magnetite and ilmenite (Martin, 1994). Compared with the Proterozoic and Phanerozoic granodiorites, TTG rocks typically contain more Na_2O, MgO and Al_2O_3 and less K_2O (Table 26.2).

Further important fingerprints of parental TTG magmas are high La/Nb and Pb/Nd ratios, high Sr abundances and high Sr/Nd ratios (Fig. 26.3(a)). These magmas show steep REE patterns with high LREE/HREE ratios (Fig. 26.3(b)). This is

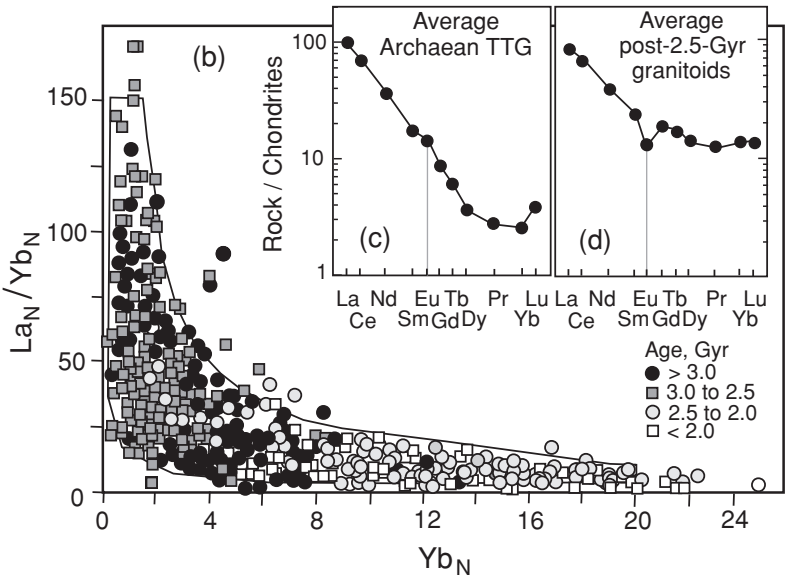

Fig. 26.3 (*cont.*)

in contrast with the REE pattern observed in ancient shales; the low La/Yb ratios ($\sim$ 10) in the latter resemble those of mafic rocks, which are characterized by relatively flat HREE abundances (La/Yb between 3 and 10). Because the shales portray the REE abundances of the source rocks, Condie (1993) considered that the Archaean crust contained a higher proportion of basaltic material than is presently observed. It is noteworthy that Eu anomalies are not a characteristic feature of TTGs.

26.3 Sedimentary rocks and processes related to them

Fine-grained clastic sediments

The bulk present-day mass of sediments is $\sim 2.7 \times 10^{24}$ g, of which 75% is situated within the continents, $\sim$ 15% at the continental margins and $\sim$ 10% on the ocean floor (Ronov, 1982; Hay *et al.*, 2001). The ocean-floor sediments, even though comprising so little of the bulk inventory, are important because their subduction flux constitutes the principal feedback between the upper crustal and mantle reservoirs (Chapters 25 and 27).

Sediments are highly variable in their mineralogy and major-element chemistry, ranging from carbonates and evaporites that are essentially monomineral to shales, which consist of a multitude of minerals. As a consequence their trace-element contents and abundance patterns also vary widely. Volumetrically, fine-grained sediments (FGSs) are the most abundant (about three-quarters of the

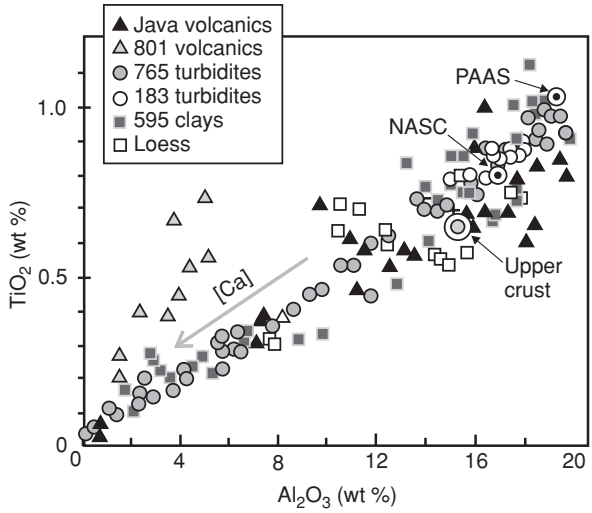

Fig. 26.4 Co-variations of Al_2O_3 and TiO_2 in fine-grained oceanic sediments from different localities. Three average composition values are shown for comparison: post-Archaean Australian shale, North American shale composite (PAAS and NASC respectively, after Taylor and McLennan, 1985) and upper crust (Rudnick and Gao, 2003). The numbers in the key correspond to the boreholes. The grey arrow shows the direction of decreasing calcium concentration. After Plank and Langmuir (1998), © Elsevier Science 1998, reproduced by permission.

total budget; Taylor and McLennan, 1985) and generally these rocks have detrital, biogenic and chemically precipitated components in variable proportions. The mixed siliciclastic–biogenic sedimentary facies holds records of different terrestrial ecosystems, crustal, oceanic and atmospheric, and of their interactions. Of the sedimentary columns accumulated in the oceans and intracontinental seas, FGSs constitute the major part. Therefore we will focus on these sediments in this section.

The concentrations of major elements in FGSs vary by a factor of ≥ 10, even within the same sedimentary sequence (Fig. 26.4). Samples with low contributions of carbonates and biogenic silica (both "diluents" derived from ocean waters) are similar to the continental composites. As the contribution of the diluents increases, the concentrations of Al_2O_3, TiO_2 and K_2O decrease proportionally but their ratios, e.g. TiO_2/Al_2O_3 in Fig. 26.4, remain constant. These elements, among others, are clearly hosted by the detrital component.

In contrast, some other elements, such as Na, Ca and Mg, are preferentially dissolved during continental weathering and have very long residence times in the ocean waters. These elements do not follow the fluxes of the detrital component and their concentrations in FGSs are mainly controlled by (1) the rates of production and death of organisms in the ocean, (2) precipitation conditions and (3) flux ratios of the terrigenous and water-derived components.

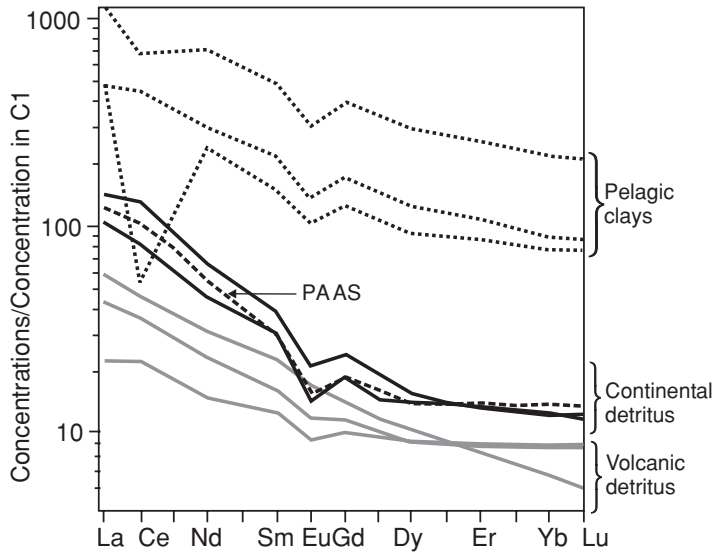

Fig. 26.5 Rare earth element patterns in oceanic fine-grained sediments (FGSs). Extremely thin dispersed slowly accumulating pelagic clays, one with a large Ce anomaly, as well as volcanic detritus, are shown for comparison. After Plank and Langmuir (1998), © Elsevier Science 1998, reproduced by permission.

The REEs are poorly soluble, and the abundance patterns of representative abyssal-plain FGS samples are almost indistinguishable from crustal composite samples (e.g. PAAS in Fig. 26.5), with La $\sim 100 \times$ C1 and a flat HREE tail. These similarities show that there is a dominant terrigenous detrital component in these ocean-floor sediments and that, generally, its transport does not affect the REE abundances. In pelagic clay sediments, which have accumulated very slowly, the REE pattern is at a first approximation similar to that for PAAS but the absolute concentrations are generally much higher. Negative Eu anomalies of a similar size are seen in both sample sets, thus reproducing this feature of the parent post-Archaean granitoids. Also, positive or negative Ce anomalies can occur in pelagic sediments.

The La/Nb ratios of FGSs are much higher than all the average values for MORBs and OIBs and those suggested for the MORB-source mantle (Fig. 26.6). Similarly, both FGSs and continental sediments have much lower La/Pb ratios than MORBs or OIBs (Fig. 26.7). For both these ratios, the similarity of the sediment values to those of andesites and the average continental crust is striking.

Notwithstanding the many similarities, there are significant differences between continental-crust and average fine-grained sediment compositions regarding soluble elements. For instance, GLOSS has higher Ba/Rb, Lu/Hf and Pb/U ratios than the continental crust. Erosion, transport and sedimentation must have fractionated certain elements independently of other processes such as continental growth or lithospheric foundering (Plank and Langmuir, 1998), and this fractionation signal

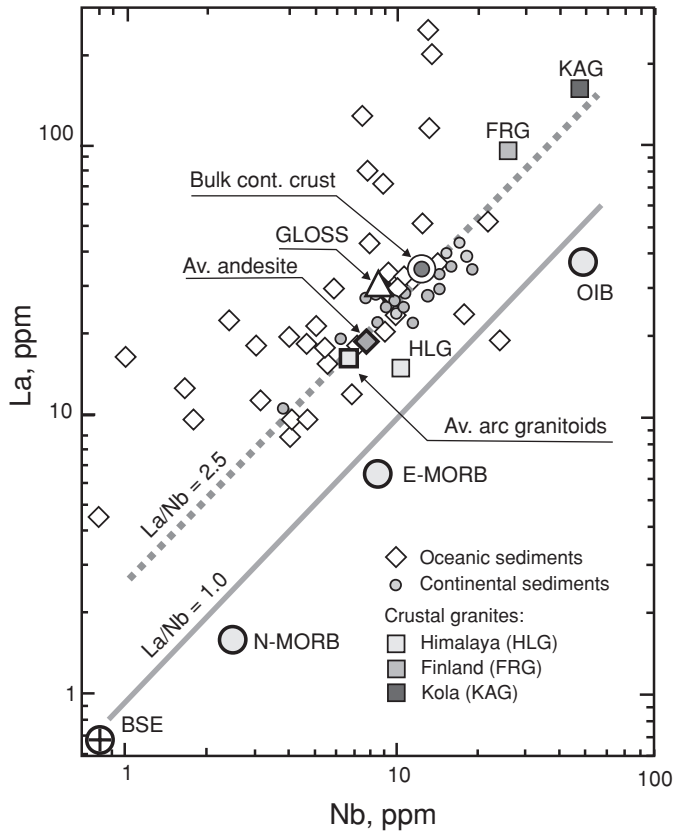

Fig. 26.6 Abundances of La and Nb in continental and oceanic sediments. Lines (broken and solid) for La/Nb = 1.0 and 2.5 are shown for comparison. Note that the Archaean upper crustal rocks show even higher La/Nb ratios, with average values of 2.8 and 3.6 for the Archaean shales and bulk crust respectively. Sources of data: continental sediments, McLennan (2001); oceanic sediments and global subducting sediment composition (GLOSS), Plank and Langmuir (1998); bulk silicate Earth (BSE), Table 17.1; granite compositions, Table 26.2; normal mid-ocean basalts (N-MORBs), enriched mid-ocean basalts (E-MORBs), and ocean-island basalts (OIBs), Sun and McDonough (1989); primitive andesite average, Av. andesite, Kelemen *et al.* (2003).

is in part carried to the mantle by subduction. The isotopic data enable us to look at this fractionation and yield important clues on the sources and processes involved in sediment formation.

Sources and mechanisms of sedimentation

The observed compositions of sediments are controlled by several factors which can be grouped into four sets: (1) the site of weathering and erosion, (2) the transport

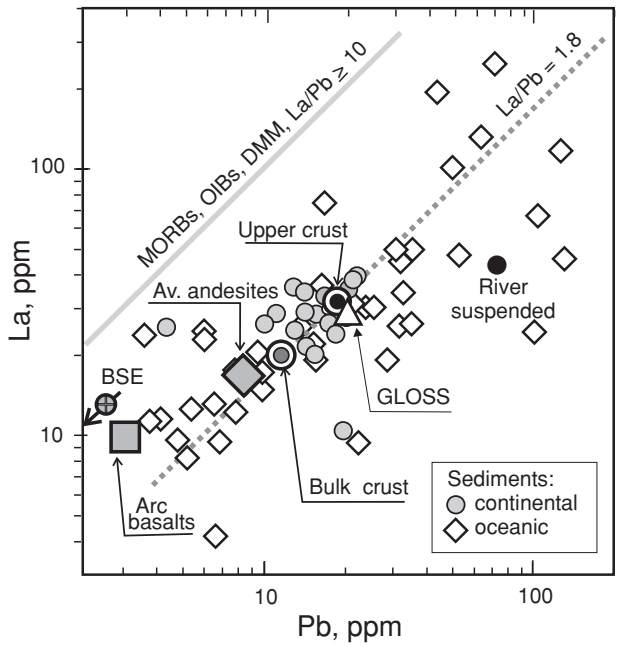

Fig. 26.7 Abundances of La and Pb in continental and oceanic sediments. Lines for La/Pb = 1.8, 10 and 4.7 (black with circle and arrow, pointing to BSE composition) are shown for comparison. Note the complementarity of crustal and mantle materials. The data sources are the same as for Fig. 26.6.

path, (3) the site of deposition, (4) the burial conditions (Sageman and Lyons, 2003). Water is the principal substance involved in each stage, although wind transport is also important for slowly accumulating pelagic sediments far from land. Water–rock interactions and water-derived organic and chemical precipitates are of prime importance in most sedimentation-related processes. Below we briefly discuss those leading to FGS formation.

(1) Bedrock lithologies, tectonics and the climate determine the rates of chemical weathering and physical erosion and the proportions of dissolved, detrital and reprecipitated components. The present-day global river-denudation flux is $\sim 2 \times 10^{16}$ g yr^{-1}, of which $\sim 80\%$ and $\sim 20\%$ are subfluxes of suspended and dissolved materials respectively (Veizer and Mackenzie, 2003). The river mass flux, 4.3×10^{19} g yr^{-1}, then gives a mean value 0.45×10^{-3} g g^{-1} for the bulk concentration of the load; the actual value varies by three orders of magnitude between individual rivers. The composition of the suspended load differs from its precursor bedrocks mainly in the depletion of water-soluble major elements (e.g. Ca, Na, K) and trace elements (e.g. Ba, Sr, Rb, U). Generally Ca, Mg, Na, Si, C, Cl and S are major components of the dissolved load, and Ba, B, Sr, Rb and Li are relatively abundant trace elements

(Meybeck, 2003; Gaillardet *et al.*, 2003). Sedimentary rocks are on the whole less resistant to erosion than magmatic ones, leading to the so-called cannibalistic recycling of sediments. The rate of such transformation of older sediments into younger ones is impressive, approaching $\sim 90\%$ since the early Proterozoic (Veizer and Jansen, 1979; Veizer and Mackenzie, 2003).

(2) The main outcome of the riverine transport of eroded material is a decrease in the grain size and a corresponding increase in the bulk-water–mineral interaction surface. This leads to progressive leaching of water-soluble elements and a corresponding increase in the ratio of dissolved and suspended loads, as well as to enhanced adsorption and chemical reactions at the interface. These factors and chemical reactions in solution further modify the chemistry of the riverine load, leading in some cases even to REE fractionation. The load is further affected by atmospheric sources (e.g. Cl and C are abundant in rain water) and sinks (e.g. biogenic calcite precipitation in lakes; Meybeck, 2003; Gaillardet *et al.*, 2003) in the pathway.

(3) At the deposition site, the dissolved load is mixed with that already present in the basin (lake, sea or ocean) and the suspended load settles along with material segregated from the water itself. Here a set of physical, chemical and biological processes controls the rate of sedimentation and the compositions, structures and textures of the sediments; all these parameters could be highly variable even at the same site. Among major elements, the sedimentation of Ca and Si depends particularly strongly on the biological activity.

Generally the REEs remain in particulate matter during weathering, erosion and subsequent transport and are thus generally not (or only a little) fractionated. Therefore the REE patterns in FGSs mimic those of the most abundant precursor crustal rocks, i.e. granites and shales. The concentrations of REEs in PAAS and some FGSs exceed those of the bulk crustal model by $\sim 20\%$, which is readily understood since other sedimentary rocks such as sandstones and carbonates, with low REE abundances, balance the total sediment REE budget (Taylor and McLennan, 1995).

Pelagic clays accumulating at slow sedimentation rates show much higher total REE concentrations (Fig. 26.5) and have positive or negative Ce anomalies, which are due to the partial oxidation of Ce to Ce^{4+}. Iron–manganese "flocks" preferentially scavenge Ce^{4+}, causing a positive Ce anomaly in such sediments and leaving behind Ce-depleted water. Apatite, a bone-forming phosphate mineral, readily concentrates REEs. Fish bones accumulate REEs from the water without substantial fractionation during life and become sedimented into FGSs after disaggregation. For these sediments, the two competing mechanisms yield a positive (high Mn/P) Ce anomaly, a negative (low Mn/P) Ce anomaly or no anomaly at all (Elderfield

and Pagett, 1986; Toyoda *et al.*, 1990). The composition of the dissolved load at a sedimentation site can be modified further by the hydrothermal flux from the oceanic crust (clearly recorded by ocean-water Sr-isotope compositions, Fig. 27.20) and the authigenic flux from sediments.

The tectonic position of a depositional site dictates: (i) the lifetime of sedimentary rocks and (ii) the ultimate fate of the sediments. The first can vary from a few million years, e.g. for sedimentation near a trench, to thousands of millions of years, for sedimentary basins within continental plates and cratons (Ingersoll and Busby, 1995; Veizer and Mackenzie, 2003). Of the possible mechanisms causing sediment destruction, two are the most common: uplift followed by cannibalistic recycling and subduction followed by metamorphism and partial mixing into the mantle.

(4) After sediments are buried underneath the overlying strata to some depth, the increasing pressure and temperature lead to their diagenetic transformation into solid rock. The pressure results in compaction of the sediments and their (micro)fracturing, whereas the interactions of pore fluids with solid phases cause dissolution and/or precipitation. One of the volumetrically most important processes of diagenesis in siliciclastic sediments, including FGSs, is the dissolution of Ca-feldspar and clay minerals, with the partial removal of Ca, Si and K by pore water and their partial replacement by precipitated albite, illite and other secondary minerals (kaolinite, chlorite, etc.) that form largely as cements. The upward transport of Ca, Si and K affects both the younger overlying sediments and the water chemistry of the immediate sedimentary environment.

While there is a continuum in pressure and temperature from diagenesis to low-grade metamorphism (Section 25.4), the latter requires tectonism to increase P and T to values that cannot be achieved by mere burial underneath younger sediments.

26.4 The lower continental crust: complement to the upper?

The composition of the deep continental crust, typical rocks of which are little exposed on the Earth's surface, is poorly constrained and much more model dependent than that of the upper crust. The model composition is based on a combination of rock and mineral data, i.e. observational and experimental petrology, geochemistry, mineralogy and seismological and geothermal studies. This multidisciplinary approach allows a lower crust having a different overall composition from that of the upper crust to be distinguished at depths below $\sim$ 20 km (Rudnick and Fountain, 1995; Rudnick and Gao, 2003).

The lower crust is composed of magmatic and metamorphic rocks. The latter are generally in granulite facies characterized by mostly anhydrous silicate minerals: with increasing T, amphibole is replaced by pyroxene as the main Fe–Ca–Mg

bearing mineral, although biotite may be present as the sole hydrous phase. The mineral assemblages equilibrate under high *PT*, typically at $T \sim 700$–$900\ ^{\circ}C$, $P \sim 0.600$–1 GPa, corresponding to depths between 20 and 30 km (Harley, 1989). At present the high temperatures required for this metamorphism can only be achieved, even at the base of the crust, by magmatic underplating or slab break-off mechanisms leading to strongly enhanced heat flow (Davies and von Blanckenburg, 1995). However, in the Archaean and early Proterozoic, provinces with average crustal U, Th and K concentrations could have achieved these temperatures by internal radioactive heating (Kramers *et al.*, 2001).

Xenoliths are quite different from rocks of the exposed granulite terrains in their composition. Most terrains are composed of high-silica rocks with $\sim 70\%$ SiO_2, which is a concentration typical of granitic rocks, and only $\sim$ one-third of terrains have mafic compositions with $\sim 50\%$ SiO_2. These are, however, typical of granulite xenoliths in volcanic rocks.

It is shown by both the compositional and the chronological evidence that the granulite xenoliths are not related to their host magmas and therefore represent a reservoir through which the magmas have ascended. An important question that then arises is why xenoliths represent mainly the mafic subset of granulites. One possible answer is that felsic lithologies are characterized by relatively low melting temperatures and therefore could be readily melted and dissolved in host magmas (Downes, 1993). Another view is that the deep crust is broadly layered and that exhumed granulite terrains and xenoliths represent upper and lower layers of the lower crust respectively. The geophysical constraints lend support to such a layered model of the lower crust, in which the deepest levels have a higher density and are therefore likely to be enriched in mafic rocks (Rudnick and Fountain, 1995).

Compositionally, the lower-crustal xenoliths are rather diverse; even within one locality, e.g. the Massif Central in France, major- and trace-element concentrations in meta-igneous xenoliths vary within wide ranges (wt %): $45 \leq [SiO_2] \leq 70$, $7 \leq [Al_2O_3] \leq 22$, $2 \leq [MgO] \leq 20$ and $0.1 \leq K_2O/Na_2O \leq 5$ (Downes, 1993). Some xenoliths are interpreted as magmatic cumulates, i.e. this part of the lower crust would consist of a layered complex with pyroxene- and plagioclase-rich layers. In this context it should be noted that, for these chemical compositions, the granulite-facies metamorphic minerals are the same as those that would crystallize from magma, so that it is difficult to say whether these xenoliths are metamorphic or magmatic rocks. Metasedimentary xenoliths are also present in the Massif Central, showing lower CaO concentrations (owing to weathering) but a high SiO_2 content (between 60% and 70%) and a high K_2O/Na_2O ratio, ~ 2.

The REEs allow further insight into the origin of precursor materials of the lower crustal xenoliths. Several features stand out. First, almost all xenoliths, even those of mafic composition, are LREE-enriched relative to both BSEs and MORBs. Mafic granulites (Hungary, Eifel) show smooth patterns reminiscent of

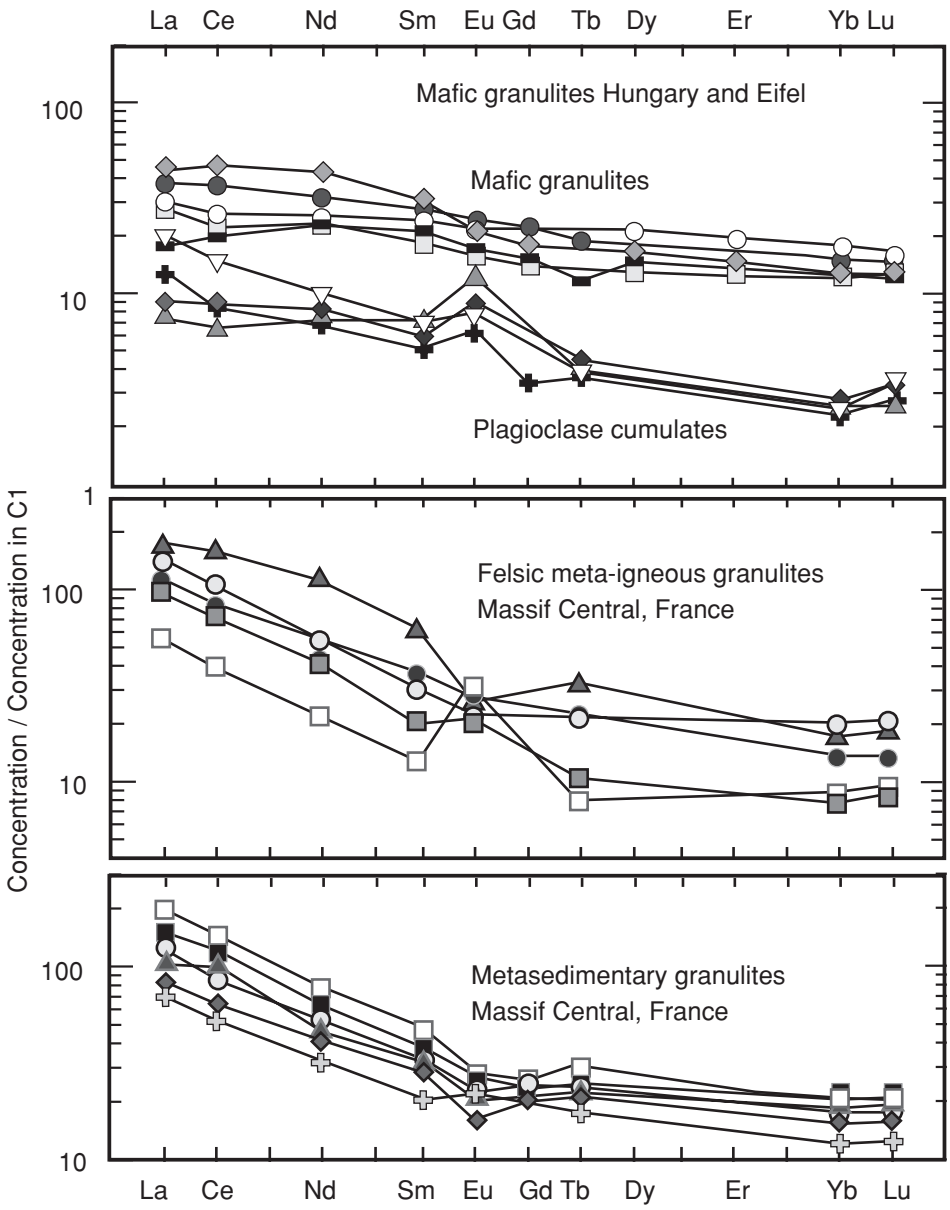

Fig. 26.8 Rare-Earth-element abundance patterns in lower-crustal xenoliths. Modified after Downes (1993).

average arc volcanics (Fig. 26.8). Second, Eu anomalies are quite common, and plagioclase-rich rocks with low overall REE-contents have positive Eu anomalies, in accord with the notion that they are cumulates. In the case of the Massif Central, the most REE-enriched sample has a complementary negative Eu anomaly. Third, felsic granulites show LREE enrichment and a flat HREE tail, comparable with the

upper-crustal REE pattern (e.g. PAAS) if a negative Eu anomaly is present (Fig. 26.5) and otherwise to high-K andesites (Taylor and McLennan, 1985). The general impression is that the magmatic lower-crustal xenolith suites reflect primitive and evolved melts as well as various cumulates arising from the differentiation of an arc basaltic or andesitic magma. The common negative Eu anomaly of upper-crust rocks may also be related to such a differentiation (Rudnick and Presper, 1990; Rudnick and Fountain, 1995).

The rare earth elements in metasedimentary granulites present a uniform group (reflecting efficient mixing prior to metamorphism) with a clearly negative Eu anomaly, a general signature of upper-crustal matter.

The La/Nb ratios present another independent view of the origin of the lower crustal materials. Mafic xenoliths from the lower crust show rather variable La/Nb ratios, from 0.5 to 10, overlapping with those observed in MORBs, OIBs and arc volcanics. However, the mean value, 2.1, is quite close to that of the upper crust (Fig. 26.6). Lanthanum–niobium ratios much greater than 1 are typical of exhumed granulite terrains (irrespectively of their composition and age) and metasedimentary and felsic xenoliths.

Large-ion lithophile-element concentrations in granulite terrains and in xenoliths vary in a wide range, up to a factor ~ 100 for K and a factor ~ 1000 for U and Th. Generally xenoliths show depletion in U and Th, with concentrations a factor ~ 10 below upper-crustal abundances and those often observed in exhumed granulite provinces (Rudnick and Presper, 1990). In granulites having $K > 1\%$ the K/Rb ratios are indistinguishable from those seen in Archaean and post-Archaean terrains as well as in common igneous and sedimentary rocks, for which $K/Rb \sim 300$. However this ratio rises to 6000 in granulites with low potassium concentrations, $K < 1\%$, implying specific Rb depletion in the lower crust, possibly related to dehydration reactions in prograde granulite metamorphism followed by upward transport by fluids (Rudnick and Presper, 1990). This feature is further highlighted by radiogenic isotope systematics (Section 27.6).

26.5 The crustal age distribution function

The present-day continental crust consists of crustal domains of different ages. The masses of crustal domains M_{DOM} that formed at time θ and were preserved until time t are expressed by the age distribution function $AGE(\theta, t)$.

The age distribution function relates to the total crustal mass at time t as follows:

$$M_{\mathrm{CCR}}(t) = \sum_{\theta} AGE(\theta, t) \tag{26.1}$$

and the difference between $AGE(\theta, t)$ for $\theta = t$ and the crustal mass derivative (or

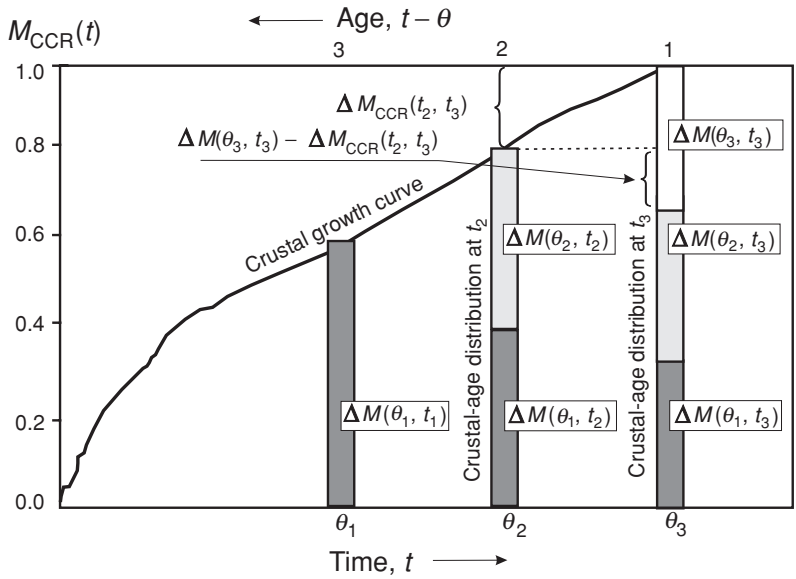

Fig. 26.9 Crustal-age distribution: masses and mass fluxes. Qualitative graph showing the principle of relationships between the crustal-growth curve, the crustal-age distribution and mass fluxes ΔM into and from the crust. All masses are shown as portions of the present-day continental crust mass. The crustal-growth curve defines the mass of the crust at any time t. The crustal-age distribution shows the masses of blocks of different age for any t. For example, at time t_3 the crust consists of only three blocks with ages θ_1 (old), θ_2 (intermediate) and θ_3 (young) $\equiv t_3$. The mass flux into the crust during the interval (t_2, t_3) is then $\Delta M(\theta_3, t_3)/(t_3 - t_2)$. The flux out of the continental crust is the difference between the flux into the crust and the real increase in mass of the continent during the time interval (t_2, t_3), $\Delta M_{CCR}(t_2, t_3)$. Adapted from Azbel and Tolstikhin (1988, 1990).

crustal growth rate) $\Delta M_{CCR}(t)/\Delta t$ determines the bulk erosion flux $EROSION(t)$ from the crust (Fig. 26.9):

$$EROSION(t) = AGE(t = \theta, t) - \Delta M_{CCR}(t)/\Delta t. \tag{26.2}$$

Here $AGE(t = \theta, t)$ is the mass ΔM of the new crustal domain added in a given time interval Δt. Also $AGE(\theta, t)$ determines another important parameter, the mean age of the continental crust at time t, $T_{CCR}(t)$:

$$\langle T_{CCR}(t)\rangle \equiv [M_{CCR}(t)]^{-1} \sum_{\theta} (t - \theta) \times AGE(\theta, t) \tag{26.3}$$

where $t - \theta$ is the age. For example, if the masses of the three crustal domains, which have different mean ages as shown in Fig. 26.9, are equal at time $t = t_3$ then Eqn (26.3) gives 2 Gyr as the mean age of the crust at $t = t_3$. For the present time,

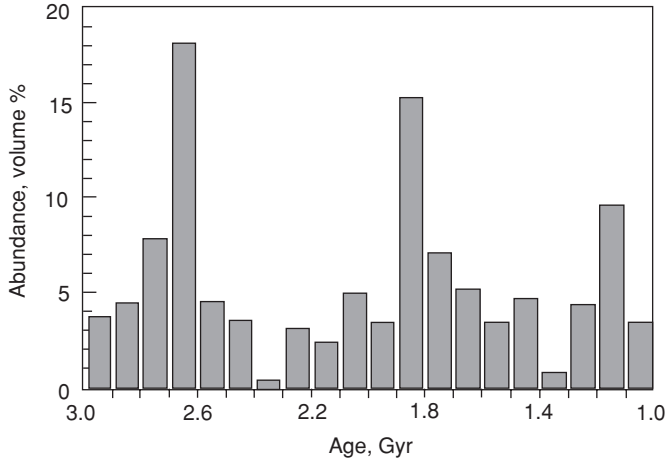

Fig. 26.10 Crustal-age distribution: zircon ages. The distribution of U/Pb zircon ages recalculated as the relative abundance of the crustal domains. Note that the largest portion of the continents appears to have originated at ~ 2.7 Gyr ago. From Condie (2000), © Elsevier Science 2000, reproduced by permission.

for instance, careful analysis of the Nd model ages (Fig. 21.5) gives $\langle T_{\mathrm{CCR}} \rangle \approx 1.8$ Gyr for a large part of North America (DePaolo *et al.*, 1991) and a similar value, $\sim$ 2 Gyr, is generally assumed for the bulk continental crust and used for modelling crustal evolution (Chapter 28).

Further, Eqn (26.3) may be modified to express the mean age (or residence time) ${}^{i}\tau_{\mathrm{CCR}}(t)$ of species i in a reservoir, e.g. in the continental crust as a whole or in crustal subreservoirs. Assuming for simplicity that matter with a concentration ${}^{i}C(\theta)$ of the stable species i was added to the crust at time θ and retained this concentration unchanged till time t; then

$$\langle {}^{i}\tau_{\mathrm{CCR}}(t) \rangle \equiv \left[{}^{i}C_{\mathrm{CCR}}(t) M_{\mathrm{CCR}}(t) \right]^{-1} \sum_{\theta} (t - \theta) \times {}^{i}C(\theta) \times AGE(\theta, t). \quad (26.4)$$

The concepts of $AGE(\theta, t)$ and the mean-age/residence-time ratio reflect the dynamics of the formation and destruction of a given reservoir and therefore give important constraints on evolutionary models. Age density as a function of age is used as a first-order proxy for the present-day value, $AGE(t_{\mathrm{FIN}} = \theta, t_{\mathrm{FIN}})$. Along with progress in geochronology, an increasing amount of dates constrain this function further. If the difference in erosion rate between crustal domains of different ages is known (the so-called erosion law, Allègre and Rousseau, 1984), then the present-day $AGE(t_{\mathrm{FIN}} = \theta, t_{FIN})$ can be extrapolated into the geological past.

An episodic history of crustal growth has been inferred by a number of authors (e.g. Condie, 1998, 2000; Albarede, 1998b) from the clustering of U–Pb zircon dates in specific, relatively narrow, age intervals: 2.6 to 2.8 and 1.7 to 1.9 Gyr (Fig. 26.10).

This may have implications for models of crustal-growth mechanisms, as will be discussed in Section 26.7 below. However, it should be noted that U–Pb zircon ages, on which this inferred age distribution rests, may be minimum ages for the crustal provinces in which they occur, as many granites result from the remelting of earlier crust. It is expected that future Hf-isotope studies on dated zircon populations will establish whether the age distribution of the latter truly reflects crustal-growth rates.

In Section 26.2 we have discussed the contrasting chemical compositions of crustal domains of different age. Such comparisons are important because they shed light on major changes in crust-feeding materials and processes through time (see e.g. Condie, 1994, 2005; Rudnick and Fountain, 1995; Hawkesworth and Kemp, 2006 for more detailed discussions of this problem). It is of equal importance that they provide the key to a more accurate estimate of the bulk chemical composition of the continental crust, via $AGE(t_{\mathrm{FIN}} = \theta, t_{\mathrm{FIN}})$.

26.6 The mean composition of crustal reservoirs

Rudnick and Fountain (1995) developed the most comprehensive compositional model of the continental crust (Table 26.3), which takes into account its layered structure and the secular (long-term non-periodic) variations of the compositions along with the seismological and heat-flow constraints. A comparison of their inferred compositions with those of other authors shows that different studies, utilizing diverse data bases, have yielded remarkably similar results. A feature that stands out is that incompatible lithophile trace elements are extremely strongly concentrated in the crust. Despite its relatively small mass, it contains as much of these elements as the whole mantle, excluding the core–mantle transition zone, D″, which we consider as a separate, somewhat enriched, reservoir (Chapter 19).

Observations on trace-element abundances, summarized for the bulk continental crust in Figs. 25.1 and 26.3(a), imply that the magma sources and magmatic processes that generated the continental crust were similar to those of modern arc environments throughout most of Earth history. Thus, the La/Nb ratios in the Archaean upper crust, ~ 3, and in the bulk crustal reservoirs (Table 26.3, Fig. 26.6) are all well above those for both MORB and OIB magmas. Other typical crustal fingerprints are the enhanced abundances of several fluid-soluble elements such as B, Li and Pb (Fig. 26.3(a)).

Regarding the intracrustal structure, the concentrations presented in Table 26.3 suggest at first glance that they could have resulted from intracrustal fractionation: the upper crust has a greater enrichment in LREEs, the highest abundance of the most incompatible elements, Rb, U and Th, a significant negative Eu anomaly and a relatively low Sr/Nd ratio, while most lower-crustal rocks present a complementary pattern (Rudnick and Gao, 2003). Important evidence on the coupled evolution

of the lower and upper crusts is recorded by the ^{176}Lu–^{176}Hf and ^{147}Sm–^{143}Nd isotopic systematics, as follows. Data from both reservoirs define a single crustal array, suggesting that the lower crust is similar to the upper crust in terms of its present-day parent/daughter values, Hf/Nd ratios and time-integrated Lu/Hf and Sm/Nd ratios (Section 27.7). This feature also implies broadly similar mean ages for the lower and upper crustal reservoirs, which places important constraints on the major crust formation and destruction mechanisms discussed in the next section.

While the above concept may be valid in a broad sense, however, some important problems with it become apparent on closer scrutiny. First, the complementarity pattern appears not to be a robust feature and is rarely observed when upper-crustal granitoids are compared with e.g. lower-crustal rocks within a given crustal domain. In particular mafic granulites, the potential residue or cumulate associated with granitoid melts, often do not show the expected complementary positive Eu anomalies (Fig. 26.8; see also Rudnick, 1992). Second, the bulk crustal concentrations of the highly incompatible elements Rb and Th are higher than those in any present-day candidates for crust-feeding magmas, especially in the most abundant arc basalts (Tables 24.1 and 26.3). Therefore to have produced a melt as enriched as the upper crust in such elements, the mass of the residual or cumulate material must have greatly exceeded the lower crustal mass (Hawkesworth and Kemp, 2006). This conclusion is also valid for major crustal constituents that are incompatible, such as K_2O (Arndt and Goldstein, 1989). The removal of mafic material from the lower crust to the mantle would reconcile most of these contradictions (Section 26.7).

26.7 Processes governing crustal mass and composition

Feeding, developing and destroying the continental crust: an introduction

The data presented above indicate that a complex interplay of magmatic, metamorphic and sedimentary processes governs the mass and composition of the continental crust.

Obviously magmatism is of first importance because it feeds the crust, delivers the energy that causes major intracrustal differentiation and initiates a number of important crustal processes. There are two major tectonic settings where crust-feeding processes operate. Converging plate boundaries with intense arc magmatism (Chapter 25) constitute the first of these. Here new crust is formed via fractionation in the subducting slab and overlying mantle, followed by the ascent of hybrid magmas, whereas the residual slab material is transferred into the mantle. These mechanisms are directly observed at present, have almost certainly operated during at least the

second half of Earth's history and were probably important during the first half, as well. The second setting is presented by already existing mature crustal domains underplated by mafic-to-intermediate mantle magmas.

Whereas the above processes result in the growth and development of the continental crust, two complementary crust-destroying mechanisms are crustal erosion (already discussed in Section 26.3) and the foundering of dense mafic lower crustal domains, known as delamination (see below).

Was a subduction-type magmatic source possible in early Earth history?

The major constituents of the Archaean upper crust, tonalite–trondhjemite–granodiorite (TTG, Section 26.2) rocks have low *mg*#, values precluding their direct generation by the melting of mantle rocks or much interaction with a mantle wedge (de Wit, 1998). Experimental petrology has shown that melts with the TTG major-element composition can result from the partial melting of a hydrated basaltic precursor at pressures up to 3 GPa and temperatures between 800 and 1100 °C, without subsequent magmatic differentiation (Winther, 1996).

A subducting slab indeed includes hydrated basalt; therefore some authors have suggested that TTG magmas could be generated via partial slab melting in the course of low-angle subduction, when the thickness of the overlying mantle wedge is minimal (e.g. Smithies *et al.*, 2003). In this proposal it is surmised that the Archaean oceanic crust was hotter, thicker and more buoyant than it is at present. Because of these features, the crust was not dragged by the sinking plate, as generally occurs at present, but was pushed by the young plate slipping from the ridge. Also, the plates were smaller and spreading rates were faster, so the subducting plates were hotter compared with modern regimes. These factors would all have promoted subduction at a smaller angle to the horizontal, so that melting of the subducting slab could have started at comparatively shallow depths and felsic melts could have risen into the crust without significant equilibration with the mantle wedge.

The generally strongly fractionated REE patterns of Archaean TTG rocks with highly depleted HREEs (Fig. 26.3(b)) have also been interpreted by Martin (1994) as an indication that the TTG rocks formed by melting in the downgoing slab, with possibly even a component from eclogite melting. The presence of garnet in the residue would then lead to a depletion of HREEs in the melts. Following this idea, the TTG magma would be similar in origin to the so-called adakites, magmas that are rare today and originated by the melting of downgoing slabs at great depth. Many (but not all) of the most ancient TTG rocks show less extreme Yb depletion ($Yb_N \sim 5$, $La_N/Yb_N \sim 20$, Fig. 26.3(b)) than somewhat younger TTG rocks ($Yb_N \sim 2$, $La_N/Yb_N \sim 50$), which would be in accord with an increasing influence of garnet

in the residue mineral assemblages, i.e. progressively deeper melting (Lagabrielle *et al.*, 1997; Martin and Moyen, 2002; Smithies *et al.*, 2003).

Apart from garnet, amphibole can also cause REE fractionation, yielding a concave-up HREE pattern as seen in many TTG rocks. Foley *et al.* (2002) found that TTGs typically have low Nb/Ta ratios and showed that these are a clear pointer to amphibole, either in a cumulate or in the residue. They demonstrated that such cumulate or residual amphibole would also lead to the high La/Nb ratios (the negative Nb anomaly) seen in TTGs, and concluded that these rocks were probably the product of the melting of amphibolite, i.e. metamorphosed hydrated basalt.

The hydrated-slab-melting hypothesis can thus account for the major-element and many trace-element features of Archaean TTG rocks. However, it does not offer a simple explanation of certain observations such as the relative enrichment of B, Pb and Li seen in the most ancient crustal rocks (for Pb see Figs. 25.1 and 26.3(a)). These elements are particularly transported by fluids and their enrichment is therefore proof that dehydration from the slab, or part of it, played a role in the formation of TTG magmas (Kamber *et al.*, 2002; Condie, 2005; Kleinhanns *et al.*, 2003). The last authors proposed a more intense dehydration from slabs in the Archaean than today. Correspondingly, water-saturated magmas that originated in the mantle wedge underplated the lower crust and underwent crystallization differentiation. If this occurred at 40 to 80 km depth and 700 to 800 °C, the cumulate would be dominated by garnet and amphibole, with clinopyroxene, orthopyroxene and minor plagioclase. A melt in equilibrium with such an assemblage would have all the major TTG characteristics: Mg depletion (complementary to its abundance in the mafic cumulate), a highly fractionated REE pattern with depleted HREEs (consumed by garnet and amphibole) and an absent or small Eu^* anomaly, depending on the mass balance of plagioclase and mafic components in the residue. Kleinhanns *et al.* (2003) speculated that a more intense hydrothermal activity at Archaean mid-ocean ridges was the ultimate cause of the different types of dominant granitoids that existed in the Archaean compared with today. Clearly variations in these models are possible, including fluid-induced (flush) melting within the slab itself.

Irrespective of which concept will stand the test of future studies, it is important that essentially all these models envisage a subduction-related environment as the principal site of formation of ancient crust provinces, as for younger ones, so that the transition could have been gradual. Indeed, seismic and geochemical studies have revealed traces of ancient subduction (e.g. Calvert *et al.*, 1995; Smithies *et al.*, 2005). de Wit (1998) discussed arguments for and against ancient plate tectonics and surmised that the "geologic evidence in favour of Early Archaean plate tectonic[s] is more than compelling". This is the background for the discussion of related problems hereafter in this book (Chapter 28).

Underplating

Lower-crustal xenoliths indicate that mafic mantle-derived magmas have on occasion intruded into mature crust and assimilated crustal matter (Section 26.4). Also, the elemental and isotopic characteristics of upper-crustal, e.g. granitic, rocks in many cases indicate a contribution by mantle magmas (Section 26.2). To account for these observations, a mechanism of crust–mantle interactions termed "underplating" is invoked. This takes place when mafic magmas ascend as far as the crust–mantle boundary and then intrude sideways into a giant sill, because of a difference in densities and/or because the boundary is a zone of weakness. Some portions of such magmas may intrude into the crust.

In principle, underplating could operate in both subduction and non-subduction environments. In the latter case OIB-like magma sources could play a role, and this means that subduction zones are not the sole providers of the continental crust. Trace-element signatures typical of arc magmas and of the continental crust at large, such as Nb depletion (and thereby high La/Nb ratios) and high Pb/La ratios, can be used to distinguish between OIB- and arc-type sources. Barth *et al.* (2000) used La/Nb ratios as a measure of the contribution of OIB-type magma sources to the bulk continental crust and found this to be between 5% and 20%.

As mentioned in Section 26.5, zircon-date clustering gives the impression that crustal growth was episodic rather than steady (Fig. 26.10). Condie (1998, 2000) has interpreted the zircon record as portraying "super-events" of mantle dynamics during which plume activity would be strongly enhanced. Other authors (e.g. Albarède, 1998b) have proposed that the episodic addition of differentiated plume-derived magma to the continents could have produced the episodicity of crustal growth. However, even if the zircon date record truly reflects episodic crustal growth (which is uncertain), it is now clear that the crust that would have formed in such episodes of intensified growth could not have been fed directly from plumes. The plume component in the bulk continental crust, discussed above, is insufficient for this. Instead, plumes would preferentially feed the oceanic crust, as this has always covered a larger surface of the planet than the continents. Therefore in times of more intense plume activity the oceanic crust would have become thicker, and its subduction and related magmatism would have produced continental crust at higher rates than in periods of quiet mantle evolution.

Underplating and the associated intrusion of mantle melts bring heat into the lower crust, which causes crustal metamorphism and in some cases partial melting and the ascent of mainly granitic magmas. Further, heating decreases the viscosity of the lower crust and thus changes the style of crustal tectonism, allowing the flow of rock masses without folding (McKenzie *et al.*, 2000). This also enables gravitational redistribution, such as the sinking of dense upper-crustal

sedimentary and volcanic series into the lower crust, where they become granulites. Thus lower-crustal rocks can have upper-crustal trace-element and isotope fingerprints (e.g. a negative Eu anomaly, Fig. 26.8, or enhanced $^{87}Sr/^{86}Sr$ ratios, Fig. 27.10).

Intracrustal magmatism

Heating of the continental crust by underplating or following tectonic thickening initiates the intracrustal magmatism that generates mostly granitic melts, because the eutectic melt composition of any assemblage containing plagioclase, K-feldspar and quartz lies within the granitic field. The Himalayan peraluminous granites (Section 26.2) are an example. Whereas these occupy only a small percentage of the mass or volume of the upper crust, crustal remelting was a common phenomenon, producing large granite provinces, in the Archaean and early Proterozoic eras. Next to the fractionation of primary crust-forming melts, this is probably the most important process that has, over time, led to the compositional difference between the lower and upper crust.

Under moderate-*PT* conditions (typically $\sim$ 0.7 to 1 GPa and 800–900 °C), the melting of metabasalts, metapelites or metagreywackes produces typically 30 to 40 vol. % of melt, even if a H_2O fluid phase is absent. A greater content of hydrous minerals results in higher melt fractions. An important consequence of intracrustal fractional melting is that it consumes large amounts of heat, which is advected upwards, so that it imposes an upper temperature limit over relatively large crustal domains. This explains the rather uniform temperatures of regional crustal metamorphism (Vielzeuf *et al.*, 1990).

The major-element concentrations of magmas depend chiefly on the composition of their protoliths: the partial melting of metabasaltic rocks yields tonalites or trondhjemites, with higher CaO and Na_2O and lower K_2O concentrations than the granites that formed by melting of metapelites and metagreywackes. These differences readily follow from the depletion in soluble Ca and Na of terrigenous sediments and their secondary K-enrichment (Taylor and McLennan, 1985). The fluid regime and *PT-t* conditions during partial melting also affect the melt composition. This is subsequently modified to varying degrees by the segregation of viscous granitoid melts, i.e. the disaggregated residue entrained by the melt, as well as by the mixing of melt with coeval magmas from other sources and interactions with wall rocks. In contrast with mantle-derived magmas, however, crustal melts are not normally strongly modified by fractional crystallization as they are highly viscous and often not much hotter than their own solidus. They "freeze" at upper-crustal levels, as H_2O fluid exsolves from the melt and the solidus temperature is thereby sharply raised.

The abundances of the major and trace elements, especially of REEs, in protoliths and related melts allow the consequences of intracrustal melting to be assessed. Trace-element abundances of shales, fine-grained sediments and metapelites are nearly uniform and therefore allow the adequate modelling of intracrustal melting and the resulting formation of granites, in particular peraluminous ones. Radiogenic (Sr, Nd) and stable (O) isotope abundances as well as field relationships (the occurrence of granites in metamorphic terrains without any association with basaltic magmatism) indicate that most peraluminous granites could have originated from pure crustal melts. In the case of the Himalayan leucogranites, typical crustal $\varepsilon_{143,\mathrm{INI}}$ values and anomalously high $^{87}Sr/^{86}Sr$ ratios (Fig. 27.9) definitely point to the involvement of high Rb/Sr material, mica, in the generations of the parental melts. The experimentally reproduced reaction

$$\begin{aligned} &22\ \text{muscovite} + 7\ \text{plagioclase} + 8\ \text{quartz} \\ &\rightarrow 25\ \text{melt} + 5\ \text{alkali feldspar} + 5\ \text{sillimanite} + 2\ \text{biotite} \end{aligned} \tag{26.5}$$

describes the fluid-absent dehydration melting of a muscovite-bearing protolith and the production of the high-$^{87}Sr/^{86}Sr$, low-[Sr] subset of Himalayan leucogranites. Tectonically enhanced compaction and feedback mechanisms between melting and deformation may in this case have promoted rapid extraction of the melts, thereby arresting the isotopic exchange between melt and source before complete equilibration, so that the high-^{87}Sr-isotope signature, derived mainly from mica, could have been preserved. Varieties of leucogranites with higher Sr concentrations and lower $^{87}Sr/^{86}Sr$ ratios could have resulted from H_2O-fluxed melting, which would consume plagioclase in greater proportions than muscovite:

$$9\ \text{muscovite} + 15\ \text{plagioclase} + 7\ \text{quartz} + x\ H_2O \rightarrow 31\ \text{melt}, \tag{26.6}$$

where x is the stoichiometric coefficient for the H_2O added to the experiment (Patino and Harris, 1998; Knesel and Davidson, 2002).

The above reactions proceed at moderate pressures; in the case of deep intracrustal melting of metasedimentary rocks, garnet becomes important in the residual mineral assemblage (Vielzeuf *et al.*, 1990):

$$\begin{aligned} &\text{muscovite} + \text{biotite} + \text{plagioclase} + \text{quartz} \\ &\rightarrow \text{garnet} + \text{K-feldspar} + \text{melt} \end{aligned} \tag{26.7}$$

and

$$\begin{aligned} &\text{biotite} + \text{alkali feldspar} + \text{quartz} + \text{plagioclase} \\ &\rightarrow \text{garnet} + \text{K-feldspar} + \text{melt}. \end{aligned} \tag{26.8}$$

Rudnick and Presper (1990) modelled REE partitioning between melts and residue in the course of partial melting of a metapelitic protolith. A very steep REE pattern, with high La/Yb values ~ 100 (a consequence of melting in the garnet stability field), and a pronounced negative Eu anomaly were obtained for the melt, while the model residue had a flat REE pattern with La/Yb ~ 1 and a weak positive Eu anomaly. Real crustally derived granites have much less fractionated REE patterns than the model, and the discrepancy can be reconciled by assuming that the separation of melt and residue phases was incomplete: viscous granitic melts could have trapped residue and ascended as a mush, and some melt could have stayed behind in the residue (e.g. Jackson *et al.*, 2003 and references therein).

Rare earth element fractionation affects the evolution of the Sm–Nd and Lu–Hf isotope systematics. With the efficient separation of intracrustal melts from a garnet-bearing residue, the lower crust would be expected to develop high $^{143}Nd/^{144}Nd$ and, in particular, $^{176}Hf/^{177}Hf$ ratios, and the upper crust lower ratios. Contrary to this expectation, the $^{176}Hf/^{177}Hf$ versus $^{143}Nd/^{144}Nd$ terrestrial array (Fig. 27.13) shows the lower- and upper-crustal materials to be similar in these systematics: the preferential partitioning of Lu into garnet must have been greatly diminished or may not have occurred at all. This can only be the result of inefficient melt–residue separation, as assumed above in the case of the REE patterns. The observation that intracrustal melting, even when garnet occurs in equilibrium with the nascent melt, does not lead to a crustal-scale REE fractionation between the lower and the upper crust is very important for global models of crust–mantle evolution. With regard to the intracrustal melting of a mafic protolith, the positive Eu anomalies seen in xenoliths are generally interpreted as the result of fractional crystallization and Eu partitioning in plagioclase cumulates rather than as a complementary feature of crustal-scale fractionation (Rudnick and Taylor, 1987).

Delamination

The highly incompatible trace elements (e.g. Rb, Ba, Th) are too abundant in the bulk continental crust to have been delivered by any directly mantle-derived melts (Fig. 25.1). This means that fractionation must have taken place in the course of crust formation and that (probably mafic) cumulates, highly depleted in these elements, were removed from the crust. This is also valid for K, which is moderately incompatible (Tables 24.1 and 26.3).

Such removal of mafic material clearly cannot have occurred via crustal weathering, erosion and subsequent subduction. The concentrations of incompatible elements in GLOSS are similar to those in the upper crust (K, Rb) or even exceed them (Th, Ba). Therefore the subduction of sediments with the GLOSS average composition removes an incompatible-enriched component from the crust and thus deepens the problem.

These observations point to a flux of, presumably mafic, depleted lower-crustal matter from the crust to the mantle. Below this is referred to as delamination, irrespective of the precise transport mechanism. The ultra-high-pressure metamorphic complexes indicate directly that some dense lower-crustal material finds its way into the mantle below mature crustal cratons (Chopin, 2003). The residua after the extraction of granitoid melt or cumulates of the crystallization differentiation of mafic melts in both cases contain dense minerals such as garnet, pyroxene, olivine, rutile and ilmenite (Table 25.1). Lower-crustal or uppermost-mantle-wedge-domains consisting of such matter may become gravitationally unstable and sink into the less dense underlying mantle.

This delamination mechanism could be promoted in situations where the base of the crust is particularly hot, so that the crustal structure is weakened. The tectonic settings for this include crustal underplating by plume magmas, rifting and subduction leading to arc magmatism. Isotopic and chronological arguments, e.g. similar mean ages of the upper and lower crust, indicate that these reservoirs evolved together and therefore preclude a substantial delamination flux beneath mature crustal cratons; this would cause rejuvenation of the lower crust. The delamination process would therefore have particularly affected young or nascent continental crust, not only by removing the mafic component but also by stimulating crust-feeding magmatism (Kay and Kay, 1993).

Arcs thus appear to be the most plausible tectonic sites for delamination of the lower crust for several reasons. (1) Delamination in this case does not lead to different evolutionary parameters of the lower and upper reservoirs (see above): both reservoirs are created by the intrusion of basaltic to andesitic melts, intracrustal differentiation and the (almost simultaneous) removal of most of the mafic component. (2) The trace-element signatures of arc magmas intruding the crust fit the respective crustal characteristics (Fig. 25.1); therefore intracrustal fractionation produces a crust that is not only enriched in incompatible elements but also has the "correct" abundance pattern. (3) A crust base rich in newly formed cumulate matter would be mechanically weak, being close to the solidus temperature. (4) A cold strong delamination-resistant subcontinental mantle is absent below the arcs. (5) Drag by the downgoing slab may assist the process and also stimulate the ascent and decompressional melting of mantle wedge material (Section 25.7).

A further mechanism that enables the foundering of lower-crustal material into the subcontinental mantle is lower-crust subduction during continental collision, as indicated by crustal xenoliths delivered to the crust by mantle melts and also by ultra-high-pressure rock units in mountain chains.

The net flux of delaminated crustal matter appears to have been quite large (Arndt and Goldstein, 1989; Jull and Kelemen, 2001; Kelemen *et al.*, 2003). This is illustrated by a model in which the incompatible trace-element enrichment in the continental crust is achieved by partial melting alone, without fractional

crystallization. The model melt fraction required for this is ~ 0.01 (Section 28.3). This is much lower than the melt fraction of ~ 0.1 estimated from the major-element compositions of arc-related magmas (Section 25.7). The discrepancy could be resolved by invoking a flux of up to ~ 0.9 of the crust-feeding material back into the mantle. This flux would be made up of dense mafic cumulates, formed in intracrustal fractionation processes and depleted in incompatible elements.

26.8 Summary

The most important questions relating to the history of the continental crust are as follows. Which processes produced the continental crust and what material did these involve? What were the transport and fractionation mechanisms occurring within the crust? How was the crust destroyed? The answers to these questions are fundamental for building a (semi-)quantitative chemical transport crust–mantle model and applying it to achieve a better understanding of the Earth's evolution.

The crustal abundances of indicative trace elements, such as enhanced Pb/La, Ba/Th and La/Nb ratios, point to subduction-related magmatism as the major crustal feeding process (Chapter 25). Moreover, because these arc-related signatures are also typical of ancient crustal rocks (Fig. 26.3(a)), arc-like magmas most probably also fed the crust in the geological past of the planet. During the Hadean and Archaean eras, subduction and arc-melt generation were different from that in the late Proterozoic and Phanerozoic: this difference is reflected in the chemical compositions of the Archaean and post-Archaean crustal rocks. Although the underplating and intrusions of mafic magmas in mature crustal domains are clearly seen to have made some contribution to crustal growth, it appears that subduction magmatism generated by far the greatest crust-feeding flux throughout Earth's history. This simplified solution of the first problem is used in the chemical Earth model (Chapter 28).

Intracrustal magmatism leading to the redistribution of chemical elements between these reservoirs is one of the most complicated geological phenomena. Different sources of heat initiate the magmatism, and highly differing *PT-t* conditions, source and wall-rock compositions and variable fluid contributions strongly affect the melt generation, transport and emplacement processes. This results in a great variety of both extracted magmas and residual matter. Because of this complexity it is difficult to establish whether the lower and upper crust are truly complementary reservoirs.

The continental crust is growing mainly by the addition of arc-generated magmas, but it is also being destroyed. Weathering and erosion along with sediment transfer from the continents are obvious processes. The dissolved and suspended riverine

as well as aeolian sediment fluxes into the ocean are important, as they affect the composition of the oceans and (via subduction) introduce specific elemental and isotopic signatures into the mantle. The composition of this flux is in most respects close to the mean composition of the upper crust.

A comparison of the crustal abundances of incompatible elements (alkali metals but also U, Th, Ba and others) and those in potential crust-feeding magmas shows that the latter are not sufficiently enriched to supply the crust (Fig. 25.1). This means that crust-feeding magmas must have evolved by fractional crystallization and that cumulates sank back into the mantle. The process is known as delamination.

Chapter 27 shows how these processes, through geological time, have left their mark in the heterogeneous isotope ratios of reservoirs.

27

Isotopic records of the evolution of Earth's accessible reservoirs

27.1 Introduction

In this chapter we discuss the present-day isotopic characteristics of the principal terrestrial reservoirs and the evolutionary trends that could have led to their diversity, starting from a common chondrite-type origin. Ultimately, these data allow the modelling of Earth's evolution. The main reservoirs considered in this book are the core (COR, Chapter 18), the core–mantle transition zone (D″ or DDP, Chapter 19), the depleted MORB-source mantle (DMM), the continental crust (CCR) and the atmo-hydrosphere (AHS). Of these the latter three can be considered to be the Earth's accessible reservoirs (EARs), as they can be directly or indirectly sampled, and these are the main reservoirs discussed below. The two silicate reservoirs, DMM and CCR, constitute the major part of the bulk silicate Earth (BSE). This is generally considered to have chondrite-like relative abundances of the refractory lithophile elements, and hence the name CHUR (chondritic uniform reservoir) is also used.

The complexity of the terrestrial transport processes discussed in Chapters 24–26 in many cases prevents the reconstruction of remote source domains using the chemical compositions of the sedimentary or magmatic rocks that resulted. However, isotope ratios preserve a unique record of the chemical composition and evolution of the sources, and reading this record is the major aim of isotope geochemistry and geochronology. These are multifarious branches of Earth sciences, and in this chapter we mainly (but not exclusively) concentrate on how radiogenic isotope systematics shed light on both the composition and evolution of major terrestrial reservoirs.

Thus, radiogenic/stable isotope ratios in young oceanic basalts directly represent a fingerprint of their mantle sources, as since eruption there has not been time for further radiogenic isotope ingrowth. That is why the mantle, even including its deep regions, can be considered an accessible reservoir. Similarly, the isotope

ratios of young sedimentary rocks yield the average of their continental source regions even if the weathering and transport processes fractionate the element ratios.

The ingrowth of radiogenic isotopes in rocks is governed by the time-integrated ratios of radioactive parent isotopes and stable daughter isotopes ($^{r}R/^{s}D$). Radiogenic isotope systematics in which the parent and daughter isotopes belong to elements that behave very differently in magmatic processes are particularly useful in tracing the history of terrestrial reservoirs. One of the most fundamental problems to which radiogenic-isotope systematics are applied is the depletion of the mantle in incompatible elements and the growth of long-lived reservoirs that are enriched in these elements. Among EARs, this is the continental crust alone. In the Earth as a whole, the inaccessible D″ is considered as another ancient enriched reservoir complementary to the mantle, with characteristics that can be evaluated within the frame of the chondritic Earth model and from noble-gas isotope systematics.

In the ^{147}Sm–^{143}Nd systematics the daughter, ^{143}Nd, belongs to a lighter REE than the parent ^{147}Sm, and LREEs are more incompatible than HREEs (Fig. 24.8). In ^{176}Lu–^{176}Hf the parent is a heavy REE and the daughter is a more incompatible high-field-strength element (HFSE). Therefore the Sm/Nd and Lu/Hf ratios in mantle residues are higher than they were in the mantle reservoir before melting. As a result, the ^{143}Nd/^{144}Nd and ^{176}Hf/^{177}Hf ratios in a depleted mantle reservoir grow more rapidly than in an undifferentiated chondritic reservoir. The melt, its complement, has lower Sm/Nd and Lu/Hf ratios than the source rocks; therefore in the continental crust, sourced by mantle melts, the ^{143}Nd/^{144}Nd and ^{176}Hf/^{177}Hf ratios evolve the most slowly of all.

The behaviour of the ^{87}Rb–^{87}Sr systematics is antithetic to this. The parent isotope belongs to an alkali metal more incompatible in mantle melting than Sr, which includes the daughter isotope. The ingrowth of the ^{87}Sr/^{86}Sr ratio is expected to be fastest in the continental crust and slowest in the depleted mantle. The ^{143}Nd/^{144}Nd and ^{87}Sr/^{86}Sr isotope ratios of the mantle and crustal reservoirs therefore give us an insight into the history of mantle melting and crust generation.

The U–Th–Pb isotope systematics are more complicated: in an ancient object the growth of the ^{207}Pb/^{204}Pb and ^{206}Pb/^{204}Pb ratios describes a curve, with an initially faster growth of the ^{207}Pb/^{204}Pb ratio (owing to the fast decay of ^{235}U) and after $\sim$ 3 Gyr ago the increase in the ^{206}Pb/^{204}Pb ratio is more rapid than that for ^{207}Pb/^{204}Pb (because of the comparatively rapid depletion of ^{235}U by decay, Fig. 10.3). The fractionation behaviour of the trio Th, U and Pb in terrestrial processes is also more complicated than those of the Rb–Sr, Sm–Nd and Lu–Hf duos. Thorium and uranium are highly incompatible elements in mantle melting, and

lead less so: it has a similar incompatibility to Ce and La (Table 24.2). However, in subduction zones Pb shows strong partitioning into fluids and is therefore found to be enriched in arc volcanics and in the continental crust (Fig. 25.1). In weathering processes and sediment transport, Th is insoluble whereas U is mobile, as UO_2^{++}, in oxidizing conditions but immobile in reducing environments. Lead is moderately soluble in weathering. In different ways, all these features are reflected in the Pb-isotope characteristics of the Earth's accessible reservoirs.

Noble-gas abundances and isotope ratios play a unique role in the study of mantle dynamics and evolution. The reason is that the Earth was highly degassed and lost atmophile elements in its very early history (Section 16.2) and is therefore extremely depleted in these elements. Even small additions of radiogenic, fissiogenic or primordial isotopes are readily seen above this very low background. The noble-gas family contains several radiogenic and fissiogenic daughters: ^{4}He is the particle emitted in α-decay of (predominantly) U and Th; ^{3}He and ^{21}Ne are yielded by nuclear reactions; ^{40}Ar is the decay product of ^{40}K; Xe has a radiogenic isotope (^{129}Xe from extinct ^{129}I) as well as fissiogenic ones (^{131,132,134,136}Xe from live ^{238}U and extinct ^{244}Pu). Noble gases thus provide a window on the occurrence and distribution of their respective radioactive (and incompatible) parent elements in the mantle, as well as on the degassing history of the Earth.

It is, further, important to note that during partial melting the noble gases behave as incompatible elements even at high pressures (Hiyagon and Ozima, 1986; Schmidt and Keppler, 2002; Heber *et al*., 2007) and therefore magmatism appears to be an efficient process for the degassing of the solid Earth. While He is continuously dissipated from the atmosphere, the heavier noble gases are retained in it, so that it has become the main reservoir of these elements.

While magmatic and weathering processes differentiate trace elements and lead to variations in isotope ratios, the mixing of materials with different isotope signatures can produce ranges of intermediate compositions or an entirely rehomogenized composition. In mixing arrays, data from several different isotopic systematics in some cases allow "end-members" of this mixing to be characterized and identified. In this context it is worth noting that the U-, Th–He- and Ne-isotope systematics and terrestrial xenology are unique in that the mixing of the depleted MORB-source mantle and the enriched crustal end-members does not produce the isotope signatures observed in most OIBs.

Although this section is chiefly focussed on isotope abundances and their interpretation in the solid Earth, some records in sedimentary rocks that yield clues on the evolution of the atmo-hydrosphere will also be discussed. These demonstrate that the evolution of the solid Earth and the atmosphere are closely linked (Section 27.9).

Table 27.1 *Enrichment factors* $[A]_{CCR}$ / $[A]_{DMM}$ *from Table 17.1 for parent and daughter elements of the isotopic systematics discussed in Chapter 27*

Element	Enrichment factor CCR/DMM
Rb	557
Sr	33
Nd	28
Sm	14
Lu	4.7
Hf	19
Pb	474
Th	409
U	277

27.2 The Lu–Hf, Sm–Nd, Rb–Sr and Th–U–Pb isotopic systematics of the mantle

Isotopic signatures of the depleted MORB-source mantle

A comparison of the concentrations of the parent and daughter elements in the depleted MORB-source mantle and in the continental crust (Table 17.1) gives the enrichment factors reproduced in Table 27.1. These enrichment factors show that the continental crust, with a mass about 0.6% of the total mass of the silicate Earth, is the most important reservoir of Rb, Pb, U and Th, and the depletion of these elements in the MORB-source mantle is extreme (Fig. 24.2).

The Pb-, Nd- and Sr-isotope data of the depleted MORB-source mantle (DMM) are summarized in Figs. 27.1(a), (b) and 27.2(a). The Nd-isotope compositions are well above the BSE value and the Sr-isotope ratios are low, as expected in a long-lived depleted reservoir. This, and the inverse correlation between the $^{143}Nd/^{144}Nd$ and $^{87}Sr/^{86}Sr$ ratios seen in Fig. 27.2, confirm the predictions, from the relative incompatibilities of parent–daughter pairs, of how these ratios should develop with time in depleted reservoirs.

The MORB Pb isotope compositions further allow two important observations. First, in the $^{207}Pb/^{204}Pb$ versus $^{206}Pb/^{204}Pb$ plot in Fig. 27.1(b) the relatively compact data field is clearly well to the right of the meteorite isochron (grey line), showing that the DMM has not evolved as a closed system since the origin of the Earth. More precisely, its μ value has increased in the course of geological time. Second, in the $^{208}Pb/^{204}Pb$ versus $^{206}Pb/^{204}Pb$ plot in Fig. 27.1(a), the data indicate development from primordial Pb with a κ value of 3.8 (the assumed BSE value) in an apparently closed system, in contrast with the actual value, $\kappa \sim 2.6$ to 2.8,

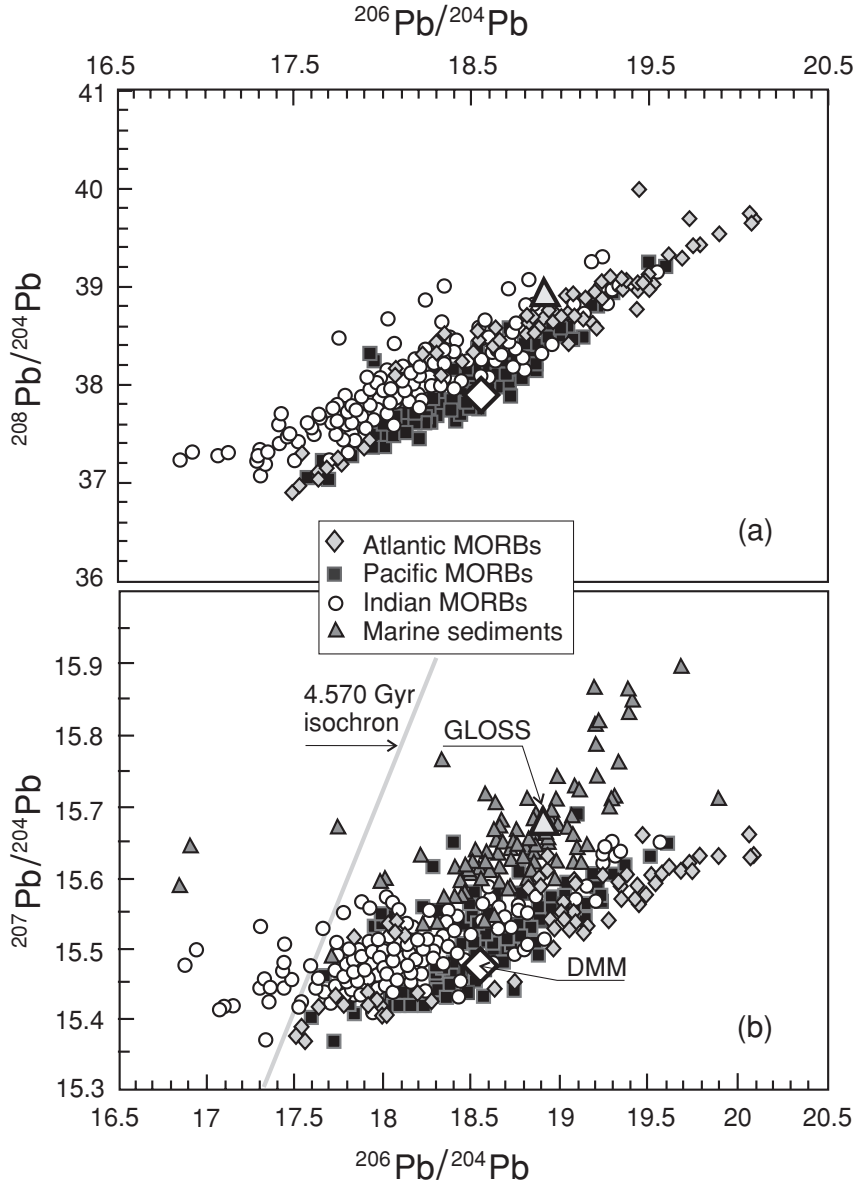

Fig. 27.1 Plots of $^{208}Pb/^{204}Pb$ (a) and $^{207}Pb/^{204}Pb$ (b) vs. $^{206}Pb/^{204}Pb$ for MORB samples. After Hofmann (2003). The average compositions for GLOSS and MORBs are from Plank and Langmuir (1998) and Kramers and Tolstikhin (1997), respectively, © Elsevier Science 2003, reproduced by permission.

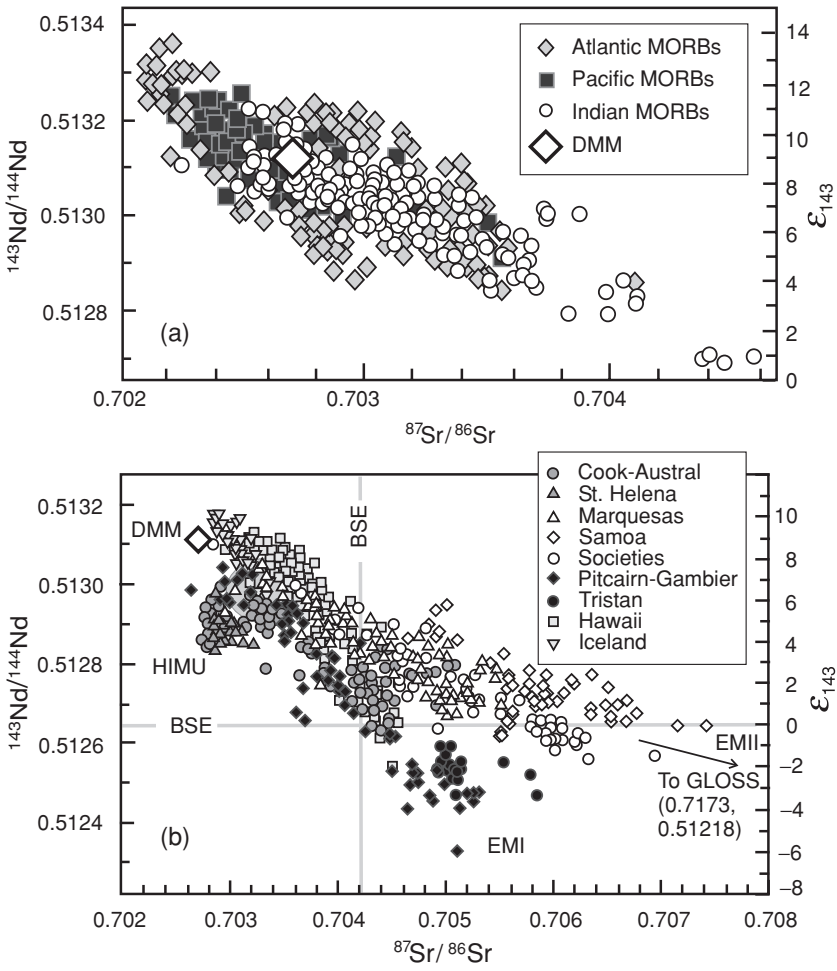

Fig. 27.2 Neodymium–strontium isotope plot for MORBs (a) and OIBs (b) samples. (a) The Sr and Nd compositions of Pacific (the most depleted) and Indian (the least depleted) MORBs are distinct, whereas the Atlantic MORB composition overlaps both. (b) The OIBs show much more heterogeneous isotope signatures than the MORBs. Model-derived BSE compositions are shown (grey lines) for comparison. The positions of the labels HIMU, EMI and EMII show distinct mantle domains that are sources of mantle plumes (Zindler and Hart, 1986). After Hofmann (2003), © Elsevier Science 2003, reproduced by permission.

for the DMM. This is known as the mantle Th/U paradox and is also proof of the open-system behaviour of the DMM (Galer and O'Nions, 1985; O'Nions and McKenzie, 1993). Both problems may be solved via the (reasonable) assumption that U became soluble owing to weathering after $\sim$ 2.2 Gyr, when the atmosphere had become oxidizing (Section 27.9). Uranium from sea water is incorporated in

altered oceanic basalt and is largely subducted, while Pb is mainly released from the slab by fluids (Kelley *et al*., 2005). The μ value of the mantle is thereby raised and its κ value lowered. Meanwhile, Pb isotope ratios in the mantle retain a memory of pre-oxygen times, when U was not preferentially recycled (Kramers and Tolstikhin, 1997; Elliott *et al*., 1999).

Without doubt the relatively large total melt fraction and polybaric melt region involved in MORB generation has helped to iron out small-scale heterogeneities in the source rocks. Also, the similarity of the isotope ratios over thousands of kilometres of ridge length characterizes the depleted MORB-source mantle (DMM) as a relatively homogeneous reservoir. However, a closer look reveals some differences between the major ridge systems, Pacific, Atlantic and Indian, and slight heterogeneities within them, for all three isotope systems. While MORBs from the East Pacific Rise are especially homogeneous (e.g. Meibom and Andersen, 2003), the Indian MORBs plot away from these in Fig. 27.2(a) and the Atlantic MORBs overlap both. Within the Atlantic oceanic basin, the $^{87}Sr/^{86}Sr$ and $^{143}Nd/^{144}Nd$ ratios vary coherently between 0.7022 and 0.7035 and from 12 to 5 ε_{143} units, respectively (e.g. Hofmann, 2003 and references therein), and the spread in the Pb isotopes is also greater than for the two other ridge systems. In the $^{208}Pb/^{204}Pb$ versus $^{206}Pb/^{204}Pb$ plot (Figure 27.1(a)), the Indian MORB field does not overlap that of the Pacific MORBs, and the Indian $^{206}Pb/^{204}Pb$ ratios are clearly lower than those in both the Atlantic and Pacific. The source region of the Indian MORBs thus contains an ancient component with slightly higher Rb/Sr and lower Sm/Nd ratios than the other basins, and relatively high κ and low μ values.

Isotopic signatures and sources of OIB magmatism: the importance of subduction

The mantle provinces that act as sources for OIB magmas show far greater isotopic variations than those of MORBs (Figs. 27.2(b), 27.3 and 27.4), which must reflect long-lived mantle heterogeneities, as first pointed out by Gast *et al*. (1964). In the Nd versus Sr as well as in the Pb-isotope plots, the points appear to radiate in different directions from a single compositional field, which is best represented by the large Hawaii and Iceland plumes. This field is very similar to the MORB source in its Pb-isotope compositions and overlaps with MORBs in its Nd and Sr isotopes, although the most depleted MORB Sr and Nd compositions are not represented in it. Although this compositional field is only poorly resolvable from the DMM in terms of Sr, Nd and Pb isotopes, the two reservoirs have not generally been considered identical and a number of names have been used for this component, mainly PREMA (prevalent mantle) or FOZO (focal zone; see Hofmann, 2003, for a review).

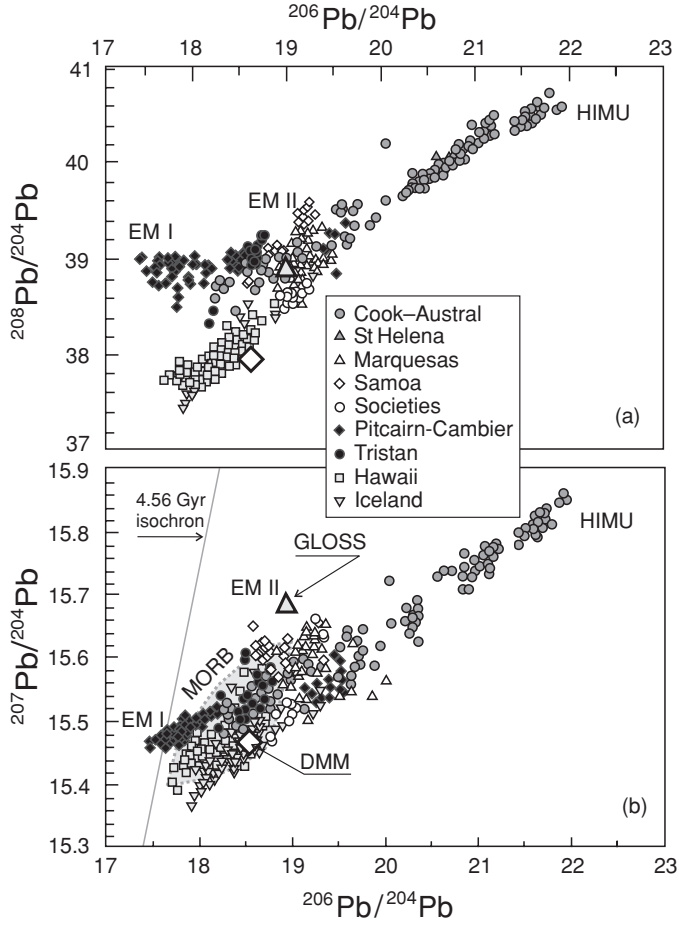

Fig. 27.3 Plots of $^{208}Pb/^{204}Pb$ (a) and $^{207}Pb/^{204}Pb$ (b) vs. $^{206}Pb/^{204}Pb$ for OIB samples. Interpreted in a chronological sense (Section 10.3), $^{207}Pb^*/^{206}Pb^*$ systematics yield a mean age of 1.85 Gyr for the high-μ OIB source (e.g. Allègre and Lewin, 1995, and references therein). After Hofmann (2003), © Elsevier Science 2003, reproduced by permission.

This nomenclature has its roots in models of separate upper- and lower-mantle convection. However, mantle tomography has clearly shown that the large Iceland, Hawaii, Cape Verde and Réunion plumes represent upwelling from the lowermost into the upper mantle (Nataf, 2000; Nolet *et al.*, 2006), and this demonstrates that the lower mantle (PREMA) is depleted, although possibly less so than the typical MORB-source mantle. As on the one hand the DMM is shown to be heterogeneous and on the other hand the PREMA field is very similar to the DMM in Sr, Nd and Pb isotopes, we will combine the PREMA and DMM reservoirs in the following discussions (and in our modelling in Chapter 28) under the name DMM (depleted

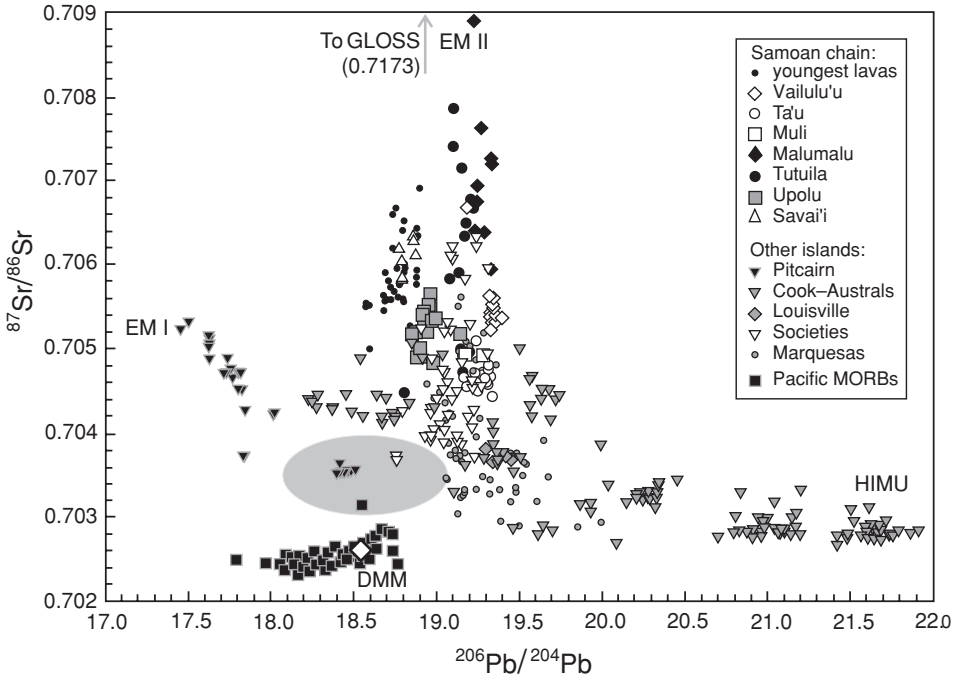

Fig. 27.4 Strontium and lead isotopic compositions for islands of the Pacific Ocean. Note the mixing of several mantle components within the Samoan volcanic chain. EM II dominates the spread in composition for the volcanoes Malumalu and Tutuila. The Upolu volcano has a significant DMM component and Vailulu'u and Ta'u have been contaminated by HIMU from the Cook–Austral underplated Pacific lithosphere. The shaded oval shows the Pb- and Sr-isotope compositions of OIBs with $^4He/^3He$ ratios well below the MORB value. These include large plumes such as Hawaii and Iceland. GLOSS and data for several other islands are shown for comparison. After Workman *et al.* (2004), © 2004 American Geophysical Union, modified by permission.

mixed mantle). Thus in this and the following sections the name DMM should be taken to include the PREMA compositional field.

In the most marked deviations from the DMM isotope composition, correlations between Sr-, Nd- and Pb-isotope patterns emerge that have led to the identification of three further specific component types: EM I, EM II (enriched mantle domains I and II) and HIMU (high-μ domains, Zindler and Hart, 1986), and OIB isotope signatures may be viewed as mixtures between these components and DMM. These components are also readily seen (and are even more pronounced) in isotope compositions of the above elements in melt inclusions from OIBs (e.g. Saal *et al.*, 2005).

The HIMU signature is most pronounced in basalts from the Cook and St Helena islands. It is particularly impressive in Pb isotopes and requires high time-integrated

μ values and relatively low κ ratios: the slope of the $^{207}Pb/^{204}Pb$ versus $^{206}Pb/^{204}Pb$ array yields an apparent age of $\sim$ 1.8 Gyr (Fig. 27.3(b)). In the Nd–Sr isotope plot it is set apart from the main array by having very low $^{87}Sr/^{86}Sr$ ratios and moderately low $^{143}Nd/^{144}Nd$ ratios (Fig. 27.2(b)).

The EM I component is mainly seen in rocks from Pitcairn Gambier and Tristan da Cunha islands. It has a distinct Pb-isotope range, with $^{208}Pb/^{204}Pb$ ratios similar to those of the most radiogenic MORB values, whereas the $^{206}Pb/^{204}Pb$ ratios are anomalously unradiogenic (Fig. 27.3). These mantle domains stand out by the fact of having had a high Th/U ratio, due to strong depletion in U. However, its Nd- and Sr-isotope ratios are below and above the BSE respectively (Fig. 27.2(b)), indicating, in contrast with the U-depletion, a slight time-integrated enrichment in incompatible elements.

The EM II signature is observed in the Marquesas, Samoa and the Society Islands. It departs from the MORB array in the direction of high $^{87}Sr/^{86}Sr$ and intermediate $^{143}Nd/^{144}Nd$ ratios such as characterize GLOSS, the average of globally subducted sediments (Fig. 27.2(b)), and its high $^{207}Pb/^{204}Pb$ ratios at moderate $^{206}Pb/^{204}Pb$ values point to a source that had an enhanced μ value in early Earth history (Fig. 27.3(b)).

As seen from the above discussion, the same anomalous component types are observed in different parts of the globe. Further, the signatures of several components can appear in a single plume over time, such as in the Pitcairn Gambier plume where a signal similar to HIMU appears in addition to the EM I end-member (Figs. 27.3 and 27.4). The different enriched mantle types are thus thought to represent specific types of rock units in the mantle rather than provinces (Hofmann, 2003). A large body of literature deals with the possible processes that might have generated their isotope signatures; the main points are discussed below.

Even though there is little doubt that variably ancient subducted or delaminated materials contributed to plume basalts and caused the deviations in their Sr-, Nd- and Pb-isotope signatures from those of the DMM, the characterization and identification of these materials is a matter of ongoing debate. This is of extreme importance because it will allow an understanding of where, when and how fractionated material was introduced into the mantle and therefore will allow its evolution to be traced in space and time (e.g. McKenzie and O'Nions, 1995). Below, several possible scenarios are discussed and compared.

27.3 Sources of OIB magmatism

According to a popular concept proposed by A. Hofmann and colleagues (e.g. Hofmann and White, 1982; Chauvel *et al.*, 1995), the subduction of metasedimentary and metabasaltic residues after dehydration and partial melting of the oceanic crust

would have introduced "metacrustal" material of variable composition into the depleted mantle. As discussed in Chapter 25, both the initial composition of subducting slabs and their chemical development in the course of subduction depend on a number of highly variable parameters; therefore the compositions of subducted rocks introduced into the mantle are also highly variable, as are the mixing proportions of these and the ambient mantle materials. For example, hydrophilic and incompatible Pb is readily removed from the subducting slab and transferred into the continental crust by arc magmas (Fig. 25.1), thus providing enhanced U/Pb ratios in the residual slab material. If such a slab were stored in the mantle as an isolated domain, it would accumulate highly radiogenic Pb and could become a source of ocean-island basalts showing the HIMU signature (Fig. 27.3(a), (b)). Highly incompatible and moderately hydrophilic Rb is also underabundant in HIMU rocks (Fig. 24.9), leading to their low $^{87}Sr/^{86}Sr$ ratios (Fig. 27.4). The $^{207}Pb/^{206}Pb$ age, ~ 1.8 Gyr for the HIMU source (see the previous section) is then interpreted as the approximate time interval between the subduction of high-μ material and OIB magmatism. This would place limits on the rate of mantle convective stirring.

Other OIB end-members could be partially sourced by a subducted metasedimentary component. Thus Eisele *et al.* (2002) interpreted the isotopic (Os, Pb, Hf, Nd, Sr systematics) and trace-element data obtained for Pitcairn basalts, which define the EM I mantle domain, in terms of multicomponent mixing. These authors identified subducted oceanic-crust residue as the major mixing component but also emphasized the contribution of metasediments, both pelagic and terrigenous. Identification of the sedimentary material involved high time-integrated Th/U ratios (up to 14; these are also recorded by the $^{208}Pb/^{206}Pb$ ratios, Fig. 27.3(a), (b)) and somewhat enhanced Lu/Hf values (recorded by the $^{176}Hf/^{177}Hf$ ratios). The latter feature is typical of pelagic metasediments that inherited high Lu/Hf ratios from ocean water (Fig. 27.13).

From a study of the trace-element and Sr–Nd–Pb–He–Os–O isotope abundances in lavas of the Samoan hot spot, Workman *et al.* (2004) concluded that the major chemical and isotopic features of Samoan volcanic rocks could have resulted from the mixing of several mantle materials (enriched, depleted and high-^{3}He). From their mixing model these authors derived a composition for the EM II end-member, i.e. the ancient metasomatized oceanic lithosphere transferred into the deep mantle via subduction or delamination.

Small-volume continental and oceanic alkali basalts (e.g. in the Cameroon volcanic chain; Fitton and Dunlop, 1985) can be strongly similar in their chemical and isotopic compositions. Based on this, McKenzie and O'Nions (1995) presented a quantitative model for their formation. In a first magmatic episode, melts which originated in the DMM via a small degree of melting (well below 0.01) and which are therefore highly enriched in incompatible elements (Eqns 12.4, 12.6)

penetrate into the subcontinental mantle lithosphere, thus producing metasomatized (refertilized) domains. Such domains would age, and their rock units would acquire enriched time-integrated isotopic signatures, set apart from the conservative host reservoir, on a reasonably short time scale, $\sim$ 1 Gyr. The authors noted that such an enrichment could hardly be achieved within a subducted slab because of insufficient fractionation of the parent–daughter elements in slab rocks. Later, a second magmatic event, i.e. partial melting within a given domain, generates continental alkali magmas, whereas delamination of the domain, followed by melting, gives rise to ocean-island and seamount volcanoes. Along with delamination of the mantle lithosphere, delamination of the lower crust could also introduce isotopic heterogeneities into the mantle.

Recently McKenzie *et al*. (2004) developed a new model in which compositions related to a plume source can be distinguished from those that originated in the course of formation of plume melts. Correlations between isotope ratios (unaffected during partial melting or fractionation) and elemental concentrations (depending on both source composition(s) and fractionation) are used to reveal isotopic and elemental heterogeneities in the source region. Solution of the model is possible only if extensive isotopic and trace-element data sets exist for a restricted region and if it is assumed that the plume-source geochemistry was modified in a single event. The model was applied to comprehensive data sets for Theistareykir (Iceland), Kilauea (Hawaii) and the Pitcairn hot spot (Pacific Ocean). The principal outcome from the modelling is the cannibalistic recycling of OIB materials: ancient ocean-island basalts, subducted at some time in the past (400 Myr for the Theistareykir source and 1.2 Gyr for Kilauea) and stored in the mantle appear to be the most suitable materials to generate the presently observed OIBs. There are two surprising features of this solution. The first is the preservation of the subducted OIB without its being affected by the subduction process or mantle convection. The other feature is the absence in these test cases of any obvious evidence of melts from the sediments that are expected to be subducted along with the OIB materials and whose traces emerge in Figs. 27.2 and 27.4.

Thus a number of subduction- and delamination-related scenarios would result in fits to the data. While they have not been firmly established, the most important general observation is that these isotopic-component signatures cannot have been generated by melting and melt differentiation in the mantle alone, as they depart from the geochemical and isotope correlation trends that would be expected in that case. In connection with models of mixing in the mantle, it is also important to realize that the plume source material itself is likely to be heterogeneous ("mingled" rather than mixed) and that the actual mixing probably occurs between melts extracted from the different subsources. This would also help to explain the heterogeneities observed at very small scales.

27.4 Light rare gases in the mantle

Terrestrial U–Th–He–Ne isotopic systematics

Soon after the discovery of primeval solar-type He in the deep Earth (Mamyrin *et al*., 1969; Clarke *et al*., 1969) it became clear that the U–Th–He trio is unique and the He-isotope record is different from other isotopic systematics. As He is continuously degassing from the solid Earth and dissipating from the Earth's atmosphere (Section 20.3), the "complementary" inventory of accessible Earth reservoirs is not valid for He (Mamyrin and Tolstikhin, 1984). Further, air–He contamination or He recycling into the mantle is insignificant, so that subtle He fluxes can be clearly traced.

In ordinary terrestrial rocks ^{4}He and ^{3}He are produced in the proportion $^4\mathrm{He}/^3\mathrm{He}_{\mathrm{RAD}} \sim 10^8$ by radioactive decay (^{4}He) and by the natural nuclear reaction $^6\mathrm{Li}(\mathrm{n}, \alpha)^3\mathrm{H}$ followed by $^3\mathrm{H} \rightarrow \beta^- \rightarrow {}^3\mathrm{He}$, for which the half-life $\tau_3 = 10.2$ yr. The sources of the natural neutron flux are (α, n) reactions and the spontaneous fission of ^{238}U (Mamyrin and Tolstikhin, 1984). The above production ratios exceed typical mantle values by a factor 1000. Therefore mantle ^{3}He may be considered as essentially a primordial isotope, and mantle ^{4}He as a partially primordial and partially radiogenic one. The closed-system $^4\mathrm{He}/^3\mathrm{He}$ ratio is approximately given by Eqns (10.7), where $^{\mathrm{r}}R$ includes ^{238}U, ^{235}U and ^{232}Th, $B_{\mathrm{r}} = 1$ and Y_{r} and λ_{r} are taken from Table 28.1. In terrestrial environments the least abundant Ne isotope, ^{21}Ne, also includes a considerable nucleogenic component (Leya and Wieler, 1999).

The continental crust, being enriched in the parent elements, is a source of radiogenic He, Ar and other radiogenic and fissiogenic noble-gas nuclides. As a noble-gas reservoir it is, however, insignificant. It is produced from highly degassed matter and only young mantle-derived crustal rocks and related fluids preserve traces of mantle rare gases (Fig. 27.5). As a given crustal domain becomes more mature, generally within ~ 0.5 Gyr after crust formation, radiogenic isotopes with fixed production ratios completely overshadow any mantle rare gas signature (Polyak and Tolstikhin, 1985). Moreover, because of the relatively young mean age of the crust (Section 26.5) and because part of its radiogenic rare gases are lost via magmatism, metamorphism, weathering and diagenesis, the continental crust is also an unimportant reservoir of radiogenic rare gas nuclides, in contrast with their parent isotopes (Table 28.3).

Mantle domains, however, reveal intriguing relationships between solar-type and terrestrial radiogenic He and Ne. A relatively uniform $^4\mathrm{He}/^3\mathrm{He}$ ratio in MORBs ($^4\mathrm{He}/^3\mathrm{He} = 86\,000 \pm 8000$) contrasts with much more variable ratios in basalts derived from mantle plumes (Fig. 27.6). These can be quite low, a factor ~ 5 below those seen in MORBs (Kurz *et al*., 1982a). This is also valid for mantle Ne: the $^{21}\mathrm{Ne}/^{22}\mathrm{Ne}$ ratios in plume-related rocks, e.g. 0.03 in the Iceland and Kola plumes,

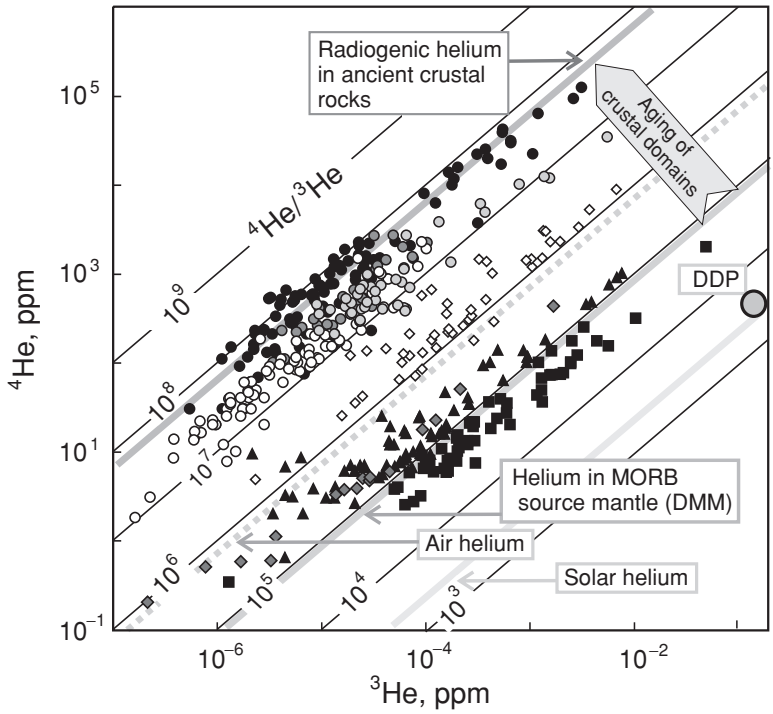

Fig. 27.5 Helium-isotope evolution in fluids of crustal domains of different ages, shown for comparison with the values for mantle domains. Black circles, pre-Ryphean Eastern European Platform (EEP); dark-grey circles, Baikalides (Timan-Pechora region); light-grey circles, parts of the EEP activated in the Ryphean-Paleozoic; open circles, Hercynides (Scythian plate, Cis-Caucasian foredeeps); open diamonds, Cis-Caucasian Hercynides activated in Cenozoic; black diamonds, Hercynian Central French Massif activated in Cenozoic; black triangles, Italian volcanic areas; black squares, Iceland "Hot Spot". Concentrations are in ppm by volume. The ^{4}He/^{3}He ratios vary insignificantly in fluids of a given crustal domain, in contrast with the highly variable concentrations. These ratios increase with the time elapsed after magmatic activity ceased (as indicated by the grey arrow in the top-right corner of the plot), from regions with high present-day magmatism and mantle-derived He in fluids to ancient plates (where magmatism ceased ~ 1 Gyr ago) with radiogenic He in groundwaters. Only data for Europe are shown, but a similar pattern is characteristic of other continents too. Note that the ^{4}He/^{3}He ratios in the He from Iceland volcanics cannot be reproduced by the mixing of DMM-He with the He of any crustal domain(s) or atmospheric He; however, the assumption of a small flux of He and/or He-bearing material from D$''$ (model-derived He concentrations are shown, 10^{-6} cm^3 STP g^{-1}, Table 28.3) allows the abundances of He isotopes in the mantle to be reconciled. After Azbel and Tolstikhin (1988), Polyak and Tolstikhin (1985) and Polyak *et al.* (1979).

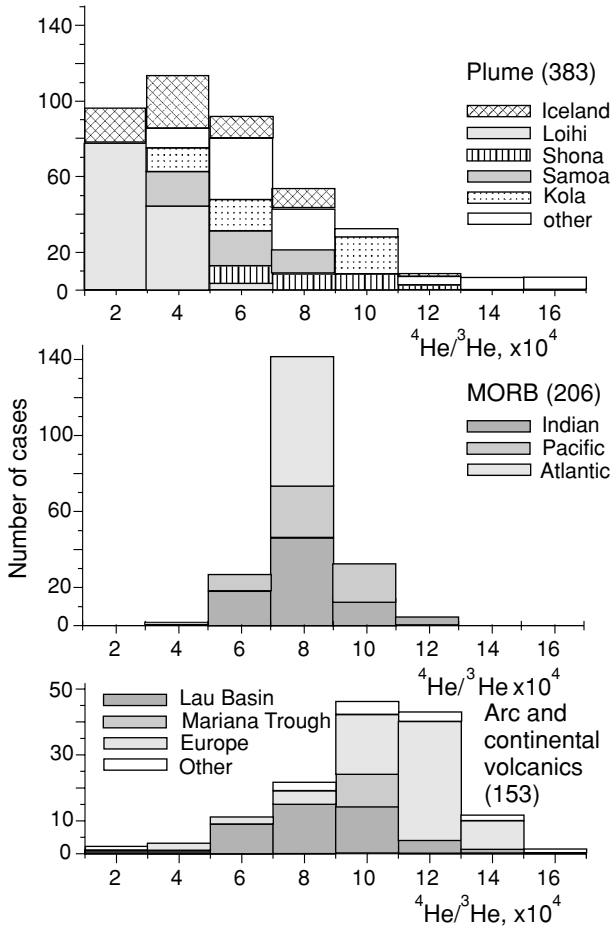

Fig. 27.6 Histogram of He-isotope compositions in plume, MORB, arc and continental volcanics. Note the narrow range of ^{4}He/^{3}He ratios in the MORB samples, in contrast with their highly variable concentrations, $10^{-13} < [^3\text{He}] < 10^{-9}$ cm^3 STP g^{-1}. Back-arc rocks generally show higher ratios, indicating a contribution of crustal radiogenic He. The ^{4}He/^{3}He ratios in plume-related rocks vary within a wide range, but a number of plumes show low ratios that cannot be reproduced by mixing MORB-source mantle He and crustal He. After Tolstikhin and Hofmann (2005); see the data sources in that paper, © Elsevier Science 2005, reproduced by permission.

are well below the MORB end-member value, 0.06 (Moreira *et al*., 2001; Tolstikhin *et al*., 2002).

Thus, in contrast with the isotope systematics discussed in Section 27.3, the plume-related noble-gas isotope signatures cannot have been produced by the mixing of MORB-source mantle and any subducted matter.

Decoupling of rare gases from other isotopic families: the need for a reservoir unrelated to subduction

The above important conclusion is further strengthened by the observation that the $^{4}He/^{3}He$ (and $^{21}Ne/^{22}Ne$) ratios in plume materials are decoupled from other isotopic systematics. The mantle sources of the Hawaii and Iceland plumes, which of all plume sources are the most similar to the MORB source in their Sr-, Nd- and Pb-isotope compositions, are the most different from the MORB source in He isotopes (Figs. 27.6 and 24.9). In contrast, some of the plumes with anomalous Sr, Nd and Pb isotopes, such as Samoa, which has a strong EM II signature, have $^{4}He/^{3}He$ ratios closer to MORB, overlapping with it.

Considering MORB, and using the mean Atlantic isotopic ratios as a reference, in Iceland quite low $^{4}He/^{3}He$ ratios in rocks and fluids (Figs. 27.5 and 27.6) accompany enhanced $^{206}Pb/^{204}Pb$ and $^{87}Sr/^{86}Sr$ ratios. Along the Atlantic ridge to the south, in most Azores and Sierra Leone rocks all three ratios exceed the average MORB values. Still further to the south, at Shone, the relationships between the trio are again similar to those seen in Iceland rocks (Kurz *et al*., 1982b; Graham, 2002).

Within plumes, interrelationships between isotopic signatures of He, Ne and other daughter nuclides have occasionally been observed. The U–Th–Pb systematics appear to be the most promising for finding recurring patterns; the parent isotopes are the same and Pb is more depleted in the DMM than Sr and Nd. Indeed, Eiler *et al*. (1998) reported a co-variation of ^{3}He and the enhanced $^{208}Pb^{*}/^{204}Pb$ ratios on Hawaii, which could be modelled as the three-component mixing of distinct end-member compositions. They considered that a contribution of primitive mantle material caused an enhancement of both ^{3}He and $^{208}Pb^{*}/^{204}Pb$. However, this type of relationship has not been observed in other plumes yet; therefore it is not clear whether excess $^{208}Pb^{*}$ is a real feature of ^{3}He-rich material or whether the observed co-variation results from occasional mixing between $^{208}Pb^{*}$-rich and ^{3}He-rich "carriers" belonging to different mantle domains. For example, Moreira *et al*. (1999) showed that the highest abundances of ^{3}He in lavas of the Azores archipelago coincided with enhanced $^{206}Pb^{*}/^{204}Pb$ ratios due to the mixing of subducted crust (a source of $^{206}Pb^{*}$) and enriched deep-mantle material (^{3}He).

As discussed in Section 27.3, in OIBs, Sr-, Nd- and Pb-isotope deviations from the DMM signatures are generally considered as resulting from subducted or delaminated matter stored in the mantle (up to $\sim$ 2 Gyr ago). For ^{3}He, this presents problems. The recycled materials are either almost He-free or contain radiogenic He, so that their $^{4}He/^{3}He$ ratios are expected to exceed both the MORB and OIB values. The subduction of continuously accreting ^{3}He-rich cosmic dust together with oceanic sediments has been proposed by e.g. Anderson (1993) as a mechanism for introducing He with low $^{4}He/^{3}He$ ratios into the mantle. This mechanism is

unlikely, however, as He is easily released from the tiny dust grains, so that little He could survive the devolatilization and partial melting of subducting slabs (Hiyagon, 1994). Also, plume-like low ^{4}He/^{3}He ratios are not at all typical for arc magmatic rocks and fluids (Hilton *et al.*, 2002). Thus it would appear that no ^{3}He-enriched matter can be introduced into the mantle by subduction or delamination. This is in accord with the observed decoupling of high-^{3}He material from Sr, Nd and Pb carriers and highlights the need for a specific noble-gas-bearing reservoir (Graham, 2002). The entrainment of noble-gas-rich material or a diffusion flux from such a reservoir could maintain the noble-gas isotope abundances in the MORB source mantle (Chapter 28).

Characteristics of the ^{3}He-bearing reservoir and solar-type light rare gases

The low initial ^{4}He/^{3}He ratio ($< 15\,000$) required for a ^{3}He-bearing reservoir must be due either to a low time-integrated (U + Th)/^{3}He ratio or to a young age.

The latter alternative is in contradiction with analyses on ancient rocks such as 370 Myr ultramafic–carbonatitic intrusive complexes (Tolstikhin *et al.*, 2002), Archaean komatiites (Matsumoto *et al.*, 2002) and other examples. Therefore the required deep-seated ancient reservoir must have a low time-integrated (U + Th)/^{3}He ratio.

As such a reservoir was formed early in Earth history, the time-integrated (U and Th)/^{3}He ratios in it must always have been at least a factor ~ 100 lower than the DMM values (Table 28.3). As was shown in Section 24.3, no large reservoir with $[U] \ll [U]_{DMM} \approx 5$–$7$ ppb exists in the silicate Earth. Also, as discussed above, the relations between U–Th–He and other isotopic systematics do not point to a reservoir that is much more depleted in incompatible elements than the DMM (e.g. Graham, 2002).

It is now generally accepted that the mantle was almost completely degassed after the Moon-forming giant impact (Section 16.2), and thus material with such a high ^{3}He concentration can only be of post-giant-impact extraterrestrial origin. Its identification from He isotopes alone is hardly possible, because He has only two stable isotopes. In this respect a major advance has come from Ne-isotope studies (Honda *et al.*, 1993): Ne has three isotopes and, after correction for atmospheric contamination, Ne-isotope compositions in most MORB and plume-related samples are similar to those observed in implanted solar gases, plus a nucleogenic ^{21}Ne component (Table 11.3). After correction for elemental fractionation, a ^{3}He/^{22}Ne elemental ratio $\sim 7 \pm 3$ is derived for MORBs and OIBs (Graham, 2002). This is only slightly above the solar value, 3.6 (Table 11.3). The difference could result from the better retention of He, which is more soluble in melts than Ne, in the course of mantle degassing (Azbel and Tolstikhin, 1990). Overall, an important inference

from these observations is that implanted solar gases appear to fit the primordial light-noble-gas component in the mantle best of all.

27.5 Mantle xenology

Xenon, with its five radiogenic and fissiogenic isotopes, has yielded important clues on the loss of the Earth's earliest atmosphere, as discussed in Chapter 20. Here we consider these isotopes in the mantle in order to shed Xe-light on the formation of the noble-gas-bearing ancient mantle reservoir and on the timing and scales of mantle degassing. To do this the parents of the fissiogenic Xe isotopes must be identified, which is possible using the $^{136}Xe/^{130}Xe$ versus $^{134}Xe/^{130}Xe$ isotope plot (Fig. 27.7). The regression line touches the air Xe data point without any forcing, thus indicating the mixing of fissiogenic and atmosphere-type components in the mantle. The spontaneous fission of ^{238}U and ^{244}Pu produces ^{136}Xe and ^{134}Xe in subtly different proportions, shown in the lower panel in Fig. 27.7 as different mixing lines for fissiogenic Xe and air Xe. The regression coincides with the Xe_{ATM}–Xe(U) mixing line, and its error envelope does not overlap the Xe_{ATM}–Xe(Pu) mixing line. This shows a dominance of ^{238}U-fission Xe. From the error limits of the regression, the maximum contribution of Xe(Pu) to fission mantle Xe appears to be up to $\sim 30\%$, and we will use this value below: the ratio $^{136}Xe(Pu)/[^{136}Xe(U) + {}^{136}Xe(Pu)]_{DMM} \approx 0.3$ was suggested by Kunz *et al.* (1998) and was later confirmed by Pepin and Porcelli (2006).

A comparison of these data with the $^{136}Xe(Pu)/^{136}Xe(U)$ ratio in a hypothetical closed-system reservoir quantifies the deficit of mantle $^{136}Xe(Pu)$. Taking into account that all the ^{244}Pu and about half the initial ^{238}U has decayed since the SOS formation and, using the initial ratio of parent isotopes $^{244}Pu/^{238}U$, and the branching ratios and yields B and Y for these isotopes from Table 28.1, we obtain a calculated value for the closed-system ratio:

$$\begin{aligned} {}^{136}Xe(Pu)/{}^{136}Xe(U) &\approx 2({}^{244}Pu/{}^{238}U)_{INI} \\ &\quad \times B_{244}\ Y_{244}({}^{136}Xe)_{244}/B_{238}\ Y_{238}({}^{136}Xe)_{238} \\ &\approx 40. \end{aligned} \tag{27.1}$$

This is ~ 80 times the observed value: almost all the Xe(Pu) has been lost from the silicate Earth, indicating intense early mantle degassing, after which $^{136}Xe(U)$ was replenished by ^{238}U fission, lowering the ratio.

Another important correlation is seen between the $^{129}Xe/^{130}Xe$ and $^{136}Xe/^{130}Xe$ ratios (Fig. 27.8). This gives a presently observed average value of $^{129}Xe(I)/[^{136}Xe(U) + {}^{136}Xe(Pu)]$ equal to 2.7 and, along with the above

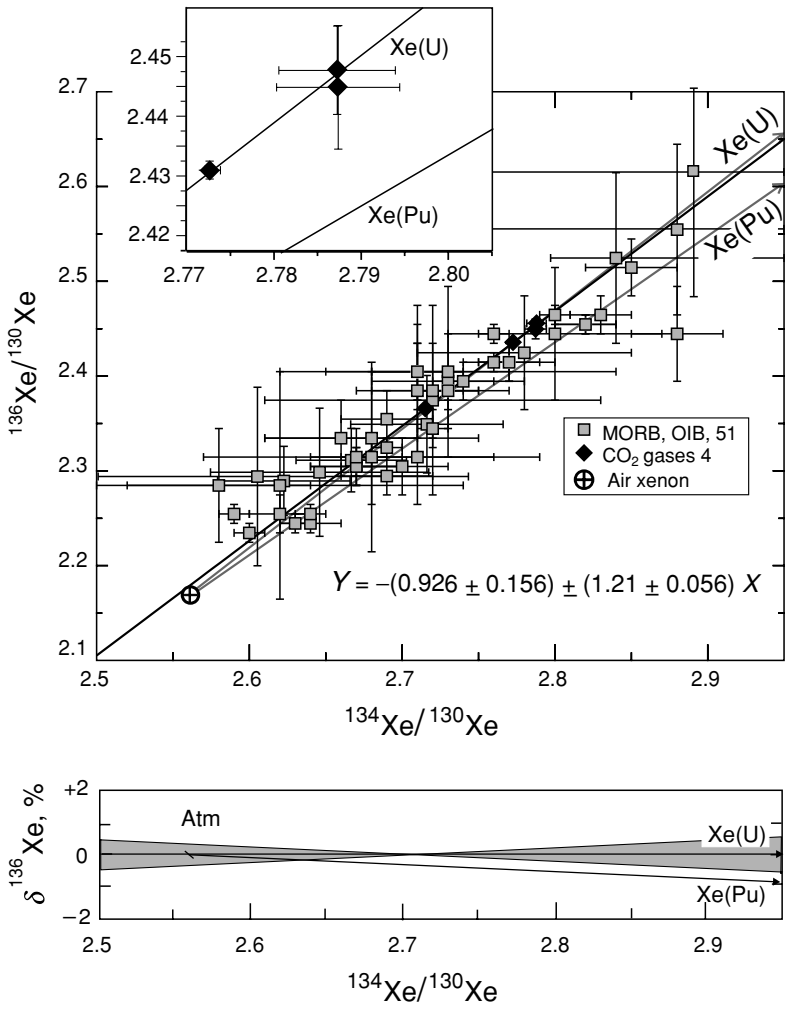

Fig. 27.7 Plots of $^{136}Xe/^{130}Xe$ vs. $^{134}Xe/^{130}Xe$. Top: the best-fit regression line almost coincides with the mixing line for air Xe_{ATM} and fission Xe(U). The equation of the regression line is shown (with 2σ errors). The error bars are 1σ. The inset highlights some CO_2-gas Xe data points that are right on the Xe_{ATM}–Xe(U) mixing line. Bottom: the result of York's (1967) regression of the data shown in the top plot. The vertical scale shows the relative percentage deviation of $^{136}Xe/^{130}Xe$ from the best-fit regression line, $\delta^{136}Xe/^{130}Xe = 100 \times [(^{136}Xe/^{130}Xe)_{sample} / (^{136}Xe/^{130}Xe)_{regression} - 1]$. The uncertainties and error envelope are 2σ and the correlation coefficient is 0.85. The regression-derived $^{136}Xe/^{134}Xe$ ratio, 1.21 ± 0.056, exactly fits the ^{238}U-fission yield of these isotopes, 1.20 ± 0.017, but differs from the ^{244}Pu yield, 1.075 ± 0.006 (e.g. Ozima and Podosek, 2002). After Tolstikhin and O'Nions (1996); see the source data references therein and in Phinney *et al.* (1978), Kunz *et al.* (1998) and Caffee *et al.* (1999), © Elsevier Science 1996, reproduced by permission.

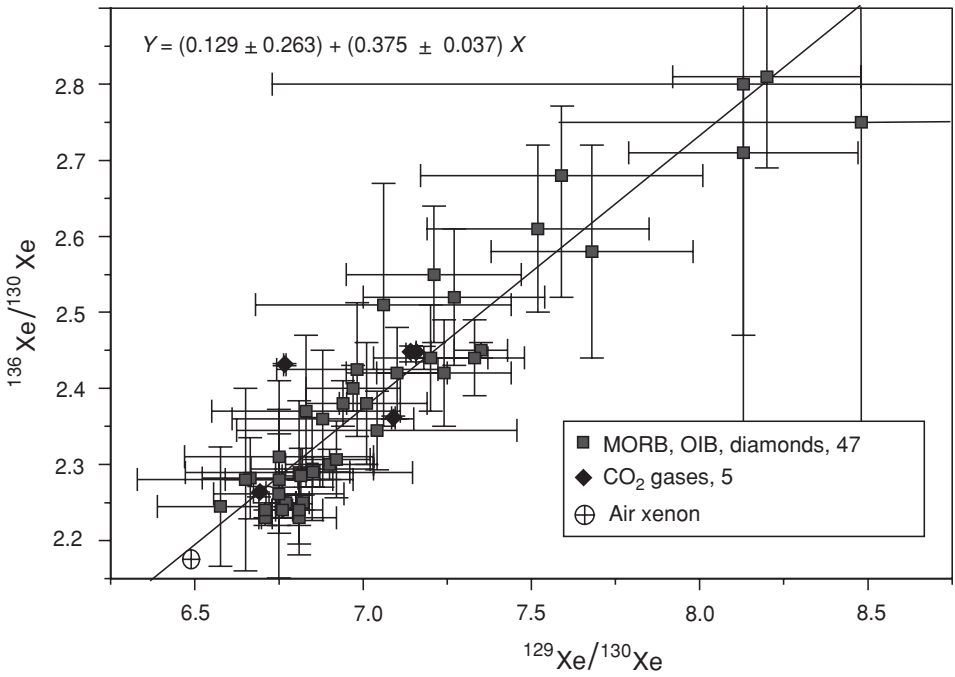

Fig. 27.8 Plot of $^{129}Xe/^{130}Xe$ vs. $^{136}Xe/^{130}Xe$. The equation of the best-fit regression for uncorrelated errors is shown (with 2σ error bars). This correlation determines the ratio $^{129}Xe(I)/^{136}Xe(U + Pu)$ in the present-day mantle as the reciprocal of the slope, 2.7 (see the main text). Other notation and sources of data are the same as in Fig. 27.7. After Tolstikhin and O'Nions (1996), © Elsevier Science 1996, reproduced by permission.

$^{136}Xe(Pu)/[^{136}Xe(U) + {}^{136}Xe(Pu)]_{DMM} \approx 0.3$ this gives $^{129}Xe(I)/^{136}Xe(Pu) \approx 10$ and $^{129}Xe(I)/^{136}Xe(U) \approx 4$.

The $^{129}Xe(I)/^{136}Xe(U)$ ratio for a hypothetical closed system, found by writing down Eqn (27.1) for ^{129}I decay instead of ^{244}Pu fission (substituting $^{129}I/^{238}U_{INI}$ from Table 28.1), is 2700, which exceeds the observed value by a factor ~ 700. This implies an early severe loss of $^{129}Xe(I)$ from the mantle, as in the case of Xe(Pu). As the radiogenic and fissiogenic Xe isotopes are produced in the solid Earth (an early loss of these isotopes from the Earth as a whole has already been discussed in Section 20.3), this qualitative result is more or less trivial. However, the data give a more differentiated perspective of mantle degassing. Fitting the data requires a much longer degassing time scale for the Pu–U–Xe subsystem than for I–U–Xe (e.g. Kunz *et al.*, 1998). A traditional way to reconcile the two subsystems (since the inspiring pioneer paper by Butler *et al.*, 1963) makes use of two mantle reservoirs: (1) an ancient reservoir that contains most of the $^{129}Xe(I)$ and $^{136}Xe(Pu)$ and (2) the convecting continuously degassing mantle (DMM), which communicates

with the atmosphere through volcanism and subduction. The first reservoir is envisaged as being incompletely closed, so that the observed ^{129}Xe(I)/^{136}Xe(U) ratio would result from the "leakage" of ^{129}Xe(I) and some other species, e.g. ^{3}He, into the second reservoir and its mixing with the (mainly) U-fission Xe generated there. We favour the D″ layer (DDP) as the location of the first reservoir (Chapter 19), and its time of formation after SOS (t_{DDP}) can be estimated from the ^{129}Xe(I)/^{136}Xe(Pu) ratio, as follows. Assuming a complete Xe loss before the reservoir's formation and negligible "leakage" afterwards and substituting the relevant parameters from Table 28.1 into Eqn (1.2), we obtain

$$
\begin{aligned}
{}^{129}\mathrm{Xe(I)}/{}^{136}\mathrm{Xe(Pu)} &= \frac{{}^{129}\mathrm{I}/{}^{244}\mathrm{Pu}\exp(-\lambda_{129}t_{\mathrm{DDP}})}{B_{244}Y_{244}\exp(-\lambda_{244}\ t_{\mathrm{DDP}})} \\
&\approx 10, \qquad (27.2)
\end{aligned}
$$

which gives $t_{\mathrm{DDP}} \sim 60$ Myr as the formation time. This is a very rough estimate, which however illustrates that the reservoir would probably have been formed within ~100 Myr after SOS formation, in agreement with estimates from the formation mechanism (Section 19.3), with the core-segregation time scale (Section 18.3) and with that of atmosphere loss relating to the giant impact (Section 20.2).

A degassing model with two mantle reservoirs, constrained by the observed ratios of radiogenic and fissiogenic Xe, suggests extreme degassing of the convecting mantle, with the retention of only a fraction $\sim 10^{-6}$ of its initial abundance of non-radiogenic noble gases (Tolstikhin and Marty, 1998; see Chapter 28). Degassing may be seen as a measure of mantle convection, which is the only mechanism capable of transporting mantle matter to a position close to the Earth's surface, where partial melting and melt degassing can occur. Very fast convection during at least the first 600 Myr of Earth history, i.e. the time interval in which 99% of the ^{244}Pu available in the Earth (Turner *et al*., 2004a) decayed, releasing the daughter Xe(Pu), is therefore implied.

Of the unradiogenic Xe component in the mantle, most appears to be recycled atmospheric Xe (Tolstikhin and Marty, 1998). However, the light Xe-isotope abundances in precisely measured CO_2 gases indeed indicate the presence of non-fractionated SW-like or Q-like Xe (Phinney *et al*., 1978; Tolstikhin and O'Nions, 1996; Caffee *et al*., 1999), and recently such a component has been identified in MORB samples (Pepin and Porcelli, 2006). These results strengthen the case for a non-fractionated initial terrestrial Xe-isotope composition and for Xe fractionation during the early atmosphere loss, in contrast with scenarios envisaging the delivery of fractionated noble gases from the outer solar system (e.g. Owen and Bar-Nun, 2001). Model-derived abundances of extraterrestrial noble gases in D″ imply the

occurrence of Q-like Xe in this reservoir: the $^{3}He/^{130}Xe_{DDP}$ ratio (Table 28.3) is a factor $\sim$ 1000 less than the SW value (Fig. 20.1).

At present the most likely explanation for the mantle noble-gas isotope systematics invokes an ancient noble-gas-bearing reservoir, the source of solar-type He and Ne, as well as early-generated Xe isotopes. Small amounts of material entrained from this reservoir into the DMM are enough to maintain the flux of these species throughout Earth history. The observed spectrum of noble-gas isotope compositions in mantle rocks of various ages could have resulted from the mixing of the noble gases that migrated from their host reservoir into the DMM with their radiogenic component. Such a hypothesis is in accord with mantle-convection models invoking a noble-gas tracer (Samuel and Farnetani, 2003) and offers explanations for several other independent observations (Section 19.1).

27.6 Isotopes of Sr, Nd and Pb in the continental crust

The continental crust is highly heterogeneous in Sr and Nd isotopes (Fig. 27.9). The positions of MORB and crustal data on opposite sides of the BSE composition clearly show the complementarity between the MORB-source mantle, which is depleted in incompatible elements (LREEs and Rb in this case), and the continental crust, which is enriched in these elements (Table 17.1).

In the upper crust the present-day ε_{143} values vary from $\sim +10$, observed in young mantle-derived granitoids, down to a relatively sharp lower limit at $\varepsilon_{143} \sim -22$. As the crustal REE patterns (and thus the Sm/Nd ratios) are relatively uniform (Table 26.3), the heterogeneity in ε_{143} must mainly reflect differences in age. However, the mixing between ancient rocks with negative ε_{143} values and mafic materials with positive ε_{143} similar to the mantle could also generate intermediate values (Section 26.2). The I-type granitoids deviate less from the mantle rocks than the S-type granitoids.

Neodymium-isotope compositions of lower-crustal xenoliths vary within the same range as the upper-crustal rocks, a number of samples being well below the mean crustal value (Fig. 27.10). This is in accord with the observation that the REE patterns are not much changed in intracrustal melting (Section 26.4). Generally, the Sm/Nd ratios also are not significantly affected by metamorphic processes or weathering and sedimentation. Because of this important feature, the model age of a rock sample may be found directly from measurement of its $^{143}Nd/^{144}Nd$ and Sm/Nd ratios (Fig. 21.5). A large number of Nd model ages allows a relatively reliable estimate of the mean age of crustal reservoirs (DePaolo *et al.*, 1991).

A comparison of the distribution of the Sm–Nd data for lower- and upper-crustal sample sets shows that these reservoirs have broadly similar mean model Nd ages (Figs. 27.9 and 27.10). This means that the delamination of a mafic cumulate

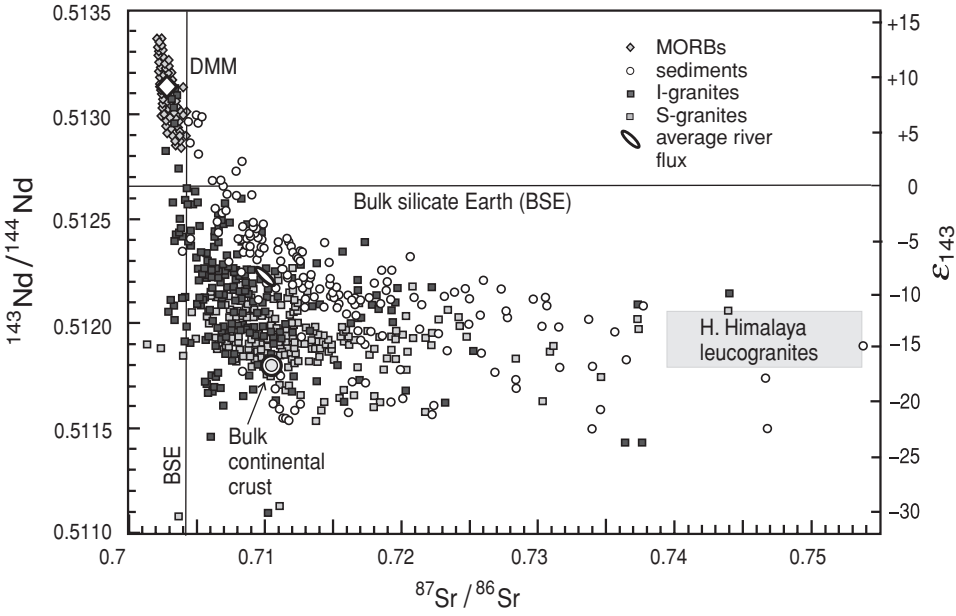

Fig. 27.9 Neodymium vs. strontium isotope plot for upper-crustal rocks. The I-granites are those produced by differentiation of a mafic melt and S-granites by the melting of (meta)sedimentary rocks (e.g. Himalayan leucogranites). Mid-ocean ridge basalts (MORBs) are included for comparison. Average ratios for the river-load flux and the bulk continental crust ($^{87}Sr/^{86}Sr \approx 0.710$, $\varepsilon(Nd) \approx -17$, see Table 28.2) are also shown. Some samples, for example the Himalayan leucogranites, have $^{87}Sr/^{86}Sr$ ratios > 0.8 and plot outside the figure. After Kostitsyn (2000), also using data from Goldstein and Jacobsen (1987, 1988), LeFort *et al.* (1987) and Ayres and Harris (1997).

component, which is required by the trace-element mass balances (Section 26.7) must occur soon after magmatic fractionation. The delamination of mature lower-crustal domains would have caused a deficit of ancient low-crustal rocks with negative ε_{143} values. This strengthens the case for arcs as the tectonic settings in which all the main processes associated with continental-crust formation occur on a relatively short time scale, in accord with the similar mean ages of the lower- and upper-crustal reservoirs (Kelemen *et al.*, 2003). Interestingly, the mean model age of river loads is less than the crustal average: presumably, proportionately more erosion takes place in mountain chains than in plains, and so young crustal domains (e.g. arcs) are over-represented in such elevated areas.

The Sr-isotope systematics of the continental crust are much more complicated than those of Nd. The $^{87}Sr/^{86}Sr$ ratios vary widely from 0.703, which is similar to the mantle value, to high values ~ 0.8 (Fig. 27.9). In part this reflects different crustal ages, as for the Nd isotopes. However, unlike Sm/Nd, Rb/Sr is highly

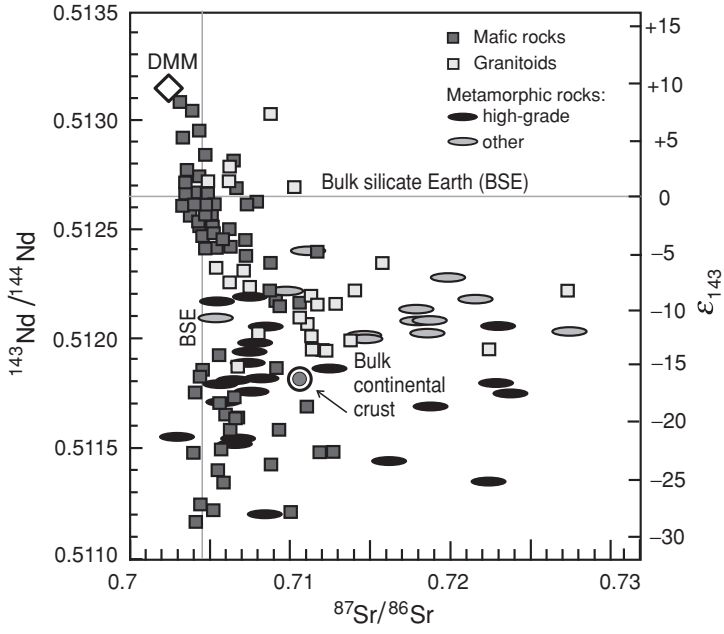

Fig. 27.10 Neodymium vs. strontium isotope plot for lower-crustal xenoliths. Three distinct end-members are seen (similarly to Fig. 27.9): mafic rocks with MORB-like isotope signatures, ancient rocks with low time-integrated Sm/Nd and Rb/Sr ratios and ancient rocks with low to intermediate Sm/Nd ratios but enhanced Rb/Sr ratios. However, the distributions of the data points are quite different: high $^{87}Sr/^{86}Sr$ ratios are much rarer in xenoliths than in the upper-crustal rocks. The low time-integrated Rb/Sr ratios imprinted in low $^{87}Sr/^{86}Sr$ ratios indicate a depletion of the lower crust in Rb. After Downes (1993) and Liu *et al.* (2004).

variable between crustal domains, because Rb and Sr behave differently in intracrustal fractionation processes. In melting Rb is much more incompatible than Sr, in metamorphism Rb is more easily removed via rock–fluid partitioning and fluid removal and in weathering and sediment transport Sr is more soluble. All these processes thus lead to an increase of the Rb/Sr ratio in the upper crust (Sections 26.4 and 26.7), the most extreme values being reached in fine clastic sediments. The preferential removal of Rb over Sr from the lower-crust results in low $^{87}Sr/^{86}Sr$ values in this reservoir (generally below 0.710, Fig. 27.10). For example, in the case of the High Himalayan granites (Section 26.2), the breakdown of micas, important concentrators of Rb, generates ^{87}Sr-enriched granitoid magmas, leaving behind residua depleted in Rb, a typical feature of lower-crustal rocks.

Because of intracrustal Rb/Sr fractionation and the great diversity of $^{87}Sr/^{86}Sr$ ratios in both crustal reservoirs, the systematics do not lend themselves to calculations of model ages in the same way as for Sm–Nd, and the average values for the

upper and lower crust are not well constrained. Broad estimates have been made in various ways. Using correlations between Sr- and Nd-isotope compositions for upper-crustal materials and the better defined mean $^{143}Nd/^{144}Nd_{CCR}$ ratio yields $^{87}Sr/^{86}Sr \approx 0.716$ for the upper crust (Goldstein and Jacobsen, 1988). The crust–mantle correlation of Sr- and He-isotope compositions, in magmatic rocks and in the associated groundwaters respectively, and a value $\sim 5 \times 10^7$ for the crustal $^4He/^3He$ end-member gives an upper-crustal average $^{87}Sr/^{86}Sr$ ratio ≈ 0.722 (Polyak *et al.*, 1979). The estimates of this ratio by Azbel and Tolstikhin (1988), 0.7045 and 0.7174 for the lower and upper crust respectively, appear to be reasonable.

The U–Th–Pb isotope systematics reflects the complexity of the different fractionating mechanisms that govern the abundances of these elements in the continental crust. The latter shows a true continuum in the relative abundance of the radiogenic Pb isotopes, portraying great heterogeneity in the time-integrated U/Pb and Th/Pb ratios (Fig. 27.11). The ancient rocks show a greater Pb-isotope spread than the younger ones, which means that the U–Th–Pb heterogeneity is mainly in the crust itself. The older set displays a large spread in $^{207}Pb/^{204}Pb$ ratios, which can only have been generated in early Earth history. Relatively unradiogenic samples of all ages are close to the general tendency of the data in Fig. 27.12(b). The least radiogenic samples, generally Pb ores of various ages with zero U/Pb ratios and therefore a "frozen" Pb-isotope record, indeed describe a curve in $^{207}Pb/^{204}Pb$ versus $^{206}Pb/^{204}Pb$ space, conjoined by the initial Pb-isotope ratios for rock suites. In the $^{208}Pb/^{204}Pb$ versus $^{206}Pb/^{204}Pb$ plot, the same sample set shows that the Th/U ratios for the system as a whole have not been greatly fractionated over geological time; the slight upward curvature results from the more rapid decay of ^{238}U than ^{232}Th (Fig. 27.12(a)).

In intracrustal melting processes, U and Th are normally more strongly partitioned into the melt than Pb; the latter is compatible in K-feldspar, which can form in some melting reactions (e.g. those involving muscovite breakdown). Therefore Pb can partially remain in the residue. It is thus expected that the upper crust has higher U and Th concentrations and also higher U/Pb and Th/Pb ratios than the lower crust (Table 26.3). In accord with the above prediction, many samples with unradiogenic Pb represent metamorphic provinces exhumed from mid-crustal to even-lower-crustal levels, e.g. the 3700 Myr Amîtsoq gneisses (West Greenland) and the Lewisian (Scotland) or the Labrador granulitic gneisses (summarized in Kramers and Tolstikhin, 1997). However, these are not mafic rocks. Further, the Pb-isotope variations cannot generally be correlated with the upper- or lower-crustal reservoirs or rock types. For instance, upper-crustal rocks of the Archaean Kaapvaal craton, South Africa, have unradiogenic Pb (Kreissig *et al.*, 2000), whereas granulitic units arguably exhumed from deep in the crust, e.g. the Northern Marginal Zone of the Limpopo Belt, Zimbabwe, are characterized by highly radiogenic Pb

and high U and Th concentrations (Berger and Rollinson, 1997). Also, true (mostly mafic) lower-continental-crust xenoliths do not have uniformly unradiogenic Pb (Rudnick and Goldstein, 1990). Thus the upper–lower-crust subdivision is poorly reflected in the Pb isotopes.

However, a supraregional diversity in the U–Th–Pb systematics has been noted among the Archaean cratons (Kamber *et al*., 2003), and this accounts for much of the global Pb-isotope heterogeneity seen in older rocks. Typical high-μ cratons are the Slave craton (Canada), the Wyoming Province (US), the Yilgarn craton (western Australia) and the Zimbabwe craton. Low-μ cratons include the South African Kaapvaal craton, the west Australian Pilbara craton and Labrador. This diversity has deep implications for very early Earth history, as discussed further below.

Given the heterogeneity seen in Fig. 27.11 and the difficulties in fully understanding the cause for it, it is at present nearly impossible to define an average Pb-isotope composition for the continental crust. Analogously to the case of the Nd-isotope systematics, sediments have been used as a proxy for this. Fine-grained river-load samples provide regional averages (Asmerom and Jacobsen, 1993), and pelagic sediments, largely wind-transported, plot in a relatively narrow field worldwide (Ben Othman *et al*., 1989); this is shown as the GLOSS value in Fig. 27.11.

If the pelagic sediments truly reflect the average Pb-isotope composition of the continental crust, a problem arises. Both major Pb reservoirs of the silicate Earth, the mantle and crust, would plot well to the right of the 4.56 Gyr reference isochron (Figs. 27.1(b), 27.3(b), 27.11(b) and 27.12(b)). This is known as the first Pb paradox or the "future" paradox (Sinha and Tilton, 1973). As the Earth is known to have accreted mainly in the first 40 Myr after SOS (Sections 18.3), the bulk Earth must plot on or very close to this isochron. There should then be a hidden reservoir with a Pb-isotope composition plotting to the left of the 4.56 Gyr line. In attempts to solve this problem, models of late formation of all or part of the core have been explored (e.g. Allègre, 1982; Galer and Goldstein, 1996; Wood and Halliday, 2005) or it has been postulated that ancient low-μ lower-crust or large subducted slabs could have balanced the terrestrial Pb (Kramers and Tolstikhin, 1997; Murphy *et al*., 2002).

However, the discrepancy in ε_{143} values between average river loads and the average crust, discussed above, may indicate that the Pb-isotope composition of pelagic sediments is likewise biased towards younger rocks. Given the extreme heterogeneity of the continental crust and that it holds a large proportion of the Earth's Pb, it is then possible that the "future" paradox is not real or at least is not as important as previously considered. Because of this large uncertainty, global modelling of Pb-isotope systematics has not been included in Chapter 28 of this book, in which we describe a chemical model for the accretion and evolution of the Earth.

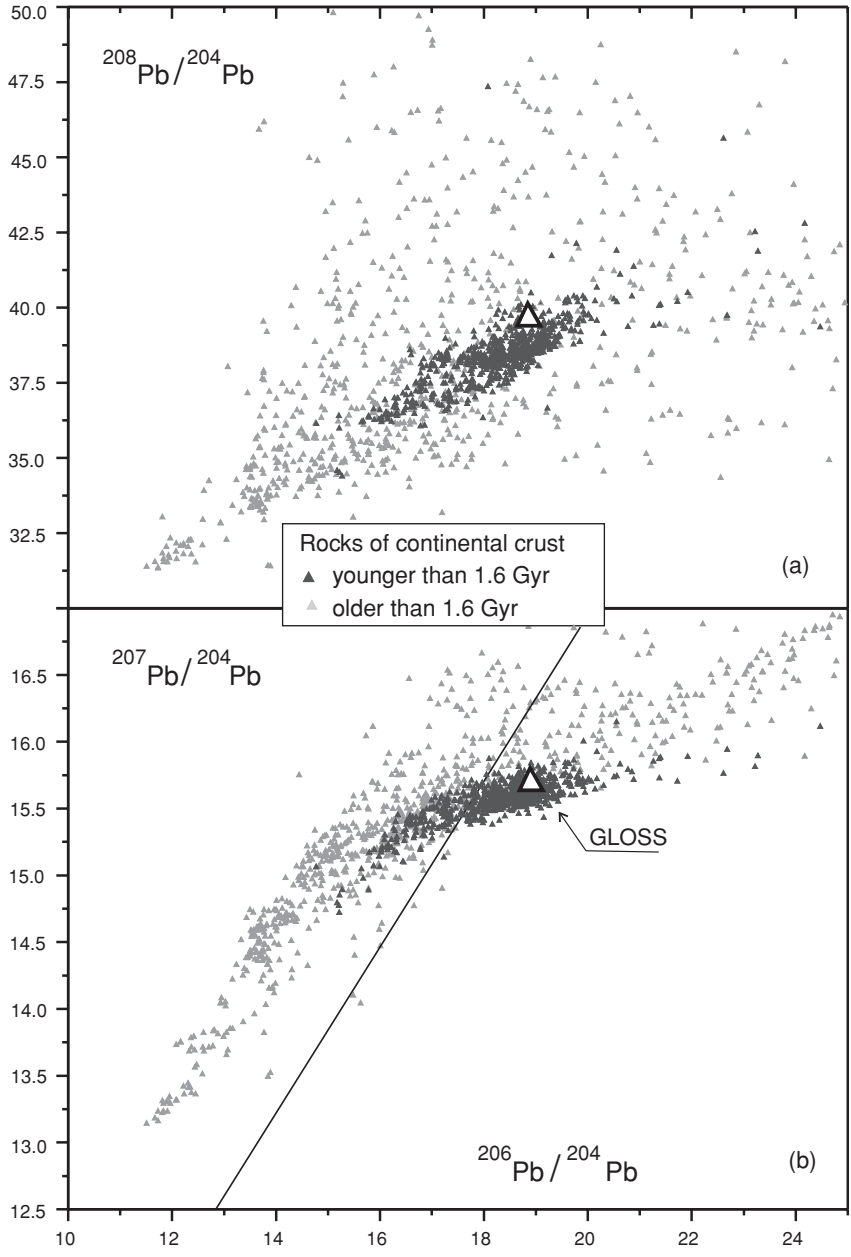

Fig. 27.11 Present-day Pb-isotope ratios in rocks of the continental crust. In the upper panel a large variation in the time-integrated Th/U ratios is reflected in the >1.6 Gyr samples. In the lower panel, note the banana shape of the data-populated area: in early Earth history ^{235}U was still relatively abundant, and variations in the U/Pb ratio produced a significant range in the ^{207}Pb/^{204}Pb ratio. By 1.6 Gyr ago, ^{235}U had decayed to $< 5\%$ of its original amount, so that variations in ^{206}Pb/^{204}Pb predominate. The relative uniformity of ^{207}Pb/^{204}Pb in the younger sample set is a result of mixing in the mantle and crustal domains. After Kramers and Tolstikhin (1997), © Elsevier Science 1997, reproduced by permission.

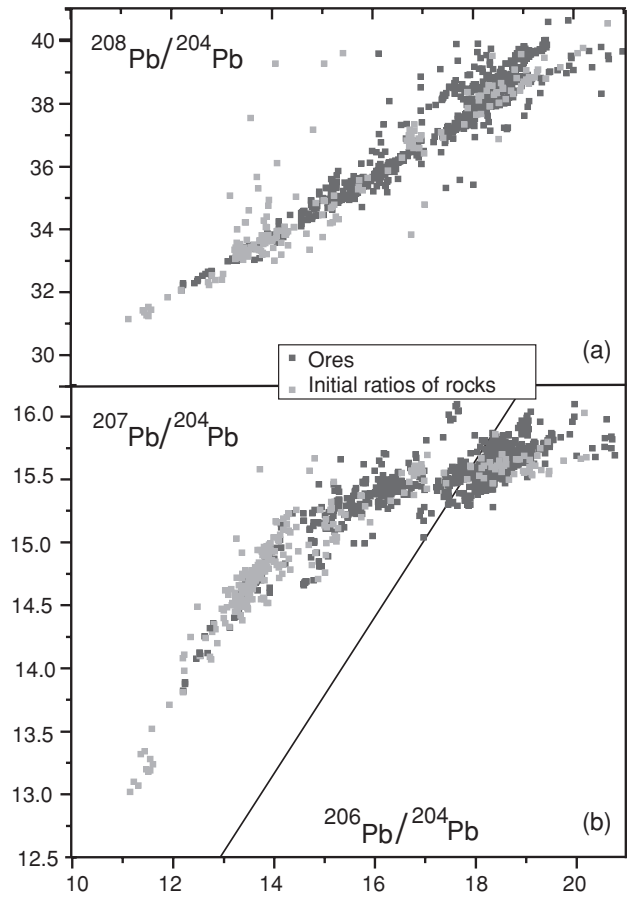

Fig. 27.12 Lead-isotope compositions in Pb-rich ores and initial Pb ratios for rock suites. From Kramers and Tolstikhin (1997), © Elsevier Science 1997, reproduced by permission.

27.7 Relationships between the Sm–Nd and Lu–Hf isotope families

As was convincingly demonstrated by Vervoort *et al*. (1996, 1999, 2000), the isotopic $^{143}Nd/^{144}Nd$ and $^{176}Hf/^{177}Hf$ ratios in terrestrial rocks constitute a single narrow terrestrial array, which includes essentially all mantle-derived and crustal rocks: MORBs, OIBs, granitoids, sediments, metamorphic rocks and lower-crustal xenoliths (Fig. 27.13). This important observation indicates that on a global scale the Sm/Nd and Lu/Hf ratios fractionate coherently: in each fractionating event, these ratios change in similar proportions to each other, so that the ingrowth of radiogenic $^{143}Nd^*$ and $^{176}Hf^*$ results in the narrow band seen in Fig. 27.13. As Nd and Hf are partitioned preferentially into melts, evolved magmatic rocks develop towards less radiogenic compositions (e.g. upper-crustal rocks) whereas the

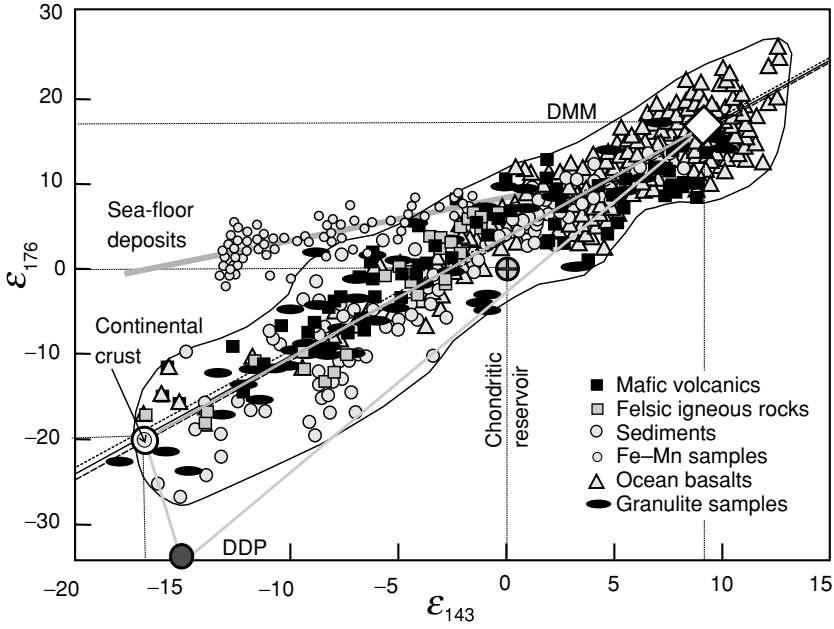

Fig. 27.13 The terrestrial ε(Hf) vs. ε(Nd) array. The three regression lines (solid, broken and dotted) for the mantle- and crustal-derived subsets and for the complete data set are very similar; $\varepsilon_{176} = 1.36\ \varepsilon_{143} + 2.95$. All three lines pass about +3 ε(Hf) units above the chondritic ε(Nd) and ε(Hf) values (assumed to correspond to the bulk silicate Earth). All samples are grouped within $\pm 8\ \varepsilon_{176}$ units of this regression line. The diamond and circles are average ε values derived from the reference solution of the model for the three reservoirs involved (Chapter 28). The model-derived mantle–crust connection (the thin darker-grey line) is indistinguishable from the regressions of the data. The sea-floor deposit array (Fe–Mn samples) shows the enhanced values of the time-integrated Lu/Hf ratio typical of ocean water (see the text for an explanation and Section 21.3 for a presentation of the Lu–Hf and Sm–Nd systematics). After Vervoort *et al.* (1996, 1999, 2000) and Goldstein and Hemming (2003); see the references for data sources in these publications.

residual matter exhibits a complementary evolution towards more radiogenic values (e.g. the DMM).

The overall similarity of the lower- and upper-crustal Nd-isotope characteristics has been noted above. The fact that the lower-crustal samples plot on the terrestrial Nd–Hf isotope array is an additional surprise, as garnet is the principal concentrator of Lu and is abundant in lower-crustal rocks and xenoliths. A much stronger Lu/Hf fractionation than that for Sm/Nd is therefore expected in lower-crustal melting processes but is rarely observed (Vervoort and Patchett, 1996). This may be due to the partial entrainment of residue by lower-crustal melts (Section 26.7), and is in contrast with what occurred in lunar mare magmatism (Section 21.4). Further,

the coherence of the lower-crustal samples and the Nd–Hf array strengthens the conclusion from Nd isotopes that the lower and upper crust are broadly coeval (DePaolo *et al.*, 1991; Vervoort *et al.*, 2000), and thus further emphasizes the importance of arcs as the principal crust-forming environment.

There are some exceptions to the coherence of terrestrial Nd and Hf isotopes. Iron- and manganese-rich nodules and crusts, formed by chemical precipitation on the ocean floor, represent one example. Their Hf- and Nd-isotope compositions reflect those of ocean water. They are offset from the terrestrial array towards enhanced $^{176}Hf/^{177}Hf$ ratios (Fig. 27.13), and this offset is greatest at low $^{143}Nd/^{144}Nd$ ratios. Note that the solubility of both Nd and Hf in ocean water is poor, and the residence times are short. The Nd and Hf in ocean water stems from weathering and from leaching of the suspended load in transit, and the anomaly is most likely due to detrital zircon. This Hf-bearing mineral is resistant to weathering and, although only accessory in amount, zircon grains constitute an important insoluble low-Lu/Hf subreservoir in sediments. Other minerals, which have complementary enhanced Lu/Hf (and thus higher $^{176}Hf/^{177}Hf$) ratios, are more readily leached, contributing to the river-load flux of Hf into the oceans. In contrast, Sm and Nd, as well-behaved members of the REE family, are not separated during the sedimentation cycle, and the $^{143}Nd/^{144}Nd$ ratios in ocean water are representative of the respective sediment sources (Patchett *et al.*, 1984; Goldstein and Hemming, 2003).

Another example of an Hf–Nd isotope anomaly, relating to the process of mantle refertilization, is given by a case study on spinel peridotite xenoliths in Hawaiian basalt (Fig. 27.14(a)). Among generally somewhat LREE-enriched patterns, one sample (W in the figure) seems to be the most primitive. However, if this sample represented a primitive mantle it would have ε_{143} and ε_{176} values close to zero. This is not the case: Hf is extremely radiogenic, particularly in sample W (Fig. 27.14(b)). A plausible explanation is that these mantle peridotites were strongly depleted owing to partial melting in a paleo-ridge $\sim$ 100 Myr ago, whereby their Lu/Hf and Sm/Nd ratios increased so much that positive ε_{143} and ε_{176} values evolved. Recently ascending melts related to the Hawaiian magmatism then refertilized these peridotites and carried them to the surface as xenoliths. Different mass balances for Nd and Hf caused the resetting of Nd-isotope compositions of the refertilized rocks towards those in the Nd-rich melts (HV in Fig. 27.14(b)) whereas Hf preserved an excess radiogenic signature, betraying the non-primitive character of these samples (Bizimis *et al.*, 2003). This example again shows the power of isotopic data to trace episodes of which the geochemical record has otherwise been obliterated.

Finally, a very important feature of the Nd–Hf terrestrial array is that the regression line for the whole data set as well as those for the mantle and continental subsets all lie about $+3$ ε_{176} units above the chondritic value, which is thought to represent the bulk silicate Earth (Fig. 27.13). One possible explanation favoured

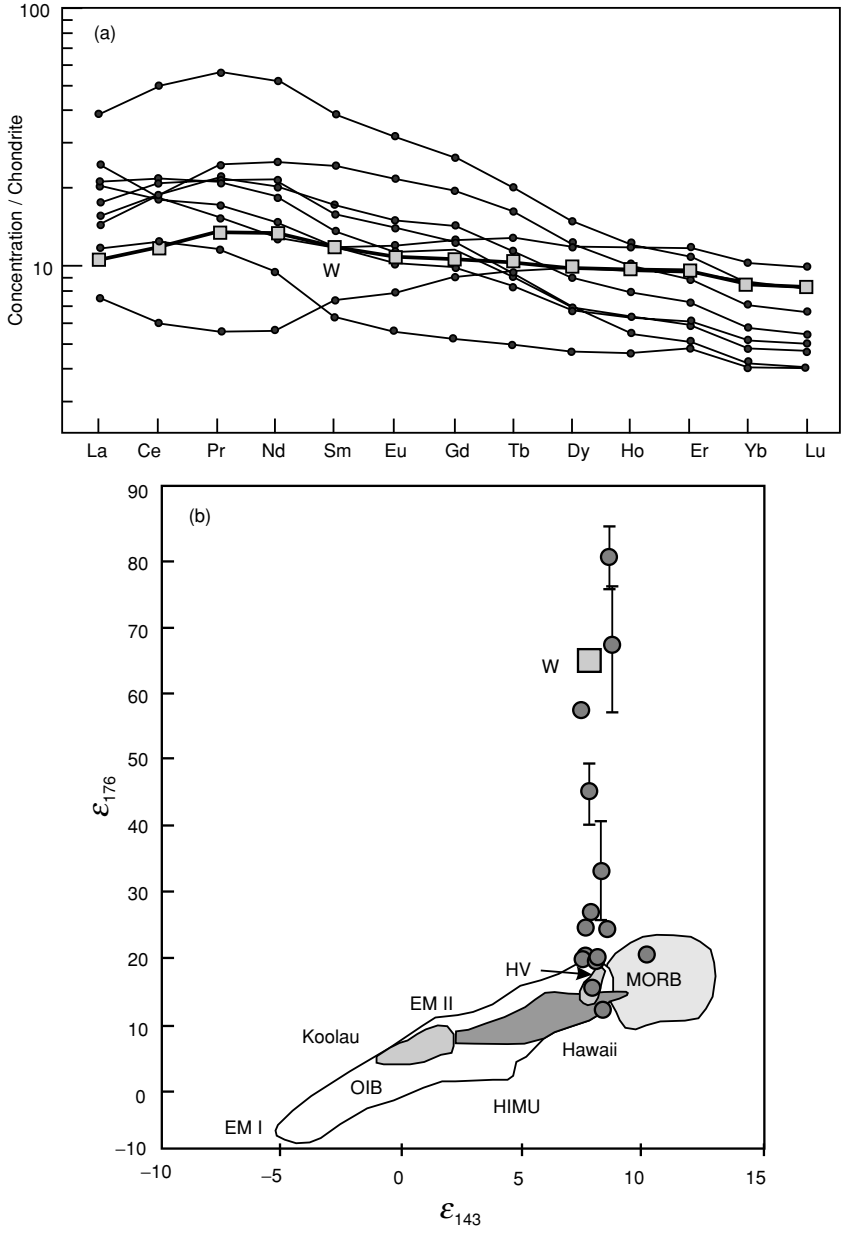

Fig. 27.14 Rare earth element and Hf–Nd isotopic systematics in refertilized peridotites, Oahu, Hawaii. (a) The REE abundances in clinopyroxenes (the principal hosts of REEs in peridotites); note the almost flat pattern for the sample labelled W (thick curve with squares). (b) Hafnium vs. neodymium isotope compositions of the clinopyroxenes: note the highly radiogenic Hf in several samples (e.g. in sample W), lying well above the terrestrial array in Fig. 27.13. The Nd- and Hf-isotope compositions in Honolulu volcanic rocks, whose parental melts refertilized the lithospheric mantle represented by the peridotites, are indicated by HV. After Bizimis *et al.* (2003), © Elsevier Science 2003, reproduced by permission.

in this book is that the superchondritic Lu/Hf ratios in the mantle and crust are balanced by subchondritic values in a hidden fractionated early-formed reservoir, the D″ layer (Chapter 19). Another possibility is that the terrestrial-chondrite matter had a somewhat higher Lu/Hf ratio than the carbonaceous chondrites: some heterogeneity among chondrites is indeed observed (Patchett *et al.*, 2004).

27.8 Isotopic traces from earliest Earth history and evolutionary trends

A window on fractionation events in the early history of the crust and mantle is provided by radioactive isotope systematics with a relatively short half-life, such as ^{235}U–^{207}Pb and ^{146}Sm–^{142}Nd and by Hf isotopes in very ancient detrital zircon grains, which act as time capsules.

In a case study of Pb isotopes in $\sim$ 3.7 Gyr metasediments and gneisses in the Godthaabsfjord area, West Greenland, a large discrepancy in the ^{207}Pb/^{204}Pb ratios for similar ^{206}Pb/^{204}Pb ratios is revealed (Fig. 27.15). Chemical metasediments (cherts and banded-iron formations, BIF) as well as gneisses and clastic metasediments define arrays that yield ^{207}Pb/^{206}Pb ages of $\sim$ 3.7 Gyr, but the chemical metasediment data are offset to higher ^{207}Pb/^{204}Pb values by a large amount, $\sim$ 0.5. To explain this discrepancy, a differentiation event at 4.3 Gyr is envisaged, in which a high-μ enriched material, with $\mu = 10.3$, is extracted from a BSE with an average $\mu = 7.7$ (Fig. 27.15). The ^{207}Pb/^{204}Pb and ^{206}Pb/^{204}Pb ratios increase faster in this material than in the BSE. As ^{235}U was abundant in early Earth history, the difference in the ^{207}Pb/^{204}Pb ratios is particularly pronounced. Fractionation of BSE-like (or slightly depleted) matter gives rise to ages for the Amîtsoq and South of Isua gneisses between 3.8 and 3.7 Gyr, and the enriched material provides Pb to the chemical sediments. Kamber *et al.* (2003) argued that the enriched material was a protocrust segment preserved at the Earth's surface from 4.3 to 3.7 Gyr and subsequently destroyed. Late bombardment of the Earth (by analogy with the Moon, Section 21.5) could have played a role in the destruction of this Hadean crust, as is also implied by the ^{146}Sm–^{142}Nd data in West Greenland gneisses (see below).

Less pronounced but nevertheless significant variations in ^{207}Pb/^{204}Pb values at a given ^{206}Pb/^{204}Pb value are quite common in the Archaean continental crust, leading to a broadening in the growth curve array (Fig. 27.11). In contrast, Pb-isotope compositions in Archaean volcanic rocks portray a much more uniform (or much better mixed) reservoir, with respect to both the U–Pb and Th–U–Pb prehistories, than the Archaean crust (Tilton, 1983). In the generation of tholeiitic and ultramafic melts, or their early differentiation, no fractionation of the Th/U ratio is expected (both are highly incompatible and melt fractions are large), so that the Th/U ratio of their mantle source can be estimated from the ^{208}Pb/^{204}Pb versus ^{206}Pb/^{204}Pb array. For the Archaean data this gives a value of 3.32, which is much higher than the present-day value of about 2.6 (Section 27.2).

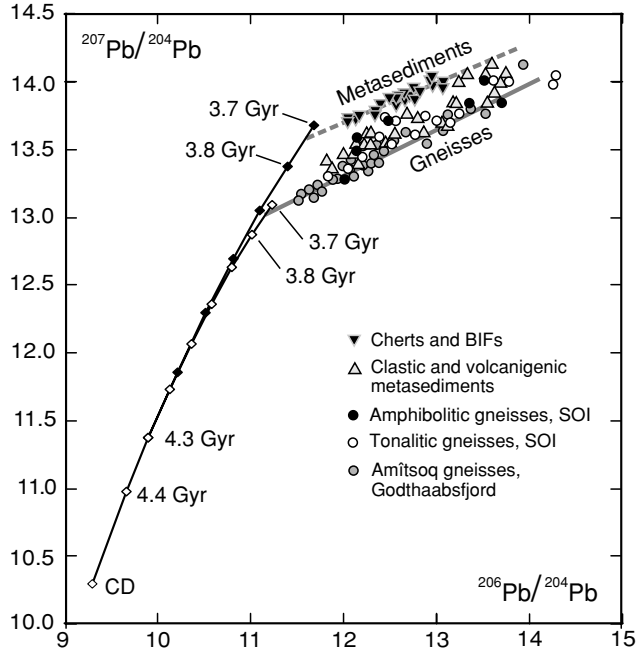

Fig. 27.15 Lead-isotope data for chemical metasediments (banded-iron formations and cherts) and for the Amîtsoq and South of Isua gneisses (SOI), West Greenland. Reference lines: chemical sediments (thick broken line); gneisses (thick solid line). Both portray ages close to 3.75 Gyr. The arrays are offset in their $^{207}Pb/^{204}Pb$ ratios. In the simplified model shown, a system with $\mu = 7.7$ starts with Canyon Diablo primordial Pb (CD) and accumulates radiogenic ^{206}Pb and ^{207}Pb from 4.55 Gyr onwards (open diamonds, shown at 100 Ma intervals from 4.4 Gyr). At 4.3 Gyr, differentiation produces a subsystem with $\mu = 10.3$ (solid diamonds). Gneisses are chiefly produced from the first system and the Pb in chemical sediments is derived from the second. After Kramers (2007). Reproduced by permission of the Geological Society, London.

An important observation relevant to the formation and early evolution of terrestrial materials is that the $^{142}Nd/^{144}$ Nd ratios in all terrestrial samples exceed the chondritic value by $+0.2\,\varepsilon_{142}$ units (Fig. 27.16(a), (b)). Assuming a chondritic-Earth model, this would imply that the Earth's mantle acquired a subchondritic Sm/Nd ratio during the first $\sim$ 100 Myr of Earth history, when the parent ^{146}Sm was still live. Assuming a chondritic-Earth model, such fractionation could have resulted from the extraction of enriched crust-like material, which would be then apparently isolated from Earth's accessible reservoirs (EARs). This hidden reservoir could possibly be the D$''$ layer (Chapter 19).

Further, after much uncertainty it has been confirmed that in the Godthaabsfjord area, West Greenland, the $\sim$ 3.7 Gyr gneisses as well as metasediments have $^{142}Nd/^{144}Nd$ ratios higher by $\sim$ 0.1 ε_{142} units than those of all the other

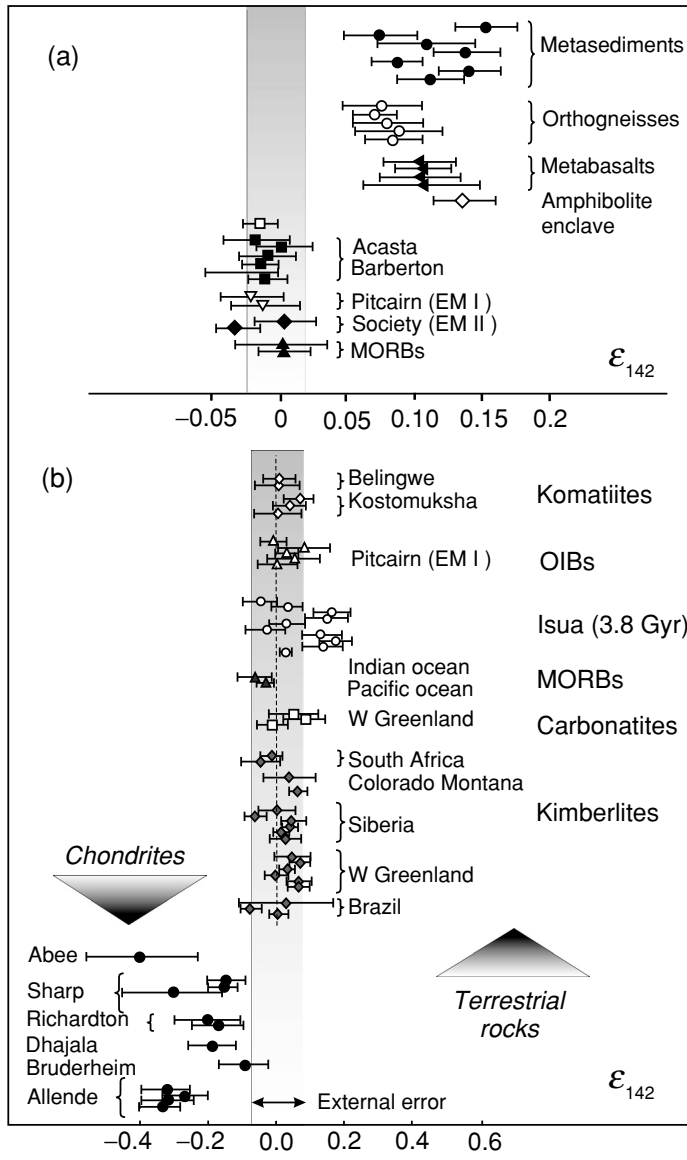

Fig. 27.16 Meteoritic and terrestrial $^{142}Nd/^{144}Nd$ ratios. The ratios are expressed in the ε_{142} notation (Eqn 19.1b). The grey vertical bars show the average external precision obtained on repeat analyses of the same sample. Error bars on the individual points show the 2σ deviation obtained for multiple measurements of each sample. See Section 21.3 and Tables 3.3 and 28.1 for the Sm–Nd systematics data. (a) Several samples from the Godthaabsfjord area, West Greenland, indicate a more depleted source than other terrestrial samples. (b) The terrestrial samples are all depleted relative to the chondritic composition. After Boyet *et al.* (2003), Boyet and Carlson (2005, 2006) and Caro *et al.* (2003, 2006), © Elsevier Science 2006, reproduced by permission (both (a) and (b)).

terrestrial rocks measured; these included samples from many Archaean cratons (Fig. 27.16(a)). Irrespective of which precise mechanism is invoked to explain this difference, it requires that some reservoir, depleted in incompatible trace elements, has remained isolated since the earliest few hundred Myr of Earth history to give rise to this regional anomaly. The analogy to the above-discussed Pb-isotope case is only partial, as the reservoir required there should have been enriched.

Zircon has proved to be a most useful mineral for studying differentiations in the earliest history of the Earth. It can be accurately dated, with U/Pb systematics, and because of its intrinsic high-Hf content and low Lu/Hf ratios, the $^{176}Hf/^{177}Hf$ ratios have not substantially changed within it. Thus the $^{176}Hf/^{177}Hf$ ratios of the parental magmas can be readily reconstructed. Further, zircon is a chemically and mechanically highly resistant mineral, which is not destroyed in sediment transport (Fig. 27.17).

The most ancient terrestrial matter hitherto found consists of detrital zircon grains in metasediments in the Mt Narryer and Jack Hills areas of the Yilgarn craton, western Australia. Among the most ancient zircons there are samples with $^{176}Hf/^{177}Hf$ ratios lying above the bulk silicate Earth development line. This shows the occurrence of depleted-magma-source regions as early as ~ 4.5 Gyr ago. However, most data, particularly from the somewhat younger detrital zircons, plot variably below this line. This points to enriched rock provinces, with Lu/Hf ratios below BSE values, that originated a few hundred Myr before they partially melted and the zircons were formed. From a comparison with the $^{176}Hf/^{177}Hf$-ratio development slopes in Fig. 27.17, such rock provinces appear on average to have had the Lu/Hf ratio of continental crust generated from a BSE-type mantle.

Non-detrital zircons from Archaean gneiss terrains do not show a large scatter in $^{176}Hf/^{177}Hf$ ratios around the BSE development line but plot mainly below it (Fig. 27.17). These zircons thus probably crystallized either from mantle-derived evolved melts (e.g. the Itsaq, Barberton and Pilbara samples) or via the remelting of pre-existing enriched crust (the Acasta samples). Thus, even if depleted domains were generated in the mantle in the first few hundred Myr of Earth history, they appear to have been obliterated by the time of the early Archaean (~ 3.8 Gyr), presumably by remixing.

Numerous Nd-isotope data on whole-rock samples, spanning all the 3.8 Gyr geological history, illustrate an increasing diversity of ε_{143} in the DMM and continental crust as time progresses (Fig. 27.18). This is expected as the differentiated reservoirs age. In the oldest rocks, the Sm–Nd systematics have been modified mostly by episodes of metamorphism, so that careful selection is needed before applying these data to Nd-isotope evolution modelling (Nägler and Kramers, 1998). The upper bound of the data envelope in Fig. 27.18 approximately defines the growth in

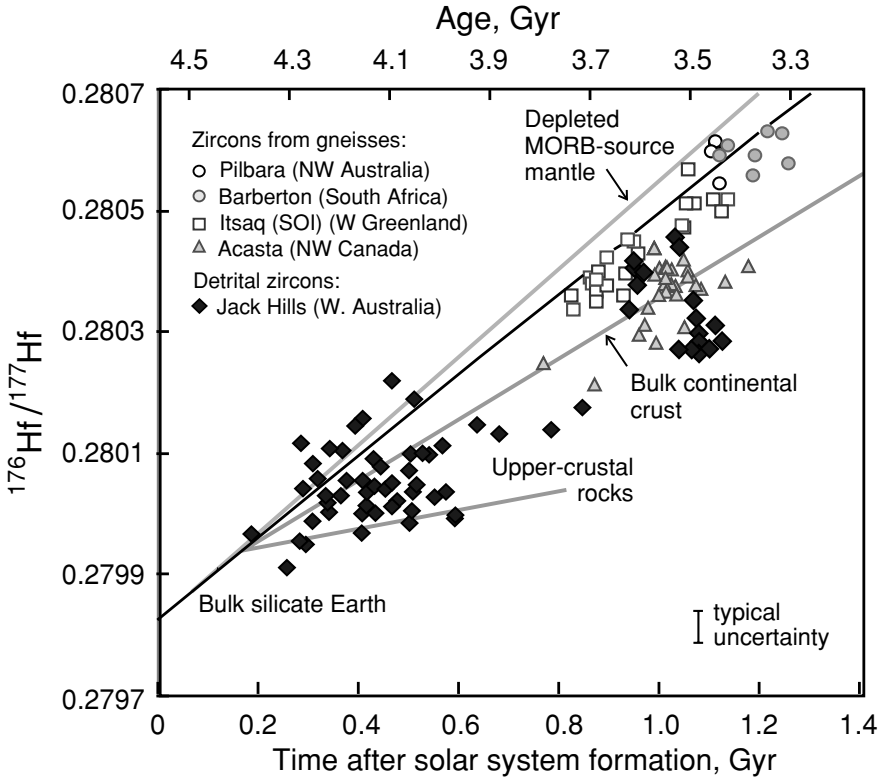

Fig. 27.17 Hafnium-isotope composition in ancient zircons. Hafnium is compatible in zircon and its isotope composition has been frozen in this mineral since its crystallization. The spread of the data points indicates magmatic differentiation that started ~ 100 Myr after SOS formation. The line of lowest gradient shows possible $^{176}Hf/^{177}Hf$ development in 4.4-Gyr-old continental crust (with Lu/Hf ratio from Table 26.3). The grey lines show the model development of DMM and CCR reservoirs, discussed in Chapter 28. Note that the CCR model incorporates both ancient and newly formed crust and is therefore intermediate between the lowest-gradient line and the DMM line. Data from Wilde *et al.* (2001), Amelin *et al.* (1999, 2000) and Harrison *et al.* (2005).

the DMM with age. A similar pattern appears for the ε_{176} evolution (e.g. Vervoort and Blichert-Toft, 1999; Bennett, 2003).

These trends are used to constrain chemical Earth-evolution models (Chapter 28). A simple approach already allows us to resolve a controversy on the continental crust growth since the Archaean (e.g. Taylor and McLennan, 1995). Extreme end-member hypotheses are (1) that the crust grew without any recycling into the mantle, and (2) that the mass of continental crust has been constant since the Archaean because recycling into the mantle has kept pace with the generation of new crust (see inset in Fig. 27.18). Both hypotheses allow a mean crust age of 2 Gyr and the observed

present-day ε_{143} values of the crust and the DMM. However, their resulting mantle-evolution trends for $\varepsilon_{143}(T)$ are totally different from that observed; it is obvious from this simple test that neither of these extreme hypotheses is correct. In detailed modelling an intermediate crustal-growth model produces a good fit to the upper bound of the data envelope (the curve DMM in Fig 27.18). Further, the model described in Chapter 28 envisages a wholly convective mantle and an apparently isolated enriched D″ reservoir (Chapters 17 and 19). The very early formation of this reservoir would have caused initial mantle depletion $\sim$ 4.5 Gyr ago, leading to the early growth of mantle $\varepsilon_{143}(T)$ even if very little or no continental crust was present prior to 4 Gyr.

27.9 Evolutionary trends recorded by sedimentary rocks

Throughout Earth history there have been changes in processes in the Earth's surface environment that can be traced by variations in the stable and radiogenic isotope ratios. In this section we show examples that demonstrate fundamental secular changes: Sr isotopes reflect the varying relative inputs of volcanism and continental weathering in the oceans, whereas the mass-independent fractionation of S and the mass-dependent fractionation of Mo are indicators of the redox state of the atmosphere and oceans. Other very important isotope tracers, primarily the mass-dependent fractionation of C and S, are intimately connected to biogeochemical cycles, which are outside the scope of this book and therefore are not discussed here.

Sedimentary rocks and processes: the strontium-isotope record

Important constraints on crust–mantle evolution come from the Rb–Sr systematics (introduced in Section 12.4), particularly from the Sr-isotope inventory in sea water. Because the Sr residence time in the oceans, $\sim$ 6 Myr, is much longer than the ocean mixing time, $\sim$ 1 kyr, the Sr-isotope composition in sea water is homogenized and thus may be considered as a representative global average for any given time. The present-day ratio $^{87}Sr/^{86}Sr = 0.7092$. Strontium, the geochemical twin of calcium, is transported by surface and hydrothermal waters. Correspondingly, the riverine flux from the continents and the hydrothermal flux of water recycled through the oceanic lithosphere together determine the $^{87}Sr/^{86}Sr$ ratio in the oceans.

Highly incompatible Rb is concentrated in the continental crust, which therefore has a high Rb/Sr ratio (Table 17.1) and a correspondingly high $^{87}Sr/^{86}Sr$ ratio. Radiogenic Sr appears in the riverine flux with a bulk river-load $^{87}Sr/^{86}Sr$ ratio equal to 0.7119, comprising both dissolved (0.7101) and suspended (0.7165)

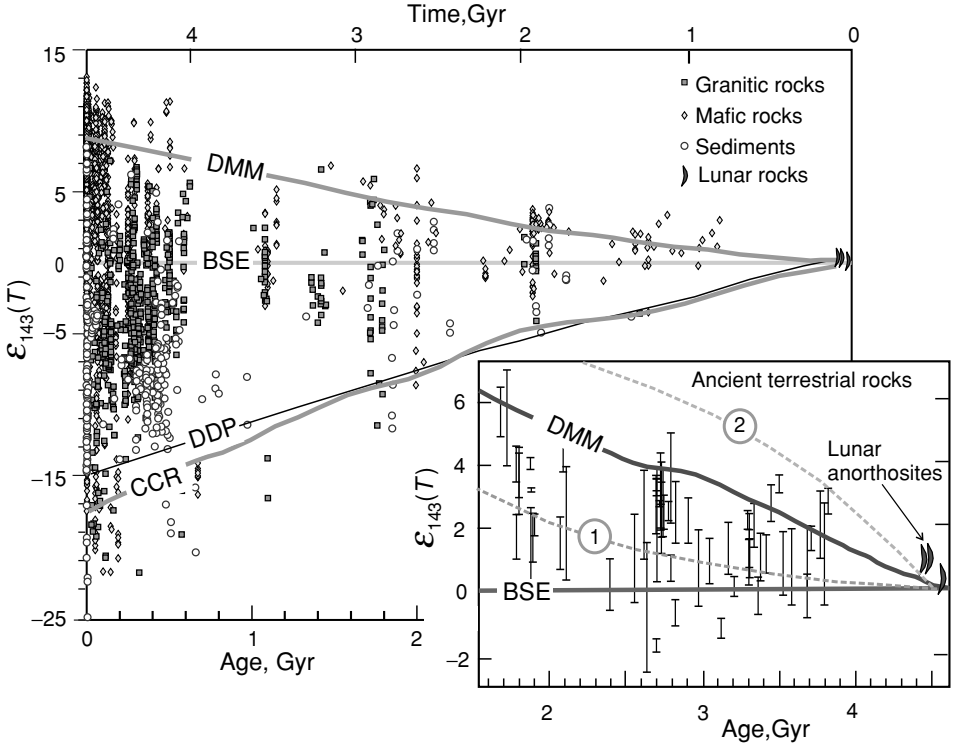

Fig. 27.18 Initial Nd-isotope compositions in terrestrial rocks. The $\varepsilon_{143}(T)$ evolution lines predicted by our reference solution (Chapter 28) are shown along with the data. Of the total $\varepsilon_{143}(0) \approx +9$ for the present depleted MORB-source mantle, $+5$ is due to the early formation of D$''$ and $+4$ is due to extraction of the continental crust. The inset shows the data and evolution lines for the most ancient rocks. The broken curves illustrate two extreme hypotheses for crustal growth: (1) continuous crustal growth without recycling; (2) early-formed crust with constant mass and recycling (the fluxes into and from the crust are equal). Both give the correct 2 Gyr average crustal age as well as the present-day mantle and crustal $\varepsilon_{143}(0)$ values; nevertheless, both fail the test since the corresponding $\varepsilon_{143}(T)$ curves do not fit the data. After Kostitsyn (2004) and Nägler and Kramers (1998); see also the data sources in these publications.

components (Fig. 27.19; Goldstein and Jacobsen, 1988; Palmer and Edmond, 1989). The dissolved riverine Sr is mainly derived from the weathering of marine precipitates, e.g. carbonates, which generally (but not always, see below) contain Sr with lower $^{87}Sr/^{86}Sr$ ratios. Continental silicate bedrocks, the principal source of the suspended load, contribute Sr with enhanced $^{87}Sr/^{86}Sr$ ratios, as also seen in GLOSS, for which $^{87}Sr/^{86}Sr = 0.7173$ (Plank and Langmuir, 1998).

In complement, the mantle is depleted in Rb and shows low Rb/Sr ratios (Table 17.1) and low $^{87}Sr/^{86}Sr$ ratios ≈ 0.703 (Fig. 27.2). That the $^{87}Sr/^{86}Sr$ values

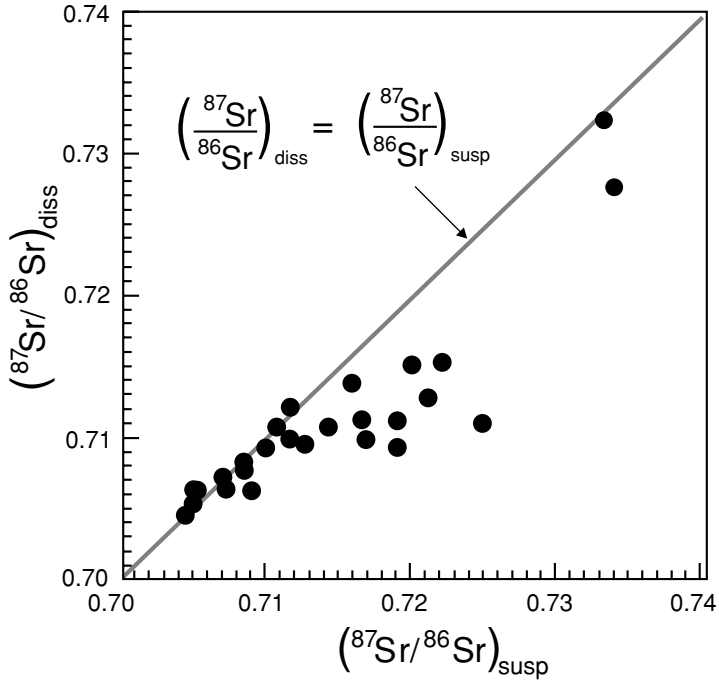

Fig. 27.19 Strontium isotopes in dissolved and suspended river loads. The relationship between the Sr-isotope compositions in the dissolved and suspended loads is controlled by the source-rock composition. If there are only silicate rocks in the source area, the dissolved and suspended loads have the same $^{87}Sr/^{86}Sr$ ratio. If marine carbonate rocks are also present, these are more readily weathered and, as they have lower $^{87}Sr/^{86}Sr$ ratios, the data points are shifted to the right of the line of equal values. After Goldstein and Jacobsen (1987), © Elsevier Science 1987, reproduced by permission.

in ocean water are lower than in the riverine Sr flux indicates a hydrothermal input of strontium from the oceanic-crust and suboceanic-lithosphere reservoirs into the oceans. The resulting mixed $^{87}Sr/^{86}Sr$ ratio of ocean-water Sr is then recorded in hydrogenous and biogenic carbonates.

Strontium-isotope signals from ancient oceans

The $^{87}Sr/^{86}Sr$ ratios of crust and mantle have evolved over geological time by the ingrowth of radiogenic ^{87}Sr and the exchange of matter between the two reservoirs; however, the continental crust has always been a greater source of radiogenic Sr than the mantle. The two fluxes of crustal and mantle Sr have varied through time, causing fluctuations in the $^{87}Sr/^{86}Sr$ ratio in the oceans and thus reflecting a specific feature of geotectonics, the distinctive rate of crustal erosion versus that of hydrothermal activity in the oceanic crust (Fig. 27.20). Until $\sim$ 2.5 Gyr ago,

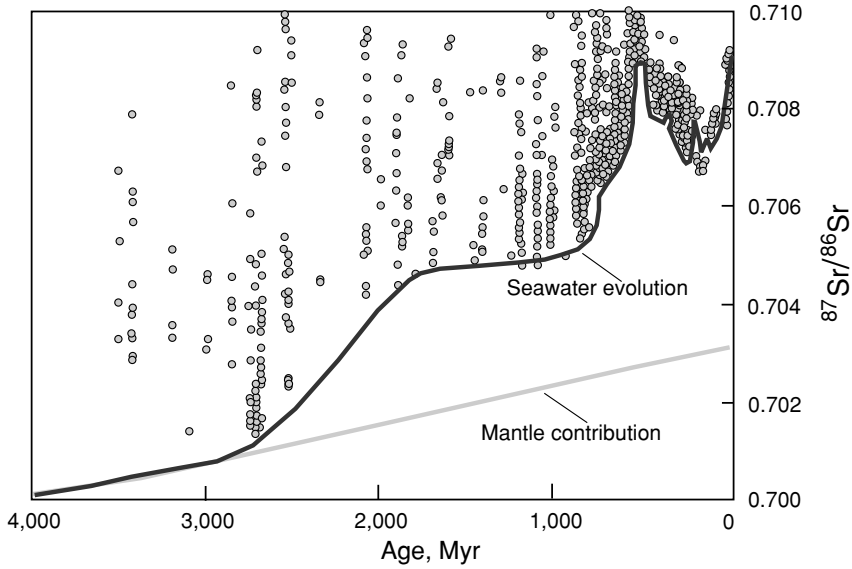

Fig. 27.20 Evolution of Sr-isotope composition of (meta)sedimentary carbonate rocks. The lower envelope of the data represents ocean-water Sr, whereas the more radiogenic compositions could reflect the contamination of the samples by continental radiogenic Sr in detrital grains. The sources of Sr in the oceans have changed with time, from a predominantly mantle source in the Archaean to a mainly crustal source at present. After Veizer and Mackenzie (2003), © Elsevier Science 2003, reproduced by permission.

the lower envelope of the Sr-isotope trend seen in Fig. 27.20 appears to follow mantle values, indicating a dominance of hydrothermal activity over continental erosion in the Archaean era. Since the Proterozoic the contribution of crustal Sr has been increasing, and at present this source prevails. Interestingly, modelling the U–Th–Pb systematics has led to a similar conclusion (Kramers and Tolstikhin, 1997).

While the strontium-isotope ratio of the "mantle" flux has always been low, developing smoothly, the "river" flux may have varied widely both in strontium abundance and isotope ratio. For example, the rapid Tertiary rise in the $^{87}Sr/^{86}Sr$ ratio (Fig. 27.20) is commonly interpreted as reflecting the uplift of the Himalayas (Veizer and Mackenzie, 2003). A good correlation between the Phanerozoic seawater strontium-isotope curve and the estimated sediment fluxes in the geological past supports this interpretation (Hay *et al.*, 2001). Assuming a similar flux of Sr isotopes from the continents during the last few millions of years, i.e. a time scale comparable with the mean Sr residence time in ocean water, then an additional input flux of less radiogenic Sr is needed to obtain the present-day Sr-isotope composition in ocean water (Davis *et al.*, 2003).

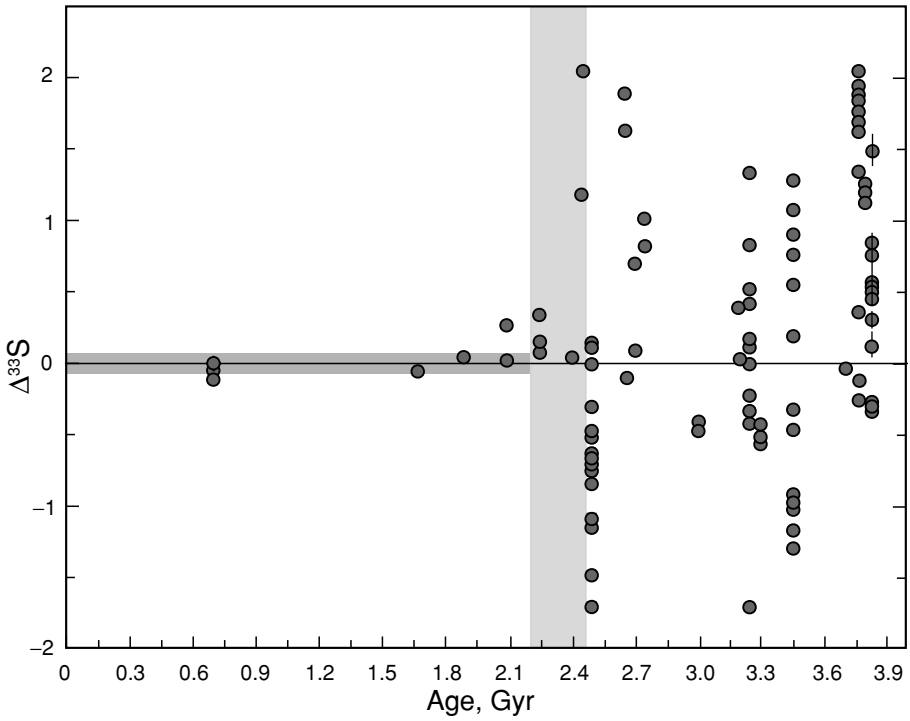

Fig. 27.21 Mass-independent fractionation of sulphur isotopes in (meta)sedimentary rocks reflecting the oxygen content in the Earth's atmosphere and hydrosphere through Earth history. Three stages are seen in the evolution of sulphur-isotope abundances in terrestrial metasedimentary rocks. The period from 3.8 Gyr to 2.45 Gyr is characterized by a variation in $\Delta^{33}S$ (defined in Section 10.2) between -2 and 2 ppm. From 2.45 to 2 Gyr the variations in $\Delta^{33}S$ are modest, 0 to 0.5 ppm (light-grey band), and after 2 Gyr the $\Delta^{33}S$ variability is much less than 0.2 ppm. The shaded rectangle along $\Delta^{33}S = 0$ represents hundreds of analyses of samples younger than ~ 2.0 Gyr (only a few representative results are shown as data points). After Farquhar and Wing (2003), © Elsevier Science 2003, reproduced by permission.

Stable-isotope signals from the ancient atmosphere

The isotopic compositions of sulphur, in rocks younger than the earliest Proterozoic, fractionate following a mass-dependent trend, giving $\delta^{33}S \approx 0.515 \times \delta^{34}S$ and $\Delta^{33}S \approx 0$ (Section 10.2). In sharp contrast, the $\Delta^{33}S$ values in early Proterozoic and Archaean samples vary from $-2‰$ to $+2‰$ (Fig. 27.21; Farquhar *et al.*, 2001; Farquhar and Wing, 2003). In ancient rocks, the $\Delta^{36}S$ values also deviate from the mass-dependent trend and correlate with $\Delta^{33}S$.

The interpretation of these important observations is in progress. At present the most likely proposal invokes photolysis reactions caused by deep ultraviolet penetration of the atmosphere. Some of these reactions, particularly those involving

SO_2 and SO, exhibit strong wavelength dependence and can therefore generate large mass-independent isotopic fractionation (MIF) effects. Elemental sulphur and some sulphur-bearing molecules would then transfer the MIF signatures from the atmosphere into sediments preserving the record. Via this chain of processes, the observed relationships between $\delta^{34}S$, $\Delta^{33}S$ and $\Delta^{36}S$ in ancient terrestrial samples can be reproduced (Fig. 27.21).

It is important that within the frame of this interpretation the early atmosphere must have been transparent at ultraviolet wavelengths, and therefore the ozone (and to a lesser degree O_2 and CO_2) ultraviolet shield, absorbing the UV-radiation, was much less efficient before 2400 Myr ago (Farquhar and Wing, 2003). A threshold for the oxygen content in the early atmosphere model was derived as $\sim 10^{-5}$ times the present-day atmospheric level (PAL, Pavlov and Kasting, 2002). The MIF of sulphur isotopes and recent studies of Fe-isotope compositions in ancient sediments (Rouxel *et al*., 2005) are in accord with earlier evidence for an oxygen-poor pre-Proterozoic atmosphere and a sharp increase in the oxygen level in the paleo-Proterozoic, as reviewed recently by Catling and Claire (2005).

These conclusions are further supported by recent work on Mo-isotope fractionation in black shales. The record (Fig. 27.22) shows a large range of mass-dependent Mo fractionation, of up to 0.8‰ per amu, in such sediments since about 2.5 Gyr. Before 3 Gyr, such fractionation effects are very small or absent, and the main increase in range appears to have occurred between 2.7 and 2.5 Gyr. The change over time is interpreted as resulting from the secular increase in the free oxygen content of the atmosphere and oceans. The solubility of Mo at surface temperatures (i.e. in rock weathering) is strongly redox sensitive, as Mo^{4+} is insoluble whereas Mo^{6+} forms the highly soluble MoO_4^{2-} (molybdate) ion. Molybdenum-isotope fractionation is not seen in igneous rocks and cannot occur in the surface environment unless Mo is in solution. In sedimentation under oxic or suboxic conditions, lighter Mo isotopes are preferentially sequestered, leaving isotopically heavy ocean water, whereas anoxic sedimentation removes all Mo from the water, so that the Mo in euxinic sediments reflects the sea-water composition. The upper envelope of the data set of Fig. 27.22 is thought to reflect the fractionated Mo-isotope composition of ocean water. At $\sim$ 2.5 Gyr both Mo-isotope fractionation and sulphur mass-independent fractionation are seen, and it thus appears that minor Mo dissolution and fractionation can occur at or even below the upper limit of $\sim 10^{-5}$ times the PAL value found for sulphur MIF. The Mo-isotope record complements the MIF record because of these very low threshold values for oxygen detection. This research is still in its infancy but has already extended the record of incipient oxygenation of the atmosphere, showing that it goes back to the late Archaean era (Siebert *et al*., 2005; Wille *et al*., 2007, and references therein).

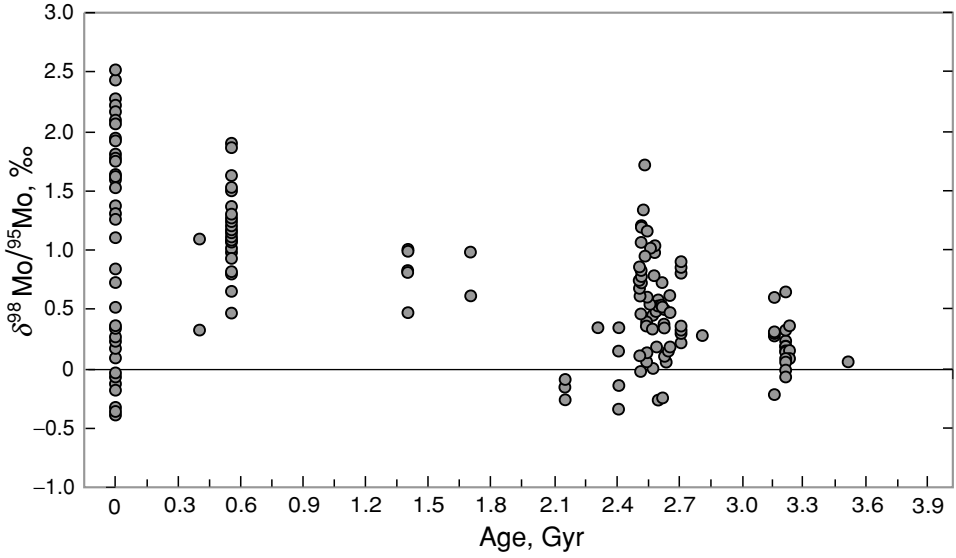

Fig. 27.22 Mass-dependent fractionation of Mo isotopes in suboxic and anoxic sediments, indicating a rise in the oxygen content in the Earth's atmosphere and hydrosphere 2.5 Gyr ago. The δ^{98}Mo/^{95}Mo value is relative to the Johnson Matthey ICP Mo standard solution (lot 602332B), with an Mo composition similar to the average continental crust. The typical analytical uncertainty on this value is 0.05‰ to 0.1‰. The Mo^{4+} ion is insoluble, whereas Mo^{6+} is soluble as MoO_4^{2-} if free oxygen is present. The ocean-water value is raised when the chemical (oxic or suboxic) sedimentation of Mo occurs, which favours the lighter isotopes; Mo-isotope fractionation is therefore an indication of oxic conditions. Suboxic sediments have variably lower δ^{98}Mo/^{95}Mo values than the Mo dissolved in the coeval sea water, and therefore the dissolved Mo (and thus oxygenated water in the oceans) at a time in the past is reflected by the large range of these values in such sediments. Data sources: Arnold *et al.* (2004) and references therein, Siebert *et al.* (2003, 2005), Wille *et al.* (2007), Nägler *et al.* (2005).

The rate of change in the oxygen concentration in the atmosphere, $dM(O_2)/dt$, is determined by the flux into this reservoir, $\varphi(t)\uparrow$, and the flux out, $\varphi(t)\downarrow$: thus $dM(O_2)/dt = \varphi(t)\uparrow + \varphi(t)\downarrow$. It is generally assumed that the major contribution to $\varphi(t)\uparrow$ comes from oxygenic photosynthesis, and that CH_2O represents the stoichiometry of its average product. Therefore $\varphi(t)\uparrow$ is represented by the reaction $CO_2 + H_2O \rightarrow CH_2O + O_2$, providing that part of the CH_2O was isolated from the atmosphere (e.g. buried in sediments) and therefore the reverse reaction is inhibited. In early Earth history, oxidation of the atmosphere was probably also promoted by H_2O and CH_4 photolysis, followed by the irreversible dissipation of hydrogen from the Earth's atmosphere (Section 20.3). The reverse flux $\varphi(t)\downarrow$ is mainly due to oxidative weathering and reactions with reducing, mainly volcanic, gases (Catling and Claire, 2005). As the ratio of $\varphi(t)\uparrow$ and $\varphi(t)\downarrow$ gradually shifted, an oxic

transition occurred (Kasting *et al*., 1993; Holland, 2002; Catling *et al*., 2001; Catling and Claire, 2005).

A rise in the oxygen concentration in the atmosphere between $\sim$ 2.6 and $\sim$2.2 Gyr ago allows an explanation of the Th/U mantle paradox, i.e. the mismatch of the Pb-isotope ratios and the actual Th/U ratios in the DMM (Section 27.2): U is oxidized to U^{6+} and becomes highly soluble as UO_2^{2+}, whereas Th remains insoluble. This leads to the efficient removal of U after weathering (Asmerom and Jacobsen, 1993; Kramers and Tolstikhin, 1997; Elliott *et al*., 1999). Turner *et al*. (2003) and Kelley *et al*. (2005) have shown that the U/Th ratios in altered oceanic crust are up to an order of magnitude higher than the average continental value, $\sim$ 4, which is in accord with the preferential subduction of U over Th. Interestingly, life on the Earth's surface has thus, via photosynthesis, led to enhanced U recycling into the mantle, which has boosted internal heat production and therefore supported plate tectonics: a paradigm of environmental feedback to the interior.

27.10 Summary

Several important requirements and constraints related to the global geochemical Earth model (to be discussed in the next chapter) follow from the above compilation of the relevant isotopic systematics.

Regarding the present-day isotopic characteristics of the principal Earth's accessible reservoirs (EARs), the data accumulated during the last decade, especially on melt inclusions, indicate substantial geochemical heterogeneities within both the MORB-source and, especially, the OIB-source mantle domains. The former has a major contribution of highly depleted material; the latter indicates variable contributions of generally enriched materials. At mid-ocean ridges, large magma generation rates may have allowed efficient mixing, obliterating small- and medium-scale heterogeneities. It could be partially for this reason that the MORB-source mantle appears less heterogeneous than the OIB-source mantle domains. A true relative homogeneity of the most depleted mantle material could be another reason.

As a paradigm, the East Pacific ridge (EPR) is characterized by the highest volume of magma generated per unit time and unit ridge length, and indeed EPR MORBs are the most homogeneous and the most depleted. The average $^{87}Sr/^{86}Sr$ and $^{143}Nd/^{144}Nd$ ratios in Atlantic MORBs appear to be slightly less depleted, and almost all the Indian MORB isotopic ratios are distinct from the EPR and Atlantic DMM characteristics (Fig. 27.2). Because the sub-Indian-Ocean MORB-source mantle is generally considered as an anomalous reservoir we have chosen, for the purpose of modelling, the average isotopic compositions of Sr, Nd and Hf in Atlantic and Pacific MORBs as representative for the MORB-source mantle as a whole (see Table 28.2 and its footnotes). As discussed in Section 27.2, the mantle

source (PREMA or FOZO) of deep plumes such as those of Hawaii and Iceland, which is also a significant component of other plumes, is similar to the DMM, and so we have included these two depleted mantle reservoirs as a single DMM in modelling. The other, highly diverse, mixing components in OIBs, which appear to be related in different ways to subduction and not to represent large reservoirs (Section 27.3), are not taken into account in our global modelling.

As emphasized in Chapter 26 and Section 27.6, the continental crust is the most heterogeneous reservoir. However, the REE abundance in the crust is relatively well constrained, thanks to the similar abundances of the middle REEs in the upper- and lower-crustal reservoirs (Table 26.3). Also, because of the global correlation of the Hf- and Nd-isotope ratios, the average crustal isotope compositions are constrained with some confidence: these values should lie on the regression line and the mean crustal ε_{143} value should be to the left of the "ocean array" (< -12, Fig. 27.13), as relatively young crustal rocks are preferentially weathered and transferred to the oceans. The model discussed in Chapter 28 operates with a single continental crust reservoir, which is sufficient for the Nd, Hf and noble-gas isotope systematics.

Because of the much more complicated behaviour of members of the Rb–Sr and Th–U–Pb families within the crustal reservoirs, the Sr and Pb crustal compositions are so diverse that two subreservoirs (a lower and upper crust to fit Rb–Sr) and even four (for the U–Th–Pb systematics) have been suggested for the proper modelling of their present-day characteristics, which in fact are highly model dependent (Kramers and Tolstikhin, 1997). The model of Chapter 28 therefore does not include the U–Th–Pb systematics, although that for Rb–Sr is considered.

The evolutionary trends display several important features, starting with the $^{142}Nd/^{144}Nd$ and $^{176}Hf/^{177}Hf$ records of the very early differentiation of the Earth, within the first few 100 Myr. In the model of Chapter 28, the formation of the core and core–mantle transition zone is the principal outcome of this early differentiation. The essence of the two-reservoir mantle model is that a flux of material carries primordial and early-produced radiogenic noble-gas species (and other relevant elements) from the apparently, but not completely, isolated small D″ reservoir into the convective degassing mantle, which acts as a source of radiogenic noble gases.

The continuous evolutionary trends of the post-Hadean era convincingly show the complementary development of the Earth's mantle and continental crust. The distribution of the data indicates that this development was not smooth. Substantial erosion of the continents appears to have started 2.7 to 2.5 Gyr ago, at the end of the Archaean, which period was also characterized by intense crustal growth and a gradual transition from a reducing to an oxidizing atmosphere.

28

Geochemical Earth model

28.1 Introduction to geochemical modelling

Generally, quantitative models are considered as the most advanced, final, step in the interpretation of experimental and analytical data. Three types of chemical evolutionary Earth model may be distinguished (in order of increasing complexity): (1) transport chemical models envisaging distinct homogeneous reservoirs and applying mainly mass-balance considerations (e.g. O'Nions *et al.*, 1979; Jacobsen and Wasserburg, 1979); (2) transport chemical models that take the temporal preservation of chemical and isotopic heterogeneities within reservoirs into account, highlighting the behaviour of the species within each reservoir (Kellogg *et al.*, 2002); (3) physical models with chemical tracers in them (Christensen and Hofmann, 1994; van Keken *et al.*, 2002; Samuel and Farnetani, 2003).

The models are best applied progressively, increasing the complexity only when simpler approaches and their deficiencies are understood. In this chapter we discuss the simplest model involving the transfer of material and species between distinct principal long-lived terrestrial reservoirs. The model includes two major stages of Earth history, accretion (Chapters 18 to 20) and post-accretion evolution. The data related to the isotopic systems modelled, ^{244}Pu–Xe(Pu), ^{129}I–^{129}Xe(I), ^{40}K–^{40}Ar, U–Th–He–Ne, ^{147}Sm–^{143}Nd, ^{87}Rb–^{87}Sr, ^{176}Lu–^{176}Hf and ^{87}Rb–^{87}Sr, were discussed in the previous chapter.

It should be emphasized that neither the model itself (Section 28.2) nor its reference solution (Section 28.3) are unique: they only illustrate one possible way to describe the Earth's materials, and the processes transferring and developing them, within the frame of a self-consistent semiquantitative concept, applying reasonable input parameters. Also only one reference solution is presented here, without analyses of the relationships between the input and output parameters: this work is in progress. The primary purpose of this model is to provide a quantitative test for

the concept of an Earth fractionated from originally chondritic-type matter into the reservoirs discussed in the earlier chapters of this Part, with their observed chemical and isotopic inventories and recorded evolutionary trends.

28.2 Multireservoir Earth model

The post-accretion evolutionary chemical model

We will describe the evolution of the principal terrestrial reservoirs (excluding the core and early atmo-hydrosphere) by a transport model similar to those published previously (Kramers and Tolstikhin, 1997; Tolstikhin and Marty, 1998; Tolstikhin *et al.*, 2006). As in the last of these, the mantle and crust are modelled as single non-subdivided reservoirs, and the D″ (DDP) layer is included as an almost fully isolated reservoir formed very early in Earth history, as discussed in Chapter 19 (Fig. 28.1).

After accretion and core segregation have ceased, decompression-related partial melting and fractionation in a mantle fractionation zone MFZ continued, producing a flux of liquid silicates that forms a short-lived "oceanic" crust (BOC, Fig. 28.1). This flux decreases with time, in accordance with the global heat loss from the Earth. The noble-gas constituents of this flux are quantitatively released into the atmo-hydrosphere (ATM). The oceanic crust is being contaminated by material eroded from the continents and by atmospheric gases. The outflux of the contaminated crust is split: the major part returns to the mantle, whereas a minor portion enters the subduction-related fractionation zone SFZ where continental crust is generated; the splitting proportion is governed by the continental-crust-generating flux of liquid silicate.

The model envisages the subduction-related fractionation at *sfz* as the only process supplying the continental crust (CCR) with mass and species (Fig. 28.1). To model crustal growth, the age distribution function $AGE(t_{\mathrm{FIN}} = \theta, t_{\mathrm{FIN}})$ is used as an input parameter that constrains the flux of liquid silicate from SFZ into the continental crust (Fig. 26.9). This flux and the fraction of liquid silicates in *sfz* determine the total influx, which is equal to the sum of two fluxes, that from the mantle wedge and that from the oceanic crust. We used a value for the flux ratio inferred from Th–U–Pb modelling (Kramers and Tolstikhin, 1997).

The crustal growth curve, $\mathrm{d}M_{\mathrm{CCR}}/\mathrm{d}t$, is a free parameter constrained by modelling. The flux of eroded material is the difference $AGE(t = \theta, t) - \mathrm{d}M_{\mathrm{CCR}}/\mathrm{d}t$. In this simple model with just one crustal reservoir, the composition of the eroded material is the same as the bulk crustal composition at a given time. The degassing flux from the crust into the atmosphere is described by the product of the degassing coefficient $L_{\mathrm{CCR,ATM}}$ (Gyr^{-1}) and the total amount of volatile species ${}^{i}N_{\mathrm{CCR}}$ (atoms

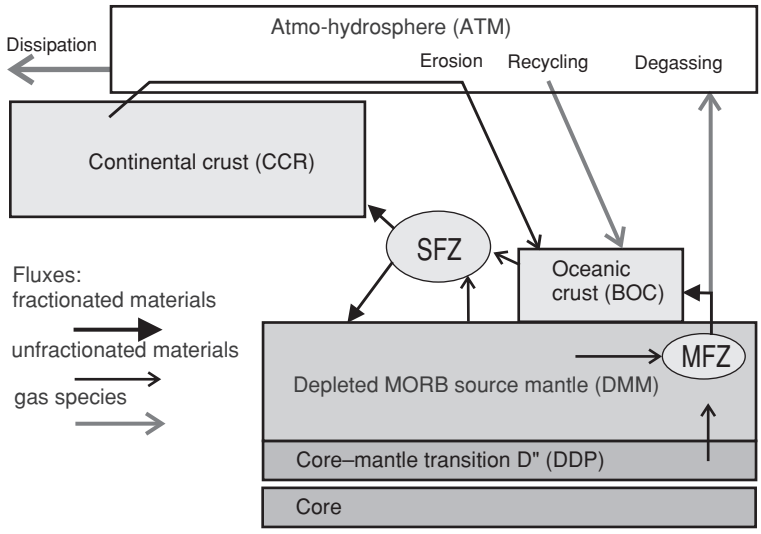

Fig. 28.1 Schematic presentation of chemical transport model: the post-accretion fluxes and processes. The partial melting and fractionation domains are MFZ for MORB-production and SFZ for continental-crust formation (equivalent to the mantle wedge above subduction zones). After Tolstikhin *et al.* (2006), © Elsevier Science 2006, reproduced by permission.

per reservoir) in the crust (i.e., $L_{\mathrm{CCR,ATM}} \times {}^{i}N_{\mathrm{CCR}}$), and the recycling flux of atmospheric noble gases into the mantle is described in a similar way.

Accreting materials

Even though proto-terrestrial material cannot be wholly identified with any known type of chondritic meteorite (Chapter 17), in our model we use chondrite-like initial elemental and isotopic abundances for the involatile elements Sm, Nd, Lu, Hf, W, U, Th and Sr (Table 28.1). The Rb–Sr and K–Ar systematics are also included: even though Rb and K are moderately volatile elements, their terrestrial initial abundances are reconstructed via the K/U and Rb/U ratios and the absolute initial concentration of involatile U (Figs. 14.4, 17.2).

For the absolute initial concentrations of the highly volatile noble gases in the "terrestrial regolith" that partially formed D″, only upper limits can be given: they should not be higher than those observed in solar-noble-gas-rich meteorites and the lunar regolith: $^{3}\mathrm{He}_{\mathrm{SIN}} < 1 \times 10^{-5}$ cm^3 STP g^{-1} (Table 11.3). The relative initial abundances of the light noble gas isotopes (He, Ne and Ar) are considered as solar by analogy with solar-implanted gases and taking into account the solar-like light-noble-gas signatures in the mantle. Chondrite-like material, the principal

Table 28.1 *Input parameters: the mass and composition of proto-terrestrial matter (at the time when the solar system was formed) and the corresponding decay constants. From Tolstikhin* et al. *(2006), © Elsevier Science 2006, reproduced by permission*

Parameter	Dimensions	Value	Footnote
mass of reservoir	g	5.98×10^{27}	*a*
metal/total mass ratio	ratio	0.3275	*a*
chondrite/basalt ratio for D″	ratio	0.2	*a*
^{232}Th	atoms g^{-1}	1.57×10^{14}	*b*
^{232}Th/^{238}U	atomic ratio	2.41	*b*
^{235}U/^{238}U	atomic ratio	0.316	
^{244}Pu/^{238}U	atomic ratio	0.01	*c*
^{127}I/^{232}Th	atomic ratio	0.206	*d*
^{129}I/^{127}I	atomic ratio	0.0001	*e*
^{40}K/^{238}U	atomic ratio	52	*f*
^{144}Nd	atoms g^{-1}	8.4×10^{14}	*g*
^{143}Nd/^{144}Nd	atomic ratio	0.506 673	*h*
^{147}Sm/^{144}Nd	atomic ratio	0.1964	*h*
^{144}Nd/Nd	atomic ratio	0.237 94	*h*
^{177}Hf	atoms g^{-1}	1.21×10^{14}	*i*
^{176}Hf/^{177}Hf	atomic ratio	0.279 82	*j*
^{176}Lu/^{177}Hf	atomic ratio	0.036 15	*j*
^{177}Hf/Hf	atomic ratio	0.185 99	*j*
^{86}Sr	atoms g^{-1}	9.15×10^{15}	*k*
^{87}Sr/^{86}Sr	atomic ratio	0.698 76	*l*
^{87}Rb/^{86}Sr	atomic ratio	0.0864	*m*
Co, Ni, Mo, Ir, Re, Au	norm. ratio	0.6725	*n*
^{184}W	norm. ratio	0.6725	*o*
^{182}W/^{184}W	atomic ratio	0.864 48	*p*
^{180}Hf/^{184}W	atomic ratio	1.325	*p*
^{182}Hf/^{180}Hf	atomic ratio	1.01×10^{-4}	*p*
^{4}He/^{3}He$_{SIN}$	atomic ratio	2310	*q*
^{36}Ar/^{3}He$_{SIN}$	atomic ratio	0.066	*r*
^{40}Ar/^{36}Ar$_{SIN}$	atomic ratio	0.01	*r*
^{130}Xe/^{3}He$_{SIN}$	atomic ratio	1.6×10^{-7}	*r*
^{3}He/^{130}Xe$_{Q}$	atomic ratio	0.323	*s*
^{4}He/^{130}Xe$_{Q}$	atomic ratio	2300	*s*
^{36}Ar/^{130}Xe$_{Q}$	atomic ratio	470	*s*
^{40}Ar/^{130}Xe$_{Q}$	atomic ratio	4.7	*s*
^{129}Xe/^{130}Xe$_{Q}$	atomic ratio	6.43	*s*
^{136}Xe/^{130}Xe$_{Q}$	atomic ratio	1.95	*s*
λ_{244}	Gyr^{-1}	8.41	*t*
$B_{244,fis}$	ratio	1.25×10^{-3}	
$Y(^{136}Xe)_{244}$	ratio	0.056	
λ_{238}	Gyr^{-1}	0.155 125	
$B_{238,fis}$	ratio	5.45×10^{-7}	
$Y(^{136}Xe)_{238}$	ratio	0.063	
$Y(^{4}He)_{238}$	ratio	8	
λ_{235}	Gyr^{-1}	0.984 85	
$Y(^{4}He)_{235}$	ratio	7	

Table 28.1 (*cont.*)

Parameter	Dimensions	Value	Footnote
λ_{232}	Gyr^{-1}	0.0494 75	
$Y(^4He)_{232}$	ratio	6	
λ_{182}	Gyr^{-1}	77.016 35	
λ_{176}	Gyr^{-1}	0.018 65	
λ_{147}	Gyr^{-1}	0.006 54	
λ_{129}	Gyr^{-1}	44.15	
λ_{87}	Gyr^{-1}	0.014 02	
λ_{40}	Gyr^{-1}	0.5543	

[a] First two rows, same as for the present-day Earth; third row, this proportion of chondrite-like material is enough to increase the mean basalt + regolith density by 7% and to stabilize this mixed material at the bottom of the convective mantle (Kellogg, 1997).
[b] Corresponds to U = 19 ppb and Th/U = 3.9 in the present-day BSE (Rocholl and Jochum, 1993).
[c] Meteoritic mean; this is close to the upper limit of the canonical ratio $^{244}Pu/^{238}U_{INI} = 0.0068 \pm 0.003$ (see compilation by Azbel and Tolstikhin, 1993).
[d] Corresponds to 10 ppm of ^{127}I in the BSE (Deruelle *et al.*, 1992). A somewhat lower $[^{127}I]_{BSE}$ value, ~ 3 ppm, is also possible (Muramatsu *et al.*, 2001; Muramatsu and Wedepohl, 1998): this difference does not change the important conclusion that the Earth has lost most of $^{129}Xe(I)$, Section 20.2.
[e] Meteoritic mean (Fig. 11.9).
[f] Corresponds to the present-day mass ratio $K/U_{BSE} = 12\,000$ (Jochum *et al.*, 1983).
[g] Corresponds to 1250 ppb of Nd in BSE (McDonough and Sun,1995).
[h] Chondritic systematics (Jacobsen and Wasserburg, 1984; Amelin and Rotenberg, 2004).
[i] From McDonough and Sun (1995).
[j] From Blichert-Toft and Albarède (1997).
[k] From McDonough and Sun (1995).
[l] From Wasserburg *et al.* (1977).
[m] From Hofmann (1988) and McDonough and Sun (1995); it corresponds to present-day K/Rb = 400 and $^{87}Sr/^{86}Sr_{BSE} = 0.7041$. The latter is slightly below the value 0.7045 (Jacobsen and Wasserburg, 1979), which is widely used but not really constrained (Blichert-Toft and Albarède, 1997).
[n] Chondritic abundances normalized to C1 and Al that would give 1 in the mantle if siderophile elements had not been sequestered into the core.
[o] In the case of tungsten, ^{184}W is the reference isotope for ^{182}Hf–^{182}W systematics.
[p] From Jacobsen (2005).
[q, r] The solar-implanted nuclide (SIN) abundances could be different from the solar-wind (SW) values because of the much more intense solar radiation during the first ~100 Myr after solar system (SOS) formation (see Wood *et al*., 2002). Also the astrophysical environment in which the implantation occurred is unknown. To highlight this possible difference we have used another abbreviation. The value listed for note *q* is after Pedroni and Begemann (1994); values for note *r* are assumed to be similar to the implanted solar wind (Anders and Grevesse, 1989). The isotope composition of Xe_{SIN} is not important because Xe_Q is by far the major Xe component.
[s] From Busemann *et al.* (2000).
[t] λ_{244} and all lines below: decay constants and $^{40}K \rightarrow {}^{40}Ar$ branching ratio 0.1048 from Villa and Renne (1998); the fission branching ratios and ^{136}Xe yields from Ozima and Podosek (2002).

constituent of D″, could preserve Q-type noble gases with enhanced abundances of heavy species (Fig. 11.5). Mixtures of solar-like and Q components (subsolar noble gases) are a general feature of chondritic meteorites, in particular enstatite chondrites (Busemann *et al.*, 2003). A mixture of Q- and solar-implanted gases appears to be a suitable starting composition (Kramers, 2003). The proportion of mixing is an unknown parameter constrained by modelling (Table 28.3).

28.3 Results: isotope geochemical constraints on Earth's evolution

The Hadean era (4.4 to 3.8 Gyr ago)

To reconstruct the rate of mantle fractionation in the Hadean era, we have assumed that this rate (equal to the rate of MORB + OIB production) and the corresponding "degassing" flux of liquid silicates was intense in early Earth history and then decreased gradually through time down to the present-day value. Taking into account (1) that no significant energy input from external sources (impacts) into the Earth is expected (at least after the late bombardment event at $\sim$ 3.9 Gyr ago), (2) that radioactive heat-producing isotopes are decaying and (3) that the Earth is gradually releasing energy acquired during accretion and core segregation, this assumption appears to be reasonable. We varied the rate of mantle-melt production (and adequate degassing) through time until the calculated present-day mantle ratio for ^{136}Xe(Pu)/^{136}Xe(U) approached the observed value (Table 28.3). In the reference solution thus obtained, the time-averaged rate of mantle fractionation and the attendant flux of silicate melt are $\sim$ two orders of magnitude greater during the Hadean era than they are at present.

Extremely efficient mantle degassing is a very robust result, constrained by the low ^{136}Xe(Pu)/^{136}Xe(U) ratio in mantle xenon. The effective mantle ^{130}Xe-depletion factor is of the order of 10^{-6}, and a similar value was derived by Tolstikhin and Marty (1998).

Because mantle convection governs post-accretion melt generation and degassing, the high rate of degassing during the first 1 Gyr or so of Earth history indicates vigorous convection within this reservoir. Energy released in the course of accretion and core formation and still available in the Earth was probably the major moving force of this early intense convection and degassing. However, the degassing rate could also have been enhanced by late impacts (between 4.5 and 3.9 Gyr ago) that disrupted the crust, leading to the uplift of hot mantle material, melting and degassing. Such effects could have been considerable even if the total flux of impactors was small (Pritchard and Stevenson, 2000). Correspondingly, in this model we assume that the late bombardment caused intense melt production and degassing.

Geological evolution (from 4.0 Gyr ago to the present): Sm–Nd, Lu–Hf and Rb–Sr isotope systematics

The rate of crustal growth and mass fluxes into and from the crust are very similar to those constrained by the Th–U–Pb systematics (Kramers and Tolstikhin, 1997). A similar crustal-growth curve was derived by Jacobsen (1988) and Azbel and Tolstikhin (1988). Other parameters that govern the distribution of the elements of interest among the three reservoirs are the melt fractions in the mantle and subduction fractionation zones and the respective partition coefficients.

The mean fraction of liquid silicates in the mantle fractionation zone (MFZ) during accretion, 0.3, is constrained by the modelling of siderophile-element partitioning into the metal phase (Kramers, 1998). Afterwards this fraction smoothly decreases to the present-day value, ~ 0.1, derived from models of mantle melt generation at ridges (e.g. McKenzie and O'Nions, 1991).

The melt fraction in the subduction fractionation zone (SFZ) appears to be a more complicated parameter. Enhanced values, ~ 0.1, were derived for the major-element compositions of arc volcanics (Chapter 25). These values do not allow sufficient fractionation of the melts produced and their enrichment in highly incompatible elements. This is illustrated by the Rb/Sr ratio of modern arc basalts, ~ 0.04 (well below the mean crustal value, 0.15; see Tables 24.1 and 26.3). To reconcile the crustal budget of highly incompatible elements, small melt fractions in the subduction fractionation zone have been invoked: 0.005 (Jacobsen and Wasserburg, 1979), 0.01 (Albarède, 1998a), 0.015 (Azbel and Tolstikhin, 1988; Kramers and Tolstikhin, 1997; Nägler and Kramers, 1998). An estimate inferred from our model, 0.01, is similar to those above.

A possible interpretation of this result is that these small melt fractions reflect a difference between the total amount of melt that was generated at subduction zones and underwent crystallization differentiation and a mafic cumulate that was delaminated and sank back into the mantle (Section 26.7). Although delamination was been included in the modelling, in a simple batch-melting model the enrichment of incompatible elements in a small primary melt fraction is similar to that for a large melt fraction when followed by crystal fractionation giving the same final fraction of melt. The result is the accepted crustal composition for the elements of interest. The discrepancy discussed above implies that delamination is substantial; the melt flux into the crust should be ~ 10 times that shown in Fig. 28.2, of which 90% would have been delaminated. Further, the model-derived value of the upper-crustal erosion flux, mainly constrained by Pb and U recycling to solve the second lead paradox, exceeds the value indicated by direct observations on sediment subduction by a factor ~ 2 (Section 25.1). Because the model does not include a delamination flux from the crust, the reference solution generates a more intense sedimentary

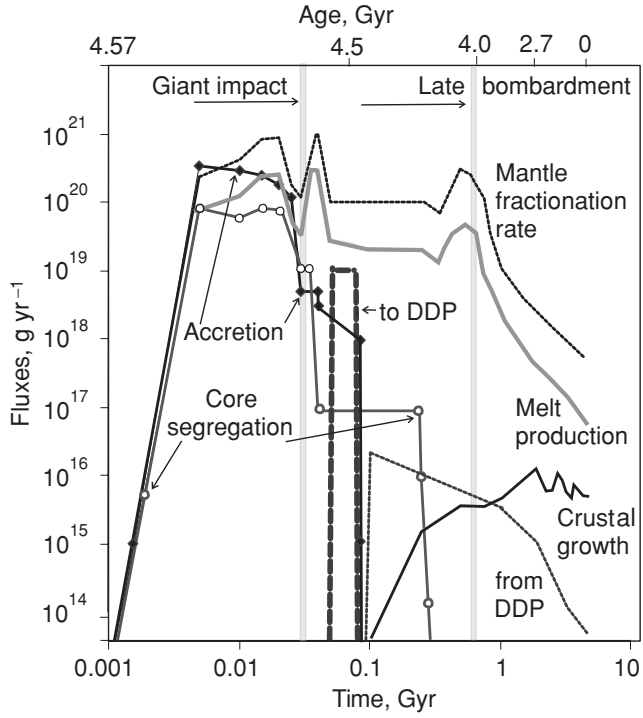

Fig. 28.2 Mass fluxes inferred from the reference model solution. The accretion mass flux is constrained by the Earth's mass and the Earth accretion time scale (obtained from the Hf–W systematics, e.g. Section 18.3), and by the mass of D″ (which is similar to the present-day value, Table 28.3), its formation time scale ($\sim$ 70 Myr, from mantle xenology, e.g. Kunz *et al.*, 1998) and the fraction of chondritic material in D″ (0.2, see the footnotes to Table 28.3); correspondingly, the flux of proto-terrestrial material constitutes one-fifth of the total flux into D″. The core-segregation mass flux is constrained by the core mass and the accretion time scale, with a tailing-off constrained by the noble-metal abundances in the mantle (Chapter 18). The melt production in the mantle is constrained by the core segregation rate for the first $\sim$ 100 Myr and by mantle xenology thereafter (Section 27.5); this flux in turn constrains the mantle fractionation rate via the melt fraction coefficient (see footnote 11 to Table 28.2). The mass flux from D″ is constrained by the mantle noble-gas systematics (Section 27.4). The crustal-growth flux (right-hand bottom corner of the figure) and the erosion flux (not shown) have been adopted from the Th–U–Pb model (Kramers and Tolstikhin, 1997). After Tolstikhin *et al.* (2006), © Elsevier Science 2006, reproduced by permission.

flux instead. Even though the delaminated material is predicted to be depleted, the delamination/sediment flux ratio, $\sim$ 20, implies that a comparable rate of U removal could be associated with delamination.

The model-derived abundances of Lu, Hf, Sm and Nd, along with the isotopic compositions of the daughter elements in differentiated reservoirs rely on the melt–solid partition of these elements. The REE bulk partition coefficients are reasonably

well constrained for mantle mineralogy (see Table 24.2 and its footnotes). For a mantle peridotite residue with 3% garnet, we used $D(\mathrm{Sm}) = 0.065$ and $D(\mathrm{Nd}) = 0.03$ (very similar to the values inferred by Jacobsen and Wasserburg (1979) for fractionation processes occurring in both MFZ and SFZ zones. This gives good agreement between the calculated and observed abundances of the species of interest in the accessible reservoirs, the mantle and the continental crust (Table 28.2 and Fig. 27.13). Because D″ largely consists of fractionated material that was separated from the bulk silicate Earth very early, its time-integrated isotopic effect on the mantle is large, $\varepsilon_{143} \approx +5$. Continuous extraction of the continental crust over time leads to the value $\varepsilon_{143} \approx +4$ for the mantle, ending up with a present-day total $\varepsilon_{143} \approx +9$ (Figs. 27.2(a), 27.18).

The bulk partition coefficient for Hf, like those for Sm and Nd, is considered in the model to be identical in both mantle fractionation processes occurring in MFZ and SFZ (Fig. 28.1). It is adjusted to produce a crustal Hf/Nd ratio of 0.18 (Table 26.3). The value derived from the model is $D(\mathrm{Hf}) = 0.0385$. The partition coefficient for Lu in the mantle fractionation zone MFZ, $D(\mathrm{Lu, MFZ}) = 0.190$, is adjusted to obtain a somewhat Lu-enriched mantle, so that the mixing line between the mantle and crustal end-members approaches the regression of the observed terrestrial Hf–Nd array in Fig. 27.13. This enhanced value leads to relatively low Lu/Hf ratios and ultimately low ε_{176} values in D″ (Table 28.2). This could reflect deep partial mantle melting (in the presence of garnet) in the early, hotter, mantle, when D″ was formed. Such partitioning of Hf allows an explanation of the Hf–Nd isotope relationships (Fig. 27.13).

The bulk partition coefficients for Sm, Nd, Lu and Hf listed above can be independently derived for a melt equilibrated with mantle peridotite consisting of Ol = 67%, Opx = 20%, Cpx = 10% and Garnet = 3%, applying the mineral partition coefficients from McKenzie and O'Nions (1991). A similar abundance of garnet in a mantle mineral assemblage (a few per cent) was derived by Blichert-Toft and Arndt (1999) from their study of how mantle fractionation causes enhanced initial $^{176}\mathrm{Hf}/^{177}\mathrm{Hf}$ ratios in ancient komatiites.

The subduction–fractionation bulk partition coefficient for Lu, 0.145, fits the mantle and crustal end-members, so that the mean ε_{176} values approach the regression line of the terrestrial Hf–Nd array (Fig. 27.13).

The Rb and Sr isotope abundances in the two accessible reservoirs, the mantle and crust (Table 28.2), are in overall agreement with observation (Chapter 27). Thus, Jacobsen (1988) inferred from a layered mantle model that Sr = 15 ppm and Rb/Sr = 0.022 for the MORB-source mantle. Recently Workman and Hart (2005) suggested a much lower Rb/Sr ratio, 0.0065. The reason for the difference is that in the latter model a late start for mantle depletion is assumed (3 Gyr), based on the concept of gradual crustal growth. Further, Workman and Hart (2005) assumed the

Table 28.2 *Calculated abundances of Sm, Nd, Lu, Hf, Rb and Sr isotopes in the principal terrestrial reservoirs: D″ (DDP), the mantle (DMM) and the continental crust (CCR) together with the solid–melt bulk partition coefficients*[11]

			DDP	DMM	CCR
	Parameter	Dimension	*a*	*b*	*c*
1	mass	10^{25} g	24.5	372	2.26
2	Nd	ppm	5.4	0.86	22.6
3	$^{147}Sm/^{144}Nd$ (Sm/Nd)	ratio	0.17 (0.28)	0.22 (0.37)	0.115 (0.19)
4	ε_{143}	ratio	−15	9	−17
5	Hf	ppm	1.150	0.203	4.370
6	$^{176}Lu/^{177}Hf$ (Lu/Hf)	ratio	0.021 (0.15)	0.040 (0.29)	0.012 (0.087)
7	ε_{176}	ratio	−35	16.4	−20
8	Sr	ppm	83	14	360
9	$^{87}Rb/^{86}Sr$ (Rb/Sr)	ratio	0.092 (0.03)	0.045 (0.015)	0.28 (0.1)
10	$^{87}Sr/^{86}Sr$	ratio	0.7048	0.7029	0.7102

[1] Mass ratios are shown within parentheses.
[2b] Comparable with 0.8 ppm from McKenzie and O'Nions (1991), 0.77 ppm from Nägler and Kramers (1998), 0.7 ppm from Salters and Stracke (2004, Table 24.1) and somewhat above 0.58 ppm from Workman and Hart (2005).
[2c, 3c] Calculated crustal Nd concentrations and Sm/Nd, Hf/Nd ratios are within the range of estimates suggested by different authors (see Table 11 in Rudnick and Fountain, 1995).
[3b] Indistinguishable from the ratio derived by Chauvel and Blichert-Toft (2001) from MORB-source mantle-melting models.
[4, 7] Present-day SOS ratios (to calculate ε values): $^{143}Nd/^{144}Nd = 0.512\,638$ and $^{176}Hf/^{177}Hf = 0.282\,772$.
[4b,c, 7b,c] The ε-coordinates of mantle and crustal end-members lie on the Hf–Nd isotope terrestrial array regression line (Fig. 27.13). $^{143}Nd/^{144}Nd_{DMM} = 0.513\,13$ ($\varepsilon_{143} = +9$) as in Workman and Hart (2005); $^{176}Hf/^{177}Hf_{DMM}$ is in between estimates presented by these authors, $\varepsilon_{176} = +17.6$, and by Salters and Stracke (2004), $\varepsilon_{176} = +15.5$.
[6b] Same as inferred by Blichert-Toft and Arndt (1999) for the source of ancient komatiites. Chauvel and Blichert-Toft (2001) derived Lu/Hf = 0.28 from MORB-source mantle-melting models.
[6c] The model-derived $^{176}Lu/^{177}Hf$ ratio is indistinguishable from the average ratio in sedimentary rocks, 0.0117, which could be a proxy for the continental crust (see Table 2 in Vervoort *et al.*, 1999).
[8c] Slightly above the value in Table 26.3.
[9b] Slightly above that proposed by Salters and Stracke (2004).
[9c] Between those suggested by Jacobsen and Wasserburg (1979) and Taylor and McLennan (1985).
[10b] Corresponds to the MOR-segment-arranged data base (307 MOR segments, totally 1300 ratios) of Su (2002), $^{87}Sr/^{86}Sr = 0.702\,85 \pm 0.000\,39$ ($\pm 1\sigma$). Salters and Stracke (2004) and Workman and Hart (2005) suggested somewhat lower ratios, 0.7027 and 0.702 63, respectively.
[10c] Within the limits suggested for the total continental crust by Jacobsen and Wasserburg (1979).
[11] Solid–melt bulk partition coefficients are as follows. In the mantle fractionation zone (MFZ, Fig. 28.1): Nd, 0.025; Sm, 0.065; Hf, 0.0385; Lu, 0.19; Sr, 0.033; Rb, 0.001. In subduction-related fractionation (SFZ, Fig. 28.1): Nd, 0.03; Sm, 0.065; Hf, 0.0385; Lu, 0.145; Sr, 0.033; Rb, 0.0002. The model melt fraction in the mantle fractionation zone is a linear function of time decreasing from 0.3 at $t = 0$ (the start of accretion) to 0.1 (at the present time); it is a constant equal to 0.01 in the subduction fractionation zone (see the main text for a discussion).
From Tolstikhin *et al.* (2006), © Elsevier Science 2006, reproduced by permission.

depletion of a relatively small portion of the mantle only. Our reference-solution ratio, 0.015, is intermediate between the two models. A low Sr for the mantle was obtained from the Sr–Ce correlation in MORB samples and a Ce concentration derived from mantle-melting models (Workman and Hart, 2005). However, in other investigations of mantle melting (e.g. McKenzie and O'Nions, 1991) Ce (and Sr) concentrations for the depleted mantle ~ 1.5 higher have been adopted, closer to our estimate.

The model Sr concentration and the Rb/Sr ratio in the bulk continental crust shown in Table 28.2 are close to the value [Sr] = 325 ppm of Rudnick and Fountain (1995) and the value Rb/Sr = 0.12 of Taylor and McLennan (1985) respectively.

Geological evolution from 4.0 Gyr until the present: the noble gases

According to the reference solution of our model, the D″ layer is an important reservoir of the radioactive heat-generating elements, U, Th and K: the model-derived abundances of these elements in D″ are $\sim 20\%$ of the BSE amounts (Table 28.3). The high abundance of K means that the amount of $^{40}Ar^*$ hidden in D″ allows a terrestrial inventory of the ^{40}K–$^{40}Ar^*$ systematics having $K/U_{BSE} = 12\,000$. The abundances of light solar noble gases are constrained by a low (U and Th)/^{3}He ratio, indicating an almost-solar isotope composition of He. The ^{3}He concentration in the model terrestrial regolith is about 0.01 times that observed in lunar ilmenites (Benkert *et al.*, 1993). From the concentrations of other solar nuclides implanted in the terrestrial regolith can be derived (see the entries for $^4He/^3He_{SIN}$, $^{36}Ar/^3He_{SIN}$ and $^{130}Xe/^3He_{SIN}$ in Table 28.1). The contribution of solar-particle-implanted material in the flux from D″ into the mantle is less than 0.05% of the Earth's mass over geological time. A prediction (which also follows from the model of Tolstikhin and Marty, 1998) is that very primitive He and Ne may be found in plume-derived samples, in which a D″-derived solar-like component prevails over mantle radiogenic and recycled atmospheric noble gases.

The D″ layer is the source of early produced $^{129}Xe(I)$ and $^{131–136}Xe(Pu)$ in the solid Earth. A high $^{129}Xe(I)/^{136}Xe(Pu)$ ratio, inferred for mantle xenon, constrains the early formation of the layer (Fig. 28.2). The contribution of a heavy-noble-gas-enriched unfractionated Q component (Table 28.3) is derived using the ratio of $^{129}Xe(I)$ and unfractionated ^{130}Xe, ~ 12, as observed in CO_2-gas Xe (Phinney *et al.*, 1978; Tolstikhin and O'Nions, 1996; Caffee *et al.*, 1999); our reference solution gives a slightly higher ratio. The concentrations of Q gases in D″ predicted by the reference solution (Table 28.3) appear to be quite reasonable: they are a factor $\sim 10^3$ lower than those observed in C1 chondrites (Fig. 11.5). The mixing proportion is $Xe_Q/Xe_{SIN} = 340$, and Q noble gases contribute ~ 0.4 of the $^{36}Ar_Q$ in D″. The occurrence of Q noble gases in D″ allows a more general

Table 28.3 *Calculated abundances of noble-gas species[13,14] and parent elements in the principal terrestrial reservoirs*

			D″	Mantle	Cont. crust
	Parameter	Dimensions	*a*	*b*	*c*
1	Mass	10^{25} g	24.5	372	2.26
2	U	ppb	71.5	7.7	1300
3	^{3}He	cm^3 STP g^{-1}	2.5×10^{-7}	6.7×10^{-11}	5×10^{-12}
4	^{4}He/^{3}He	ratio	2.8×10^{3}	8.5×10^{4}	1×10^{8}
5	^{40}Ar	cm^3 STP g^{-1}	6.7×10^{-5}	2.3×10^{-6}	1.7×10^{-4}
6	^{40}Ar/^{36}Ar	ratio	2.9×10^{3}	4.8×10^{4}	—
7	^{130}Xe	cm^3 STP g^{-1}	1.4×10^{-11}	3.5×10^{-14}	0
8	^{129}Xe/^{130}Xe	ratio	17.5	7.6	—
9	^{136}Xe/^{130}Xe	ratio	2.47	2.54	—
10	^{136}Xe(U)	cm^3 STP g^{-1}	2.3×10^{-13}	1.2×10^{-14}	1.1×10^{-12}
11	^{129}Xe(I)/^{136}Xe(U)	ratio	664	4.5	0
12	^{136}Xe(Pu)/{^{136}Xe(U) + ^{136}Xe(Pu)}	ratio	0.97	0.28	0.02

[1a] The initial model D″ mass is 2.46×10^{26} g, so only 6% of the D″ mass ($\leq 0.05\%$ $M_\oplus$) was entrained by mantle convective flow and maintained the D″-sourced noble gas flux through the mantle in the course of Earth history.

[2a,b,c] The crustal concentration of U is equal to that suggested by Weaver and Tarney (1984) and is $\sim 10\%$ below the estimate of Rudnick and Fountain (1995). The mantle U concentration is the same as that derived from U–Th–Pb modelling by Kramers and Tolstikhin (1997) for the depleted upper mantle.

[3a] This concentration of $^{3}He_{DDP}$ corresponds to $^{3}He_{SIN} = 1.25 \times 10^{-6}$ cm^3 STP g^{-1} implanted in the "terrestrial regolith", e.g. slightly below the concentrations actually observed in solar-noble-gas-rich meteorites (e.g. Acfer, Table 11.3).

[3b] The model-derived $[^{4}He]_{DMM}$ and $[^{3}He]_{DMM}$ are somewhat higher than those derived for layered mantle models (Marty and Tolstikhin, 1998), because of the higher U and Th concentrations and their mantle residence time.

[3c] $[^{3}He]_{CCR}$ in this cell is computed as a product of U and Th decay in the crust; this concentration and the ^{4}He/^{3}He ratio below (cell 4*c*) give the mean (U and Th)–He age of the continental crust as 1.7 Gyr, similar to the mean K–Ar age: for simplicity the crustal degassing coefficients for radiogenic Ar and He were assumed to be equal.

[4a] All ^{4}He/^{3}He and ^{21}Ne/^{22}Ne ratios, observed in plume-derived rocks, minerals and fluids, can be obtained by mixing of noble gases from D″, plume-source and DMM.

[5a] The portion of terrestrial $^{40}Ar^{*}$ generated and preserved in D″ amounts to 24% of the terrestrial inventory. Along with the atmospheric $^{40}Ar^{*} = 3.69 \times 10^{22}$ cm^3 STP, the values in cells (5*a*, *b*, *c*) add up to 6.55×10^{22} cm^3 STP, which is 88% of the total $^{40}Ar^{*}$ generated by terrestrial potassium; 12% of terrestrial $^{40}Ar^{*}$ was lost along with ^{129}Xe(I) and ^{136}Xe(Pu).

[6b] The ^{40}Ar/$^{36}Ar_{DMM}$ ratio results mainly from $^{36}Ar_{ATM}$ recycling into the mantle.

[7a] $[^{130}Xe]_{Q,DDP}$ is determined from the model-derived $[^{129}Xe(I)]_{DDP}$ and Xe isotope systematics in CO_2-gas xenon (cell 8*a*). In turn, $[^{130}Xe]_{Q,DDP}$ and $[^{3}He]_{SIN}$ determine the mixing proportion of Q and solar initial noble gas components. The model-derived ratio of $^{130}Xe_Q/^{130}Xe_{SIN} = 340$, and the ratio of $^{36}Ar_Q/^{36}Ar_{SIN} = 0.39$. $[^{130}Xe]_{Q,DDP}$ is a factor ~ 50 below those observed in bulk carbonaceous chondrites (Fig. 11.5).

solution of the model, which now does not require the degassing of Q noble gases from a chondrite matter at a late stage of accretion.

The values of the flux from D″ into the mantle, the mantle degassing flux and the recycling rate of atmospheric Xe and Ar were adjusted to obtain model He, Ar and Xe isotope compositions and a ^{3}He-concentration (Table 28.3) similar to the values accepted for the MORB-source mantle (Section 27.4). Atmosphere recycling into the mantle is essential: without it, the ^{40}Ar/^{36}Ar ratio derived for the mantle Ar could be as high as $\sim 300\,000$.

As mentioned above the crust is not an important reservoir for the terrestrial inventory of radiogenic noble gases. Setting the value of the degassing coefficient $L_{\mathrm{CCR,ATM}}$ to 0.5 Gyr^{-1} yields a mean ^{40}Ar–^{40}K age for the continental crust that is $\sim 30\%$ younger than the Sm–Nd age, 2.2 Gyr. Then the total present-day amount of radiogenic ^{40}Ar* in the partially degassed crust is $\sim 6\%$ of the total terrestrial inventory of this nuclide. The model-derived crustal and mantle concentrations of U and other radioactive elements (Table 28.3) are in reasonable agreement with the available estimates (Table 17.1).

Summarizing, the reference solution shows that a D″ layer of the type assumed in this model enables one to resolve terrestrial paradoxes of both solar and radiogenic noble gases and also of the inventory of incompatible elements (Chapter 19). As D″ was formed from slightly fractionated (enriched) matter and was isolated very early, it acts as a second enriched reservoir (in addition to the continental crust). The two reservoirs balance, within the framework of the chondritic Earth model, a wholly depleted mantle in terms of incompatible-element concentrations and the Sm–Nd, Lu–Hf and Rb–Sr isotopic systematics.

←

[7b] ^{130}Xe in the present-day mantle is mainly air-derived recycled Xe (Tolstikhin and O'Nions, 1996; Tolstikhin and Marty, 1998).
[8a] Similar to the ratio of ^{129}Xe over the light-isotope-enriched fraction of ^{130}Xe observed in CO_2-gas xenon (Tolstikhin and O'Nions, 1996).
[8b, 9b] These ratios fit the observed ^{129}Xe/^{130}Xe versus ^{136}Xe/^{130}Xe mantle correlation (Fig. 27.8).
[12a] Xe(Pu) is by far the most important fission Xe component in D″.
[12b] Contribution of Xe(Pu) as proposed by Kunz *et al.* (1998).
[13] Noble gases are treated as incompatible elements with a solid–melt bulk partition coefficient = 0.001 for all noble gas species. In the course of mantle magmatism (for which the rate is shown in Fig. 28.2) all noble gases are transferred from the respective melt flux into the atmosphere and only this degassing flux is envisaged in the model.
[14] Noble-gas recycling from the atmosphere into the mantle is treated as a flux proportional to the atmospheric abundances, with constant coefficients, 0.001 Gyr^{-1} for Ar and 0.004 Gyr^{-1} for Xe (see Tolstikhin and Marty, 1998, and Ballentine and Barfod, 2000, for a detailed discussion of the noble-gas-recycling contamination problem).

28.4 Summary

In this modelling process, it has been shown that the observed inventories and isotope characteristics of noble-gas and other incompatible trace elements in the Earth's mantle and continental crust can be reproduced by a transport-balance model based on a single convecting mantle and starting from accreting matter that had, on average, a chondrite-like composition. An early-formed D″ layer, consisting of sunken oceanic crust and including a chondritic regolith component, is essential for this model to be successful.

Such a D″ layer could have formed in the late stages of the Earth's accretion by the subduction of basaltic/komatiitic crust loaded with chondritic regolith (as proposed by Tolstikhin and Hofmann, 2005). The subducted material (containing metal as a major constituent of the regolith and therefore intrinsically more dense than the silicate mantle) could have accumulated at the base of the mantle above the core and stabilized there (as proposed by e.g. Samuel and Farnetani, 2003; Mao *et al.*, 2004). This scenario has important geochemical consequences and enables one to reconcile mass balances with whole-mantle convection in the framework of a chondritic Earth model.

The model D″ is an important reservoir containing $\sim 20\%$ of the terrestrial incompatible trace elements. These include heat-generating U, Th and K, and therefore a significant portion of radiogenic heat is generated at the base of the silicate mantle, stimulating mantle convection and increasing the heat flow from the depleted mantle.

Because of its early formation and efficient isolation, the D″ layer is the major store for early-generated radiogenic noble gas isotopes, as well as solar and planetary ones (Q). Fluxes of mass and/or species from the D″ layer into the convecting mantle and the mixing of D″-derived species with the radiogenic components generated in the mantle and a recycled air component can explain the observed noble-gas isotope patterns, which range from almost solar in some plume-related samples to those typical of MORBs. A small amount of solar-particle-implanted material, less than 0.0005 $M_{\oplus}$, is enough to maintain the mantle's noble-gas flow throughout geological history.

The model predicts an extremely high degree of mantle degassing, constrained by a low $^{136}Xe(Pu)/^{136}Xe(Pu, U)$ ratio, < 0.3, in the mantle Xe, especially taking into account that the major portion of $^{136}Xe(Pu)$ is transferred into the mantle from the D″ layer, and so the intrinsic mantle ratio (the ratio for the degassed mantle in the absence of fluxes from D″ and the atmosphere) should be much less than the observed value.

For the degassing to reach the levels required by the model, the mantle fractionation rate in the Hadean and the corresponding flux of liquid silicates would

need to have been on average two to three orders of magnitude greater than their present-day values. With the exception of helium and (in some cases) neon, the heavier non-radiogenic mantle noble-gas species are mainly recycled atmospheric components.

Although the Sm/Nd and Lu/Hf fractionation of D″ relative to that of the BSE is weak, its early isolation causes a substantial isotopic time-integrated effect and thus allows the signatures of ^{147}Sm–^{143}Nd and ^{176}Lu–^{176}Hf in the mantle and crustal reservoirs to be reconciled.

Much work is still needed to verify the proposed origin, history and significance of D″ as an important geochemical reservoir, including the modelling of terrestrial regolith accumulation on the surface of an early basaltic crust, its subduction and stabilization at the base of a convecting mantle. The search for such deep ancient reservoir(s) through new isotopic tracers (such as ^{182}W and ^{142}Nd) and noble-metal isotope systematics (e.g. Pt–Os and Re–Os; Brandon *et al.*, 2003) is important. We have merely demonstrated that a D″ mass (2.3×10^{26} g) in agreement with seismic observations, and the one-fifth proportion of regolith material to crustal material required to stabilize D″, allows fits to geochemical data in an Earth model with whole-mantle convection.

References

Abe, Y. (1993). Physical state of the very early earth. *Lithos*, **30**, 223–35.

Abia, C., Busso, M., Gallino, R., Dominguez, I., Straniero, O. and Isern, J. (2001). The ^{85}Kr s-process branching and the mass of carbon stars. *Astrophys. J.*, **559**, 1117–34.

Adams, F. C. and Laughlin, G. (2000). Protostellar disk formation and early evolution. In *From Dust to Terrestrial Planets*, eds. W. Benz, R. Kallenbach and G. W. Lugmair. Dordrecht: Kluwer Acad. Pub., pp. 23–38.

Agnor, C. B., Canup, R. M. and Levison, H. F. (1999). On the character and consequences of large impacts in the late stage of terrestrial planet formation. *Icarus*, **142**, 219–37.

Ahrens, T. J. (1990). Earth accretion. In *Origin of the Earth,* eds. H. E. Newsom and J. H. Jones. Oxford: Oxford University Press, pp. 211–27.

Ahrens, T. J. (1993). Impact erosion of terrestrial planetary atmospheres. *Ann. Rev. Earth Planet. Sci.*, **21**, 525–55.

Akulov, Y. A. and Mamyrin, B. A. (2004). Difference between the triton beta decay constants in atomic and molecular tritium measured by the helium isotope method. *Phys. Lett. B*, **600**, 41–7.

Albarède, F. (1998a). Time-dependent models of U–Th–He and K–Ar evolution and the layering of mantle convection. *Chem. Geol.*, **145**, 413–29.

Albarède, F. (1998b). The growth of continental crust. *Tectonophysics*, **296**, 1–14.

Aleon, J., Robert, F., Duprat, J. and Derenne, S. (2005). Extreme oxygen isotopic ratios in the early solar system. *Nature*, **437**, 385–8.

Alexander, C. M. O. (1994). Trace-element distributions within ordinary chondrite chondrules – implications for chondrule formation conditions and precursors. *Geochim. Cosmochim. Acta*, **58**, 3451–67.

Alexander, C. M. O. (1996). Recycling and volatile loss in chondrule formation. In *Chondrules and the Protoplanetary Disk*, eds. R. H. Hewins, R. H. Jones and E. R. D. Scott. Cambridge: Cambridge University Press, pp. 233–41.

Alexander, C. M. O. (2004). Chemical equilibrium and kinetic constraints for chondrule and CAI formation conditions. *Geochim. Cosmochim. Acta*, **68**, 3943–69.

Alexander, C. M. O., Arden, J. W., Ash, R. D. and Pillinger, C. T. (1990a). Presolar components in the ordinary chondrites. *Earth Planet. Sci. Lett.*, **99**, 220–9.

Alexander, C. M. O., Swan, P. and Walker, R. M. (1990b). *In situ* measurement of interstellar silicon carbide in two CM chondrite meteorites. *Nature*, **348**, 715–7.

Alfe, D., Gillan, M. J. and Price, G. D. (2000). Constraints on the composition of the Earth's core from *ab initio* calculations. *Nature*, **405**, 172–5.

Alibert, C., Norman, M. D. and McCulloch, M. T. (1994). An ancient Sm–Nd age for a ferroan noritic anorthosite clast from lunar breccia 67016. *Geochim. Cosmochim. Acta*, **58**, 2921–6.

Alibes, A., Labay, J. and Canal R. (2001). Galactic chemical abundance evolution in the solar neighborhood up to the iron peak. *Astron. Astrophys*., **370**, 1103–21.

Allan, N. L., Du, Z., Lavrentiev, M. Y., Blundy, J. D., Purton, J. A. and van Westrenen, W. (2003). Atomistic simulation of mineral–melt trace-element partitioning. *Phys. Earth Planet. Inter.*, **139**, 93–111.

Allègre, C. J. (1982). Chemical geodynamics. *Tectonophysics*, **81**, 109–32.

Allègre, C. J. (1997). Limitation on the mass exchange between the upper and lower mantle: the evolving convection regime of the Earth. *Earth Planet. Sci. Lett.*, **150**, 1–6.

Allègre, C. J. and Lewin, E. (1995). Isotopic systems and stirring times of the Earth's mantle. *Earth Planet. Sci. Lett.*, **136**, 629–46.

Allègre, C. J. and Rousseau, D. (1984). The growth of continents through geological time studied by Nd isotope analysis of shales. *Earth Planet. Sci. Lett.*, **67**, 19–34.

Allègre, C. J., Manhes, G. and Goepel, C. (1995a). The age of the Earth. *Geochim. Cosmochim. Acta*, **59**, 1445–56.

Allègre, C. J., Poirier, J. P., Humler, E. and Hofmann, A. W. (1995b). The chemical composition of the Earth. *Earth Planet. Sci. Lett.*, **134**, 515–26.

Allègre, C., Manhes, G. and Lewin, E. (2001). Chemical composition of the Earth and the volatility control on planetary genetics. *Earth Planet. Sci. Lett.*, **185**, 49–69.

Aller, L. H. (1971). *Atoms, Stars, and Nebulae*. Cambridge, MA: Harvard University Press, p. 352.

Amari, S., Gao, X., Nittler, L. R., Zinner, E., Jose, J., Hernanz, M. and Lewis, R. S. (2001a). Presolar grains from novae. *Astrophys. J.*, **551**, 1065–72.

Amari, S., Nittler, L. R., Zinner, E., Lodders, K. and Lewis, R. S. (2001b). Presolar SiC grains of type A and B: their isotopic compositions and stellar origins. *Astrophys. J.*, **559**, 463–83.

Amelin, Y. and Rotenberg, E. (2004). Sm–Nd systematics of chondrites. *Earth Planet. Sci. Lett.*, **223**, 267–82.

Amelin, Y., Lee, D.-C., Halliday, A. N. and Pidgeon, R. T. (1999). Nature of the Earth's earliest crust from hafnium isotopes in single detrital zircons. *Nature*, **399**, 252–5.

Amelin, Y., Lee, D.-C. and Halliday, A. N. (2000). Early-middle Archaean crustal evolution deduced from Lu–Hf and U–Pb isotopic studies of single zircon grains. *Geochim. Cosmochim. Acta*, **64**, 4205–25.

Amelin, Y., Krot, A. N., Hutcheon, I. D. and Ulyanov, A. A. (2002). Lead isotope ages of chondrules and calcium–aluminum-rich inclusions. *Science*, **297**, 1678–83.

Anders, E. and Grevesse, N. (1989). Abundances of the elements: meteoritic and solar. *Geochim. Cosmochim. Acta*, **53**, 197–214.

Anderson, D. L. (1993). He-3 from the mantle – primordial signal or cosmic dust. *Science*, **261**, 170–6.

Anderson, O. L. and Isaak, D. G. (2002). Another look at the core density deficit of Earth's outer core. *Phys. Earth Planet. Inter.*, **131**, 19–27.

Andersson, U. B., Neymark, L. A. and Billstrom, K. (2002). Petrogenesis of Mesoproterozoic (Subjotnian) rapakivi complexes of central Sweden: implications from U–Pb zircon ages, Nd, Sr and Pb isotopes. *Trans. Roy. Soc. Edinburgh: Earth Sci.*, **92**, 201–28.

Andreasen, R. and Sharma, M. (2006). Heterogeneous distribution of p-process Sm and Nd isotopes in the solar nebula. *Geochim. Cosmochim. Acta* (**Suppl. 6**), A18.

Aoki, W., Ryan, S. G., Norris, J. E. *et al*. (2001). Neutron capture elements in s-process rich, very metal-poor stars. *Astrophys. J.*, **561**, 346–63.
Arculus, R. J., Holmes, R. D., Powell, R. and Righter, K. (1990). Metal–silicate equilibrium and core formation. In *Origin of the Earth*, eds. H. E. Newsom and J. H. Jones. Oxford: Oxford University Press, pp. 251–71.
Arlandini, C., Kappeler, F., Wisshak, K. *et al*. (1999). Neutron capture in low-mass asymptotic giant branch stars: cross sections and abundance signatures. *Astrophys. J.*, **525**, 886–900.
Arndt, N. T. and Goldstein, S. L. (1989). An open boundary between lower continental crust and mantle: its role in crust formation and crustal recycling. *Tectonophysics*, **161**, 201–12.
Arnold, G. L., Anbar, A. D., Barling, J. and Lyons, T. W. (2004). Molybdenum isotope evidence for widespread anoxia in Mid-Proterozoic oceans. *Science*, **304**, 87–90.
Arnould, M., Paulus, G. and Meynet, G. (1997). Short-lived radionuclide production by non-exploding Wolf–Rayet stars. *Astron. Astrophys.*, **321**, 452–64.
Ashwal, L. D. (1993). *Anorthosites*. New York: Springer-Verlag, pp. 422.
Asmerom, Y. and Jacobsen, S. B. (1993). The Pb isotopic evolution of the Earth: inferences from river water suspended loads. *Earth Planet. Sci. Lett.*, **115**, 245–56.
Ayres, M. and Harris, N. (1997). REE fractionation and Nd-isotope disequilibrium during crustal anatexis: constraints from Himalayan leucogranites. *Chem. Geol.*, **139**, 249–69.
Azbel, I. Y. and Tolstikhin, I. N. (1988). *Radiogenic Isotopes and the Evolution of the Earth's Mantle, Crust and Atmosphere*. Apatity, Russia: Kola Sci. Center Publ., pp. 140.
Azbel, I. Y. and Tolstikhin, I. N. (1990). Geodynamics, magmatism, and degassing of the Earth. *Geochim. Cosmochim. Acta*, **54**, 139–54.
Azbel, I. Y. and Tolstikhin, I. N. (1993). Accretion and early degassing of the Earth: constraints from Pu–U–I–Xe isotopic systematic. *Meteoritics*, **28**, 609–21.
Azbel, I. Y., Tolstikhin, I. N., Kramers, J. D., Pechernikova, G. V. and Vitiazev, A. V. (1993). Core growth and siderophile element depletion of the mantle during homogeneous Earth accretion. *Geochim. Cosmochim. Acta*, **57**, 2889–98.
Baker, J., Bizzarro, M., Wittig, N., Connelly, J. and Haack, H. (2005). Early planetesimal melting from an age of 4.5662 Gyr for differentiated meteorites. *Nature*, **436**, 1127–31.
Balashov, Y. A. (2004). Geochemical peculiarities and genesis of alkaline granites of Keivy region (Kola Peninsula). In *Proc. Conf. Isotope Geochim.*, Vol. 17. Moscow: Vernadsky Inst. Geochemistry Analyt. Chem., pp. 22–3.
Ballentine, C. J. and Barfod, D. N. (2000). The origin of air-like noble gases in MORB and OIB. *Earth Planet. Sci. Lett.*, **180**, 39–48.
Barbarin, B. (1999). A review of the relationships between granitoid types, their origins and their geodynamic environments. *Lithos*, **46**, 605–26.
Barling, J. and Anbar, A. D. (2004). Molybdenum isotope fractionation during adsorption by manganese oxides. *Earth Planet. Sci. Lett.*, **217**, 315–29.
Barth, M. G., McDonough, W. F. and Rudnick, R. L. (2000). Tracking the budget of Nb and Ta in the continental crust. *Chem. Geol.*, **165**, 197–213.
Basford, J. R., Dragon, J. C., Pepin, R. O., Coscio, M. R. J. and Murthy, V. R. (1973). Krypton and xenon in lunar fines. In *Proc. Lunar Planet. Sci. Conf.*, Vol. 2, pp. 1915–55.

Batiza, R. (1982). Abundances, distribution and sizes of volcanoes in the Pacific Ocean and implications for the origin of non-hotspot volcanoes. *Earth Planet. Sci. Lett.*, **60**, 195–206.

Beard, B. L., Taylor, L. A., Scherer, E. E., Jonson, C. M. and Snyder, G. A. (1998). The source region and melting mineralogy of high-titanium and low-titanium lunar basalts deduced from Lu–Hf isotope data. *Geochim. Cosmochim. Acta*, **62**, 525–44.

Becker, H., Jochum, K. P. and Carlson, R. W. (2000). Trace element fractionation during dehydration of eclogites from high-pressure terranes and the implications for element fluxes in subduction zones. *Chem. Geol.*, **163**, 65–99.

Becker, H., Horan, M. F., Walker, R. J., Gao, S., Lorand, J.-P. and Rudnick, R. L. (2006). Highly siderophile element composition of the Earth's primitive upper mantle: constraints from new data on peridotite massifs and xenoliths. *Geochim. Cosmochim. Acta*, **70**, 4528–50.

Beckett, J. R. and Stolper, E. (1994). The stability of hibonite, melilite and other aluminous phases in silicate melts: implications for the origin of hibonite-bearing inclusions from carbonaceous chondrites. *Meteoritics*, **29**, 41–65.

Beckwith, S., Sargent, A. I., Chini, R. S. and Gusten, R. (1990). A survey for circumstellar disks around young stellar object. *Astron. J.*, **99**, 924–45.

Beech, M. and Mitalas, R. (1994). Formation and evolution of massive stars. *Astrophys. J. Suppl.*, **95**, 517–34.

Beers, T. C. and Christlieb, N. (2005). The discovery and analysis of very metal-poor stars in the Galaxy. *Ann. Rev. Astron. Astrophys.*, **43**, 531–80.

Bejina, F., Jaoul, O. and Liebermann, R. C. (2003). Diffusion in minerals at high pressure: a review. *Phys. Earth Planet. Inter.*, **139**, 3–20.

Bell, D. R. and Rossman, G. R. (1992). Water in the Earth's mantle: the role of nominally anhydrous minerals. *Science*, **255**, 1391–7.

Ben Othman, D., White, W. M. and Patchett, J. (1989). The geochemistry of marine sediments, island arc magma genesis, and crust–mantle recycling. *Earth Planet. Sci. Lett.*, **94**, 1–21.

Benkert, J.-P., Baur, H., Signer, P. and Wieler, R. (1993). He, Ne, and Ar from the solar wind and solar energetic particles in lunar ilmenites and pyroxenes. *J. Geophys. Res.*, **98** (E7), 13147–62.

Bennett, V. C. (2003). Compositional evolution of the mantle. In *The Mantle and Core*, Vol. 2, ed. R. W. Carlson. Amsterdam: Elsevier-Pergamon, pp. 493–519.

Benz, W. (2000). Low velocity collisions and the growth of planetesimals. In *From Dust to Terrestrial Planets*, eds. W. Benz, R. Kallenbach and G. W. Lugmair. Dordrecht: Kluwer, pp. 279–94.

Benz, W. and Asphaug, E. (1999). Catastrophic disruptions revisited. *Icarus*, **142**, 5–20.

Benz, W. and Cameron, A. G. W. (1990). Terrestrial effects of the giant impact. In *Origin of the Earth*, eds. H. E. Newsom and J. H. Jones. Oxford, UK: Oxford University Press, pp. 61–7.

Benz, W., Slattery, W. L. and Cameron, A. G. W. (1986). The origin of the Moon and the single-impact hypothesis. 1. *Icarus*, **66**, 515–35.

Benz, W., Slattery, W. L. and Cameron, A. G. W. (1987). The origin of the Moon and the single-impact hypothesis. 2. *Icarus*, **71**, 30–45.

Benz, W., Cameron, A. G. W. and Melosh, H. J. (1989). The origin of the Moon and the single-impact hypothesis. 3. *Icarus*, **81**, 113–31.

Benz, W., Asphaug, E. and Ryan, E. V. (1994). Numerical simulations of catastrophic disruption – recent results. *Planet. Space Sci.*, **42**, 1053–66.

Berger, M. and Rollinson, H. (1997). Isotopic and geochemical evidence for crust–mantle interaction during late Archaean crustal growth. *Geochim. Cosmochim. Acta*, **61**, 4809–29.

Bernard-Griffiths, J., Peucat, J. J. and Menot, R. P. (1991). Isotopic (Rb–Sr, U–Pb and Sm–Nd) and trace element geochemistry of eclogites from Pan-African belt: a case study of REE fractionation during high-grade metamorphism. *Lithos*, **27**, 43–57.

Bernatowicz, T. J., Podosek, F. A., Swindle, T. D. and Honda, M. (1988). I–Xe systematic in LL chondrites. *Geochim. Cosmochim. Acta*, **52**, 1113–21.

Betehtin, A. G. (1951). *The Course of Mineralogy*. Moscow: State Publ. Geol. Literature, pp. 543.

Binzel, R. P., Gaffey, M. J., Thomas, P. C., Zellner, B. H., Storrs, A. D. and Wells, E. N. (1997). Geologic mapping of Vesta from 1994 Hubble Space Telescope images. *Icarus*, **128**, 95–103.

Birch, F. (1952). Elasticity and constitution of the earth's interior. *J. Geophys. Res.*, **57**, 227–86.

Birck, J. L. and Allègre, C. J. (1978). Chronology and chemical history of the parent body of basaltic achondrites studied by the ^{87}Rb–^{87}Sr method. *Earth Planet. Sci. Lett.*, **39**, 37–51.

Bizimis, M., Sen, G. and Salters, V. J. M. (2003). Hf–Nd isotope decoupling in the oceanic lithosphere: constraints from spinel peridotites from Oahu, Hawaii. *Earth Planet. Sci. Lett.*, **217**, 43–58.

Bizzarro, M., Baker, J. A. and Haack, H. (2004). Mg isotope evidence for contemporaneous formation of chondrules and refractory inclusions. *Nature*, **431**, 275–8.

Black, D. C. and Matthews, M. S., eds. (1985). *Protostars and Planets II*. Tucson, AZ: University of Arizona Press, pp. 1313.

Blichert-Toft, J. and Albarède, F. (1997). The Lu–Hf isotope geochemistry of chondrites and the evolution of the mantle–crust system. *Earth Planet. Sci. Lett.*, **148**, 243–58.

Blichert-Toft, J. and Arndt, N. T. (1999). Hf isotope compositions of komatiites. *Earth Planet. Sci. Lett.*, **171**, 439–51.

Bloemen, H., Wijnands, R., Bennet, K. *et al*. (1994). COMPTEL observations of the Orion complex: evidence for cosmic-ray induced gamma-ray lines. *Astron. Astrophys.*, **281**, L5–L8.

Bochsler, P. (1987). Solar wind ion composition. *Physica Scripta*, **18**, 55–60.

Bodinier, J.-L. and Godard, M. (2003). Orogenic, ophiolitic, and abyssal peridotites. In *The Mantle and Core*, Vol. 2, ed. R. W. Carlson. Amsterdam: Elsevier-Pergamon, pp. 103–70.

Boehler, R. (1996). Melting temperature of the Earth's mantle and core: Earth's thermal structure. *Ann. Rev. Earth Planet. Sci.*, **24**, 15–40.

Boesenberg, J. S. and Delaney, J. S. (1997). A model composition of the basaltic achondrite planetoid. *Geochim. Cosmochim. Acta*, **61**, 3205–25.

Bogard, D. D., Clayton, R. N., Marti, K., Owen, T. and Turner, G. (2001). Martian volatiles: isotopic composition, origin, and evolution. *Space Sci. Rev.*, **96**, 425–58.

Bolhar, R., Kamber, B. S., Moorbath, S., Fedo, C. M. and Whitehouse, M. J. (2004). Characterisation of early Archaean chemical sediments by trace element signatures. *Earth Planet. Sci. Lett.*, **222**, 43–60.

Bolhar, R., Kamber, B. S., Moorbath, S., Whitehouse, M. and Collerson, K. D. (2005). Chemical characterization of earth's most ancient clastic metasediments from the Isua Greenstone Belt, southern West Greenland. *Geochim. Cosmochim. Acta*, **69**, 1555–73.

Borg, L., Norman, M., Nyquist, L. *et al*. (1999). Isotopic studies of ferroan anorthosite 62236: a young lunar crustal rock from a light rare-earth-element-depleted source. *Geochim. Cosmochim. Acta*, **63**, 2679–91.

Borisov, A. and Palme, H. (1997). Experimental determination of the solubility of platinum in silicate melts. *Geochim. Cosmochim. Acta*, **61**, 4349–57.

Borisov, A., Palme, H. and Spettel, B. (1994). Solubility of palladium in silicate melts – implications for core formation in the Earth. *Geochim. Cosmochim. Acta*, **58**, 705–16.

Boss, A. P. (1996). A concise guide to chondrule formation models. In *Chondrules and the Protoplanetary Disk*, eds. R. H. Hewins, R. H. Jones and E. R. D. Scott. Cambridge, UK: Cambridge University Press, pp. 257–63.

Boss, A. P. and Graham, J. A. (1993). Clumpy disk accretion and chondrule formation. *Icarus*, **106**, 168–78.

Boss, A. P. and Vanhala, H. A. T. (2000). Triggering protostellar collapse, injection, and disk formation. In *From Dust to Terrestrial Planets*, eds. W. Benz, R. Kallenbach and G. W. Lugmair. Dordrecht: Kluwer, pp. 13–22.

Bourdon, B., Langmuir, C. H. and Zindler, A. (1996a). Ridge-hotspot interaction along the Mid-Atlantic Ridge between 37°30′ and 40°30′N: the U–Th disequilibrium evidence. *Earth Planet. Sci. Lett.*, **142**, 175–89.

Bourdon, B., Zindler, A., Elliott, T. and Langmuir, C. H. (1996b). Constraints on mantle melting at mid-ocean ridges from global ^{238}U-^{230}Th disequilibrium data. *Nature*, **384**, 231–5.

Bourdon, B., Turner, S. and Dosseto, A. (2003). Dehydration and partial melting in subduction zones: constraints from U-series disequilibria. *J. Geophys. Res.*, **108** (B6), 2291–310.

Bourles, D. L., Brown, E. T., Raisbeck, G. M., Yiou, F. and Gieskes, J. M. (1992). Beryllium isotope geochemistry of hydrothermally altered sediments. *Earth Planet. Sci. Lett.*, **109**, 47–56.

Boyet, M. and Carlson, R. W. (2005). ^{142}Nd evidence for early (> 4.53 billion year) global differentiation of the silicate Earth. *Science*, **309**, 576–81.

Boyet, M. and Carlson, R. W. (2006). A new geochemical model for the Earth's mantle inferred from ^{146}Sm–^{42}Nd systematics. *Earth Planet. Sci. Lett.*, **250**, 254–68.

Boyet, M., Blichert-Toft, J., Rosing, M., Storey, M., Teoluk, P. and Albarede, F. (2003). ^{142}Nd evidence for early Earth differentiation. *Earth Planet. Sci. Lett.*, **214**, 427–42.

Boynton, W. V. (1984). Cosmochemistry of the rare earth elements: meteorite studies. In *Rare Earth Element Geochemistry*, ed. P. Henderson. Amsterdam: Elsevier, pp. 63–114.

Boynton, W. V. (1985). Meteoritic evidence concerning conditions in the solar nebula. In *Protostars and Planets II*, eds. D. C. Black and M. S. Matthews. Tucson, AZ: University of Arizona Press, pp. 772–87.

Branch, D. (1998). Type Ia Supernovae and the Hubble constant. *Ann. Rev. Astron. Astrophys.*, **36**, 17–55.

Brandon, A. D., Walker, R. J., Puchtel, I. S., Becker, H., Humayun, M. and Revillon, S. (2003). ^{186}Os–^{187}Os systematics of Gorgona Island komatiites: implications for very early growth of the inner core. *Earth Planet. Sci. Lett.*, **206**, 411–26.

Brandon, A. D., Walker, R. J. and Puchtel, I. S. (2006). Platinum–osmium isotope evolution of the Earth's mantle: constraints from chondrites and Os-rich alloys. *Geochim. Cosmochim. Acta*, **70**, 2093–103.

Brazzle, R. H., Pravdivtseva, O. V., Meshik, A. P. and Hohenberg, C. M. (1999). Verification and interpretation of the I–Xe chronometer. *Geochim. Cosmochim. Acta*, **63**, 739–60.

Brearley, A. J. (2003). Nebular versus parent-body processing. In *Meteorites, Comets, and Planets*, Vol. 1, ed. A. M. Davis. Amsterdam: Elsevier-Pergamon, pp. 247–68.
Bridges, J. C., Franchi, I. A., Hutchison, R., Sexton, A. S. and Pillinger, C. T. (1998). Correlated mineralogy, chemical compositions, oxygen isotopic compositions and size of chondrules. *Earth Planet. Sci. Lett.*, **155**, 183–96.
Bridges, J. C., Franchi, I. A., Sexton, A. S. and Pillinger, C. T. (1999). Mineralogical controls on the oxygen isotopic compositions of UOCs. *Geochim. Cosmochim. Acta*, **63**, 945–51.
Broecker, W. S. (1985). *How to Build a Habitable Planet*. Tucson, AZ: Eldigio Press, pp. 291.
Bromm, V. and Larson, R. B. (2004). The first stars. *Ann. Rev. Astron. Astrophys.*, **42**, 79–118.
Brown, E. T., Measures, C. I., Edmond, J. M., Bourles, D. L., Raisbeck, G. M. and Yiou F. (1992b). Continental input of beryllium to the oceans. *Earth Planet. Sci. Lett.*, **114**, 101–11.
Brown, G., Hawkesworth, C. and Wilson, C. (1992a). *Understanding the Earth*. Cambridge, UK: Cambridge University Press, pp. 563.
Brown, G. C. and Mussett, A. E. (1981). *The Inaccessible Earth*. London, UK: Allen and Unwin, pp. 261.
Burbidge, E. M., Burbidge, G. R., Fowler, W. A. and Hoyle, F. (1957). Synthesis of the elements in stars. *Rev. Modern Phys.*, **29**, 547–650.
Burles, S., Nollett, K. M. and Turner, M. S. (2001). Big Bang nucleosynthesis predictions for precision cosmology. *Astrophys. J.*, **552**, L1–5.
Burris, D. L., Pilachowski, C. A., Armandroff, T. E., Sneden, C., Cowan, J. J. and Roe, H. (2000). Neutron-capture elements in the early galaxy: insights from a large sample of metal-poor giants. *Astrophys. J.*, **544**, 302–19.
Burrows, A. (2000). Supernova explosions in the Universe. *Nature*, **403**, 727–33.
Busemann, H. and Eugster, O. (2002). The trapped noble gas component in achondrites. *Meteorit. Planet. Sci.*, **37**, 1865–91.
Busemann, H., Baur, H. and Wieler, R. (2000). Primordial noble gas in "phase Q" in carbonaceous and ordinary chondrites studied by closed-system stepped etching. *Meteorit. Planet. Sci.*, **35**, 949–73.
Busemann, H., Eugster, O., Baur, H. and Wieler, R. (2003). The ingredients of the "subsolar" noble gas component. In *Proc. Lunar Planet. Sci. Conf.*, Vol. 34, p. 1674.
Busso, M., Gallino, R. and Wasserburg G. J. (1999). Nucleosynthesis in asymptotic giant branch stars: relevance for Galactic enrichment and solar system formation. *Ann. Rev. Astron. Astrophys.*, **37**, 239–309.
Busso, M., Gallino, R., Lambert, D. L., Travaglio, C. and Smith, V. V. (2001). Nucleosynthesis and mixing on the asymptotic giant branch. III. Predicted and observed s-process abundances. *Astrophys. J.*, **557**, 802–21.
Butler, W. A., Jeffery, P. M., Reynolds, J. H. and Wasserburg, G. J. (1963). Isotopic variations in terrestrial gases. *Geophys. Res.*, **68**, 3283–91.
Caffee, M. W., Hudson, G. B., Velsko, C., Huss, G. R., Alexander, E. C., Jr. and Chivas, A. R. (1999). Primordial noble gases from Earth's mantle: identification of a primitive volatile component. *Science*, **285**, 2115–18.
Calvert, A. J., Sawyer, E. W., Davis, W. J. and Ludden, J. N. (1995). Archean subduction inferred from seismic images of a mantle suture in the Superior province. *Nature*, **375**, 670–4.

Cameron, A. G. W. (1976). Final stage of solar evolution. In *Frontiers of Astrophysics*, ed. E. H. Avrett. Cambridge, MA: Harvard University Press, pp. 131–59.
Cameron, A. G. W. (1983). Origin of the atmospheres of terrestrial planets. *Icarus*, **56**, 195–201.
Cameron, A. G. W. (1995). The first 10-million years in the Solar nebula. *Meteoritics*, **30**, 133–61.
Cameron, A. G. W. (2000). Higher-resolution simulations of the giant impact. In *Origin of the Earth and Moon*, eds. R. M. Canup and K. Righter. Tucson, AZ: University of Arizona Press, pp. 133–44.
Cameron, A. G. W. (2001a). Extinct radioactivities, core-collapse supernovae, jets, and the r-process. *Nucl. Phys.*, **A688**, 289C–96C.
Cameron, A. G. W. (2001b). From interstellar gas to the Earth–Moon system. *Meteorit. Planet. Sci.*, **36**, 9–22.
Cameron, A. G. W. (2001c). Some properties of r-process: accretion disks and jets. *Astrophys. J.*, **562**, 456–69.
Cameron, A. G. W. and Benz, W. (1991). The origin of the Moon and the single impact hypothesis – IV. *Icarus*, **92**, 204–16.
Cameron, A. G. W., Hoflich, P., Myers, P. C. and Clayton, D. D. (1995). Massive supernovae, Orion gamma-rays, and the formation of the Solar system. *Astrophys. J.*, **447**, L53–7.
Cameron, A. G. W., Vanhala, H. and Hoflich, P. (1997). Some aspects of triggered star formation. In *Astrophysical Implications of the Laboratory Study of Presolar Materials*, eds. T. I. Bernatowicz and E. Zinner. New York: Amer. Inst. Physics, pp. 665–93.
Canup, R. M. (2004). Simulations of a late lunar-forming impact. *Icarus*, **168**, 433–56.
Canup, R. M. and Asphaug, E. (2001). Origin of the Moon in a giant impact near the end of the Earth's formation. *Nature*, **412**, 708–13.
Canup, R. M. and Righter, K., eds. (2000). *Origin of the Earth and Moon*. Tucson, AZ: University of Arizona Press, pp. 555.
Carlson, R. W. and Hauri, E. H. (2001). Extending the Pd-107–Ag-107 chronometer to low Pd/Ag meteorites with multicollector plasma-ionization mass spectrometry. *Geochim. Cosmochim. Acta*, **65**, 1839–48.
Carlson, R. W. and Lugmair, G. W. (1988). The age of ferroan anorthosite 60025: oldest crust on a young Moon. *Geochim. Cosmochim. Acta*, **90**, 119–30.
Carlson, R. W. and Lugmair, G. W. (2000). Timescales of planetesimal formation and differentiation based on extinct and extant radioisotopes. In *Origin of the Earth and Moon*, eds. R. M. Canup and K. Righter. Tucson, AZ: University of Arizona Press, pp. 25–44.
Carlson, R. W., Pearson, D. G. and James, D. E. (2005). Physical, chemical, and chronological characteristics of continental mantle. *Rev. Geophys.*, **43**, RG1001, doi:10.1029/2004 RG000156.
Caro, G., Bourdon, B., Birck, J.-L. and Moorbath, S. (2003). ^{146}Sm–^{142}Nd evidence for early differentiation of the earth mantle. *Nature*, **423**, 428–31.
Caro, G., Bourdon, B., Birck, J.-L. and Moorbath, S. (2006). High-precision ^{142}Nd / ^{144}Nd measurements in terrestrial rocks: constraints on the early differentiation of the Earth's mantle. *Geochim. Cosmochim. Acta*, **70**, 164–91.
Cartigny, P., Harris, J. W. and Javoy, M. (2001). Diamond genesis, mantle fractionations and mantle nitrogen content: a study of δ^{13}C–N concentrations in diamonds. *Earth Planet. Sci. Lett.*, **185**, 85–98.

Cassen, P. (1996). Models for the fractionation of moderately volatile elements in the solar nebula. *Meteorit. Planet. Sci.*, **31**, 793–806.
Catling, D. C. and Claire, M. W. (2005). How Earth's atmosphere evolved to an oxic state: a status report. *Earth Planet. Sci. Lett.*, **237**, 1–20.
Catling, D. C., Zahnle, K. J. and McKay, C. P. (2001). Biogenic methane, hydrogen escape, and the irreversible oxidation of early Earth. *Science*, **293**, 839–43.
Cayrel, R., Hill, V., Beers, T. C. *et al*. (2001). Measurement of stellar age from uranium decay. *Nature*, **409**, 691–2.
Chabaux, F., Riotte, J. and Dequincey, O. (2003). Weathering and surface waters. *Rev. Mineral. Geochem.*, **52**, 533–76.
Chambers, J. E. (2004). Planetary accretion in the inner Solar System. *Earth Planet. Sci. Lett.*, **223**, 241–52.
Chambers, J. E. and Wetherill, G. W. (1998). Making the terrestrial planets: N-body integrations of planetary embryos in three dimensions. *Icarus*, **136**, 304–27.
Chambers, J. E. and Wetherill, G. W. (2001). Planets in the asteroids belts. *Meteorit. Planet. Sci.*, **36**, 381–99.
Chase, C. G. and Patchett, P. J. (1988). Stored mafic/ultramafic crust and early Archean mantle depletion. *Earth Planet. Sci. Lett.*, **91**, 66–72.
Chaussidon, M., Robert, F. and McKeegan, K. D. (2006). Li and B isotopic variations in an Allende CAI: evidence for the *in situ* decay of short-lived ^{10}Be and for the possible presence of the short-lived nuclide ^{7}Be in the early solar system. *Geochim. Cosmochim. Acta.*, **70**, 224–45.
Chauvel, C. and Blichert-Toft, J. (2001). A hafnium isotope and trace element perspective on melting of the depleted mantle. *Earth Planet. Sci. Lett.*, **190**, 137–51.
Chauvel, C., Goldstein, S. L. and Hofmann, A. W. (1995). Hydration and dehydration of oceanic crust controls Pb evolution in the mantle. *Chem. Geol.*, **126**, 65–75.
Chen, G. Q. and Ahrens, T. J. (1997). Erosion of terrestrial planet atmosphere by surface motion after a large impact. *Phys. Earth Planet. Inter.*, **100**, 21–6.
Chen, J. H. and Wasserburg, G. J. (1981). The isotopic composition of uranium and lead in Allende inclusions and meteoritic phosphates. *Earth Planet. Sci. Lett.*, **52**, 1–15.
Chen, J. H. and Wasserburg, G. J. (1996). Live ^{107}Pd in the early solar system and implications for planetary evolution. In *Earth Processes: Reading the Isotopic Code*, eds. A. R. Basu and S. R. Hart. A.G.U. Monograph no. 95, pp. 1–20.
Chiappini, C. and Matteucci, F. (2001). Galactic chemical evolution. In *Solar and Galactic Composition*, ed. R. F. Wimmer-Schweingruber. New York: Amer. Inst. Physics, pp. 227–38.
Chiappini, C., Matteucci, F. and Romano, D. (2001). Abundance gradients and the formation of the Milky Way. *Astrophys. J.*, **554**, 1044–58.
Choi, B.-G., Krot, A. N. and Wasson, J. T. (2000). Oxygen isotopes in magnetite and fayalite in CV chondrites Kaba and Mokoia. *Meteorit. Planet. Sci.*, **35**, 1239–48.
Chokshi, A., Tielens, A. G. M. and Hollenbuch, D. (1993). Dust coagulation. *Astrophys. J.*, **407**, 806–19.
Chopin, C. (2003). Ultrahigh-pressure metamorphism: tracing continental crust into the mantle. *Earth Planet. Sci. Lett.*, **212**, 1–14.
Christensen, U. (1995). Effects of phase-transitions on mantle convection. *Ann. Rev. Earth Planet. Sci.*, **23**, 65–87.
Christensen, U. R. and Hofmann, A. W. (1994). Segregation of subducted oceanic-crust in the convecting mantle. *J. Geophys. Res. – Solid Earth*, **99** (B10), 19, 867–84.
Christlieb, N., Gustafsson, B., Korn, A. J. *et al*. (2004). HE 0107–5240, a chemically ancient star. A detailed abundance analysis. *Astrophys. J.*, **603**, 708–28.

Clarke, D. B. (1996). Two centuries after Hutton's "Theory of the Earth": the status of granite science. *Trans. Roy. Soc. Edinburgh: Earth Sci.*, **87**, 353–9.
Clarke, W. B., Beg, M. A. and Craig, H. (1969). Excess ^{3}He in the sea: evidence for terrestrial primordial helium. *Earth Planet. Sci. Lett.*, **6**, 213–20.
Clayton, D. D. (1994). Production of ^{26}Al and other extinct radionuclides by low energy heavy cosmic ray in molecular clouds. *Nature*, **368**, 222–4.
Clayton, D. D. and Jin, L. (1995). Gamma rays, cosmic rays, and extinct radioactivity in molecular clouds. *Astrophys. J.*, **451**, 681–99.
Clayton, D. D. and Timmes, F. X. (1997). Implications of presolar grains for galactic chemical evolution. In *Astrophysical Implications of the Laboratory Study of Presolar Materials*, eds. T. I. Bernatowicz and E. Zinner. New York: Amer. Inst. Physics, pp. 237–64.
Clayton, R. N. (1993). Oxygen isotopes in meteorites. *Ann. Rev. Earth Planet. Sci.*, **21**, 115–49.
Clayton, R. N. (2002). Self-shielding in the Solar nebula. *Nature*, **415**, 860–1.
Clayton, R. N. (2003). Oxygen isotopes in the Solar system. *Space Sci. Rev.*, **106**, 19–32.
Clayton, R. N., Grossman, L. and Mayeda, T. K. (1973). A component of primitive nuclear composition in carbonaceous meteorites. *Science*, **182**, 485–8.
Clayton, R. N., Mayeda, T. K. and Molini-Velsko, C. (1985). Isotopic variations in Solar System material: evaporation and condensation of silicates. In *Protostars and Planets II*, eds. D. C. Black and M. S. Matthews. Tucson, AZ: University of Arizona Press, pp. 755–71.
Clayton, R. N., Hinton, R. W. and Davis, A. M. (1988). Isotopic variations in the rock-forming elements in meteorites. *Phil. Trans. Roy. Soc. London*, **A325**, 483–501.
Clayton, R. N. and Mayeda, T. K. (1996). Oxygen isotope studies of achondrites. *Geochim. Cosmochim. Acta*, **60**, 1999–2017.
Clayton, R. N. and Mayeda, T. K. (1999). Oxygen isotope studies of carbonaceous chondrites. *Geochim. Cosmochim. Acta*, **63**, 2089–104.
Coffin, M. F. and Eldholm, O. (1994). Large igneous provinces: crustal structure, dimensions, and external consequences. *Rev. Geophys.*, **32**, 1–36.
Collier, M. R., Hamilton, D. C. and Gloeckler, G. (1998). Oxygen 16 to oxygen 18 abundance ratio in the solar wind observed by Wind/Mass. *J. Geophys. Res.*, **103** (A1), 7–14.
Coltice, N. and Ricard, Y. (1999). Geochemical observations and one layer mantle convection. *Earth Planet. Sci. Lett.*, **174**, 125–37.
Conder, J. A., Wiens, D. A. and Morris, J. (2002). On the decompression melting structure at volcanic arcs and back-arc spreading centers. *Geophys. Res. Lett*. **29**, 1727–31.
Condie, K. C. (1993). Chemical composition and evolution of the upper continental crust – contrasting results from surface samples and shales. *Chem. Geol.*, **104**, 1–37.
Condie, K. C. (1994). Greenstones through time. In *Archean Crustal Evolution*, ed. K. C. Condie. Amsterdam: Elsevier, pp. 85–120.
Condie, K. C. (1998). Episodic continental growth and supercontinents: a mantle avalanche connection? *Earth Planet. Sci. Lett.*, **163**, 97–108.
Condie, K. C. (2000). Episodic continental growth models: afterthoughts and extensions. *Tectonophysics*, **322**, 153–62.
Condie, K. C. (2005). TTGs and adakites: are they both slab melts? *Lithos*, **80**, 33–44.
Connolly, H. C., Jr. and Hewins, R. H. (1995). Chondrules as products of dust collisions with totally molten droplets within a dust-rich nebular environment – an experimental investigation. *Geochim. Cosmochim. Acta*, **59**, 3231–46.

Connolly, H. C., Jr. and Love, S. G. (1998). The formation of chondrules: petrologic tests of the shock wave model. *Science*, **280**, 62–7.
Cowan, J. and Sneden, C. (2006). Heavy element synthesis in the oldest stars and the early Universe. *Nature*, **440**, 1151–6.
Cowan, J. J., Pfeiffer, B., Kratz, K. L., Thielemann, F. K., Sneden, C., Burles, S., Tytler, D. and Beers, T. C. (1999). *r*-Process abundances and chronometers in metal-poor stars. *Astrophys. J.*, **521**, 194–205.
Crabb, J., Lewis, R. S. and Anders, E. (1982). Extinct ^{129}I in C3 chondrites. *Geochim. Cosmochim. Acta*, **46**, 2511–25.
Crisp, J. A. (1984). Rates of magma emplacement and volcanic output. *J. Volcanol. Geotherm. Res.*, **20**, 177–211.
Cuzzi, J. N., Dobrovolskis, A. R. and Hogan, R. C. (1996). Turbulence, chondrules and planetesimals. In *Chondrules and the Protoplanetary Disk*, eds. R. H. Hewins, R. H. Jones and E. R. D. Scott. Cambridge, UK: Cambridge University Press, pp. 35–43.
Cuzzi, J. N., Davis, S. S. and Dobrovolskis, A. R. (2003). Blowing in the wind. II. Creation and redistribution of refractory inclusions in turbulent protoplanetary nebula. *Icarus*, **166**, 385–402.
Dalpe, C. and Baker, D. R. (2000). Experimental investigation of large-ion-lithophile-element-, high-field-strength-element-, and rare-earth-element-partitioning between calcic amphibole and basaltic melt: the effects of pressure and oxygen fugacity. *Contrib. Mineral. Petrol.*, **140**, 223–50.
Davies, G. F. (1990). Heat and mass transport in the early Earth. In *Origin of the Earth*, eds. H. E. Newsom and J. H. Jones. Oxford, UK: Oxford University Press, pp. 175–94.
Davies, J. H. and von Blanckenburg, F. (1995). Slab break off – a model of lithosphere detachment and its test in the magmatism and deformation of collisional orogens. *Earth Planet. Sci. Lett.*, **129**, 85–102.
Davis, A. C., Bickle, M. J. and Teagle, D. A. H. (2003). Imbalance in the oceanic strontium budget. *Earth Planet. Sci. Lett.*, **211**, 173–87.
Day, J. M. D., Floss, C., Taylor, L. A., Anand, M. and Patchen, A. D. (2006). Evolved mare basalt magmatism, high Mg/Fe feldspathic crust, chondritic impactors, and the petrogenesis of Antarctic lunar breccia meteorites Meteorite Hills 01210 and Pecora Escarpment 02007. *Geochim. Cosmochim. Acta*, **70**, 5957–89.
Deloule, E. and Robert, F. (1995). Interstellar water in meteorites? *Geochim. Cosmochim. Acta*, **59**, 4695–706.
Deloule, E., Robert, F. and Doukhan, J. C. (1998). Interstellar hydroxyl in meteoritic chondrules: implications for the origin of water in the inner solar system. *Geochim. Cosmochim. Acta*, **62**, 3367–78.
DePaolo, D. J., Linn, A. M. and Schubert, G. (1991). The continental crustal age distribution – methods of determining mantle separation ages from Sm–Nd isotopic data and application to the Southwestern United States. *J. Geophys. Res.*, **96** (B2), 2071–88.
Deruelle, B., Dreibus, G. and Jambon, A. (1992). Iodine abundances in oceanic basalts: implications for Earth dynamics. *Earth Planet. Sci. Lett.*, **108**, 217–27.
de Wit, M. J. (1998). On Archean granites, greenstones, cratons and tectonics: does the evidence demand a verdict? *Precambrian Res.*, **91**, 181–226.
Dikov, Y. P., Ivanov, A. V., Wlotzka, F., Galimov, E. M. and Wänke, G. (2002). The nature of volatiles in the lunar regolith. *Solar System Res.*, **36**, 1–11.
Dobson, D. P. (2000). ^{57}Fe and Co tracer diffusion in liquid Fe–FeS at 2 and 5 GPa. *Phys. Earth Planet. Inter.*, **120**, 137–44.

Downes, H. (1993). The nature of the lower continental crust of Europe: petrological and geochemical evidence from xenoliths. *Phys. Earth Planet. Inter.*, **79**, 195–218.
Draine, B. T. (2003). Interstellar dust grains. *Ann. Rev. Astron. Astrophys.*, **41**, 241–89.
Drake, M. J. (1986). Is lunar bulk material similar to earth's mantle? In *Origin of the Moon*, eds. W. K. Hartmann, R. J. Phillips and G. J. Taylor. Houston, TX: Lunar Planet. Inst., pp. 105–24.
Drake, M. J. (2001). The eucrite/Vesta story. *Meteorit. Planet. Sci.*, **36**, 501–13.
Dreibus, G., Bruckner, J. and Wänke, H. (1997). On the core mass of the asteroid Vesta. *Meteorit. Planet. Sci.*, **32**, A-36.
Drouart, A., Dubrulle, B., Gautier, D. and Robert, F. (1999). Structure and transport in the solar nebula from constraints on deuterium enrichment and giant planets formation. *Icarus*, **140**, 129–55.
Drozd, R. J. and Podosek, F. A. (1976). Primordial ^{129}Xe in meteorites. *Earth Planet. Sci. Lett.*, **31**, 15–30.
Ducea, M. and Saleeby, J. B. (1998). The age and origin of a thick mafic-ultramafic keel from beneath the Sierra Nevada batholith. *Contrib. Mineral. Petrol.*, **133**, 169–85.
Ebel, D. S. and Grossman, L. (2000). Condensation in dust-enriched systems. *Geochim. Cosmochim. Acta*, **64**, 339–66.
Edvardsson, B., Andersen, J., Gustafsson, B., Lambert, D. L., Nissen, P. E. and Tomkin, J. (1993). The chemical evolution of the galactic disk. 1. Analysis and results. *Astron. Astrophys.*, **275**, 101–52.
Eiler, J. M., Farley, K. A. and Stolper, E. M. (1998). Correlated helium and lead isotope variations in Hawaiian lavas. *Geochim. Cosmochim. Acta*, **62**, 1977–84.
Eiler, J. M., Crawford, A., Elliott, T., Farley, K. A., Valley, J. W. and Stolper, E. M. (2000). Oxygen isotope geochemistry of oceanic-arc lavas. *J. Petrol.*, **41**, 229–56.
Eisele, J., Sharma, M., Galer, S. J. G., Blichert-Toft, J., Devey, C. W. and Hofmann, A. W. (2002). The role of sediment recycling in EM-1 inferred from Os, Pb, Hf, Nd, Sr isotope and trace element systematics of the Pitcairn hotspot. *Earth Planet. Sci. Lett.*, **196**, 197–212.
Elderfield, H. and Pagett, R. (1986). Rare earth elements in ichthyolites: variations with redox conditions and depositional environment. *Sci. Total Envir.*, **49**, 175–97.
Elkins-Tanton, L. T., Hager, B. H. and Grove, T. L. (2004). Magmatic effects of the lunar late heavy bombardment. *Earth Planet. Sci. Lett.*, **222**, 17–27.
Elliott, B. A. (2001). Crystallization conditions of the Wiborg rapakivi batholith, SE Finland: an evaluation of amphibole and biotite mineral chemistry. *Mineral. Petrol.*, **72**, 305–24.
Elliott, T., Plank, T., Zindler, A., White, W. and Bourdon, B. (1997). Element transport from slab to volcanic front at the Mariana Arc. *J. Geophys. Res.*, **102**, 14 991–15 019.
Elliott, T., Zindler, A. and Bourdon, B. (1999). Exploring the kappa conundrum: the role of recycling in the lead isotope evolution of the mantle. *Earth Planet. Sci. Lett.*, **169**, 129–45.
Elmegreen, B. G. (1981). Grain formation behind shocks and the origin of isotopically anomalous meteorite inclusions. *Astrophys. J.*, **251**, 820–33.
Elmegreen, B. G. (1985). Molecular clouds and star formation: an overview. In *Protostars and Planets II*, eds. D. C. Black and M. S. Matthews. Tucson, AZ: University of Arizona, Press, pp. 33–58.
Endress, M. and Bischoff, A. (1996). Carbonates in CI chondrites: clues to parent body evolution. *Geochim. Cosmochim. Acta*, **60**, 489–507.
Ernst, W. G. (2001). Subduction, ultrahigh-pressure metamorphism, and regurgitation of buoyant crustal slices – implications for arcs and continental growth. *Phys. Earth Planet. Inter.*, **127**, 253–75.

Essene, E. J. (1989). The current status of thermobarometry in metamorphic rocks. In *Evolution of Metamorphic Belts*, Vol. 43, eds. J. S. Daily, R. A. Cliff and B. W. D. Yardley. Geol. Soc. Spec. Pub., pp. 1–44.

Evans II, N. J. (1999). Physical conditions in regions of star formation. *Ann. Rev. Astron. Astrophys.*, **37**, 311–62.

Fagan, T. J., McKeegan, K. D., Krot, A. N. and Keil, K. (2001). Calcium–aluminum-rich inclusions in enstatite chondrites (II): oxygen isotopes. *Meteorit. Planet. Sci.*, **36**, 223–30.

Fahey, A. J., Zinner, E. K., Crozaz, G. and Kornacki, A. S. (1987). Micro distributions of Mg isotopes and REE abundances in a Type A calcium–aluminum-rich inclusion from Efremovka. *Geochim. Cosmochim. Acta*, **51**, 3215–29.

Farouqi, K., Freiburghaus, C., Kratz, K.-L., Pfeiffer, B., Rauscher, T. and Thielemann, F.-K. (2005). Astrophysical conditions for an r-process in the high-entropy wind scenario of type II supernovae. *Nuclear Physics*, **A758**, 631c-4.

Farquhar, J. and Wing, B. A. (2003). Multiple sulfur isotopes and the evolution of the atmosphere. *Earth Planet. Sci. Lett.*, **213**, 1–13.

Farquhar, J., Chacko, T. and Frost, B. R. (1993). Strategies for high-temperature oxygen isotope thermometry: a worked example from the Laramie Anorthosite Complex, Wyoming, USA. *Earth Planet. Sci. Lett.*, **117**, 407–22.

Farquhar, J., Chacko, T. and Ellis, D. J. (1996). Preservation of oxygen isotope compositions in granulites from Northwestern Canada and Enderby Land, Antarctica: implications for high-temperature isotopic thermometry. *Contrib. Mineral. Petrol.*, **125**, 213–24.

Farquhar, J., Savarino, J., Airieau, S. and Thiemens, M. H. (2001). Observation of wavelength-sensitive mass-independent sulfur isotope effects during SO_2 photolysis: implications for the early atmosphere. *J. Geophys. Res.*, **106** (E12), 32, 829–39.

Feigelson, E. D. and Montmerle, T. (1999). High-energy processes in young stellar objects. *Ann. Rev. Astron. Astrophys.*, **37**, 363–408.

Fitton, J. G. and Dunlop, H. M. (1985). The Cameroon line, West Africa, and its bearing on the origin of oceanic and continental alkali basalts. *Earth Planet. Sci. Lett.*, **72**, 23–38.

Flam, F. (1991). Seeing stars in a handful of dust. *Science*, **253**, 380–1.

Floss, C., James, O. B., McGee, J. J. and Crozaz, G. (1998). Lunar ferroan anorthosite petrogenesis: clues from trace element distributions in FAN subgroups. *Geochim. Cosmochim. Acta*, **62**, 1255–83.

Foley, S., Tiepolo, M. and Vannucci, R. (2002). Growth of early continental crust controlled by melting of amphibolite in subduction zones. *Nature*, **412**, 837–40.

Forsyth, D. and Uyeda, S. (1975). On the relative importance of the driving forces of plate motion. *Geophys. J. Roy. Astron. Soc.*, **43**, 163–200.

Fortenfant, S. S., Rubie, D. C., Reid, J., Dalpé, C., Capmas, F. and Gessmann, C. K. (2003). Partitioning of Re and Os between liquid metal and magnesiowüstite at high pressure. *Phys. Earth Planet. Inter.*, **139**, 77–91.

Francois, P., Spite, M. and Spite, F. (1993). On the galactic age problem – determination of the [Th/Eu] ratio in halo stars. *Astron. Astrophys.*, **274**, 821–4.

Frebel, A., Aoki, W., Christlieb, N. *et al*. (2005). Nucleosynthetic signatures of the first stars. *Nature*, **434**, 871–3.

Freedman, W. L. and Turner, M. S. (2003). Measuring and understanding the universe. *Rev. Mod. Phys.*, **75**, 1433–48.

Freedman, W. L., Madore, B. F., Gibson, B. K. *et al*. (2001). Final results from the Hubble space telescope key project to measure the Hubble constant. *Astrophys. J.*, **553**, 47–72.

Frick, U. and Chang, S. (1978). Elimination of chromite and novel sulfides as important carrier phases of noble gases in carbonaceous chondrites. *Meteoritics*, **13**, 465–70.
Friedmann, A. (1922). On the curvature of space. *Zeitschrift fur Physik*, **10**, 377–86.
Gaillardet, J., Viers, J. and Dupré, B. (2003). Trace elements in river waters. In *Surface and Ground Water, Weathering, and Soils*, Vol. 5, ed. J. I. Drever. Amsterdam: Elsevier-Pergamon, pp. 225–72.
Galer, S. J. G. and Goldstein, S. L. (1996). Influence of accretion on the lead in the Earth. In *Earth Processes: Reading the Isotopic Code*, eds. A. Basu and S. Hart. A.G.U. Monograph no. 95, pp. 75–98.
Galer, S. J. G. and O'Nions, R. K. (1985). Residence time of thorium, uranium and lead in the mantle and implications for mantle convection. *Nature*, **316**, 778–82.
Gallino, R., Busso, M. and Lugaro, M. (1997). Neutron capture nucleosynthesis in AGB stars. In *Astrophysical Implications of the Laboratory Study of Presolar Materials*, eds. T. J. Bernatowicz and E. Zinner. New York: Amer. Inst. Physics Vol. 402, pp. 115–53.
Gary, M., McAfee, R. Jr. and Wolf, C. L. (1973). *Glossary of Geology*. New York: Amer. Geol. Inst. Publ., pp. 805.
Gast, P. W. (1968). Upper mantle chemistry and the evolution of the earth's crust. In *The History of the Earth's Crust*, ed. R. A. Phinney. Princeton, NJ: Princeton University Press, pp. 15–27.
Gast, P. W., Tilton, G. R. and Hedge, C. (1964). Isotopic composition of lead and strontium from Ascension and Gough Islands. *Science*, **145**, 1181–5.
Geiss, J. and Gloeckler, G. (1998). Abundances of deuterium and helium-3 in the protosolar cloud. In *Primordial Nuclei and their Galactic Evolution*, eds. N. Prantzos, M. Tosi and R. von Steiger. Dordrecht: Kluwer Acad. Publ., pp. 239–50.
Geiss, J. and Reeves, H. (1972). Cosmic and solar system abundances of deuterium and helium-3. *Astron. Astrophys.*, **18**, 126–32.
Genda, H. and Abe, Y. (2003). Survival of a proto-atmosphere through the stage of giant impacts: the mechanical aspects. *Icarus*, **164**, 149–62.
Gerling, E. K. and Levsky, L. K. (1956). On the origin of inert gases in stony meteorites. *Geochimiya*, **7**, 59–64.
Gessmann, C. K., Wood, B. J., Rubie, D. C. and Kilburn, M. R. (2001). Solubility of silicon in liquid metal at high pressure: implications for the composition of the Earth's core. *Earth Planet. Sci. Lett.*, **184**, 367–76.
Ghosh, A. and McSween, H. Y. J. (1998). A thermal model for the differentiation of asteroid 4 Vesta, based on radiogenic heating. *Icarus*, **134**, 187–206.
Gibert, B., Schilling, F. R., Tommasi, A. and Mainprice, D. (2003). Thermal diffusivity of olivine single-crystals and polycrystalline aggregates at ambient conditions – a comparison. *Geophys. Res. Lett.*, **30**, 2172–7.
Gill, J. A. (1981). *Orogenic Andesites and Plate Tectonics*. New York: Springer-Verlag, pp. 390.
Gilroy, K. K., Sneden, C., Pilachowski, C. A. and Cowan, J. J. (1988). Abundances of n-capture elements in Population II stars. *Astrophys. J.*, **327**, 298–320.
Gilmour, J. D., Whitby, J. A., Turner, G., Bridges, J. C. and Hutchison, R. (2000). The iodine–xenon system in clasts and chondrules from ordinary chondrites: implications for early solar system chronology. *Meteorit. Planet. Sci.*, **35**, 445–55.
Gloeckler, G. and Geiss, J. (2001). Composition of the local interstellar cloud from observations and interstellar pickup ions. In *Solar and Galactic Composition*, ed. R. F. Wimmer-Schweingruber. New York: Amer. Inst. Phys., pp. 281–90.

Godard, M., Jousselin, D. and Bodinier, J.-L. (2000). Relationships between geochemistry and structure beneath a palaeo-spreading centre: a study of the mantle section in the Oman ophiolite. *Earth Planet. Sci. Lett.*, **180**, 133–48.

Goldstein, S. L. and Hemming, S. R. (2003). Long-lived isotopic tracers in oceanography, paleo-oceanography, and ice-sheet dynamics. In *The Oceans and Marine Geochemistry*, Vol. 6, ed. H. Elderfield. Amsterdam: Elsevier-Pergamon, pp. 453–90.

Goldstein, S. J. and Jacobsen, S. B. (1987). The Nd and Sr isotopic systematics of river-water dissolved material: implications for the sources of Nd and Sr in seawater. *Chem. Geol.,* **66**, 245–72.

Goldstein, S. J. and Jacobsen, S. B. (1988). Nd and Sr isotopic systematics of river water suspended material: implications for crustal evolution. *Earth Planet. Sci. Lett.*, **87**, 249–65.

Göpel, C., Manhes, G. and Allègre, C. J. (1994). U–Pb systematics of phosphates from equilibrated ordinary chondrites. *Earth Planet. Sci. Lett.*, **121**, 153–71.

Gounelle, M., Shu, F. H., Shang, H., Glassgold, A. E., Rehm, K. E. and Lee, T. (2001). Extinct radioactivities and protosolar cosmic rays: self-shielding and light elements. *Astrophys. J.*, **548**, 1051–70.

Gounelle, M., Shu, F. H., Shang, H., Glassgold, A. E., Rehm, K. E. and Lee, T. (2006). The irradiation origin of beryllium radioisotopes and other short-lived radionuclides. *Astrophys. J.*, **640**, 1163–70.

Grady, M. M. and Wright, L. P. (2003). Elemental and isotopic abundances of carbon and nitrogen in meteorites. *Space Sci. Rev.*, **106**, 231–48.

Graham, A. L., Bewan, A. W. R. and Hutchison, R. (1985). *Catalogue of Meteorites*. Tucson, AZ: University of Arizona Press, pp. 199.

Graham, D. W. (2002). Noble gas isotope geochemistry of mid-ocean ridges and ocean island basalts: characterization of mantle source reservoirs. In *Noble Gases in Geochemistry and Cosmochemistry*, Vol. 47, eds. D. Porcelli, C. J. Ballentine and R. Wieler. Washington DC: Mineral. Soc. Amer., pp. 247–318.

Grand, S. P. (1994). Mantle shear structure beneath the Americas and surrounding oceans. *J. Geophys. Res.*, **99** (B6), 11 591–621.

Graner, F. and Dubrulle, B. (1994). Titius–Bode laws in the solar system: I. Scale invariance explains everything. *Astron. Astrophys.*, **282**, 262–8.

Gratton, R. G. and Sneden, C. (1994). Abundances of neutron-capture elements in metal-poor stars. *Astron. Astrophys*., **287**, 927–46.

Gray, C. M., Papanastassiou, D. A. and Wasserburg, G. J. (1973). The identification of early condensates from the solar nebula. *Icarus*, **20**, 213–39.

Green, D. H. and Ringwood, A. E. (1963). Mineral assemblages in a model mantle composition. *J. Geophys. Res.*, **68**, 937–45.

Green, D. H. and Ringwood, A. E. (1967). The genesis of basaltic magmas. *Contrib. Mineral. Petrol.*, **15**, 103–90.

Grevesse, N. and Sauval, A. J. (1998). Standard solar composition. *Space Sci. Rev.*, **85**, 161–74.

Grossman, J. N., Rubin, A. E., Nagahara, N. and King, E. A. (1988). Properties of chondrules. In *Meteorites and the Early Solar System*, eds. J. F. Kerridge and M. S. Matthews. Tucson, AZ: University of Arizona Press, pp. 619–59.

Grossman, L. (1972). Condensation in the primitive solar nebula. *Geochim. Cosmochim. Acta*, **36**, 597–619.

Grossman, L. (1975). Petrography and mineral chemistry of Ca-rich inclusions in the Allende meteorite. *Geochim. Cosmochim. Acta*, **39**, 433–54.

Grossman, L., Ganapathy, R. and Davis, A. M. (1977). Trace elements in the Allende meteorite – III. Coarse-grained inclusions revisited. *Geochim. Cosmochim. Acta* **41**, 1647–64.

Grossman, L., Ebel, D. S., Simon, S. B., Davis, A. M., Richter, F. M. and Parsad, N. M. (2000). Major element chemical and isotopic compositions of refractory inclusions in C3 chondrites: the separate roles of condensation and evaporation. *Geochim. Cosmochim. Acta*, **64**, 2879–94.

Grossman, L., Ebel, D. S. and Simon, S. B. (2002). Formation of refractory inclusions by evaporation of condensate precursors. *Geochim. Cosmochim. Acta*, **66**, 145–61.

Grove, T. L. (2000). Origin of magmas. In *Encyclopedia of Volcanoes*. San Diego, CA: Academic Press, pp. 133–47.

Haack, H., Rasmussen, K. L. and Warren, P. H. (1990). Effects of regolith/megaregolith insulation on the cooling histories of differentiated asteroids. *J. Geophys. Res.*, **95**, 5111–24.

Haapala, I. and Ramo, O. T. (1999). Rapakivi granites and related rocks: an introduction. *Precambrian Res.*, **95**, 1–7.

Haapala, I., Ramo, O. T. and Frindt, S. (2005). Comparison of Proterozoic and Phanerozoic rift-related basaltic–granitic magmatism. *Lithos*, **80**, 1–32.

Haederle, M. and Atherton, M. P. (2002). Shape and intrusion style of the Coastal Batholith, Peru. *Tectonophysics*, **345**, 17–28.

Halliday, A. N. and Porcelli, D. (2001). In search of lost planets – the paleocosmochemistry of the inner solar system. *Earth Planet. Sci. Lett.*, **192**, 545–59.

Halliday, A. N., Lee, D.-C. and Jacobsen, S. B. (2000). Tungsten isotopes, the timing of metal–silicate fractionation and the origin of the Earth and Moon. In *Origin of the Earth and Moon*, eds. K. Righter and R. Canup. Tucson, AZ: University of Arizona Press, pp. 45–62.

Hanowski, N. P. and Brearley, A. J. (2000). Iron-rich aureoles in the CM carbonaceous chondrites Murray, Murchison and Allan Hills 81002: evidence for *in situ* aqueous alteration. *Meteorit. Planet. Sci.*, **35**, 1291–308.

Hansen, B. M. S. and Liebert, J. (2003). Cool white dwarfs. *Ann. Rev. Astron. Astrophys.*, **41**, 465–515.

Hansen, U. and Yuen, D. A. (1988). Numerical simulation of thermal–chemical instabilities at the core–mantle boundary. *Nature*, **334**, 237–40.

Harley, S. L. (1989). The origins of granulites: a metamorphic perspective. *Geol. Mag.*, **126**, 215–47.

Harris, M. J., Lambert, D. L. and Goldman, A. (1987). The $^{12}C/^{13}C$ and $^{16}O/^{18}O$ ratios in the solar photosphere. *Mon. Not. Roy. Astr. Soc.*, **224**, 237–55.

Harris, W. E., Durrell, P. R., Pierce, M. J. and Secker, J. (1998). Constraints on the Hubble constant from observations of the brightest red-giant stars in a Virgo-cluster galaxy. *Nature*, **395**, 45–7.

Harrison, T. M., Blichert-Toft, J., Muller, W., Albarède, F., Holden, P. and Mojzsis, S. J. (2005). Heterogeneous hadean hafnium: evidence of continental crust at 4.4 to 4.5 Gyr. *Science*, **310**, 1947–50.

Hart, S. R. and Zindler, A. (1986). In search of a bulk-earth composition. *Chem. Geol.*, **57**, 247–67.

Hartmann, L. (2000). Observational constraint on transport (and mixing) in pre-main sequence disks. In *From Dust to Terrestrial Planets*, eds. W. Benz, R. Kallenbach and G. W. Lugmair. Dordrecht: Kluwer, pp. 55–68.

Hartmann, L. and Kenyon, S. J. (1985). On the nature of FU Orionis objects. *Astrophys. J.*, **299**, 462–78.

Hartmann, L., Ballesteros-Paredes, J. and Bergin, E. A. (2001). Rapid formation of molecular clouds and stars in the solar neighborhood. *Astrophys. J.*, **562**, 852–68.
Hartmann, W. K., Phillips, R. J. and Taylor, G. J., eds. (1984). *Origin of the Moon*. Houston: Lunar and Planetary Inst., pp. 781.
Hawkesworth, C. J. and Kemp, A. I. S. (2006). The differentiation and rates of generation of the continental crust. *Chem. Geol.*, **226**, 134–43.
Hay, W. W., Wold, C. N., Soding, E. and Floegel, E. (2001). Evolution of sediment fluxes and ocean salinity. In *Geologic Modeling and Simulation: Sedimentary Systems*, eds. D. F. Merriam and J. C. Davis. Dordrecht: Kluwer/Plenum, pp. 153–67.
Hayashi, C., Nakazava, K. and Mizuno, H. (1979). Earth melting due to the blanketing effect of the primordial dense atmosphere. *Earth Planet. Sci. Lett.*, **43**, 22–48.
Heber, V. S., Brooker, R. A., Kelley, S. P. and Wood, B. J. (2007). Crystal–melt partitioning of noble gases (helium, neon, argon, krypton, and xenon) for olivine and clinopyroxene. *Geochim. Cosmochim. Acta*, **71**, 1041–61.
Herzog, G. F., Anders, E., Alexander, E. C., Jr., Davis, P. K. and Lewis, R. S. (1973). Iodine-129 / Xenon-129 age of magnetite from the Orgueil meteorite. *Science*, **180**, 489–91.
Hewins, R. H. (1988). Experimental studies of chondrules. In *Meteorites and the Early Solar System*, eds. J. F. Kerridge and M. S. Matthews. Tucson, AZ: University of Arizona Press, pp. 660–79.
Hewins, R. H. (1996). Chondrules and protoplanetary disk: an overview. In *Chondrules and the Protoplanetary Disk*, eds. R. H. Hewins, R. H. Jones and E. R. D. Scott. Cambridge, UK: Cambridge University Press, pp. 3–9.
Hewins, R. H. and Newsom, H. E. (1988). Igneous activity in the early solar system. In *Meteorites and the Early Solar System*, eds. J. F. Kerridge and M. S. Matthews. Tucson, AZ: University of Arizona Press, pp. 73–101.
Hewins, R. H., Jones, R. H. and Scott, E. R. D., eds. (1996). *Chondrules and the Protoplanetary Disk*. Cambridge, UK: Cambridge University Press, pp. 346.
Hewitt, J., McKenzie, D. P. and Weiss, N. O. (1975). Dissipative heating in convective flows. *J. Fluid Mech.*, **68**, 721–38.
Hillebrandt, W. and Niemeyer, J. C. (2000). Type Ia supernova explosion models. *Ann. Rev. Astron. Astrophys.*, **38**, 191–230.
Hilton, D. R., Fischer, T. P. and Marty, B. (2002). Noble gases and volatiles recycling at subduction zones. In *Noble Gases in Geochemistry and Cosmochemistry*, Vol. 47, eds. D. Porcelli, C. J. Ballentine and R. Wieler. Washington DC: Mineral. Soc. Amer., pp. 319–70.
Hinton, R. W., Davis, A. M., Scatena-Wachel, D. E., Grossman, L. and Draus, R. J. (1988). A chemical and isotopic study of hibonite-rich refractory inclusions in primitive meteorites. *Geochim. Cosmochim. Acta*, **52**, 2573–98.
Hiroi, T., Pieters, C. M., Zolensky, M. E. and Lipschutz, M. E. (1993). Evidence of thermal metamorphism on the C-asteroid, G-asteroid, B-asteroid, and F-asteroid. *Science*, **261** (5124), 1016–18.
Hiyagon, H. (1994). Retention of solar helium and neon in IDPs in deep-sea sediment. *Science*, **263** (5151), 1257–9.
Hiyagon, H. and Ozima, M. (1986). Partition of noble gases between olivine and basalt melt. *Geochim. Cosmochim. Acta*, **50**, 2045–57.
Hoefs, J. (2005). *Stable Isotope Geochemistry* (3rd edition). Berlin: Springer-Verlag, pp. 197.
Hofmann, A. W. (1988). Chemical differentiation of the Earth: the relationship between mantle, continental crust, and oceanic crust. *Earth Planet. Sci. Lett.*, **90**, 297–314.

Hofmann, A. W. (2003). Sampling mantle heterogeneity through oceanic basalts: isotopes and trace elements. In *The Mantle and Core*, Vol. 2, ed. R. W. Carlson. Amsterdam: Elsevier-Pergamon, pp. 61–101.

Hofmann, A. W. and White, W. M. (1982). Mantle plumes from ancient oceanic crust. *Earth Planet. Sci. Lett.*, **57**, 421–36.

Hohenberg, C. M., Hudson, B., Kennedy, B. M. and Podosek, F. A. (1981). Noble gas retention chronologies for the St Severin meteorite. *Geochim. Cosmochim. Acta*, **45**, 535–46.

Holland, H. D. (2002). Volcanic gases, black smokers, and the great oxidation event. *Geochim. Cosmochim. Acta*, **66**, 3811–26.

Holloway, J. R. (1998). Graphite–melt equilibria during mantle melting: constraints on CO_2 in MORB magmas and the carbon content in the mantle. *Chem. Geol.*, **147**, 89–97.

Holzheid, A., Sylvester, P., O'Neill, H. S. C., Rubie, D. C. and Palme, H. (2000). Evidence for a late chondritic veneer in the Earth's mantle from high-pressure partitioning of palladium and platinum. *Nature*, **406**, 396–9.

Honda, M., McDougall, I., Patterson, D. B., Doulgeris, A. and Clague, D. A. (1993). Noble-gases in submarine pillow basalt glasses from Loihi and Kilauea, Hawaii – a solar component in the Earth. *Geochim. Cosmochim. Acta*, **57**, 859–74.

Honda, S., Aoki, W., Kajino, T. *et al*. (2004). Spectroscopic studies of extremely metal-poor stars with the Subaru high dispersion spectrograph. II. The r-process elements, including thorium. *Astrophys. J.*, **607**, 474–98.

Hood, L. L. (1998). Thermal processing of chondrule precursors in planetesimal bow shocks. *Meteorit. Planet. Sci.*, **33**, 97–107.

Hood, L. L. and Ceisla, F. (2001). The scale size of chondrule formation regions: constraints imposed by chondrule cooling rates. *Meteorit. Planet. Sci.*, **36**, 1571–85.

Hood, L. L. and Horanyi, M. (1993). The nebular shock-wave model for chondrule formation – one-dimensional calculations. *Icarus*, **106**, 179–89.

Hood, L. L. and Kring, D. A. (1996). Models for multiple heating mechanisms. In *Chondrules and the Protoplanetary Disk*, eds. R. H. Hewins, R. H. Jones and E. R. D. Scott. Cambridge, UK: Cambridge University Press, pp. 265–76.

Hood, L. L. and Zuber, M. T. (2000). Recent refinements in geophysical constraints on Lunar origin and evolution. In *Origin of the Earth and Moon*, eds. R. M. Canup and K. Righter. Tucson, AZ: University of Arizona Press, pp. 397–409.

Hoppe, P. and Ott, U. (1997). Mainstream silicon carbide grains from meteorites. In *Astrophysical Implications of the Laboratory Study of Presolar Materials*, eds. T. I. Bernatowicz and E. Zinner. New York: Amer. Inst. Phys., pp. 27–57.

Hsu, W. B., Wasserburg, G. J. and Huss, G. R. (2000). High time resolution by use of the ^{26}Al chronometer in the multistage formation of a CAI. *Earth Planet. Sci. Lett.*, **182**, 15–29.

Hubble, E. P. (1929). A clue to the structure of the Universe. *Astron. Soc. Pacific Leaflets*, **1**, 93.

Humayun, M. and Cassen, P. (2000). Processes determining the volatile abundances of the meteorites and terrestrial planets. In *Origin of the Earth and Moon*, eds. R. M. Canup and K. Righter. Tucson, AZ: University of Arizona, Press, pp. 3–23.

Humler, E., Langmuir, C. and Daux, V. (1999). Depth versus age: new perspectives from the chemical compositions of ancient crust. *Earth Planet. Sci. Lett.*, **173**, 7–23.

Hunten, D. M., Pepin, R. O. and Walker, J. C. G. (1987). Mass fractionation in hydrodynamic escape. *Icarus*, **69**, 532–49.

Hurley, P. M. (1968). Absolute abundance and distribution of Rb, K, and Sr in the Earth. *Geochim. Cosmochim. Acta*, **32**, 273–84.
Huss, G. R. (1990). Ubiquitous interstellar diamond and SiC in primitive chondrites: abundances reflect metamorphism. *Nature*, **347**, 159–62.
Huss, G. R., Lewis, R. S. and Hemkin, S. (1996). The "normal planetary" noble gas component in primitive chondrites: compositions, carrier, and metamorphic history. *Geochim. Cosmochim. Acta*, **60**, 3311–40.
Huss, G. R., Hutcheon, I. D. and Wasserburg, G. J. (1997). Isotopic systematic of presolar silicon carbide from the Orgueil (CI) chondrite: implication for Solar system formation and stellar nucleosynthesis. *Geochim. Cosmochim. Acta*, **61**, 5117–48.
Huss, G. R., MacPherson, G. J., Wasserburg, G. J., Russell, S. S. and Srinivasan, G. (2001). Aluminum-26 in calcium–aluminum-rich inclusions and chondrules from unequilibrated ordinary chondrites. *Meteorit. Planet. Sci.*, **36**, 975–97.
Huss, G. R., Meshik, A. P., Smith, J. B. and Hohenberg, C. M. (2004). Presolar diamond, silicon carbide, and graphite in carbonaceous chondrites: implications for thermal processing in the solar nebula. *Geochim. Cosmochim. Acta*, **67**, 4823–48.
Ingersoll, R. V. and Busby, C. J. (1995). Tectonics of sedimentary basins. In *Tectonics of Sedimentary Basins*, eds. C. J. Busby and R. V. Ingersoll. Oxford, UK: Blackwell, pp. 1–51.
Isern, J., Bravo, E., Garcia-Berro, E., Dominguez, I. and Salaris, M. (2001). On the internal composition of white dwarfs. *Nucl. Phys.*, **A688**, 122c–5.
Israelian, G., Lopez, R. J. G. and Rebolo, R. (1998). Oxygen abundances in unevolved metal-poor stars from near-ultraviolet OH lines. *Astrophys. J.*, **507**, 805–17.
Israelian, G., Rebolo, R., Basri, G., Casares, J. and Martin, E. L. (1999). Evidence of a supernova origin for the black hole in the system GRO J1655-40. *Nature*, **401**, 142–4.
Israelian, G., Rebolo, R., Garcia, L. G. *et al*. (2001). Oxygen in the very early galaxy. *Astrophys. J.*, **551**, 833–51.
Istomin, V. G., Grechnev, K. V. and Kochnev, V. A. (1983). Venera-13 and Venera-14: mass spectrometry of the atmosphere. *Kosmicheskie Issledovaniya*, **21**, 410–20.
Iwamori, H. (1994). ^{238}U–^{230}Th–^{226}Ra and ^{235}U–^{231}Pa disequilibria produced by mantle melting with porous and channel flows. *Earth Planet. Sci. Lett.*, **125**, 1–16.
Jackson, M. D., Cheadle, M. J. and Atherton, M. P. (2003). Quantitative modeling of granitic melt generation and segregation in the continental crust. *J. Geophys. Res.*, **108** (B7), 2332–53.
Jacobsen, S. B. (1988). Isotopic constraints on crustal growth and recycling. *Earth Planet. Sci. Lett.*, **90**, 315–29.
Jacobsen, S. B. (2005). The Hf–W isotopic system and the origin of the Earth and Moon. *Ann. Rev. Earth Planet. Sci.*, **33**, 18.1–40.
Jacobsen, S. B. and Wasserburg, G. J. (1979). The mean age of mantle and crustal reservoirs. *J. Geophys. Res.*, **84**, 7411–27.
Jacobsen, S. B. and Wasserburg, G. J. (1984). Sm–Nd isotopic evolution of chondrites and achondrites, II. *Earth Planet. Sci. Lett.*, **67**, 137–50.
Jagoutz, E., Palme, H., Baddenhausen, H. *et al*. (1979). The abundance of major, minor and trace elements in the earth's mantle as derived from primitive ultramafic nodules. In *Proc. Lunar Planet. Sci. Conf.*, Vol. 10, pp. 2031–50.
Jakosky, B. M., Pepin, R. O., Johnson, R. E. and Fox, J. L. (1994). Mars atmospheric loss and isotopic fractionation by solar-wind-induced sputtering and photochemical escape. *Icarus*, **111**, 271–88.

Jana, D. and Walker, D. (1997a). The influence of silicate melt composition on distribution of siderophile elements among metal and silicate liquids. *Earth Planet. Sci. Lett.*, **150**, 463–72.

Jana, D. and Walker, D. (1997b). The influence of sulfur on partitioning of siderophile elements. *Geochim. Cosmochim. Acta*, **61**, 5255–77.

Javoy, M. (1998). The birth of the Earth's atmosphere: the behaviour and fate of its major elements. *Chem. Geol.*, **147**, 11–25.

Jerram, D. A. and Widdowson, M. (2005). The anatomy of continental flood basalt provinces: geological constraints on the processes and products of flood volcanism. *Lithos*, **79**, 385–405.

Jewitt, D., Luu, J. and Trujillo, C. (1998). Large Kuiper Belt objects: the Mauna Kea 8K CCD survey. *Astron. J.*, **115**, 2125–35.

Jochum, K. P., Hofmann, A. W., Ito, E., Seufert, H. M. and White, W. M. (1983). K, U and Th in mid-ocean ridge basalt glasses and heat production, K/U and K/Rb in the mantle. *Nature*, **306**, 431–6.

Jochum, K. P., Hofmann, A. W. and Seufert, H. M. (1993). Tin in mantle-derived rocks: constraints on Earth evolution. *Geochim. Cosmochim. Acta*, **57**, 3585–95.

John, T., Scherer, E. E., Haase, K. and Schenk, V. (2004). Trace element fractionation during fluid-induced eclogitization in a subducting slab: trace element and Lu–Hf–Sm–Nd isotope systematics. *Earth Planet. Sci. Lett.*, **227**, 441–56

Johnson, K. T. M. (1998). Experimental determination of partition coefficients for rare earth and high-field-strength elements between clinopyroxene, garnet, and basaltic melt at high pressures. *Contrib. Mineral. Petrol.*, **133**, 60–8.

Jolliff, B. L., Wieczorek, M. A., Shearer, C. K. and Neal, C. R., eds. (2006). New views of the Moon. In *Reviews in Mineralogy and Geochemistry*, Vol. 60. Washington DC: Mineral. Soc. Amer., pp. 721.

Jones, J. H. (1996). Chondrite models for the composition of the Earth's mantle and core. *Phil. Trans. Roy. Soc. London*, **A354**, 1481–94.

Jones, J. H. and Drake, M. J. (1986). Geochemical constraints on core formation in the Earth. *Nature*, **322**, 221–8.

Jones, J. H. and Hood, L. L. (1990). Does the Moon have the same chemical composition as the Earth's upper mantle? In *Origin of the Earth*, eds. H. E. Newsom and J. H. Jones. Oxford, UK: Oxford University Press, pp. 85–98.

Jones, J. H. and Palme, H. (2000). Geochemical constraints on the origin of the Earth and Moon. In *Origin of the Earth and Moon*, eds. R. M. Canup and K. Righter. Tucson, AZ: University of Arizona Press, pp. 197–216.

Jull, M. and Kelemen, P. B. (2001). On the conditions for lower crustal convective instability. *J. Geophys. Res.*, **106** (B4), 6423–46.

Jull, M., Kelemen, P. B. and Sims, K. (2002). Consequences of diffuse and channelled porous melt migration on uranium series disequilibria. *Geochim. Cosmochim. Acta*, **66**, 4133–48.

Jurewicz, A. J. G., Mittlefehldt, D. W. and Jones, J. H. (1993). Experimental partial melting of the Allende (CV) and Murchison (CM) chondrites and the origin of asteroidal basalts. *Geochim. Cosmochim. Acta*, **57**, 2123–39.

Jurewicz, A. J. G., Mittlefehldt, D. W. and Jones, J. H. (1995). Experimental partial melting of the St Severin (LL) and Lost City (H) chondrites. *Geochim. Cosmochim. Acta*, **59**, 391–408.

Kallemeyn, G. W. and Wasson, J. T. (1981). The compositional classification of chondrites: I, The carbonaceous chondrite groups. *Geochim. Cosmochim. Acta*, **45**, 1217–30.

Kallenbach, R. (2001). Isotopic composition measured *in situ* in different solar wind regimes by CELIAS/MTOF on board SOHO. In *Solar and Galactic Composition*, ed. R. F. Wimmer-Schweingruber. New York: Amer. Inst. Phys, pp. 113–19.

Kallenbach, R. and Ott, U. (2003). Glossary. *Space Sci. Rev.*, **106**, 413–22.

Kamber, B. S., Ewart, A., Collerson, K. D., Bruce, M. C. and McDonald, G. D. (2002). Fluid-mobile trace element constraints on the role of slab melting and implications for Archaean crustal growth models. *Contrib. Mineral. Petrol.*, **144**, 38–56.

Kamber, B. S., Collerson, K. D., Moorbath, S. and Whitehouse, M. J. (2003). Inheritance of early Archaean Pb-isotope variability from long-lived Hadean protocrust. *Contrib. Mineral. Petrol.*, **145**, 25–46.

Kappeler, F., Beer, H. and Wisshak, K. (1989). s-Process nucleosynthesis – nuclear physics and the classical model. *Rep. Progress Phys.*, **52**, 945–1013.

Karato, S. and Murthy, V. R. (1997). Core formation and chemical equilibrium in the Earth. 1. Physical considerations. *Phys. Earth Planet. Inter.*, **100**, 61–79.

Kasting, J. F., Eggler, D. H. and Raeburn, S. P. (1993). Mantle redox evolution and the oxidation-state of the Archean atmosphere. *J. Geol.*, **101**, 245–57.

Kato, T., Ringwood, A. E. and Irifune, T. (1988). Constraints on element partition coefficients between $MgSiO_3$ perovskite and liquid determined by direct measurements. *Earth Planet. Sci. Lett.*, **90**, 65–8.

Kaula, W. M. (1999). Constraint on Venus evolution from radiogenic argon. *Icarus*, **139**, 32–39.

Kay, R. W. and Kay, S. M. (1993). Delamination and delamination magmatism. In *Plate Tectonic Signatures in the Continental Lithosphere*, eds. A. G. Green, A. Kroner, H.-J. Gotze and N. Pavlenkova. Tectonophysics, Vol. 219, pp. 177–89.

Kelemen, P. B., Hanghoj, K. and Greene, A. R. (2003). One view of the geochemistry of subduction-related magmatic arcs, with an emphasis on primitive andesite and lower crust. In *The Crust*, Vol. 3, ed. R. L. Rudnick. Amsterdam: Elsevier-Pergamon, pp. 593–659.

Kelemen, P. B., Yogodzinski, G. M. and Scholl, D. W. (2004). Along-strike variation in lavas of the Aleutian island arc: implications for the genesis of high *Mg*# andesite and the continental crust. In *Inside the Subduction Factory*, Vol. 138, ed. J. Eiler. Washington DC: AGU Monograph, pp. 223–76.

Kelley, K. A., Plank, T., Farr, L., Ludden, J. and Staudigel, H. (2005). Subduction cycling of U, Th, and Pb. *Earth Planet. Sci. Lett.*, **234**, 369–83.

Kellogg, J. B., Jacobsen, S. B. and O'Connell, R. J. (2002). Modeling the distribution of isotopic ratios in geochemical reservoirs. *Earth Planet. Sci. Lett.*, **204**, 183–202.

Kellogg, L. H. (1997). Growing the Earth's D″ layer: effect of density variations at the core–mantle boundary. *Geophys. Res. Lett.*, **24**, 2749–52.

Kellogg, L. H., Hager, B. H. and van der Hilst, R. D. (1999). Compositional stratification in the deep mantle. *Science*, **283**, 1881–4.

Kemp, A. I. S. and Hawkesworth, C. J. (2003). Granitic perspectives on the generation and secular evolution of the continental crust. In *The Crust*, Vol. 3, ed. R. L. Rudnick. Amsterdam: Elsevier-Pergamon, pp. 350–410.

Kendall, J.-M., Stuart, G. W., Ebinger, C. J., Bastow, I. D. and Keir, D. (2005). Magma-assisted rifting in Ethiopia. *Nature*, **433**, 147–9.

Kerridge, J. F. (1993). What can meteorites tell us about nebular conditions and processes during planetesimal accretion? *Icarus*, **106**, 135–50.

Kerridge, J. F. and Matthews, M. S., eds. (1988). *Meteorites and the Early Solar System*. Tucson, AZ: University of Arizona Press, 1286. pp.

Kessel, R., Schmidt, M. W., Ulmer, P. and Pettke, T. (2005). Trace element signature of subduction-zone fluids, melts and supercritical liquids at 120–180 km depth. *Nature*, **437**, 724–7.

Kilburn, M. R. and Wood, B. J. (1997). Metal–silicate partitioning and the incompatibility of S and Si during core formation. *Earth Planet. Sci. Lett.*, **152**, 139–48.

Kim, J. S. and Marti, K. (1992). Solar-type xenon: isotopic abundances in Pesyanoe. In *Proc. Lunar Planet. Sci. Conf.*, Vol. 22, pp. 145–51.

Kirschbaum, C. (1987). Carrier phases for iodine in the Allende meteorite and their associated $^{129}Xe/^{127}I$ ratios: a laser microprobe study. *Geochim. Cosmochim. Acta*, **52**, 679–99.

Kirsten, T. (1983). Geochemical double beta decay experiments. In *Science Underground*, Vol. 96, eds. M. M. Nieto, W. C. Haxton, C. M. Hofman, E. W. Kolb, V. D. Sandberg and J. W. Toevs. New York: Amer. Inst. Phys, pp. 396–410.

Klein, E. M. (2003). Geochemistry of the igneous oceanic crust. In *The Crust*, Vol. 3, ed. R. L. Rudnick. Amsterdam: Elsevier-Pergamon, pp. 433–63.

Klein, E. M. and Langmuir, C. H. (1987). Global correlations of oceanic basalt chemistry with axial depth and crustal thickness. *J. Geophys. Res.*, **92**, 8089–115.

Kleine, T., Munker, C., Mezger, K. and Palme, H. (2002). Rapid accretion and early core formation on asteroids and the terrestrial planets from Hf–W chronometry. *Nature*, **418**, 952–5.

Kleinhanns, I. C., Kramers, J. D. and Kamber, B. S. (2003). Importance of water for Archaean granitoid petrology: a comparative study of TTG and potassic granitoids from Barberton Mountain Land, South Africa. *Contrib. Mineral. Petrol.*, **145**, 377–89.

Knesel, K. M. and Davidson, J. P. (2002). Insights into collisional magmatism from isotopic fingerprints of melting reactions. *Science*, **296**, 2206–8.

Knittle, E. and Jeanloz, R. (1991). Earth's core–mantle boundary: results of experiments at high pressures and temperatures. *Science*, **251**, 1438–43.

Kohut, E. J., Stern, R. J., Kent, A. J. R., Nielsen, R. L., Bloomer, S. H. and Leybourne, M. (2006). Evidence for adiabatic decompression melting in the Southern Mariana Arc from high-Mg lavas and melt inclusions. *Contrib. Mineral. Petrol.*, **152**, 201–21.

Kong, P. and Ebihara, M. (1997). The origin and nebular history of the metal phase of ordinary chondrites. *Geochim. Cosmochim. Acta*, **61** (11), 2317–29.

Kong, P. and Palme, H. (1999). Compositional and genetic relationship between chondrules, chondrule rims, metal, and matrix in the Renazzo chondrite. *Geochim. Cosmochim. Acta*, **63**, 3673–82.

Kong, P., Ebihara, M. and Palme, H. (1999). Distribution of siderophile elements in CR chondrites: evidence for evaporation and recondensation during chondrule formation. *Geochim. Cosmochim. Acta*, **63**, 2637–52.

Kortenkamp, S. J., Kokubo, E. and Weidenschilling, S. J. (2000). Formation of planetary embryos. In *Origin of the Earth and Moon*, eds. R. M. Canup and K. Righter. Tucson, AZ: University of Arizona Press, pp. 85–100.

Kostitsyn, Y. A. (2000). Origin of peraluminous rare-metal granites: a review of Rb–Sr and Sm–Nd isotopic data. In *Ore-Bearing Granites of Russia and Adjacent Countries*, eds. A. Kremenetsky, B. Lehmann and R. Seltmann. Moscow: IMGRE, pp. 143–55.

Kostitsyn, Y. A. (2004). Terrestrial Sm–Nd and Lu–Hf isotopic systematics: do they correspond to chondrites? *Petrologiya*, **12**, 451–66.

Kramers, J. D. (1998). Reconciling siderophile element data in the Earth and Moon, W isotopes and the upper lunar age limit in a simple model of homogeneous accretion. *Chem. Geol.*, **145**, 461–78.

Kramers, J. D. (2003). Volatile element abundance patterns and the early liquid water ocean on Earth. *Precambrian Res.*, **126**, 379–94.
Kramers, J. D. (2007). Hierarchical Earth accretion and the Hadean Eon (Invited bicentennial review). *J. Geol. Soc.*, **164**, 2–17.
Kramers, J. R. and Tolstikhin, I. N. (1997). Two terrestrial lead isotope paradoxes, forward transport modeling, core formation and the history of the continental crust. *Chem. Geol.*, **139**, 75–110.
Kramers, J. D., Kreissig, K. and Jones, M. Q. W. (2001). Crustal heat production and style of metamorphism: a comparison between two Archean high grade provinces in the Limpopo Belt, Southern Africa. *Precambrian Res.*, **112**, 149–63.
Kratz, K.-L. (2001). Measurements of r-process nuclei. *Nucl. Phys.*, **A688**, 308c-17.
Kratz, K.-L., Bitouzet, J.-P., Thielemann, F.-K., Moeller, P. and Pfeiffer, B. (1993). Isotopic r-process abundances and nuclear structure far from stability – implications for the r-process mechanism. *Astrophys. J.*, **403**, 216–38.
Kreissig, K., Nagler, T. F., Kramers, J. D., van Reenen, D. D. and Smit, C. A. (2000). An isotopic and geochemical study of the northern Kaapvaal Craton and the Southern Marginal Zone of the Limpopo Belt: are they juxtaposed terranes? *Lithos*, **50**, 1–25.
Krot, A. N., Hutcheon, I. D., Yurimoto, H., Cuzzi, J. N., McKeegan, K. D., Scott, E. R. D., Libourel, G., Chaussidon, M., Aleon, J. and Petaev, M. I. (2005). Evolution of oxygen isotopic composition in the inner solar nebula. *Astrophys. J.*, **622**, 1333–42.
Krot, A. N., McKeegan, K. D., Huss, G. R., Liffman, K., Sahijpal, S., Hutcheon, I. D., Srinivasan, G., Bischoff, A. and Keil, K. (2006). Aluminum–magnesium and oxygen isotope study of relict Ca–Al-rich inclusions in chondrules. *Astrophys. J.*, **639**, 1227–37.
Kuehner, S. M., Laughlin, J. R., Grossman, L., Johnson, M. L. and Burnett, D. S. (1989). Determination of trace element mineral/liquid partition coefficients in melilite and diopside by ion and electron microprobe techniques. *Geochim. Cosmochim. Acta*, **53**, 3115–30.
Kung, C. C. and Clayton, R. N. (1978). Nitrogen abundances and isotopic compositions in stony meteorites. *Earth Planet. Sci. Lett.*, **38**, 421–35.
Kunz, J., Staudacher, T. and Allègre, C. J. (1998). Plutonium-fission xenon found in Earth's mantle. *Science*, **280**, 877–80.
Kuramoto, K. (1997). Accretion, core formation, H and C evolution of the Earth and Mars. *Phys. Earth Planet. Inter.*, **100**, 3–20.
Kurz, M. D., Jenkins, W. J. and Hart, S. R. (1982a). Helium isotopic systematics of oceanic islands and mantle heterogeneity. *Nature*, **297**, 43–7.
Kurz, M. D., Jenkins, W. J., Schilling, J. G. and Hart, S. R. (1982b). Helium isotopic variations in the mantle beneath the central North Atlantic Ocean. *Earth Planet. Sci. Lett.*, **58**, 1–14.
Lackey, J. S., Valley, J. W. and Saleeby, J. B. (2005). Supracrustal input to magmas in the deep crust of Sierra Nevada batholith: evidence from high-δ^{18}O zircon. *Earth Planet. Sci. Lett.*, **235**, 315–30.
Lagabrielle, Y., Goslin, J., Martin, H., Thirot, J.-L. and Auzende, J.-M. (1997). Multiple active spreading centers in the hot North Fiji Basin (Southwest Pacific): a possible model for Archaean seafloor dynamics? *Earth Planet. Sci. Lett.*, **149**, 1–13.
Laming, J. M. (2001). The electron temperature and ^{44}Ti decay rate in Cassiopeia A. In *Solar and Galactic Composition*, ed. R. F. Wimmer-Schweingruber. New York: Amer. Inst. Phys, pp. 411–16.

Larsen, T. B., Yuen, D. A. and Storey, M. (1999). Ultrafast mantle plumes and implications for flood basalt volcanism in the Northern Atlantic Region. *Tectonophysics*, **311**, 31–43.

Larson, R. B. (1981). Turbulence and star formation in molecular clouds. *Mon. Not. Roy. Astr. Soc.*, **194**, 809–26.

LaTourrette, T. and Wasserburg, G. J. (1998). Mg diffusion in anorthite: implications for the formation of early solar system planetesimals. *Earth Planet. Sci. Lett.*, **158**, 91–108.

Lecluse, C. and Robert, F. (1994). Hydrogen isotope-exchange reaction-rates – origin of water in the inner Solar-System. *Geochim. Cosmochim. Acta*, **58**, 2927–39.

Lecuyer, C., Gillet, P. and Robert, F. (1998). The hydrogen isotope composition of seawater and the global water cycle. *Chem. Geol.*, **145**, 249–61.

Lecuyer, C., Simon, L. and Guyot, F. (2000). Comparison of carbon, nitrogen and water budgets on Venus and the Earth. *Earth Planet. Sci. Lett.*, **181**, 33–40.

Lee, H. Y. and Ganguly, J. (1988). Equilibrium composition of coexisting garnet and orthopyroxene: experimental determinations in the system FeO–MgO–Al_2O_3–SiO_2, and applications. *J. Petrol.*, **29**, 93–113.

Lee, T., Papanastassiou, D. A. and Wasserburg, G. J. (1976). Demonstration of ^{26}Mg excess in Allende and evidence for ^{26}Al. *Geophys. Res. Lett.*, **3**, 109–12.

Le Fort, P., Cuney, M., Deniel, C., France-Lanord, C., Sheppard, S. M. F., Upreti, B. N. and Vidal, P. (1987). Crustal generation of the Himalayan leucogranites. *Tectonophys*., **134**, 39–57.

Lehmann, B. E., Lehmann, M., Neftel, A., Gut, A. and Tarakanov, S. V. (1999). Radon-220 calibration of near-surface turbulent gas transport. *Geophys. Res. Lett.*, **26**, 607–10.

Le Pichon, X. (1968). Sea-floor spreading and continental drift. *J. Geophys. Res.*, **73**, 3660–97.

Lewis, J. S. (2004). *Physics and Chemistry of the Solar System*. London, UK: Academic Press, pp. 655.

Lewis, R. S. and Anders, E. (1975). Condensation time of the solar nebula from extinct ^{129}I in primitive meteorites. *Proc. Nat. Acad. Sci. USA*, **72**, 268–73.

Lewis, R. S., Srinivasan, B. and Anders, E. (1975). Host phase of a strange xenon component in Allende. *Science*, **190**, 1251–62.

Leya, I. and Wieler, R. (1999). Nucleogenic production of Ne isotopes in Earth's crust and upper mantle induced by alpha particles from the decay of U and Th. *J. Geophys. Res. – Solid Earth*, **104**, 15, 439–50.

Leya, I., Halliday, A. N. and Wieler, R. (2003). The predictable collateral consequences of nucleosynthesis by spallation reaction in the early Solar system. *Astrophys. J.*, **594**, 605–16.

Li, J. and Agee, C. B. (2001). Element partitioning constraints on the light element composition of the Earth's core. *Geophys. Res. Lett.*, **28**, 81–4.

Liffman, K. and Toscano, M. (2000). Chondrule fine-grained mantle formation by hypervelocity impact of chondrules with a dusty gas. *Icarus*, **143**, 106–25.

Lin, J.-F., Heinz, D. L., Campbell, A. J., Devine, J. M. and Shen, G. (2002). Iron–silicon alloy in Earth's core? *Science*, **295**, 313–15.

Lin, J.-F., Campbell, A. J., Heinz, D. L. and Shen, G. (2003). Static compression of iron–silicon alloys: implications for silicon in the Earth's core. *J. Geophys. Res. – Solid Earth*, **108**, 2045.

Lissauer, J. J. and Safronov, V. S. (1991). The random component of planetary rotation. *Icarus*, **93**, 288–97.

Liu, L.-G. and Huh, C.-A. (2000). Effect of pressure on the decay rate of ^{7}Be. *Earth Planet. Sci. Lett.*, **180**, 163–7.

Liu, Y., Gao, S., Yuan, H., Zhou, L., Liu, X., Wang, X., Hu, Z. and Wang, L. (2004). U–Pb zircon ages and Nd, Sr, and Pb isotopes of lower crustal xenoliths from North China Craton: insights on evolution of lower continental crust. *Chem. Geol.*, **211**, 87–109.

Lodders, K. and Fegley, B., Jr. (1992). Trace element condensation in circumstellar envelopes of carbon stars. *Meteoritics*, **27**, 250.

Lowrie, W. (1997). *Fundamentals of Geophysics*. Cambridge, UK: Cambridge University Press, pp. 368.

Lugmair, G. W. and Galer, S. J. G. (1992). Age and isotopic relationships among the angrites Lewis Cliff 86010 and Angra dos Reis. *Geochim. Cosmochim. Acta*, **56**, 1673–94.

Lugmair, G. W. and Shukolyukov, A. (1998). Early solar system timescales according to ^{53}Mn–^{53}Cr systematics. *Geochim. Cosmochim. Acta*, **62**, 2863–86.

Lugmair, G. W. and Shukolyukov, A. (2001). Early solar system events and time scales. *Meteorit. Planet. Sci.*, **36**, 1017–26.

Lux, G. (1987). The behavior of noble gases in silicate liquids: solution, diffusion, bubbles and surface effects, with implications to natural samples. *Geochim. Cosmochim. Acta*, **51**, 1549–60.

Lynden-Bell, D. and Pringle, J. S. (1974). The evolution of viscous discs and the origin of nebular variables. *Mon. Not. Roy. Astr. Soc.*, **168**, 603–37.

Lyons, J. R. and Young, E. D. (2005). CO self-shielding as the origin of oxygen isotope anomalies in the early solar nebula. *Nature*, **435**, 317–20.

MacPherson, G. J. and Davis, A. M. (1993). A petrologic and ion microprobe study of a Vigarano type B refractory inclusion. Evolution by multiple stages of alteration and melting. *Geochim. Cosmochim. Acta*, **57**, 231–43.

MacPherson, G. J. and Davis, A. M. (1994). Refractory inclusions in the prototypical CM chondrite Mighei. *Geochim. Cosmochim. Acta*, **58**, 5599–625.

MacPherson, G. J., Bar-Matthews, M., Tanaka, T., Olsen, E. and Grossman, L. (1983). Refractory inclusions in the Murchison meteorite. *Geochim. Cosmochim. Acta* **47**, 823–39.

MacPherson, G. J., Crozaz, G. and Lundberg, L. L. (1989). The evolution of a complex type B Allende inclusion: an ion microprobe trace element study. *Geochim. Cosmochim. Acta*, **53**, 2413–27.

MacPherson, G. J., Davis, A. M. and Zinner, E. K. (1995). The distribution of Al-26 in the early Solar-system – a reappraisal. *Meteoritics* **30** (4), 365–86.

Mahaffy, P., Donahue, T. M., Atreya, S. K., Owen, T. C. and Niemann, H. B. (1998). Galileo probe measurements of D/H and ^{3}He/^{4}He in Jupiter's atmosphere. In *Primordial Nuclei and their Galactic Evolution*, eds. N. Prantzos, M. Tosi and R. von Steiger. Dordrecht: Kluwer, pp. 251–63.

Makalkin, A. B. and Dorofeeva, V. A. (1995). Structure of proto-planetary accretion disk around the Sun on the T-Tauri stage: initial data, equations and modeling. *Astron. Vestnik*, **29**, 99–122.

Malamud, B. D. and Turcotte, D. L. (1999). How many plumes are there? *Earth Planet. Sci. Lett.*, **174**, 113–24.

Mamyrin, B. A. and Tolstikhin, I. N. (1984). *Helium Isotopes in Nature*. Amsterdam: Elsevier, pp. 273.

Mamyrin, B. A., Tolstikhin, I. N., Anufriev, G. S. and Kamensky, I. L. (1969). Anomalous helium isotopic composition in volcanic gases. *Dokl. Acad. Nauk USSR*, **184**, 1197–9.

Manhes, G., Allègre, C. J. and Provost, A. (1984). U–Th–Pb systematics of the eucrite Juvinas: precise age determination and evidence for exotic lead. *Geochim. Cosmochim. Acta*, **48**, 2247–64.

Mao, W. L., Shen, G., Prakapenka, V. B., Meng, Y., Campbell, A. J., Heinz, D. L., Shu, J., Hemley, R. J. and Mao, H. (2004). Ferromagnesian postperovskite silicates in the D″ layer of the Earth. *Proc. Nat. Acad. Sci.*, **101**, 15, 867–9.

Marhas, K. K., Goswami, J. N. and Davis, A. M. (2002). Short-lived nuclides in hibonite grains from Murchison: evidence for solar system evolution. *Science*, **298**, 2182–5.

Martin, H. (1994). The Archean grey gneisses and genesis of continental crust. In *Archean Crustal Evolution*, ed. K. C. Condie. Amsterdam: Elsevier, pp. 205–59.

Martin, H. (1999). Adakitic magmas: modern analogues of Archaean granitoids. *Lithos*, **46**, 411–29.

Martin, H. and Moyen, J.-F. (2002). Secular changes in tonalite–trondhjemite–granodiorite composition as markers of the progressive cooling of Earth. *Geology*, **30**, 319–22.

Marty, B. and Marti, K. (2002). Signatures of early differentiation of Mars. *Earth Planet. Sci. Lett.*, **196**, 251–63.

Marty, B. and Tolstikhin, I. N. (1998). CO_2 fluxes from mid-ocean ridges, arcs and plumes. *Chem. Geol.*, **145**, 233–48.

Marty, B. and Zimmermann, L. (1999). Volatiles (He, C, N, Ar) in mid-ocean ridge basalts: assessment of shallow-level fractionation and characterization of source composition. *Geochim. Cosmochim. Acta*, **63**, 3619–33.

Mason, B. (1962). *Meteorites*. New York: Wiley and Sons, pp. 274.

Mathew, K. J. and Marti, K. (2002). Martian atmospheric and interior volatiles in the meteorite Nakhla. *Earth Planet. Sci. Lett.*, **199**, 7–20.

Mathew, K. J., Kim, J. S. and Marti, K. (1998). Martian atmospheric and indigenous components of xenon and nitrogen in the Shergotty, Nakhla, and Chassigny group meteorites. *Meteorit. Planet. Sci.*, **33**, 655–64.

Matsui, T. and Abe, Y. (1986). Evolution of an impact-induced atmosphere and magma ocean on the accreting Earth. *Nature*, **319**, 303–5.

Matsumoto, T., Seta, A., Matsuda, J., Takebe, M., Chen, Y. and Arai, S. (2002). Helium in the Archean komatiites revisited: significantly high $^{3}He/^{4}He$ ratios revealed by fractional crushing gas extraction. *Earth Planet. Sci. Lett.*, **196**, 213–25.

Matteucci, F. and Recchi, S. (2001). On the typical timescale for the chemical enrichment from type Ia Supernovae in Galaxies. *Astrophys. J.*, **558**, 351–8.

McDade, P., Blundy, J. D. and Wood, B. J. (2003). Trace element partitioning on the Tinaquillo Lherzolite solidus at 1.5 GPa. *Phys. Earth Planet. Inter.*, **139**, 129–47.

McDonough, W. F. and Sun, S.-S. (1995). The composition of the Earth. *Chem. Geol.*, **120**, 223–53.

McKenzie, D. P. (1968). The influence of the boundary conditions and rotation on convection in the Earth's mantle. *Geophys. J. Roy. Astron. Soc.*, **15**, 457–500.

McKenzie, D. P. (1984). The generation and compaction of partially molten rock. *J. Petrol.*, **25**, 713–65.

McKenzie, D. (1985). $^{230}Th–^{238}U$ disequilibrium and the melting processes beneath ridge axes. *Earth Planet. Sci. Lett.*, **72**, 149–57.

McKenzie, D. (2000). Constraints on melt generation and transport from U-series activity ratios. *Chem. Geol.*, **162**, 81–94.

McKenzie, D. P. and Bickle, M. J. (1988). The volume and composition of melt generated by extension of the lithosphere. *J. Petrol.*, **29**, 625–79.

McKenzie, D. and O'Nions, R. K. (1991). Partial melt distributions from inversion of rare earth element concentrations. *J. Petrol.*, **32**, 1021–91.
McKenzie, D. and O'Nions, R. K. (1995). The source regions of ocean island basalts. *J. Petrol.*, **36**, 133–59.
McKenzie, D. and O'Nions, R. K. (1998). Melt production beneath oceanic islands. *Phys. Earth Planet. Inter.*, **107**, 143–82.
McKenzie, D., Nimmo, F., Jackson, J. A., Gans, P. B. and Miller, E. L. (2000). Characteristics and consequences of flow in the lower crust. *J. Geophys. Res. – Solid Earth)*, **105** (B5), 11, 029–46.
McKenzie, D., Stracke, A., Blichert-Toft, J., Albarede, F., Gronvold, K. and O'Nions, R. K. (2004). Source enrichment processes responsible for isotopic anomalies in oceanic island basalts. *Geochim. Cosmochim. Acta*, **68**, 2699–724.
McLennan, S. M. (2001). Relationships between the trace element composition of sedimentary rocks and upper continental crust. *Geochem. Geophys. Geosyst.*, **2**, 2000GC000109.
McWilliam, A. (1997). Abundance ratios and galactic chemical evolution. *Ann. Rev. Astron. Astrophys.*, **35**, 503–56.
McWilliam, A. (1998). Ba abundances in extremely metal-poor stars. *Astron. J.*, **115**, 1640–7.
McWilliam, A., Preston, G. W., Sneden, C. and Searle, L. (1995). Spectroscopic analysis of 33 of the most metal poor stars. II. *Astron. J.*, **109**, 2757–99.
Meibom, A. and Anderson, D. L. (2003). The statistical upper mantle assemblage. *Earth Planet. Sci. Lett*., **217**, 123–39.
Meibom, A. and Clark, B. E. (1999). Evidence for the insignificance of ordinary chondritic material in the asteroid belt. *Meteorit. Planet. Sci.*, **34**, 7–24.
Meisel, T., Walker, R. J., Irving, A. J. and Lorand, J.-P. (2001). Osmium isotopic compositions of mantle xenoliths: a global perspective. *Geochim. Cosmochim. Acta*, **65**, 1311–23.
Melosh, H. J. (2003). The history of air. *Nature*, **424**, 22–3.
Melosh, H. J. and Tonks, W. B. (1993). Swapping rocks: ejection and exchange of surface material among the terrestrial planets. *Meteoritics*, **28**, 398.
Melosh, H. J., Vickery, A. M. and Tonks, W. B. (1993). Impacts and the early environment and evolution of the terrestrial planets. In *Protostars and Planets, III*, eds. E. H. Levy and J. I. Lunine. Tucson, AZ: University of Arizona Press, pp. 1339–70.
Metzler, K., Bischoff, A. and Stoffler, D. (1992). Accretionary dust mantles in CM chondrites – evidence for solar nebula processes. *Geochim. Cosmochim. Acta*, **56**, 2873–97.
Meybeck, M. (2003). Global occurrence of major elements in rivers. In *Surface and Ground Water, Weathering, and Soils*, Vol. 5, ed. J. I. Drever. Amsterdam: Elsevier-Pergamon, pp. 207–23.
Meyer, B. S. (1997). Supernova nucleosynthesis. In *Astrophysical Implications of the Laboratory Study of Presolar Materials*, eds. T. I. Bernatowicz and E. Zinner. New York: Amer. Inst. Phys., pp. 155–78.
Meyer, B. S. and Clayton, D. D. (2000). Short-lived radioactivities and the birth of the Sun. In *From Dust to Terrestrial Planets*, eds. W. Benz, R. Kallenbach and G. W. Lugmair. Dordrecht: Kluwer, pp. 133–52.
Millar, T. J., Bennett, A. and Herbst, E. (1989). Deuterium fractionation in dense interstellar clouds. *Astrophys. J. Suppl.*, **340**, 906–20.
Minster, J.-F., Birck, J.-L. and Allègre, C. J. (1982). Absolute age of formation of chondrites by the ^{87}Rb–^{87}Sr method. *Nature*, **300**, 414–19.

Mitchell, R. C., Baron, E., Branch, D., Lundqvist, P., Blinnikov, S., Hauschildt, P. H. and Pun, C. S. J. (2001). ^{56}Ni mixing in the outer layers of SN 1987A. *Astrophys. J.*, **556**, 979–86.

Mittlefehldt, D. W., McCoy, V. J., Goodrich, C. A. and Kracher, A. (1998). Non-chondritic meteorites from asteroidal bodies. In *Reviews in Mineralogy: Planetary Materials*, Vol. 36, ed. J. J. Papike. Washington DC: Mineral. Soc. Amer., pp. 4.1–4.195.

Mochizuki, Y. (2001). ^{44}Ti: its initial abundance in Cas A and its detection possibility in SNe 1987 A with INTEGRAL. *Nucl. Phys.*, **A688**, 58c–61c.

Moecher, D. P. and Sharp, Z. D. (1999). Comparison of conventional and garnet-aluminosilicate-quartz O isotope thermometry: insights for mineral equilibration in metamorphic rocks. *Amer. Mineral.*, **84**, 1287–303.

Molnar, P. and Stock, J. (1987). Relative motions of hotspots in the Pacific, Atlantic and Indian oceans since late Cretaceous time. *Nature*, **327**, 587–91.

Morbidelli, A., Chambers, J., Lunine, J. I. *et al.* (2000). Source regions and timescales for the delivery of water to the Earth. *Meteorit. Planet. Sci.*, **35**, 1309–20.

Moreira, M., Doucelance, R., Kurz, M. D., Dupre, B. and Allègre, C. J. (1999). Helium and lead isotope geochemistry of the Azores Archipelago. *Earth Planet. Sci. Lett.*, **169**, 189–205.

Moreira, M., Breddam, K., Curtice, J. and Kurz, M. D. (2001). Solar neon in the Icelandic mantle: new evidence for an undegassed lower mantle. *Earth Planet. Sci. Lett.*, **185**, 15–23.

Morfill, G., Spruit, H. and Levy, E. H. (1993). Physical processes and conditions associated with the formation of protoplanetary disks. In *Protostars and Planets, III*, eds. E. H. Levy and J. Lunine. Tucson, AZ: University of Arizona Press, pp. 939–78.

Morgan, J. W. and Anders, E. (1980). Chemical composition of Earth, Venus and Mercury. *Proc. Nat. Acad. Sci. USA*, **77**, 6973–7.

Morgan, J. W., Walker, R. J., Brandon, A. D. and Horan, M. F. (2001). Siderophile elements in Earth's upper mantle and lunar breccias: data synthesis suggests manifestations of the same late influx. *Meteorit. Planet. Sci.*, **36**, 1257–75.

Morgan, W. J. (1968). Rises, trenches, great faults, and crustal blocks. *J. Geophys. Res.*, **73**, 1959–83.

Morlok, A., Bischoff, A., Stephan, T., Floss, C., Zinner, E. and Jessberger, E. K. (2006). Brecciation and chemical heterogeneities of CI chondrites. *Geochim. Cosmochim. Acta*, **70**, 5371–94.

Morris, J. D. and Ryan, J. G. (2003). Subduction zone processes and implications for changing composition of the upper and lower mantle. In *The Mantle and Core*, Vol. 2, ed. R. W. Carlson. Amsterdam: Elsevier-Pergamon, pp. 451–70.

Morris, J., Gosse, J., Brachfeld, S. and Tera, F. (2002). Cosmogenic ^{10}Be and the solid earth: studies in active tectonics, geomagnetism and subduction zone processes. In *Reviews in Mineralogy*, Vol. 50, ed. E. Grew. Washington DC: Mineral. Soc. Amer., pp. 207–70.

Morse, J. W. (2003). Formation and diagenesis of carbonate sediments. In *Sediments, Diagenesis and Sedimentary Rocks*, Vol. 7, ed. F. T. Mackenzie. Amsterdam: Elsevier-Pergamon, pp. 67–85.

Mostefaoui, S., Lugmair, G. W., Hoppe, P. and Goresy, A. E. (2004). Evidence for live ^{60}Fe in meteorites. *New Astron. Rev.*, **48**, 155–9.

Mundt, R., Stocke, J., Strom, S. E., Strom, K. M. and Anderson, E. R. (1985). The optical spectrum of L1551 IRS 5. *Astrophys. J.*, **297**, L41–5.

Muramatsu, Y. and Wedepohl, K. H. (1998). The distribution of iodine in the earth's crust. *Chem. Geol.*, **147**, 201–16.

Muramatsu, Y., Fehn, U. and Yoshida, S. (2001). Recycling of iodine in fore-arc areas: evidence from the iodine brines in Chiba, Japan. *Earth Planet. Sci. Lett.*, **192**, 583–93.

Murphy, D. T., Kamber, B. S. and Collerson, K. D. (2002). A refined solution to the first terrestrial Pb-isotope paradox. *J. Petrol.*, **43**, 39–53.

Murthy, V. R. and Karato, S. (1997). Core formation and chemical equilibrium in the Earth. 2. Chemical consequences for the mantle and core. *Phys. Earth Planet. Inter.*, **100**, 81–95.

Nagataki, S., Hashimoto, M., Sato, K., Yamada, S. and Mochizuki, Y. S. (1998). The high ratio of Ti-44/Ni-56 in Cassiopeia A and the axisymmetric collapse-driven supernova explosion. *Astrophys. J.*, **492**, L45–8.

Nägler, T. F. and Kramers, J. D. (1998). Nd isotopic evolution of the upper mantle during the Precambrian: models, data and the uncertainty of both. *Precambrian Res.*, **91**, 233–52.

Nägler, T. F., Siebert, J., Luschen, H. and Bottcher, M. E. (2005). Sedimentary Mo isotope record across the Holocene fresh–brackish water transition of the Black Sea. *Chem. Geol.*, **219**, 283–95.

Nakajima, J., Takei, Y. and Hasegawa, A. (2005). Quantitative analysis of the inclined low-velocity zone mantle wedge of northeastern Japan: a systematic change in melt-filled pore shapes with depth and its implications for melt migration. *Earth Planet. Sci. Lett.*, **234**, 59–70.

Nakamura, T., Nagao, K. and Takaoka, N. (1999a). Microdistribution of primordial noble gases in CM chondrites determined by *in situ* laser microprobe analysis: decipherment of nebular processes. *Geochim. Cosmochim. Acta*, **63**, 241–55.

Nakamura, T., Nagao, K., Metzler, K. and Takaoka, N. (1999b). Heterogeneous distribution of solar and cosmogenic noble gases in CM chondrites and implications for the formation of CM parent bodies. *Geochim. Cosmochim. Acta*, **63**, 257–73.

Nataf, H. C. (2000). Seismic imaging of mantle plumes. *Ann. Rev. Earth Planet. Sci.*, **28**, 391–417.

Nemchin, A. A., Pidgeon, R. T. and Whitehouse, M. J. (2006). Re-evaluation of the origin and evolution of >4.2 Gyr zircons from the Jack Hills metasedimentary rocks. *Earth Planet. Sci. Lett.*, **244**, 218–33.

Newman, W. I., Symbalisty, E. M. D., Ahrens, T. J. and Jones, E. M. (1999). Impact erosion of planetary atmospheres: some surprising results. *Icarus*, **138**, 224–40.

Newsom, H. E. (1990). Accretion and core formation in the Earth: evidence from siderophile elements. In *Origin of the Earth*, eds. H. E. Newsom and J. H. Jones. Oxford, UK: Oxford University Press, pp. 273–88.

Newsom, H. E. (1995). Composition of the Solar system, planets, meteorites, and major terrestrial reservoirs. In *Global Earth Plysics: A Handbook of Physical Constants*, Vol. 1, ed. T. J. Ahrens. AGU Reference Shelf, pp. 159–89.

Newsom, H. E. and Sims, K. W. W. (1991). Core formation during early accretion of the Earth. *Science*, **252**, 926–33.

Newsom, H. E. and Taylor, S. R. (1989). Geochemical implications of the formation of the Moon by a single giant impact. *Nature*, **338**, 29–34.

Nicolet, M. (1957). The aeronomic problem of helium. *Ann. Geophys.*, **13**, 1–21.

Niida, K. and Green, D. H. (1999). Stability and chemical composition of pargasitic amphibole in MORB pyrolite under upper mantle conditions. *Contrib. Mineral Petrol*, **135**, 18–40.

Nittler, L. R. (1997). Presolar oxide grains in meteorites. In *Astrophysical Implications of the Laboratory Study of Presolar Materials*, eds. T. I. Bernatowicz and E. Zinner. New York: Amer. Inst. Phys., pp. 59–81.

Nittler, L. R., Alexander, C. M. O., Gao, X., Walker, R. M. and Zinner, E. (1994). Interstellar oxide grains from the Tieschitz ordinary chondrite. *Nature*, **370**, 443–6.
Nolet, G., Karato, S.-I. and Montelli, R. (2006). Plume fluxes from seismic tomography. *Earth Planet. Sci. Lett.*, **248**, 685–99.
Norman, M. D., Borg, L. E., Nyquist, L. E. and Bogard, D. D. (2003). Chronology, geochemistry, and petrology of a ferroan noritic anorthosite clast from Descartes breccia 67215: clues to the age, origin, structure, and impact history of the lunar crust. *Meteorit. Planet. Sci.*, **38**, 645–61.
Norman, M. D., Yaxley, G. M., Bennett, V. C. and Brandon, A. D. (2006). Magnesium isotopic composition of olivine from the Earth, Mars, Moon, and pallasite parent body. *Geophys. Res. Lett.*, **33**, L15202 doi:10.1029/2006GL026446.
Nutman, A. P., Bennett, V. C., Friend, C. R. L. and Rosing, M. T. (1997). 3710 and 3790 Myr volcanic sequences in the Isua (Greenland) supracrustal belt; structural and Nd isotope implications. *Chem. Geol.*, **141**, 271–87.
Ohtani, E., Yurimoto, H. and Seto, S. (1997). Element partitioning between metallic liquid, silicate liquid, and lower-mantle minerals: implications for core formation of the Earth. *Phys. Earth Planet. Inter.*, **100**, 97–114.
Okuchi, T. (1997). Hydrogen partitioning into molten iron at high pressure: implications for Earth's core. *Science*, **278**, 1781–4.
Olsen, E. J. and Bunch, T. E. (1984). Equilibration temperatures of the ordinary chondrites; a new evaluation. *Geochim. Cosmochim. Acta*, **48**, 1363–5.
Olsen, E. J., Mayeda, T. K. and Clayton, R. N. (1981). Cristobalite-pyroxene in an L6 chondrite – implication for metamorphism. *Earth Planet. Sci. Lett.*, **56**, 82–8.
O'Neil, J. R. (1986). Theoretical and experimental aspects of isotopic fractionation. In *Reviews in Mineralogy,* Vol. 16, *Stable Isotopes*, ed. P. Ribbe. New York: Mineral. Soc. Amer., pp. 1–40.
O'Neill, H. S. (1991a). The origin of the Moon and the early history of the Earth – a chemical model. Part 1: the Moon. *Geochim. Cosmochim. Acta*, **55**, 1135–57.
O'Neill, H. S. (1991b). The origin of the Moon and the early history of the Earth – a chemical model. Part 2: the Earth. *Geochim. Cosmochim. Acta*, **55**, 1159–72.
O'Neill, H. S., Canil, D. and Rubie, D. C. (1998). Oxide-metal equilibria to 2500 degrees C and 25 GPa: implications for core formation and the light component in the Earth's core. *J. Geophys. Res. – Solid Earth*, **103**, 12, 239–60.
O'Nions, R. K. and McKenzie, D. (1993). Estimates of mantle thorium/uranium ratios from Th, U and Pb isotope abundances in basaltic melts. *Phil. Trans. Roy. Soc. London A*, **342**, 65–77.
O'Nions, R. K. and Oxburgh, E. R. (1983). Heat and helium in the Earth. *Nature*, **306**, 429–32.
O'Nions, R. K., Evensen, N. M. and Hamilton, P. J. (1979). Geochemical modelling of mantle differentiation and crustal growth. *J. Geophys. Res.*, **84**, 6091–101.
Ott, U. (1996). Interstellar diamond xenon and timescales of supernova ejecta. *Astrophys. J.*, **463**, 344–8.
Ott, U. (2002). Noble gases in meteorites – trapped components. In *Noble Gases in Geochemistry and Cosmochemistry*, Vol. 47, eds. D. Porcelli, C. J. Ballentine and R. Wieler. Washington DC: Mineral. Soc. Amer., pp. 71–100.
Ott, U. (2003). Isotopes of volatiles in pre-solar grains. *Space Sci. Rev.*, **106**, 33–48.
Ott, U., Kronenbitter, J., Flores, J. and Chang, S. (1984). Colloidally separated samples from Allende residues: noble gases, carbon and an ESCA study. *Geochim. Cosmochim. Acta*, **48**, 267–80.
Owen, C. and Bar-Nun, A. (2001). Contributions of icy planetesimals to the earth's early atmosphere. *Origins of Life and Evolution of the Biosphere*, **31**, 435–58.

Owen, T. and Encrenaz, T. (2003). Element abundances and isotope ratios in the giant planets and Titan. *Space Sci. Rev.*, **106**, 121–38.
Ozima, M. and Podosek, F. A. (2002). *Noble Gas Geochemistry*. Cambridge, UK: Cambridge University Press, pp. 286.
Ozima, M., Wieler, R., Marty, B. and Podosek, F. A. (1998). Comparative studies of solar, Q-gases and terrestrial noble gases, and implications on the evolution of the solar nebula. *Geochim. Cosmochim. Acta*, **62**, 301–14.
Ozima, M., Podosek, F. A., Higuchi, T., Yin, Q.-Z. and Yamada, A. (2007). On the mean oxygen isotope composition of the Solar System. *Icarus*, **186**, 562–70.
Pagel, B. E. J. (1994). Chemical evidence on galaxy formation and evolution. In *The Formation and Evolution of Galaxies*, eds. C. Munoz-Tunon and F. Sanchez. Cambridge, UK: Cambridge University Press, pp. 149–230.
Pagel, B. E. J. (2001). Chemical evolution of galaxies. *Publ. Astronom. Soc. Pacific*, **113**, 137–41.
Palme, H. (2000). Are there chemical gradients in the inner solar system? In *From Dust to Terrestrial Planets*, eds. W. Benz, R. Kallenbach and G. W. Lugmair. Dordrecht: Kluwer, pp. 237–62.
Palme, H. and Jones, A. P. (2003). Solar system abundances of the elements. In *Meteorites, Comets, and Planets*, Vol. 1, ed. A. M. Davis. Amsterdam: Elsevier-Pergamon, pp. 41–61.
Palme, H. and Nickel, K. G. (1985). Ca/Al ratio and composition of the Earth's upper mantle. *Geochim. Cosmochim. Acta*, **49**, 2123–32.
Palme, H. and O'Neill, H. S. C. (2003). Cosmochemical estimates of mantle composition. In *The Mantle and Core*, Vol. 2, ed. R. W. Carlson. Amsterdam: Elsevier-Pergamon, pp. 1–38.
Palmer, M. R. and Edmond, J. M. (1989). The strontium isotope budget of the modern ocean. *Earth Planet. Sci. Lett.*, **92**, 11–26.
Papanastassiou, D. A. and Wasserburg, G. J. (1969). Initial strontium isotopic abundances and the resolution of small time differences in formation of planetary objects. *Earth Planet. Sci. Lett.*, **5**, 361–76.
Parada, M. A., Nyström, J. O. and Levi, B. (1999). Multiple sources for the Coastal Batholith of central Chile (31–34 °S): geochemical and Sr–Nd isotopic evidence and tectonic implications. *Lithos*, **46**, 505–21.
Patchett, P. J., White, W. M., Feldmann, H., Kielinczuk, S. and Hofmann, A. W. (1984). Hafnium/rare earth element fractionation in the sedimentary system and crustal recycling into the Earth's mantle. *Earth Planet. Sci. Lett.*, **69**, 365–78.
Patchett, P. J., Vervoort, J. D., Soderlund, U. and Salters, V. J. M. (2004). Lu–Hf and Sm–Nd isotopic systematics in chondrites and their constraints on the Lu–Hf properties of the Earth. *Earth Planet. Sci. Lett.*, **222**, 29–41.
Patino, D. A. E. and Harris, N. (1998). Experimental constraints on Himalayan anatexis. *J. Petrol.*, **39**, 689–710.
Pattison, D. R. M. and Newton, R. C. (1989). Reversed experimental calibration of the garnet-clinopyroxene Fe–Mg exchange thermometer. *Contrib. Mineral. Petrol.*, **101**, 87–103.
Pavlov, A. and Kasting, J. F. (2002). Mass-independent fractionation of sulfur isotopes in Archean sediments: strong evidence for an anoxic Archean atmosphere. *Astrobiology*, **2**, 27–41.
Pavlov, A. K. and Pavlov, A. A. (1997–1998). Atmospheric losses under dust bombardment in the ancient atmospheres. *Earth, Moon and Planets*, **76**, 157–83.

Peacock, J. A. (1999). *Cosmological Physics*. Cambridge, UK: Cambridge University Press, pp. 682.

Peacock, S. M., van Keken, P. E., Holloway, S. D., Hacker, B. R., Abers, G. A. and Fergason, R. L. (2005). Thermal structure of the Costa Rica–Nicaragua subduction zone. *Phys. Earth Planet. Inter.*, **149**, 187–200.

Pearson, D. G., Canil, D. and Shirey, S. B. (2003). Mantle samples included in volcanic rocks: xenoliths and diamonds. In *The Mantle and Core*, Vol. 2, ed. R. W. Carlson. Cambridge, UK: Elsevier-Pergamon, pp. 171–275.

Peck, W. H., Valley, J. W., Wilde, S. A. and Grahams, C. M. (2001). Oxygen isotope ratios and rare earth elements in 3.3 to 4.4 Ga zircons: ion microprobe evidence for high δ^{18}O continental crust and oceans in the Early Archean. *Geochim. Cosmochim. Acta*, **65**, 4215–29.

Pedroni, A. and Begemann, F. (1994). On unfractionated solar gases in the H3-6 meteorite Acfer 111. *Meteoritics*, **29**, 632–42.

Penzias, A. A. and Wilson, R. W. (1965). A measurement of excess antenna temperature at 4080 mc/S. *Astrophys. J.*, **142**, 419.

Pepin, R. O. (1991). On the origin and early evolution of terrestrial planet atmospheres and meteoritic volatiles. *Icarus*, **92**, 1–79.

Pepin, R. O. (1992). Origin of noble-gases in the terrestrial planets. *Ann. Rev. Earth Planet. Sci.*, **20**, 389–430.

Pepin, R. O. (1994). Evolution of the Martian atmosphere. *Icarus*, **111**, 289–304.

Pepin, R. O. and Phinney, D. (1978). Components of xenon in the Solar System. Unpublished preprint, Minneapolis, Minnesota: University of Minnesota, pp. 176.

Pepin, R. O. and Porcelli, D. (2002). Origin of noble gases in the terrestrial planets. In *Noble Gases in Geochemistry and Cosmochemistry*, Vol. 47, eds. D. Porcelli, C. J. Ballentine and R. Wieler. Washington DC: Mineral. Soc. Amer., pp. 191–246.

Pepin, R. O. and Porcelli, D. (2006). Xenon isotope systematics, giant impacts, and mantle degassing on the early Earth. *Earth Planet. Sci. Lett.*, **250**, 470–85.

Petaev, M. I. and Wood, J. A. (1998). The condensation with partial isolation (CWPI) model of condensation in the solar nebula. *Meteorit. Planet. Sci.*, **33**, 1123–37.

Pettini, M. and Bowen, D. V. (2001). A new measurement of the primordial abundance of deuterium: toward convergence with the baryon density from the cosmic microwave background? *Astrophys. J.*, **560**, 41–8.

Pfeiffer, B., Ott, U. and Kratz, K.-L. (2001). Stellar and nuclear-physics constraints on two r-process components in the early Galaxy. *Nucl. Phys.*, **A688**, 575c-7.

Phinney, D., Tennyson, J. and Frick, U. (1978). Xenon in CO_2 well gas revisited. *J. Geophys. Res.*, **83** (B5), 2313–19.

Pinto, P. A., Eastman, R. G. and Rogers, T. (2001). A test for the nature of the Type Ia Supernova explosion mechanism. *Astrophys. J.*, **551**, 231–43.

Plank, T. and Langmuir, C. H. (1993). Tracing trace elements from sediment input to volcanic output at subduction zones. *Nature*, **362**, 739–42.

Plank, T. and Langmuir, C. H. (1998). The chemical composition of subducting sediment and its consequences for the crust and mantle. *Chem. Geol.*, **145**, 325–94.

Podosek, F. A. (1970). Dating of meteorites by high-temperature release of iodine-correlated ^{129}Xe. *Geochim. Cosmochim. Acta*, **34**, 341–65.

Podosek, F. A. and Cassen, P. (1994). Theoretical, observational, and isotopic estimates on the lifetime of the solar nebula. *Meteoritics*, **29**, 6–25.

Poirier, J. P. (1994). Light elements in the earth's outer core – a critical review. *Phys. Earth Planet. Inter.*, **85**, 319–37.

Pollack, H. N., Hurter, S. J. and Johnston, R. (1993). Heat loss from the earth's interior: analysis of the global data set. *Rev. Geophys.*, **31**, 267–80.

Polyak, B. G. and Tolstikhin, I. N. (1985). Isotope composition of Earth's helium and the problem of the motive forces of tectogenesis. *Chem. Geol.*, **52**, 9–33.

Polyak, B. G., Prasolov, E. M., Buachidze, G. I., Kononov, V. I., Mamyrin, B. A., Surovtseva, L. I., Khabarin, L. V. and Yudenich, V. S. (1979). He and Ar isotopic compositions in the fluids of Alp–Appenine region and their connection with volcanism. *Dokl. Acad. Nauk USSR*, **247**, 1220–6.

Porcelli, D. and Ballentine, C. J. (2002). Models for distribution of terrestrial noble gases and evolution of the atmosphere. In *Noble Gases in Geochemistry and Cosmochemistry*, Vol. 47, eds. D. Porcelli, C. J. Ballentine and R. Wieler. Washington DC: Mineral. Soc. Amer., pp. 411–80.

Porcelli, D. and Halliday, A. N. (2001). The core as a possible source of mantle helium. *Earth Planet. Sci. Lett.*, **192**, 45–56.

Premo, W. R., Tatsumoto, M., Misawa, K., Nakamura, N. and Kita, N. I. (1999). Pb-isotopic systematics of lunar highland rocks (> 3.9 Ga): constraints on early lunar evolution. *Int. Geol. Rev.*, **41**, 95–128.

Pritchard, M. E. and Stevenson, D. J. (2000). Thermal aspects of a lunar origin by giant impact. In *Origin of the Earth and Moon*, eds. R. M. Canup and K. Righter. Tucson, AZ: University of Arizona Press, pp. 179–96.

Pudovkin, M. I., Tolstikhin, I. N. and Golovchanskaya, I. V. (1981). Recent achievements in helium isotope dissipation research. *Geochim. J.*, **15**, 51–61.

Puster, P. and Jordan, T. H. (1997). How stratified is mantle convection? *J. Geophys. Res. – Solid Earth*, **102**, 7625–46.

Pyle, J. M. and Spear, F. S. (2000). An empirical garnet (YAG) – xenotime thermometer. *Contrib. Mineral. Petrol.*, **138**, 51–8.

Qian, Y.-Z. (2002). Neutrino-induced fission and r-process nucleosynthesis. *Astrophys. J.*, **569**, L103–6.

Qian, Y.-Z. and Wasserburg, G. J. (2003). Stellar sources for heavy r-process nuclei. *Astrophys. J.*, **588**, 1099–109.

Qian, Y. Z., Vogel, P. and Wasserburg, G. J. (1999). Neutrino fluence after r-process freezeout and abundances of Te isotopes in presolar diamonds. *Astrophys. J.*, **513**, 956–60.

Quitté, G., Birck, J. L. and Allègre, C. J. (2000). ^{182}Hf–^{182}W systematics in eucrites: the puzzle of iron segregation in the early solar system. *Earth Planet. Sci. Lett.*, **184**, 83–94.

Ragnarsson, S.-I. (1995). Planetary distances: a new simplified model. *Astron. Astrophys.*, **301**, 609–12.

Raheim, A. and Green, D. H. (1974). Experimental determination of temperature and pressure-dependence of Fe–Mg partition coefficient for coexisting garnet and clinopyroxene. *Contrib. Mineral. Petrol.*, **48**, 179–203.

Rankenburg, K., Brandon, A. D. and Neal, C. R. (2006). Neodymium isotope evidence for a chondritic composition of the Moon. *Science*, **312**, 1369–72.

Rea, D. K. and Ruff, L. J. (1996). Composition and mass flux of sediment entering the world's subduction zones: implications for global sediment budgets, great earthquakes, and volcanism. *Earth Planet. Sci. Lett.*, **140**, 1–12.

Reagan, M. K., Morris, J. D., Herrstrom, E. A. and Murrell, M. T. (1994). Uranium series and beryllium isotope evidence for an extended history of subduction modification of the mantle below Nicaragua. *Geochim. Cosmochim. Acta*, **58**, 4199–212.

Reddy, B. E., Tomkin, J., Lambert, D. L. and Allende, P. C. (2003). The chemical compositions of Galactic disc F and G dwarfs. *Mon. Not. Roy. Astron. Soc.*, **340**, 304–40.

Reeves, H. (1998). Concluding remarks. In *Primordial Nuclei and their Galactic Evolution*, eds. N. Prantzos, M. Tosi and R. von Steiger. Dordrecht: Kluwer, pp. 319–24.

Reifarth, R., Arlandini, C., Heil, M., Kappler, F., Sedyshev, P., Mengoni. A., Herman, M., Rauscher, T., Gallino, R. and Travaglio, C. (2003). Stellar neutron capture on Promethium: implications for the s-process neutron density. *Astrophys. J.*, **582**, 1251–62.

Richter, S., Ott, U. and Begemann, F. (1998). Tellurium in pre-solar diamonds as an indicator for rapid separation of supernova ejecta. *Nature*, **391**, 261–3.

Righter, K. (2002). Does the Moon have a metallic core? Constraints from giant impact modeling and siderophile elements. *Icarus*, **158**, 1–13.

Righter, K. and Drake, M. J. (1996). Core formation in Earth's Moon, Mars and Vesta. *Icarus*, **124**, 513–29.

Righter, K. and Drake, M. J. (1997). A magma ocean on Vesta: core formation and petrogenesis of eucrites and diogenites. *Meteorit. Planet. Sci.*, **32**, 929–44.

Righter, K. and Drake, M. J. (1999). Effect of water on metal–silicate partitioning of siderophile elements: a high pressure and temperature terrestrial magma ocean and core formation. *Earth Planet. Sci. Lett.*, **171**, 383–99.

Righter, K. and Drake, M. J. (2000). Metal–silicate equilibrium in the early Earth – new constraints from the volatile moderately siderophile elements Ga, Cu, P, and Sn. *Geochim. Cosmochim. Acta*, **64**, 3581–97.

Righter, K., Drake, M. J. and Yaxley, G. (1997). Prediction of siderophile element metal–silicate partition coefficients to 20 GPa and 2800 °C: the effects of pressure, temperature, oxygen fugacity, and silicate and metallic melt compositions. *Phys. Earth Planet. Inter.*, **100**, 115–34.

Ringwood, A. E. (1975). *Composition and Petrology of the Earth's Mantle*. New York: McGraw-Hill, pp. 618.

Ringwood, A. E. (1979). *Origin of the Earth and Moon*. New York: Springer-Verlag, pp. 295.

Ringwood, A. E. (1984). The earth's core: its composition, formation and bearing upon the origin of the earth. *Proc. Roy. Soc. Lond.*, **A395**, 1–46.

Ringwood, A. E. (1990). Earliest history of the Earth–Moon system. In *Origin of the Earth*, eds. H. E. Newsom and J. H. Jones. Oxford, UK: Oxford University Press, pp. 101–34.

Robert, F. (2001). The origin of water on Earth. *Science*, **293**, 1056–8.

Robert, F. (2003). The D/H ratio in chondrites. *Space Sci. Rev.*, **106**, 87–101.

Robert, F., Gautier, D. and Dubrulle, B. (2000). The solar system D/H ratio: observations and theories. In *From Dust to Terrestrial Planets*, eds. W. Benz, R. Kallenbach and G. W. Lugmair. Dordrecht: Kluwer, pp. 201–24.

Rocholl, A. and Jochum, K. P. (1993). Th, U and other trace-elements in carbonaceous chondrites: implications for the terrestrial and solar-system Th/U ratios. *Earth Planet. Sci. Lett.*, **117**, 265–78.

Ronov, A. B. (1982). The Earth's sedimentary shell (quantitative patterns of its structure, compositions, and evolution). *Int. Geol. Rev.*, **24**, 1313–88.

Ronov, A. B. and Yaroshevsky, A. A. (1976). A new model of chemical composition of the Earth crust. *Geochimiya*, **12**, 1763–96.

Rood, R. T., Bania, T. M., Balser, D. S. and Wilson, T. L. (1998). Helium-3: status and prospects. In *Primordial Nuclei and their Galactic Evolution*, eds. N. Prantzos, M. Tosi and R. von Steiger. Dordrecht: Kluwer, pp. 185–98.

Rouxel, O. J., Bekker, A. and Edwards, K. J. (2005). Iron isotope constraints on the Archean and Paleoproterozoic ocean redox state. *Science*, **307**, 1088–91.

Rubin, A. E. (1995). Petrologic evidence for collisional heating of chondritic asteroids. *Icarus*, **113**, 156–67.

Rubin, A. E. (1997). Mineralogy of meteorite groups. *Meteorit. Planet. Sci.*, **32**, 231–47.

Rubin, A. E. (2000). Petrologic, geochemical and experimental constraints on models of chondrule formation. *Earth Sci. Rev.*, **50**, 3–27.

Rubin, A. M. and Krot, A. N. (1996). Multiple heating of chondrules. In *Chondrules and the Protoplanetary Disk*, eds. R. H. Hewins, R. H. Jones and E. R. D. Scott. Cambridge, UK: Cambridge University Press, pp. 173–80.

Rubin, K. H., van der Zander, I., Smith, M. C. and Bergmanis, E. C. (2005). Minimum speed limit for ocean ridge magmatism from ^{210}Pb–^{226}Ra–^{230}Th disequilibria. *Nature*, **437**, 534–8.

Rudnick, R. L. (1992). Restites, Eu anomalies, and the lower continental crust. *Geochim. Cosmochim. Acta*, **56**, 963–70.

Rudnick, R. and Fountain, D. M. (1995). Nature and composition of the continental crust: a lower crustal perspective. *Rev. Geophys.*, **33**, 267–309.

Rudnick, R. L. and Gao, S. (2003). Composition of the continental crust. In *The Crust*, Vol. 3, ed. R. L. Rudnick. Amsterdam: Elsevier-Pergamon, pp. 1–64.

Rudnick, R. and Goldstein, S. L. (1990). The Pb isotopic composition of lower crustal xenoliths and the evolution of lower crustal Pb. *Earth Planet. Sci. Lett.*, **98**, 192–207.

Rudnick, R. L. and Presper, T. (1990). Geochemistry of intermediate- to high-pressure granulites. In *Granulites and Crustal Evolution*, eds. D. Vielzeuf and P. Vidal. Dordrecht: Kluwer, pp. 523–50.

Rudnick, R. and Taylor, S. R. (1987). The composition and petrogenesis of lower crust: a xenolith study. *J. Geophys. Res.*, **92**, 13 981–14 005.

Rudnick, R. L., Barth, M., Horn, I. and McDonough, W. F. (2000). Rutile-bearing refractory eclogites: missing link between continents and depleted mantle. *Science*, **287**, 278–81.

Russell, S. S., Srinivasan, G., Huss, G. R., Wasserburg, G. J. and MacPherson, G. J. (1996). Evidence for widespread ^{26}Al in the solar nebula and constraints for nebula time scales. *Science*, **273**, 757–62.

Russell, S. S., Huss, G. R., Fahey, A. J., Greenwood, R. C., Hutchison, R. and Wasserburg, G. J. (1998). An isotopic and petrologic study of calcium–aluminum-rich inclusions from CO3 meteorites. *Geochim. Cosmochim. Acta*, **62**, 689–714.

Ruzicka, A., Snyder, G. A. and Taylor, L. A. (2001). Comparative geochemistry of basalts from the Moon, Earth, HED asteroid, and Mars: implications for the origin of the Moon. *Geochim. Cosmochim. Acta*, **65**, 979–97.

Rydgren, A. E. and Cohen, M. (1985). Young stellar objects and their circumstellar dust: an overview. In *Protostars and Planets II*, eds. D. C. Black and M. S. Matthews. Tucson, AZ: University of Arizona Press, pp. 371–85.

Saal, A. E., Hart, S. R., Shimizu, N., Hauri, E. H., Layne, G. D. and Eiler, J. M. (2005). Pb isotopic variability in melt inclusions from the EMI–EMII–HIMU mantle end-members and the role of the oceanic lithosphere. *Earth Planet. Sci. Lett.*, **240**, 605–20.

Safronov, V. S. (1966). Sizes of largest bodies falling onto the planets during their formation. *Sov. Astronomy*, **9**, 987–91.

Safronov, V. S. (1969). Evolution of the protoplanetary cloud and formation of the earth and planets. NASA Technical publication TT F-667.
Sageman, B. B. and Lyons, T. W. (2003). Geochemistry of fine-grained sediments and sedimentary rocks. In *Sediments, Diagenesis and Sedimentary Rocks*, Vol. 7, ed. F. T. Mackenzie. Amsterdam: Elsevier-Pergamon, pp. 116–58.
Sahijpal, S., Goswami, J. N., Davis, A. M., Grossman, L. and Lewis, R. S. (1998). A stellar origin for the short-lived nuclides in the early Solar system. *Nature*, **391**, 559–61.
Salaris, M., degl'Innocenti, S. and Weiss, A. (1997). The age of the oldest globular clusters. *Astrophys. J.*, **479**, 665–72.
Salerno, E., Buhler, F., Bochsler, P. *et al*. (2001). Direct measurement of ^{3}He/^{4}He in the LISM with the COLLISA experiment. In *Solar and Galactic Composition*, ed. R. F. Wimmer-Schweingruber. New York: Amer. Inst. Phys., pp. 275–80.
Salters, L., McKenzie, D., Grönvold, K. and Shimizu, N. (2001). Melt generation and movement beneath Theistareykir, NE Iceland. *J. Petrol.*, **42**, 321–54.
Salters, V. J. M. and Stracke, A. (2004). Composition of the depleted mantle. *Geochem. Geophys. Geosyst*., **5**, 1–27, doi:10.1029/2003GC000597.
Samuel, H. and Farnetani, C. G. (2003). Thermochemical convection and helium concentrations in mantle plumes. *Earth Planet. Sci. Lett.*, **207**, 39–56.
Sano, Y. and Williams, S. N. (1996). Fluxes of mantle and subducted carbon along convergent plate boundaries. *Geophys. Res. Lett.*, **23**, 2749–52.
Schatz, H., Aprahamian, A., Barnard, V. *et al*. (2001). End point of the rp-process on accreting neutron stars. *Phys. Rev.*, **86**, 3471–4.
Schatz, H., Toenjes, R., Pfeiffer, B. *et al*. (2002). Thorium and uranium chronometers applied to CS 31082–001. *Astrophys. J.*, **579**, 626–38.
Schmidt, B. C. and Keppler, H. (2002). Experimental evidence for high noble gas solubilities in silicate melts under mantle pressures. *Earth Planet. Sci. Lett.*, **195**, 277–90.
Schmidt, M. (1959). The rate of star formation. *Astrophys. J.*, **129**, 243–58.
Schmidt, M. W. and Poli, S. (2003). Generation of mobile components during subduction of oceanic crust. In *The Crust*, Vol. 3, ed. R. L. Rudnick. Amsterdam: Elsevier-Pergamon, pp. 567–91.
Schmidt, M. W., Vielzeuf, D. and Auzanneaub, E. (2004). Melting and dissolution of subducting crust at high pressures: the key role of white mica. *Earth Planet. Sci. Lett.*, **228**, 65–84.
Schmitt, W., Palme, H. and Wänke, H. (1989). Experimental determination of metal–silicate partition coefficients for P, Co, Ni, Cu, Ga, Ge, Mo and W and some implications for the early evolution of the Earth. *Geochim. Cosmochim. Acta*, **53**, 173–85.
Schneider, R. (2006). Constraining the epoch of very massive star formation. *New Astron. Rev.*, **50**, 64–9.
Schodel, R., Ott, T., Genzel, R. *et al*. (2002). A star in a 15.2-year orbit around the supermassive black hole at the centre of the Milky Way. *Nature*, **419**, 694–6.
Schoenberg, R., Kamber, B. S., Collerson, K. D. and Moorbath, S. (2002). Tungsten isotope evidence from ~3.8-Gyr metamorphosed sediments for early meteorite bombardment of the Earth. *Nature*, **418**, 403–5.
Schramm, D. N. and Turner, M. S. (1998). Big-bang nucleosynthesis enters the precision era. *Rev. Mod. Phys.*, **70**, 303–18.
Scott, E. R. D. (1972). Chemical fractionation in iron meteorites and its interpretation. *Geochim. Cosmochim. Acta*, **36**, 1205–36.

Scott, E. R. D. and Krot, A. N. (2005). Thermal processing of silicate dust in the solar nebula: clues from primitive chondrite matrices. *Astrophys. J.*, **623**, 571–8.

Sears, D. W. G., Lu, J., Benoit, P. H., DeHart, J. M. and Lofgren, G. E. (1992). A compositional classification scheme for meteoritic chondrules. *Nature*, **357**, 207–10.

Sears, D. W. G., Huang, S. and Benoit, P. H. (1996). Open-system behaviour during chondrule formation. In *Chondrules and the Protoplanetary Disk*, eds. R. H. Hewins, R. H. Jones and E. R. D. Scott. Cambridge, UK: Cambridge University Press, pp. 221–31.

Sedlmayr, E. and Kruger, D. (1997). Formation of dust particles in cool stellar outflows. In *Astrophysical Implications of the Laboratory Study of Presolar Materials*, eds. T. I. Bernatowicz and E. Zinner. New York: Amer. Inst. of Physics, pp. 425–50.

Shang, H., Shu, F. H., Lee, T. and Glassgold, A. E. (2000). Protostellar winds and chondritic meteorites. In *From Dust to Terrestrial Planets*, eds. W. Benz, R. Kallenbach and G. W. Lugmair. Dordrecht: Kluwer, pp. 153–76.

Shaw, D. M. (1970). Trace element fractionation during anatexis. *Geochim. Cosmochim. Acta*, **34**, 237–43.

Shearer, C. K. and Floss, C. (2000). Evolution of the moon's mantle and crust as reflected in trace-elements microbeam studies of lunar magmatism. In *Origin of the Earth and Moon*, eds. R. M. Canup and K. Righter. Tucson, AZ: University of Arizona Press, pp. 339–59.

Shearer, C. K. and Papike, J. J. (2005). Early crustal building processes on the Moon: models for the petrogenesis of the magnesium suite. *Geochim. Cosmochim. Acta*, **69**, 3445–61.

Shimizu, N. (1998). The geochemistry of olivine-hosted melt inclusions in a FAMOUS basalt ALV519-4-1. *Phys. Earth Planet. Inter.*, **107**, 183–201.

Shklovsky, I. S. (1977). *Stars, their Birth, Life and Death*. Moscow, USSR: Nauka, pp. 384.

Shu, F. H., Adams, F. C. and Lizano, S. (1987). Star formation in molecular clouds – observation and theory. *Ann. Rev. Astron. Astrophys*., **25**, 23–72.

Shu, F. H., Shang, H., Gounelle, M., Glassgold, A. E. and Lee, T. (2001). The origin of chondrules and refractory inclusions in chondritic meteorites. *Astrophys. J.*, **548**, 1029–50.

Shukolyukov, A. and Lugmair, G. W. (2006). Manganese–chromium isotope systematics of carbonaceous chondrites. *Earth Planet. Sci. Lett.*, **250**, 200–13.

Siebert, C., Nägler, T. F., von Blanckenburg and F. Kramers, J. D. (2003). Molybdenum isotope records as a potential new proxy for paleoceanography. *Earth Planet. Sci. Lett.*, **211**, 159–71.

Siebert, C., Kramers, J. D., Meisel, T., Morel, P. and Nägler, T. F. (2005). PGE, Re–Os, and Mo isotope systematics in Archean and early Proterozoic sedimentary systems as proxies for redox conditions of the early Earth. *Geochim. Cosmochim. Acta*, **69**, 1787–801.

Siebert, C., McManus, J., Bice, A., Poulson, R. and Berelson, W. M. (2006). Molybdenum isotope signatures in continental margin marine sediments. *Earth Planet. Sci. Lett.*, **241**, 723–33.

Sigmarsson, O., Chmeleff, J., Morris, J. and Lopez-Escobar, L. (2002). Origin of ^{226}Ra–^{230}Th disequilibria in arc lavas from southern Chile and implications for magma transfer time. *Earth Planet. Sci. Lett.*, **196**, 189–96.

Silk, J. (1980) *The Big Bang (The Creation and Evolution of the Universe)*. San Francisco, CA: Freeman and Co., pp. 391.

Silk, J. and Bouwens, R. (2001). The formation of galaxies. *New Astron. Rev.*, **45**, 337–50.

Simmons, N., Forte, A. and Grand, S. P. (2006). Constraining mantle flow with seismic and geodynamic data: a joint approach. *Earth Planet. Sci. Lett.*, **246**, 109–24.

Simon, S. B., Grossman, L. and Davis, A. M. (1997). Multiple generation of hibonite in spinel–hibonite inclusions from Murchison. *Meteorit. Planet. Sci.*, **32**, 259–69.

Simon, S. B., Grossman, L., Krot, A. N. and Ulyanov, A. A. (2002). Bulk chemical compositions of type B refractory inclusions. In *Proc. Lunar Planet. Sci. Conf.*, Vol. 33, 1620.pdf.

Sims, K. W. W., DePaolo, D. J., Murrell, M. T. *et al*. (1999). Porosity of the melting zone and variations in the solid mantle upwelling rate beneath Hawaii: inferences from ^{238}U–^{230}Th–^{226}Ra and ^{235}U–^{231}Pa disequilibria. *Geochim. Cosmochim. Acta*, **63**, 4119–38.

Sims, K. W. W., Goldstein, S. J., Blichert-Toft, J. *et al*. (2002). Chemical and isotopic constraints on the generation and transport of magma beneath the East Pacific Rise. *Geochim. Cosmochim. Acta*, **66**, 3481–504.

Sinha, A. K. and Tilton, G. R. (1973). Isotopic composition of common lead. *Geochim. Cosmochim. Acta*, **37**, 1823–49.

Slater, L., McKenzie, D., Gronvold, K. and Shimizu, N. (2001). Melt generation and movement beneath Theistareykir, NE Iceland. *J. Petrol.*, **42**, 321–54.

Smithies, R. H., Champion, D. C. and Cassidy, K. F. (2003). Formation of Earth's early Archaean continental crust. *Precambrian Res.*, **127**, 89–101.

Smithies, R. H., Champion, D. C., Van Kranendonk, M. J., Howard, H. M. and Hickman, A. H. (2005). Modern-style subduction processes in the Mesoarchaean: geochemical evidence from the 3.12 Gyr Whundo intra-oceanic arc. *Earth Planet. Sci. Lett.*, **231**, 231–7.

Smoliar, M. I. (1993). A survey of Rb–Sr systematics of eucrites. *Meteoritics*, **28**, 105–13.

Snyder, G. A., Taylor, L. A. and Halliday, A. N. (1995). Processes involved in the formation of magnesium-suite plutonic rocks from the highlands of the Earth's moon. *J. Geophys. Res.*, **100**, 9365–88.

Snyder, G. A., Borg, L. E., Nyquist, L. E. and Taylor, L. A. (2000). Chronology and isotopic constraints on lunar evolution. In *Origin of the Earth and Moon*, eds. R. M. Canup and K. Righter. Tucson, AZ: University of Arizona Press, pp. 361–95.

Sobolev, A. V. (1996). Melt inclusions in minerals as a source of principal petrological information. *Petrology*, **4**, 209–20.

Sobolev, A. V. and Chaussidon, M. (1996). H_2O concentrations in primary melts from supra-subduction zones and mid-ocean ridges: implications for H_2O storage and recycling in the mantle. *Earth Planet. Sci. Lett.*, **137**, 45–55.

Sobolev, A. V. and Shimizu, N. (1993). Ultra-depleted primary melt included in an olivine from the Mid-Atlantic Ridge. *Nature*, **363**, 151–4.

Sollerman, J. (2002). Optical and infrared observations of radioactive elements in supernovae. *New Astron. Rev.*, **46**, 493–8.

Solomatov, V. S. (2000). Fluid dynamics of a terrestrial magma ocean. In *Origin of the Earth and Moon*, eds. R. M. Canup and K. Righter. Tucson, AZ: University of Arizona Press, pp. 323–38.

Solomatov, V. S. and Stevenson, D. J. (1993a). Suspension in convective layers and style of differentiation of a terrestrial magma ocean. *J. Geophys. Res.*, **98** (E3), 5375–90.

Solomatov, V. S. and Stevenson, D. J. (1993b). Kinetics of crystal growth in a terrestrial magma ocean. *J. Geophys. Res.*, **98** (E3), 5407–18.

Spergel, D. N., Verde, L., Peiris, H. V. *et al*. (2003). First-year Wilkinson microwave anisotropy probe (WMAP) observations: determination of cosmological parameters. *Astrophys. J.*, **148**, 175–94.

Spicuzza, M. J., Day, J. M. D., Taylor, L. A. and Valley, J. W. (2007). Oxygen isotope constraints on the origin and differentiation of the Moon. *Earth Planet. Sci. Lett.*, **253**, 254–65.

Spiegelman, M. and Elliott, T. (1993). Consequences of melt transport for uranium series disequilibrium in young lavas. *Earth Planet. Sci. Lett.*, **118**, 1–20.

Srinivasan, G. and Bischoff, A. (2001). Ca–K and Al–Mg studies of CAIs from CH and CR chondrites. *Meteorit. Planet. Sci.*, **36**, A196.

Srinivasan, G., Sahijpal, S., Ulyanov, A. A. and Goswami, J. N. (1996). Ion microprobe studies of Efremovka CAIs: II. Potassium isotope composition and ^{41}Ca in the early Solar System. *Geochim. Cosmochim. Acta*, **60**, 1823–35.

Stachel, T., Aulbach, S., Brey, G. P. *et al*. (2004). The trace element composition of silicate inclusions in diamonds: a review. *Lithos*, **77**, 1–19.

Staudigel, H. (2003). Hydrothermal alteration processes in the oceanic crust. In *The Crust*, Vol. 3, ed. R. L. Rudnick. Amsterdam: Elsevier-Pergamon, pp. 511–35.

Steinberger, B. and O'Connell, R. J. (1998). Advection of plumes in mantle flow: implications for hotspot motion, mantle viscosity and plume distribution. *Geophys. J. Inter*., **132**, 412–34.

Stern, S. A. (1999). The Lunar atmosphere: history, status, current problems, and context. *Rev. Geophys*., **37**, 453–91.

Stevenson, D. J. (1987). Origin of the Moon – the collision hypothesis. *Ann. Rev. Earth Planet. Sci.*, **15**, 271–315.

Stevenson, D. J. (1990). Fluid dynamic of core formation. In *Origin of the Earth*, ed. H. E. Newsom and J. H. Jones. Oxford, UK: Oxford University Press, pp. 231–49.

Stoffler, D. and Ryder, G. (2001). Stratigraphy and isotope ages of lunar geologic units: chronological standard for the inner solar system. *Space Sci. Rev.*, **96**, 9–54.

Stolper, E. (1977). Experimental petrology of eucrite meteorites. *Geochim. Cosmochim. Acta*, **41**, 587–611.

Straub, S. M., Layne, G. D., Schmidt, A. and Langmuir, C. H. (2004). Volcanic glasses at the Izu arc volcanic front: new perspectives on fluid and sediment melt recycling in subduction zones. *Geochem. Geophys. Geosyst*., **5**, Q01007, doi:10.1029/2002GC000408.

Strom, K. M., Strom, S. E., Edwards, S., Cabrit, S. and Skrutskie, M. F. (1989). Circumstellar material associated with solar-type pre-main sequence starts: a possible constraint on the time scale for planet building. *Astrophys. J.*, **97**, 1451–70.

Strom, S. E. (1985). Protostars and planets: overview from an astronomical perspective. In *Protostars and Planets II*, eds. D. C. Black and M. S. Matthews. Tucson, AZ: University of Arizona Press, pp. 17–32.

Su, Y. J. (2002). *Mid-ocean Ridge Basalt Trace Element Systematics: Constraints from Database Management, ICPMS Analyses, Global Data Compilation, and Petrologic Modeling*. Columbia, USA: Columbia University, Graduate School of Arts and Sciences, pp. 457.

Sun, S.-S. and McDonough, W. F. (1989). Chemical and isotopic systematics of oceanic basalts: implications for mantle composition and processes. In *Magmatism in the Ocean Basins*, Vol. 42, eds. A. D. Saunders and M. J. Norry. Oxford: Geol. Soc. Spec. Publ., pp. 313–45.

Swindle, T. D. (1998). Implications of iodine–xenon studies for the timing and location of secondary alteration. *Meteorit. Planet. Sci.*, **33**, 1147–55.

Swindle, T. D. and Jones, J. H. (1997). The xenon isotopic composition of the primordial Martian atmosphere: contributions from solar and fission components. *J. Geophys. Res.*, **102** (E1), 1671–8.

Swindle, T. D. and Podosek, F. A. (1988). Iodine–xenon dating. In *Meteorites and the Early Solar System*, eds. J. F. Kerridge and M. S. Matthews. Tucson, AZ: University of Arizona Press, pp. 1127–46.

Swindle, T. D., Caffee, M. W., Hohenberg, C. M. and Lindstrom, M. M. (1983). I–Xe studies of individual Allende chondrules. *Geochim. Cosmochim. Acta*, **47**, 2157–77.

Swindle, T. D., Caffee, M. W. and Hohenberg, C. M. (1988). Iodine–xenon studies of Allende inclusions: eggs and the pink angel. *Geochim. Cosmochim. Acta*, **52**, 2215–27.

Swindle, T. D., Caffee, M. W., Hohenberg, C. M., Lindstrom, M. M. and Taylor, G. J. (1991). Iodine–xenon studies of petrographically and chemically characterized Chainpur chondrules. *Geochim. Cosmochim. Acta*, **55**, 861–80.

Swindle, T. D., Davis, A. M., Hohenberg, C. M., MacPherson, G. J. and Nyquist, L. E. (1996). Formation times of chondrules and Ca–Al-rich inclusions: constraints from short-lived radionuclides. In *Chondrules and the Protoplanetary Disk*, eds. R. H. Hewins, R. H. Jones and E. R. D. Scott. Cambridge, UK: Cambridge University Press, pp. 77–86.

Tachibana, S. and Huss, G. R. (2003). The initial abundances of ^{60}Fe in the Solar system. *Astrophys. J.*, **588**, L41–4.

Tackley, P. J. (2000). Mantle convection and plate tectonics: toward an integrated physical and chemical theory. *Science*, **288**, 2002–6.

Takahashi, E. and Kushiro, I. (1983). Melting of a dry peridotite at high pressures and basalt magma genesis. *Amer. Mineral.*, **68**, 859–79.

Takahashi, K. and Yokoi, K. (1987). Beta-decay rates of highly ionized heavy atoms in stellar interiors. *Atomic Data and Nuclear Data Tables*, **36**, 375–409.

Takaoka, N. (1972). An interpretation of general anomalies of xenon and the isotopic composition of primitive xenon. *Mass Spectrometry*, **20**, 287–302.

Taylor, G. J., Scott, E. R. D. and Keil, K. (1983). Cosmic setting for chondrule formation. In *Chondrules and their Origins*, ed. E. A. King. Houston, TX: Lunar Planet. Inst., pp. 262–78.

Taylor, G. J., Keil, K., McCoy, T. J., Haack, H. and Scott, E. R. D. (1993). Asteroid differentiation: pyroclastic volcanism to magma oceans. *Meteoritics*, **28**, 34–52.

Taylor, S. R. (2001). *Solar System Evolution: a New Perspective. An Inquiry into the Chemical Composition, Origin and Evolution of the Solar System*. Cambridge, UK: Cambridge University Press, pp. 460.

Taylor, S. R. and McLennan, S. M. (1985). *The Continental Crust: its Composition and Evolution*. Oxford, UK: Blackwell, pp. 312.

Taylor, S. R. and McLennan, S. M. (1988). The significance of the rare earths in geochemistry and cosmochemistry. In *Handbook on the Physics and Chemistry of Rare Earths*, Vol. 11, eds. K. A. Geschneidner and L. Eyring. Amsterdam: Elsevier, pp. 485–578.

Taylor, S. R. and McLennan, S. M. (1995). The geochemical evolution of the continental crust. *Rev. Geophys.*, **33**, 241–65.

Taylor, S. R., Taylor, G. J. and Taylor, L. A. (2006). The moon: a Taylor perspective. *Geochim. Cosmochim. Acta*, **70**, 5904–18.

Tera, F., Brown, L., Morris, J., Sacks, I. S., Klein, J. and Middleton, R. (1986). Sediment incorporation in island-arc magmas: inference from ^{10}Be. *Geochim. Cosmochim. Acta*, **50**, 535–50.

Thiemens, M. H. (1988). Heterogeneity in the nebula: evidence from stable isotopes. In *Meteorites and the Early Solar System*, eds. J. F. Kerridge and M. S. Matthews. Tucson, AZ: University of Arizona Press, pp. 899–923.

Thiemens, M. H. (1996). Mass-independent isotopic effects in chondrites: the role of chemical processes. In *Chondrules and the Protoplanetary Disk*, eds. R. Hewins, R. Jones and E. Scott. Cambridge, UK: Cambridge University Press, pp. 107–18.

Thielemann, F.-K., Hauser, P., Kolbe, E. *et al*. (2002). Heavy elements and age determinations. *Space Sci. Rev.*, **100**, 277–96.

Tilton, G. R. (1973). Isotopic lead ages of chondritic meteorites. *Earth Planet. Sci. Lett.*, **19**, 321–9.

Tilton, G. R. (1983). Evolution of the depleted mantle: the lead perspective. *Geochim. Cosmochim. Acta*, **47**, 1191–7.

Tilton, G. R. (1988). Age of the solar system. In *Meteorites and the Early Solar System*, eds. J. F. Kerridge and M. S. Matthews. Tucson, AZ: University of Arizona Press, pp. 259–75.

Timmes, F. X., Woosley, S. E. and Weaver, T. A. (1995). Galactic chemical evolution: hydrogen through zinc. *Astrophys. J. Suppl.*, **98**, 617–58.

Tolstikhin, I. and Hofmann, A. W. (2005). Early crust on top of the Earth's core. *Phys. Earth Planet. Inter.*, **148**, 109–30.

Tolstikhin, I. N. and Marty, B. (1998). The evolution of terrestrial volatiles: a view from helium, neon, argon and nitrogen isotope modelling. *Chem. Geol.*, **147**, 27–52.

Tolstikhin, I. N. and O'Nions, R. K. (1994). The earth's missing xenon: a combination of early degassing and of rare gas loss from the atmosphere. *Chem. Geol.*, **115**, 1–6.

Tolstikhin, I. N. and O'Nions, R. K. (1996). Some comments on isotopic structure of terrestrial xenon. *Chem. Geol.*, **129**, 185–99.

Tolstikhin, I. N., Kamensky, I. L., Marty, B. *et al*. (2002). Rare gas isotopes and parent trace elements in ultrabasic–alkaline–carbonatite complexes, Kola Peninsula: identification of lower mantle plume component. *Geochim. Cosmochim. Acta*, **66**, 881–901.

Tolstikhin, I. N., Kramers, J. D. and Hofmann, A. W. (2006). A chemical Earth model with whole mantle convection: the importance of a core–mantle boundary layer (D″) and its early formation. *Chem. Geol.*, **226**, 79–99.

Tonks, W. B. and Melosh, H. J. (1990). The physics of crystal settling and suspension in a turbulent magma ocean. In *Origin of the Earth*, eds. H. E. Newsom and J. H. Jones. Oxford, UK: Oxford University Press, pp. 151–74.

Toyoda, K., Nakamura, Y. and Masuda, A. (1990). Rare earth elements of Pacific pelagic sediments. *Geochim. Cosmochim. Acta*, **54**, 1093–103.

Travaglio, C., Burkert, A. and Galli, D. (2001a). Inhomogeneous chemical evolution of the galactic halo. *Nucl. Phys.*, **A688**, 396c-8.

Travaglio, C., Galli, D. and Burkert, A. (2001b). Inhomogeneous chemical evolution of the galactic halo: abundance of r-process elements. *Astrophys. J.*, **547**, 217–30.

Travaglio, C., Gallino, R., Busso, M. and Gratton, R. (2001c). Lead: asymptotic giant branch production and galactic chemical evolution. *Astrophys. J.*, **549**, 346–52.

Treiman, A. H. (1997). The parent magmas of the cumulate eucrites: a mass balance approach. *Meteorit. Planet. Sci.*, **32**, 217–30.

Tricca, A., Wasserburg, G. J., Porcelli, D. and Baskaran, M. (2001). The transport of U- and Th-series nuclides in a sandy unconfined aquifer. *Geochim. Cosmochim. Acta*, **65**, 1187–210.

Trieloff, M. and Kunz, J. (2005). Isotope systematics of noble gases in the Earth's mantle: possible sources of primordial isotopes and implications for mantle structure. *Phys. Earth Planet. Inter.*, **148**, 13–38.

Trubitsyn, V. P. (2000). Principles of the tectonics of floating continents. *Izvestiya Physics of the Solid Earth*, **36**, 708–41.

Truran, J. W., Cowan, J. J. and Fields, B. D. (2001). Halo star abundances and r-process synthesis. *Nucl. Phys.*, **A688**, 330c-9.

Turcotte, D. and Schubert, G. (1982). *Geodynamics*. New York: Wiley and Sons, pp. 450.

Turner, G., Harrison, T. M., Holland, G., Mojzsis, S. J. and Gilmour, J. (2004a). Extinct ^{244}Pu in ancient zircons. *Science*, **306**, 89–91.

Turner, S., Blundy, J., Wood, B. and Hole, M. (2000). Large ^{230}Th-excesses in basalts produced by partial melting of spinel lherzolite. *Chem. Geol.*, **162**, 127–36.

Turner, S., Bourdon, B. and Gill, J. (2003). Insights into magma genesis at convergent margins from U-series isotopes. In *Rev. Mineral. Geochem.: Uranium Series Geochemistry*, Vol. 52, ed. G. M. Henderson, C. Lundstrom and S. Turner. Washington DC: Amer. Mineral. Soc., pp. 255–315.

Turner, S., Black, S. and Berlo, K. (2004b). ^{210}Pb–^{226}Ra and ^{228}Ra–^{232}Th systematics in young arc lavas: implications for magma degassing and ascent rates. *Earth Planet. Sci. Lett.*, **227**, 1–16.

Twarog, B. A. (1980). The chemical evolution of the solar neighborhood. 1. A bias-free reduction technique and data sample. *Astrophys. J. Supplement Ser.*, **44**, 1–29.

Ulmer, P. (2001). Partial melting in the mantle wedge – the role of H_2O in the genesis of mantle-derived "arc-related" magmas. *Phys. Earth Planet. Inter.*, **127**, 215–32.

Urey, H. C. (1947). The thermodynamic properties of isotopic substances. *J. Chem. Soc. Lond.*, 562–81.

van Andel, T. (1992). Seafloor spreading and plate tectonics. In *Understanding the Earth*, eds. G. Brown, C. Hawkesworth and C. Wilson. Cambridge, UK: Cambridge University Press, pp. 167–85.

van Keken, P. E., Ballentine, C. J. and Porcelli, D. (2001). A dynamical investigation of the heat and helium imbalance. *Earth Planet. Sci. Lett.*, **188**, 421–34.

van Keken, P. E., Hauri, E. H. and Ballentine, C. J. (2002). Mantle mixing: the generation, preservation, and destruction of chemical heterogeneity. *Ann. Rev. Earth Planet. Sci.*, **30**, 493–525.

van Keken, P. E., Ballentine, C. J. and Hauri, E. H. (2003). Convective mixing in the earth's mantle. In *The Mantle and Core*, Vol. 2, ed. R. W. Carlson. Amsterdam: Elsevier-Pergamon, pp. 471–91.

Vannay, J.-C. and Sharp, Z. D. (1999). Bernhard Grasemann Himalayan inverted metamorphism constrained by oxygen isotope thermometry. *Contrib. Mineral. Petrol.*, **137**, 90–101.

Veizer, J. and Jansen, S. L. (1979). Basement and sedimentary recycling and continental evolution. *J. Geol.*, **87**, 341–70.

Veizer, J. and Jansen, S. L. (1985). Basement and sedimentary recycling – 2: time dimension to global tectonics. *J. Geol.*, **93**, 625–43.

Veizer, J. and Mackenzie, F. T. (2003). Evolution of sedimentary rocks. In *Sediments, Diagenesis and Sedimentary Rocks*, Vol. 7, ed. F. T. Mackenzie. Amsterdam: Elsevier-Pergamon, pp. 370–409.

Verchovsky, A. B., Sephton, M. A., Wright, I. P. and Pillinger, C. T. (2002). Separation of planetary noble gas carrier from bulk carbon in enstatite chondrites during stepped combustion. *Earth Planet. Sci. Lett.*, **199**, 243–55.

Vervoort, J. D. and Blichert-Toft, J. (1999). Evolution of the depleted mantle: Hf isotope evidence from juvenile rocks through time. *Geochim. Cosmochim. Acta*, **63**, 533–56.
Vervoort, J. D. and Patchett, P. J. (1996). Behavior of hafnium and neodymium isotopes in the crust: constraints from Precambrian crustally derived granites. *Geochim. Cosmochim. Acta*, **60**, 3717–33.
Vervoort, J. D., Patchett, P. J., Gehrels, G. E. and Nutman, A. P. (1996). Constraints on early Earth differentiation from hafnium and neodymium isotopes. *Nature*, **379**, 624–7.
Vervoort, J. D., Patchett, P. J., Blichert-Toft, J. and Albarède, F. (1999). Relationships between Lu–Hf and Sm–Nd isotopic systems in the global sedimentary system. *Earth Planet. Sci. Lett.*, **168**, 79–99.
Vervoort, J. D., Patchett, P. J., Albarède, F., Blichert-Toft, J., Rudnick, R. and Downes, H. (2000). Hf–Nd isotopic evolution of the lower crust. *Earth Planet. Sci. Lett.*, **181**, 115–29.
Vetrin, V. R., Kamensky, I. L., Bayanova, T. B. *et al*. (1999). Melanocratic enclaves and petrogenesis of alkaline granites of the Ponoy massif (Kola Peninsula). *Geochimiya*, **11**, 1178–90.
Vielzeuf, D., Clemens, J. D., Pin, C. and Moinet, E. (1990). Granites, granulites, and crustal differentiation. In *Granulites and Crustal Evolution*, eds. D. Vielzeuf and P. Vidal. Dordrecht: Kluwer, pp. 59–85.
Villa, I. M. and Renne, P. R. (1998). Decay constants in geochronology. *Episodes*, **20**, 1–2.
Vink, J. (2005). Gamma-ray observations of explosive nucleosynthesis products. *Adv. Space Res.*, **35**, 976–86.
Visona, D. and Lombardo, B. (2002). Two-mica and tourmaline leucogranites from the Everest–Makalu region (Nepal–Tibet). Himalayan leucogranite genesis by isobaric heating? *Lithos*, **62**, 125–50.
Vityazev, A. V., Pechernikova, G. V. and Saphronov, V. S. (1990). *Terrestrial Planets: Origin and Early Evolution*. Moscow: Nauka, pp. 296.
von Blanckenburg, F., O'Nions, R. K., Belshaw, N. S., Gibb, A. and Hein, J. R. (1996). Global distribution of beryllium isotopes in deep oceanic water as derived from Fe–Mn crusts. *Earth Planet. Sci. Lett.*, **141**, 213–26.
Vuong, M. H., Montmerle, T., Grosso, N., Feigelson, E. D., Verstraete, L. and Ozawa, H. (2003). Determination of the gas-to-dust ratio in nearby dense clouds using X-ray absorption measurements. *Astron. Astrophys.*, **408**, 581–99.
Walker, D., Longhi, J., Stopler, E. N., Grove, T. L. and Hays, J. F. (1975). Origin of titaniferous lunar basalts. *Geochim. Cosmochim. Acta*, **39**, 1219–35.
Wallerstein, G., Iben, I., Parker, P. *et al*. (1997). Synthesis of the elements in stars: forty years of progress. *Rev. Mod. Phys.*, **69**, 995–1084.
Wang, L., Howell, D. A., Hoflich, P. and Wheeler, J. C. (2001). Bipolar supernova explosions. *Astrophys. J.*, **550**, 1030–5.
Wänke, H., Dreibus, G. and Jagoutz, E. (1984). Mantle chemistry and accretion history of the Earth. In *Archaean Geochemistry*, ed. A. Kroner, G. N. Hanson and A. M. Goodwin. Berlin: Springer-Verlag, pp. 1–24.
Warren, P. H. (2003). The Moon. In *Meteorites, Comets, and Planets*, Vol. 1, eds. A. M. Davis. Amsterdam: Elsevier-Pergamon, pp. 559–99.
Warren, P. H. (2005). "New" lunar meteorites: implications for composition of the global lunar surface, lunar crust, and the bulk Moon. *Meteorit. Planet. Sci.*, **40**, 477–506.
Warren, P. H. and Kallemeyn, G. W. (1993). The ferroan-anorthositic suite, the extent of primordial lunar melting, and the bulk composition of the moon. *J. Geophys. Res.*, **98** (E3), 5445–55.

Wasserburg, G. J., Tera, F., Papanastassiou, D. A. and Huneke, J. C. (1977). Isotopic and chemical investigations on Angra dos Reis. *Earth Planet. Sci. Lett.*, **35**, 294–316.
Wasserburg, G. J., Busso, M., Gallino, R. and Raiteri, C. M. (1994). Asymptotic Giant Branch stars as a source of short-lived radioactive nuclei in the solar nebula. *Astrophys. J.*, **424**, 412–28.
Wasserburg, G. J., Boothroyd, A. I. and Sackmann, I. J. (1995a). Deep circulation in red giant stars: a solution to the carbon and oxygen isotope puzzles? *Astrophys. J.*, **447** (1), L37–L40.
Wasserburg, G. J., Gallino, R., Busso, M., Goswami, J. N. and Raiteri, C. M. (1995b). Injection of freshly synthesized ^{41}Ca in the early solar nebula by an Asymptotic Giant Branch Star. *Astrophys. J.*, **440**, L101–4.
Wasson, J. T. (1985). *Meteorites: Their Record of Early Solar-System History*. New York: Freeman and Co, pp. 274.
Wasson, J. T. (1996). Chondrule formation: energetic and length scales. In *Chondrules and the Protoplanetary Disk*, eds. R. H. Hewins, R. H. Jones and E. R. D. Scott. Cambridge, UK: Cambridge University Press, pp. 45–54.
Wasson, J. T. (1999). Trapped melt in IIIAB irons; solid/liquid elemental partitioning during the fractionation of the IIIAB magma. *Geochim. Cosmochim. Acta*, **63**, 2875–89.
Wasson, J. T. and Kallemeyn, G. W. (1988). Compositions of chondrites. *Phil. Trans. Roy. Soc. London*, **A325**, 535–44.
Weaver, B. L. and Tarney, J. (1984). Major and trace element composition of the continental lithosphere. *Phys. Chem. Earth*, **15**, 39–68.
Weber, M., Davis, J. P., Thomas, C., Kruger, F., Scherbaum, F., Schlittenhardt, J. and Kornig, M. (1996). The structure of the lowermost mantle as determined from using seismic arrays. In *Seismic Modelling of Earth Structure*, eds. E. Boschi, G. Ekstrom and A. Morelli, pp. 399–442.
Wedepohl, K. H. (1995). The composition of the continental crust. *Geochim. Cosmochim. Acta*, **59**, 1217–32.
Wegener, A. (1915). *Die Entstehung der Kontinente und Ozeane*.
Weidenschilling, S. J. (2000). Formation of planetesimals and accretion of the terrestrial planets. In *From Dust to Terrestrial Planets*, eds. W. Benz, R. Kallenbach and G. W. Lugmair. Dordrecht: Kluwer, pp. 295–310.
Weisberg, M. K. and Prinz, M. (1996). Agglomeratic chondrules, chondrule precursors, and incomplete melting. In *Chondrules and the Protoplanetary Disk*, eds. R. H. Hewins, R. H. Jones and E. R. D. Scott. Cambridge, UK: Cambridge University Press, pp. 119–28.
Wen, L. X., Silver, P., James, D. and Kuehnel, R. (2001). Seismic evidence for a thermo-chemical boundary at the base of the Earth's mantle. *Earth Planet. Sci. Lett.*, **189**, 141–53.
Wessel, P. and Lyons, S. (1997). Distribution of large Pacific seamounts from Geosat/ERS-1: implications for the history of intraplate volcanism. *J. Geophys. Res. – Solid Earth*, **102**, 22 459–75.
Wetherill, G. W. (1990). Formation of the earth. *Ann. Rev. Earth Planet. Sci.*, **18**, 205–56.
Wetherill, G. W. and Inaba, S. (2000). Planetary accumulation with continuous supply of planetesimals. In *From Dust to Terrestrial Planets*, eds. W. Benz, R. Kallenbach and G. W. Lugmair. Dordrecht: Kluwer, pp. 311–20.
Wetherill, G. W. and Stewart, G. R. (1993). Formation of planetary embryos: effects of fragmentation, low relative velocity, and independent variation of eccentricity and inclination. *Icarus*, **106**, 190–209.

Whalen, J. B., Currie, K. L. and Chappell, B. W. (1987). A-type granites: geochemical characteristics, discrimination and petrogenesis. *Contrib. Mineral. Petrol.*, **95**, 407–19.

Wiechert, U., Halliday, A. N., Lee, D.-C., Snyder, G. A., Taylor, L. A. and Rumble, D. (2001). Oxygen isotopes and the moon-forming giant impact. *Science*, **294**, 345–8.

Wieler, R. and Baur, H. (1994). Krypton and xenon from the solar wind and solar energetic particles in two lunar ilmenites of different antiquity. *Meteoritics*, **29**, 570–80.

Wieler, R., Anders, E., Baur, H., Lewis, R. S. and Signer, P. (1991). Noble gases in "phase Q": closed-system etching of an Allende residue. *Geochim. Cosmochim. Acta*, **55**, 1709–22.

Wieler, R., Humbert, F. and Marty, B. (1999). Evidence for a predominantly non-solar origin of nitrogen in the lunar regolith revealed by single grain analyses. *Earth Planet. Sci. Lett.*, **167**, 47–60.

Wiens, R. C., Huss, G. R. and Burnett, D. S. (1999). The solar oxygen-isotopic composition: predictions and implications for solar nebula processes. *Meteorit. Planet. Sci.*, **34**, 99–107.

Wilde, S. A., Valley, J. W., Peck, W. H. and Graham, C. M. (2001). Evidence from detrital zircons for the existence of continental crust and oceans on the Earth 4.4 Gyr ago. *Nature*, **409**, 175–8.

Wille, M., Kramers, J. D., Nägler, T. F. *et al*. (2007). Evidence for a gradual rise of oxygen between 2.6 and 2.5 Ga from Mo isotopes and Re-PGE signatures in shales. *Geochim. Cosmochim. Acta*, **71**, 2417–35.

Williams, Q. and Hemley, R. J. (2001). Hydrogen in the deep Earth. *Ann. Rev. Earth Planet. Sci.*, **29**, 365–418.

Williams, Q. and Knittle, E. (1997). Constraints on core chemistry from the pressure dependence of the bulk modulus. *Phys. Earth Planet. Inter.*, **100**, 49–59.

Wilson, T. L., Serabyn, E. and Henkel, C. (1986). The high-velocity CO outflow in Orion. *Astron. Astrophys*., **167**, L17–L20.

Wimmer-Schweingruber, R. F., Bochsler, P. and Kern, O. (1998). First determination of the silicon isotopic composition of the solar wind: WIND/MASS results. *J. Geophys. Res.*, **103** (A9), 20 621–30.

Wimmer-Schweingruber, R. F., Bochsler, P. and Wurz, P. (1999a). Isotopes in the solar wind: new results from ACE, SOHO and WIND. In *Solar Wind*, Vol. 9, eds. S. R. Habbal, R. Esser, J. V. Hollweg and P. A. Isenberg. New York: Amer. Inst. Phys., pp. 147–152.

Wimmer-Schweingruber, R. F., Boschsler, P., Gloeckler, G. *et al*. (1999b). On the bulk isotopic composition of magnesium and silicon during the May 1998 CME: ACE/SWIMS. *Geophys. Res. Lett.*, **26**, 165–8.

Winther, K. T. (1996). An experimentally based model for the origin of tonalitic and trondhjemitic melts. *Chem. Geol.*, **127**, 43–59.

Wisshak, K., Guber, K., Voss, F., Kappeler, F. and Reffo, G. (1993). Neutron-capture in Sm-148, Sm-150 – a sensitive probe of the s-process neutron density. *Phys. Rev.*, **48**, 1401–19.

Wolf, R. and Anders, E. (1980). Moon and Earth: compositional differences inferred from siderophiles, volatiles and alkalis in basalts. *Geochim. Cosmochim. Acta*, **44**, 2111–24.

Wood, B. E., Muller, H.-R., Zank, G. P. and Linsky, J. (2002). Measured mass-loss rates of solar-like stars as a function of age and activity. *Astrophys. J.*, **574**, 412–25.

Wood, B. J. and Halliday, A. N. (2005). Cooling of the Earth and core formation after the giant impact. *Nature*, **437**, 1345–8.
Wood, J. A. (1967). Olivine and pyroxene compositions in Type II carbonaceous chondrites. *Geochim. Cosmochim. Acta*, **31**, 2095–108.
Wood, J. A. (1981). The interstellar dust as a precursor of Ca, Al-rich inclusions in carbonaceous chondrites. *Earth Planet. Sci. Lett.*, **56**, 32–44.
Wood, J. A. (1985). Meteoritic constraints on processes in the solar nebula. In *Protostars and Planets II*, eds. D. C. Black and M. S. Matthews. Tucson, AZ: University of Arizona Press, pp. 687–702.
Wood, J. A. (1988). Chondritic meteorites and the solar nebula. *Ann. Rev. Earth Planet. Sci.*, **16**, 53–72.
Wood, J. A. (1996). Unresolved issues in the formation of chondrules and chondrites. In *Chondrules and the Protoplanetary Disk*, eds. R. H. Hewins, R. H. Jones and E. R. D. Scott. Cambridge, UK: Cambridge University Press, pp. 55–69.
Wood, J. A. (2000). Pressure and temperature profiles in the solar nebula. In *From Dust to Terrestrial Planets*, eds. W. Benz, R. Kallenbach and G. W. Lugmair. Dordrecht: Kluwer, pp. 87–96.
Wooden, D. H. (1997). Observational evidence for mixing and dust condensation on core-collapse supernovae. In *Astrophysical Implications of the Laboratory Study of Presolar Materials*, eds. T. I. Bernatowicz and E. Zinner. New York: Amer. Inst. Phys, pp. 317–76.
Woolf, V. M., Tomikin, J. and Lambert, D. L. (1995). The r-process element europium in galactic disc F and G dwarf stars. *Astrophys. J.*, **453**, 660–72.
Woosley, S. E. (1997). Neutron-rich nucleosynthesis in carbon deflagration supernovae. *Astrophys. J.*, **476**, 801–10.
Woosley, S. E. (2001). Models for type Ia supernovae. *Nucl. Phys.*, **A688**, 9c–16c.
Woosley, S. and Janka, T. (2005). The physics of core-collapse supernovae. *Nature (Physics)*, **1**, 147–54.
Woosley, S. E. and Weaver, T. A. (1995). The evolution and explosion of massive stars. II. Explosive hydrodynamics and nucleosynthesis. *Astrophys. J. Suppl.*, **101**, 181–235.
Woosley, S. E., Hartmann, D. H., Hofmann, R. D. and Haxton, W. C. (1990). The neutrino process. *Astrophys. J.*, **356**, 272–301.
Woosley, S. E., Heger, A. and Weaver, T. A. (2002). The evolution and explosion of massive stars. *Rev. Mod. Phys.*, **74**, 1015–72.
Workman, R. K. and Hart, S. R. (2005). Major and trace element composition of the depleted MORB mantle (DMM). *Earth Planet. Sci. Lett.*, **231**, 53–72.
Workman, R. K., Hart, S. R., Jackson, M. D. *et al*. (2004). Recycled metasomatized lithosphere as the origin of the Enriched Mantle II (EM2) end-member: evidence from the Samoan Volcanic Chain. *Geochem. Geophys. Geosyst*., **5**, Q04008, doi:10.1029/2003GC000623.
Yin, Q.-Z., Lee, C.-T. and Ott, U. (2006). Signatures of the s-process in presolar silicon carbide grains: barium through hafnium. *Astrophys. J.*, **647**, 676–84.
Yoder, H. S., Jr. and Tilley, C. E. (1962). Origin of basalt magmas: an experimental study of natural and synthetic rock systems. *J. Petrol.*, **3**, 342–532.
Yoneda, S. and Grossman, L. (1995). Condensation of CaO–MgO–Al_2O_3–SiO_2 liquids from cosmic gases. *Geochim. Cosmochim. Acta*, **59**, 3413–44.
York, D. (1967). The best isochron. *Earth Planet. Sci. Lett.*, **2**, 479–82.
Young, E. D. and Russell, S. S. (1998). Oxygen reservoirs in the early solar nebula inferred from an Allende CAI. *Science*, **282**, 452–5.

Young, E. D., Simon, J. I., Galy, A., Russell, S. S., Tonui, E. and Lovera, O. (2005). Supra-canonical ^{26}Al / ^{27}Al and the residence time of CAIs in the solar protoplanetary disk. *Science*, **308**, 223–7.

Yurimoto, H. and Kuramoto, K. (2004). Molecular cloud origin for the oxygen isotope heterogeneity in the Solar system. *Science*, **305**, 1763–6.

Yurimoto, H., Ito, M. and Nagasawa, H. (1998). Oxygen isotope exchange between refractory inclusion in Allende and solar nebula gas. *Science*, **282**, 1874–7.

Zack, T., Moraes, R. and Kronz, A. (2004). Temperature dependence of Zr in rutile: empirical calibration of a rutile thermometer. *Contrib. Mineral. Petrol.*, **148**, 471–88.

Zahnle, K. and Kasting, J. F. (1986). Mass fractionation during transonic escape and implications for loss of water from Mars and Venus. *Icarus*, **68**, 462–80.

Zaikowski, A. (1980). I–Xe dating of Allende inclusions: antiquity and fine structure. *Earth Planet. Sci. Lett.*, **47**, 211–22.

Zeng, L., Saleeby, J. B. and Asimow, P. (2005). Nd isotope disequilibrium during crustal anatexis: a record from the Goat Ranch migmatite complex, southern Sierra Nevada batholite, California. *Geology*, **33**, 53–6.

Zhang, Y., Huang, S., Schneider, D. *et al*. (1996). Pyroxene structures, cathodoluminescence and the thermal history of the enstatite chondrites. *Meteoritics*, **31**, 87–96.

Zhao, D. (2004). Global tomographic images of mantle plumes and subducting slabs: insight into deep Earth dynamics. *Phys. Earth Planet. Inter.*, **146**, 3–34.

Zharkov, V. N. (1983). *Internal Structure of Earth and Planets*. Moscow: Nauka, pp. 415.

Zindler, A. and Hart, S. (1986). Chemical geodynamics. *Ann. Rev. Earth Planet. Sci.*, **14**, 493–571.

Zinner, E. (1998). Stellar nucleosynthesis and the isotopic composition of presolar grains from primitive meteorites. *Ann. Rev. Earth Planet. Sci.*, **26**, 147–88.

Zinner, E. K. and Goepel, C. (1992). Evidence for ^{26}Al in feldspars from the H4 chondrite Ste. Marguerite. *Meteoritics*, **27**, 311–12.

Zinner, E., Nittler, L. R., Alexander, C. M. O. and Gallino, R. (2006). The study of radioisotopes in presolar dust grains. *New Astron. Rev.*, **50**, 574–7.

Zolensky, M. E., Weisberg, M. K., Buchanan, P. C. and Mittlefehldt, D. W. (1996). Mineralogy of carbonaceous chondrite clasts in HED achondrites and the Moon. *Meteorit. Planet. Sci.*, **31**, 518–37.

Zozulya, D. R., Bayanova, T. B. and Eby, G. N. (2005). Geology and age of the late Archean Keivy alkaline province, Northeastern Baltic Shield. *J. Geol.*, **113**, 601–8.

Glossary

Words in italics are to be found in a separate entry. For a description of rock types, see the list of meteorites, rocks and minerals.

ablation Removal of material by attrition, e.g. by passage through the *atmosphere*, where a major process is evaporation.

abundance:

- The abundance of element X in an object relative to a reference composition is defined as X_{OBJECT} / X_{REF}, where the concentrations X_{OBJECT} and X_{REF} are measured in g g^{-1} or in atomic ratios.
- The abundance of *volatile* element in an object relative to *involatile* element Y and to a reference composition is $(X/Y)_{\mathrm{OBJECT}}/(X/Y)_{\mathrm{REF}}$.
- The isotopic abundance in a sample relative to a reference composition is defined as $\varepsilon_X \equiv 10\,000 \times \{[(X/Y)_{\mathrm{SAM}}/(X/Y)_{\mathrm{REF}}] - 1\}$ or as $\delta_X \equiv 1000 \times \{[(X/Y)_{\mathrm{SAM}}/(X/Y)_{\mathrm{REF}}] - 1\}$, where X and Y are the concentrations of two different *isotopes* of the same element (the daughter and stable *isotopes* respectively in the case where the contribution of a radiogenic daughter isotope, e.g. $^{143}\mathrm{Nd}^*$, is small).
- The abundance relative to solar is written as $[X/Y] \equiv \log_{10}(X/Y) - \log_{10}(X/Y)_{\odot}$; here the ratios are atomic.
- The absolute number density for element X is $\log \varepsilon(X) \equiv \log(X/\mathrm{H}) + 12$.
- The metallicity is

$$ {}^{X}Z \equiv \log_{10}\left(\frac{\text{mass of element } X \text{ in a given object}}{\text{mass of H in the object}}\right) - \log_{10}\left(\frac{\text{mass of element } X \text{ in the Sun}}{\text{mass of H in the Sun}}\right), $$

  where X is an element heavier than He.
- The total metallicity of an object,

$$ \Sigma\,{}^{X}Z \equiv \log_{10}\left(\frac{\text{total mass of elements heavier than He in object}}{\text{mass of H in object}}\right) - \log_{10}\left(\frac{\text{total mass of such elements in the Sun}}{\text{mass of H in the Sun}}\right). $$

- The metallicity index for a single heavy element X is defined as $[X/\mathrm{H}] \equiv \log_{10}(X/\mathrm{H}) - \log_{10}(X/\mathrm{H})_{\odot}$, where X/H is a ratio of atomic concentrations, i.e. an element abundance as defined above.

accessory phase A *mineral* present in low *abundance* in rocks but which may contain a significant proportion of the incompatible trace-element inventory of the rock. Examples include monazite and zircon.

accretion disk A rotating disk of gas and *dust* falling into a newborn star.

accretion Growth by *assimilation* of material from the outside, e.g. the formation of planets and planetesimals by the accumulation of smaller objects in the primordial nebula.

accumulated minerals These are crystals in *lavas* that are in excess of the amounts that could crystallize from a melt in a closed system. Like *cumulates*, some cases of accumulated crystals may be impossible to detect but others stand out because they result in rock compositions different from all or most terrestrial melts.

achondrites *Meteorites* in which *chondrules* are not visible; they are formed from the complete melting or partial melting of the original chondritic material, which occurred owing to the *differentiation* of the parent body (planet or *asteroid*). Achondrites are found in several rare types: *evolved* or *differentiated* achondrites such as the HED *meteorites* (the howardites, eucrites and diogenites), presumably from the *asteroid* Vesta, *Angrites*, *Aubrites*, *SNC meteorites* and *primitive* achondrites.

activation energy The minimum quantity of energy needed to initiate a process such as a chemical reaction.

activity The dimensionless effective concentration, a. For a solute species i the activity is given by $a_i = \gamma_i m_i$, where m_i is the concentration in mol kg^{-1} and γ_i is the activity coefficient (in kg mol^{-1}), which takes account of interference by other ions and molecules in a real solution.

activity ratio The ratio of the products of the concentrations C and decay constants λ of two neighbouring radioactive isotopes i, j in a radioactive chain, $(\lambda_i{}^i C)/(\lambda_j{}^j C)$. If $\lambda_i{}^i C = \lambda_j{}^j C$ then the numbers of each isotope decaying per unit time are equal; this state is known as secular radioactive equilibrium.

adiabatic process A thermodynamic process in which a substance is expanded or compressed without exchanging heat with its surroundings.

adsorption The adherence of gas molecules to solid surfaces with which they are in contact.

aeolian processes Wind processes, from the Greek *aeolus*.

aerosol Particles of liquid or solid dispersed as a *suspension* in a gas.

agglutinate A *lithology* characteristic of planetary surfaces, consisting of regolith particles bonded together with impact-generated *glass*. Correspondingly agglutinates are glass-bonded rock, *mineral* and glass fragments, generally seen in planetary *regoliths*.

albedo The fraction of incident light that is reflected away from a surface.

ALL Abbreviation for the Allende *chondrite*; also the lowest initial $^{87}Sr/^{86}Sr$ ratio measured in a CAI in the Allende *carbonaceous chondrite*, $0.698\,77 \pm 0.000\,02$.

alkane One of a series of saturated open-chain organic compounds, i.e. containing no double or triple bonds.

alteration A change in mineralogy owing to chemical reactions between solids and fluids at subsolidus temperatures.

amphibolite facies The set of *metamorphic mineral* assemblages in which *mafic* rocks are composed of amphibole and plagioclase. The facies is typical of regional metamorphism at moderate to high pressures and temperatures (i.e. > 300 MPa, 450–700 °C).

amu Atomic mass unit, defined as one-twelfth of the mass of a ^{12}C atom; $1\ \text{amu} = 1.660\,53 \times 10^{-24}$ g.

angrites *Achondrite meteorites*, chiefly consisting of clinopyroxene, anorthitic plagioclase and olivine (with chemical formula $CaFeSiO_4$).

angular momentum The *angular momentum* of a system about a specified origin is the sum over all the particles in the system (or an integral over the different elements of the system if it is continuous) of the vector products of the radius vector joining each particle to the origin and the momentum of the particle.

aphelion That point in the orbit of a body, gravitationally bound to the Sun, at which the body is furthest from the Sun. The term is also used for non-heliocentric orbits.

aquifer A water-carrying rock formation below a planet's surface.

Archean–Proterozoic transition The time span of about 3.2 to 2.5 Gyr ago, which incorporates the major tectonic stabilization (cratonization) near or at the end of the Archean. The transition is generally short-lived on any given *craton* but is found at different times in different places. This term is to be distinguished from the Archean–Proterozoic boundary, which is commonly dated at 2.5 Gyr.

assimilation The incorporation of material originally present in the surrounding wall-rock into a magma. If the wall-rock is incorporated into the liquid, thermal energy is required to heat and melt the solid rock.

asteroids Mainly rocky metallic objects, 1–1000 km in size, that are orbiting the Sun, mostly in the asteroid main belt between the orbits of Mars and Jupiter; they consist of pristine solar system material and it is likely that these bodies never coalesced into a planet.

asthenosphere The part of the upper *mantle* beneath the *lithosphere* that deforms by plastic flow as a result of the high temperatures at this depth in the Earth.

asymptotic giant branch A phase in stellar evolution when helium or hydrogen is burning in the shells above the *core*, and the star again (after the RGB stage) expels its outer shells;

atmophile elements Those elements that tend to be present in planetary bodies as gases, e.g. the inert (noble, rare) gases and nitrogen.

atmosphere The mixture of gases and traces of *dust*, ices and droplets gravitationally bound to a planet. Within the first ≈ 90 km above the Earth's surface the composition is uniform (homosphere) except for the presence of some condensable and trace gases such as H_2O and O_3. In the *troposphere*, the lowest layer of the homosphere, atmospheric temperatures decrease with height but they rise again in the second layer, the stratosphere. The third layer is the mesosphere, where again very low temperatures prevail. Above about 95 km the atmosphere changes considerably and becomes the heterosphere: molecular diffusion dominates the transport of mass and energy and gases start to separate according to their molecular mass. Higher still, in the thermosphere, temperatures rise rapidly until at the highest part of the atmosphere, known as the exosphere, isothermal conditions under high temperatures are found (~ 1500 K at ~ 500 km). Light gases such as H and He now escape.

atomic mass number The total number A of protons Z and neutrons N in a nucleus, $A \equiv Z + N$.

atomic mass unit See *amu.*

aubrite An *evolved achondrite* of *igneous* origin, consisting primarily of enstatite.

average-carbonaceous-chondrite-Kr, -Xe (AVCC-Kr, -Xe) Krypton and xenon as found in *primitive (carbonaceous) chondrites*. These nuclides are dominated by the Q component.

baryon A nucleon (proton or neutron), or any elementary particle that can be transformed into a nucleon and some number of mesons and lighter particles.

basaltic achondrite best initial (BABI) ratio This refers to the value for the initial ratio of $^{86}Sr/^{87}Sr$ that characterizes *achondrites*, 0.698 98.

beta decay Radioactive decay taking place by emission of an electron or positron.

binding energy The measure of the strength of a nucleus. The measured mass of an isotope $M(A, Z)$ is always smaller than the sum of the masses of the constituent particles, which are protons + neutrons + electrons: the mass deficit is given by $[ZM_p + (A - Z)M_n + Zm_e] - M(A, Z) \equiv \Delta M > 0$. Here Z is the number of protons or electrons and M_p, M_e are their respective masses; A is the atomic mass number, the total number of *baryons* in the nucleus; $A - Z$ is the number of neutrons and M_n is the mass of the neutron. The energy $\Delta W = \Delta M\, c^2$ (c is the velocity of light in a vacuum) is termed the total binding energy ΔW, and the ratio $\varepsilon = \Delta W/A$ is the binding energy per nucleon, which is specific to each nuclide.

branching ratio The probability of realization of a given nuclear process among all possible ones; for example, the probability that ^{238}U will decay by *fission*, $B_{238} = \lambda_{fiss}/(\lambda_\alpha + \lambda_{fiss})$.

bulk composition The chemical composition of an object averaged over its whole volume.

calc-alkaline magmas These have, at high *mg*#, both high Na + K and high SiO_2 (i.e. high SiO_2 at low Fe/Mg); tholeiitic magmas have lower SiO_2 and Na + K for a given *mg*# than calc-alkaline magmas.

caldera A volcanic depression that is usually roughly circular or oval, caused by collapse and often found on the summit of a *volcano*.

carbon star A rather loosely defined category of red-giant stars whose spectra show strong bands of C, CN or other C compounds.

carbonaceous (C) chondrites Primitive – though complex – *meteorites* containing more than about 0.2 wt % carbon, including organic compounds and water-bearing *minerals* that are evidence for the inclusion of water not long after formation. Chemical and mineralogical differences are named for the type specimens Ivuna (CI), Mighei (CM), Vigarano (CV), Ornans (CO), Karoonda (CK) and Renazzo (CR). The petrologic grade designations of C chondrites indicate increasing *metamorphism* of the meteorite by water (grades 1 and 2) or by heat (grades 3 to 6). Most such chondrites are highly oxidized and of nearly solar composition except for the most *volatile elements*.

cataclysm, terminal cataclysm Hypothetical short episode of intense bombardment of the Moon, and possibly all terrestrial planets, about 3.9–4.0 Gyr ago.

cerium anomaly Enrichment (positive anomaly) or depletion (negative anomaly) of Ce compared with the level predicted from a smooth *chondrite*-normalized REE pattern.

chalcophile elements Metals of the centre and right-hand side of the periodic table (e.g. Cu, Zn, Sb, As, Pb, Sn, Cd, Hg, Ag); they occur chiefly in sulphide *minerals*.

Chandrasekhar limit The limiting mass for *white dwarf* stars. If the mass of a star exceeds this critical mass (1.44 $M_\odot$ for the expected mean molecular mass, 2), the load of the overlying layers will be so great that degeneracy pressure will be unable to support it and no configuration will be stable.

chassignite A very rare type of *achondrite* (only one known, Chassigny) consisting of olivine with minor amounts of pyroxene, plagioclase, chromite and sulphide.

chemical fractionation The redistribution of chemical elements among coexisting or originating phases or the redistribution by a specific transport process; see also *differentiation*.

chondrites A class of primitive *meteorites* containing *chondrules* within their primary *matrix*. They were formed shortly after the Sun's birth (4.570 Gyr ago); the subclasses are *carbonaceous*, *ordinary* and *enstatite* chondrites.

chondrules Small (0.1 to 1 mm) approximately spherical assemblages, characteristic of most *chondrites*, that existed independently prior to incorporation in the meteorite and show evidence for partial or complete melting.

clast An individual lithic unit, e.g. a *mineral* grain or rock fragment, produced by the disintegration of a larger rock unit; a rock fragment within a breccia.

closure The start of retention within a substance, e.g. of the stable products of radioactive decay within a *mineral* grain.

clouds, interstellar See *interstellar medium*.

CNO cycle H burning in a stellar *core* via reactions with C, N and O nuclei.

column density The number of atoms or molecules per cm^2 in a line of sight.

coma The spherical envelope of gas and *dust* surrounding the nucleus of an active comet, created when ambient heat causes the vaporization of comet material.

compatible element An element with equilibrium solid–melt (or solid–fluid) concentration ratio (*partition coefficient*) >1.

condensation Transformation from the gaseous to a solid or liquid phase. In the context of this book, it is generally taken to refer to the formation of solid grains from nebular gas.

continent–continent collision zone A special type of *convergent margin* where a continent on the subducting plate collides with another on the overriding plate.

convergent margin The zone where two tectonic plates converge and one is subducted beneath the other.

core The central portion of a *differentiated planet* chiefly consisting of Fe and Ni; also, the central region of a star.

core formation The process that gravitationally segregates metallic iron in the (partially) molten interior of a planet (planetesimal) to form a metallic *core*.

corona The greatly extended and very hot outermost region of a main-sequence star such as the Sun; the term is sometimes used for a similar region in a planetary *atmosphere*.

cosmic rays High-energy rays (up to 10^{20} eV) in a galaxy mainly consisting of protons (90%), heavier particles (mainly α-particles; 9%) and electrons (1%).

cosmogenic nuclide A nuclide produced by interaction with cosmic radiation.

Coulomb barrier The repulsive force between charged particles of the same sign that acts to prevent positively charged particles penetrating the nucleus.

crater A bowl-shaped depression with a raised rim, formed by a meteoroid impact (an *impact* or meteorite crater); not applied to *volcanic* features, in modern technical usage.

craton An area of *crust* that has remained stable for a very long period of time.

crust The outer layer of a terrestrial planet. On the Earth the continental crust ranges from 30 to 80 km in thickness and the oceanic *crust* from 6 to 20 km.

crystalline substance One constituted by small crystals that are distinguishable by conventional optical microscopy.

cumulate A rock formed by the partial crystallization of a melt, after which the remaining melt was removed. While some cumulates may be difficult to recognize, others are evident because the cumulate *mineral* assemblage has major- and/or trace-element contents distinct from all or most other terrestrial melts, easily understood as the result of crystal/melt partitioning.

daughter nuclide A nuclide produced by the decay of a radioactive parent. A daughter nuclide may be stable or radioactive.

decay constant The decay constant multiplied by the number of atoms of a radioactive nuclide equals the instantaneous decay rate. It is also equal to the natural logarithm of 2 divided by the *half-life*. The units are reciprocal time.

delamination A process by which dense segments of the lower *crust* (and *lithospheric mantle*) sink into the convecting *asthenosphere* as a result of their negative buoyancy.

density and surface density of the terrestrial feeding zone

- The **surface density** is $\sigma_p \approx (1/{}^{\Sigma X}Z_{SOS})\ \Sigma M_p/S$, where $S = \pi[r^2(\text{Mars}) - r^2(\text{Venus})]$, ΣM_p is the total mass of the *terrestrial planets*, r is the Sun to planet distance and ${}^{\Sigma X}Z_{SOS}$ is the total *metallicity* index; ${}^{\Sigma X}Z_{SOS} \sim 1/200$ for the terrestrial-planet feeding zone. Values for σ_p are as follows: $\sigma_p \approx 2.5 \times 10^3$ g cm^{-2} using Vityazev *et al.* (1990); $\sigma_p \approx 4.2 \times 10^3$ g cm^{-2} using Cameron (1995).
- The **density** is $\rho(H_2) \approx \sigma_p/h$, where h is the nebular thickness and is ~ 0.1 of the distance between Sun and Earth.

depletion factor The ratio of the presently observed concentration of given element or isotope in a reservoir (from which it is released) and its concentration in this reservoir at some fixed time ago.

diagenetic change A chemical and or physical change brought about in a sediment after it is buried.

differentiated meteorites These exhibit the type of *chemical fractionation* that one would expect to occur on a differentiated planet.

differentiated planet A planet that has separated into regions of different composition, for instance *core*, *mantle* and *crust*; heavier material sinks to the core and lighter materials rise toward the surface.

differentiation The process by which more than one type of *igneous* rock develops *in situ* from a common *magma*; also, the chemical separation of materials in a planetary body during melting, allowing heavier elements to sink towards the centre of the layered mass to form chemically distinct zones, e.g. *core*, *mantle* and *crust*.

diogenites *Igneous achondrites* from the mantle of the *asteroid* Vesta, composed of Mg-rich orthopyroxene and minor amounts of olivine and plagioclase.

dust Solid particles in the interstellar clouds (or planetary nebulae). In cold molecular clouds (including the presolar cloud) the *dust*/gas mass ratio is $\sim 1/100$.

Earth's accessible reservoirs (EARs) These are the MORB-source depleted mantle, the continental crust and the atmo-hydrosphere.

eclogite facies This term represents high-pressure and relatively low-temperature *metamorphic* parageneses with omphacitic clinopyroxene and pyrope-rich garnet.

ejecta Materials ejected either from a *crater* by the action of volcanism or a *meteoroid* impact or from a stellar object, such as a *supernova*, by shock waves.

elements, n-capture Heavy elements ($A > 60$) having more neutrons than protons.

endogenic process A process arising from the interior of the Earth (as opposed to an *exogenic process*).

endothermic reaction A reaction that consumes energy.

enstatite (E) chondrites Rare *chondrites* rich in enstatite; most of their iron is in the form of metal or sulphide, rather than oxides in *silicates*, implying that they originate from an oxygen-poor region of the *solar nebula*, possibly inside the present orbit of Mars; they are further classified by petrologic grades 3 to 6 and according to their Fe content (EH indicates approximately 30% Fe and EL about 25% Fe).

e-process An equilibrium process. A complex set of nucleosynthetic reactions in which the photodisintegration of previously synthesized nuclides leads to a population of

nuclides that approaches local statistical equilibrium. The e-process is believed to be largely responsible for the so-called iron peak and the enhanced abundances of strong α-nuclides (e.g. ^{24}Mg, ^{28}Si, ^{32}S, ^{36}Ar, ^{40}Ca).

erosion The removal of broken crustal rocks by water, ice or wind flow.

eucrites *Igneous achondrites* presumably representing the *crust* of the *asteroid* Vesta, primarily composed of Ca-poor pyroxene (pigeonite) and Ca-rich plagioclase (anorthite); additionally, they often contain *accessory minerals* such as silica, chromite, troilite and nickel–iron metal.

europium anomaly The Eu anomaly is expressed by $Eu/Eu^* = 2Eu_n/(Sm_nGd_n)^{0.5}$, where the asterisk indicates the normal abundance of Eu and the subscripted "n" indicates that the values are normalized to chondritic *meteorites*. Europium is the only rare earth element (REE) that can occur in the 2+ valence state under the oxygen-fugacity conditions found in the Earth. The Eu^{2+} ion is larger than its REE^{3+} neighbours and has a charge and radius similar to that of Sr. It therefore substitutes for Sr in feldspars, and the *fractionation* of feldspar will lead to an Eu anomaly.

eutectic The lowest temperature at which an alloy can be wholly or partly liquid. Crystallization under these conditions frequently leads to a petrologically distinctive texture.

evolved rock An intermediate or *felsic* igneous rock (or its metamorphosed equivalent) that is derived from a rock of a more *mafic* composition through the processes of *magmatic differentiation* or partial melting.

exhumation Exposure of the underlying *terrain* by the erosional removal of matter overlying it.

exogenic process A process arising from the surface of the Earth (as opposed to an *endogenic* process) or even originating externally.

exothermic reaction A reaction that liberates heat energy.

exotic noble-gas component For such noble gases the isotope compositions are very different from solar values. This noble-gas component is generally found in presolar grains and is probably a product of a single or a few nucleosynthetic events.

exposure age The time spent by given material in exposure to cosmic radiation. Nuclear reactions between the cosmic radiation and nuclides in the material produce new nuclides (or associated phenomena such as tracks), whose *abundances* can be used to estimate the exposure age.

extinct nuclides Radioactive nuclides with *half-lives* that are short compared with the age of the solar system, which were present when a meteorite or meteoritic component formed but which have now decayed below detection limits. Their one-time presence in the material is indicated by their decay products.

extrusion *Igneous* rocks erupted on the surface.

fall The observed arrival of a *meteorite* on Earth. Such meteorites are usually recovered soon after fall and are relatively free of terrestrial contamination and *weathering* effects.

felsic rock A rock composed mainly of light-coloured *minerals*.

fertile peridotite A peridotite not depleted in incompatible elements.

find The unobserved arrival of a *meteorite*, which was not seen to *fall* but which was found and recognized subsequently.

fission A decay process in which a nucleus fragments into two or more pieces of roughly equal mass. The process can be spontaneous or induced by particle bombardment.

fissure A crack extending far into a planet through which *magma* erupts.

fractional crystallization The crystallization of *minerals* from a *silicate* liquid (a magma) during cooling causes the liquid to change composition. The possible compositional variations that can occur through this process are governed by the thermodynamic state functions for the crystals and melt.

fractionation The separation of one phase, element or isotope from another.

galactic halo Spherical regions around spiral galaxies that contain dim stars and globular clusters. The radius of the halo surrounding the Milky Way extends some 50 kpc from the Galactic centre (Earth is at $\approx$ 28 kpc from the centre, in the Galactic disk).

gardening The reworking and overturning of a *regolith*, principally by micrometeoroid bombardment.

gas-retention age The age of a meteorite as calculated from the abundance of gaseous daughter products.

Gd_N/Yb_N The ratio of the chondrite-normalized concentrations (denoted by subscript N) of Gd and Yb.

giant impact The collision and possible merging of two planet-sized bodies during the late stage of planetary accretion. Probably the Moon was formed as a result of the giant collision of the proto-Earth and a Mars-sized impactor.

geobarometry Determination of the pressure at which an assemblage (of *mineral* pairs, minerals and a presumed gas or liquid of different phases of a given mineral) was formed.

glass A substance that is non-crystalline, fused from dissolved *silica* and *silicates*; glasses may also contain soda and lime.

graben An elongate depressed crustal unit, bounded by faults on its long sides.

granulite facies The set of *metamorphic mineral* assemblages in which *mafic* rocks are represented by diopside + hypersthene + plagioclase. The facies is typical of deep-seated regional metamorphism at temperatures above 650 °C and pressures greater than 600 MPa.

granulite terrain A large tract of land composed of rocks at the *granulite facies*.

H II region A region of ionized hydrogen in interstellar space. H II regions occur near stars with high luminosities and high surface temperatures. Ionized hydrogen, having no electrons, does not produce spectral lines; however, occasionally a free electron will be captured by a free proton and the resulting radiation can be studied optically. H II regions have lifetimes of only a few Myr.

half-life The length of time required for half the atoms in a given sample of a radioactive nuclide to decay; the notation for half-life in this book is τ.

heat-producing elements Those elements that generate heat as a result of their radioactive decay (e.g. K, Th and U).

Hertzsprung–Russell (HR) diagram In present usage, a plot of bolometric magnitude against effective temperature for a population of stars. Related plots are the colour–magnitude plot and the spectrum–magnitude plot (visual magnitude versus spectral type), the original form of the HR diagram.

high-field-strength elements Those with a high charge-to-ionic-radius ratio (Nb, Zr, Ti, V).

highlands The oldest *cratered* lunar surface areas, chemically distinct from the maria.

howardite Polymict brecciated *achondrite* consisting predominantly of lithic units similar to *eucrites* and *diogenites*, though more extreme compositions are also found.

HREEs The heavy rare earth elements, Gd through Lu.

hydrosphere The portion of Earth, or other planet, that is water, including liquid water, ice and water vapour on the surface, underground or in the *atmosphere*.

ices Constituents of cold molecular interstellar clouds and cold regions of planetary nebulae. Icy grains are mainly composed of frozen water and other volatile compounds, e.g. CO, CO_2 etc., including organic molecules. Sizes vary from a few molecules to $\sim$ 1 cm but are generally $\sim$ 1 μm. Ices are often seen as mantles on refractory grains. Chemical reactions on the surfaces of ice grains are important as they stimulate the formation of *molecular clouds*.

igneous rock Rock from the solidification of hot, molten, *magma* or *lava*.

impact erosion The loss of *volatiles*, especially atmospheric, during impact events.

impact melt Rock that melts during impact *crater* formation.

impact parameter The closest distance between the pre-impact trajectories of the centres of colliding bodies.

inclusions Aggregates of *mineral* grains, melts or fluids within solid host materials.

incompatible element An element that tends to be excluded from a crystal and concentrated into the *magmatic* liquid, commonly because its ionic radius is too large to fit comfortably into the crystal lattice.

interstellar medium (ISM) The material found between the stars, consisting of gas, *dust* (H mass fraction $\sim$ 70%, He $\sim$ 28%, the heavier elements O, C, N, Ne, S, Ar, Fe and others contributing all together $\sim$ 2%), mineral grains and cosmic rays. It comprises about 10% of the visible matter in the disk of our Galaxy (the Milky Way). The denser regions are also termed interstellar clouds.

intrusion A body of *igneous* rocks forced as *magma* into other rock formations underground.

ion–molecule reaction A reaction between an ionized atom or molecular fragment and a neutral atom or molecule. In the interior of interstellar molecular clouds, ions are initially produced by the interaction of galactic cosmic rays with neutral atoms or molecules.

ionosphere The region of charged particles in a planet's upper *atmosphere*; the Earth's ionosphere is at an altitude $\sim$ 40–400 km.

iron meteorites These represent only $\sim$ 5% of meteorite *falls*; some are thought to be pieces of the shattered *cores* of *differentiated asteroids*; the structure varies, depending upon the ratio of the two Ni–Fe alloys, kamacite ($\sim$ 27%–65% Ni) and taenite ($\leq$ 7.5% Ni).

iron–wustite (IW) buffer A reference buffer to which the oxygen fugacity of a system may be compared (wustite is FeO).

island arc An arc-like string of volcanic islands formed above zones of descending oceanic *crust* (above subduction zones).

isobaric cooling A pressure–temperature path followed by *metamorphic* rocks in which the temperature decreases while pressure remains at approximately the same high value.

isobars Atoms with an equal number of protons + neutrons in the nuclei, i.e. with the same atomic mass number, A.

isochron As used in this book it refers to a line of equal age for a sample suite when the concentration of a radiogenic *daughter nuclide* is plotted against the radioactive parent nuclide. The two nuclide concentrations are usually normalized to a non-radiogenic nuclide.

isomer One of a number of molecules that all have the same elemental composition but which differ from each other in structure.

isothermal decompression The pressure–temperature path followed by *metamorphic* rocks in which the pressure decreases while temperature remains at approximately the same high value.

isotopes Atoms with the same number of protons in the nuclei but different numbers of neutrons.

Jeans escape The escape of the fastest atoms in a Maxwell–Boltzmann distribution when their speed exceeds the escape velocity.

Kepler velocity The orbital velocity of a gravitationally bound object around the central massive object, i.e. the velocity that leads to a "centrifugal force" exactly balancing the gravitational attraction between the two objects.

KREEP A basaltic rock found on the Moon, characterized by its high content of K, the rare earth elements and P.

Kuiper Belt A flat region of space in the radial zone extending outwards from the orbit of Neptune (at 30 AU) to 50 AU, containing at least 70 000 objects with diameters larger than 100 km on low-eccentricity low-inclination orbits.

large-ion lithophile elements (LILEs) These *lithophile* elements comprise Rb, Ra, Ba, K and Ce. Although they are not, strictly speaking, LILEs sometimes Th and U are grouped with the LILEs when referring to elements that are highly incompatible.

latent heat of melting or latent heat of crystallization The heat of reaction required to accomplish the phase change from solid to liquid form.

lava The *magma* that flows onto the surface of a planet after erupting from a *volcano* or *fissure*. Such magmas solidify at the surface to *crystalline* or *glassy igneous* rocks, which are referred to as volcanic rocks.

light curve Brightness values plotted as a function of time.

light–dark The structure displayed by gas-rich regolith breccias in which light-coloured *clasts* are located in a dark *matrix*.

light year The distance travelled by light in a vacuum during one year, 9.46×10^{22} cm.

liquidus The line or surface in a phase diagram above which the system is completely liquid.

lithology The physical character of a rock.

lithophile One of the geochemical classes of elements. *Lithophile* elements are those that tend to concentrate in the *silicate* phase, e.g. Si, Mg, Ca, Al, Na, K and the rare earth elements.

lithosphere The portion of the Earth's *crust* and upper *mantle* (above the *asthenosphere*) that is rigid and deforms by brittle fracture as a result of its lower temperature.

lithospheric mantle That portion of the Earth's *mantle* that immediately underlies, and is coupled to, the *crust*.

lithostatic pressure The pressure due to the weight of overlying rock.

local interstellar cloud (LIC) The interstellar medium near the Sun, with a number density ≈ 0.5 cm^{-3}, a temperature ≈ 7000 K and a size of several parsecs. The Sun is expected to leave the LIC in about 10 000 years.

luminosity, bolometric The total output of stellar radiative energy.

Lyman lines Ultraviolet spectral lines due to H atoms.

mafic The term used to describe a *silicate mineral* whose cations are predominantly Mg and/or Fe. It is also used for rocks made up principally of such *minerals*.

magma Molten rock that consists of up to three components: liquid *silicate* melt, suspended *crystalline* solids and gas bubbles. When magma cools in the interior of the Earth, the resulting *igneous* rocks are referred to as intrusive or plutonic rocks.

magma ocean A hypothetical stage in the evolution of a planetary object during which virtually the entire surface of the object is covered with molten *lava*.

magmatic material Molten *silicate* material.

magnesium number The molar ratio $mg\# \equiv \mathrm{Mg}/(\mathrm{Mg} + \mathrm{Fe})$.

main sequence A stage of evolution in which stars spend the major part of their lifetimes. Main-sequence stars produce energy in their *cores* by hydrogen fusion. Their luminosity and surface temperatures are well correlated.

mantle The portion of the Earth's interior lying below the Mohorovičić discontinuity and above the outer *core*. It is divided into the upper mantle, which extends to a depth $\sim$ 400 km; the transition zone, which extends to $\sim$ 670 km; the lower mantle, which extends to the core–mantle transition zone at $\sim$ 2600 km; the region from the core–mantle transition zone down to the outer core boundary at 2900 km depth.

mantle wedge A region triangular in cross section underlying arc *crust* and overlying a subduction zone, extending to perhaps 400 km depth.

mare martian meteorites These are also called SNC meteorites; they include the three meteorite classes named after the location of the *fall* of a prominent member of each class: *shergottites*, *nakhlites*, *chassignites*. They are identified as originating from Mars because of their young ages, *basaltic* composition and inclusion of martian atmospheric gas.

mass-dependent fractionation A process that causes the proportions of *isotopes* or elements to change in a manner dependent on the differences in their mass. Thus the $^{18}O/^{16}O$ ratio changes twice as much, for a given physical or chemical process, as the $^{17}O/^{16}O$ ratio. Consequently, samples that were originally similar in their proportion of O isotopes are found along a line with slope 0.5 (the mass fractionation line) on a plot of $^{17}O/^{16}O$ against $^{18}O/^{16}O$ after they have experienced the usual chemical and physical processes.

mass-independent fractionation This can result from different processes, for example from quantum-mechanical symmetry effects in molecules. In reactions involving ozone, molecular symmetry kinetically favours the yield of $^{17}O^{16}O^{16}O$ and $^{18}O^{16}O^{16}O$ relative to $^{16}O^{16}O^{16}O$; therefore such reactions as $2O_3 \rightarrow 3O_2$ leave behind ^{16}O-depleted ozone O_3 and ^{16}O-enriched residual oxygen O_2.

matrix The fine-grained material that occupies the space in a rock such as a meteorite, between larger, well-characterized, components such as *chondrules*, *inclusions* etc.

mesosiderites A broad class of *stony-iron meteorites*, surface *regolith*, fragment mixture (breccia) of *mantle* rock and Ni–Fe alloy, with metal compositions that are much more uniform than *iron meteorites*; they are stirred up and fused by repeated impacts.

mesostasis Interstitial, generally fine-grained, material occupying the space between the larger *mineral* grains in an *igneous* rock; generally, therefore, the last material to solidify from a melt.

metallicity See *abundance*.

metamorphic rocks Rocks that have recrystallized in a solid state as a result of changes in temperature, pressure and chemical environment.

metamorphism The solid-state modification of a rock, e.g. recrystallization, caused by elevated temperatures (and possibly pressures).

meteorites Fragments of small interplanetary debris from *asteroids*, comets, Mars or the Moon, that survive atmospheric entry (at speeds of 15–70 km s^{-1}) and can be recovered on the ground; they are categorized as stony, iron or *stony-iron*.

mica Hydrous *silicates* of Al with various bases (K, Mg, Fe or Li).

mineral An inorganic substance of definite chemical composition and usually of definite crystal structure; some rocks consist of only one type of mineral such as quartz or feldspar; most rocks contain several minerals, however.

modal mineralogy The volumetric proportion of *minerals* in a rock.

model age A radiometric age determination based on parameters at least one of which is assumed rather than measured. (The assumed value is generally the initial concentration of the *daughter nuclide*.) Strictly, it might be argued that even *mineral isochrons* are model ages in that their interpretation rests upon assumptions such as common initial concentrations, but in most cases the quality of the *isochron* itself can be taken as an adequate test of those assumptions.

molecular cloud An interstellar cloud with a relatively high density and very low temperature, consisting of gas (roughly 75% molecular hydrogen, 21%–24% helium and a large variety of heavier molecules), *dust* and *mineral* grains. Our solar system formed out of a molecular cloud 4570 billion years ago

monoclinic A crystal system characterized by a single two-fold symmetry axis, a single symmetry plane or a combination of the two.

nakhlite A rare type of achondrite meteorite consisting of calcic pyroxene (augite) and olivine.

nebula

- **planetary nebula** An expanding envelope (typical expansion rate 30 to 50 km s^{-1}) of ionized gas surrounding a hot *white dwarf*. The envelope receives ultraviolet radiation from the central star and re-emits it as visible light by the process of fluorescence.
- **solar nebula** A disk of gas + *dust* around the nascent Sun present during solar accretion.

neon-B (helium-B, argon-B) A Ne (He, Ar) component, found in gas-rich *meteorites* (and most clearly identified for Ne), that is a mixture of solar-wind and fractionated Ne (He, Ar).

neon-E Presolar ^{22}Ne-rich Ne in *primitive meteorites*.

neutron star A star whose *core* is composed primarily of neutrons, as is expected to occur when the mean core density is in the range 10^{13}–10^{14} g cm^{-3} (which may be compared with a *white dwarf's* maximum density, $\sim 10^8$ g cm^{-3}). Under current theories pulsars are thought to be rotating magnetic neutron stars with diameters $\sim$ 10–15 km and with a magnetic field of about 10^{12} gauss.

nova A star that exhibits a sudden surge of energy, temporarily (over a period of a few days) increasing its luminosity by as much as 17 magnitudes or more (although magnitude changes of 12 to 14 are typical). Novae are old disk-population stars and are all in close binary systems, one component being a *main sequence* star filling its Roche lobe and the other a *white dwarf*. This eventually leads to a thermonuclear explosion of the *white dwarf* (a *supernova* Ia). Unlike *supernovae*, novae retain their stellar form and most of their substance after the outburst.

obliquity The tilt of a planet's axis from the perpendicular to the plane of the ecliptic.

Occam's razor An axiom enunciated by William of Ockham (?–1348) of which one translation is "It is vain to do with more what may be done with less." Briefly, "keep it simple."

onion-shell A hypothetical chondrite parent body in which petrographic types are arranged concentrically.

Oort cloud A spherical cloud of comets having semimajor axes $> 20\,000$ AU found by J. H. Oort in his empirical study of the orbits of long-period comets. Comets in this shell can be sufficiently perturbed by passing stars or giant molecular clouds that a fraction of them acquire orbits that take them within the orbits of Jupiter and Saturn.

ordinary chondrites (OC) These are the most common type of *meteorite fall* on Earth. They are further classified by their Fe content: H denotes an Fe content $\approx$ 27% by

weight, L corresponds to ≈ 23% Fe and LL means "low iron" or "low metal" (≈ 20% Fe); the numbers 3–7 following the H, L or LL classifications are petrographic grades indicating the degree of *chondrule alteration* by heating.

organic compounds These are carbon-containing compounds. Organic compounds can be formed by both biological and non-biological processes.

orogenic belt A linear or arc-like belt of crust that has been subjected to folding and deformation during a mountain-building event.

oxidation The process of adding O to, or removing H from, an element (or of increasing the element's valence, i.e. oxidation state).

oxygen fugacity A function expressing the molar free energy of O in a manner analogous to the way in which pressure measures the free energy of an ideal gas. In practice, oxygen fugacity is equivalent to the partial pressure of O.

paleothermometry The determination of the temperature at which processes have occurred. The method usually involves an elemental or isotopic distribution between *mineral* pairs, or temperature-dependent phase transformations, and the temperature obtained strictly refers to the temperature at which the system was last able to equilibrate.

pallasites A class of *stony-iron meteorites*; their metallic *matrix* contains large green olivine crystals; they were probably formed at the *core–mantle* boundaries of asteroids.

parent body The object on or in which a given *meteorite*, or class of meteorites, was located prior to ejection as a metre-sized object.

parent nuclide A radioactive nuclide, e.g. ^{238}U.

parsec (pc) A measure of distance used in astronomy. One parsec is the distance at which a 1 AU base line subtends an angle of 1 arcsecond; 1 pc = 3.26 *light years* = 3.08×10^{18} cm.

partition coefficient For trace element i the partition coefficient between two coexisting phases, 1 and 2, which are in contact long enough for diffusion to take place, so that equilibrium has been achieved, is the ratio $D_{i,2/1} \equiv C_{i,2}/C_{i,1}$, where $C_{i,1}$ and $C_{i,2}$ are the concentrations of i in the two phases. Generally D_i depends on pressure, temperature and the chemical compositions of the phases.

Pauli pressure In a degenerate star, where the electrons are roaming freely throughout the star, each electron must occupy a different energy level. If the star is small, the levels are far apart; consequently there are many high-energy electrons, which exert a pressure that may stabilize a dead star.

Pee Dee Belemnite (PDB) A fossil carbonate from the Cretaceous Pee Dee formation in South Carolina. The isotopic composition of its carbon is used as the international standard for comparing ^{13}C/^{12}C ratios.

pelitic rock A sedimentary rock composed of clay.

percentage mean deviation (pmd) A statistical term commonly used as a measure of how far the *silicate minerals* in a *chondrite* are from chemical equilibrium.

perihelion The point at which a body's orbital motion takes it closest to the Sun.

phase transition Transition of matter from one state with specific physical and chemical properties to another, e.g. the transition of a solid from one crystal structure to another.

phenocryst A relatively large, and therefore conspicuous, grain in a porphyritic rock.

photolysis Chemical decomposition brought about by the action of light.

photosphere The normally visible region of a main-sequence star such as the Sun. Most solar spectroscopic abundance data have been obtained for this region.

phyllosilicates Products of the hydrous alteration of olivine and pyroxene, i.e. saponite, serpentine and smectite clays; they also generally contain hydrated oxides and sulphides.

planetary gases The inventory of all trapped gases in *meteorites* not of solar composition; in general this inventory is dominated in Ar, Kr, Xe by the Q-gas component and in He and Ne by a component concentrated in presolar diamonds and identified by a specific isotopic composition of Xe having enhanced abundances of heavy and light isotopes, so-called HL-xenon.

planetesimals These are bodies 1–100 km in size that were formed in the early solar system by the *accretion* of *dust* (rock) and ice (if present) in the central plane of the *solar nebula*. Most planetesimals accreted to planets, but many, such as the *asteroids*, never combined to form large bodies.

plate tectonics *Activity* associated with the break-up of the *lithosphere* into moving pieces, or "plates".

plume A buoyant upwelling or downwelling of material whose buoyancy results from temperature contact with the surrounding material.

polymict Description of a breccia in which the *clasts* and/or *matrix* have differing compositions.

polymorph A *mineral* with the same composition as another, but with a different crystal structure; e.g. diamond and graphite are well-known carbon polymorphs.

porosity The percentage of the total rock or *soil* volume that consists of open spaces.

porphyritic A texture found in many *igneous* rocks, characterized by relatively large crystals, known as *phenocrysts*, set in a fine-grained or *glassy matrix*.

p-process The name of the hypothetical nucleosynthetic process thought to be responsible for the synthesis of the rare heavy proton-rich nuclei that are bypassed by the r- and s- processes. It is manifestly less efficient (and therefore rarer) than the s- or r-process because the protons must overcome the *Coulomb barrier*, and it may in fact work as a secondary process for the r- and s-process nuclei. It seems to involve primarily (p, γ) reactions at masses above cerium (where neutron separation energies are low). The p-process is assumed to occur in *supernova* envelopes at a temperature $\leq 10^9$ K and at densities $\leq 10^4$ g cm^{-3}

pressure units 1 hectopascal = 100 pascal = 0.001 bar = 10.2 kg m^{-1} s^{-2} $\approx$ 0.75 mm mercury $\approx$ 0.001 atm; 1 GPa = 10 kbar $\approx$ 31 km of Earth's depth; the terrestrial upper-mantle pressure gradient is 0.033 GPa km^{-1} (in the Moon it is 0.005 GPa km^{-1}).

primary magma A liquid produced by the partial melting of a source region and unmodified by any post-segregation process.

primitive fluids *Lavas*, melts and liquids with *mg*# > 60. Primitive *cumulates* have *mg*# ~ 85.

primitive meteorites These contain chemically unmodified or relatively unaltered material representative of the *solar nebula*; they are the opposite of *differentiated meteorites*.

primordial nucleosynthesis The process of formation of nuclei in the early Universe.

prograde reactions *Mineral* reactions occurring under increasing temperature and pressure conditions.

proto-star A star in the process of formation, which has not yet become hot enough in its *core* to initiate the process of nuclear fusion (which requires a temperature $\approx 10^7$ K) and so halt its gravitational collapse. It is luminous owing to the release of gravitational potential energy from the infall of nebula material from its *accretion disk*.

Q gases These comprise a major part of the "planetary" Ar, Kr and Xe; Ar-Q, Kr-Q, Xe-Q usually dominate the inventory of these gases in *primitive meteorites*. The Q gases show strong elemental *fractionation* in relation to solar.

quantum tunnelling Penetration by a particle into a potential energy region that is classically forbidden.

radioactive equilibrium (RE) A situation where the rate of production of a radioactive isotope is equal to the rate of its decay.

radiogenic nuclide A nuclide produced by the decay of a radioactive parent nuclide, e.g. $^{206}Pb^{*}$, which is produced by the decay of ^{238}U.

radiometric age The "absolute age" of an geologic event, feature, fossil or rock; it is determined by using natural radioactive "clocks", e.g. the radioactive decay of naturally occurring ^{40}K to stable ^{40}Ar with a *half-life* $\sim$1.3 Gyr.

radionuclide A nuclide that is unstable against radioactive decay.

ratio In Sm–Nd, Lu–Hf and some other isotopic systematics it is convenient to express a parent–daughter concentration ratio relative to its value in a reference reservoir, e.g. the chondritic reservoir; for example $f(\mathrm{Sm/Nd}) = [(\mathrm{Sm/Nd})/(\mathrm{Sm/Nd})_{\mathrm{CHUR}}] - 1$.

red giant A late-type high-luminosity star of very large radius that occupies the upper-right portion of the *HR diagram*. It has a surface temperature of $\approx$ 2000–3000 K and a diameter of 10–100 $R_{\odot}$. Red giants are post-main-sequence stars which have exhausted the H fuel in their *cores* and whose luminosity is supported by energy production in an H-burning shell. The red-giant phase corresponds to the establishment of a deep convective envelope.

reduction A process involving the addition of H or removal of O or a decrease in the valence of an element; the opposite of *oxidation*.

REEs The rare earth elements. The light REEs (LREEs) comprise lanthanum to samarium, the middle REEs comprise europium to dysprosium and the heavy REEs (HREEs) comprise holmium to lutetium. (The actinides, i.e. the elements from actinium to lawrencium, are also known as rare earth elements.)

refractory element Any chemical element that vaporizes only at high temperatures (e.g. Ca, Al, U, and the rare earth elements, such as Ce); the opposite of a *volatile* element.

regolith A layer of loose, pulverized, debris (unconsolidated rock, *minerals*, *glass* fragments) created on the surface of a planet or satellite by *impact gardening*; regoliths were measured in the lunar *mare lavas* to be $\sim$ 5–20 m deep, grading into coarser broken materials.

resonances Gravitational relationships, mostly with Jupiter, that force the orbits of *asteroids* to change, usually toward larger eccentricity; a mechanism that ejects a continuing flux of asteroids from the main belt onto orbits that cross those of Mars and/or the Earth and Moon, creating (along with comets) the *impact crater*ing on those planets.

restite The material remaining behind after the extraction of a partial melt.

retrograde *Mineral* reactions occurring under decreasing temperature and pressure conditions.

r-process The capture of neutrons on a very rapid time scale (i.e. one in which a nucleus can absorb neutrons in rapid succession, so that regions of great nuclear instability are bridged); this mechanism has been advanced to account for the existence of all elements heavier than Bi as well as the neutron-rich *isotopes* heavier than Fe. The essential feature of the r-process is the production and consumption of great numbers of neutrons in a very short time ($\leq$ 1 s). The presumed source for such a large flux of neutrons is a *supernova*, at the transition region between the nascent neutron star and the ejected material.

shergottite A rare type of meteorite, consisting of pyroxene (pigeonite) and maskelynite.

shock Momentary excursion to high pressures (and temperatures) caused by an impact or explosion.

shock wave (or shock front) A discontinuity in temperature and pressure propagating in a solid, liquid or gas with supersonic velocity, caused by an impact or explosion.

siderophile elements These elements have a high chemical affinity to Fe (e.g. Ni, Co, Au, As, Ge, Ga, Ir, Re, Os, Pt, Pd); they are found in the metal-rich interiors of chemically differentiated *asteroids*.

silicate A variety of *mineral* that contains Si, O and one or more metals.

SNC meteorites These include the three *meteorite* classes named after the location of the *fall* of a prominent member of each class: *shergottites*, *nakhlites*, *chassignites*; they have been identified as originating from Mars by their young ages, *basaltic* composition and inclusion of martian atmospheric gas (another martian meteorite is ALH 84001).

soil The upper layers of sediment.

solar flare A sudden outburst of energy on the solar photosphere.

solar nebula Gas and *dust* in the *accretion disk* of the young Sun, from which the Sun, planets and other bodies in our solar system were formed.

solar wind A supersonic flow of fully ionized plasma produced by the expansion of the solar *corona* into interplanetary space.

solid solution A substance in which two or more components, such as the atoms of two or more elements, are randomly mixed on such a fine scale that the resulting solid is homogeneous.

solidus The curved line in the phase diagram of a binary system separating a field of homogeneous *solid solution* from a field of two or more other phases.

spallogenic process A process produced by the violent partial disintegration of an atomic nucleus; in a meteoritic context, this is generally due to *cosmic-ray* bombardment.

s-process A process in which heavy stable neutron-rich nuclei are synthesized from iron-peak elements by the successive captures of free neutrons in a weak neutron flux, so that there is time for *beta decay* before another neutron is captured (cf. the *r-process*). This is a process of nucleosynthesis that is believed to take place in intershell regions during the *red-giant* phase of evolution of a star, at densities up to 10^5 g cm^{-3} and temperatures of about 3×10^8 K (neutron densities are $\leq 10^{10}$ cm^{-3}).

sputtering The expulsion of atoms or ions from a solid caused by the impact of energetic particles.

standards

- **mean ocean water (SMOW):** the reference standard for the measurement of O- and H-isotope compositions.
- **Belemnitella Americana** from PD (Cretaceous) formation (**PDB**): the reference standard for the measurement of C-isotope compositions.

Stokes' drag The viscous drag law stating that the force which retards a body moving through a fluid is directly proportional to the velocity, the radius of the body and the viscosity of the fluid. Stokes' drag applies when the Reynolds number is low and the mean free path of the fluid molecules is small compared with the body's size.

stony-iron meteorites These have both stone and metal fractions; the two main groups are *mesosiderites* and *pallasites*.

subduction-related magmatic arc (or, simply, **arc)** Chains of *volcanoes* on the overthrust plate parallel to, and $\sim$ 100–200 km horizontally away from, the surface expression of a subduction zone, together with coeval underlying plutonic rocks.

subsolar noble gases A noble-gas component with rather high Ar–Kr–Xe abundance ratios, intermediate between solar and typical-planetary values, and isotopic compositions similar to solar. Found in *enstatite chondrites* of higher petrographic type.

supernova (core-collapse SNe II) The explosive brightening of a star, in which the energy radiated increases by a factor $\sim 10^{10}$; it occurs when the star has burnt up all its available nuclear fuel and the *core* collapses catastrophically.

supracrustal rock A rock that forms at the Earth's surface.

suspension Fine particles of a given size are held in suspension in a stream of an appropriate density.

T Tauri stars Very young stars that are precursors to solar-mass stars; they are characterized by very intense emission, infrared excesses and irregular variability. The prototype for this class of stars is T Tau.

tectonics The fracturing and movement of large-scale rock masses in response to compressional, tensional or shear forces, causing faulting and folding (tectonics can create mountain ranges, rift zones, faults, fractured rock and folded rock masses).

terrain Area of a planet or moon with a distinctive geological character.

terrestrial feeding zone A flat ring in the solar nebula disk with inner and outer radii ≈ 130 and ≈ 180 million kilometres respectively. Most material from which the Earth was accreted came from this zone.

terrestrial planets Mercury, Venus, Earth and Mars.

terrigenous rock The product of the mechanical destruction of precursor bedrocks delivered to the sedimentation environment as debris or fragments.

textures These are characterized for *igneous* rocks on the basis of grain size and shape and *mineral* orientation and proportions: fine-grained (< 1 mm), medium-grained (1–5 mm), coarse-grained (5–30 mm) and pegmatitic (> 30 mm).

tidal stress The differential force per unit area acting on a planetary body due to the gravitational attraction of the Sun, a moon or another planet, resulting in periodic bulging.

troctolite *Igneous*, lunar *highland* rock composed of plagioclase and olivine.

troposphere The lowermost region of a planetary *atmosphere* where convection keeps the gas mixed and maintains a steady decrease of temperature with height. Most clouds are in the troposphere.

uncompressed density The density a planet would have if it were not compressed by its own gravity.

underplating The *intrusion* of magmas near the base of the *crust*.

ureilites Coarse-grained *primitive achondrites* that are made up of olivine and pyroxene, with graphite or diamond present in the areas between grains; they are of unresolved origin, but the diamond formation has been attributed to shock.

U-Xe (Xe only) A xenon component with a composition derived from multidimensional correlations in the stepwise release of bulk *carbonaceous chondrites*. This is perhaps the most primitive Xe in the solar system, but it has never been observed directly. Relative to U-Xe, solar-wind Xe shows overabundances of ^{134}Xe and ^{136}Xe but otherwise the compositions are identical.

Van der Waals force The relatively weak attraction force operative between neutral atoms and molecules.

vesicle A bubble-shaped cavity in a *mineral* or rock, generally produced by expansion of gas in a magma.

volatile element Any chemical element that vaporizes at relatively low temperatures (e.g. H_2O, CO_2, CO, CH_4, NH_3 and K-, Na-, Pb-compounds).

volcano A mountain formed from the eruption of *igneous* matter.

weathering The mechanical breakdown and chemical *alteration* of rocks and *minerals* during exposure to air, moisture, frost or organic matter.

white dwarf A star of high surface temperature (typically of order 3×10^4 K), low luminosity and high density (10^5 to 10^8 g cm^{-3}), with roughly the mass of the Sun (the average mass is about 0.7 $M_\odot$) and the radius of the Earth, that has exhausted most or all of its nuclear fuel; a white dwarf is believed to be a star in its final stage of evolution. The typical escape velocity from a white dwarf is 3000 km s^{-1}. Such stars have relatively low rotational velocities.

Widmanstatten Specific structure in *iron meteorites*, revealed by etching with a mild acid.

Wolf–Rayet star One of a class of very luminous, very hot stars (with surface temperatures as high as 5×10^4 K), whose spectra have broad emission lines (mainly He I and He II) that are presumed to originate from material continually ejected from the star at very high velocities (about 2000 km s^{-1}) by stellar winds. They may be the exposed helium *cores* of stars that were at one time on the H-burning *main sequence*. Some Wolf–Rayet spectra show predominantly emission lines from ions of carbon (WC stars); others show predominantly emission lines from the ions of nitrogen (WN stars).

Yield (Y_r) the number of daughter atoms produced by the decay of one atom of a parent radioactive element. For example, the *fission* of one atom of ^{238}U produces an average 0.0063 atoms of ^{136}Xe: $Y(^{136}\text{Xe})_{238} = 0.0063$; the α-decay of one atom of ^{238}U produces eight atoms of ^{4}He, $Y(^4\text{He})_{238} = 8$.

Sources for the Glossary: Black and Matthews (1985); Gary *et al*. (1973); Grove (2000); Hewins (1996); Kallenbach and Ott (2003); Kelemen *et al*. (2003); Kerridge and Matthews (1988); Ott (2002); Rudnick and Fountain (1995); Silk (1980); Stoffler and Ryder (2001); Taylor and McLennan (1995); Vityazev *et al*. (1990).

Abbreviations

Words in italics are explained in the Glossary

ADOR	Angra dos Reis *achondrite*, also the initial $^{87}Sr/^{86}Sr$ ratio in achondritic *meteorites*, $0.698\,83 \pm 0.000\,02$
AGB	*asymptotic giant branch* phase in stellar evolution
amu	*atomic mass unit*
ASI	alumina saturation index
atm	unit of pressure
ATM	*atmosphere* or *atmo-hydrosphere*
AU	astronomical unit, the mean distance of the Earth from the Sun, 1.5×10^{13} cm
AVCC	average *carbonaceous chondrite* reference composition
BABI	basaltic *achondrite* best initial ratio
BBN	Big Bang nucleosynthesis
BIF	banded-iron formation
BSE	bulk silicate Earth
C1	group of carbonaceous chondrites (CC)
CAI	calcium–aluminium-rich *inclusions*
CAR	continental arc granitic rocks
CCR	bulk continental crust
CHUR	chondritic uniform reservoir
CMB	core–mantle boundary
DDP	distinct deep solar-rare-gas-bearing reservoir, the core–mantle transition zone, also known as D″
DFSW	double-fractionated solar-wind Xe
DMM	depleted MORB-source mantle; in Section 27.2 the abbreviation is widened to "depleted mixed mantle"
EARs	Earth's accessible reservoir
ECR	radioactive equilibrium concentration ratio, *activity ratio*
EM I, EM II	enriched mantle domains, sources of OIB magmas
EPR	East Pacific Rise
FAS	ferroan anorthosite suite, rocks of the lunar crust (same as FAN)
FGS	fine-grain sediment
FRG	Finnish Rapakivi granite
FSW	fractionated *solar wind*

FUN	*fractionation* and unknown nuclear effects, specific features of some rare *inclusions* in *meteorites*
GCE	galactic chemical evolution
GIP	giant (Moon-forming) impact
GLOSS	global average subducted sediment
GPa	gigapascal (10^9 Pa)
Gyr	gigayear (10^9 yr)
HAS	high-alkali suite of the lunar crust
HED	*howardite, eucrite* and *diogenite achondrites*
HFSE	high-field-strength element
HIMU	high μ, $^{238}U/^{204}Pb$ ratio with reference to the present
HLG	Himalayan leucogranites
HMS	high-magnesium suite of the lunar crust
H–R	*Hertzsprung–Russell diagram*
HREEs	*heavy rare earth elements*
HSEs	highly siderophile elements
IAVs	island arc volcanics
IDP	interplanetary *dust* particle
ISM	*interstellar medium*
KAG	Kola alkaline granites
kappa	κ, $^{232}Th/^{238}U$ ratio with reference to the present
KREEP	lunar basalt highly enriched in K, *REE*s and P
LCC	lower continental crust
LILE	large-ion *lithophile* element
LIM	liquid metal
LIS	liquid silicate
LMB	lunar *mare* basalt
LMO	lunar *magma* ocean
LREEs	*light rare earth elements*, La through Sm
$M_\odot$	solar mass (1.989×10^{33}g)
$M_\oplus$	earth mass (5.976×10^{27}g)
MFZ	*mantle fractionation* zone
mg#	the molar ratio $Mg/(Mg + Fe^{2+})$, known as the magnesium number
MIF	mass independent *fractionation*
MOR	mid-ocean ridge
MORB	mid-ocean ridge basalt
MPa	10^6 pascals
Mpc	10^6 *parsecs*
mu	μ, $^{238}U/^{204}Pb$ ratio with reference to the present
Myr	10^6 years
NASC	North American shale composite
OIB	ocean-island basalt
PAAS	post-Archean average Australian shale
PAL	present-day atmospheric level (concentration)
PDB	Belemnitella Americana from PD formation; *standard* for C-isotope measurements
PNS	proto-neutron star
ppm	parts per million, generally by weight
PREMA	prevalent *mantle*
REEs	*rare earth elements*

RGB	*red giant branch* phase in stellar evolution
SFZ	*subduction fractionation* zone
SMOW	mean ocean water *standard* for O- and H-isotope measurements
SNC	*shergottite*, *nakhlite* and *chassignite achondrites*
SNe	*supernovae*
SOI	south of Isua gneisses (West Greenland)
SOS	solar system
SW	*solar wind*
TTG	tonalite, trondhjemite and granodiorite rocks
TW	terrawatt $= 10^{12}$ watts, unit used to express the global terrestrial heat flow
UOC	unequilibrated ordinary *chondrites*

Meteorites, rocks and minerals discussed or mentioned in the text

Meteorites : name (type) abbreviation

Abee (EH) Ab
Acapulco (Ach, achondrite) Aca (separates: f, feldspar, ph, phosphate)
Acfer 059 (CR), 111 (H3) Acf
Achondrites (Ach)
Allegan (H5) Aln
Allende (CV3) All
Alta Ameem (LL5) AlA
Angra dos Reis (Ach/angrite) AdoR
Arapahoe (L5) Are
Ausson (L5) Aus
Barwell (L6) Bar
Beaver Creek (H4) BeC
Bereba (Ach/eucrite) Ber or Be
Bishunpur (LL3) Bish
Bjurbole (LL4) Bjur
Bouvante (Ach/eucrite) Bouv
Bovedy (L3) Bov
Bruderheim (L6) Br
Caldera (Ach/eucrite) Cal
Canyon Diablo (IA) CD
Cape York (IIIAB) CaY
Carlton (IIICD) Car
Chainpur (LL3) Ch
Chervony Kut (Ach/eucrite) CK
Clovis (L3) Clo
Cold Bokkeveld (CM2) CoB
Colony (CO3) Col
Dayton (IIICD) Day
Deep Spring (ungrouped) DeS
Dhajala (H3) Dha
Efremovka (CV3) Ef
El Taco (IAB) ElT
Esquel (Pal) Es

Felix (CO3) Fe
Forest Vale (H4) FoV
Gibeon (IVA) Gib
Grosnaja (CV3) Gr
Guarena (H6) Gua
Guidder (LL5) Gu
Henbury (IIIAB) Hen
Homestead (L5) Hom
Ibitira (Ach/eucrite) Ib
Ikhrarene (L4) Ik
Indarch (EH4) In
Inman (L/LL3.3) Imn
Isna (CO3) Ia
Johnstown (Ach/diogenite) Jt
Jonzac (Ach/eucrite) Jon or Jo
Juvinas (Ach/eucrite) Juv
Kaba (CV3) Kab
Kapoeta (Ach/howardite) Kap
Karoonda (CK4) Kar
Kernouve (H6) Ker
Knyahinya (LL5) Kny
Krymka (LL3) Krym
Lance (CO3) La
Leoville (CV3) Leo
Lewis Cliff 86010 (Ach/angrite) Lew
Los Martinez (L6) LoM
Manych (LL3) Man
Marion (Iowa) (L6) Mar
Millbillillie (Ach/eucrite) Mil
Moama (Ach/eucrite) Moa
Modoc (L6) Mod
Mokoia (CV3) Mo
Moorabie (L3.6) Moor
Moore County (Ach/eucrite) MC
Mount Edith (IIIAB) MoE
Mundrabilla (IIICD) Mun
Murchison (CM2) Mu (m, magnetite)
Murray (CM2) Mur
Nadiabondi (H5) Nad
Nantan (IIICD) Nat
N'Goureyma (irons/ungrouped) NGo
Nogoya (CM2) Nog
Nuevo Laredo (Ach/eucrite) NL or NuL
Olivenza (LL5) Oli
Orgueil (C1) Or
Ornans (CO3) Orn
Pantar (H5) Pa
Parnallee (LL3) Par
Pasamonte (Ach/eucrite) Pas
Pena Blanca Spring (Ach/aubrite) PBS

Phum Sambo (H4) PhS
Pinon (ungrouped) Pin
Pomozdino (Ach/eucrite) Pom
Quinyambie (LL3) Qui
Ragland (L3.5)
Renazzo (CR2) Re
Richardton (H5) Rin or Ri
Saint Severin (LL6) StS (d, dark fraction; l, light fraction)
Semarkona (LL3) Sem
Serra de Mage (Ach/eucrite) SdM or SM
Shalka (Ach/diogenite) Sha
Shallowater (Ach/aubrite) Sh
Sioux County (Ach/eucrite) SC
Soko Banja (LL4) SoBa
St Marks (EH5) StM
Stannern (Ach/eucrite) Stan or Sta
Ste Marguerite (H4) StMg
Susuman (IIIAB)
Syromolotovo (IIIAB) Syr
Tieschitz (H/L) Tie
Tucson (irons/ungrouped) Tuc
Tuxtuac (LL5) Tux
Vigarano (CV3) Vi
Walters (L6) Wal
Y-791195 (Ach/eucrite) Y79

Rocks: name and type

alkaline granite	Granite with orthoclase/plagioclase ratio >2. Also corresponds to peralkaline chemistry with Al/(Na + K) < 1
amphibolite	Mafic rock consisting predominantly of amphibole and plagioclase
andesite	Volcanic rock containing 52% to 63% SiO_2 and with (Ca + Na) ≫ K, hence plagioclase bearing. Usually contains biotite and amphibole
anorthosite	Plutonic igneous rock composed almost entirely of plagioclase feldspar and balanced by pyroxene and olivine
authigenic r	Component of a sedimentary rock originated locally, during or after sedimentation, owing to diagenetic transformations
basalt	Fine-grained dark-coloured igneous rock; contains 48%–52% silica (SiO_2), chiefly composed of plagioclase, feldspar and pyroxene but also other minerals, e.g. olivine and ilmenite; the most common volcanic rock on the terrestrial planets
bedrock	Solid rock that underlies the soil and regolith or is exposed at the surface
breccia	Rock composed of fragments derived from previous generations of rocks cemented together
carbonatite	Magmatic rock, mainly primary carbonate, subdivided (depending on composition) into calcite, dolomite and siderite carbonatite

dacite	Volcanic rock similar to andesite but containing $> 63\%$ SiO_2, hence contains quartz
detrital	Sediments consisting of debris or fragments of precursor bedrocks
diorite	Speckled black and white, equigranular or porphyritic, rock; mainly plagioclase and hornblende, also may contain biotite and pyroxene
dunite	Coarse-grained igneous rock composed almost entirely of olivine
eclogite	Extremely high-grade metamorphic ultramafic rock containing garnet and clinopyroxene; high-pressure form of mid-ocean ridge basalts and picrite
gabbro	Coarse-grained igneous rock rich in olivine, pyroxene and plagioclase
gneiss	Metamorphic rocks, compositionally similar to granitoids
granite	Coarse-grained igneous rock containing orthoclase and plagioclase in about equal amounts, $> 20\%$ quartz and lesser amounts of mica and/or amphibole. Mean SiO_2 content is 72%
granitoids	Group name of the granite rocks from quartz diorite to leucogranite
granodiorite	Granitoid rock with orthoclase/plagioclase ratio < 0.5; otherwise similar to granite
granulite	Metamorphic rock composed of granular minerals of uniform size such as quartz, feldspar or pyroxene, formed at $\sim 800\,^{\circ}C$
harzburgite	Ultramafic rock, mainly composed of olivine and orthopyroxene
kimberlite	Group of ultramafic feldspar-free subvolcanic rocks, consisting of olivine, bronzite, green pyroxene, micas and carbonates with rare ilmenite, chromite, perovskite
komatiite	Ultramafic volcanic rock with $\sim 30\%$ MgO. Mainly limited to the Archean eon
lamprophyre	Melanocratic dyke rock with porphyritic texture, containing hornblende, pyroxene or biotite
lherzolite	Ultramafic rock composed of olivine, pyroxene, spinel, plagioclase
metapelite	Metamorphosed shale, fine-grained detrital sedimentary rock originally composed largely of consolidated clay, silt and mud
norite	A type of igneous rock containing plagioclase and in which the pyroxene is mainly orthorhombic rather than monoclinic
ophiolites	Rock complex that generally includes basic and ultrabasic deep-seated rocks (dunite, peridotite, pyroxenite, tonalite, gabbro), lavas (basaltic) and sedimentary rocks, i.e. ocean floor abducted onto continents
pelagic s	Sediments deposited in remote-from-continent sea or ocean environments
peridotite	Coarse-grained crystalline rock containing $> 40\%$ olivine accompanied by Cr-diopside, enstatite and an aluminous phase (either spinel or garnet, depending on pressure)
plutonic r	Coarse-grained intrusive igneous rock that cooled slowly at depth
pyroxenite	Igneous rock composed largely of pyroxene

rapakivi granite	Hornblende-biotite or biotite granite with large ovoids of potassium feldspar
schist	Metamorphic rock whose texture is defined by the prevalence of platy minerals: micas, chlorites, talc and hornblendes
sedimentary r	Products of the mechanical, chemical or biochemical destruction of precursor bedrocks under *PT* conditions close to those on the Earth's surface
tholeiitic basalt	Basalt with a normative composition including hypersthene
tonalite–trondhjemite–granodiorite r	Common suite of Na-rich felsic granitoids ("TTG"), abundant in Archean (> 2.5 Gyr) continental crust
trondhjemite	Plutonic rock composed of sodic plagioclase, quartz, biotite and little or no potassium feldspar
ultramafic	Igneous rock consisting predominantly of mafic silicate minerals
wiborgite	Rapakivi granite, in which ovoid grains of potassium feldspar are rimmed by oligoclase
xenolith	A rock that occurs as a fragment in another, unrelated, igneous rock (literally, a foreign rock fragment)

Minerals

albite	Sodium end-member of the plagioclase feldspar group, $Na(AlSi_3O_8)$
amphiboles	Group of ferromagnesian silicates, $(Ca, Na)_{2–3}(Mg, Fe, Al)_5[(Si, Al)Si_3O_{11}]_2[OH]_2$
anorthite	Calcium end-member of the plagioclase feldspar group, $Ca(Al_2Si_2O_8)$
apatite	Typical accessory mineral of igneous rocks, also the most abundant P-bearing mineral, $Ca_5[PO_4]_3(Fe, Cl, OH)$
biotite	Mica group mineral typical of igneous rocks, $K(Fe^{2+}, Mg)_3(AlSi_3O_{10})(OH, F)_2$
calcite	Typical mineral of chemical sediments (limestone), calcium carbonate, $CaCO_3$; also formed during the differentiation of alkaline magmas and as hydrothermal mineral
chromite	Brownish-black cubic mineral of the spinel group, typical of ultramafic (and rarely, mafic) rocks, $(Cr, Al)_2[(Fe, Mg)O_4]$
clay	Finely crystalline, hydrous silicates; weathering or hydrothermal alteration product of, e.g., feldspar, pyroxene or amphibole
clinopyroxene	Rock-forming silicate with the general formula $Ca(Mg,Fe)Si_2O_6$
coesite	High-pressure modification of quartz, SiO_2
diamond	High-pressure modification of elemental carbon. Occurs in mantle rocks; brought to the surface by kimberlite volcanism
diopside	Mineral of the pyroxene group, $CaMgSi_2O_6$; typical of igneous rocks but sometimes found in metamorphic rocks as well
enstatite	Mineral of the pyroxene group, $MgSiO_3$
epidote	Typical metasomatic and hydrothermal mineral, $Ca_2Al_2FeSi_3O_{12}(OH)$
fassaite	Mineral of the pyroxene group, $CaMgSi_2O_6$
feldspars	Abundant group of Al–Si bearing minerals. Mixed phases between end-members $KAlSi_3O_8$ (orthoclase), $NaAlSi_3O_8$ (albite) and $CaAl_2Si_2O_8$ (anorthite)
fluorite	Polygenic mineral, CaF_2

garnet	Mineral typical of high-*PT* metamorphic and metasomatic rocks, e.g. eclogites, $R_3^{2+}R_2^{3+}Si_3O_{12}$, where R^{2+} = Ca, Fe, Mg or Mn or R^{3+} = Al, Fe or Cr
graphite	Low-pressure modification of elemental carbon. Generally formed in the metamorphism of organic-rich sediments
grossular	Mineral of the Ca-garnet group, $Ca_3Al_2Si_3O_{12}$
hedenbergite	Mineral of the pyroxene group, $CaFeSi_2O_6$
hornblende	Dark-green to black mineral of the amphibole group
hypersthene	Mineral of the pyroxene group, typical orthopyroxene; a constituent of igneous ultramafic and mafic rocks, $(Mg, Fe)_2Si_2O_6$ (22%–30% $FeSiO_3$)
ice	Used by planetary scientists to refer to water, methane or ammonia occurring as solids in the outer solar system
illite	Low-temperature hydrous mica, $(K,H_2O)Al_2[(Al, Si)Si_3O_{10}](OH)_2$
ilmenite	Igneous mineral typical of igneous mafic rocks, e.g., basalts, $FeTiO_3$
jadeite	Mineral of the pyroxene group (cpx), $NaAlSi_2O_6$, typical of high-pressure metamorphic rocks
kaolinite	A clay, $Al_2Si_2O_5(OH)_4$, formed by hydrothermal alteration or weathering of aluminosilicates, especially feldspars
kyanite	High-*PT* metamorphic mineral, $Al_2[SiO_4]O$
labrador	Abundant member of plagioclase family, $NaAlSi_3O_8$ (50%–70% An)
lawsonite	Rare mineral belonging to melilite group and seen in metamorphic rocks, $CaAl_2Si_2O_7(OH)_2 \cdot H_2O$
magnetite	Magmatic (rarely hydrothermal) mineral, member of the spinel group, $FeFe_2O_4$
melilite	Mineral of metasomatic (less often, igneous) origin, $Ca_2(Al, Mg)(Si, Al)_2O_7$
monazite	Typical accessory mineral of crustal magmatic rocks, granites, syenites, pegmatites etc., $(Ce, La, Y, Th)[PO_4]$
muscovite	The most abundant mica, typical mineral of granitic and metamorphic rocks of the continental crust, $KAl_2[AlSi_3O_{10}](OH)_2$
nepheline	Typical mineral of igneous alkaline rocks, $Na[AlSiO_4]$ or $Na_2O \cdot Al_2O_3 \cdot 2SiO_2$
olivine	Rock-forming igneous silicate in the crust and mantle, $(Mg, Fe)_2SiO_4$
omphacite	Na-rich pyroxene, typical mineral of eclogites
orthopyroxene	Pyroxene-group igneous rock-forming silicate abundant in crustal and mantle mafic and ultramafic rocks, $R_2[Si_2O_6]$, where $R_2 = Mg_2$ in enstatite, R_2 = (Mg, Fe) in hypersthene and $R_2 = Fe_2$ in ferrosilite
perovskite	Mineral of igneous and metamorphic origin seen as an accessory in ultramafic and mafic alkaline rocks, $CaTiO_3$
phengite	Mica of muscovite group, typical of high-pressure metamorphic rocks. $(Na, K)(Fe, Mg)[(Al, Si)Si_3O_{10}](OH, F)_2$
phlogopite	Typical mineral of metamorphic rocks but also seen in ultramafic Mg-bearing rocks, $KMg_3[AlSi_3O_{10}](F, OH)_2$
phosphates	P-bearing minerals (almost 250 varieties, including apatite)
phyllosilicate	One of a family of silicate minerals (e.g., clay or micas) characterized by a structure that consists of sheets or layers, invariably hydrated
pigeonite	Monocline pyroxene, $(Mg, Fe, Ca)_2Si_2O_6$
plagioclase	Light-coloured feldspar ranging from $NaAlSi_3O_8$ to $CaAl_2Si_2O_8$; they include rocks composed of almost a single mineral, e.g., anorthosites
pyrope	Belongs to garnet group, $Mg_3Al_2Si_3O_{12}$; typical of ultramafic rocks

pyroxene	Group of ferromagnesian silicates with a single chain of silicon-oxygen tetrahedral (Fe, Mg, Ca)SiO_3; crystal structure monoclinic (clinopyroxene) or orthorhombic (orthopyroxene); common in basalts
quartz	Pure crystalline SiO_2
serpentine	Major rock-forming silicate formed by metamorphism and hydrothermal alteration of mafic minerals; $(Mg, Fe)_3Si_2O_5(OH)_4$
siderite	$FeCO_3$; named in 1845 from the Greek *sideros*, iron
silica	SiO_2 with other minerals. Crystalline: quartz, trydimite, coesite, stishovite, depending on *p* and *T*. Microcrystalline: Chalcedony. Amorphous: opal or glass
sillimanite	High-*PT* metamorphic mineral, Al_2SiO_5
sodalite	Typical mineral of alkaline volcanic rocks, often in association with nepheline, $Na_8[AlSiO_4]_6Cl_2$
spinel	Oxide mineral with general formula $M^{2+}M_2^{3+}O_4$, e.g. $MgAl_2O_4$
titanite	Accessory mineral of acid and alkaline igneous rocks, granites and nepheline syenites, $CaTi[SiO_4]O$
tridymite	SiO_2, with admixture of Al and Na
troilite	Pyrrohotite-group mineral, formed under reducing conditions, FeS (Fe, 63.53%; S, 36.47%)
whitlockite	P-bearing mineral, sometimes associated with apatite, $Ca_3[PO_4]_2$
xenotime	Accessory mineral of acid and alkaline rocks, also metamorphic rocks, $Y[PO_4]$
zircon	Accessory mineral in acid igneous rocks, granites, syenites etc., $ZrSiO_4$

Sources for the List of meteorites, minerals and rocks: Ashwal (1993); Betehtin (1951); Gary *et al*. (1973); Graham *et al*. (1985); Kelemen *et al*. (2003); Taylor and McLennan (1995).

Index

ablation 27, 259
accessory minerals 168, 338, 349, 356
accretion
  materials 151, 161, 205, 234, 259, 262, 264–6
  of meteorite parent bodies 27–32, 101, 143, 158, 189
  planetary 101, 199, 213, 218–26, 230, 236, 258
  prism
  rock 151
  stellar 54, 71, 76–8, 83, 102
achondrites, *see* meteorites
activity
  biological 364
  hydrothermal 143, 156, 192, 320, 374, 420
  igneous 164, 184, 293, 299, 300, 375
  magnetic 107
  ratio 313–14, 330, 340
adsorption 160, 364
age (methods) 118
  "absolute" 117
  isochron, radiometric 119, 120, 177
  isochron, stellar 81
  model 123, 277, 403
age (results)
  chondrite meteorite materials 120, 124–8, 152–8, 178, 185
  distribution function 96, 368–71, 428
  giant impact 240, 283
  lunar materials 258, 268, 278, 279
  metallicity relationships 85
  non-chondrite meteorite materials 178–85, 191–4
  presolar grains 89
  stars (lifetime of) 82, 95
  stellar clusters 82
  stellar nucleosynthesis 79–82, 91
  terrestrial materials and reservoirs 296, 348, 354–7, 391–4, 439
  universe 19, 44–50
age difference 79, 123
agglomeration 27, 104, 142–6, 205, 230
alteration 120, 127, 135, 155, 191, 355
angrites, *see* meteorites
angular momentum 102, 202, 211, 267
asteroid, *see also* meteorite
  belt 27, 33, 105, 135, 205, 215, 218, 230, 264
  cooling rate 82, 161, 168, 187, 189
atmosphere
  loss of 254, 258–61
  planetary 25, 144–49, 247, 251, 260, 266
  solar 33, 35, 251
  stellar 21, 30
  terrestrial 212–13, 250–66, 327, 387, 394, 418–26, 439
atom
  core 10, 12
  density, *see* density
  energy, *see* energy
  mass 10, 17, 42, 110
aubrites, *see* meteorites

baryon 19, 24, 45
  density, *see* density
  mass 19
  particles 50
baryonic matter 19, 44, 46, 50
beryllium isotopes 45, 92, 323, 327–31, 335–7
boron and B/Be ratio 15, 327–9, 337–9, 371
branching 9, 63–6, 118

carbon and C isotopes
  in early solar nebula (and in meteorites) 144, 151, 263
  in presolar grains 28, 30
  in terrestrial materials 363
  in stars 58–61, 67, 69, 76–8, 86–9
Chandrasekhar limit 59
chondrite 33, 130, 132, 136, 152–6, 192, 268, 429
  Ca–Al refractory inclusions in 40, 103, 108, 120, 124–33
  carbonaceous 27, 33, 135–46, 191, 264, 413, 437
  chondrules 33, 94, 132, 162, 192
  and Earth model 211, 217, 230, 231, 235, 440
  enstatite 135, 140, 163, 247, 265
  hydrous phases in 143
  matrix of 137–43, 147, 156–62, 191
  ordinary 135–44, 159, 161, 202, 265

chondrite (*cont.*)
parent body 27, 104, 129, 156, 190
presolar grains in 21, 27–31, 40, 42, 159
"terrestrial" 218, 230, 251, 413, 439
clast 163, 171, 186, 355, 405, 413
CNO cycle 56
collapse
of interstellar cloud 21, 40, 52, 54, 101–5
of stellar core 67, 68, 70–7, 87
of white dwarf 84
comet 32, 201, 266
condensation 21, 32, 42, 89, 91, 107, 119, 126, 132, 136, 230
convection 226–30
in stellar reservoirs 22, 57, 61, 67, 71, 76, 88
in terrestrial mantle 213, 216, 246, 248, 291, 298, 301, 389, 402, 432, 440
in Vesta and lunar magma oceans 188, 236, 282
core
asteroid 164–90, 242
core–mantle transition (D″) 113, 214, 245–8, 371, 382, 426, 440
lunar 269–70
mineral 108–13, 127, 132, 139, 151, 355
stellar 22, 54, 72, 76, 83, 87, 93, 147
terrestrial 202, 212, 214, 217, 231–42, 258, 382, 426, 432
cosmic rays 27, 93
Coulomb barrier 10, 22, 45, 56
cumulate 189, 284, 302, 326, 355, 372, 403, 433

decompression 237, 295, 300, 301, 317
decompression melting 319, 341, 379, 428
delamination 373, 379–81, 392, 403, 433
degassing 214, 243, 257, 260–1, 301–3, 398–402, 432–40
deformation 71, 285, 297, 377
density
baryonic 45, 51
of gas (including interstellar clouds) 53, 95, 98, 160
of lunar materials 269, 282, 285
of materials in the solar system 104, 151, 163, 187, 201–5
of nuclear matter 11, 77
of nucleosynthetic environments 45, 50
of particles (neutrons, protons, electrons, etc) 56, 59, 70
of stellar reservoirs (core, shell) 55, 71
surface 95, 209
of terrestrial materials 214, 235–6, 245–8, 296, 333, 344, 366
diagenesis 347, 365, 394
diapir 237, 285, 317, 340
differentiation (*see also* fractionation)
of lunar materials 267, 281, 286
of planetesimals, asteroids 164, 171, 181–90, 192
in solar nebulae 131
of terrestrial materials 225, 230, 236, 319, 339, 372, 379, 393, 426
diffusion 113, 126, 165, 236
thermal diffusion coefficient 301

ejecta 21, 75, 83, 87, 93, 96, 134, 151, 168, 246
elements (see also rare earth elements)
atmophile 213, 250–1, 261–4, 384
α-capture (nuclei, isotopes) 15, 76, 78, 134
n-capture 25, 39–42, 67, 72, 78, 88, 165
CNO 25, 86, 88, 97
compatible 166–75, 285, 305, 325, 340, 406
high-field-strength (HFSE) 324, 342, 383
incompatible 166–75, 187–90, 272–84, 305, 324, 340–2, 378, 384, 392
large-ion lithophile (LILE) 324, 326, 342, 368
light (fragile) 15, 37, 165
r-process 22, 72–5, 79, 83, 90, 96, 101, 270
s-process 22, 61, 84, 91, 97, 270
refractory (including involatile) 26, 32–42, 110, 134, 153, 171, 186, 215, 244, 269, 429
siderophile 140–2, 164–5, 173–9, 187–90, 231, 248, 269–70, 433
transitional 239
volatile 33–5, 106–8, 136–46, 156–62, 173–89, 205–6, 221–5, 263, 271, 336
energy
accretion (impact-released) 104, 107, 211, 214, 432
binding 11–18, 24, 37, 45, 56, 70, 78, 134
chemical 11
gravitational 53, 57, 70
interface 165
kinetic 53, 54, 77, 113, 116, 259
nuclear 11, 53, 55–8, 68, 77, 81
of radioactive decay 104, 298
shock 27, 78
equilibrium
chemical 110, 128, 133, 188, 231–7, 270, 272, 284, 332, 374
constant 333
isotopic 113–16, 144
hydrostatic 53
nuclear statistical 74
partitioning 154, 166, 187
proton–neutron 45
radioactive (secular) 311–13, 331, 340
erosion 335, 346, 364, 404, 421, 426
erosion law 370
eutectic 165, 236, 376
exposure time 62, 246
extrusion 347

facies
metamorphic 333–5, 365
sedimentary 360
faults 297, 319
fission, *see* nuclear fission
fissure 295, 301, 319
formation interval, *see* age difference
fractional crystallization 108, 133, 167, 186–8
fractionation
chemical 32–3, 110, 119, 164–8, 186, 213, 226, 250, 273, 329–32, 378, 410–14
mass-dependent isotope 113–16, 128, 142–6, 250–61

mass-independent isotope 117, 129, 423
volatility related 32, 173, 205

galaxy 19–23, 24, 31, 40, 44, 83–98, 134
glass 281, 302, 305
(gravitational)
acceleration 54
attraction 55, 104
capture 264
constant 53, 259
energy, see energy
field 226
forces 53, 58, 103, 211
instability 199, 247
interactions 208
segregation 202
gravity, effects of 165, 229, 236, 282

hafnium and related isotopic systematics 40, 92, 94, 277
^{182}Hf–^{182}W systematics 153, 182–3, 194, 240, 268
^{176}Lu–^{176}Hf systematics (extraterrestrial samples) 284, 285
^{176}Lu–^{176}Hf systematics (terrestrial samples) 226, 309, 372, 378, 383, 409–16, 426, 435
heat flow 293, 297, 366, 371, 440
helium (and He isotopes) 19, 42, 52
ash 57
burning 58, 61, 69, 76, 87
He/H ratios 44
primordial 25, 45
solar 147, 246, 429
in terrestrial materials 243, 384, 394–8, 406, 437
Hertzsprung–Russell (H-R) diagram 31, 54, 58, 81
highland 271, 286
hydrogen (and H isotopes) 15, 19, 24, 52
burning in stars 55–61, 67, 69, 88
H and D abundances
in interstellar clouds 42, 53
in meteorites 144, 265
in planets 236, 251, 259, 262
primordial 24, 44
hydrodynamic escape 212, 259–66
hydrosphere 236, 251, 262, 300, 382

ice 131, 146
impact
breccia 171, 190
crater 168, 212
erosion 260
giant 203, 210, 211, 214, 218, 228, 239, 270
parameter
inclusions
melt 302, 307, 315, 390, 425
mineral 338
refractory (Ca–Al-rich, CAI) see chondrite
interstellar medium 19, 71, 78, 83–97
clouds 19, 23, 42, 52–3, 82, 101, 106, 130, 151
dust (see also presolar grains in chondrites) 26, 42, 53, 97, 106
gas and dust/gas ratio 19, 95, 107
intrusion 282, 347, 354–5, 379
iron and Fe isotopes 17
banded formation 413
[Fe/H] ratio, *see also* metallicity 25, 60, 85, 97
isotopes 10, 62, 74, 77, 92, 164
meteorites, *see* meteorites, iron
peak elements 12, 37, 43, 52, 61, 70, 74–8, 84, 96
isobar 15–18, 38, 60, 72
isochron, *see* age (methods)
isotopes (*see also respective element*) 18

Jeans critical mass 53
Jeans escape 259–61

Kepler velocity 103
K–Rb–REE–P-enriched basalts (KREEP) 271–4

lava 295, 302, 329, 331, 341, 392
lead (and Pb isotopes)
abundances in meteorites 224
abundance in terrestrial materials 371
binding energy of 14, 17, 38
^{238}U–^{235}U–^{232}Th–Pb isotope systematics 119–20, 224, 269, 383–97, 406, 413
terrestrial paradoxes 387, 407, 433
light curve 49, 76
liquidus 165, 282
lithium and Li isotopes (*see also* elements, light) 10, 15, 92, 94, 349, 371, 394
lithosphere 228, 301
plates 291
subcontinental 298, 344, 379, 393
suboceanic 295, 299, 309, 319, 344, 392

magma (magmatism)
andesitic 324, 368
basaltic 347
lunar magma ocean 281–7
terrestrial magma ocean 213, 214, 225, 228, 246, 266
Vesta (asteroid) magma ocean 188–90
magnesium isotopes (and ^{26}Al–^{26}Mg isotope systematics) 42, 91, 125, 153, 192
magnesium number, *mg#* 239, 271, 282, 349, 356
main sequence star 31, 56–8, 69, 82, 105
mantle (asteroid) 165, 174, 186, 190
mantle (lunar) 269, 276, 277, 282, 285
mantle (terrestrial), *see also* lithosphere 202, 212, 214
ancient 225
asthenospheric 291
depleted 244, 383, 425
of grain (mineral) 110, 127, 130
primitive 221, 325, 397, 411
mantle wedge 324, 326–32, 338–43, 373–4, 379, 428
matrix (*see also* chondrites, matrix) 167, 236, 301
melts (melting) 107, 141, 164
batch 166, 167, 433
flash 139
flush 342, 374

melts (melting) (*cont.*)
fractional 166, 167, 171, 313–19, 340, 342, 376
metallic 165, 182
temperature of 108, 160, 165, 212, 338, 366
mesosiderites, *see* meteorites
mesostasis 139
metallicity 23, 24, 25, 60, 83, 95–7
metamorphism (*see also* facies) 297, 322, 332, 338
of meteorite parent bodies 27, 134, 142, 162
pressure of 332, 334, 338
prograde 332, 368
retrograde 332
temperature of 334–5, 366
meteorites (non-chondritic) 129, 191–4, 270
achondrite (differentiated, stony, aubrite, angrite) 163, 179, 186, 192
differentiated, from asteroid Vesta 164, 183, 187, 189, 206
diogenite 168–75, 184, 188–90
eucrite 168–73, 182, 188, 194, 234, 277
howardite 171
iron 163, 168, 175, 181–90, 224, 242
martian 251
stony-iron (mesosiderites, pallasites, etc.) 163, 186

nebula
planetary 91–3
solar 30, 35, 101, 113, 146, 156–62, 191–4
supernovae 78
neodymium and Sm–Nd isotopic systematics
s- and r-process abundances of 65, 270
^{146}Sm–^{142}Nd isotope systematics 226, 245, 270, 277, 413
^{147}Sm–^{143}Nd isotope systematics 244, 277, 309, 357, 378, 385–91, 409–11, 434
niobium anomaly 245, 325, 354, 374
nitrogen and N isotopes 15
in meteorites 144
in presolar grains 29, 77
in stellar atmospheres 58, 89
in terrestrial materials 251, 263
nuclear fission 10, 17, 118, 394
nuclear fusion (burning), *see* respective element
nucleosynthesis 11, 27, 40–3
in ancient stars 25
in Big Bang 24, 44, 94
ν-process 74
p-process 74
r-process 22, 68–78, 79, 83, 94
s-process 22, 26, 28, 52, 59–67

ordinary chondrites, *see* chondrite
organic matter 135, 144, 262, 363
oxygen and O isotopes
in early solar nebulae (and in meteorites) 133, 159
fugacity 166, 187, 218, 239, 330
in lunar and terrestrial materials 268, 334, 341
in presolar grains 28
in terrestrial atmosphere 423
mass-dependent isotope fractionation 114, 116, 128
mass-independent isotope fractionation 116, 128, 132
in stars (*see also* elements, – CNO) 58, 67, 69, 74, 76–8, 87–8

parent body, *see* chondrite
partition coefficient 165
metal–silicate 141, 187, 233–9, 271
mineral–melt 325, 342
mineral–mineral 334
solid-silicate–fluid 326
solid-silicate–liquid-silicate 167, 173, 284, 305, 334
pelagic sediments 328, 361, 392, 407
phase transition 113, 216, 228, 333
phenocryst 316
photolysis 422, 424
photosphere, *see* stars
phyllosilicates 139, 144
planetesimals, *see* asteroid
planets 19, 31
formation of 208–10
giant planets 33, 201, 264
terrestrial 32, 101, 134, 201–6, 217
plate tectonics 291, 298, 322, 374, 425
plume
in planets 212, 225, 246, 298–300, 317–20, 375, 388–98
in stars 76
potassium and K isotopes (including ^{41}Ca–^{41}K isotopic systematics) 9, 104, 124, 137, 173, 205, 213, 221, 318, 339, 365
porosity 317
PT conditions
in lunar and terrestrial reservoirs 211, 281, 332–40, 348, 366, 376
in meteorite parent bodies 164
in solar nebula 104, 133, 146, 166

Q gases 147, 246, 437

radioactive (nuclear) decay 10, 15, 18, 38, 68, 75, 79, 118, 162, 432
alpha 17, 384
beta 59, 61, 65, 72
chains 311
constant (rate) 63–6
double beta 15
e-capture 9
equation for
fission, *see* nuclear fission
radioactive (radiogenic) isotopes (nuclides), *see respective element*
rare earth elements (REEs) 63–65, 110–13
cerium anomaly 340, 361–4
europium (anomaly, abundance) 63, 79, 110–13, 189, 272, 281–7, 349–78
in lunar materials 272–87
in meteorites 133, 171, 189
in terrestrial materials 221, 244, 306–9, 319, 338, 349–68, 373, 378, 403, 426, 434

HREEs 309, 324, 342, 354, 373
LREEs 307, 324, 342, 357, 411
in presolar grains 63
reaction, chemical 116, 128, 143, 165, 364
condensation (gas–solid and gas–melt) 107
dehydration 144, 247, 300, 322, 326, 336, 339, 368, 374
endothermic 228
hydration 143, 247
solid-state 142, 162, 322, 332, 333, 377
reaction nuclear, *see* nucleosynthesis, nuclear fusion
red giant, see stars
regolith 147, 239, 246, 259, 268, 437
rocks 245
felsic 349–66
fertile 216, 221, 224, 230
igneous (magmatic) 114, 165, 277
mafic 354–9, 366, 372, 378
metamorphic 114, 143, 226
residual 216, 277, 295, 319, 337, 377
sedimentary (see also sedimentary facies) 297, 321, 328, 340, 365, 383, 392

shock wave
in planetary impacts 260
in solar nebula 159–62
in stellar evolution (explosion) 40, 53, 71
siderophile elements, *see* elements
silicon (Si isotopes) 217
fusion (burning) in stars 67, 68, 70, 73, 78
in presolar grains 29
in solar nebula (and meteorites) 117, 132, 142, 159
in terrestrial materials 235, 364
solar flare 92
solar nebula, *see* nebula
solar wind 25, 33, 104, 131, 147, 246
solidus 139, 165, 247, 301, 319, 340, 376
spallation 92, 327
spreading 294, 319
sputtering 260
stars (and stellar remnants) 19, 31, 77
asymptotic giant branch (AGB) 58, 61, 66, 89, 93
black hole 21, 59, 71, 83, 87
carbon 28, 89
formation of 52–5
luminosity of 49, 54–8, 71, 75
neutrino 71, 72
neutron 21, 59, 71, 78, 83
red giant branch (RGB) 58, 69, 88, 97
shells 22, 57–8, 61, 69, 72, 83, 89
stellar core, *see* core
supernovae 19, 30, 68, 87
Ia (SNe Ia) 49, 68, 76–8, 84, 96
II (SNe II) 68–71, 78, 85, 96, 97
photosphere (*see also* atmosphere) 33, 76
T Tauri 103, 104
ultra-metal-poor 87
white dwarf 21, 59, 68, 76–8, 84, 95
Stokes's law 229
stony-iron meteorites, *see* meteorites
strontium isotopes (and ^{87}Rb–^{87}Sr isotopic systematics) 35, 178
in lunar materials 269
in meteorites 178
in terrestrial materials 223, 328, 338, 349, 377, 383–97, 404, 418
subduction 248, 296, 299, 321–30, 335, 354, 373, 375, 378, 391
sulphur isotopes 117, 422
supernova Ia, II, *see* stars

terrain
Archaean 357, 416
metamorphic 366, 377
terrestrial planets, *see* planets
terrigenous sediments 321, 360, 376, 392
texture 33, 108, 139, 354
thermal diffusion coefficient 301
thermobarometry, *see PT* conditions
thorium
abundances in terrestrial reservoirs and rocks 221, 224, 309, 314, 326, 338, 368, 383, 406
as cosmochronometer 79–80
in lunar rocks 274, 285
short-life isotopes 311–15, 329, 340
U–Th–Pb isotope systematics, *see* lead
tidal motions 202

underplating 335, 348, 375
uranium (isotopes)
abundances in terrestrial reservoirs and rocks 205, 221, 257, 298, 314, 326, 368, 383
as cosmochronometer 79–80
in lunar rocks 285
short-lived isotopes of
U-Th-Pb isotope systematics, see lead

vaporization 27, 212, 230, 271
volcano 296, 328, 393

weathering 27, 360, 364, 378, 384, 394, 425
white dwarf, *see* stars
Widmanstatten structure 163, 187

Xe isotopes 63, 243
in presolar grains 71
in terrestrial and martian atmospheres 213, 253–8, 259, 260
radiogenic (^{129}I–^{244}Pu–^{238}U–Xe isotope systematics), 155, 185, 195, 399–403, 437
U–Xe 254
xenolith 108, 139, 216, 347, 357, 366, 403

yield 11, 28